Field Oriented Control of Single and Cascaded Doubly-Fed Induction Machines

Bernhard Hopfensperger

A Thesis Submitted for the Degree of
Doctor of Philosophy

Department of Electrical and Electronic Engineering
University of Newcastle upon Tyne
1998

Gewidmet
meinen Eltern
meiner Schwester mit Ihrer Familie
und meiner Freundin Bettina

Abstract

A single doubly-fed induction machine (SDFM) is a wound rotor induction machine with the stator connected to a supply network and the rotor fed by a bi-directional converter. A cascaded doubly-fed induction machine (CDFM) is a connection of two wound rotor induction machines with the rotors connected electrically and mechanically thus avoiding brushes. One stator is connected to the supply network and the other is fed by a bi-directional converter. Both schemes, the SDFM and the CDFM, have in common that the VA-rating of the power converter is reduced compared to a singly-fed system. This thesis presents investigations of the field oriented control for the SDFM and the CDFM.

After reviewing and categorising doubly-fed machines a thorough steady state analysis and stator flux oriented control treatment of the SDFM is presented. Although the steady state analysis and the field oriented control of a SDFM is well established it is necessary that this is included as foundation for the CDFM control behaviour and for the sensorless control investigations.

Steady state analysis of the CDFM highlights similarities to the SDFM. Two different field oriented control schemes are applied to the CDFM. A previously developed combined flux oriented scheme is modified to be applicable to a CDFM consisting of any machine combination. Furthermore, the scheme is simplified by removing a mathematical control extension in the q-axis, which has a stabilising effect on the control performance.
Justified by steady state analysis the stator flux oriented control structure initially developed for the SDFM is applied to the CDFM.

Two variations of a position sensorless scheme taking advantage of the proportionalities between stator and rotor quantities are applied to the SDFM. Differentiating the estimated position angle allows the schemes to be extended for speed control purposes.
The performance of the sensorless field oriented control methods are also investigated on the CDFM.

Harmonic analysis of the SDFM / CDFM system establishes harmonic sources and harmonic current propagation through the system. A theoretical harmonic current prediction process incorporating simulation and steady state modeling delivers good results.

All theoretical investigations are confirmed by experimental results. The experimental real-time controlled drive system consists of two 2.25 kW wound rotor induction machines, a bi-directional IGBT converter and the control hardware comprises two 80C167 microcontrollers.

Acknowledgments

Foremost, I want to thank my supervisor Dr. Dave Atkinson for giving me the opportunity to carry out such interesting research work. His help and support in every aspect of the project is very much appreciated.
I also want to thank other members of our research group, Alan, Barrie, John, Mark and Paul for advice.

Thanks goes to Tony Lakin and his workforce at Microtech Ltd. for coming up with the cascaded machine idea (although not entirely new), for hardware support and initial programming assistance.
Furthermore, I want to thank Dr. Ralph Kennel and Rupert Weber from Robert BOSCH GmbH, Erbach, for assistance and hardware donation.

I want to thank the Department of Electrical and Electronic Engineering for the received financial support.

I want to thank all my friends who shared some time with me on their journey through academic life in the U.G lab namely Andy, Adil, Alun, Anthony, Bayram, Brian, Chris M., Chris F., Christian, Gavin, Hassan, Hossein, Howard, Ibrahim, Jawad, Jim H., Jim K., Ken, Mohammed, Øystein, Pete, Phil, Roger, Steve, Simon, Sidik and Volker.

Thanks goes to the administrative and technical staff of the Department for their always quick and thorough support and for the special social environment in the Department.

I want to thank my house and flat mates during the time in Newcastle for their friendship, namely Chris, Simon, Yannis and Vasilis, but a special thanks goes to Becky for doing a considerable amount of cooking.

Table of Contents

List of Abbreviations and Symbols

Abbreviations

SDFM	single doubly-fed induction machine
CDFM	cascaded doubly-fed induction machine
SF-CDFM	single frame cascaded doubly-fed induction machine
BDFM	brushless doubly-fed induction machine
DFRM	doubly-fed reluctance machine
FFT	fast fourier transformation
MRAC	model reference adaptive control
VSCF	variable-speed constant-frequency
d.c., DC	direct current
a.c.	alternating current
ADC	analogue-digital conversion (card)
DAC	digital-analogue conversion (card)
µC	microcontroller
DSP	digital signal processor
EPROM	electrically programmable read only memory
RAM	random access memory
PWM	pulse width modulation
PI	proportional-integral (controller)
GTO	gate turn-off thyristor
IGBT	insulated gate bipolar transistor

Symbols

Superscripts (for reference frames):

a	stator of SDFM, side 1 of CDFM (stationary) reference frame
b	rotor of SDFM, side 2 of CDFM reference frame
c	side 3 of CDFM reference frame
d	side 4 of CDFM reference frame
e	excitation reference frame for orientation
e+	reference frame attached to the stator voltage of the SDFM or the side1 voltage of the CDFM
g	general reference frame

Subscripts:

1	stator of SDFM or side 1 of CDFM quantity
2	rotor of SDFM or side 2 of CDFM quantity
3	side 3 of CDFM quantity
4	side 4 of CDFM quantity
σ	leakage quantity

mag, μ	magnetising quantity
R	combined rotor quantity (side 2 and side 3 of CDFM)
A	machine A of CDFM quantity
B	machine B of CDFM quantity
AB	combined CDFM quantity
d	d-axis quantity
q	q-axis quantity
r	rotor quantity
m	mechanical quantity
a, b, c	electrical phases
ν	harmonic quantity
y	line-side inverter quantity
x	variac quantity
s	supply network quantity

Labeling of Quantities:

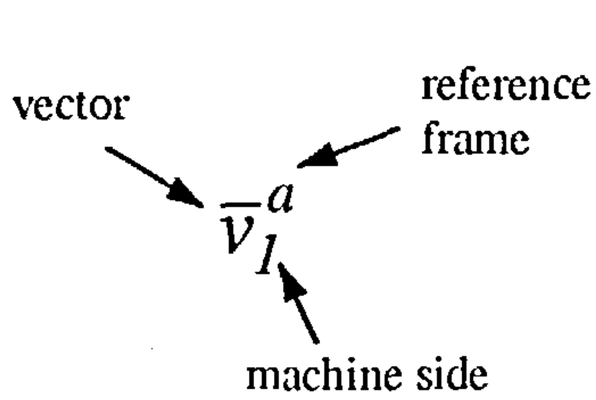

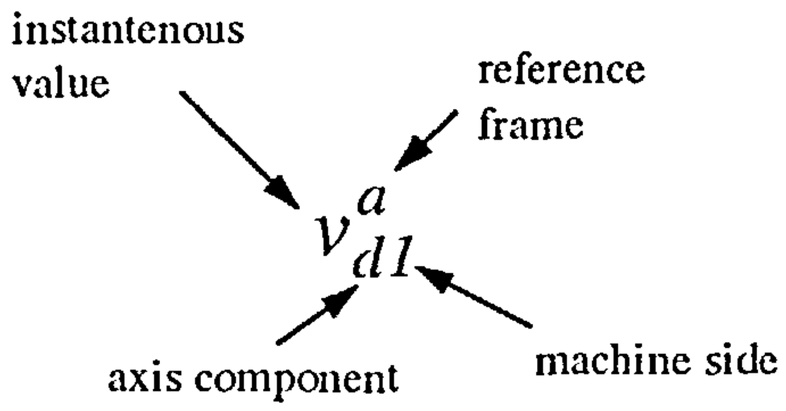

or "$vd1a$" in graphs

Voltages and Currents:

$\bar{v}_1, \bar{v}_2, \bar{v}_3, \bar{v}_4$	voltage vector of respective machine side
v_{1a}, v_{1b}, v_{1c}	Phase a, b and c instantaneous voltages of stator of SDFM
v_{2a}, v_{2b}, v_{2c}	Phase a, b and c instantaneous voltages of side 2 of CDFM
v_{3a}, v_{3b}, v_{3c}	Phase a, b and c instantaneous voltages of side 3 of CDFM
V_1	Stator of SDFM or side 1 of CDFM phase voltage in rms
$\bar{V}_1, \bar{V}_2, \bar{V}_3, \bar{V}_4$	voltage phasor of respective machine side
V_{dc}	d.c.-link voltage
$\bar{E}_{1ag}, \bar{E}_{2ag}$	
$\bar{E}_{3ag}, \bar{E}_{4ag}$	air-gap voltages of respective machine sides
$\bar{i}_1, \bar{i}_2, \bar{i}_3, \bar{i}_4$	current vector of respective machine side
i_{1a}, i_{1b}, i_{1c}	Phase a, b and c instantaneous currents of stator of SDFM
i_{2a}, i_{2b}, i_{2c}	Phase a, b and c instantaneous currents of side 2 of CDFM
i_{3a}, i_{3b}, i_{3c}	Phase a, b and c instantaneous currents of side 3 of CDFM
$\bar{I}_1, \bar{I}_2, \bar{I}_3, \bar{I}_4$	current phasor of respective machine side
$\bar{I}_{mag}$	Magnetising current phasor
$\bar{I}_{fe}$	Iron loss resistance current phasor

Flux linkages:

$\overline{\Psi}_1, \overline{\Psi}_2, \overline{\Psi}_3, \overline{\Psi}_4$	flux linkage vector of respective machine side
$\overline{\Psi}_R$	combined rotor circuit loop flux linkage vector of CDFM

$\overline{\Psi}_{\mu AB}$	combined magnetising flux linkage vector of CDFM

Torque and Power:

T_e	electromagnetic torque
T_{eA}, T_{eB}	electromagnetic torque of machine A and B of CDFM
T_{eAB}	total electromagnetic torque of CDFM
T_L	load torque
P_1, P_2, P_3, P_4	active power of respective machine side
P_m	mechanical power
P_{mA}, P_{mB}, P_{mAB}	mechanical power of machine A, B and total power of CDFM
Q_1, Q_2, Q_3, Q_4	reactive power of respective machine side
S_1, S_2, S_3, S_4	apparent power of respective machine side
Q_{12}	total reactive power of SDFM
Q_{14}	total reactive power of CDFM
Q_A, Q_B	reactive power of machine A and machine B of CDFM

Frequencies:

f_1, f_2, f_3, f_4	frequency of respective machine side in Hz
f_m	mechanical rotor frequency in mechanical Hz
f_r	mechanical rotor frequency in electrical Hz
f_{rA}, f_{rB}	mechanical rotor frequency of machine A, B of the CDFM in electrical Hz
ω_1, ω_2, ω_3, ω_4	angular frequency of respective machine side in elec. rad/s
ω_m	mechanical angular frequency of rotor in mechanical rad/s
ω_{mA}, ω_{mB}	mechanical angular frequency of rotor of machine A, B in mech. rad/s
ω_r	mechanical angular frequency of rotor in electrical rad/s
ω_{rA}, ω_{rB}	mechanical angular frequency of rotor of machine A, B in elec. rad/s
ω_{rAB}	mechanical angular frequency of side 4 relative to side 1 of the CDFM
ω_g	angular frequency of the general reference frame in elec. rad/s
ω_e	angular frequency of the excitation reference frame in elec. rad/s
s	slip
s_A, s_B	slip of machine A, B of CDFM
s_E	equivalent slip of CDFM

Angles:

Θ_m	rotor angle in mech. rad
Θ_{mA}, Θ_{mB}	rotor angle of machine A and B in mech. rad
Θ_{mAB}	combined rotor angle in mech. rad
Θ_r	rotor angle in elec. rad
Θ_{rA}, Θ_{rB}	rotor angle of machine A and B in elec. rad
Θ_{rAB}	combined rotor angle in elec. rad
Ω	angle between frame "b" and "e" of the CDFM
β_2	rotor current angle in frame "b" of the SDFM
β_4	side 4 current angle in frame "d" of the CDFM
χ	angle of controlled current vector in frame "e"
ε	angle between frame "b" and "e" or between frame "d" and "e"

Machine Parameters:

a	turns ratio of SDFM
a, b	turns ratio of machine A and B of CDFM

p_A	pole pair number of SDFM
p_A, p_B	pole pair number of machine A and machine B of CDFM
R_1, R_2, R_3, R_4	resistance of respective machine side
R_R	combined rotor resistance of CDFM
L_1, L_2, L_3, L_4	self inductance of respective machine side
L_R	combined rotor inductance of CDFM
L_{mag}	magnetising inductance
L_m	mutual inductance
L_{mA}, L_{mB}	mutual inductance of machine A and B
$L_{\sigma 1}$, $L_{\sigma 2}$, $L_{\sigma 3}$, $L_{\sigma 4}$	leakage inductance of respective machine side
J	mechanical moment of inertia

Constants:

k_1, k_2	constants for stator flux orientation controlled CDFM
m_1, m_2	constants for combined flux orientation controlled CDFM
c_1, c_2	constants for harmonic analysis

List of Figures

List of Tables

Chapter 1

Introduction

The decade about 100 years ago saw enormous efforts to achieve variable speed control of electric machines. In 1890 the DC-machine and the 3-phase induction machine, cage and wound rotor, had been established. At that time the only way to allow speed control was by resistance variation in the armature circuit of a DC-machine or the rotor circuit of a wound rotor induction machine. A brushless form of speed control was first devised in 1893 independently by Steinmetz in the USA and Görges in Germany [c4]. They connected two wound rotor induction machines together to create a cascaded machine. As shown in figure 1.1, the stator of machine A is connected to the 3-phase supply network. A direct electrical and mechanical interconnection of the rotors of the machines makes brushes for the slip-rings obsolete. The rheostat on the stator of machine B is then used for speed change in the same way as for a normal wound rotor induction machine.

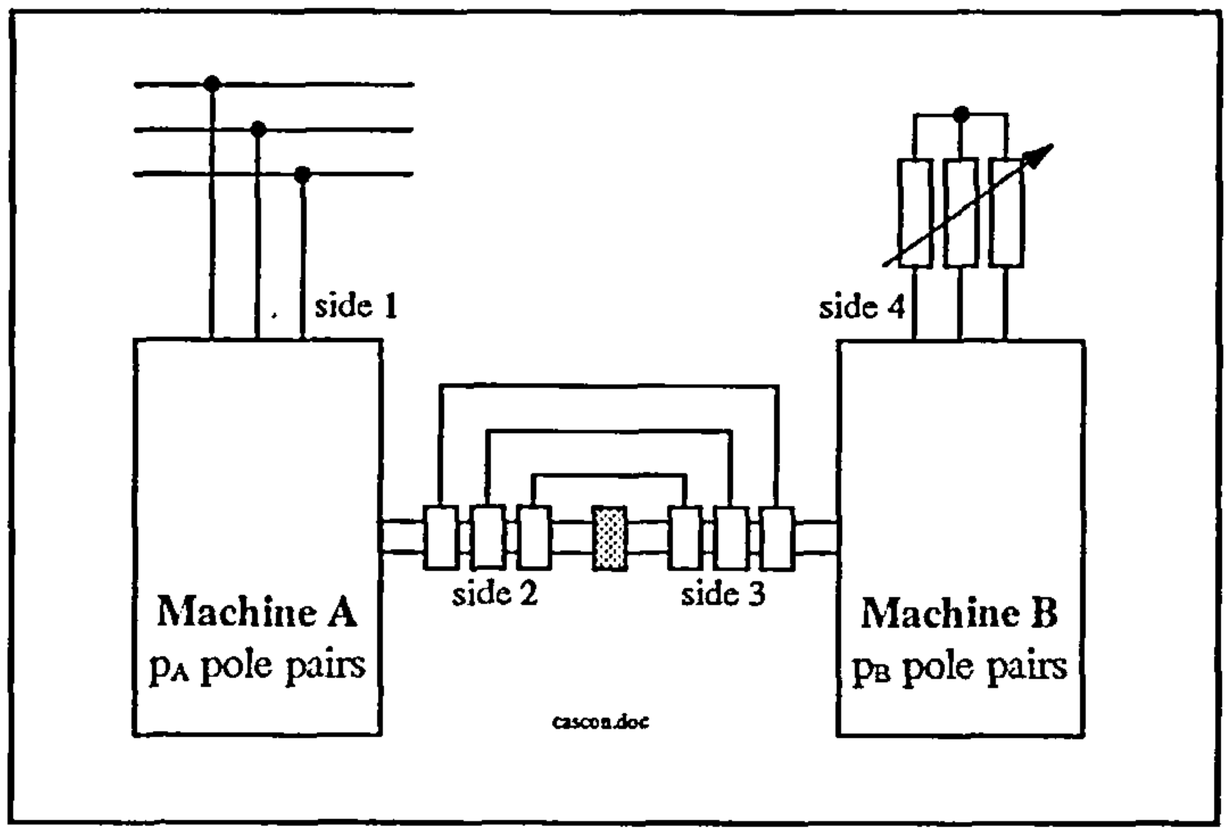

Figure 1.1: Cascaded machine connection

Apart from brushless operation the cascaded machine was utilised, when more than one base speed was needed. Four different base speeds can be accomplished, when two wound rotor machines with unequal pole pairs are available. There are first of all the base speeds of each individual machine given by the supply frequency and the respective pole pair number. Additionally, depending on the rotor phase sequence connection, two more base speeds can be achieved related to the sum and the difference of the pole pair numbers.

The drawback of cascade operation is its inherently low power factor and efficiency, but it has been applied in a.c. ship propulsion, where low maneuvering speeds are important [f1].

Nowadays, a century later, favoured by advancements in power electronics, microelectronic control hardware and modern control theory, the brushless cascaded machine is subject to renewed interest. This is particularly valid for the various emerged types of brushless doubly-fed machines, as described later. Together with the wound rotor induction machine, the cascaded brushless doubly-fed machines can generally be classified as doubly-fed machines in contrast to singly-fed machines, as illustrated in figure 1.2.

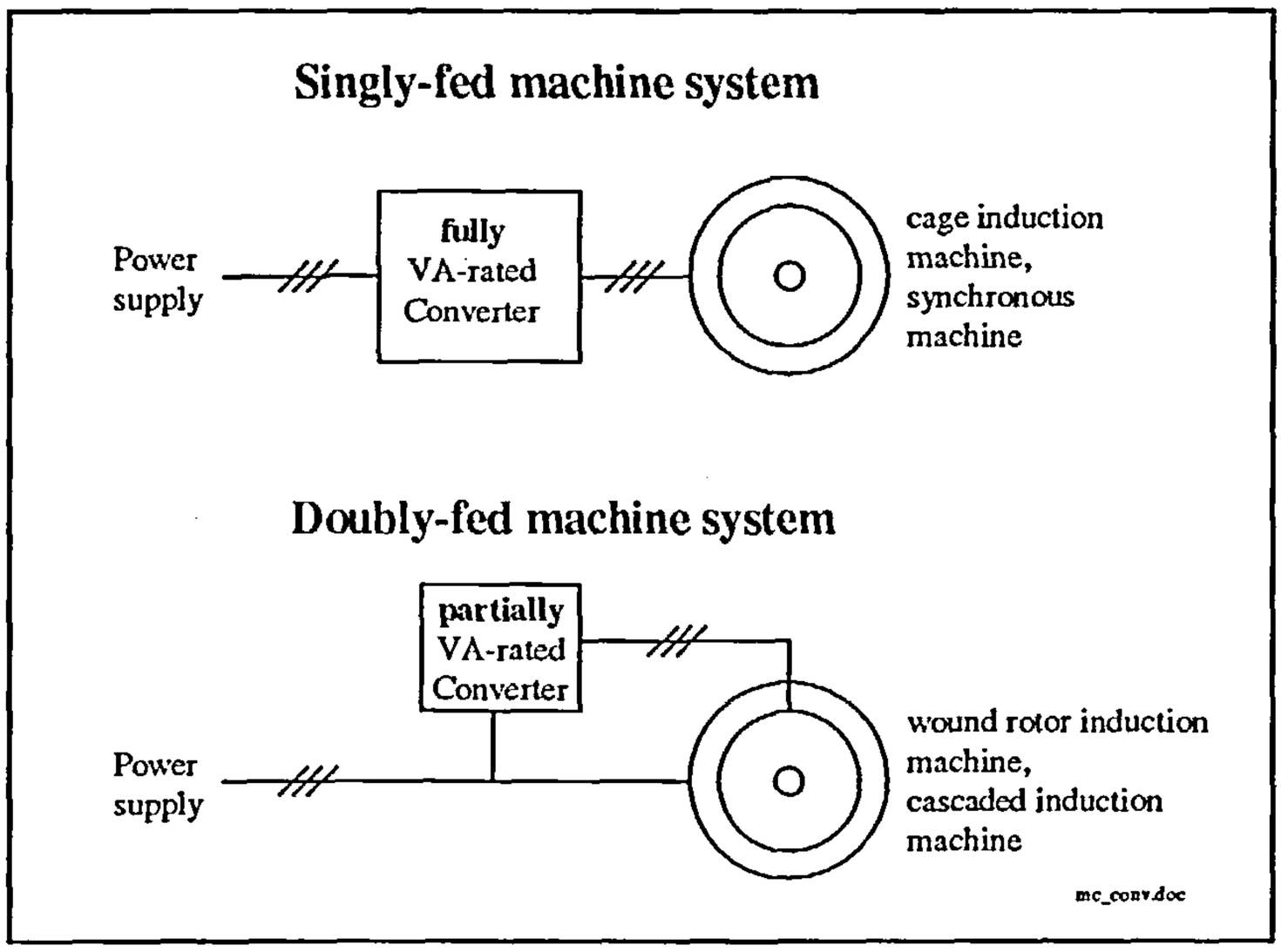

Figure 1.2: Singly-fed and doubly-fed machine system

Singly-fed refers to machines where power is fed to one set of 3-phase a.c. windings and doubly-fed refers to machines with two sets of accessible 3-phase a.c. windings. Hence, a synchronous machine qualifies as a singly-fed machine.

As pointed out in figure 1.2, a variable speed doubly-fed machine arrangement has the advantage of a reduced power converter rating compared to an equally rated singly-fed system, since only slip-power has to be handled by the converter. This can lead to cost savings of up to 30 % [c28] despite the increased machine costs for a doubly-fed system. This cost benefit factor is the main driving force behind enthusiastic research into doubly-fed machines over the last years. Althoūgh control of doubly-fed machines has found attention the main focus of world wide research is engaged with machine design improvements of brushless doubly-fed machines.

This thesis aims primarily to contribute to the control, precisely the field oriented control, of doubly-fed induction machines.

1.1 Objectives

Before laying down the objectives it is useful to define two abbreviations, which are used throughout this thesis:

SDFM - single doubly-fed (induction) machine. This term is used for a wound rotor induction machine, where the stator is connected to the supply network and the rotor is connected to a bi-directional power converter, as shown in figure 1.2.

CDFM - cascaded doubly-fed (induction) machine. In contrast to a "single" machine, this term refers to a cascade connection of two wound rotor induction machines as displayed in figure 1.1, which also contains the adopted machine side nomenclature. Side 1 for the stator of machine A and side 2 for the rotor of machine A. Side 3 is the rotor of machine B and side 4 relates to the stator of machine B. As the SDFM the CDFM is doubly-fed with side 1 connected to the supply network and side 4 connected to a power converter in accordance to figure 1.2.

The objectives of this thesis are:

- Summarise and clarify developments and state-of-the-art in doubly-fed machine design and control.
- Design and build-up of an electrical drive system suitable for field oriented control of the SDFM and the CDFM.
- Comprehensive model description and steady-state treatment of the SDFM. Implementation of field oriented control of the SDFM. (Although the theory and control of the SDFM is generally well understood it is necessary to include it as a basis for the CDFM theory)
- Comprehensive dynamic model, rotor connection and reference frame description of the CDFM. Comprehensive steady-state treatment of the CDFM, dependent on rotor connection. Investigation of pole pair relationship. Implementation of previously developed field oriented CDFM control method with focus on simplification. Implementation of same field oriented control on the CDFM as it is used for the SDFM and investigation of control performance.
- Implementation of position sensorless control methods for the SDFM and investigation of their feasibility for the CDFM.
- Inverter produced harmonic current analysis on the SDFM and CDFM system and investigation of a potential harmonic prediction method based on simulation and modeling.

1.2 Review on Doubly-Fed Machines

As mentioned at the beginning, the control of the wound rotor induction machine and the cascaded induction machine for variable speed drives relied initially on resistance variation in one of their a.c. windings. This method of torque manipulation results in energy waste.

The first truly doubly-fed variable speed systems were introduced with the so-called "slip-power recovery schemes", engaging the wound rotor induction machine in a very efficient way. Those arrangements can be divided into two groups, in mechanical and electrical recovery. The former converts the slip-power back into mechanical power to supplement the main motor, Krämer (1904), and the latter returns the frequency converted power to the main supply, Scherbius (1907). Both schemes are based on the use of auxiliary machines [f1].
With the advent of the thyristor in the 1960s and further developments in power electronic devices the auxiliary machines were replace by static power converters and the schemes became known as Static-Krämer and Static-Scherbius drives.

The brushless form of slip-power recovery was enabled with the connection of two wound rotor induction machines to a CDFM. An improved version has been accomplished with the single frame cascaded doubly-fed machine (SF-CDFM), where both stators are fitted axially aligned in a common frame. A crossed-over cage rotor, necessary for correct phase sequence connection, goes over the whole machine length [b18], figure 1.3.
Another brushless doubly-fed path was initiated by Hunt in 1907 [c1]. He aimed to unite two machines into one. A special type of stator winding sets up two rotating fields which interact with a special type of cage rotor. Further world wide research led to new stator and rotor configurations, including cage and reluctance type rotors [d6].
A third brushless doubly-fed machine path is opened up by the so-called Tandem-machine, where two stators are axially aligned, with one fixed and the other physically axially rotatable. A cage rotor is common to both stators [e2].

Figure 1.3 illustrates the different types and categorisation of doubly-fed machines, which are further reviewed in the following.

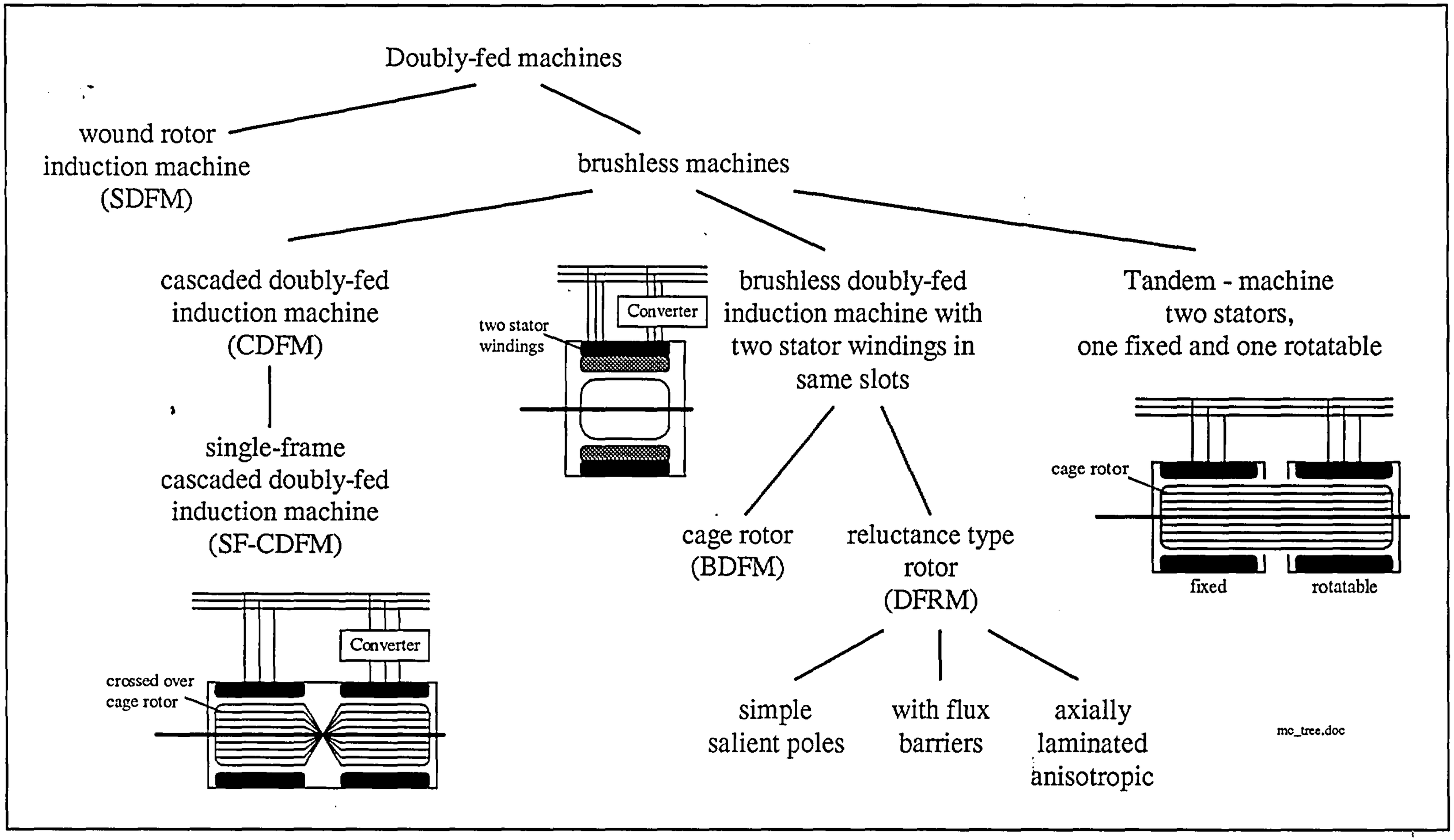

Figure 1.3: Doubly-fed machines tree

1.2.1 Review on SFDM

Riaz in 1959 [a1] gives a very detailed description of active and reactive power flow properties of a wound rotor induction machine, considering several operating conditions for motoring and generating. Based on a per-phase equivalent circuit, which is made up of two subnetworks for separately exhibiting each of the stator and rotor circuit, power and torque equations are derived. The electrical properties are summarised as four basic transformations: frequency transformation between stator and rotor, turns-ratio transformation of stator and rotor voltages, transformation of stator and rotor active power by the slip value and a reactive power transformation involving the slip.

Also based on a per-phase equivalent circuit Vicatos and Tegopoulos (1989) [a3] presented a thorough analysis of the doubly-fed induction generator under synchronous operation. Stator and rotor currents, active and reactive power as well as mechanical power and electromechanic torque are expressed as functions of the slip, the rotor excitation voltage and an angle α, which is the phase difference between the stator voltage and the rotor voltage referred to the stator. It is shown that the electromechanic torque consists of three components. Two asynchronous components produced by the stator and rotor voltage, respectively, and a synchronous torque as a consequence of the stator and rotor field interaction. Various derivations conclude that it is possible to operate the doubly-fed machine at any speed by controlling the rotor frequency. Furthermore, stator active power can be controlled by varying the angle α and reactive power can be controlled by varying the magnitude of the rotor excitation voltage.

This scalar control behaviour of the doubly-fed induction machine was taken a step further by Rifai and Ortmeyer (1993) [a5]. They investigated the dynamic control stability of a generator system with a cycloconverter in the rotor circuit. To regulate the stator reactive power, the stator reactive current component is fed back to an integral controller, which gives the exciter (rotor) voltage magnitude demand for the cycloconverter. The experimental system is described in very little detail and it remains doubtful whether it is sufficient to verify the theoretical work. Nevertheless, a two-axis mathematical model of the doubly-fed generator was developed and a linearised control stability analysis was carried out. It is stated that the implemented system is stable for slips near zero, but becomes unstable for higher magnitude slips. Instability can be overcome by modifying the cycloconverter frequency as the shaft speed changes and adding proportional feedback involving the stator and rotor current vectors. Digital computer simulations on the non-linear model are used for verification.

Probably the first reported work on field oriented control of the doubly-fed induction

machine was by Leonhard in 1979 [a2]. It is shown that the orientation of the rotor current vector relative to the stator flux vector leads to decoupled stator active and reactive power control. The rotor current quadrature component is proportional to the torque and stator power of the machine and the rotor direct component manipulates the stator reactive power. A two-axis space vector machine model is used for description of the control system dealing with an inner current control and an outer speed/power control loop. Employed classical PI-controllers have to process d.c. values in steady state, since control quantities are represented in "field coordinates". The performance of the control is shown by digital computer simulation and it is stressed that the analogy to the DC-machine control structure is the main advantage of the field oriented control.
It can be said that since that time the stator flux oriented control of the SDFM, with decoupled active and reactive power control capabilities, can be regarded as the main control principle for that type of electric machine.

Having the latest power electronic inverters and control hardware available, Tang and Xu (1993) [a13] presented work on the SDFM with dual PWM inverters with a d.c.-link in the rotor circuit. Based on the stator flux oriented control, the machine-side inverter is used for active and reactive power control of the SDFM at variable speed and the line-side inverter provides the d.c.-link voltage and is able to control the power factor at its supply interface point. The new aspect of their approach is that they consider the machine-inverter system as one unit, concerning reactive power control. Both inverters are coordinated in a way that a unity power factor is created at the grid connection point of the machine-inverter system. At the same time the reactive current flow in the SDFM, regulated by the machine-side inverter, is minimised to keep the copper losses down and improve system efficiency.
In a later paper Tang and Xu (1995) [a13] describe the stator flux oriented and fuzzy logic control of a doubly-fed variable speed drive with DSP implementation. The inner current control loop of the SDFM contains conventional PI-controllers, but an outer speed loop is closed by a fuzzy controller. Speed error and change of speed error serve as inputs to the fuzzy controller, which produces the q-axis rotor current demand value as output. It is claimed that the fuzzy logic control approach, based on field orientation principles, achieves faster speed tracking and eliminates speed overshoot compared to a PI speed controlled SDFM.

The latest contribution in the field oriented control of the doubly-fed machine is by Heller and Schumacher (1997) [a16]. They investigated the stability of the field oriented controlled SDFM. A stator flux oriented mathematical model of the SDFM with impressed rotor currents is linearised and the resulting eigenvalues are computed. It is concluded that the machine model contains a set of poorly damped eigenvalues. These eigenvalues cause flux oscillations when rotor currents or line voltage change rapidly. Their analysis is verified by

experimental work on a 33 kW machine. It is clearly shown that flux oscillations result if the control bandwidth of the inner current control loop is too high.

Yamamoto and Motoyoshi (1991) [a4] describe a decoupled active and reactive power control strategy with rotor current orientation on the air-gap flux. Outer power control and inner current control loop use PI-controllers and give a voltage demand to a cycloconverter. Moreover, the characteristics of transmission of harmonic currents, caused by the cycloconverter in the rotor, is analysed. A so-called "symmetrical coordinate method" is used for theoretical analysis and results are confirmed by experiment.

Refoufi and Pillay (1994) [a10] use a hybrid dq/abc model of the SDFM to predict current waveforms of a slip-power recovery drive with a rectifier - inverter in the rotor circuit. Their model appears to predict the waveforms very closely to measured ones. Also, the harmonic analysis of predicted and measured current waveforms is in very close agreement.

Further harmonic analysis is carried out by Hombu and co-workers (1995) [a11]. Digital simulations with an Electro Magnetic Transient Program are carried out and harmonic currents generated by three different types of GTO converters in the rotor circuit are compared.

A position sensorless stator flux oriented SDFM control scheme was described by Arsudis and Vollstedt in 1990 [a7]. With measurements of the stator voltage and current and the rotor current, the angle between rotor position and stator flux reference frame can be estimated. With the knowledge of that angle the conventional active and reactive power control can be performed as shown by measurements. Limitations of the control scheme appear for low rotor current values.

Another sensorless method is described by Bogalecka (1993) [a8] for active and reactive power control in a stator voltage and a stator flux reference frame. Utilising the active and reactive stator power an angle between the rotor current vector and the respective reference frame is calculated. An angle controller is introduced, which generates the angular frequency of the rotor current vector. Simulation results show the performance of the scheme.

Xu and Cheng (1995) [a9] present a sensorless control configuration for air-gap flux orientation of the SFDM. Only rotor current and voltage measurements are needed for a so-called torque angle estimater. The torque angle can be estimated satisfactorily except for low rotor frequencies. Simulation and experimental results confirm their control strategy.

In this thesis *the steady-state treatment and the stator flux oriented control of the SDFM are presented. Although they serve as an application and confirmation of past research, it is necessary to include SDFM theory as introduction and as a bridge to the CDFM steady state and control theory.*
New elements are brought in by the position sensorless control of the SDFM, which is initially based on the scheme by Arsudis [a7]. Furthermore, a current harmonic prediction method for the SDFM system is introduced.

1.2.2 Review on Cascaded and Brushless Doubly-Fed Machines

As shown in figure 1.3, the brushless section of the doubly-fed induction machines splits up into three branches.

The first branch, classified as the CDFM, goes back to 1893 when Steinmetz and Görges connected two wound rotor machines for speed variation with a rheostat. Over the years numerous researchers all over the world analysed and modeled the machine connection and implemented some form of control [b1-b5, b15].
This branch is continued by the single-frame CDFM (SF-CDFM) and has been mainly pursued in Germany [b17, b18]. It is manufactured by Antriebstechnik GmbH FAURNDAU up to 250 kW and used as a self-synchronous drive with a thyristor converter.

The middle branch is a merger of two machines into one, with two stator windings in the same slots and initially a special wound rotor. It was proposed by Hunt in 1907 [c1] and later improved by Creedy in 1921 [c3], both UK.
After another half a century, in 1970, the idea was taken up by Broadway in the UK who developed a special cage rotor structure to replace the wound rotor. Over the last ten years major research in that direction is due to Wallace, Spée and various co-workers at Oregon State University, USA [c15]. They coined the expression brushless doubly-fed machine (BDFM) for that type of machine and developed diverse machine models and control methods, ranging from simple V/Hz control to field orientation principles. More recently Oregon have joined forces with Cambridge University to further develop the machine design [c22]. Other BDFM control and design contributions are reported from Japan [c7] and Australia [c9].
A different type of rotor structure goes also back to Broadway. Apart from the cage rotor, he developed a reluctance type rotor for the brushless doubly-fed machine [d1]. Sparked by research fundings this idea was taken up in the USA in the mid 1980's [c28] and resulted in research concentration at Ohio State University headed by Xu [d6] in addition to GE-Corporate Research Development Center with Liao [d8]. The term doubly-fed reluctance

machine (DFRM) is used for this type of machine.

The third type of brushless doubly-fed machine, the Tandem-machine, originated from Australia in 1966 by Smith [e1]. The machine has one fixed and one movable stator frame and a common cage rotor. In the 1990s it found research attention by Perahia and Nayar [e3], Australia. A hydro power application is reported by Levy [e2] from Ireland in 1986.

The following more detailed review of brushless doubly-fed machines covers the whole branch as indicated in figure 1.3. The review is split in four groups covering CDFM / SF-CDFM, the BDFM, the DFRM and finally the Tandem-machine.
It has to be said that research in this thesis is aimed at the CDFM / SF-CDFM, so that the review on the BDFM, DFRM and the Tandem-machine is mainly undertaken to draw the whole brushless doubly-fed machine picture and to place the CDFM / SF-CDFM in respect to the other doubly-fed machine options.

CDFM / SF-CDFM - fundamentals and machine connection

Depending on the rotor phase sequence connection there are two distinct synchronous speeds for the machine set. For negative phase sequence connection the rotor fields rotate in the same direction relative to the rotor and the synchronous speed is related to the difference of both pole pair numbers. Both machines develop opposing torques. For positive phase sequence connection, counter rotating rotor fields, both machines develop torque in the same direction and the synchronous speed is related to the sum of the individual pole pair numbers. In any case, the proportional mechanical power output of the individual machine is in proportion to the pole pair number [c4].
Therefore, regardless of machine type, CDFM or SF-CDFM, the fields set up by the rotor have to be counter rotational to produce co-acting torque components.

As described, the CDFM is a connection of two wound rotor induction machines. The rotors are directly connected, mechanically and electrically, as shown in figure 1.1.

The SF-CDFM has two machines built in one common frame. Two stator windings are axially aligned next to each other as shown in figure 1.3. The cage-structured rotor is made out of rotor bars. In order to achieve counter rotational rotor fields so that the individual machine parts produce torque in the same direction, the cage rotor has to be "crossed-over". Industrial applications up to 250 kW with the SF-CDFM are reported. Both machine-halves have the same number of pole pairs [b18].

CDFM / SF-CDFM - model analysis and control

In 1967 Smith [b1] presented an analysis of the performance of the CDFM. Frequency and

power relationships are developed. Also a rotor referred per-phase equivalent circuit, consisting of a connection of two wound rotor equivalent circuits is formed. It is stated that the torque of the machine is proportional to the sine of the phase angle between the two supply voltages. Theoretical analysis is confirmed by experimental results with two identical wound rotor induction machines.

The principle of using a connection of two wound rotor induction machines as a per-phase equivalent circuit for the CDFM / SF-CDFM is moreover taken up by other researchers [b4, b5, b7, b17]. This approach is also pursued in this thesis for steady state analysis.

In 1979 Smith, together with Cook, investigated the stability of the CDFM for open-loop V/Hz control with a forced-commutated inverter on side 4 [b2]. A dynamic d-q-model of the CDFM is developed and the eigenvalues are analysed. It is shown that the operational range comprises stable and unstable regions. The unstable regions can be stabilised by introducing a phase-lag current feedback with the d.c.-link current as feedback. Experimental results verify the stabilisation effect. Later, 1983, Cook and Smith explored the influence of machine parameters on the stability of the CDFM [b3]. They concluded that practical CDFM design parameters will not produce any inherently well damped machine over a wide speed range.

Bauer [b15], 1986, also investigated the dynamic behaviour of the CDFM under open-loop operation. For V/Hz control and additionally for current control on side 4. The linearised state space model analysis confirms the results obtained by Cook and Smith [b2] for the V/Hz control. The current control turns out to be unstable over the compete operational speed range.

Nonaka and Oguchi [b4], 1977, implemented a CDFM system with a self-controlled thyristor converter with a current d.c.-link on side 4. The control strategy is not made very clear, but the machine-side converter receives its pulse signals dependent on the rotor speed and the line-side converter commutation is governed by the line voltage waveform. The proposed circuit is not able to control motor speed continuously around the cascaded synchronous speed, when the voltage on side 4 is too small.
It seems that the control of the CDFM as described in [b4] is similar to a synchronous machine in self-synchronous mode control, where the torque is controlled by varying the commutation angle of the machine-side thyristor converter.

A self-synchronous mode control is implemented by FAURNDAU in their so-called SD-drives, consisting of a SF-CDFM and a machine-side load commutated thyristor inverter and a line-side phase controlled rectifier with current d.c.-link [b18]. The speed / torque

control is accomplished by controlling the load angle of the machine-side inverter. In comparison to the system of [b4] the SD-drive rotates in the direction so that the voltage and frequency on side 4 increases linearly from standstill. The cascaded synchronous speed with the lack of sufficient commutation voltage is thus avoided. However, with the voltage increases also the power handling of the thyristor converter, but the simple control structure with the cheap thyristor modules keeps the price of such a drive to a minimum.

Bauer was the first who applied field orientation control principles to the CDFM [b14, b15]. The artificial reference frame for orientation comprises of the two stator current vectors. Controlling the inaccessible rotor current in that reference frame allows manipulation of the CDFM torque. A control structure is developed to regulate the rotor current with the side 4 current and experimental results with two 1 kW wound rotor machines show the performance of that control arrangement.

Krebs continued Bauer's work by controlling the machine in the state space [b16, b17]. To improve damping Krebs introduced an observer for the unmeasureable rotor currents. He implemented the control scheme on a 30 kW SF-CDFM with Transputer based control.

A different reference frame for field orientation is chosen by Koczara and co-workers [b11-b13]. They use the stator flux (side 1) for orientation. The space vector CDFM machine model is developed for this particular reference frame and simulation results are presented. It is concluded that the side 1 active power can be controlled by the quadrature component of the side 4 current and the reactive power on side 1 is regulated by the direct component of the side 4 current in that stator flux reference frame. However, no experimental work is shown for verification.

The above described control methods for the CDFM / SF-CDFM are for grid connected machines, where side 1 is connected to a stiff supply network and side 4 is connected to some form of converter.
In the 1980s Ortmeyer together with co-workers did a series of investigations on a CDFM system for stand-alone aircraft generation [b5-b9]. The CDFM system under consideration consists of two cascaded wound rotor induction machines together with a permanent magnet machine on the same shaft. The permanent magnet machine generates a variable frequency variable voltage, depending on speed, which is then connected to side 4 of the CDFM via a rectifier-inverter arrangement with d.c.-link.
In [b5] the fundamental characteristics of the system operation is derived and described. The basic equations relating slips, pole pair numbers and power are first developed for a lossless machine. The two rotor connection options are defined and it is found that positive phase sequence rotor connection is favourable for subsynchronous operation and negative

phase sequence connection for supersynchronous operation of machine A of the CDFM. VAr flow is studied with the help of the connection of two per-phase equivalent circuits and it is concluded that provisions of power factor compensation on side 1 are required.
Steady state measurements on an experimental 3-2 pole pair CDFM were taken [b6] to confirm the basic theoretical machine characteristics.
In [b7] a two-axis model for each individual machine is given and the two rotor connection arrangements are described. Linearised small signal analysis is used to examine system stability of a proposed scalar control scheme, which independently regulates side 4 voltage and frequency. It is shown that with current state feedback improved performance can be achieved confirmed by computer time step simulations.
[b8] extends the scalar control analysis by introducing a so called "resistance simulator" into the control structure. This simulator takes account of the side 4 and the d.c.-link resistance, when current state feedback is used. Again linearised analysis was undertaken to produce a set of root locus plots. Computer simulations and limited laboratory tests claim to confirm the validity and feasibility of the scalar control method and it is shown that "resistance simulation" has stabilising effect on the control system.

The research in this thesis *concentrates on the control of a CDFM (also applicable to the SF-CDFM). The field oriented control of Bauer [b14] (combined flux orientation) can only be applied to a CDFM, which consists of two identical machines. Investigations are carried out to see if the scheme can be modified to be used for unequal machines, such as the laboratory machines.*
Furthermore, the scheme of Bauer contains a complicated mathematical extension in the torque control axis, which is necessary for correct control. It is examined as to whether the removal of that extension and thus simplification is still sufficient for proper speed and torque control.
In addition it is explored, whether the field oriented control scheme of Bauer results in decoupled active and reactive power control as it is known from the SDFM.
As described, the field oriented control scheme of the SDFM (stator flux orientation) has been simulated on the CDFM [b13], but no experimental implementation is reported. Furthermore, it is not commented in what extend the additional closed rotor circuit of the CDFM affects the stator flux oriented control. This is researched and the decoupled active and reactive power control capabilities are investigated.
In addition, a novel sensorless control scheme for the CDFM is proposed and analysed.
Finally, harmonic analysis is carried out and a harmonic current prediction process is applied to the CDFM system.

Now to the review of the remaining brushless doubly-fed systems:

BDFM - fundamentals and machine design

The BDFM is also a single frame machine, but in comparison to the SF-CDFM, where the stator windings are physically separated, both stator windings are wound in the same slots and share a common magnetic circuit, as shown in figure 1.3. In order to avoid transformer coupling between the two stator windings they must have different pole pair numbers, which must differ by more than one to avoid unbalanced magnetic pull on the rotor [c4, c17]. Although it is possible to arrange a single stator winding to produce two different fields [c4], it is preferred to have two isolated 3-phase stator windings as they enable a better overall performance compromise and can be individually rated depending upon the drive application [c17].

The rotor has a so-called multi-circuit single-layer bar construction, which is a specialised cage structure. It consists of identical sections, or nests, equal to the sum of the pole-pairs of the two stator windings [c4, c17] as shown below in figure 1.4.

The fundamental frequency and power relations of the CDFM / SF-CDFM are applicable to the BDFM, i.e. the two fields set up in the machine must be counter rotational relative to the rotor and the proportional power handling of the stator windings is in proportion to the pole pair number [c4].

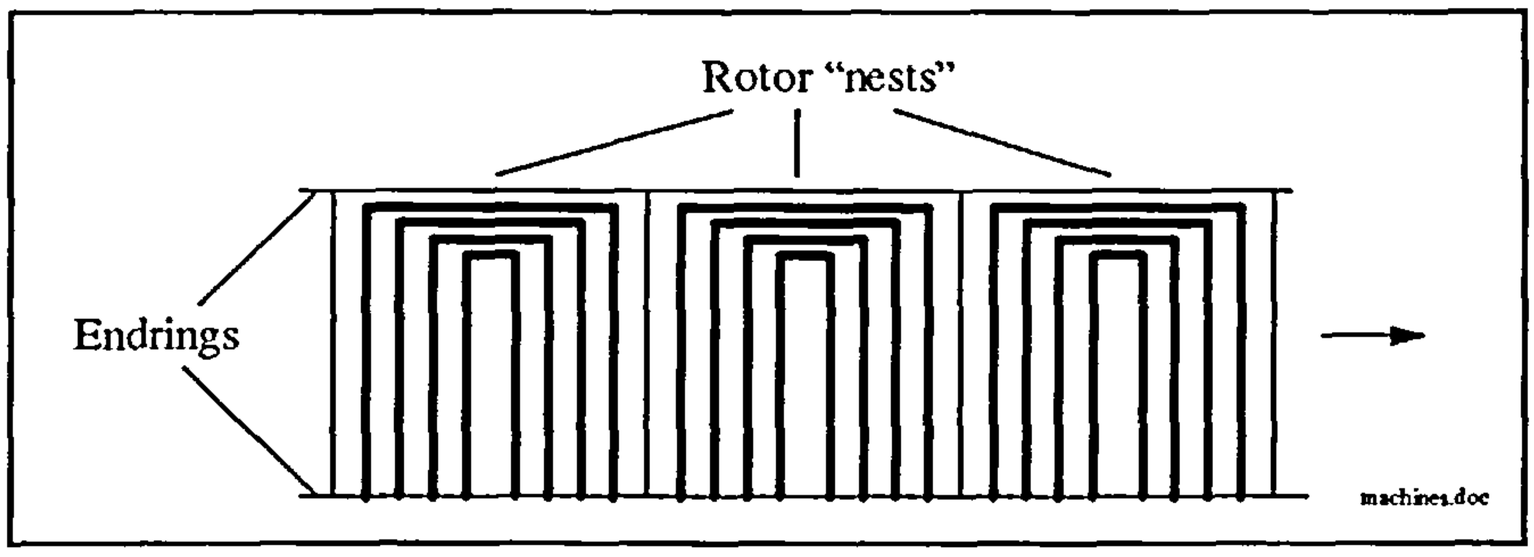

Figure 1.4: BDFM rotor configuration (surface view)

BDFM - model analysis and control

Major developments on the BDFM analysis and control are due to the work of Wallace, Spée and numerous co-workers.

Over the past decade various models have been developed. A two-axis model allowed the proper dynamic simulation of the BDFM for control purposes [c12]. Only recently, with the involvement of Cambridge University, BDFM models, which are closely related to the machine design have appeared. Among them a rigorous mathematical model based on generalised harmonic analysis [c23], a coupled circuit model [c22] and a finite element model [c21] for iron loss and saturation modeling.

Another steady state model has been developed by Perrera and Smith [c10], 1993. Their model is based on the development of a coupling impedance matrix.

Concerning the control of the BDFM Kusko and Somuah [c6], 1978, investigated the steady state performance of a BDFM for slip-power recovery. The theoretical analysis is based on the connection of two wound rotor induction machine equivalent circuits. It is found that the BDFM with the static frequency changer behaves like a separately excited DC-motor. Experimental measurements on a 0.5 HP machine confirm the theoretical analysis.
Other slip-power recovery schemes based on a BDFM are reported [c7, c8].

The open-loop stability of the BDFM for V/Hz control (on side 4) is investigated by Li, Wallace and Spée [c20], 1995. Using Floquet and Lyapunov techniques for eigenvalue computation it is concluded that the BDFM is open-loop stable over the entire speed range, which is verified by practical results.
This seems to be somewhat surprising, in conflict with the findings of other workers who report that the CDFM / SF-CDFM has unstable regions for open-loop V/Hz control [b2, b15].

Nevertheless, this open-loop stability of the BDFM forms the basis for a simple V/Hz control implementation [c20]. To achieve better dynamic performance a direct torque control structure was developed [c14] assisted by MRAC for speed control [c16], which turned out to be rather complicated for microprocessor implementation due to time-varying quantities. Despite initially ruling out field orientation principles for the BDFM, a synchronous frame d-q-model has been developed as foundation for a rotor flux oriented control algorithm [c25]. This algorithm uses a torque estimator and a predictor for the quantities of the stator winding, which is directly connected to the supply network. Later, a simplified field oriented control method has been developed, avoiding the torque estimator, and better experimental results were achieved [c26].

DFRM - fundamentals and machine design

The stator of the DFRM is identical to that of the BDFM, but instead of a cage rotor a reluctance type rotor is used. Three different rotor structures, as shown in figure 1.5, were investigated by finite element analysis [d6, d10].
Compared to the BDFM there are no rotor currents present and hence no rotor fields for interaction with the stator windings. The principle of the reluctance type rotor machines relies on the mutual magnetic coupling between the two stator windings, which is modulated by the saliency of the rotor [d10].
As for the BDFM the number of *poles* of the reluctance rotor is governed by the sum of the stator winding *pole pairs* [d10].

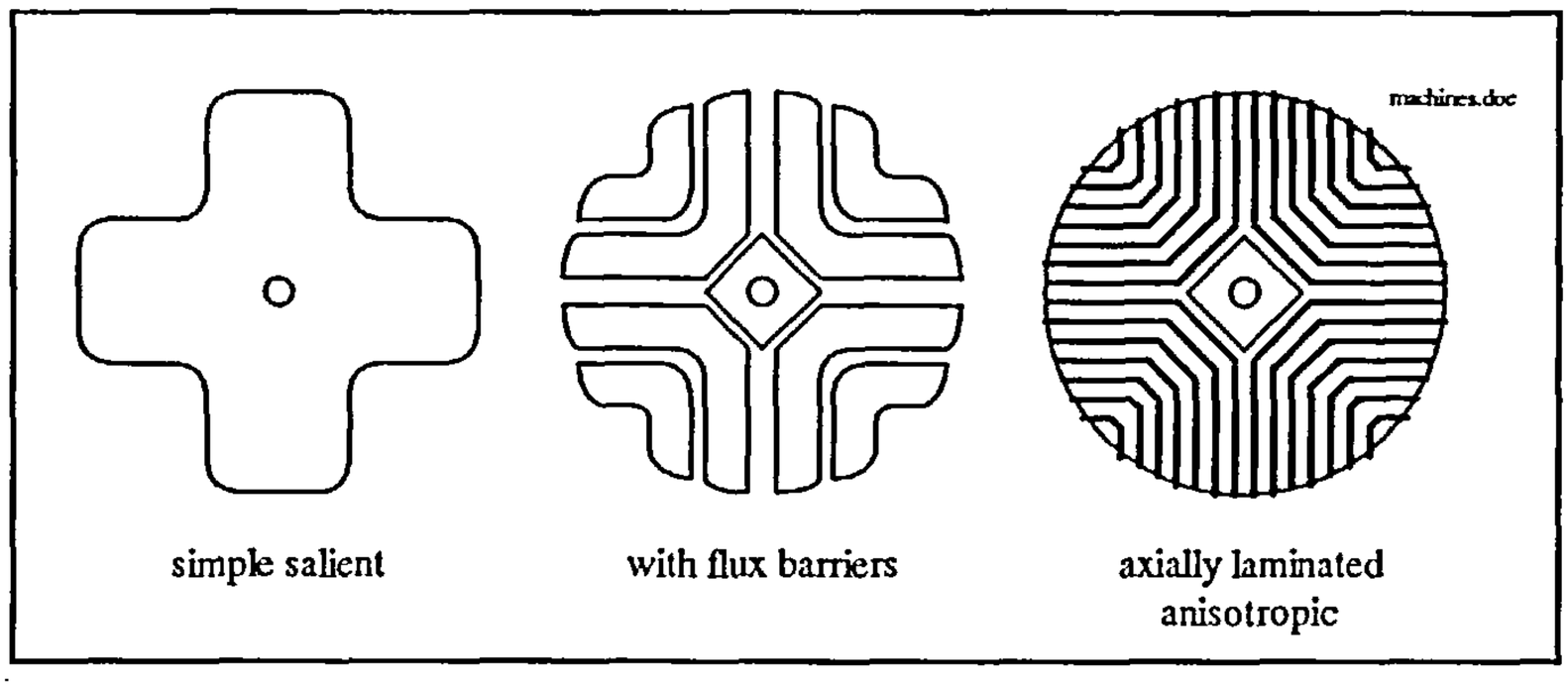

Figure 1.5: DFRM rotor types

The different rotor structures show varying degrees of mutual coupling modulation for the stator windings, with the axially laminated anisotropic rotor as a favourite [d6].

DFRM - model analysis and control

Liang, Xu and Lipo, 1991, developed a DFRM d-q-model and an equivalent circuit. It is stated that the model and equivalent circuit of the DFRM is the same as for a wound rotor induction machine, which implies that the DFRM is equivalent to a SDFM with a pole pair number made up from the sum of the two stator windings [d4].

This was proven by Xu and co-workers in 1996, who applied the SDFM stator flux field orientated control to the DFRM. Same decoupled active and reactive power control can be achieved [d7].

Furthermore, a position sensorless control scheme has been developed based on the reciprocal nature of the stator windings, which allows to derive a torque angle [d8].

Tandem - machine [e1-e4]

The last form of electric machine, which can be classified as a brushless doubly-fed machine is the so-called Tandem-machine. It consists of two axially aligned stators. One fixed and the other physically axially movable using a form of cradle. The squirrel cage rotor has skewed rotor bars extending over the full length of the two stators, as displayed in figure 1.3. The laminated core of the rotor is divided into two sections each the length of a stator winding.

The adjustment of one stator relative to the other is equivalent to the introduction of an electrical phase shift between the supply voltages on the stators. Doing so, the torque-speed curve of the Tandem-machine is effected in the same way as operating a normal cage induction machine on variable supply voltage with constant frequency.

The development of an equivalent circuit is reported and theoretical results are confirmed by experimental work [e1-e4].

The control arrangement for the Tandem-machine is straight forward and confirmed experimentally in a small scale hydropower [e2] and wind power application [e3]. A simple

power comparator is used for constant power generation or maximum power point tracking. The comparator gives a signal to a DC-motor, which is attached to a worm gear to rotate one stator to produce the desired power output.

Despite the advantage of having no power electronic converter, it seems doubtful whether the Tandem-machine will have any commercial success, mainly impaired by the special machine design, which also demands an auxiliary motor for stator frame rotation. Furthermore, the lagging power factor of the system may have to be compensated by capacitors or a parallel connected synchronous machine [e2].

1.3 Application Possibilities

Before listing potential application areas for doubly-fed machines, a price comparison between a 100 kW singly-fed and doubly-fed variable speed system is presented. Based on 4-quadrant operation, the singly-fed system requires a fully rated power converter and the doubly-fed systems a 50 % rated converter for full torque capabilities at standstill. Prices are based on major UK motor and drive manufacturers.

		Singly-fed system	*Doubly-fed system*	
Type:	*Motor:*	cage induction machine	wound rotor induction machine	
	Converter:	4-quadrant control unity power factor high performance control	4-quadrant control unity power factor high performance control	
Rating:	*Motor:*	110 kW	110 kW	
	Converter:	110 kW (155 kVA)	55 kW (83 kVA)	(50 % of singly-fed)
Price:	*Motor:*	£ 6000	£ 11400	(189 % of singly-fed)
	Converter:	£ 17600	£ 11260	(64 % of singly-fed)
	Total:	***£ 23600***	***£ 22660***	***(96 % of singly-fed)***

It can be seen that the increased motor costs of the doubly-fed system are compensated by the reduced converter costs. In the above case both systems end up at about the same amount. If the speed range is limited and hence the power converter rating of the doubly-fed system decreases a cost advantage of the doubly-fed system becomes apparent.
The motor cost ratio in the above example between a cage induction machine and a wound rotor induction machine is about 100 : 189. Comparing the ratio between a cage induction machine and a SF-CDFM for same machine ratings this ratio reduces to about 100 : 140-145 [b18]. Even for a prototype 10 HP BDFM this ratio reduces to 100 : 132 [c28]. This

shows that with brushless doubly-fed machines a clear cost advantage arises for variable speed drive systems.

Potential application areas for doubly-fed machine systems (brushed and brushless) can generally be defined as variable-speed constant-frequency (VSCF) applications, such as:

Wind Power Generation

Using variable speed wind power generation systems allows storage of kinetic energy in the moving masses of the wind turbine during wind fluctuations and gives the mechanical blade control sufficient time to respond to changing wind conditions. In that way mechanical stresses on the system components can be alleviated and the power input to the grid has a smoother shape. Furthermore, by following a maximum power curve the annual wind energy capture can be increased.

The latest commercial example is the 1.5 MW wind turbine of TACKE with a stator flux oriented controlled wound rotor induction machine [f13], resulting in decoupled active and reactive power control [a14, a15].

Also, investigations for the BDFM [c18] and the DFRM [d3] are reported.

Pumped Storage Hydro Power Plants

Power generation and power consumption must be balanced permanently in an electrical grid, otherwise the frequency will change due to acceleration / deceleration of the rotating masses of turbo generators and large motors. Therefore, by adjusting the pump load on the available grid power allows to regulate the frequency. On the other hand, during power generation the efficiency of a water turbine can be optimised by varying the speed dependent on water level and demanded power.

In order to perform power control in pump mode and efficiency optimisation in turbine mode, prevented by synchronous generators in traditional hydro power plants, wound rotor induction machines with field oriented control are becoming more popular [a16, f14].

Starter / Generator Aerospace Application

An aerospace application has following requirements: In motoring mode, a constant frequency supply provides power to an electric machine system, which acts as a starter to an aircraft engine. In generating mode, a variable speed prime mover (gas turbine) drives an electric machine system, which has to generate at constant frequency. Additionally, these generators require brushless operation. Traditionally, a synchronous generator with some form of mechanical speed conversion has been employed.

Ortmeyer investigated a CDFM system [b5] and a BDFM / DFRM system is discussed in [f12].

Fan and Pump Drives

Conventional fan and pump drives utilise a fixed speed cage induction machine at full power output. The process flow rate is mostly controlled by baffles and throttling valves. This results in high energy waste and large energy consumption. There are large efforts in industry to replace such systems by adjustable speed drives to save energy costs. The cubic power-speed curve nature of fans and centrifugal pumps requires a singly-fed variable speed power converter system to be rated at the upper limit of the load. With most applications limited to a speed range of 70% - 100% [c28] significant cost savings can be obtained with a doubly-fed system and thus shortens the payback time.

A 60 HP BDFM waste-water treatment plant is described in [c19] for example.

Ship Service Power Generation and Ship Propulsion

So-called "propulsion derived ship service" power systems have an electric a.c. generator on the same shaft with the main diesel engine, which is used for propulsion. The variable speed propulsion necessity, requires a VSCF electric system as constant frequency generator. Such a system has advantages due to fuel economy, since cheap diesel provides the energy source [f11]. Using a doubly-fed generator could further reduce electrical equipment size and costs.

On the other hand, for specialised vessels, a diesel motor drives a generator at constant speed to produce the required electrical power. In such a case the propulsion is provided by an electrical machine system, which has to be suitable for variable speed [f10].

Other potential application areas for brushless doubly-fed machines are in hazardous environments such as mining.

1.4 Thesis Organisation

After having given a detailed doubly-fed machine review in this chapter, chapter 2 describes the laboratory control set-up, which is suitable for SDFM and CDFM control implementation.

Chapter 3 starts off with space vector basics and the model description of the SDFM. The steady state analysis of the SDFM, based on the per-phase equivalent circuit, serves as a build up to the field oriented control implementation of the SDFM with decoupled active and reactive power control.

Chapter 4 deals with the dynamic model of the CDFM. The CDFM steady state theory, based on the connection of two SDFM per-phase equivalent circuits, is organised in parallel to the SDFM analysis to show similarities and to derive conclusions for the stator flux oriented control of the CDFM.

Chapter 5 covers the ficld oriented control of the CDFM. Beginning with the previously developed control of Bauer, modifications and simplifications are investigated. The second half of the chapter deals with the implementation of the CDFM stator flux oriented control.
Chapter 6 describes two sensorless control methods for the SDFM, from which one is applied to the CDFM.
Chapter 7 is dedicated to the harmonic analysis of the SDFM and the CDFM system. Also, results obtained from a harmonic simulation and modeling process are compared to the measured current harmonics.
Conclusions are given in chapter 8.

Appendices cover detailed hardware description, simulations on SDFM and CDFM, FFT summary, PWM principles and measured waveforms.

Chapter 2

Laboratory Implementation

The following chapters, which detail the machine drive systems, will be better understood if the experimental equipment is first described.

The digitally controlled electrical drive system consists of three main components: the electric machine, the power converter and the digital control hardware. Additionally, there are various interface circuits necessary connecting some of the main system elements. For experimental purposes, the prime mover is provided by another electrical machine coupled to the shaft of the experimental machine set.
This chapter describes in a condensed way the individual parts of the experimental laboratory set-up to give a foundation for the control derivation and implementation of the SDFM and CDFM control in the following chapters. More detailed information on the laboratory machine set-up, electrical circuits and microcontroller programming can be found in appendices A - C.

2.1 Complete Drive System

The complete laboratory drive system is illustrated in figure 2.1. The power part (thickened lines) consists of a bi-directional power converter and the SDFM / CDFM. A DC-machine, acting as a prime mover to the system (not shown in figure 2.1) is connected to the shaft of the wound rotor induction machines.
The control hardware used for the system, consists of two 16-bit microcontroller 80C167 (denoted as µC 1 and µC 2). They perform all control functions, analog-to-digital-conversions (ADC) and the pulse width modulation (PWM). An unidirectional fast serial communication from µC 2 to µC 1 allows data transfer in the described direction. Communications to the PC and to an oscilloscope via a digital-to-analog-card (DAC) are set up with µC 1.
Various interface circuits connect the power part to the control part of the system. At the same time they provide electrical isolation. The PWM interface produces 6 PWM signals with added dead-time from the 3 PWM signals generated by µC 1. The remaining interface circuits are used for preparing the sensed voltage, current and encoder signals to appropriate signals for further processing.

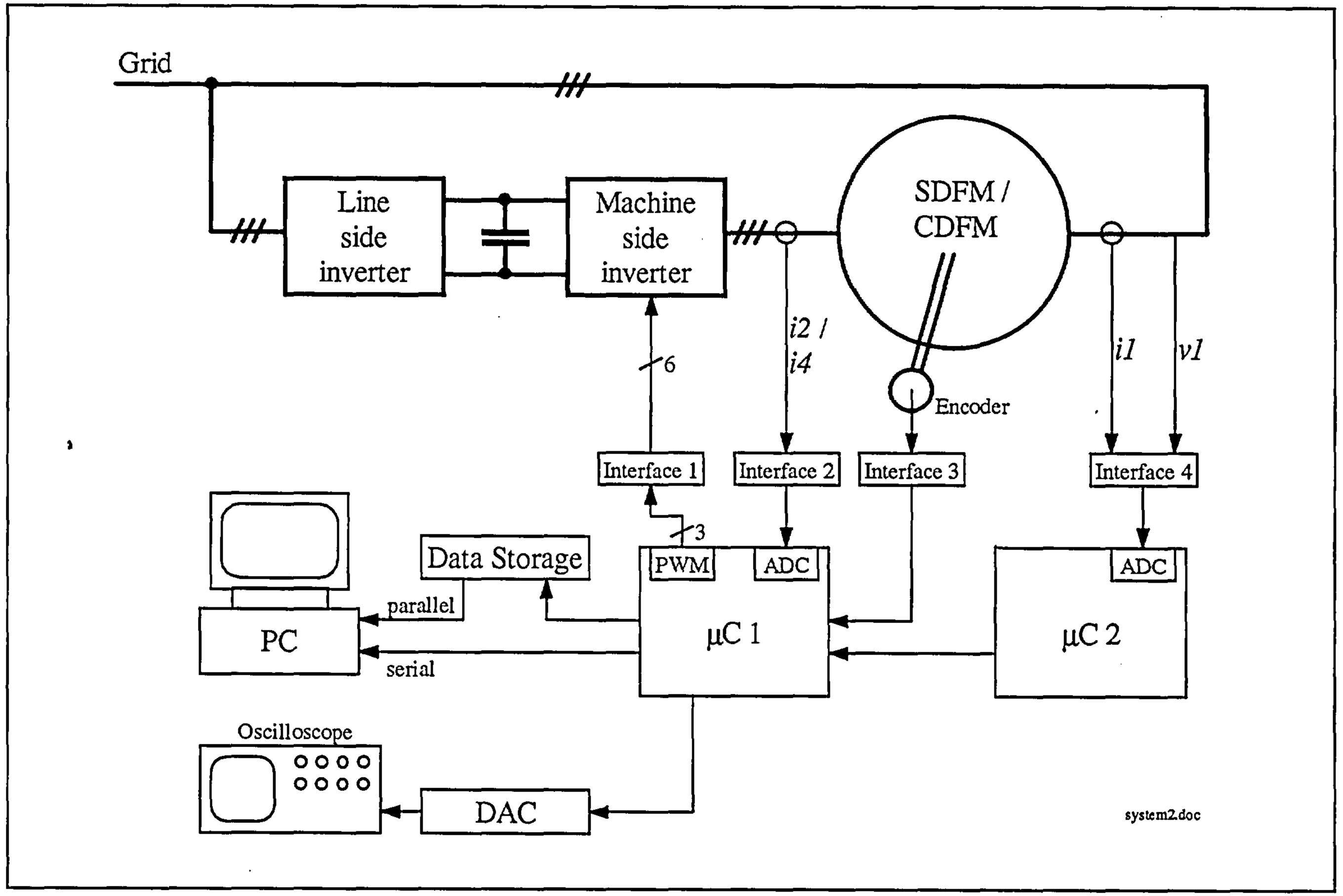

Figure 2.1: Laboratory drive set-up

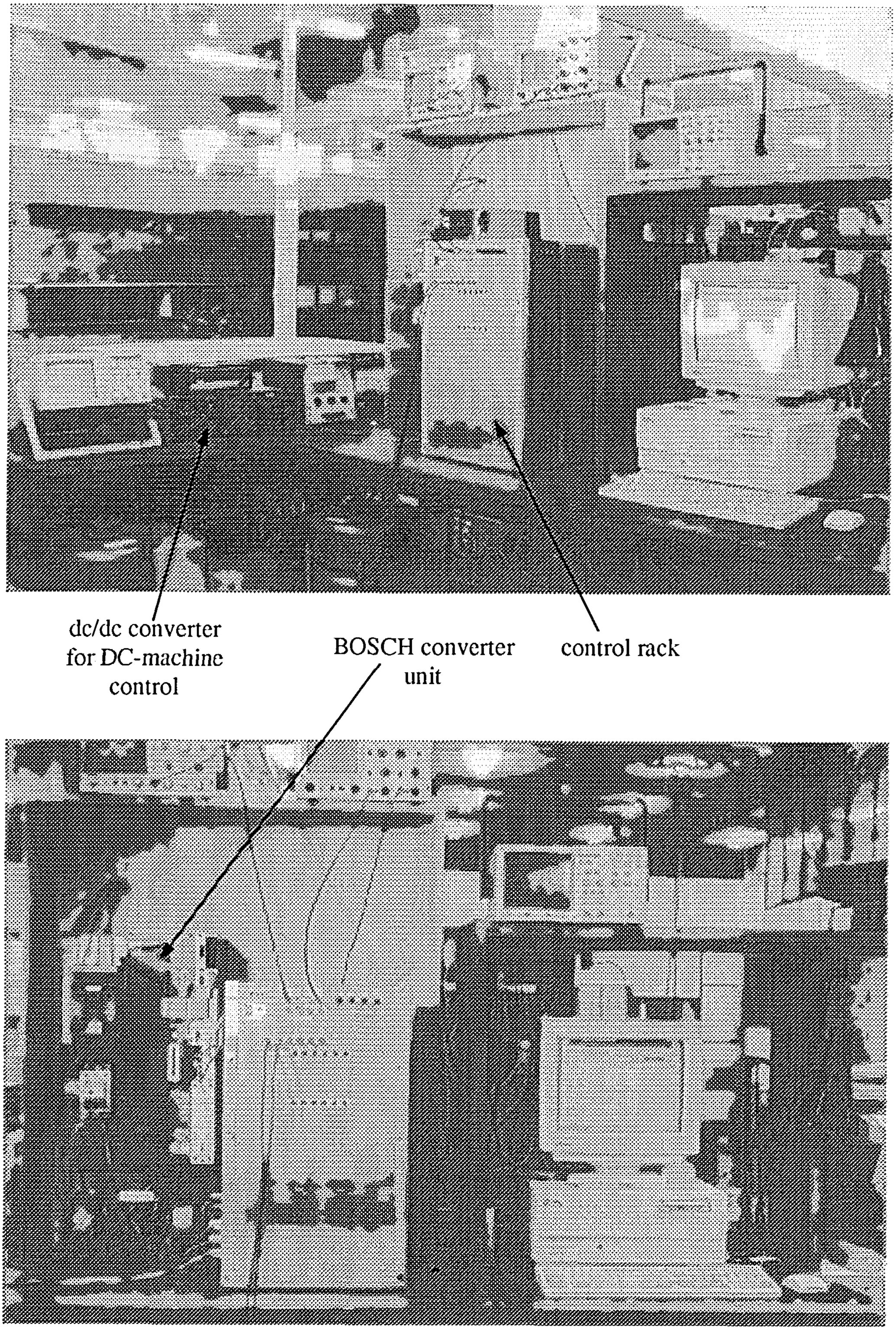

Figure 2.2: Pictures of the laboratory set-up

The physical laboratory set-up is shown in figure 2.2. The center of the arrangement is the "control rack" containing the microcontroller boards, all interface circuits and the power supply circuits. The circuits are placed on different levels with the controller boards on the top level. The front panel of the top level serves as user interface with various potentiometers, protection status indicators and enable and reset switch. BNC-connectors allow various timing and PWM signals of the microcontrollers to be brought out for monitoring purposes.
The second level from the top contains an EPROM emulator, the DAC and the data storage card. BNC-connectors from the DAC are mounted on the front-panel of this level. The remaining circuits are arranged in the levels below.

As displayed, the power converter and the PC are placed to the left and right of the control rack, respectively.
Transformers and variacs for the DC-machine supply are outlined in the left half of the top picture. They are placed underneath the bench. On top of the bench is the manually controlled dc/dc converter for the armature winding supply of the DC-machine. The electrical machines are arranged behind the benches.

2.1.1 Experimental Machines

The wound rotor induction machine used for implementation of the SDFM control is a BROOK 2.25 kW machine. As a machine with 2 pole pairs it is rated for 15.1 Nm at 1420 rpm. Both, the stator and the rotor are connected in star. The stator is directly connected to the 415 V supply network and the rotor windings are connected to the machine-side inverter. This machine is also used as machine B of the CDFM.
Machine A of the CDFM is a HOMES 2.25 kW wound rotor induction machine with 4 pole pairs and rated 32.1 Nm at 670 rpm. The stator is connected in star and the rotor is connected in delta.
In the introduction and also in the following chapters, the CDFM is described as a brushless machine arrangement with directly interconnected rotor windings. However, the laboratory machines are arranged in a slightly different way to match the voltage and current ratings of the individual machine windings. Machine A had to be connected the other way round so that following machine connection is used: side 1 is the delta connected rotor of the HOMES machine and is therefore connected via slip-rings and a variac to the supply network. The variac is needed to bring the voltage level down from the supply to the delta connected machine side. The stator of the HOMES machine, side 2, is connected to the rotor of the BROOK machine, side 3, via slip-rings. Consequently, side 4 is the stator of the BROOK machine and is connected to the machine-side inverter. Although set up in the

described way and using slip-rings the electrical behaviour of the CDFM remains unchanged.

A 3.75 kW HIGGS DC-machine acts as a prime mover for the SDFM / CDFM. Despite being of series wound machine type the connection is in separately exited mode to allow easier control. The machine is rated for 35.8 Nm at 1000 rpm. Two separate transformer arrangements are required to provide the low-voltage high-current rating of the field and armature winding.
A manually controlled dc/dc converter is connected to the armature winding. Only current control and therefore torque control of the DC-machine is possible. No closed speed loop arrangements are provided.

The DC-machine possesses a through shaft allowing mechanical connection to a wound rotor induction machine on either side. The physical bed-plate arrangement is shown in figure 2.3, where the DC-machine is the middle machine. An incremental encoder is mounted on the HOMES wound rotor induction machine generating the pulses for position measurement.

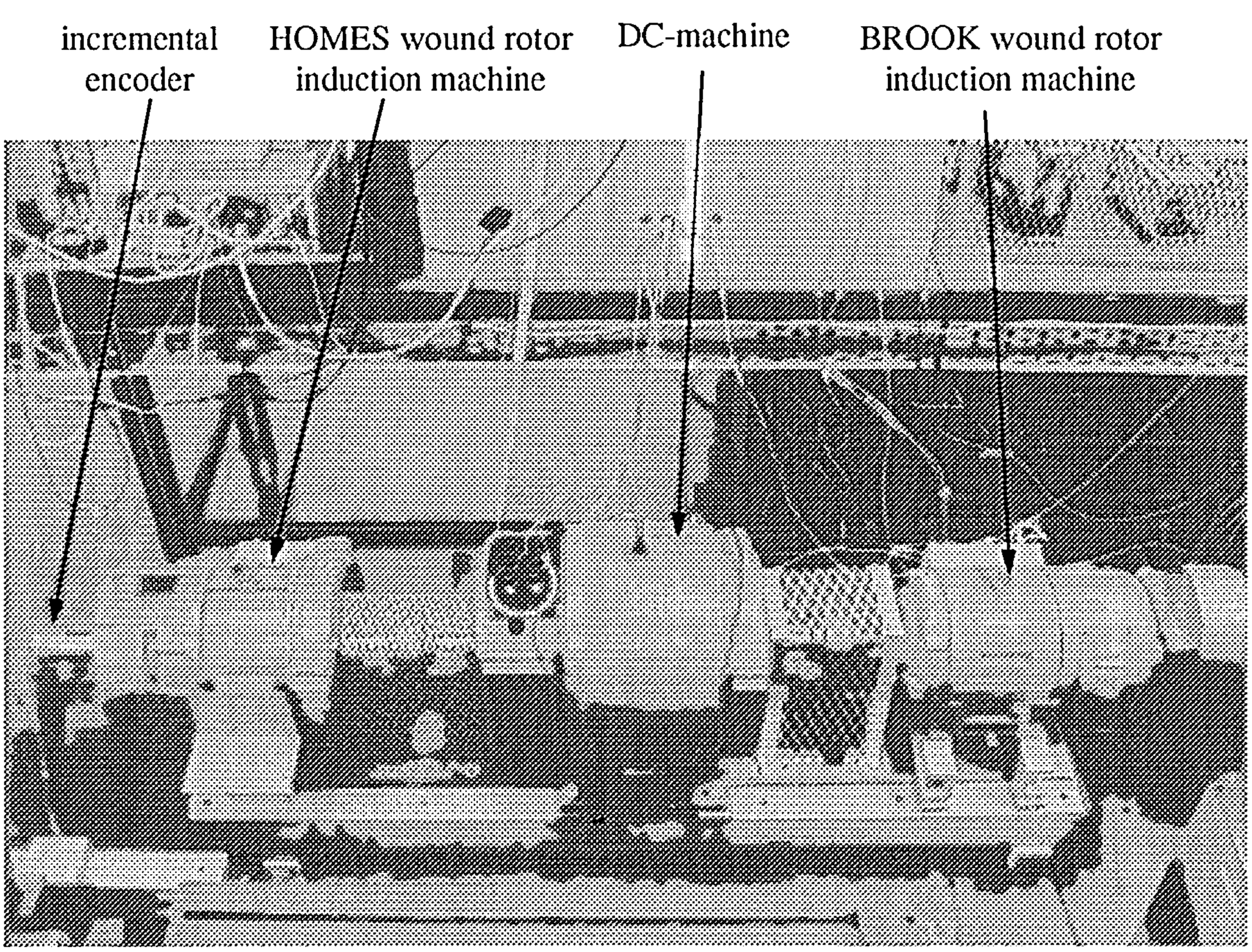

Figure 2.3: Picture of bed-plate machine arrangement

2.1.2 Power Converter

The converter is a modified BOSCH Servodyn-D [f24] power converter consisting of following modules:

- Grid connection module
- Line inductors
- Supply module
- Inverter module

The configuration of the power converter is shown in figure 2.4.

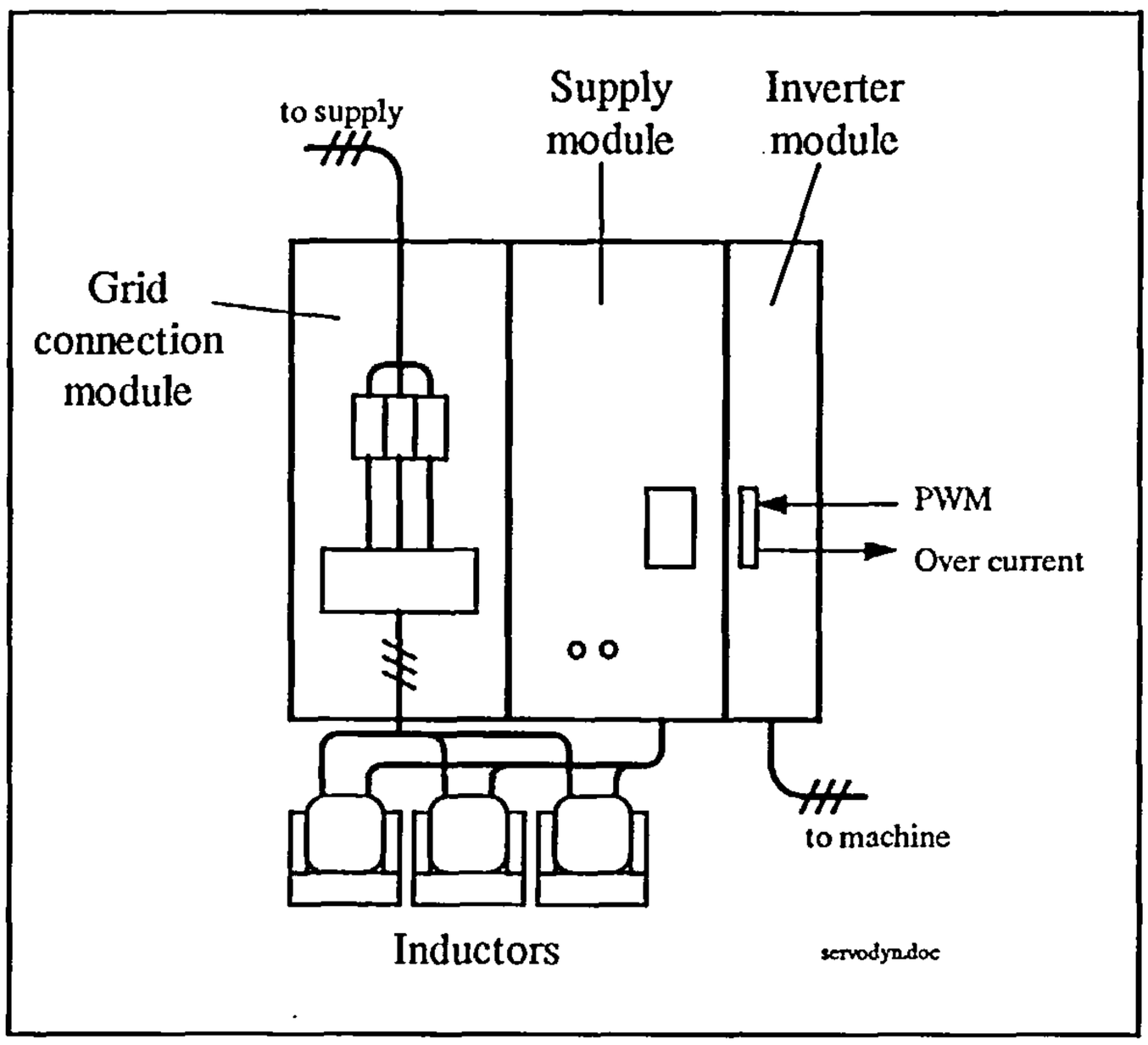

Figure 2.4: BOSCH power converter unit

The *grid connection module* contains fuses and contactors for connection to a 3-phase 380...415 V supply network.

Three 1 mH *inductors* are placed between the grid connection module and the supply module to decouple the grid from the d.c.-link.

The *supply module* contains a 4-quadrant controlled front-end or line-side inverter and provides the d.c.-link for the remaining inverter module. As an independent functioning unit it controls the d.c.-link to 650 V at unity power factor at the grid connection point. The module is rated for 47 kW / 68 A and has a switching frequency of 7.45 kHz.

The *inverter module* contains the machine-side inverter and is rated for 7 A. This module had to be modified in order to interface it with the externally used controller unit. The

original controller card in the inverter module had to be removed and was replaced by an interface circuit to provide a connection for the PWM signals to the driver circuits of the module.
An over-current signal generated by the module internal over current detection circuit is used to shut down the PWM signals coming from the microcontroller card.

The supply module and the inverter module are mounted on and connected via a back panel module which provides the d.c.-link connection.

2.1.3 Interfaces

As shown in figure 2.1 there are several interface circuits present in the laboratory drive set-up. The main task of those circuits is the electrical isolation between power and control circuits and the initial processing of sensed signals for further use.

Interface 1
The microcontroller µC 1 generates three PWM signals. An electronic circuit, on the same board as µC 1, generates the remaining three PWM signals and adds dead-time to them. The six PWM signals are then sent to the inverter module of the power converter. A circuit in the inverter module including optocouplers is responsible for electrical isolation and connection to the driver circuits for the IGBT modules of the machine-side inverter.
The interface unit 1, shown as one unit in figure 2.1, is split up in two circuits, one on the µC 1 board and one within the inverter module. This is due to the pre-designed microcontroller board.

Interface 2
The sensing of the controlled rotor current (SDFM) or side 4 current (CDFM) is accomplished with three LEM LTA 50P/SP1 current transducers. Each individual line current is sensed. An operational amplifier circuit processes the signals to give a voltage range of 0-5 V for a maximum peak current of 13.28 A. This voltage signal is fed to the ADC of µC 1.

Interface 3
The incremental encoder provides two 90° phase shifted rectangular pulse trains (5000 pulses per revolution) and a reference pulse for each revolution. A differential line receiver and an optocoupler stage provide the connection of the TTL pulses to µC 1 for position and speed calculation.

Interface 4

Interface circuit 4 is responsible for the sensing of the stator or side 1 current and voltage. Two line currents are sensed with a LEM current transducer LA 25-NP. As for interface 2, an operational amplifier prepares the signal from the transducer to produce a voltage range of 0-5 V for a peak current of 16.67 A. This signal is fed to the ADC of µC 2.
Two operational amplifier circuits are used to scale two *phase* supply voltage measurements to give a voltage range of 0 - 5 V for a peak voltage of 367 V for ADC with µC 2.

DAC - Card

A digital-analog-conversion card with six 12-bit DAC IC's allows to output internal control variables for display and data sampling purposes with an oscilloscope.

Data Storage Card

A data storage card can be used for storing the microcontroller internal 16-bit variables. After storage the data is read out via a parallel connection to the PC and saved to a data file.

EPROM Emulator

An EPROM emulator card (not shown in figure 2.1) is used during software development cycles to download compiled code. The program code is then read by the respective microcontroller. Only one microcontroller at a time can be connected to the emulator. The emulator is connected to a parallel port of the PC.
Using the EPROM emulator eases the software design process and reduces EPROM burning to a minimum.

Other connections

A serial link from µC 1 to the PC allows a screen display of non-real-time critical data such as speed, control parameters, etc.
Also, µC 1 and µC 2 output TTL signals for timing monitoring with an oscilloscope.

2.1.4 Control System

As the control hardware two 80C167 microcontroller boards are available. The boards were donated by Microtech Ltd. and are originally designed for laser firing circuit control. As a consequence, the pre-designed microcontroller boards had to be modified for the intended machine control purpose. Figure 2.5 shows a picture of the microcontroller boards, which are on the top level of the control rack.
The 80C167 [f22] is a 16-bit fixed-point microcontroller for real-time embedded control

applications. Its advantage is the high level of on-chip integration of peripheral subsystems. Among those are a 10-bit ADC unit, a PWM unit, general purpose time units and communication channels.

Both microcontrollers are used and configured as shown in figure 2.1. µC 1 performs most of the control functions, which include current control with PWM generation, position and speed calculation. Its PWM unit synchronised interrupt request sets the switching frequency of the machine-side inverter and also determines the available processing time. Initially a 4 kHz switching frequency was used and later lowered to 2.5 kHz to extend calculation time. To synchronise both microcontrollers, µC 1 generates a signal to produce an external interrupt request in µC 2. µC 2 performs the remaining functions such as angle calculation, power calculation and power control. The microcontrollers communicate via the high speed synchronous link. At the end of each cycle µC 2 sends required control variables to µC 1 for further processing in the successive control cycle. The ADC tasks are shared between the microcontrollers depending on the respective control functions.

Both microcontrollers are programmed using the high level language "C".

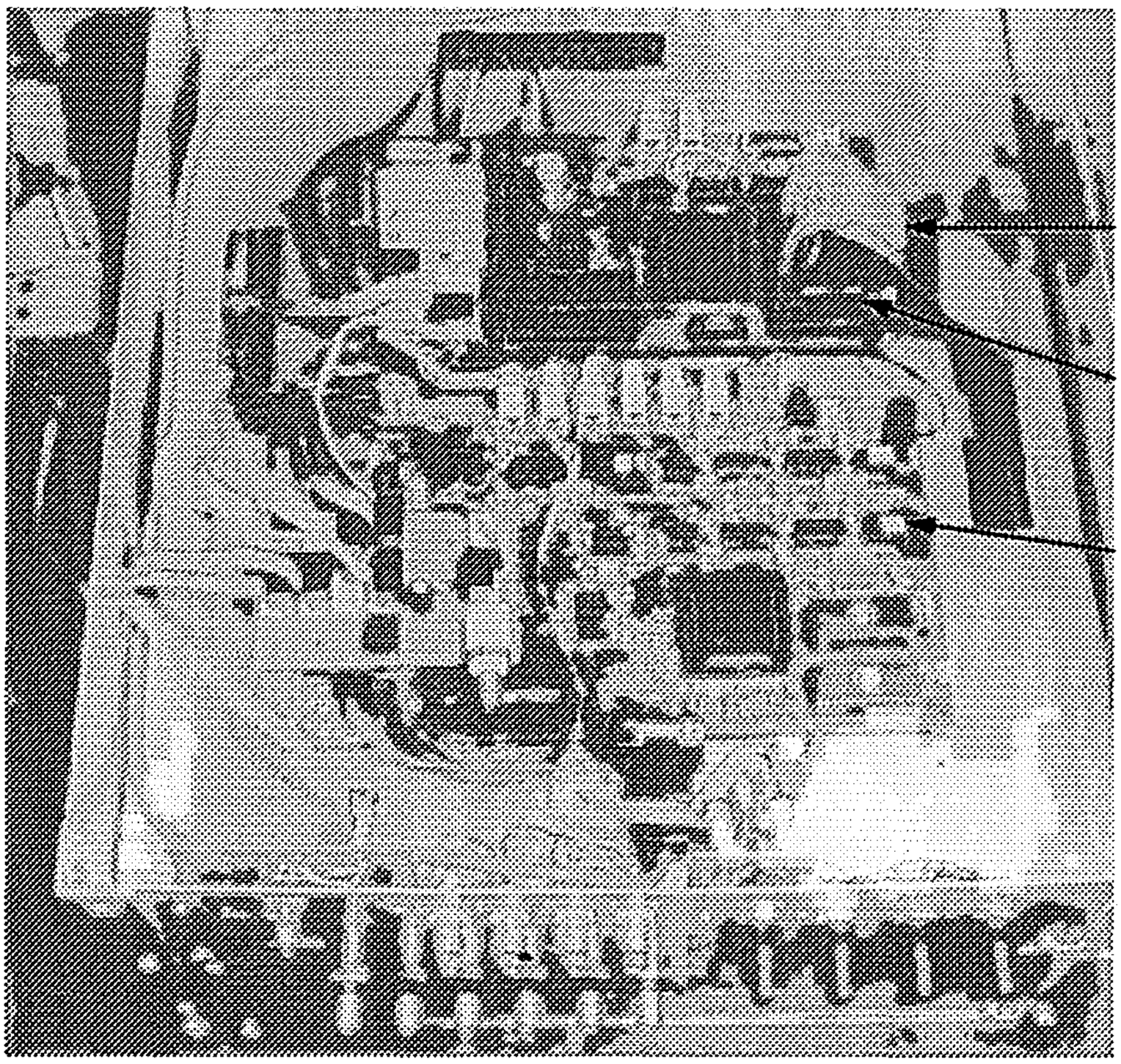

Figure 2.5: Picture of microcontroller boards

2.2 Summary

The experimental laboratory set-up with a brief explanation of the individual subsystems are described in this chapter. Also, pictures shown in the previous pages help to get an impression of the laboratory arrangement.
A more in depth treatment and description of the hardware set-up can be found in appendices A - C.

Chapter 3

Single Doubly-Fed Induction Machine

The SDFM or wound rotor induction machine can nowadays be seen as a generally well understood electrical machine. In comparison to the cage induction machine the rotor windings are not short circuited, but brought out via slip rings as shown in figure 3.1. From there, the three rotor phases are accessible with brushes. Figure 3.1 also contains the adopted nomenclature and naming of the two machine sides, side 1 and side 2.
Descriptions of SDFM's can be found in standard literature [f2, f3] together with the appropriate field oriented control structure.

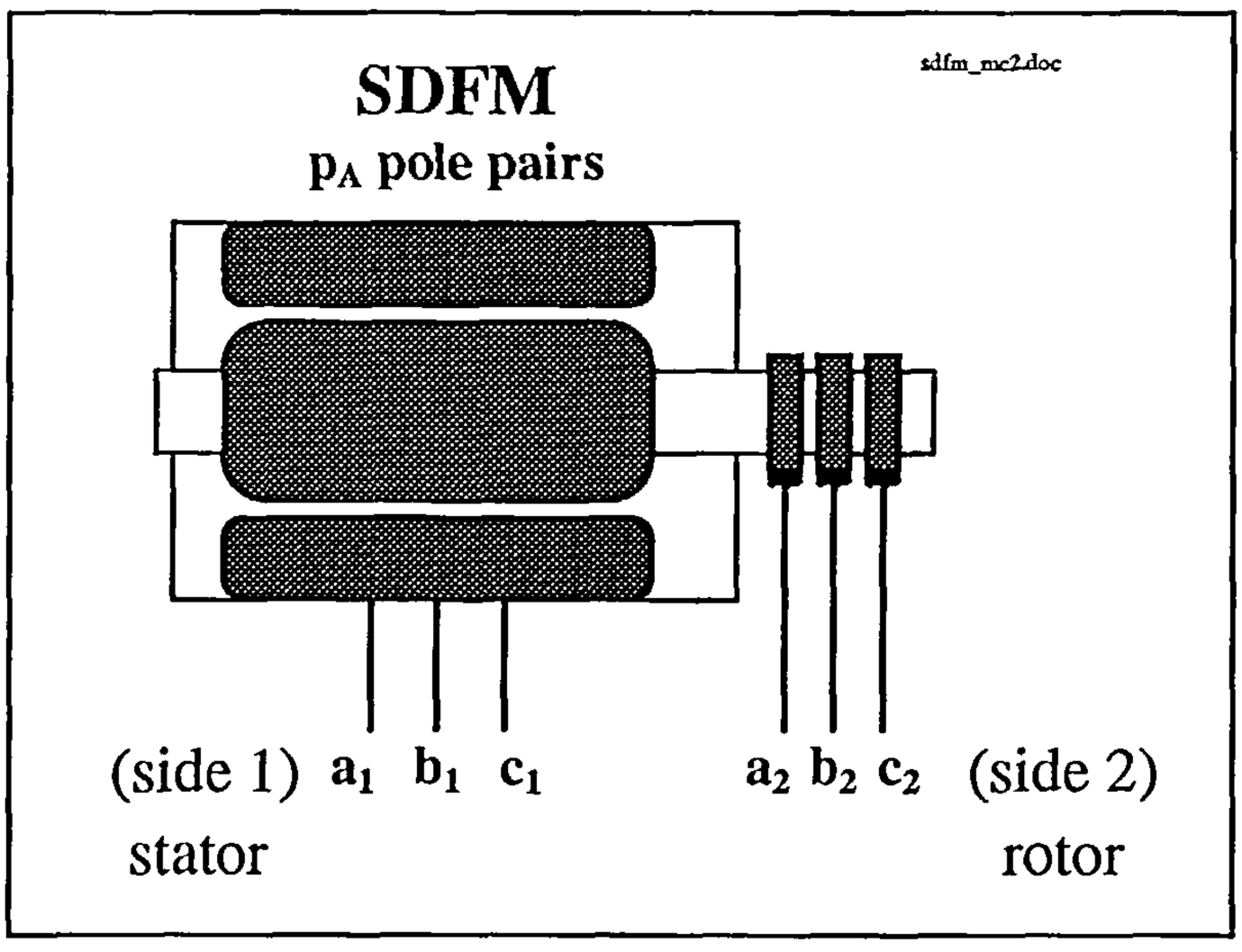

Figure 3.1: Single doubly-fed machine

This chapter serves mainly as a foundation for the CDFM theory in chapter 4 and chapter 5 and for the sensorless control of the SDFM in chapter 6. Beginning with the space vector theory and the dynamic machine model derivation of the SDFM, it moves on to the per-phase equivalent circuit and to steady state simulations. The simulations give a clear picture of the active and reactive power flow behaviour in the machine. This power flow can be controlled independently by field orientation, which is demonstrated in the last section of this chapter.

3.1 Space Vector Representation and Dynamic Model

To gain insight in the structure of the SDFM and its field oriented control a dynamic model based on space vectors is developed. The space vector method allows representation of the electrical machine quantities in a 2-phase system, 2-dimensional complex plane or reference frame instead of a 3-phase representation. This requires that 3-to-2 and 2-to-3 phase transformations are performed. A dynamic machine model of the SDFM by means of the compact space vectors yields a clear physical picture of the machine behavior and the field oriented control and incorporates all dynamic effects occurring during steady state and transient operation.

3.1.1 Space Vector Representation

The dynamic machine model is subject to following assumptions:

- the machine is a smooth-air-gap machine with radial flux density
- the windings are symmetrical three phase windings
- no zero-sequence components
- end-windings and slot effects are ignored
- permeability of iron is infinite
- saturation and iron losses are neglected

The phase voltage equation for each individual stator winding in its natural stator reference frame, denoted as frame "a", is

$$v_{1a}^{a} = R_1 i_{1a}^{a} + \frac{d\Psi_{1a}^{a}}{dt} \tag{3.1.1}$$

$$v_{1b}^{a} = R_1 i_{1b}^{a} + \frac{d\Psi_{1b}^{a}}{dt} \tag{3.1.2}$$

$$v_{1c}^{a} = R_1 i_{1c}^{a} + \frac{d\Psi_{1c}^{a}}{dt} \tag{3.1.3}$$

where

R_1 is the stator resistance per phase

v_{1a}^{a}, v_{1b}^{a} and v_{1c}^{a} are the instantaneous stator phase voltages in the stator reference frame

i_{1a}^{a}, i_{1b}^{a} and i_{1c}^{a} are the instantaneous stator phase currents in the stator reference frame

Ψ_{1a}^{a}, Ψ_{1b}^{a} and Ψ_{1c}^{a} are the instantaneous stator phase flux linkages in the stator reference frame

The reference frames of a SDFM with the appropriate 3-phase systems are depicted in figure 3.2. Reference frame "a" is attached to the stator windings and reference frame "b" is

attached to the moving rotor windings. In both cases the direct "d-axis" of the 2-phase reference frame is aligned with "phase a" and the quadrature "q-axis" is perpendicular to the "d-axis" in direction towards "phase b" of the 3-phase system. As shown, the "b"-frame is moving relative to the stationary "a"-frame with the mechanical rotor speed ω_r in electrical radians per second.

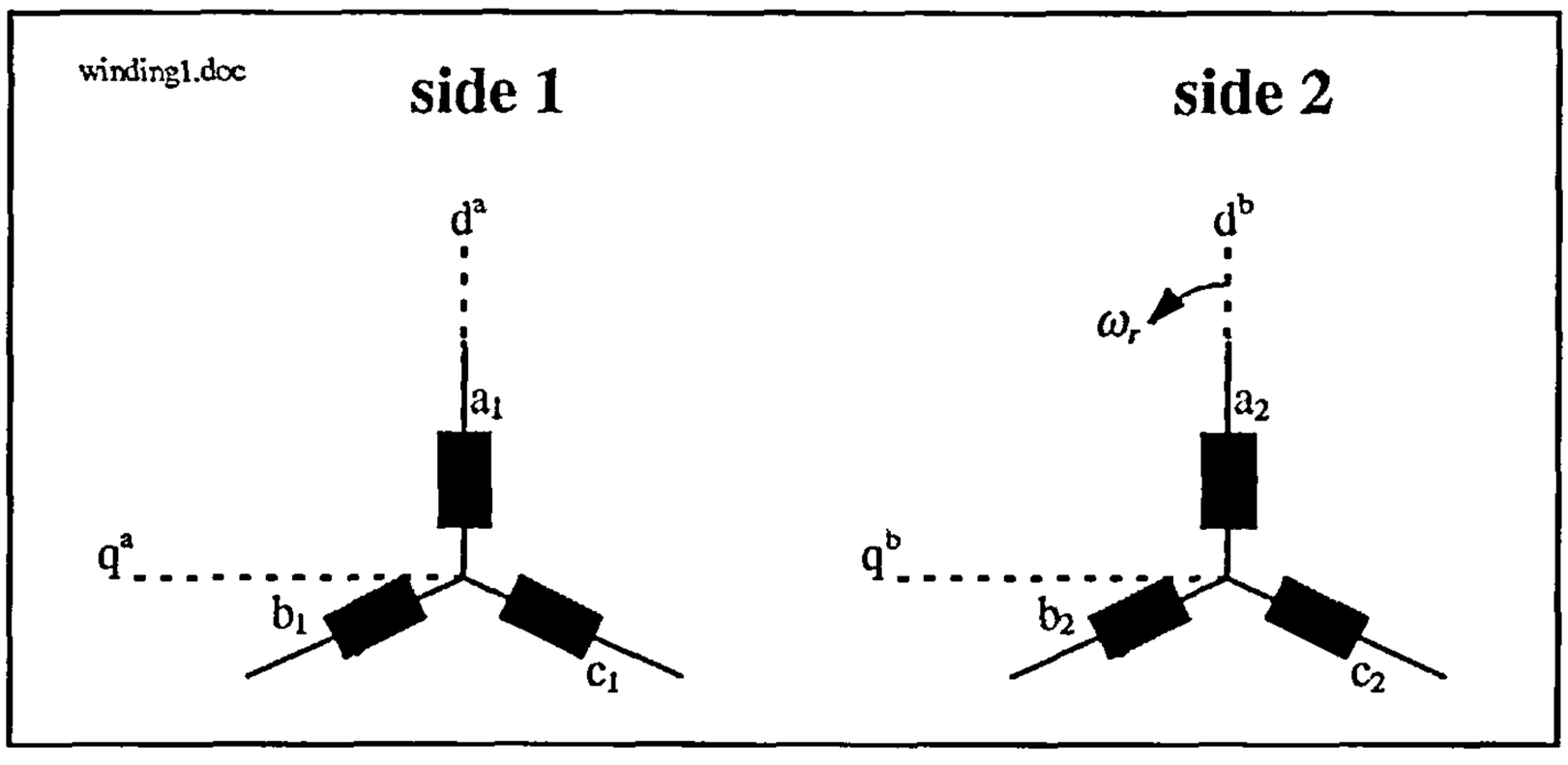

Figure 3.2: Windings and reference frames for the SDFM

The 2-dimensional stator voltage space vector in its natural reference frame is defined as

$$\bar{v}_1^a = \frac{2}{3}(v_{1a}^a + a v_{1b}^a + a^2 v_{1c}^a) \tag{3.1.4}$$

with

$$a = e^{j120^\circ} = -\frac{1}{2} + j\frac{\sqrt{3}}{2} \tag{3.1.5}$$

$$a^2 = e^{j240^\circ} = -\frac{1}{2} - j\frac{\sqrt{3}}{2} \tag{3.1.6}$$

similarly the stator current and flux linkage vectors can be defined as

$$\bar{i}_1^a = \frac{2}{3}(i_{1a}^a + a i_{1b}^a + a^2 i_{1c}^a) \tag{3.1.7}$$

$$\bar{\Psi}_1^a = \frac{2}{3}(\Psi_{1a}^a + a \Psi_{1b}^a + a^2 \Psi_{1c}^a) \tag{3.1.8}$$

It has to be noted, that the complex factor "a" of (3.1.5) and (3.1.6) is different to the reference frame naming "a".

Substituting the stator phase voltage equations (3.1.1)-(3.1.3) into (3.1.4) together with (3.1.7) and (3.1.8) then the stator voltage space vector expressed in the stator reference frame results in the form

$$\bar{v}_1^a = R_1 \bar{i}_1^a + \frac{d\bar{\Psi}_1^a}{dt} \tag{3.1.9}$$

This voltage vector determines the instantaneous magnitude and angular position of the peak of the sinusoidally distributed voltage wave in the complex plane produced by the three spatially displaced stator windings.

The flux linkage vector in (3.1.8) can be expressed in terms of stator and rotor current vectors together with L_1 as the stator self inductance and L_m as the mutual inductance as

$$\bar{\Psi}_1^a = L_1 \bar{i}_1^a + L_m \bar{i}_2^a \qquad (3.1.10)$$

It has to be pointed out that $\bar{i}_2^a$ is the rotor current vector expressed in the reference frame "a" attached to the stator.

Applying similar procedure to the rotor leads to the rotor voltage and flux linkage space vector expressed in a reference frame "b" attached to the rotor windings

$$\bar{v}_2^b = R_2 \bar{i}_2^b + \frac{d\bar{\Psi}_2^b}{dt} \qquad (3.1.11)$$

$$\bar{\Psi}_2^b = L_2 \bar{i}_2^b + L_m \bar{i}_1^b \qquad (3.1.12)$$

L_2 is the rotor self inductance and $\bar{i}_1^b$ is the stator space vector in the rotor reference frame.

Since the space vectors are represented in a complex plane it is also possible to write the stator voltage vector in terms of a direct "d" and quadrature "q" component. Equation (3.1.4) can therefore be stated as

$$\bar{v}_1^a = v_{d1}^a + j v_{q1}^a = \sqrt{2}\bar{V}_1 e^{j\omega_1 t} \qquad (3.1.13)$$

where

$\bar{V}_1 = V_1 e^{j\alpha_1}$ is the complex stator voltage phasor

ω_1 is the angular frequency of the stator quantities

The same is valid for the stator current and flux linkage vector

$$\bar{i}_1^a = i_{d1}^a + j i_{q1}^a \qquad (3.1.14)$$

$$\bar{\Psi}_1^a = \Psi_{d1}^a + j\Psi_{q1}^a \qquad (3.1.15)$$

and for the rotor voltage, current and flux linkage space vector in the rotor reference frame "b"

$$\bar{v}_2^b = v_{d2}^b + j v_{q2}^b \qquad (3.1.16)$$

$$\bar{i}_2^b = i_{d2}^b + j i_{q2}^b \qquad (3.1.17)$$

$$\bar{\Psi}_2^b = \Psi_{d2}^b + j\Psi_{q2}^b \qquad (3.1.18)$$

3-to-2 and 2-to-3 Phase Transformations

The transformation from a 3-phase system into a 2-phase quadrature system is performed with the help of the non-power-invariant transformation. The non-power-invariant form has the advantage that the projection of the space vector onto the phase axes directly yields the

instantaneous values of the phase variable of that quantity. However, this transformation requires a scaling factor in the torque and power equations as will be seen later.

The fictitious 2-phase stator voltage components of (3.1.13) are related to the physical 3-phase stator voltages as

$$v_{d1}^{a} = \frac{2}{3} v_{1a}^{a} - \frac{1}{3} v_{1b}^{a} - \frac{1}{3} v_{1c}^{a}$$

$$v_{q1}^{a} = \frac{1}{\sqrt{3}} (v_{1b}^{a} - v_{1c}^{a}) \qquad (3.1.19)$$

The corresponding transformation of the stator voltage vector from a 2-phase system into a 3-phase system follows as

$$v_{1a}^{a} = v_{d1}^{a}$$

$$v_{1b}^{a} = -\frac{1}{2} v_{d1}^{a} + \frac{\sqrt{3}}{2} v_{q1}^{a} \qquad (3.1.20)$$

$$v_{1c}^{a} = -\frac{1}{2} v_{d1}^{a} - \frac{\sqrt{3}}{2} v_{q1}^{a}$$

All the 3-to-2 and 2-to-3 transformations apply as well to the remaining stator and rotor quantities. Figure 3.3 shows the general symbolic transformation.

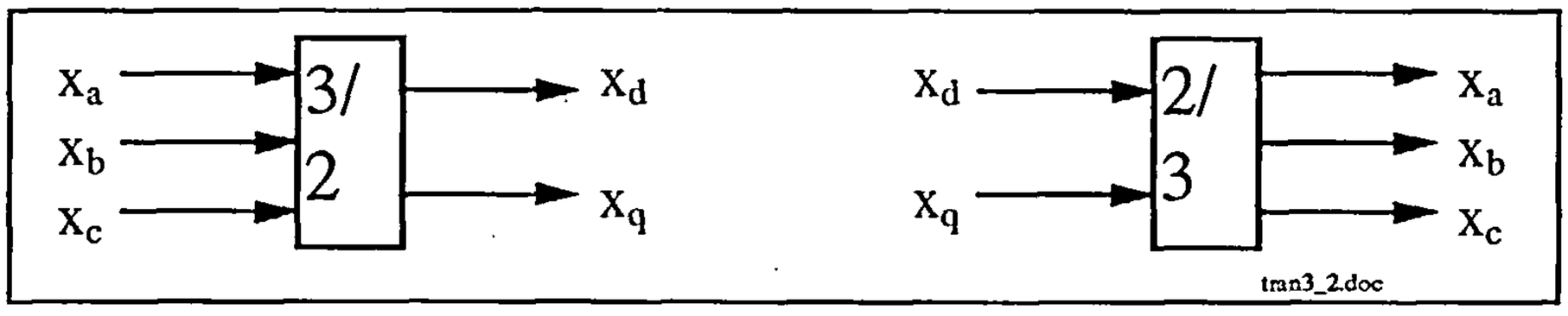

Figure 3.3: General symbolic 3-to-2 and 2-to-3 phase transformation

Reference Frame Transformations

As already introduced for equation (3.1.10) and (3.1.12) the individual space vectors can be transformed from one reference frame into another. This is necessary in order to see for example the effect of the rotor current upon the stator flux linkage in the reference frame attached to the stator as in equation (3.1.10). In this case it is important to turn or transform the rotor current vector from the rotor reference frame "b" onto the stator reference frame "a" by the angle of the mechanical rotation as

$$\bar{i}_2^{a} = \bar{i}_2^{b} e^{j\Theta_r} \quad \text{or} \quad \begin{bmatrix} i_{d2}^{a} \\ i_{q2}^{a} \end{bmatrix} = \begin{bmatrix} cos\Theta_r & -sin\Theta_r \\ sin\Theta_r & cos\Theta_r \end{bmatrix} \begin{bmatrix} i_{d2}^{b} \\ i_{q2}^{b} \end{bmatrix} \qquad (3.1.21)$$

where

Θ_r is the rotor position angle in electrical radians between side 1 reference frame "a" and side 2 reference frame "b" as illustrated in figure 3.4

For reverse rotation of the stator current vector from the stationary stator reference frame "a" to the rotor reference frame "b" as in equation (3.1.12) is as

$$\bar{i}_1^b = \bar{i}_1^a e^{-j\Theta_r} \quad \text{or} \quad \begin{bmatrix} i_{d1}^b \\ i_{q1}^b \end{bmatrix} = \begin{bmatrix} cos\Theta_r & sin\Theta_r \\ -sin\Theta_r & cos\Theta_r \end{bmatrix} \begin{bmatrix} i_{d1}^a \\ i_{q1}^a \end{bmatrix} \tag{3.1.22}$$

The rotation or transformation of space vectors is a very important feature of field oriented control. They are important to describe the dynamic model of the SDFM in different reference frames.

Generally, a space vector is multiplied by a factor of $e^{-j\alpha}$, when the rotation of the reference frame is in positive mathematical direction and multiplied by the factor $e^{j\alpha}$ in reverse direction, where α is the angle between the two reference frames.

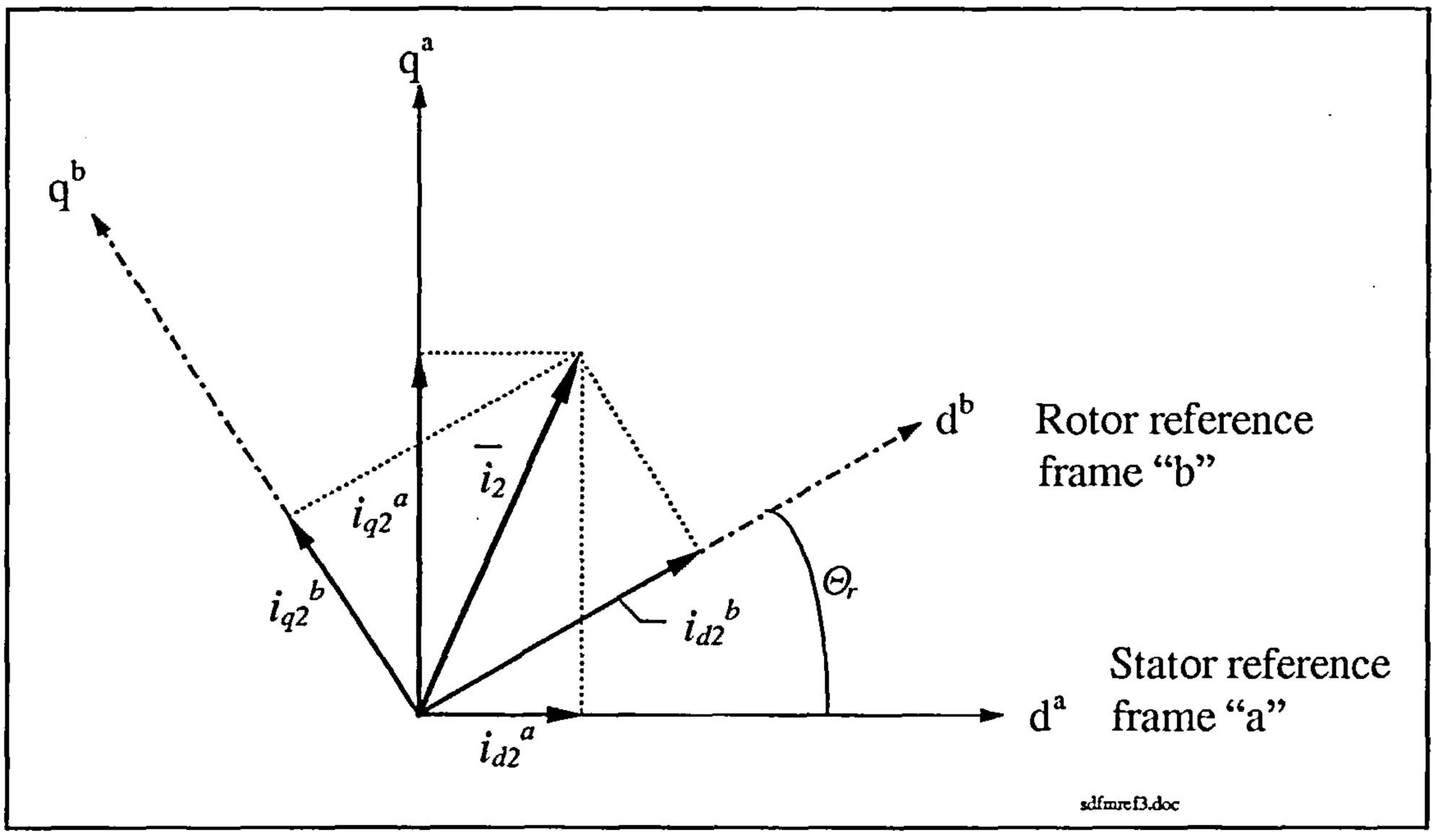

Figure 3.4: Rotor current space vector in rotor reference frame "b" and stator reference frame "a"

3.1.2 Electrical Torque and Mechanical Dynamics

The electromagnetic torque produced by the SDFM can be obtained based on energy balance [f3] and is expressed as a cross product of the stator flux linkage space vector and the rotor current space vector in the stator reference frame "a" as

$$T_e = -\frac{3}{2} p_A \frac{L_m}{L_1} (\overline{\Psi}_1^a \times \bar{i}_2^a) \qquad (3.1.23)$$

with p_A as the pole pair number of the SDFM

The torque equation is independent of the respective reference frame as long as the involved space vectors are expressed in the same reference frame.

To describe the dynamic behavior of a mechanical drive with constant inertia the equations of motion as

$$T_e - T_L = \frac{J}{p_A} \frac{d\omega_r}{dt} \qquad (3.1.24)$$

and

$$\frac{d\Theta_r}{dt} = \omega_r \qquad (3.1.25)$$

are needed. In there

T_L is the load torque

J is the mechanical inertia

ω_r is the angular rotor speed in electrical radians per second

3.1.3 Dynamic Model

To describe the dynamic model of the SDFM in a general reference frame "g" it is essential to rotate all the space vectors from their natural reference frame into the "g" frame. The model in the "g" frame has the advantage of being general, providing a platform an which to develop a model of the SDFM in a particular reference frame, as is the case with field orientation. Figure 3.5 clarifies the transformation angles and the different angular speed descriptions. The angular speeds ω_r and ω_s are relative to the stationary reference frame "a".

Based on figure 3.5 the rotations of the different space vectors into the reference frame "g" in the case of stator quantities are

$$\bar{v}_1^g = \bar{v}_1^a e^{-j\Theta_g} \qquad \bar{i}_1^g = \bar{i}_1^a e^{-j\Theta_g} \qquad \overline{\Psi}_1^g = \overline{\Psi}_1^a e^{-j\Theta_g} \qquad (3.1.26)$$

and for the rotor quantities are

$$\bar{v}_2^g = \bar{v}_2^b e^{-j(\Theta_g - \Theta_r)} \qquad \bar{i}_2^g = \bar{i}_2^b e^{-j(\Theta_g - \Theta_r)} \qquad \overline{\Psi}_2^g = \overline{\Psi}_2^b e^{-j(\Theta_g - \Theta_r)} \qquad (3.1.27)$$

The substitution of equation (3.1.26) and (3.1.27) into (3.1.9) and (3.1.11) yield the stator and rotor voltage space vectors expressed in the general reference frame "g"

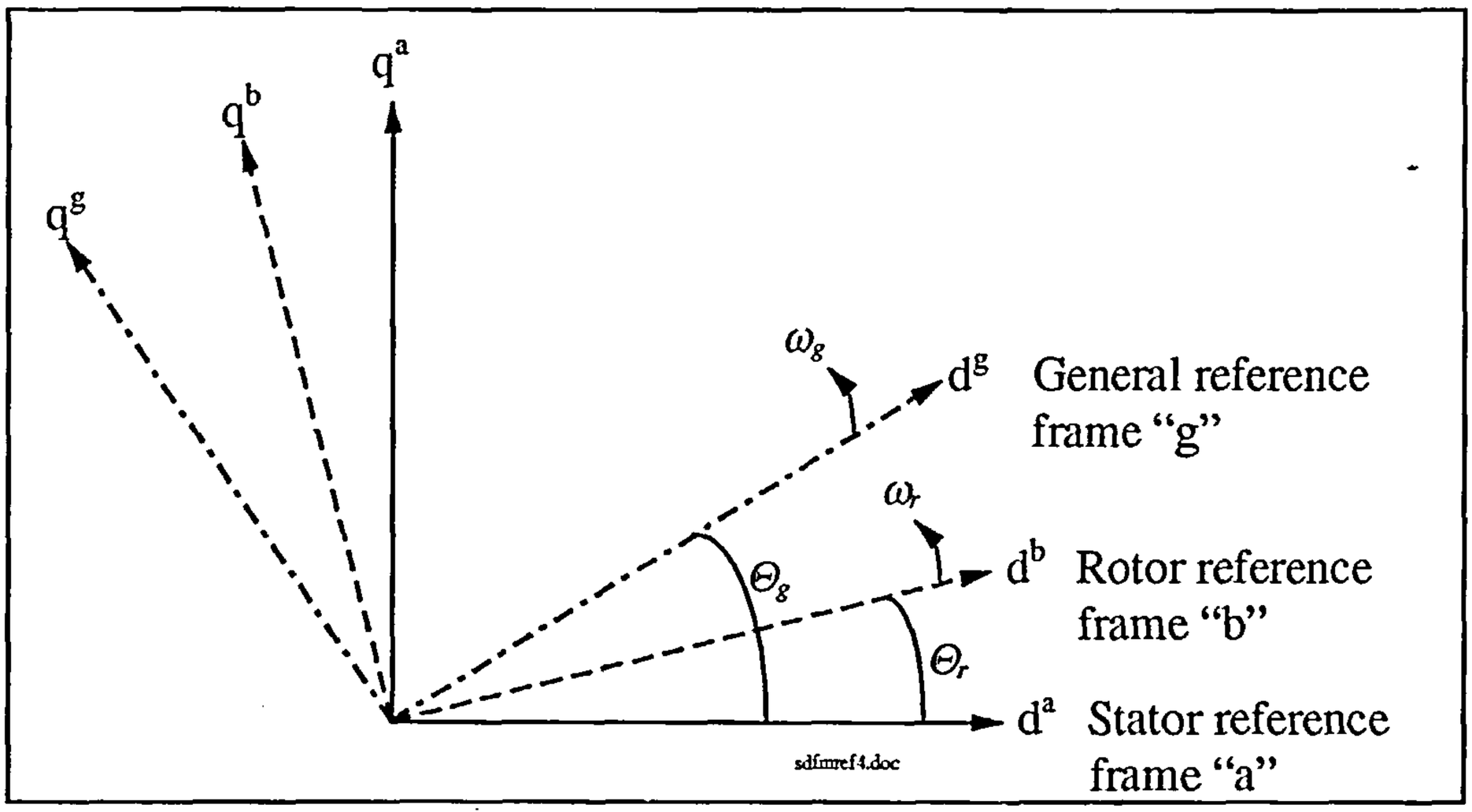

Figure 3.5: Reference frames and angles for the SDFM

$$\bar{v}_1^g = R_1\bar{i}_1^g + \frac{d\bar{\Psi}_1^g}{dt} + j\omega_g\bar{\Psi}_1^g \tag{3.1.28}$$

$$\bar{v}_2^g = R_2\bar{i}_2^g + \frac{d\bar{\Psi}_2^g}{dt} + j(\omega_g - \omega_1)\bar{\Psi}_2^g \tag{3.1.29}$$

where the stator and rotor flux linkages in the general reference frame "g" can be expressed in terms of the stator and rotor current vectors as

$$\bar{\Psi}_1^g = L_1\bar{i}_1^g + L_m\bar{i}_2^g \tag{3.1.30}$$

$$\bar{\Psi}_2^g = L_2\bar{i}_2^g + L_m\bar{i}_1^g \tag{3.1.31}$$

By combining equations (3.1.28)-(3.1.31) and employing the rules of differentiation the following two voltage equations result

$$\bar{v}_1^g = R_1\bar{i}_1^g + L_1\frac{d\bar{i}_1^g}{dt} + L_m\frac{d\bar{i}_2^g}{dt} + j\omega_g(L_1\bar{i}_1^g + L_m\bar{i}_2^g) \tag{3.1.32}$$

$$\bar{v}_2^g = R_2\bar{i}_2^g + L_2\frac{d\bar{i}_2^g}{dt} + L_m\frac{d\bar{i}_1^g}{dt} + j(\omega_g - \omega_r)(L_2\bar{i}_2^g + L_m\bar{i}_1^g) \tag{3.1.33}$$

Separating equation (3.1.32) and (3.1.33) into its 2-dimensional components and using matrix formation then the model of the SDFM expressed in the "g" frame can be written as

$$\begin{bmatrix} v_{d1}^g \\ v_{q1}^g \\ v_{d2}^g \\ v_{q2}^g \end{bmatrix} = \begin{bmatrix} R_1 + pL_1 & -\omega_g L_1 & pL_m & -\omega_g L_m \\ \omega_g L_1 & R_1 + pL_1 & \omega_g L_m & pL_m \\ pL_m & -(\omega_g - \omega_r)L_m & R_2 + pL_2 & -(\omega_g - \omega_r)L_2 \\ (\omega_g - \omega_r)L_m & pL_m & (\omega_g - \omega_r)L_2 & R_2 + pL_2 \end{bmatrix} \begin{bmatrix} i_{d1}^g \\ i_{q1}^g \\ i_{d2}^g \\ i_{q2}^g \end{bmatrix} \tag{3.1.34}$$

with

p as the differential operator $\frac{d}{dt}$

Equation (3.1.34) together with the mechanical equation (3.1.24) and (3.1.25) defines the complete dynamic model of the SDFM.

It has to be noted that in the preceding equations the effect of a possible turns-ratio between stator and rotor windings is assumed to be of unity value to simplify the derivation of the dynamic model and the field oriented control. In case a non-unity turns-ratio is involved it is necessary to refer all dynamic equations to the same number of turns, which is usually the stator number of turns (see Appendix D).

3.2 Steady State

Before dealing with the control of the SDFM it is advantageous to remain with the steady state relationships of the SDFM for a while. Initially looking at the steady state model assists in familiarising with the electrical behaviour.

3.2.1 Per-Phase Equivalent Circuit

If the stator windings are supplied by a sinusoidal voltage, then in steady state and by using complex phasor notation the stator voltage equation per phase follows as

$$\bar{V}_1 = R_1\bar{I}_1 + j\omega_1 L_{\sigma 1}\bar{I}_1 + \bar{E}_{1ag} \qquad (3.2.1)$$

where

$L_{\sigma l}$ is the stator leakage inductance

E_{1ag} is the induced stator e.m.f. due to the mutual air-gap flux in the machine

The rotor voltage equation per phase can be written as

$$\bar{V}_2 = R_2\bar{I}_2 + j\omega_2 L_{\sigma 2}\bar{I}_2 + \bar{E}_{2ag} \qquad (3.2.2)$$

with

$L_{\sigma 2}$ as the rotor leakage inductance

E_{2ag} as the induced rotor e.m.f. due to the mutual air-gap flux in the machine

ω_2 as the rotor electrical angular frequency

In comparison to the dynamic model in section 3.1 the steady state model takes account of the iron losses of the machine. As it is common practice in steady state analysis of induction

machines the iron losses are assumed to be concentrated in the stator only and are represented by a resistance R_{fe} in parallel to the magnetising inductance L_{mag}. Although the rotor of a SDFM encounters larger frequencies than that of a cage induction machine and therefore is subject to variations in iron losses it is assumed that the value of the iron loss resistor stays constant. The iron losses are included in the steady state analysis and later in the steady state simulations in order to model the behavior of the SDFM as close as possible to reality.

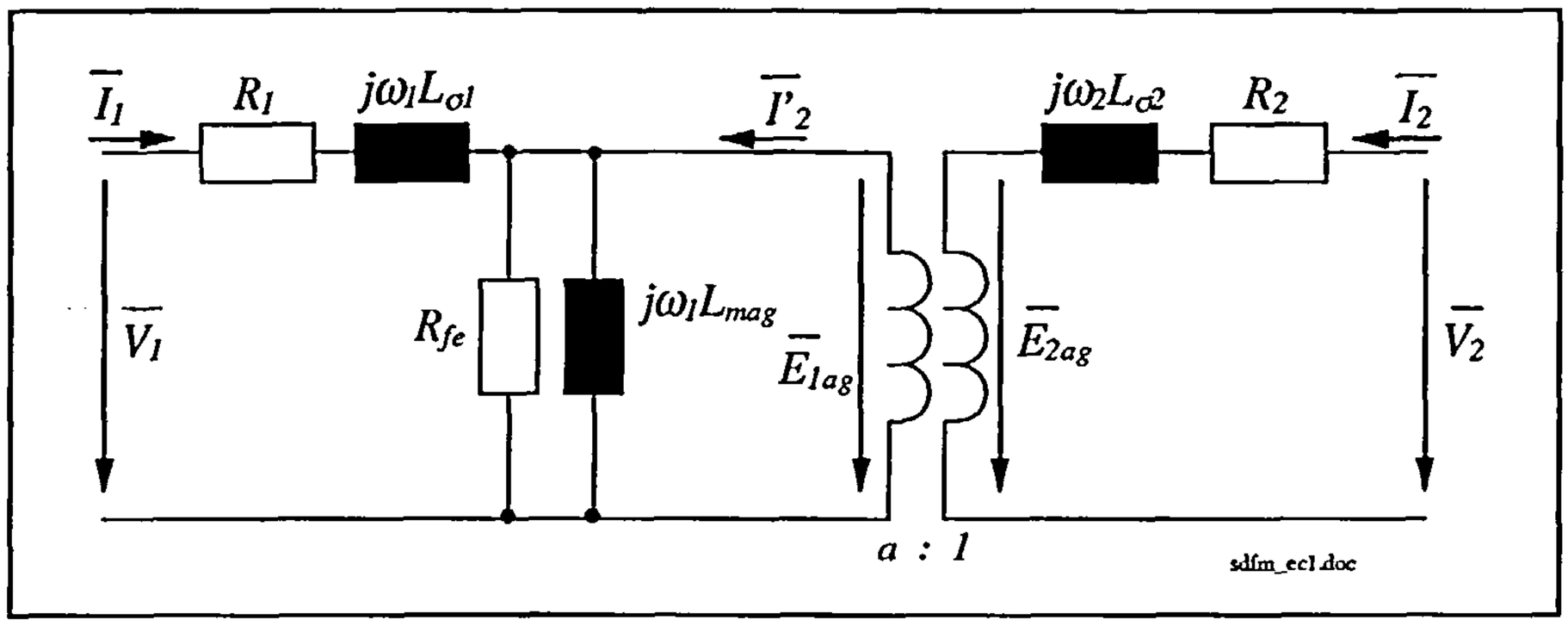

Figure 3.6: Per-phase steady state equivalent circuit of the SDFM

As can be seen in figure 3.6 the stator e.m.f. can be defined as the voltage across the magnetising path

$$\overline{E}_{1ag} = \frac{\overline{I}_1 + \overline{I}'_2}{\overline{Y}_{mag}} \tag{3.2.3}$$

with

$$\overline{Y}_{mag} = \frac{1}{R_{fe}} + \frac{1}{j\omega_1 L_{mag}} \tag{3.2.4}$$

as the magnetising admittance and

$$\overline{I}'_2 = \frac{\overline{I}_2}{a} \tag{3.2.5}$$

as the stator referred rotor current phasor. In (3.2.5) $a = \frac{N_1}{N_2}$ is the effective turns ratio between stator and rotor windings. The rotor e.m.f. can now be written as

$$\overline{E}_{2ag} = \overline{E}_{1ag} \frac{s}{a} \tag{3.2.6}$$

by introducing the slip

$$s = \frac{\omega_2}{\omega_1} = \frac{f_2}{f_1} \tag{3.2.7}$$

and f_1 as the stator frequency and f_2 as the rotor frequency.

The slip can also be defined as the relative difference between the synchronous speed n_1 of the stator m.m.f. wave and the mechanical speed of the rotor n_m

$$s = \frac{n_1 - n_m}{n_1} \tag{3.2.8}$$

The synchronous speed in mechanical rpm of the SDFM is defined in terms of stator frequency f_1 and pole pair number p_A as

$$n_1 = \frac{60 * f_1}{p_A} \tag{3.2.9}$$

In (3.2.6) the influence of the speed or slip respectively upon the rotor e.m.f. can clearly be seen. The smaller the slip or the closer the speed approaches synchronism the less e.m.f. is induced in the rotor windings, since the relative movement of the stator flux wave to the rotor winding reduces. At the synchronous speed where $s=0$ the rotor has no relative movement to the stator flux and no voltage is induced in the rotor windings.

The per-phase equivalent circuit of figure 3.6 is made up of two subnetworks representing the stator and rotor windings. In comparison to the more common referred equivalent circuit as known from the cage induction machine, the above circuit has the advantage of dealing independently with the stator quantities at stator frequency f_1 and the rotor quantities at rotor frequency f_2 omitting the referral process. The mathematical connection between the two subcircuits is accomplished with equation (3.2.6). A simplified representation of figure 3.6 is shown in figure 3.7.

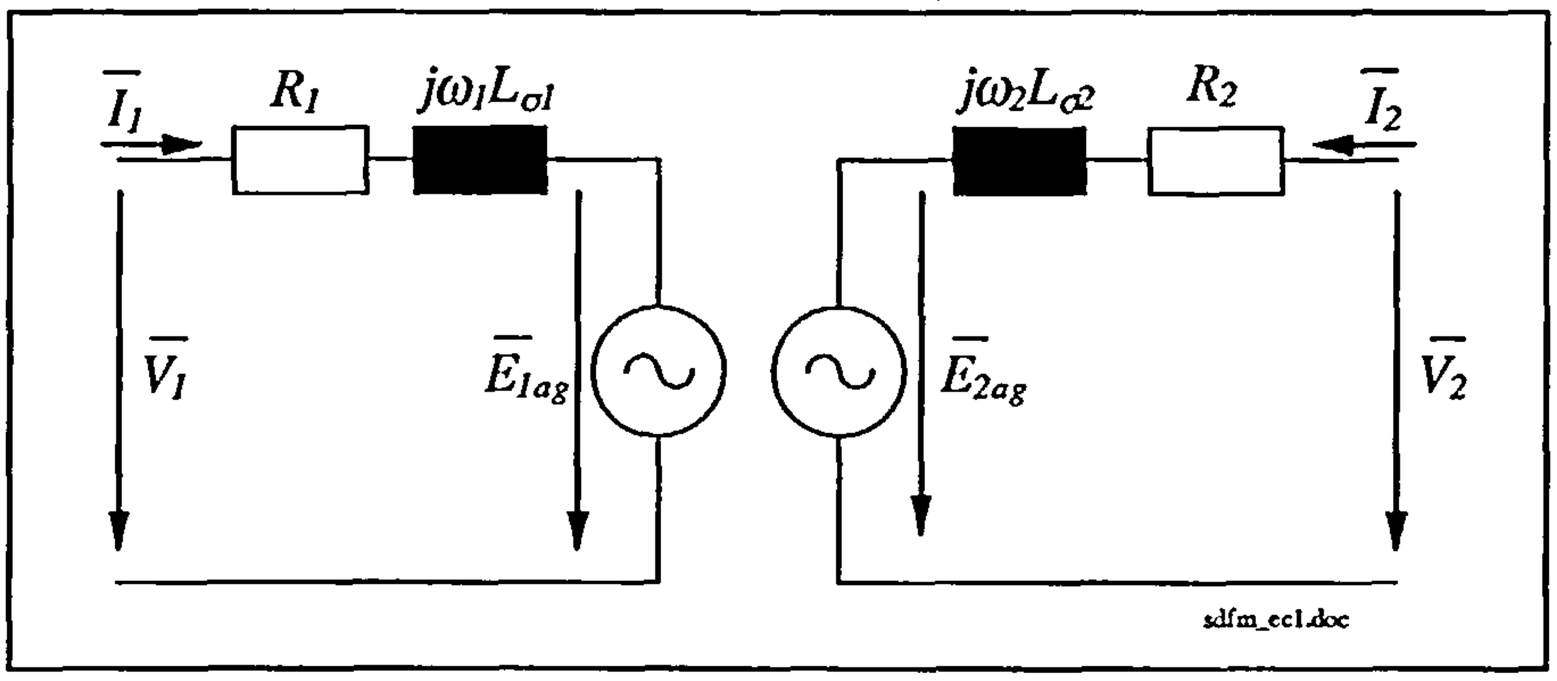

Figure 3.7: Non-referred per-phase steady state equivalent circuit of the SDFM

The voltage arrows in figure 3.6 and 3.7, indicating voltage sources, are pointing from the higher to the lower potential.

In order to make power calculations on the SDFM it is required to define the power equations. The 3-phase apparent power for the stator and the rotor is defined as

$$S_1 = 3 * \overline{V}_1 conj(\overline{I}_1) \tag{3.2.10}$$

$$S_2 = 3 * \overline{V}_2 conj(\overline{I}_2) \tag{3.2.11}$$

the real power is

$$P_1 = real(S_1) \tag{3.2.12}$$

$$P_2 = real(S_2) \tag{3.2.13}$$

and for the imaginary or reactive power of the stator and rotor can be written

$$Q_1 = imag(S_1) \tag{3.2.14}$$

$$Q_2 = imag(S_2) \tag{3.2.15}$$

The real power is taken positive when flowing into the system, i.e. the stator or rotor terminals. Delivered inductive reactive power towards the SDFM terminals is taken positive and capacitive reactive power negative.

The speed range of a SDFM can be divided in different speed sections denoted as stationary, subsynchronous, synchronous and supersynchronous speed. Depending on the speed the rotor frequency varies linearly and can take even negative values for supersynchronous speeds as following dissection describes.

Stationary (s=1): The stator or side 1 of the SDFM is connected to the 50 Hz mains supply network. It is therefore always supplied by a positive sequence 3-phase system at the frequency f_1. The positive sequence shall be denoted as "a_1-b_1-c_1". If the rotor is stationary a 3-phase voltage is induced on the rotor, or side 2, with the frequency f_2, which in the stationary case is the same as on side 1. The voltages measured on the 3-phase rotor terminals have also a positive phase sequence denoted as "a_2-b_2-c_2". In this condition the SDFM behaves merely as a transformer.

Subsynchronous (1<s<0): By rotating the rotor in the direction of the spatial flux wave of the stator the frequency f_2 on side 2 starts to be reduced accordingly to (3.2.7).
The closer the speed approaches synchronism, the smaller f_2 will be, since the slip s changes from the value 1 at standstill to the value 0 at synchronism.
Synchronous (s=0): At the point when the mechanical rotor speed reaches synchronous speed, the rotor frequency will be 0 Hz. The rotor windings rotate spatially now in synchronism with the stator flux wave. The rotor phases therefore "see" no relative movement of the stator flux wave. No voltage is induced in the rotor windings in this case.
Supersynchronous (s<0): By further acceleration, the rotor windings "overtake" the stator flux wave and the rotor frequency becomes negative in accordance with equations (3.2.7) and (3.2.8). This negative value means that the rotor phase sequence has reversed and can be regarded as "a_2-c_2-b_2". It means that the spatial rotor voltage wave rotates in negative direction relative to the rotor.
The frequency relationships between stator, side 1, and rotor, side 2, for the used SDFM with 2 pole pairs can be seen in figure 3.8, where the synchronous speed is at 1500 rpm.

Negative frequency aspect

The negative frequency aspect is generally of no importance apart from when it comes to deal with the reactive power equations as pointed out in [b10]. At positive frequencies the

reactance of an inductance is positive and therefore demands inductive reactive power, when the current phasor is lagging the voltage phasor. With a negative frequency the mathematical definition of the reactance would have a negative value and therefore represents a capacitance rather than an inductance. The current phasor is now leading the voltage phasor. However, the phasor reference system at negative frequencies is rotating in the opposite direction as for the positive frequency system. The current would therefore still be lagging the voltage phasor [f14]. Stating it in a different way, the VAr flow in negative frequency systems is towards capacitive load, rather than towards inductive load [b10]. This has to be taken into account when calculating the rotor reactive power at supersynchronous speed.

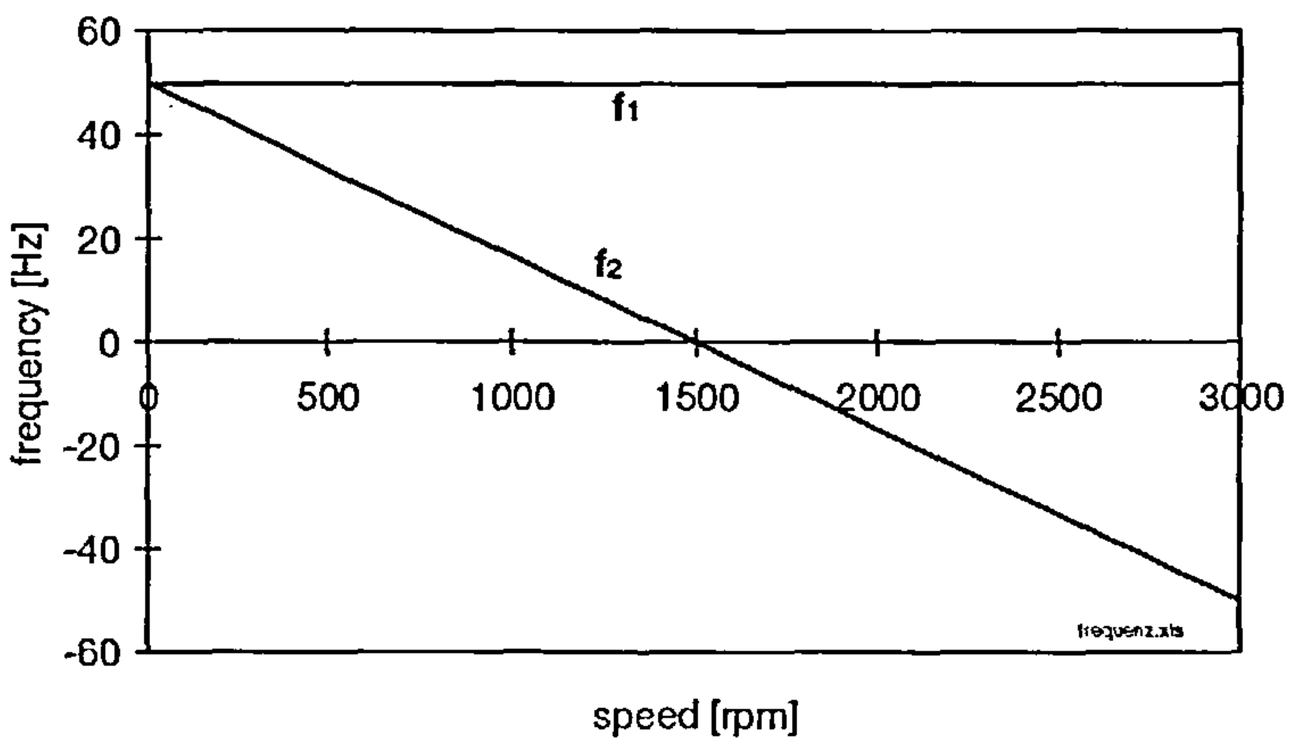

Figure 3.8: Stator and rotor frequency relationship of the SDFM with 2 pole pairs

Finally, the definition of the electromagnetic torque in steady state is given by

$$T_e = -3 * p_A * L_{mag} * (\bar{I}_{mag} \times \frac{\bar{I}_2}{a}) \tag{3.2.16}$$

where

$$\bar{I}_{mag} = \frac{\bar{E}_{1ag}}{j\omega_1 L_{mag}} \tag{3.2.17}$$

is the magnetising current flowing through the magnetising inductance.

3.2.2 Steady State Simulations

In a drive application the stator (side 1) is connected to the 3-phase mains network which has a constant line voltage at constant frequency f_1. The rotor windings (side 2) are connected via the slip-rings to a bi-directional frequency converter as depicted in figure 3.9. This converter must be able to supply the rotor with a voltage at variable amplitude, frequency and phase. When this converter is equipped with a fast current control in each winding, then it can be assumed that the rotor is fed with an impressed current. The SDFM

can therefore be seen as a "doubly-fed" system fed by a voltage source on side 1 and by a current source on side 2.

Depending on the phase and magnitude of the rotor current relative to the stator voltage, it is possible to control stator active and reactive power [f2]. To demonstrate this, steady state simulations have been carried out based on the per-phase steady state equivalent circuit equations. Parameters (Appendix A) used for simulation are taken from the experimental 2 pole pair, 2.25 kW SDFM. It has to be mentioned that the value for the iron loss resistor, acquired from tests, is multiplied by a factor of 1.8. It is usual practice with simulations on cage induction machines to modify the iron losses to get a closer agreement between simulations and measurements [f20]. All other parameters are taken as calculated from the tests.

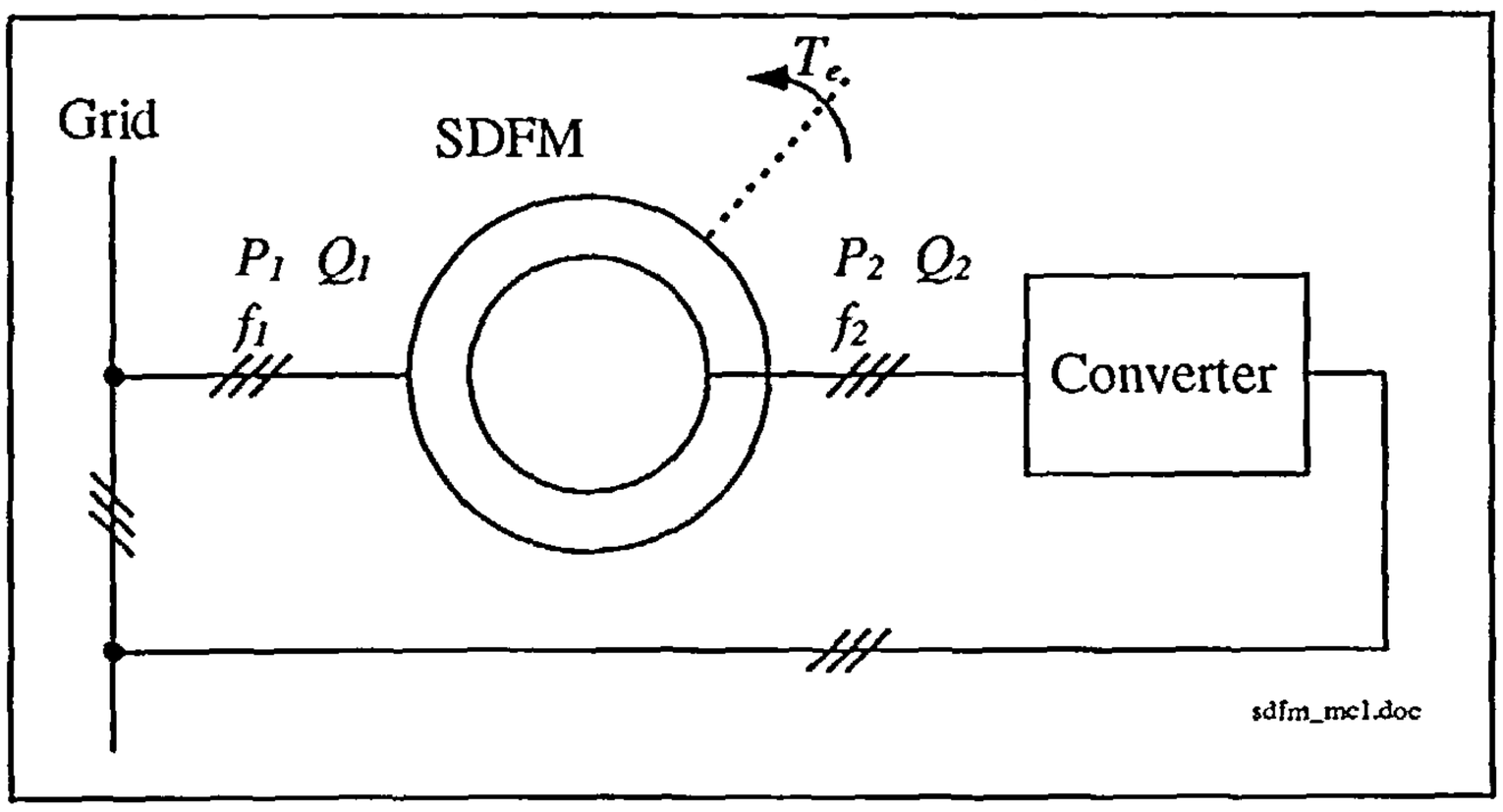

Figure 3.9: Connection of the SDFM

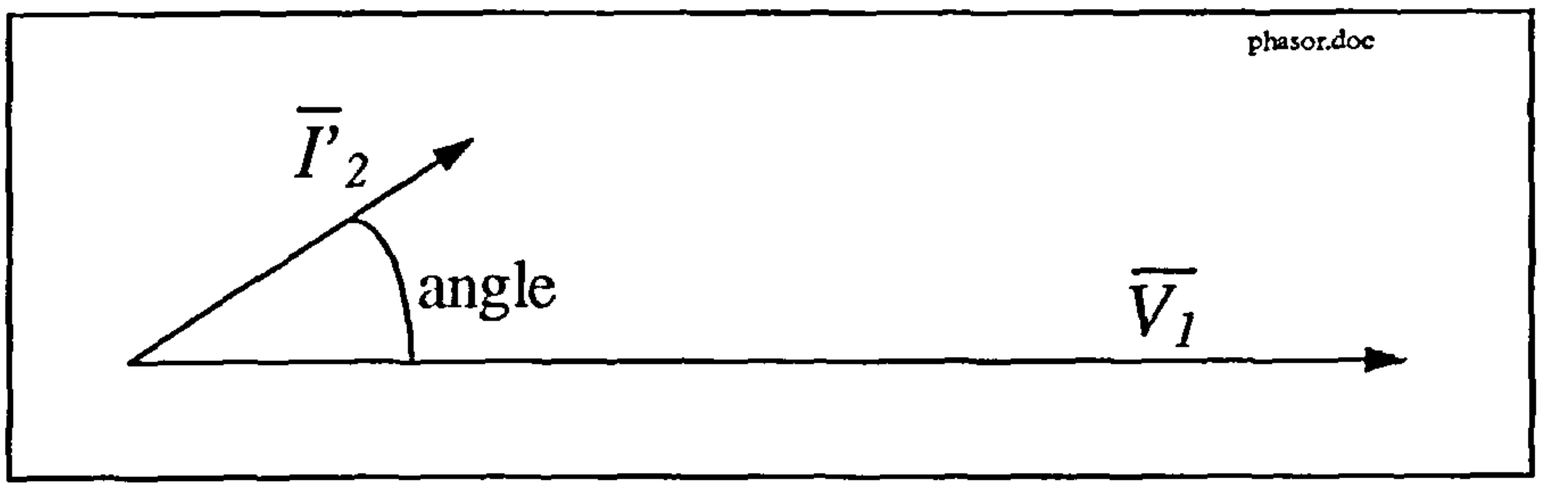

Figure 3.10: Phasor diagram of stator voltage and referred rotor current

The first set of simulations are performed at a constant speed of 1300 rpm, which is subsynchronous for the machine considered. The referred rotor current steady state phasor is rotated with a constant magnitude relative to the stator voltage phasor as indicated in figure 3.10. Various quantities expressed as a function of the rotation angle are presented in figures 3.11 to 3.13. The solid lines represent the results for the SDFM in accordance to the equivalent circuit in figure 3.7 which includes copper and iron losses.

In figure 3.11 the results are shown for the active stator and rotor active power. It can be seen that depending on the angle between the stator voltage and the rotor current, the stator active power P_1 can be controlled in a sinusoidal shape over the whole angle range. The angle between $\bar{V}_1$ and $\bar{I}'_2$ corresponds to the phase difference. At 180° P_1 reaches the maximum positive value. This means that power is flowing into the stator terminals and positive electromagnetic torque is developed (figure 3.13) demonstrating that the machine is in motoring mode. At 0° P_1 reaches the maximum negative value and power is flowing from the stator towards the supply network as the machine is in generating mode.

In addition to the simulations including all losses, simulation results, where all copper and iron losses are neglected (dashed line), are shown in figures 3.11 and 3.13. In this case the phase resistances were set to zero and the iron loss resistor was set to infinity. As can be expected the results change only slightly compared to the full loss lines, since the winding resistance and the iron losses shouldn't affect the general performance of the SDFM a great deal. In figure 3.11 it can be seen that the lossless power lines for P_1 and P_2 change their sign at the same point. Whenever P_1 has a positive value P_2 has a negative value and vice versa. That is slightly different with the solid lines. They show that when either P_1 or P_2 crosses the zero line the other one has a positive value meaning that the losses are then supplied either via side 1 or side 2. Figure 3.13 shows that the losses have also only a small effect on the torque curve.

Figure 3.12 displays the simulation results for the stator and rotor reactive power. As mentioned in [a1] the relation between stator and rotor reactive power assumes the form

$$Q_{12} = Q_1 + \frac{Q_2}{|s|} \tag{3.2.18}$$

where Q_{12} is the sum of reactive powers needed to establish leakage and magnetising flux in the machine. Alternatively it can be written as

$$Q_{12} = |\bar{I}_1|^2 X_{\sigma 1} + |\bar{I}_2|^2 X_{\sigma 2} + |\bar{I}_{mag}|^2 X_{mag}$$

where

$X_{\sigma 1}$, $X_{\sigma 2}$ and X_{mag} are the stator, rotor and magnetising reactances calculated at supply frequency f_1.

The reactive power Q_{12} is always positive, since there is inductive reactive power demanded by the SDFM to establish the excitation. This can be seen in figure 3.12, where Q_{12} has a nearly constant positive value over the whole angle range. Whenever one of the two machine terminals does not supply reactive power, i.e. has the value zero, then the other takes a positive value, i.e. all the reactive power has to be supplied via this terminal. It is even possible to supply inductive reactive power to the grid. In that case the converter generates the inductive reactive excitation power for the SDFM on top of the inductive reactive power which is fed through the machine into the grid. In reality, this can be done

only to a certain limit, because the reactive power transfer through the machine leads to higher currents and therefore to higher losses. To manipulate the side 1 reactive power with the rotor current is more favorable at low slip values in accordance to equation (3.2.18). Only a slight variation of Q_2 leads to a change of Q_1. At synchronous speed, where $s = 0$ the SDFM behaviour is identical to that of a synchronous machine.

Experimental data points for P_1 and Q_1, measured on the laboratory machine set, are added to the simulated results in figure 3.11 and 3.12. The data points were mainly taken in generating mode and having leading power factor on side 1. The simulated and experimental data are in very close agreement. This proves that simulations, based on the per-phase equivalent circuit equations are a very useful tool to model the SDFM in steady state.

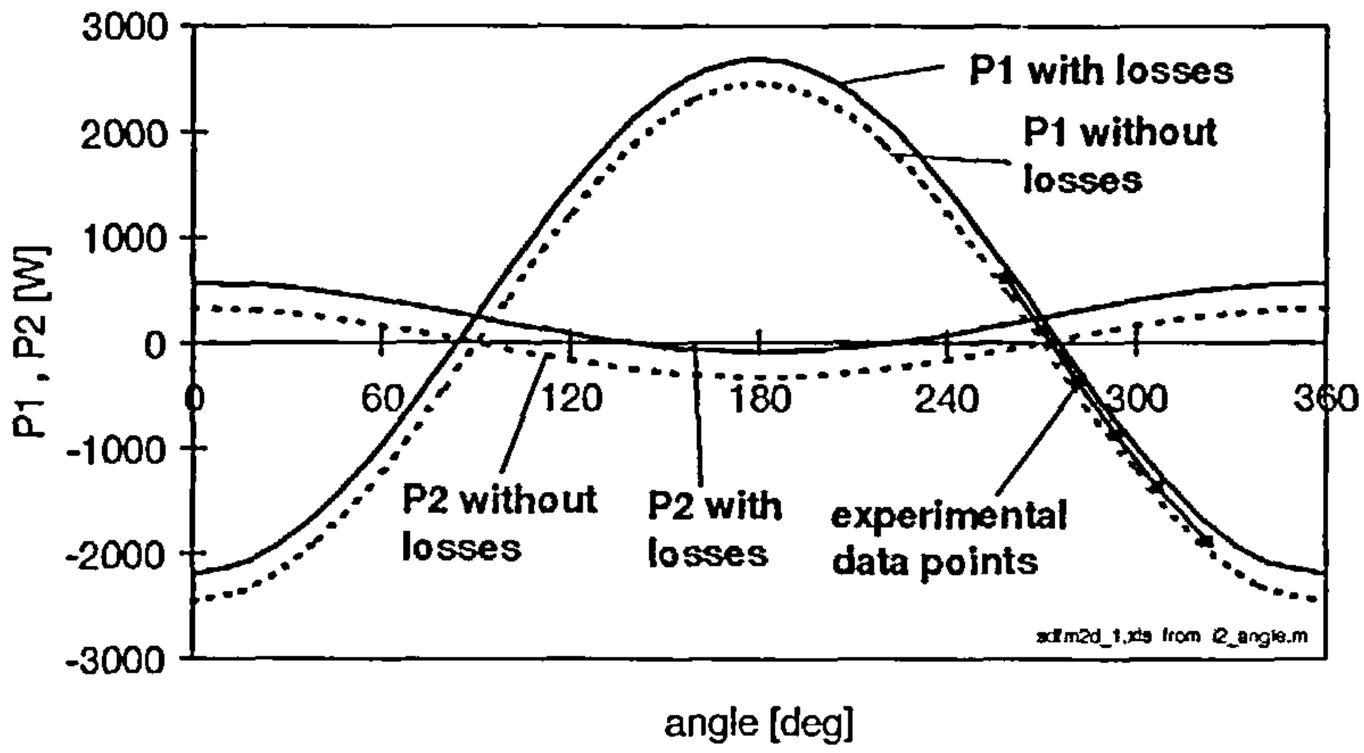

Figure 3.11: Simulated steady state values of P_1 and P_2 with and without losses together with experimental data points

($V_{1rms} = 240V$, $|I_{2peak}| = 5A$, $n_m = 1300$ rpm)

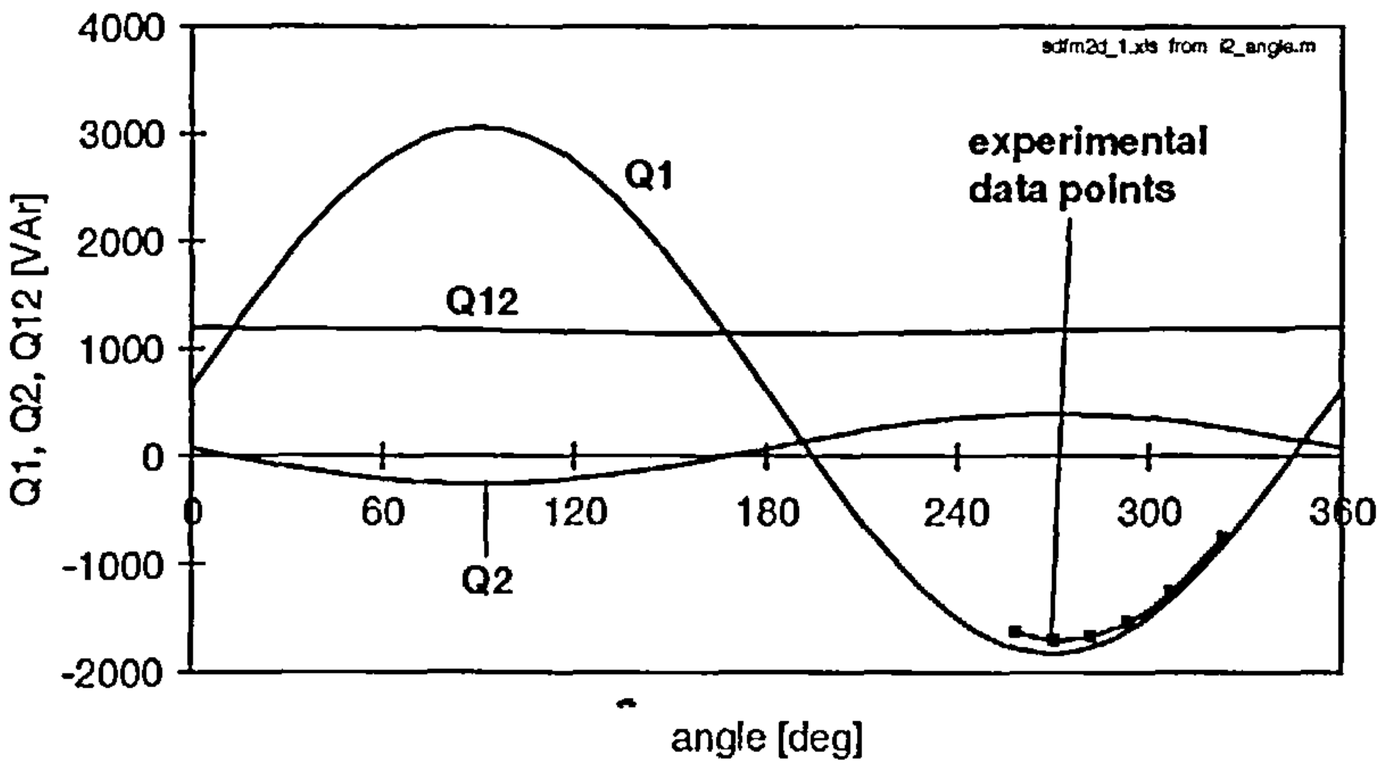

Figure 3.12: Simulated steady state values of Q_1, Q_2 and Q_{12} together with experimental data points

($V_{1rms} = 240V$, $|I_{2peak}| = 5A$, , $n_m = 1300$ rpm)

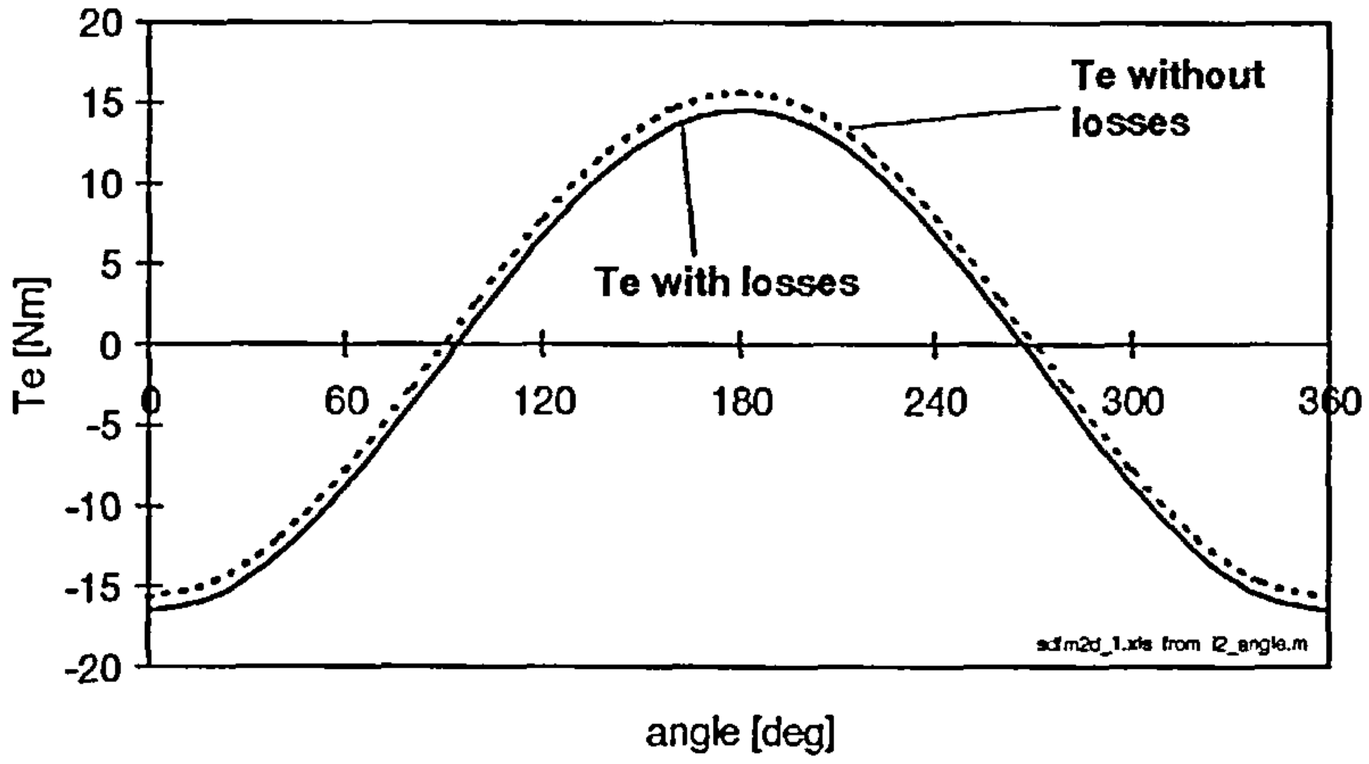

Figure 3.13: Simulated steady state values of the electric torque T_e with and without losses
($V_{1rms} = 240V$, $|I_{2peak}| = 5A$, , $n_m = 1300$ rpm)

A second set of simulations on the SDFM again rotate the rotor current phasor relative to the stator voltage phasor over the whole angle range of 0°-360°. Additionally, in the third dimension, the speed is varied from 0 rpm to 3000 rpm, that is up to double the synchronous speed of the laboratory machine. The simulations are based on the steady state per-phase equivalent circuit with copper and iron losses are included.

In figure 3.14 and 3.15 the 3-dimensional surfaces of P_1 and P_2 are displayed. It can immediately be seen, that the surface of P_1 has the sinusoidal shape, as known from figure 3.11, over the complete speed range. Side 1 active power is consequently independent of speed and is only set by the magnitude and the angle of $\bar{I}'_2$ relative to $\bar{V}_1$. It is different for the rotor active power P_2. The maximum values for P_2 in the angle-axis concur with the maximum values as in figure 3.11, which can be expected, since figure 3.11 is only a single "slice" from the shape of figure 3.15. However, now the magnitude and power flow direction (positive or negative value) of P_2 varies along the speed-axis. The smallest magnitude in dependency of speed occurs around synchronous speed, where also the power flow direction is reversed.

In figure 3.16 and 3.17 the reactive powers Q_1 and Q_2 are shown. Q_1 takes the same sinusoidal shape, as in figure 3.12, constant over the whole speed range. Hence, indicating that Q_1 is only set by the magnitude and the angle of $\bar{I}'_2$ relative to $\bar{V}_1$, as it is the case for P_1. Q_2 in comparison varies along the speed-axis in magnitude, but doesn't change the sign. This means, that for a fixed rotor current to stator voltage relation, the reactive power flow direction (inductive or capacitive) in the rotor is the same, regardless of sub- or supersynchronous speed. However, the amount of reactive power in the rotor circuit depends on speed to fulfill the requirements of equation (3.2.18).

Figures 3.14 and 3.16, clearly support the known fact, that active and reactive stator power of a SDFM can be controlled by changing rotor current magnitude and phase relative to stator voltage, and that independent of speed.

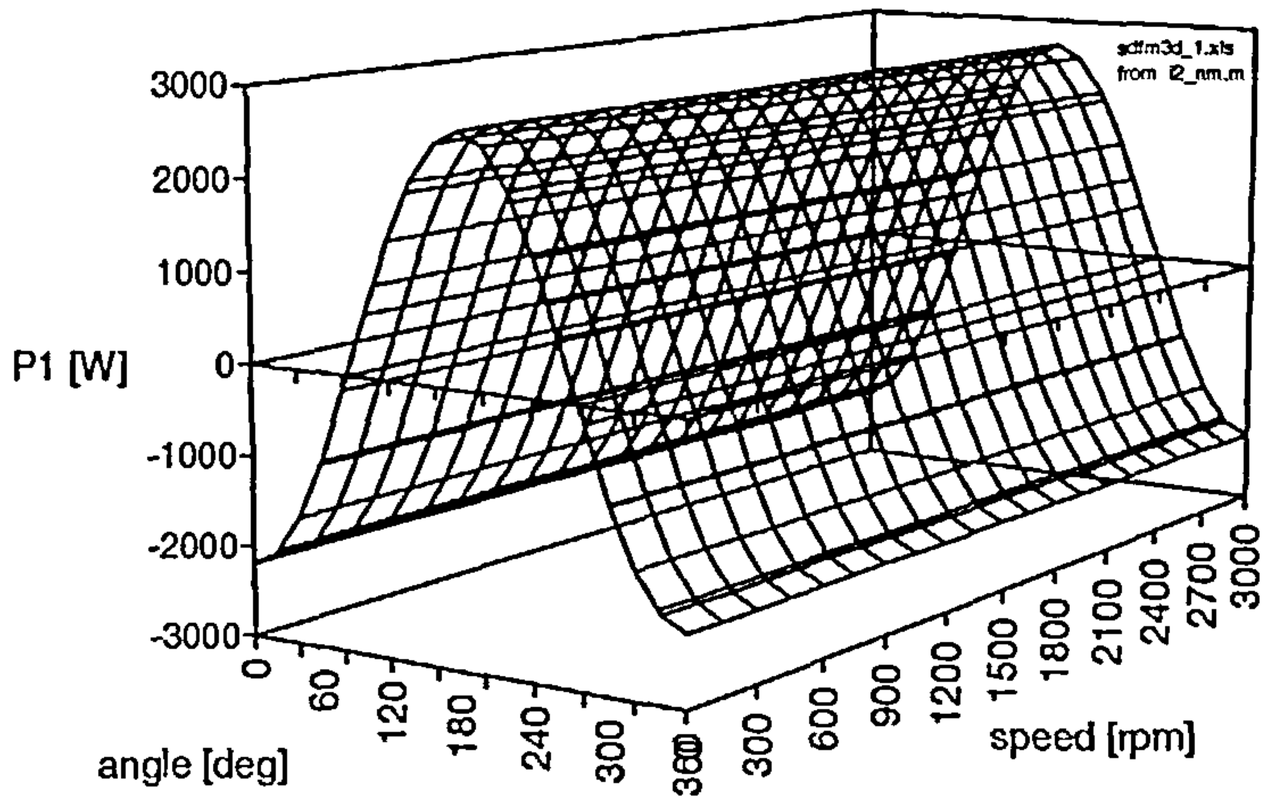

Figure 3.14: Simulated steady state values of P_1 as a function of angle and speed

($V_{1rms} = 240V$, $|I_{2peak}| = 5A$)

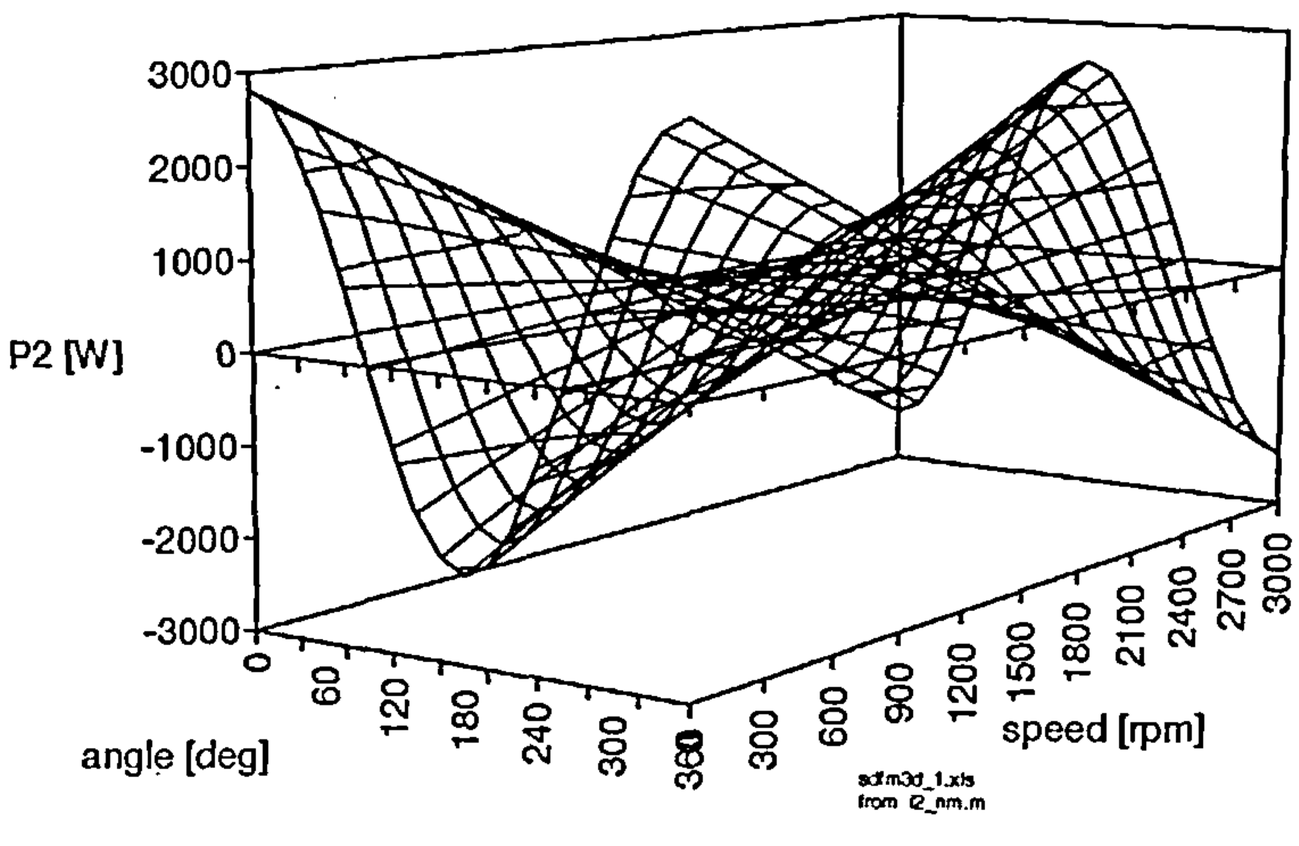

Figure 3.15: Simulated steady state values of P_2 as a function of angle and speed

($V_{1rms} = 240V$, $|I_{2peak}| = 5A$)

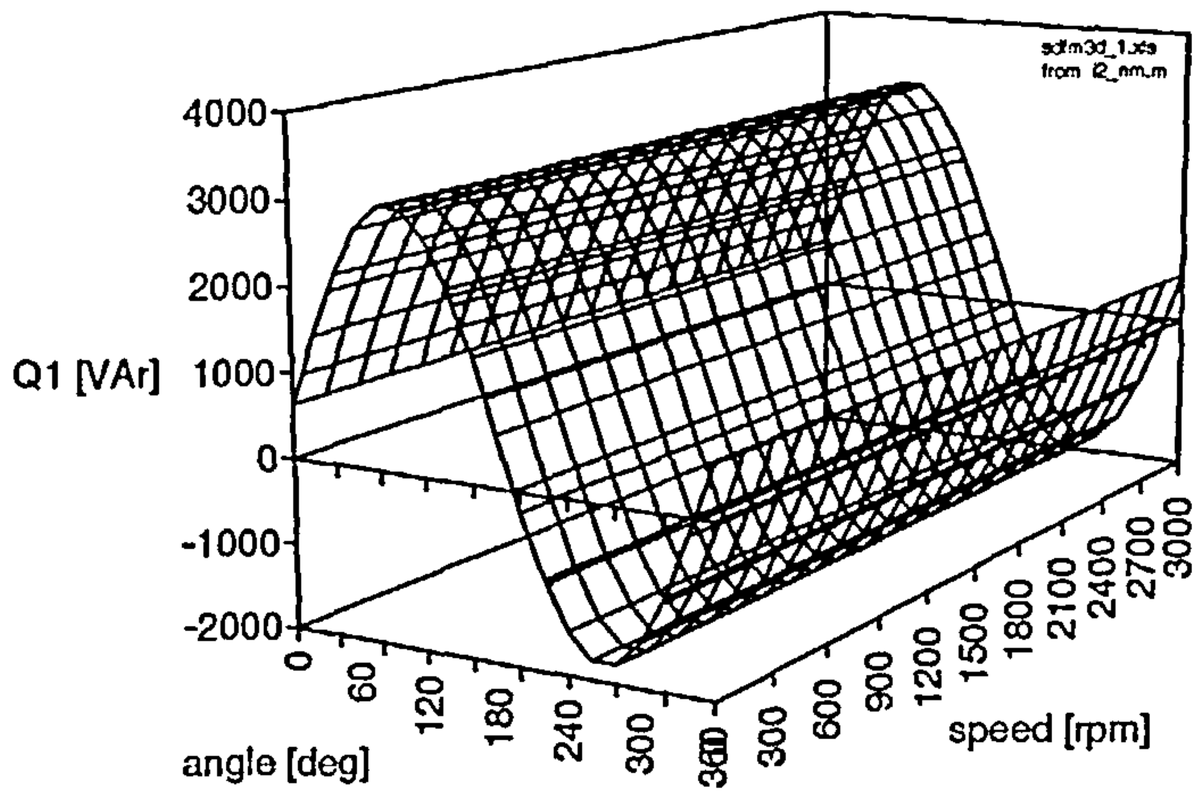

Figure 3.16: Simulated steady state values of Q_1 as a function of angle and speed

($V_{1rms} = 240V$, $|I_{2peak}| = 5A$)

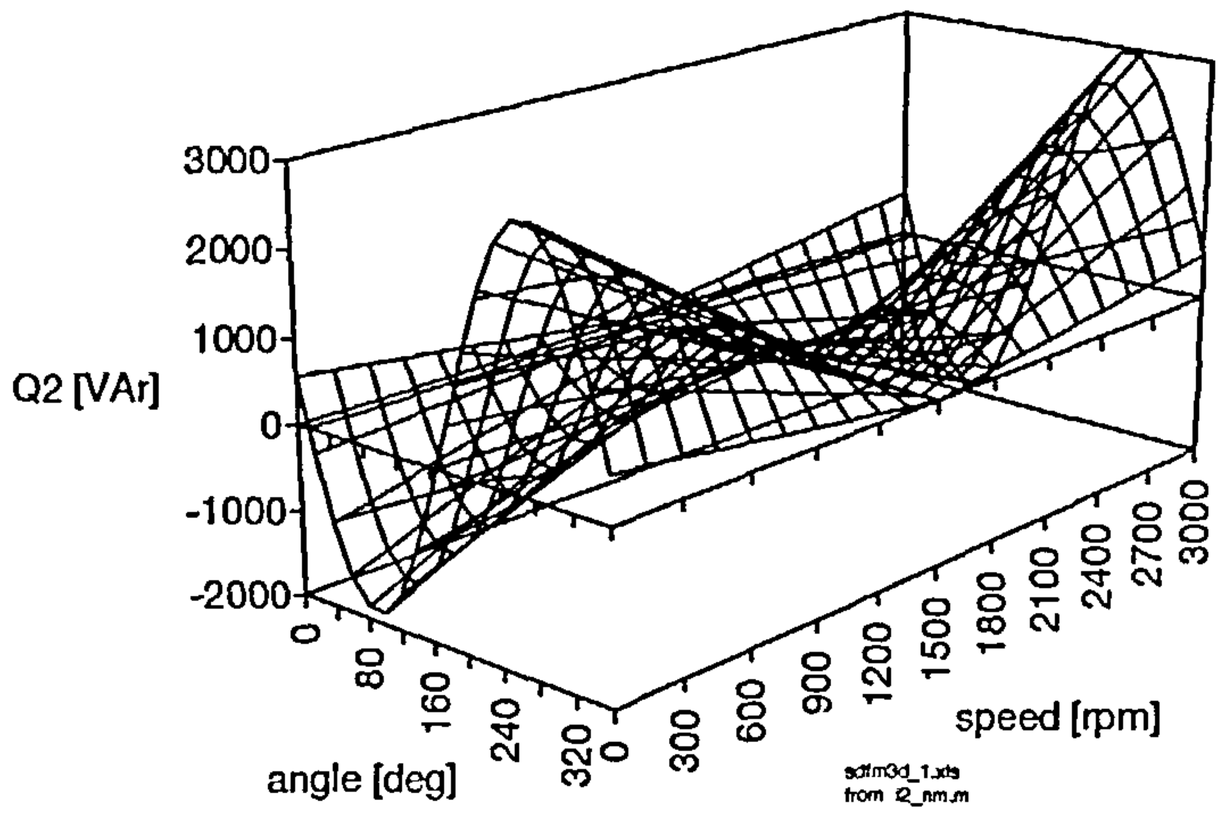

Figure 3.17: Simulated steady state values of Q_2 as a function of angle and speed

($V_{1rms} = 240V$, $|I_{2peak}| = 5A$)

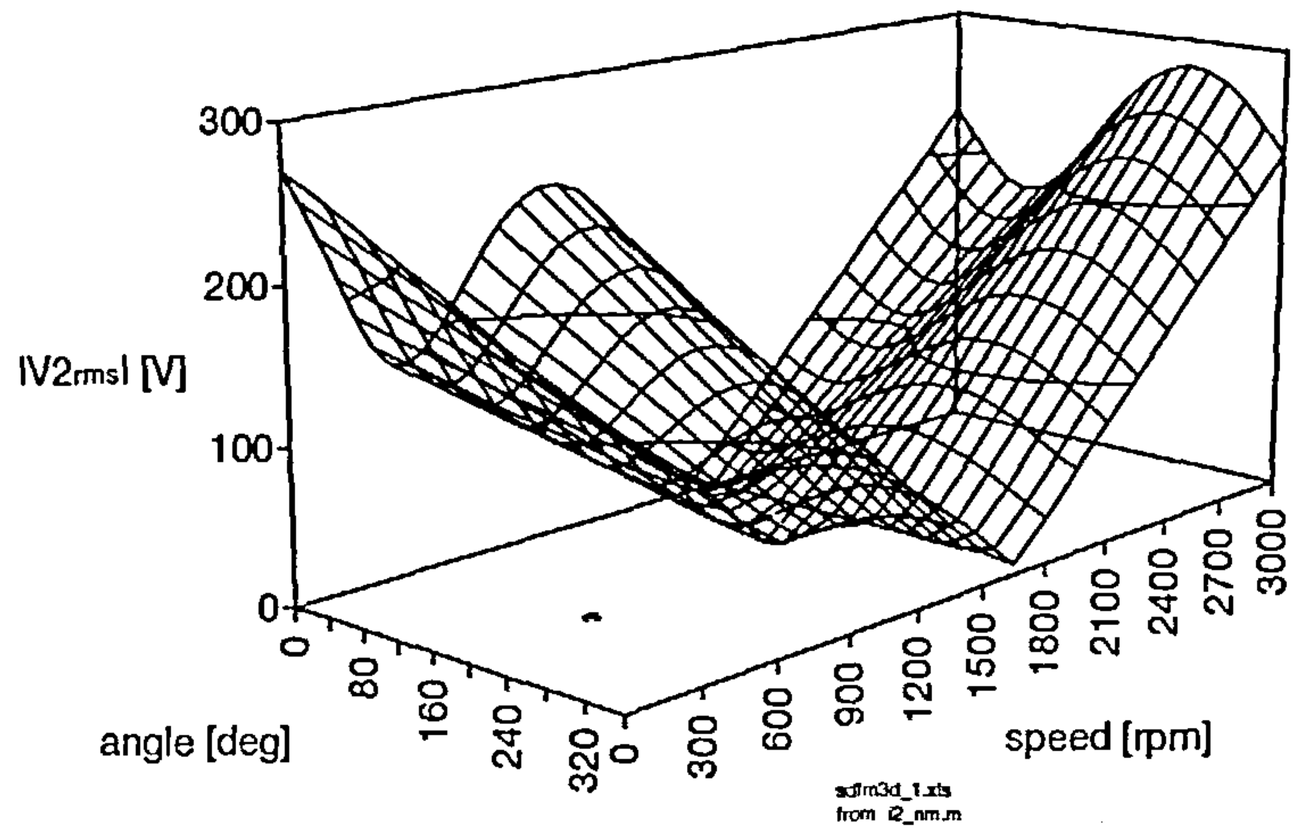

Figure 3.18: Simulated steady state values of V_2 as a function of angle and speed

($V_{1rms} = 240V$, $|I_{2peak}| = 5A$)

A 3-dimensional surface plot of the rotor voltage is shown in figure 3.18. Viewed from the speed-axis the surface forms a "V-form" with the minimum value at around 1500 rpm. Considering equation (3.2.6), which is repeated here

$$\overline{E}_{2ag} = \overline{E}_{1ag}\frac{s}{a}$$

and looking at the equivalent circuit in figure 3.7, it can be seen that the stator terminal voltage and the rotor terminal voltage differ only by the voltage drop across the phase resistances and the leakage reactances to their air-gap e.m.f. values. Neglecting that voltage drop in a first order approximation and considering only the magnitude then (3.2.6) can be rewritten in a simplified form as

$$|\overline{V}_2| \approx |\overline{V}_1|\frac{s}{a} \qquad (3.2.19)$$

3.2.3 Power Flow

The steady state simulations of the SDFM are already indicating how the power is flowing between its three ports depending on speed and the rotor current phasor position relative to stator voltage. The three ports involved are the stator windings, the rotor windings and the mechanical shaft.

Now, the relationship or conversion properties between the different machine power ports are given in an simplified analytical way with all losses neglected. A look at figures 3.11 and 3.13 justifies that assumption, since the curves with and without losses differ only by a small amount.

To have the power relations in this form allows simplified calculations to be made on the SDFM, thus permitting in a quick way to assess the involved power flow in the machine.

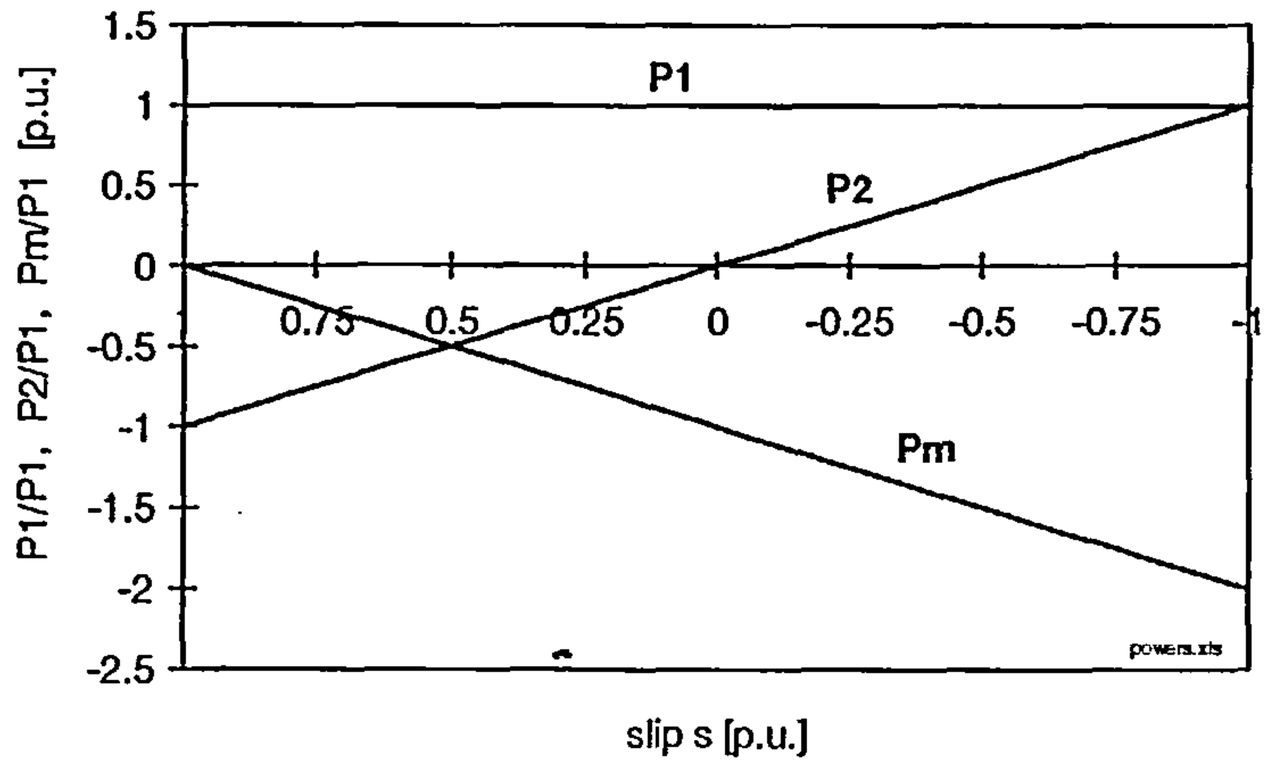

Figure 3.19: Power relations of the SDFM neglecting losses

(constant T_e)

The simplified interaction of the different power ports are given by the formulas [a1]

$$P_2 = -sP_1 \tag{3.2.20}$$

$$P_m = -(1-s)P_1 \tag{3.2.21}$$

when powers flowing towards the machine are taken positive.

The mechanical power in (3.2.21) is a function of the electromagnetic torque and the mechanical angular speed as

$$P_m = -T_e\omega_m \tag{3.2.22}$$

Figure 3.19 shows the power relations in per-unitised form at constant torque. The power handling of side 1 is always constant, whereas the power handling of the rotor varies with speed, as simulated in figure 3.15.

The speed range of the SDFM can generally be divided in two sections, subsynchronous and supersynchronous. There is also the distinction to be made between motoring and generating mode. Table 3.1 gives the power flow directions of the SDFM and the power flow diagram in figure 3.20 helps to visualise the different speed sections and operating modes. Power arrows in 3.20 are pointing towards the machine in agreement with the adopted convention.

	Motoring $P_m < 0$	***Generating*** $P_m > 0$
Subsynchronous $P_1 = -(P_m + P_2)$	$P_1 > 0$ $P_2 < 0$	$P_1 < 0$ $P_2 > 0$
Supersynchronous $P_m = -(P_1 + P_2)$	$P_1 > 0$ $P_2 > 0$	$P_1 < 0$ $P_2 < 0$

table.doc

Table 3.1: Power flow directions of the SDFM neglecting losses

As displayed by figure 3.19 the power handling of the rotor side is symmetrical to the synchronous speed of the SDFM with zero power at s = 0. The further the speed deviates from synchronous speed the more power has to be processed by the rotor, i.e. by the converter connected to the rotor windings. The operational speed range for a SDFM in a variable speed application is therefore always centered around the synchronous point as far as possible. The smaller the speed range the less power flows through the bi-directional converter. The rating of the converter depends on the maximum slip value in the speed range and the ratio between side 1 and side 2 can be written as

$$\frac{P_2}{P_1} = |s_{max}|$$

Compared to a conventional cage induction machine drive with a fully rated converter for variable speed applications, the SDFM system offers a reduced converter rating.

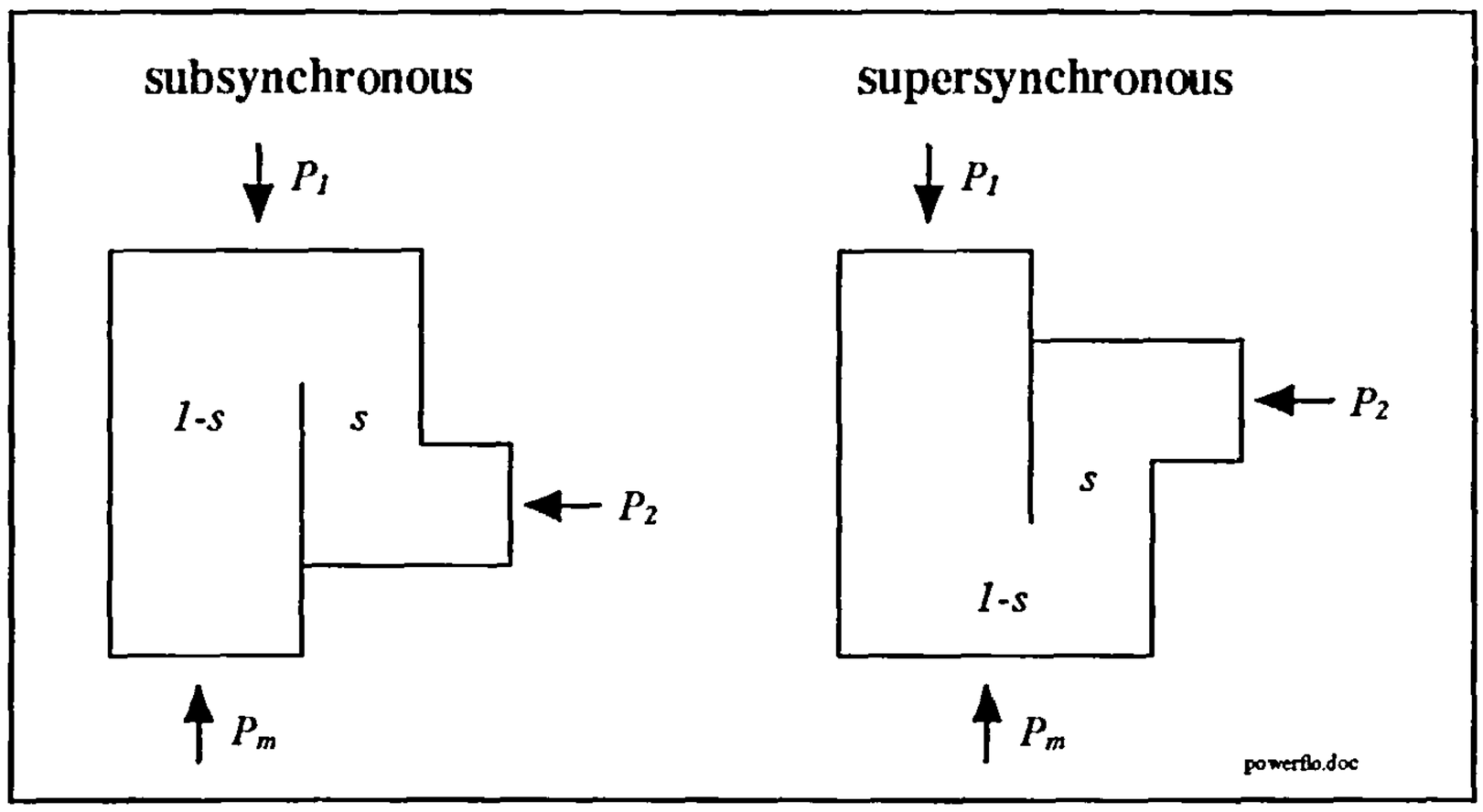

Figure 3.20: Power flow diagram for the SDFM neglecting losses

3.3 Field Oriented Control

High dynamic performance control for the SDFM can be achieved by means of field orientation [f2]. Although there are plenty of applications, where simpler control methods, such as Static-Scherbius drives, are sufficient, the field oriented approach can be regarded as the standard way of controlling the SDFM nowadays. That is mainly due to the ability to control stator active and reactive power independently from each other.

Considering the electromagnetic torque of the SDFM as in equation (3.1.23) in a general reference frame "g"

$$T_e = -\frac{3}{2} p_A \frac{L_m}{L_1} (\overline{\Psi}_1^g \times \bar{i}_2^g) = -\frac{3}{2} p_A \frac{L_m}{L_1} (\Psi_{d1}^g i_{q2}^g - \Psi_{q1}^g i_{d2}^g) \tag{3.3.1}$$

then it can be seen that for choosing a reference frame which is attached to the stator flux, equation (3.3.1) would change to the following simple form

$$T_e = -\frac{3}{2} p_A \frac{L_m}{L_1} \Psi_1^e i_{q2}^e \tag{3.3.2}$$

since

$$\Psi_{q1}^e = 0 \quad \text{and} \quad \Psi_{d1}^e = |\overline{\Psi}_1^e| = \Psi_1^e \tag{3.3.3}$$

The reference frame attached to the stator flux is denoted as excitation "e" reference frame. Equation (3.3.2) shows that the torque of the SDFM can be controlled by the q-component of the rotor current in the "e"-frame, when the stator flux is held at a constant value. As is the case with the field oriented cage induction machine this way of controlling the torque resembles the case of the separately exited DC-machine.

To develop the machine control structure, the dynamic machine model has to be presented in field coordinates. Taking the general reference frame machine equations (3.1.28) and

(3.1.29) and replacing the general angular frequency ω_g by the synchronous rotating angular frequency ω_e leads to the machine equations in frame "e" as

$$\bar{v}_1^e = R_1 \bar{i}_1^e + \frac{d\bar{\Psi}_1^e}{dt} + j\omega_e \bar{\Psi}_1^e \tag{3.3.4}$$

$$\bar{v}_2^e = R_2 \bar{i}_2^e + \frac{d\bar{\Psi}_2^e}{dt} + j(\omega_e - \omega_1)\bar{\Psi}_2^e \tag{3.3.5}$$

If it is assumed to have an inverter in the rotor circuit with fast current control, which impresses the desired current value, then the rotor voltage equation (3.3.5) is initially of no concern.

Replacing the stator current in (3.3.4) by

$$\bar{i}_1^e = \frac{\bar{\Psi}_1^e - L_m \bar{i}_2^e}{L_1} \tag{3.3.6}$$

which is based on equation (3.1.30), then (3.3.4) can be written as

$$\frac{d\bar{\Psi}_1^e}{dt} + \left(\frac{R_1}{L_1} + j\omega_e\right)\bar{\Psi}_1^e = \frac{R_1 L_m}{L_1}\bar{i}_2^e + \bar{v}_1^e \tag{3.3.7}$$

Using the constraints of the stator flux in the "e"-frame of (3.3.3) together with $T_1 = \frac{L_1}{R_1}$

and $(1+\sigma_1) = \frac{L_1}{L_m}$ and splitting (3.3.7) into d-q-components then

$$\frac{T_1}{L_m}\frac{d\Psi_{d1}^e}{dt} + \frac{1}{L_m}\Psi_{d1}^e = i_{d2}^e + \frac{1+\sigma_1}{R_1}v_{d1}^e \tag{3.3.8}$$

$$\frac{d\mu}{dt} = \omega_e = \frac{L_1}{T_1}\frac{i_{q2}^e}{\Psi_{d1}^e} + \frac{v_{q1}^e}{\Psi_{d1}^e} \tag{3.3.9}$$

σ_1 is the stator leakage factor and T_1 the stator time constant and μ is the angle between the stationary reference frame "a" and the excitation reference frame "e".

Equation (3.3.8) and (3.3.9) represent the stator dynamics in the "e"-frame. If perfect rotor current control was assumed then these equations would totally describe the machine electrical dynamics.

Reference frames for the SDFM in field orientation with the angle and angular speed definitions are displayed in figure 3.21.

To allow the transformation of the rotor currents from their natural rotor reference frame into the "e"-frame the angle

$$\varepsilon = \mu - \Theta_r \tag{3.3.10}$$

is important to know. The rotor position angle Θ_r can be obtained from incremental encoder signals, but there are three different ways on how to calculate the angle μ.

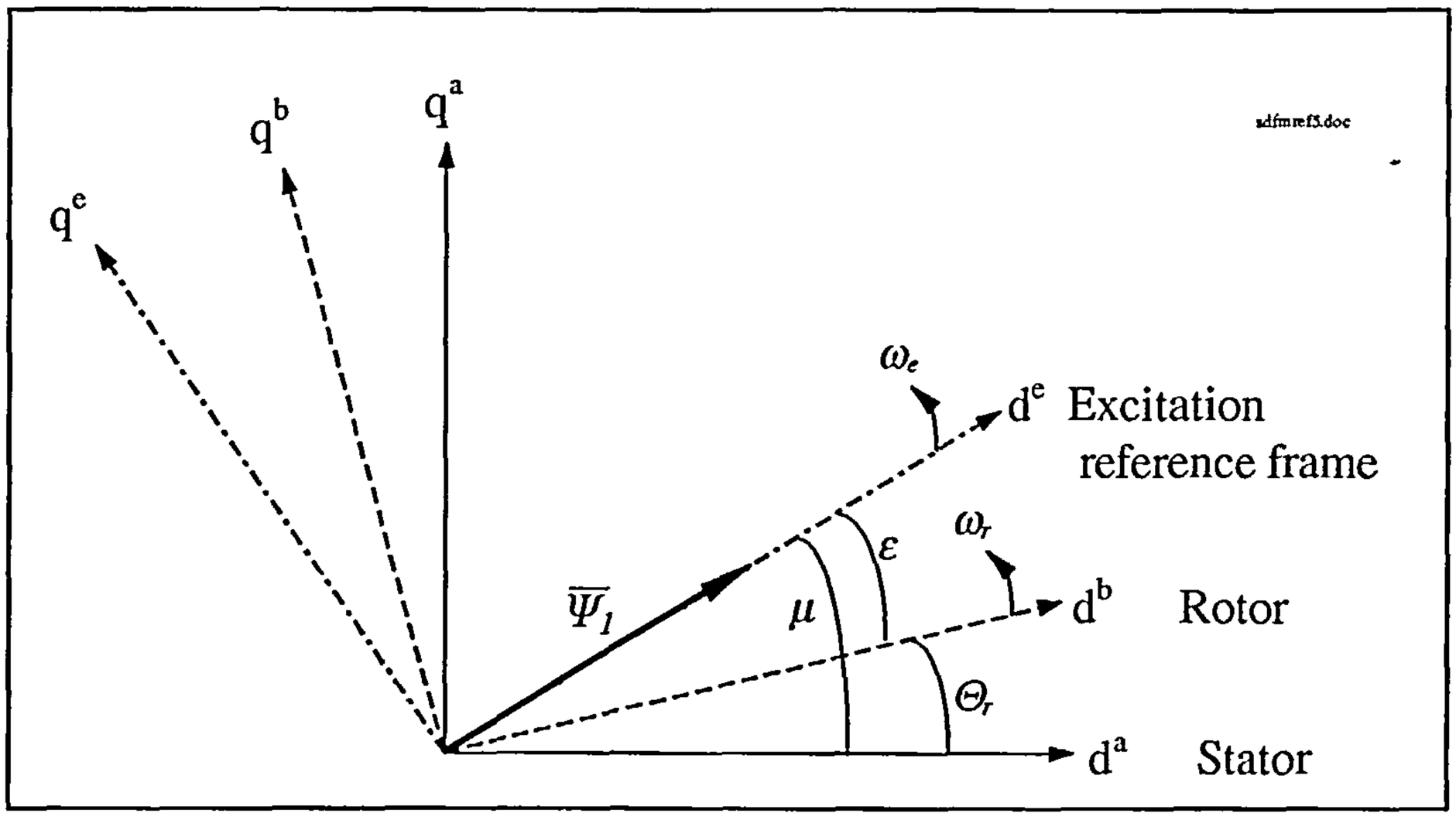

Figure 3.21: Reference frames and angles for the SDFM in field orientation

Looking at the stator flux equation (3.1.10) in the stator reference frame "a"

$$\overline{\Psi}_1^a = L_1 \bar{i}_1^a + L_m \bar{i}_2^a \qquad \text{(3.1.10 repeated)}$$

and by splitting it into its real and imaginary components then μ follows as

$$\mu = arctan \frac{\Psi_{q1}^a}{\Psi_{d1}^a} \qquad (3.3.11)$$

In this case it is first required to transform the rotor current into the stationary stator reference frame with the help of the rotor position angle. The individual stator flux component are then calculated by

$$\Psi_{d1}^a = L_1 i_{d1}^a + L_m i_{d2}^a \quad \text{and} \quad \Psi_{q1}^a = L_1 i_{q1}^a + L_m i_{q2}^a \qquad (3.3.12)$$

This way makes it essential that both currents are measured and the inductance values of the machine are known.

Another possibility of getting μ is by considering the stator voltage equation (3.1.9) in the stationary frame.

$$\bar{v}_1^a = R_1 \bar{i}_1^a + \frac{d\overline{\Psi}_1^a}{dt} \qquad \text{(3.1.9 repeated)}$$

The two flux components can now be calculated by integration

$$\Psi_{d1}^a = \int (v_{d1}^a - R_1 i_{d1}^a)dt \quad \text{and} \quad \Psi_{q1}^a = \int (v_{q1}^a - R_1 i_{q1}^a)dt \qquad (3.3.13)$$

This method may make it compelling to employ digital passband filter with a low cutoff frequency to avoid d.c.-offsets [a15], which can be associated with integrations. In addition to stator and rotor currents here the stator voltage has to be sensed as well.

A third and commonly used method simplifies equation (3.1.9) by neglecting the stator resistance. This approach can be justified for larger machines, since the resistance in

comparison to the stator reactance is quite small ($R_1 << \omega_1 L_1$). (3.1.9) and therefore in simple terms can be written as

$$\bar{v}_1^a \approx \frac{d\bar{\Psi}_1^a}{dt} \tag{3.3.14}$$

From this it can be seen that a reference frame attached to the stator flux has the same angular frequency as the stator voltage

$$\omega_e = \omega_1 = const. \tag{3.3.15}$$

By substituting $\bar{\Psi}_1^a = \left|\bar{\Psi}_1^a\right| e^{j\mu}$ in equation (3.3.14) and applying the rules of differentiation the magnitude of the stator flux expressed in the "e"-frame is given by

$$\Psi_1^e \approx \frac{\sqrt{2}V_1}{\omega_1} \tag{3.3.16}$$

where V_1 is the stator phase voltage in rms. The individual components of the stator voltage space vector in the excitation reference frame take the value

$$v_{d1}^e = 0 \quad \text{and} \quad v_{q1}^e = \omega_1 \Psi_1^e = \sqrt{2}V_1 = const. \tag{3.3.17}$$

Equation (3.3.16) and (3.3.17) show, that the magnitude of the stator flux is set by the stator voltage and that the stator voltage vector is $\pi/2$ in advance of the stator flux vector.

A simple way to obtain μ is therefore by measuring the stator voltage vector angle α_1 in the stationary reference frame and subsequently subtracting $\pi/2$. The angle α_1 can be obtained by a 3-to-2 transformation of the individual stator phase voltages, yielding the stator voltage vector in the stationary reference frame, and a cartesian-to-polar transformation. The approach to calculating the angle ε, between rotor and excitation reference frame, with incorporation of the rotor position angle Θ_r is depicted in figure 3.22.

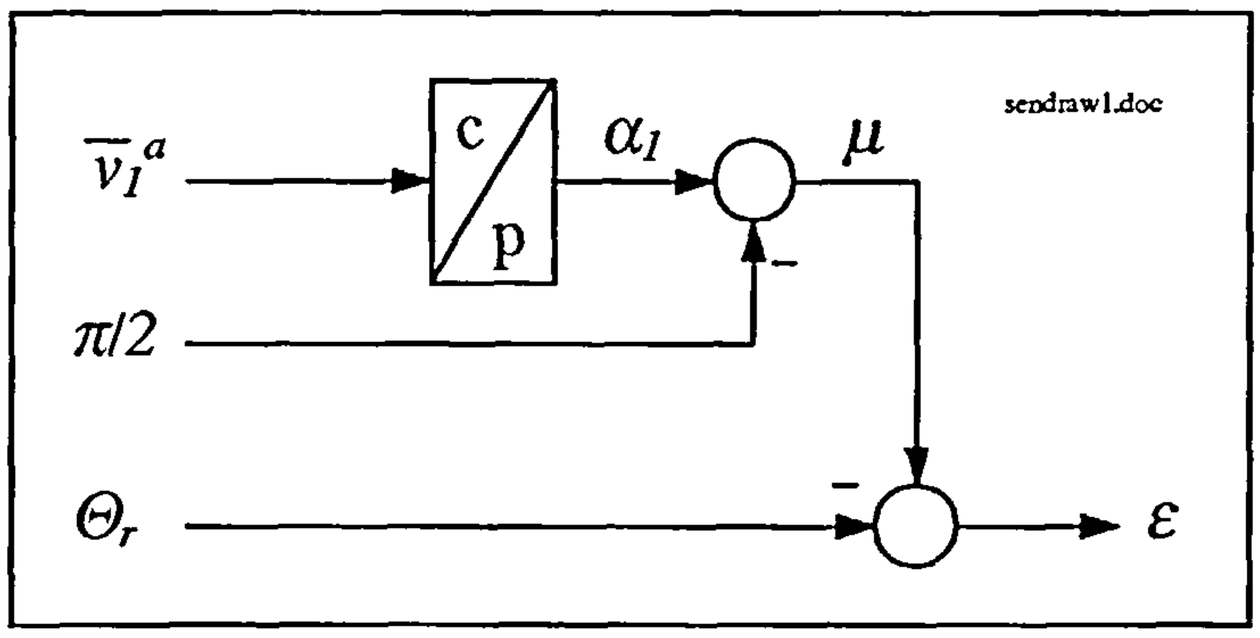

Figure 3.22: Angle construction for the SDFM

As it is the case for the second method, for this simple technique it is necessary to measure the stator voltage, but the stator voltage is anyway required, when applying a power control loop as will be the case. Additionally, there are no machine parameters involved in acquiring

the field angle. However, this method is only possible with a stiff voltage source free of fluctuations and voltage disturbances.

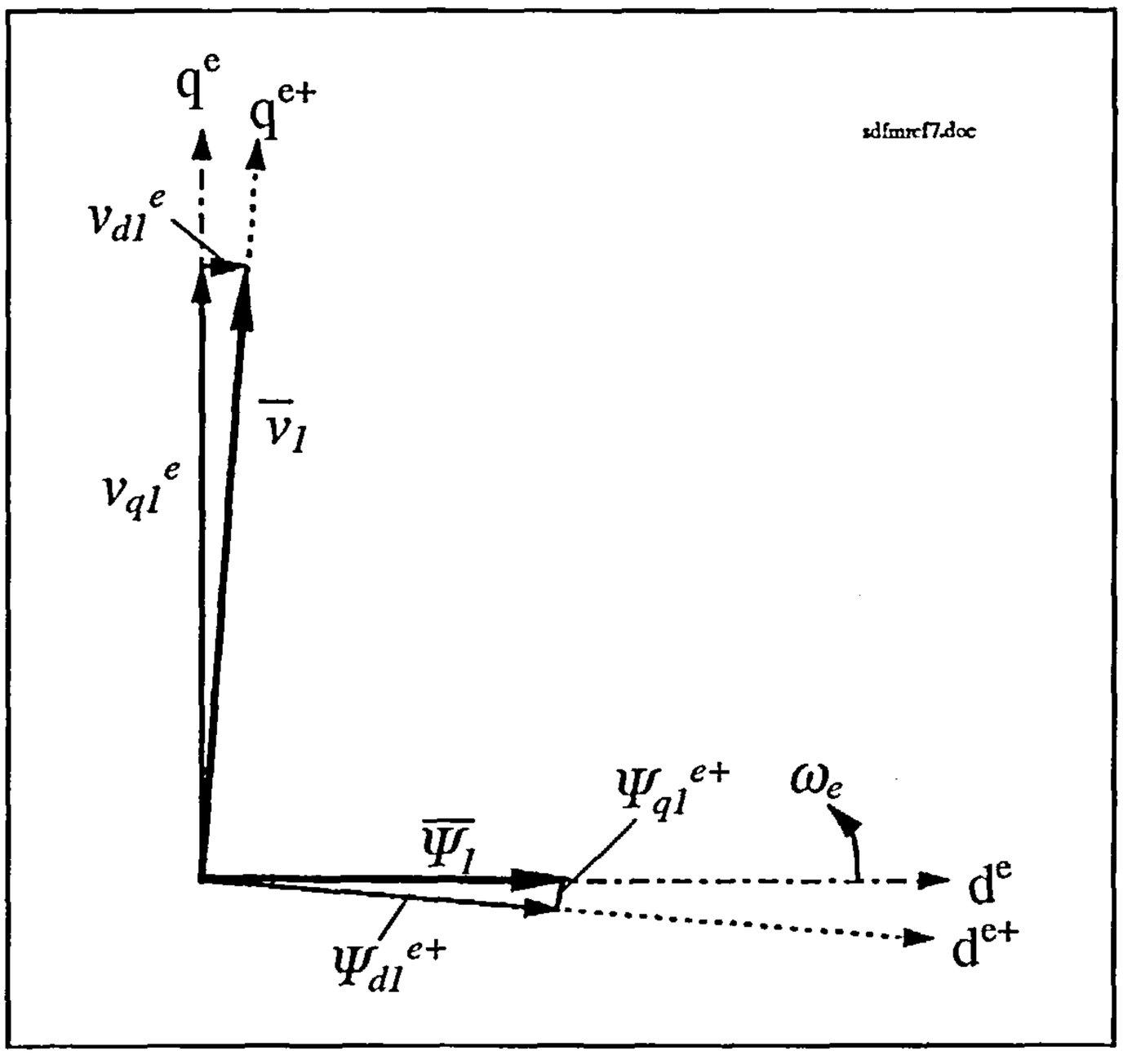

Figure 3.23: Stator voltage space vector in excitation reference frame "e"

The 2.25 kW laboratory machine used for experimental work has a relatively large stator resistance, but inspite of this it was decided to use the simple angle construction method. The influence of the resistance can be estimated by considering figure 3.23. There the stator voltage vector is expressed in the excitation reference frame "e" for the case of a lagging stator power factor. The angle between stator voltage and flux is smaller than 90°. For rated values of the laboratory SDFM in steady state the angle is 88° resulting in an error of around 2°. Although the influence of the stator resistance will be seen in experimental results, the small angle error still justifies the neglect of the stator resistance. As was discovered during experimental laboratory work, a far more important factor for the angle construction was the time difference between the sampling point of the stator voltage and the successive use of the acquired stator voltage angle. If that interval is too long the voltage and thus flux vector will have advanced in the meantime leading to an incorrect orientation of the rotor current.

Steady state analysis and machine model analysis indicate that decoupled control of rotor currents in the stator flux reference frame is possible. The stator flux is impressed by the stiff stator voltage and its magnitude is not dependent on the d-component of the rotor current in the "e"-frame as equation (3.3.8) would initially suggest. Rather the rotor current components control the stator current components in the "e"-frame as can be demonstrated

with equation (3.3.6). Rearranging (3.3.6) and splitting into d-q-components together with the constraints of equation (3.3.3) the rotor current shows following interaction with the stator current components

$$i_{d1}^{e} = \frac{1}{L_1}\Psi_1^{e} - \frac{L_m}{L_1} i_{d2}^{e} \tag{3.3.18}$$

$$i_{q1}^{e} = -\frac{L_m}{L_1} i_{q2}^{e} \tag{3.3.19}$$

When constant inductance values are assumed the d-component of the rotor current directly manipulates the stator current d-component and the rotor current q-component is a measure for the stator current q-component.

In the reference frame "e" with the simplifications of equation (3.3.17) it is obvious that because of equation (3.3.18) and (3.3.19) the stator active and reactive power are manipulated with the individual components of the rotor current. Stator active and reactive powers are calculated in terms of space vectors by stator voltage and current in a general reference frame as

$$P_1 = \frac{3}{2}(v_{d1}^{g} i_{d1}^{g} + v_{q1}^{g} i_{q1}^{g}) \quad \text{and} \quad Q_1 = \frac{3}{2}(v_{q1}^{g} i_{d1}^{g} - v_{d1}^{g} i_{q1}^{g}) \tag{3.3.20}$$

Applying the constraints of equation (3.3.17) together with (3.3.18) and (3.3.19) the active and reactive power can be expressed as

$$P_1 = -\frac{3}{2}\frac{\sqrt{2}V_1 L_m}{L_1} i_{q2}^{e} \tag{3.3.21}$$

$$Q_1 = \frac{3}{2}\frac{\sqrt{2}V_1}{L_1}\Psi_1^{e} - \frac{3}{2}\frac{\sqrt{2}V_1 L_m}{L_1} i_{d2}^{e} \tag{3.3.22}$$

It can be seen that stator active power is directly proportional to the q-component of the rotor current in the excitation reference frame and stator reactive power is proportional to the d-component of rotor current.

This was already indicated by the steady state simulations in section 3.2.2, where stator powers are dependent on the position of the rotor current phasor relative to the stator voltage phasor independent of speed.

3.3.1 Inner Current Control Loop

So far it has been assumed that an inverter in the rotor circuit resulting in perfect current control, which ensures that the demanded current values are actually present in the machine. In the laboratory set-up of the SDFM drive a voltage source inverter was used in the rotor circuit. Hence, a rotor voltage is impressed in the rotor windings, rather than a rotor

current. This makes it necessary to apply a fast current control loop to the voltage source inverter to ensure impressed rotor currents. The transformation of the rotor currents from the rotor reference frame into the excitation reference frame effectively modulates the a.c. currents at rotor frequency into d.c. values in the "e"-frame in steady state conditions. As already mentioned, the control structure of the SDFM in field coordinates resembles the control method of a separately excited DC-machine. The rotor currents in d.c. can therefore be controlled by classical PI-controller as it is the case for the DC-machine. Figure 3.24 shows the control scheme for the inner current control loop of the SDFM, which is now investigated further.

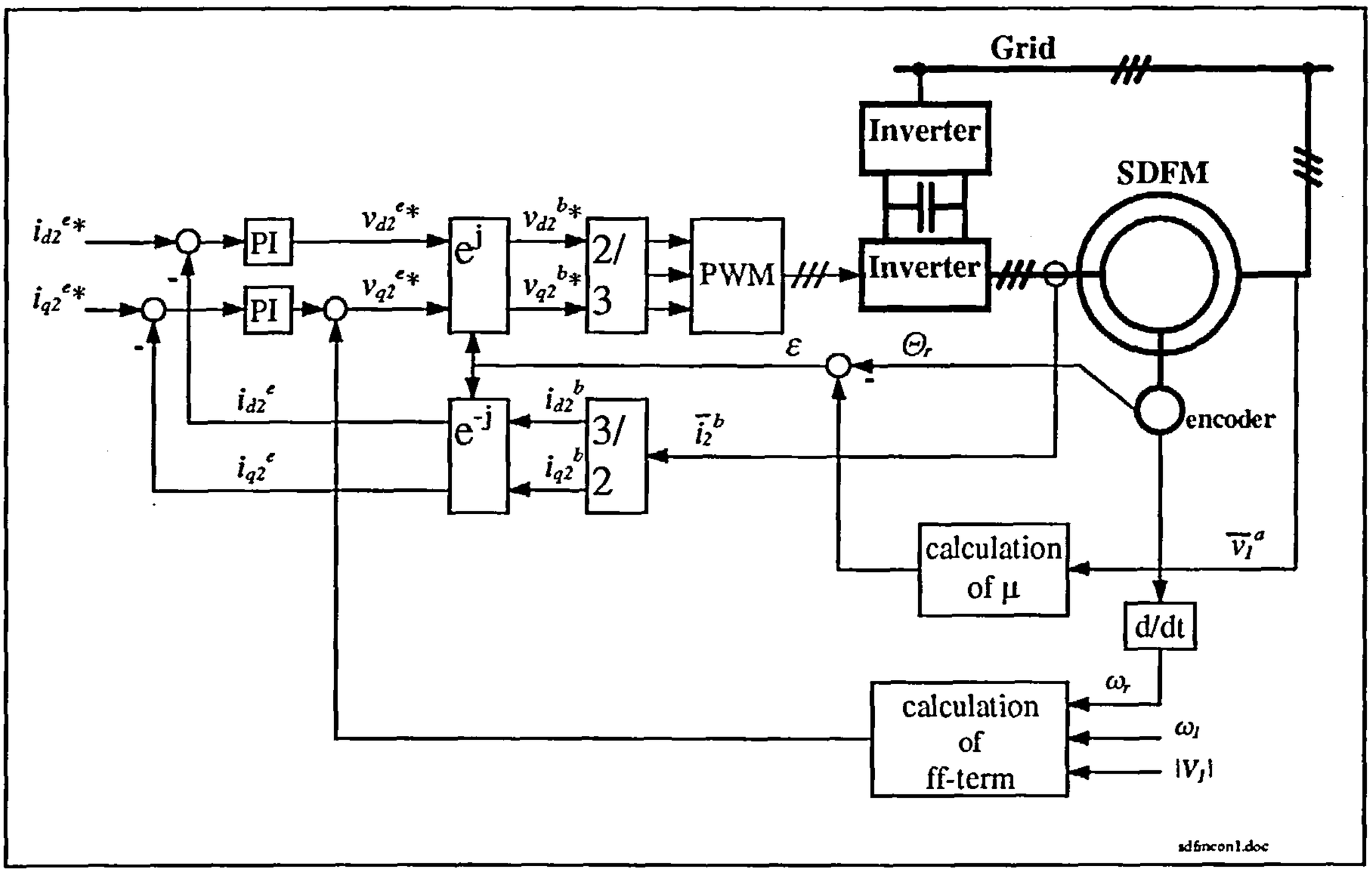

Figure 3.24: Control scheme of the SDFM - inner current control

The rotor voltage vector in the excitation reference frame is expressed in equation (3.3.5). Rotating the rotor flux vector equation (3.1.12) into the "e"-frame and by substituting the stator current with the help of equation (3.3.6), the rotor flux vector takes the form

$$\overline{\Psi}_2^e = (L_2 - \frac{L_m^2}{L_1})\bar{i}_2^e + \frac{L_m}{L_1}\overline{\Psi}_1^e \qquad (3.3.23)$$

Replacing (3.3.23) in (3.3.5) gives for the rotor voltage

$$\bar{v}_2^e = R_2\bar{i}_2^e + (L_2 - \frac{L_m^2}{L_1})\frac{d\bar{i}_2^e}{dt} + \frac{L_m}{L_1}\frac{d\overline{\Psi}_1^e}{dt} + j\omega_2(L_2 - \frac{L_m^2}{L_1})\bar{i}_2^e + j\omega_2\frac{L_m}{L_1}\overline{\Psi}_1^e \qquad (3.3.24)$$

where $\omega_2 = \omega_1 - \omega_r$.

Splitting (3.3.24) in d-q and considering only steady state ($\frac{d}{dt} = 0$) with $\Psi_{q1}^e = 0$ leads to

$$v_{d2}^{e}* = R_2 i_{d2}^{e} - \omega_2 (L_2 - \frac{L_m^{\ 2}}{L_1}) i_{q2}^{e} \qquad (3.3.25)$$

$$v_{q2}^{e}* = R_2 i_{q2}^{e} + \omega_2 (L_2 - \frac{L_m^{\ 2}}{L_1}) i_{d2}^{e} + \omega_2 \frac{L_m}{L_1} \Psi_1^{e} \qquad (3.3.26)$$

The components $v_{d2}^{e}*$ and $v_{q2}^{e}*$ are the rotor voltage components in the "e"-frame which are necessary to ensure the desired rotor current values i_{d2}^{e} and i_{q2}^{e} in the rotor circuit. As it can be seen, the second terms in those equations constitute cross coupling terms and the third term in (3.3.26) is equivalent to an speed dependent induced e.m.f. in the rotor circuit due to the stator flux. The cross coupling terms turn out to have only a marginal influence with a factor of 0.046 for the used machine and are therefore neglected, but that cannot be said for the e.m.f. term with a factor of about 0.815. This term acts as a disturbance to the output of the PI-controller in the q-axis. It is possible to compensate the influence of the back e.m.f. term by choosing high PI-controller gains, but a steady state tracking error will persist [f16]. The tracking error can be eliminated by adding a feed forward term to the output of the q-axis controller with the value

$$feed\ forward = \omega_2 \frac{L_m}{L_1} \Psi_1^{e} \qquad (3.3.27)$$

This also results in easier tuning. The inputs to the feed forward calculator in figure 3.24, equation (3.3.27) and (3.3.16), are the rotor speed, the synchronous angular frequency and the magnitude of the stator voltage. The latter two are constants, since a stiff voltage grid is presumed.

Hardware is shown in bold lines in figure 3.24. The control structure, the PWM, the calculation of the angles and the feed forward term is performed by the microcontrollers 80C167 as described in chapter 2.

Experimental results for the inner current control loop of the SDFM are presented in figures 3.26 to 3.31. The hardware set-up and configuration is described in chapter 2, but a short description of the overall configuration shall be sketched out in the following paragraphs.

Measurements were taken for the generating mode of the SDFM, permitting the later extension of the inner current control loop with an outer power control loop. For that the DC-machine was set up to act as a prime mover for the SDFM. Only manual current control of the DC-machine was possible, via a potentiometer.

As laid out in figure 3.24, side 1 of the SDFM is connected to the 415 V supply network and side 2 to the machine-side inverter, which has a switching frequency of 4 kHz allowing 250 µs for the software implementation. The tasks for the individual microcontrollers was split up in the following way

μC1 sampling and A/D conversion of the rotor current
complete inner current control loop including PWM
calculation of rotor position and speed from the encoder signals
calculation of feed-forward term

μC2 sampling and A/D conversion of stator voltage
calculation of stator flux position

The data transfer from μC1 to μC2 was carried out at the end of the interrupt routine, so that the data is available in the successive routine in μC1.

Demand values of the rotor current components, denoted by the asterisk "*", could either be set manually via potentiometer or internally programmed.
The tuning of the PI-controller parameter was carried out in a manual way with the help of two potentiometers.

In figure 3.26 and 3.27 experimental results for a step change in the d-component of the rotor current are presented. The demand value for the d-axis current was set to perform a sudden step from 0 A to 4 A and then back to 0 A, while the q-axis current was left at a constant value of 2 A. It can clearly be seen that due to that step change the stator reactive power is controlled. The slight variation in the stator active power is the basic effect of the stator resistance as can be further explained by looking at figure 3.23. In there a second reference frame, denoted as "e+", is aligned with the stator voltage vector. Field orientation actually takes place with that reference frame, since it is assumed that the stator flux is 90° lagging relative to the stator voltage. Hence, following is valid

$$v_{d1}^{e+} = 0 \quad \text{and} \quad \Psi_{q1}^{e+} \neq 0 \tag{3.3.28}$$

With that and regarding equation (3.3.20)

$$P_1 \propto i_{q1}^{e+} \quad \text{and} \quad Q_1 \propto i_{d1}^{e+} \tag{3.3.29}$$

which is clearly visible in figure 3.26, where the same influence in step responses occurs in the power and stator current graphs. The relationship between stator and rotor current has slightly changed from the situation in equation (3.3.18) and (3.3.19) to

$$i_{d1}^{e+} = \frac{1}{L_1}\Psi_{d1}^{e+} - \frac{L_m}{L_1} i_{d2}^{e+} \tag{3.3.30}$$

$$i_{q1}^{e+} = \frac{1}{L_1}\Psi_{q1}^{e+} - \frac{L_m}{L_1} i_{q2}^{e+} \tag{3.3.31}$$

The individual flux components vary in the reference frame "e+" depending on the angle between stator flux and stator voltage. This again is influenced by the voltage drop across

the stator resistance.
A step in i_{d2}^{e+}, for example, has an effect on the stator current and thus on the voltage drop, which leads to a slight position change of the stator flux linkage vector in the "e+"-frame. Due to that, Ψ_{q1}^{e+} would be affected and this would be seen in the q-component of the stator current.
Although the effect of the stator resistance can be seen, it is still small enough to justify the neglect of it.

Figure 3.27 shows the same step response in the d-axis current component together with the stator voltage and current in the same phase of the stator winding. The phase change between stator voltage and current with the change in the magnitude in the stator current clearly displays the fundamental principle of field orientation, which is basically a sudden step change from one steady state condition into another. That can also be seen in figure 3.28 for a step change in the q-component of the rotor current.

A second set of graphs for a step change in the q-component is displayed in figure 3.29. Again, the minor effect of the stator resistance can be recognised. For these measurements the speed varies across the synchronous speed of the SDFM. That is due to the constant torque mode of the prime mover. Since a change in the q-component of the rotor current in the "e"-frame manipulates the torque of the SDFM, equation (3.3.2), the machine set is speeding up and down, depending on the torque balance.

Figure 3.30 shows a wide range speed variation with constant values for the d-component and q-component of the rotor current demonstrating the independence of speed upon the current control loop. That independence is mainly due to cancellation of the slip proportional induced e.m.f. in the q-axis with the feed forward term. Figure 3.31 displays the tracking of the demand value by its actual value with and without the inclusion of the feed forward term in the control loop with same PI-controller parameter in both cases.

3.3.2 Outer Power Control Loop

The proportionality of the rotor current components to the stator active and reactive power allows the inner current control loop to be supplemented with an outer power control loop in a cascaded manner, as it is known from the DC-machine control. The extension to the inner current loop is shown in figure 3.25.

The actual values for the active and reactive power are calculated from the measured stator voltage and current in the stationary reference frame with the help of equation (3.3.20). This

task and the sampling of the stator current is carried out by µC2 as well as the complete power control. The processed demand values for the inner current control loop are transferred to µC1 at the end of the interrupt routine together with all the other transfer data.

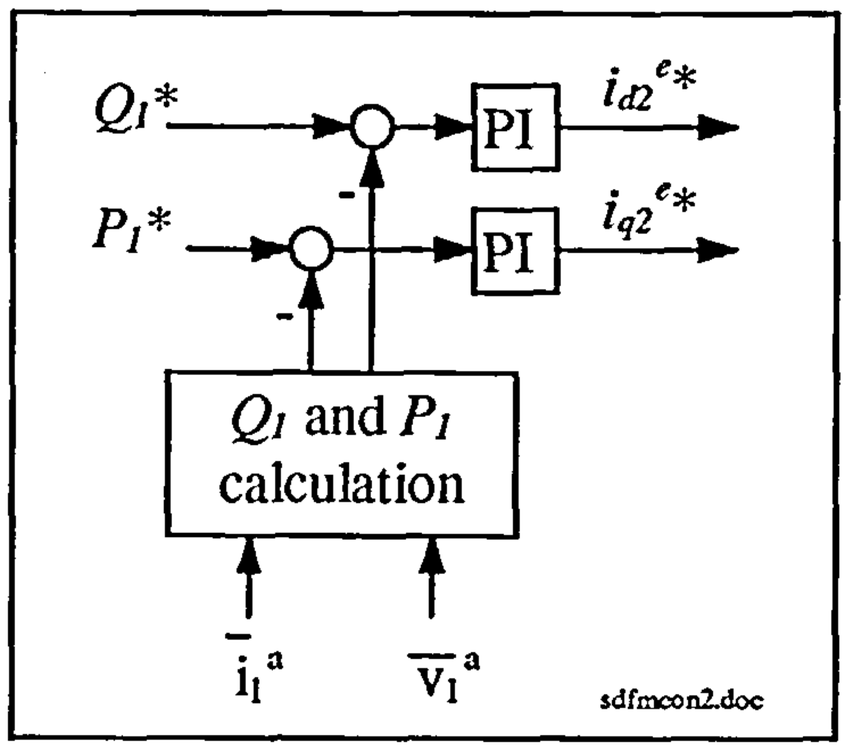

Figure 3.25: Power control loop extension

Figure 3.32 illustrates experimental results for step changes in the active and reactive power demand. Both graphs show very good decoupling. Figure 3.33 shows the results for the power control loop with constant demand values over a wide speed range and demonstrates the independence of speed upon the control of the SDFM.

3.3.3 Speed Control Loop

So far the SDFM has been used in generating mode, but for other applications, such as pump drives, torque or speed control may be appropriate. Based on equation (3.3.2) it is shown that in the field oriented reference frame the torque is proportional to the q-axis rotor current. Therefore by controlling the q-component a torque or speed control can be performed with the SDFM. Figure 3.34 illustrates experimental measurements for a speed control application. A demand speed ramp from 1000 to 1650 rpm and back is carried out at no-load. In this case the d-component of the rotor current can be set to a constant value. As equation (3.3.2) suggests the torque is manipulated by the q-component in order to follow the demand speed value, whereas the d-component is held constant across the speed variation. The necessary extension to form a speed control loop cascaded onto the q-axis rotor current control is shown in figure 3.35. In the results it can also be seen, that the stator power is proportional to the q-axis rotor current.

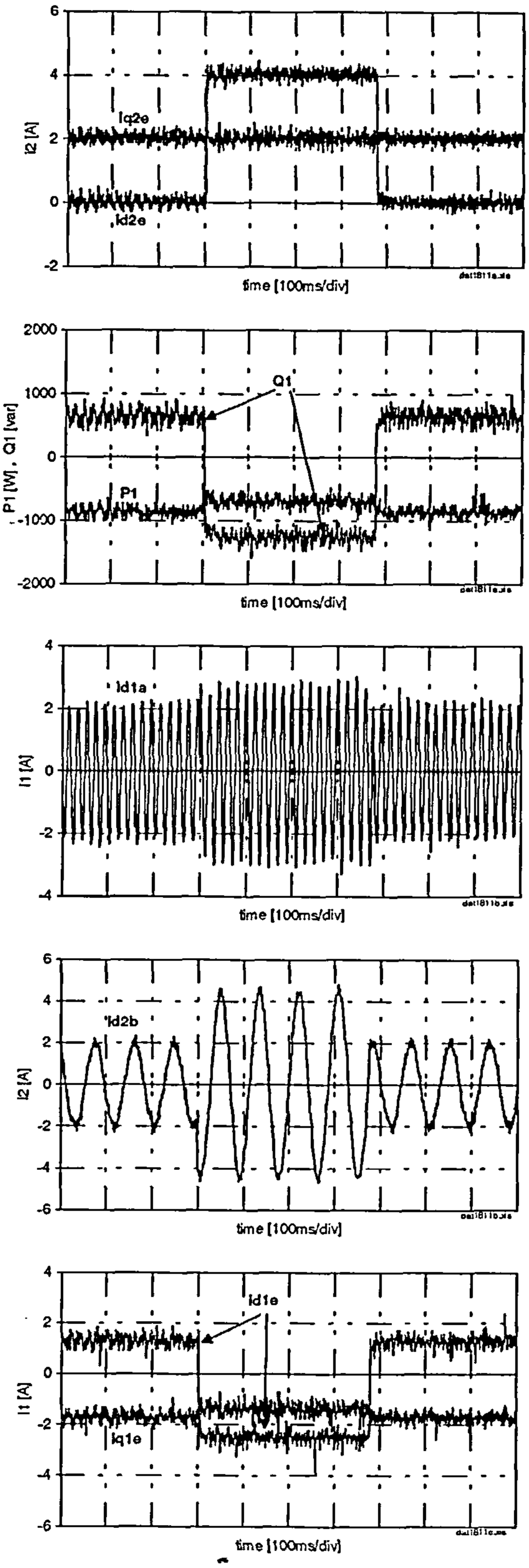

Figure 3.26: Experimental SDFM dynamics I of a step change in i_{d2}^{e*} - current control loop

(step in $i_{d2}^{e*} = 0$ to 4 A , $i_{q2}^{e*} = 2$A , n_m=1140 rpm)

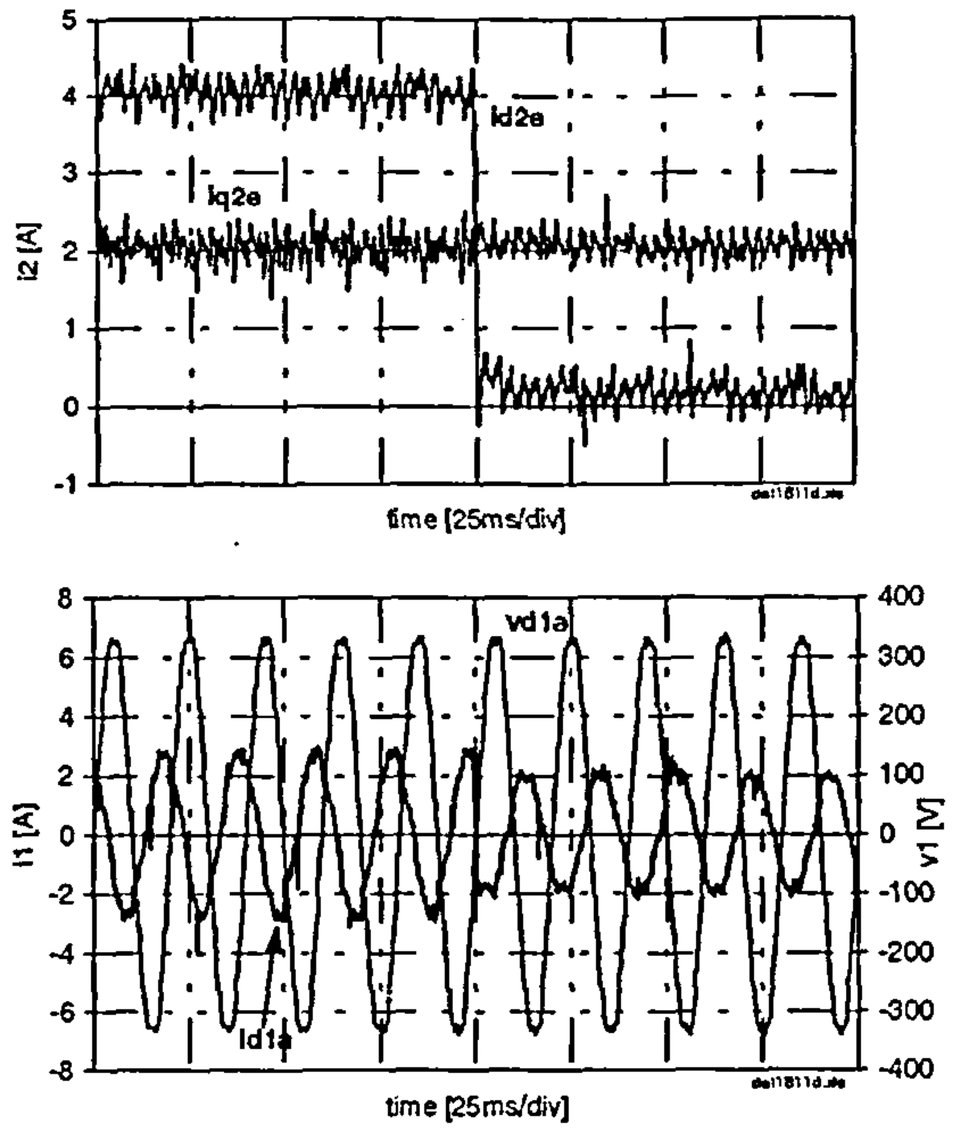

Figure 3.27: Experimental SDFM dynamics II of a step change in i_{d2}^{e*} - current control loop

(step in i_{d2}^{e*} = 4 to 0 A , i_{q2}^{e*} = 2 A , n_m=1200 rpm)

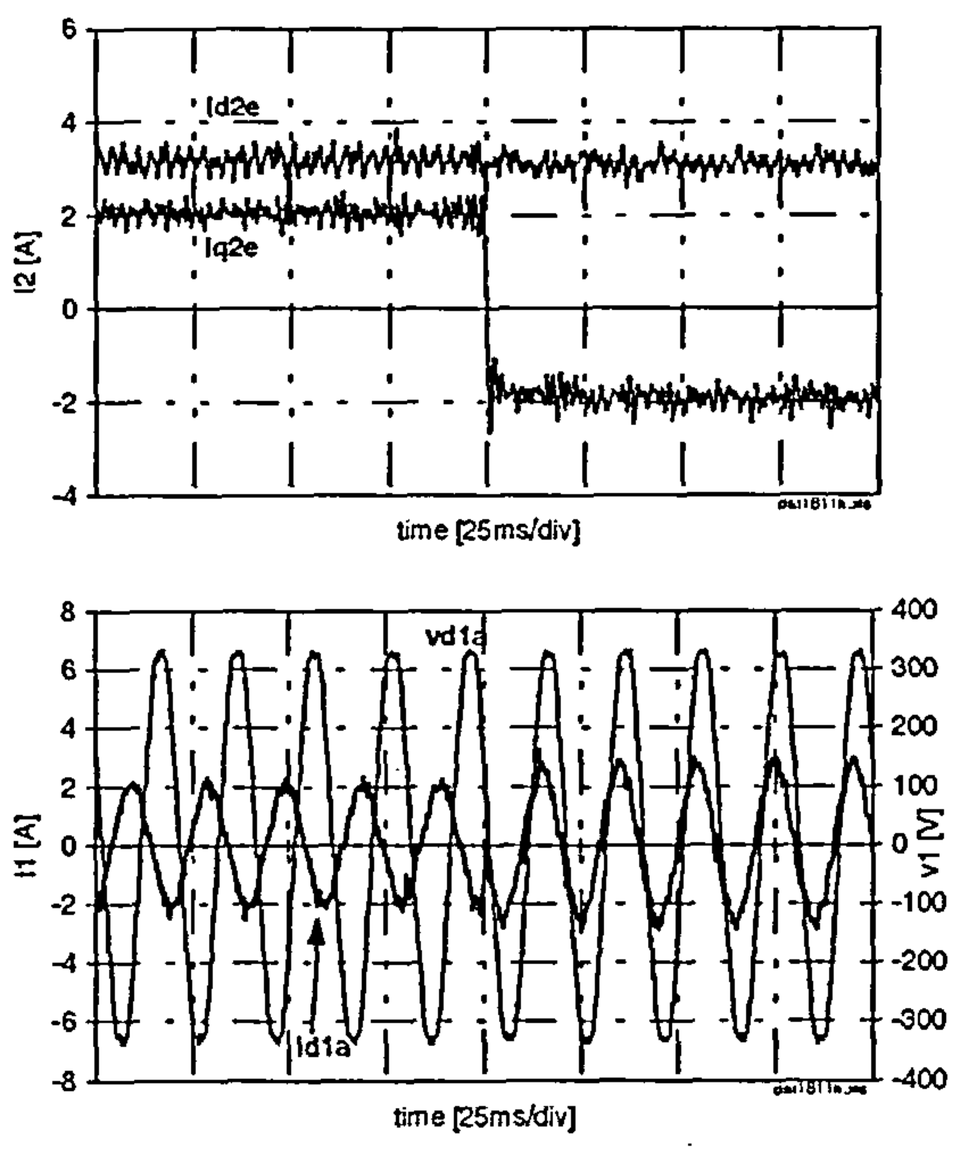

Figure 3.28: Experimental SDFM dynamics I of a step change in i_{q2}^{e*} - current control loop

(step in i_{q2}^{e*} = 2 to -2 A , i_{d2}^{e*} = 3 A , n_m=1450 rpm)

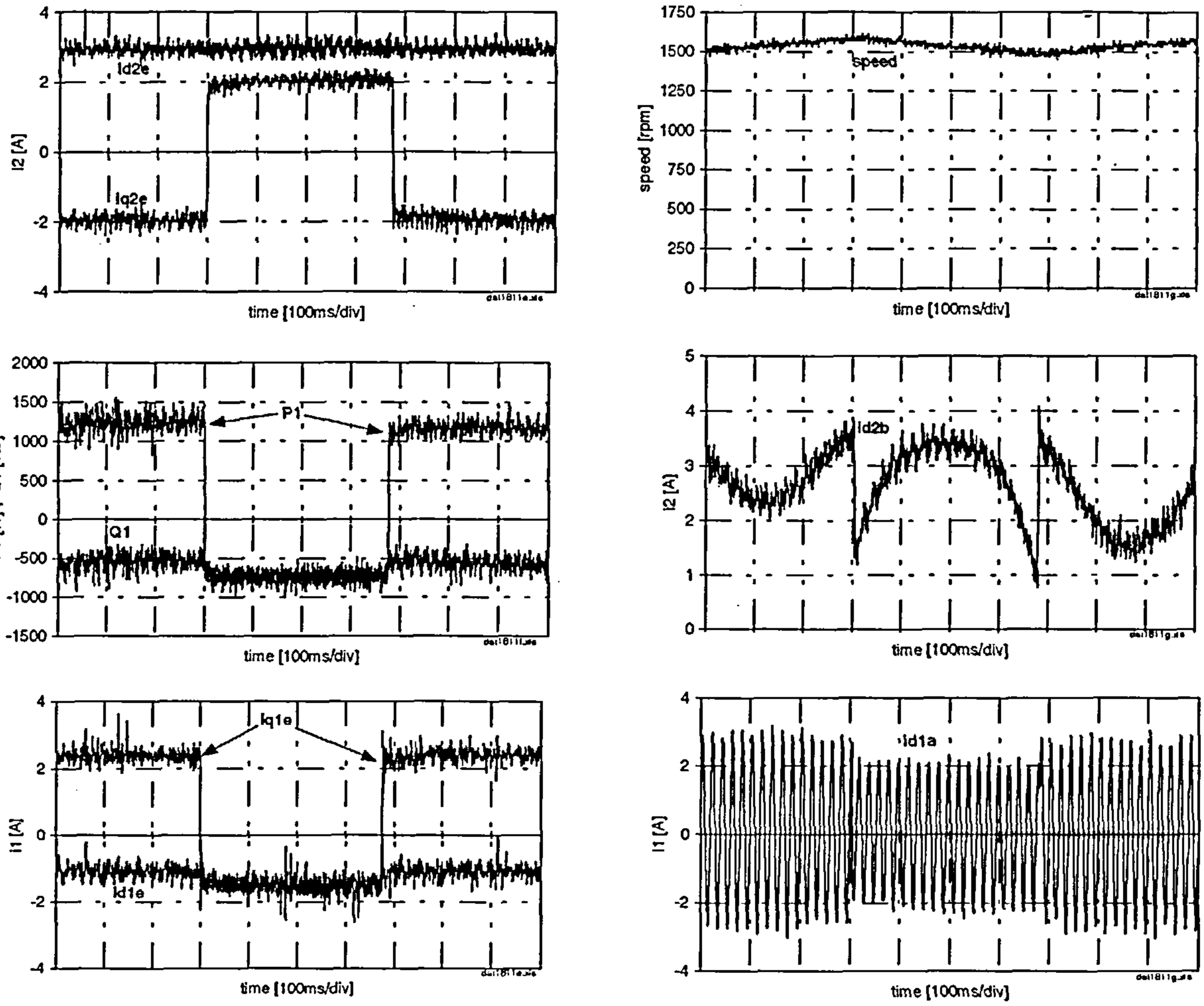

Figure 3.29: Experimental SDFM dynamics II of a step change in $i_{q2}^{e}*$ - current control loop

(step in $i_{q2}^{e}* = 2$ to -2 A , $i_{d2}^{e}* = 3$ A)

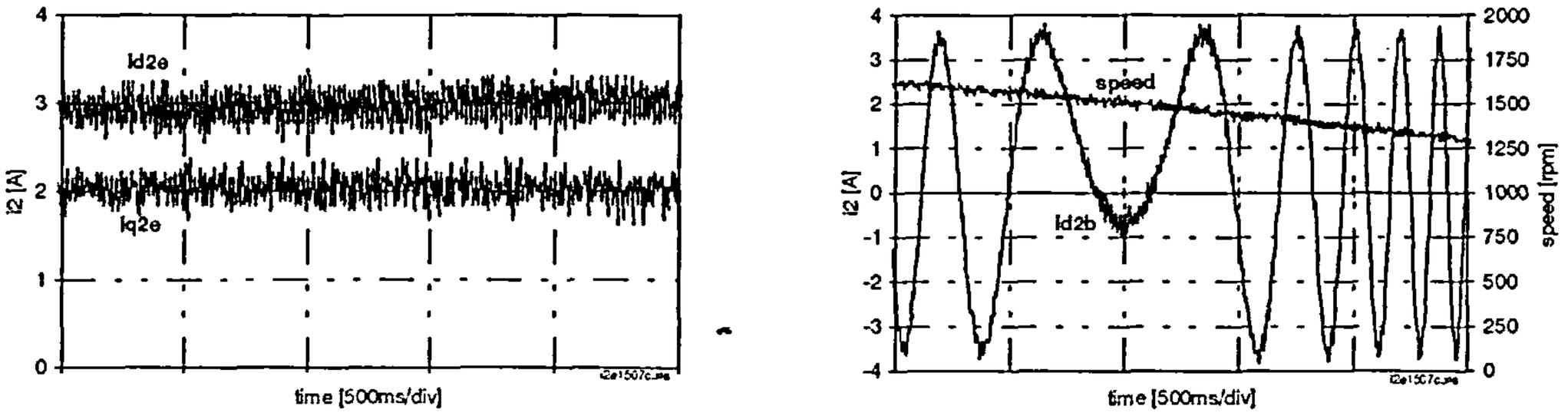

Figure 3.30: Experimental SDFM dynamics over speed range with constant demand values for $i_{d2}^{e}*$ and $i_{q2}^{e}*$ - current control loop

($i_{d2}^{e}* = 3$, $i_{q2}^{e}* = 2$ A , $n_m = 1620$ - 1280 rpm)

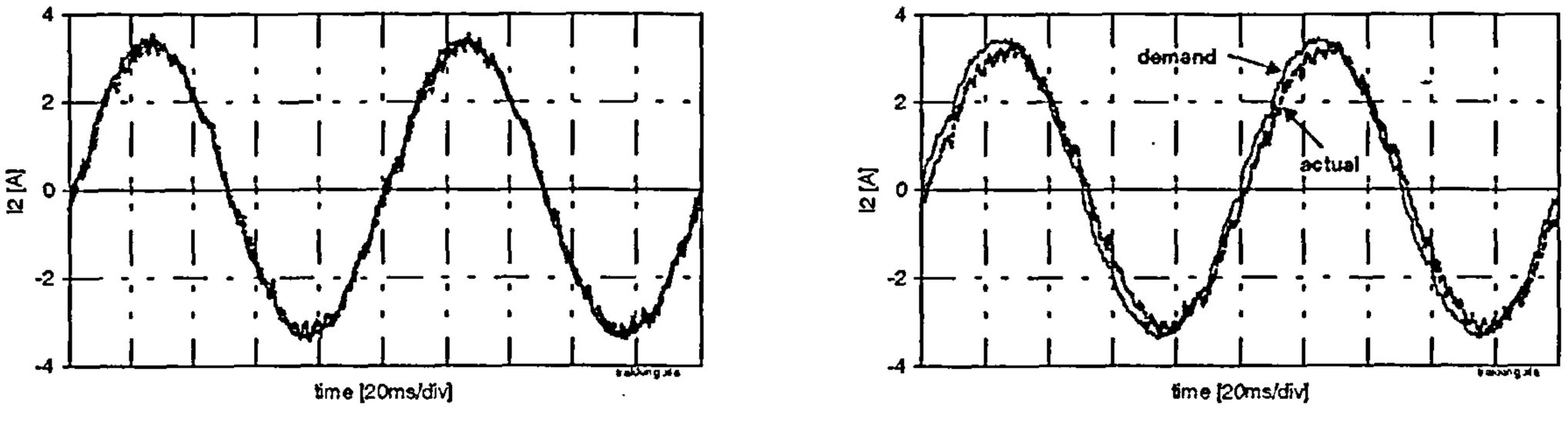

Figure 3.31: Experimental SDFM dynamics demonstrating the effect of the feed forward term in the q-axis at 1200 rpm - current control loop

(left: with feed forward term right: without feed forward term

$i_{d2}^{e*} = 3$ A , $i_{q2}^{e*} = 1.5$ A)

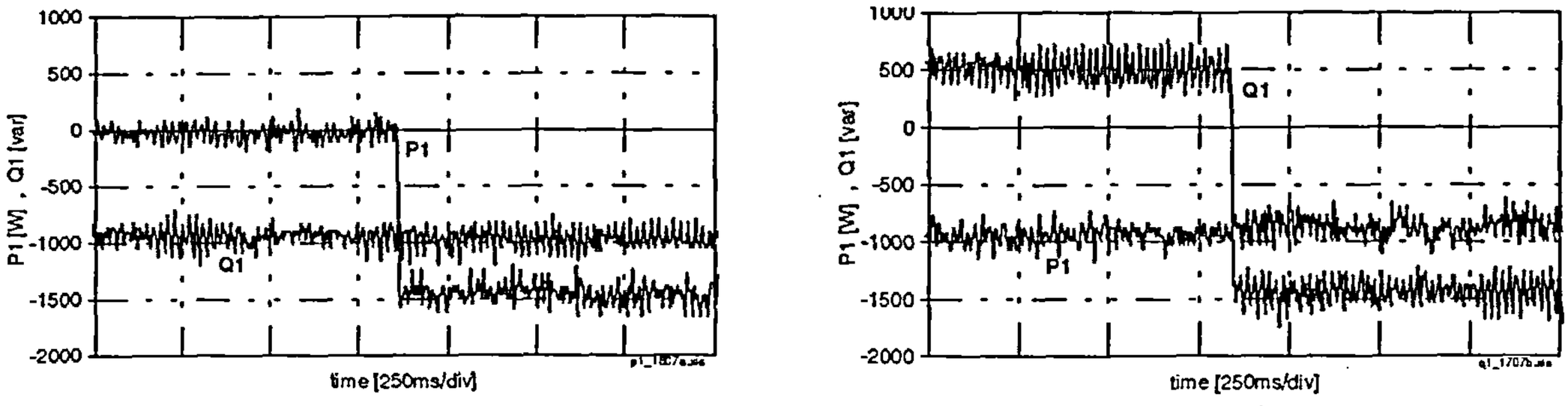

Figure 3.32: Experimental SDFM dynamics for step changes in P_1* and Q_1* - power control loop

(left: step in P_1* = 0 to -1.5 kW , Q_1* = -1 kvar , n_m = 1650 rpm

right: step in Q_1* = 0.5 to -1.5 kvar , P_1* = -1 kW , n_m = 1200 rpm)

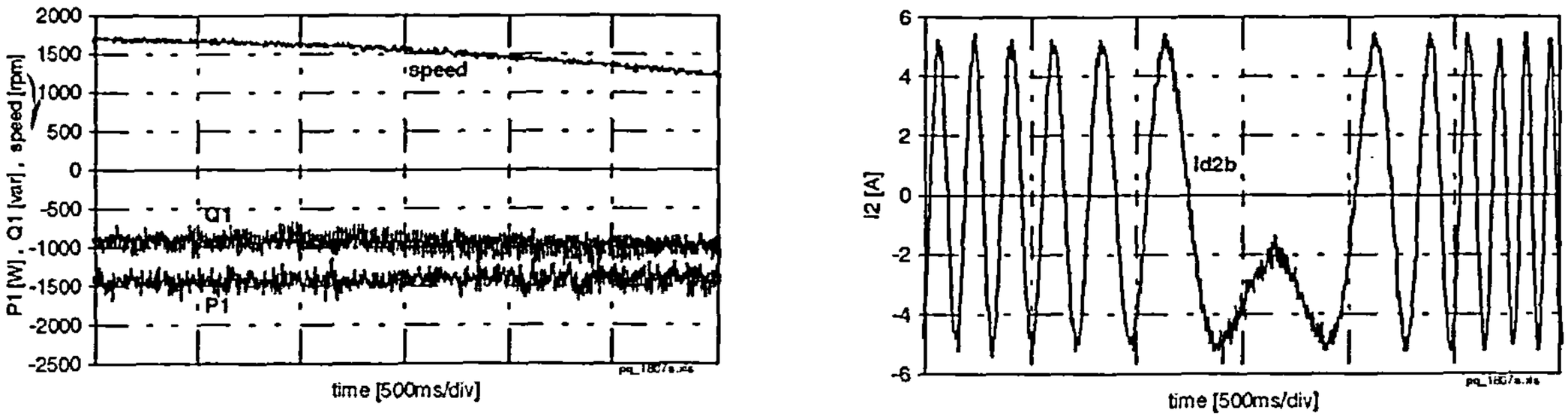

Figure 3.33: Experimental SDFM dynamics over speed range with constant demand values for P_1* and Q_1* - power control loop

(Q_1* = -1 kvar , P_1* = -1.5 kW , n_m = 1700-1200 rpm)

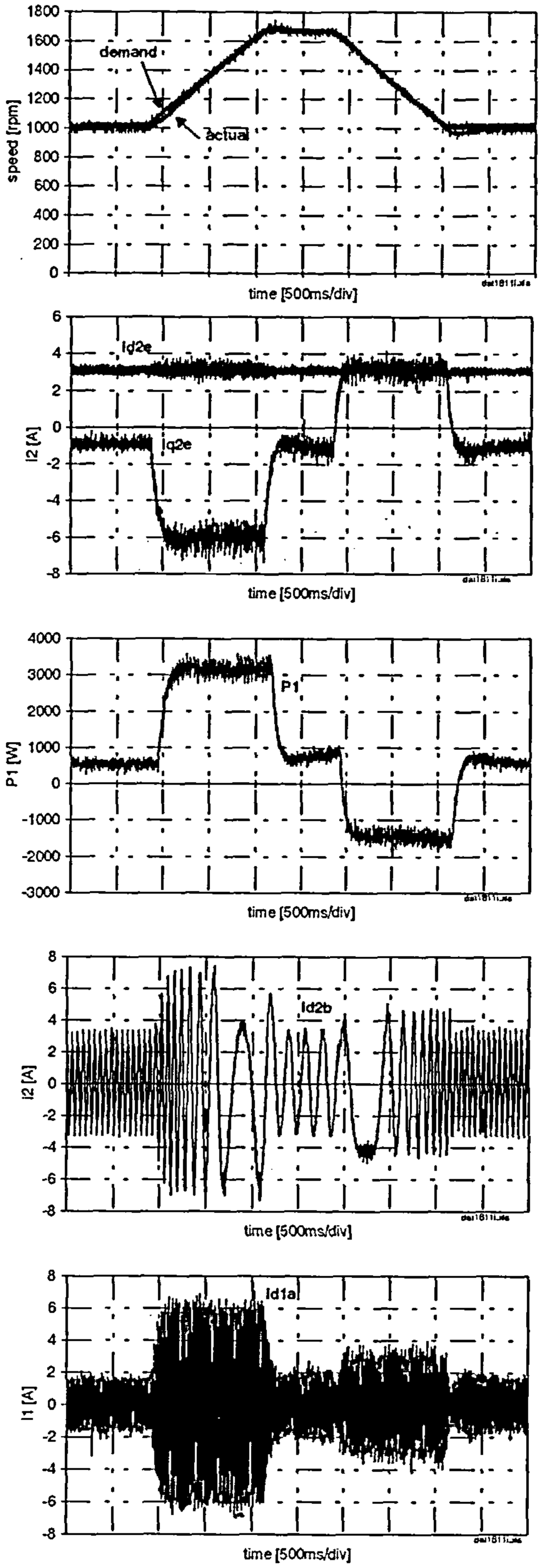

Figure 3.34: Experimental SDFM dynamics of the speed control loop for no-load

(i_{d2}^{e}* = 3 A , n_m* = 1000-1650 rpm)

The speed control loop was performed in µC1. The switching frequency of the inverter in that case was changed from 4kHz to now 2.5kHz, to allow 400µs for the implementation.

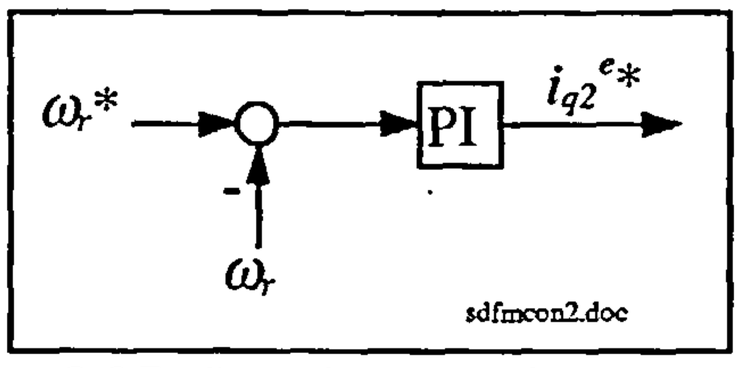

Figure 3.35: Speed control loop extension

3.4. Summary

Initially beginning with the space vector method as a tool for modeling the dynamic behaviour of the machine, the complete SDFM machine model in a general reference frame is presented in this chapter as a starting point for the field oriented approach.
Simulations based on a steady state per-phase equivalent circuit for the SDFM underline the usefulness of a steady state model for familiarising with the "doubly-fed" principle. Experimental measurements support the steady state simulations and justify the formation of a general power flow diagram.
Finally, the field oriented control of the SDFM is derived based on stator flux linkage orientation. Experimental results show the decoupled control possibilities of stator active and reactive power. The field oriented control is also applied to a speed control loop.

The thorough and extensive description and modeling of the SDFM machine with its control was necessary to help with the understanding of the CDFM, which is described in the next two chapters.

Chapter 4

Cascaded Doubly-Fed Induction Machine

The cascaded doubly-fed induction machine is a connection of two wound rotor induction machines as depicted in figure 4.1. Both, the rotor mechanical shaft and the rotor windings are directly connected to form a two-machine doubly-fed system, where the individual machines, machine A and machine B, can have any pole pair number. Due to the rotor winding connection, i.e. the direct connection of the slip rings, brushes become obsolete in contrast to the SDFM. Therefore the arrangement constitutes a brushless doubly-fed system.

The following analysis in this chapter are applicable to the CDFM and to the SF-CDFM, since there is no difference in the fundamental electrical behaviour of those machines.

The nomenclature adopted is also shown in figure 4.1, in which the particular machine sides are as follows:

side 1 - stator of machine A or stator A

side 2 - rotor of machine A or rotor A

side 3 - rotor of machine B or rotor B

side 4 - stator of machine B or stator B

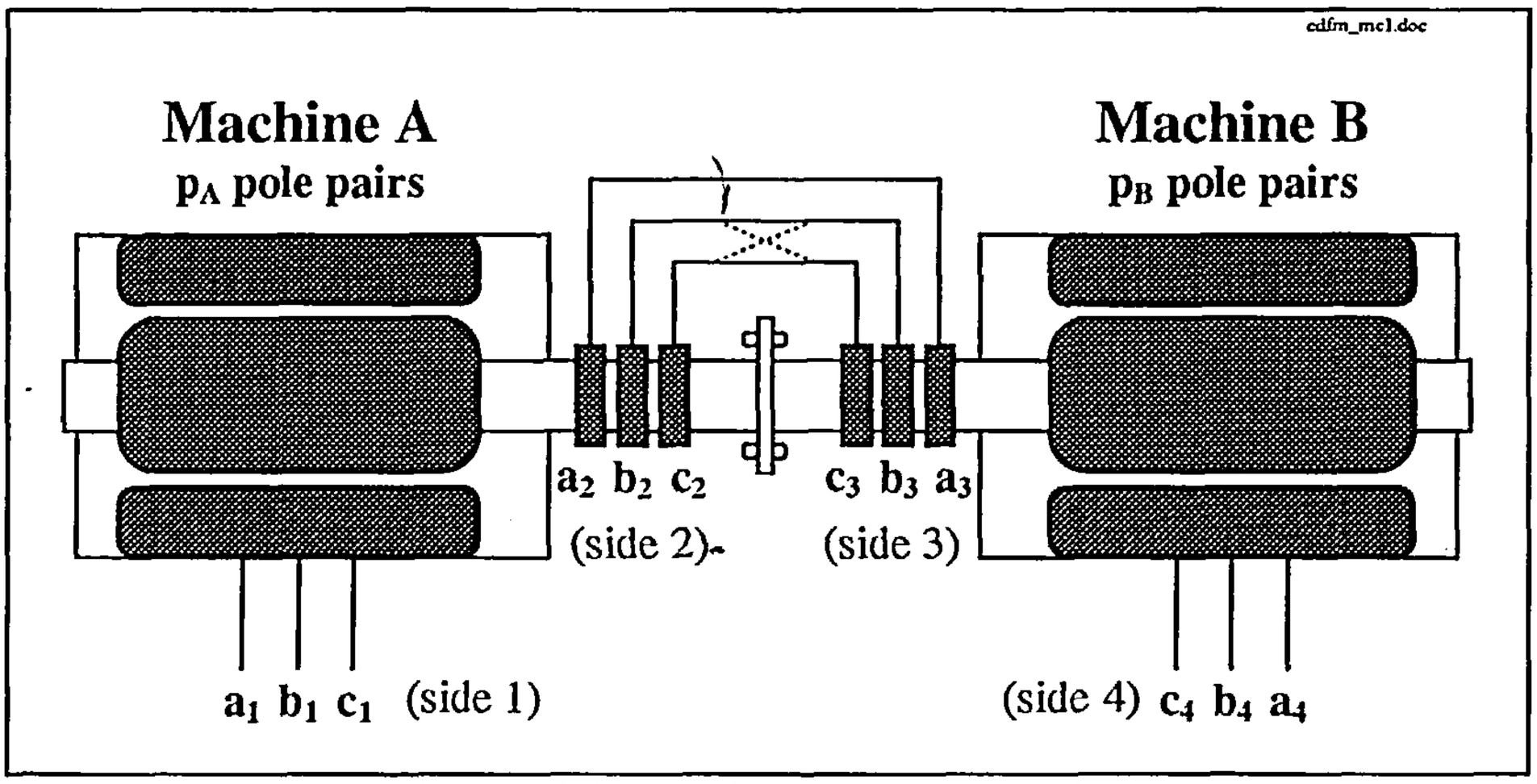

Figure 4.1: Cascaded doubly-fed induction machine arrangement

In the first section of this chapter the rotor connection possibilities are explained and a reference frame system is developed. After the introduction of the torque equation for the CDFM the dynamic machine model for both machine connection possibilities is derived. The reference frame system and the dynamic model of the CDFM serve as a foundation for the field oriented control of the CDFM in chapter 5.
Comprehensive steady state treatment is carried out in the same manner as for the SDFM to show similarities between the SDFM and the CDFM. After frequency and slip definitions the per-phase equivalent circuit is developed, always taking account of the rotor connection possibilities. Steady state simulations are performed in close relation to the steady state simulation of the SDFM. Finally, in steady state the influence of the pole pair combination is analysed.

4.1 Dynamic Model

4.1.1 Rotor Connection and Reference Frames

Before developing the dynamic model of the CDFM it is necessary to clear the matter of the rotor connection and define the reference frame relationship of all four machine sides of the CDFM.

Rotor Connection

As indicated in figure 4.1 there are two possible ways to connect the rotor windings of each machine to each other. Either a positive phase sequence mode or a negative phase sequence mode is possible. In positive phase sequence connection the individual torque components act in the same direction, but with the negative phase sequence connection the two machines develop opposing torques [c4]. Therefore the negative phase sequence connection has no real use in high power applications and is mainly only of academic interest. Despite that fact the dynamic machine model and the steady state equations are developed for both machine connections for the sake of completeness.

Positive phase sequence rotor connection

Side 2 is connected with side 3 as a_2-a_3, b_2-b_3 and c_2-c_3 (solid lines in figure 4.1). A positive phase sequence on side 2 a_2-b_2-c_2 results in a positive phase sequence on side 3 a_3-b_3-c_3 and the angular frequency definition on both sides is as

$$\omega_2 = \omega_3 \tag{4.1.1}$$

because side 2 and side 3 have always the same phase sequence. That means, that the electrical rotor quantities are counter rotational relative to the rotor, due to the back-to-

back machine arrangement. The resulting electrical connection of the rotor windings is shown in figure 4.2, in which the individual phase voltages and currents assume the relationship [b5]

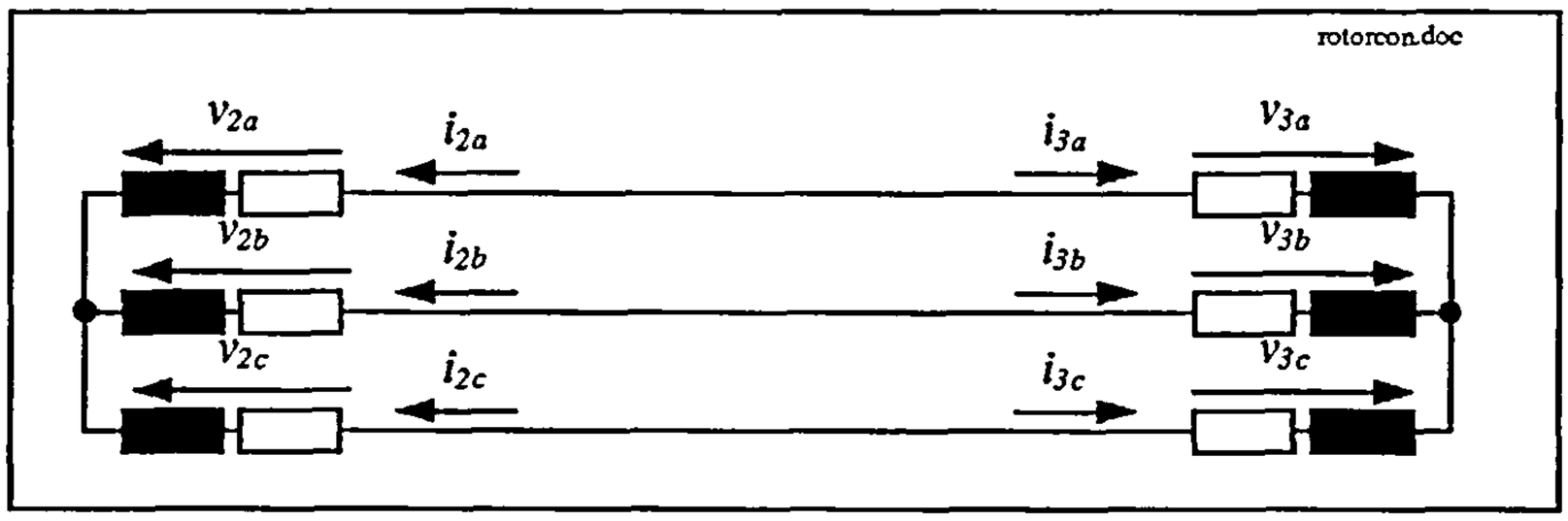

Figure 4.2: Positive phase sequence rotor connection

$$v_{2a} = v_{3a} \quad \text{and} \quad i_{2a} = -i_{3a}$$
$$v_{2b} = v_{3b} \quad \text{and} \quad i_{2b} = -i_{3b}$$
$$v_{2c} = v_{3c} \quad \text{and} \quad i_{2c} = -i_{3c}$$

By using space vector definition, the d-components and the q-components of the voltages and currents take following connection

$$v_{d2} = v_{d3} \quad \text{and} \quad v_{q2} = v_{q3}$$
$$i_{d2} = -i_{d3} \quad \text{and} \quad i_{q2} = -i_{q3}$$

which leads to the space vector connection of the voltages and currents in the form

$$\bar{v}_2 = \bar{v}_3 \quad \text{and} \quad \bar{i}_2 = -\bar{i}_3 \tag{4.1.2}$$

Negative phase sequence rotor connection

Side 2 is connected with side 3 as a_2-a_3, b_2-c_3 and c_2-b_3 (crossed over lines in figure 4.1). The electrical circuit for this connection is shown in figure 4.3. Now a positive phase sequence on side 2 results in a negative phase sequence on side 3 a_3-c_3-b_3 with

$$\omega_2 = -\omega_3 \tag{4.1.3}$$

and the electrical rotor quantities rotate in the same spatial direction relative to the rotor. In this case the phase quantities take the relation [b5]

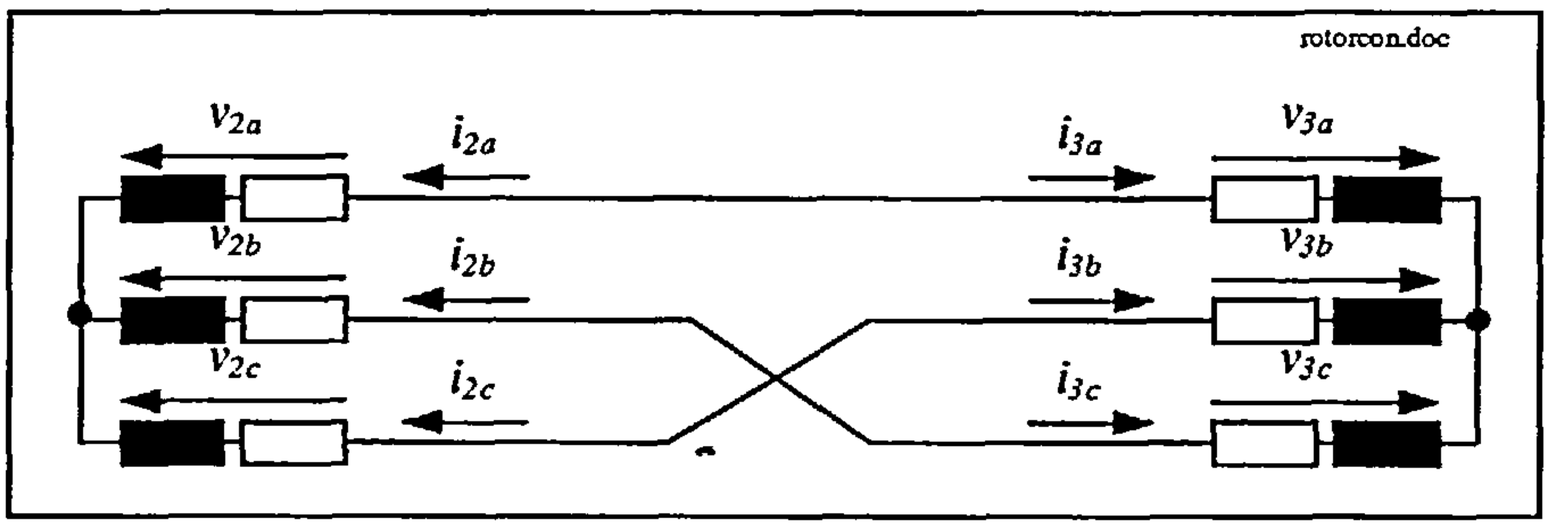

Figure 4.3: Negative phase sequence rotor connection

$$v_{2a} = v_{3a} \quad \text{and} \quad i_{2a} = -i_{3a}$$
$$v_{2b} = v_{3c} \quad \text{and} \quad i_{2b} = -i_{3c}$$

$$v_{2c} = v_{3b} \quad \text{and} \quad i_{2c} = -i_{3b}$$

and in the in d-q-system

$$v_{d2} = v_{d3} \quad \text{and} \quad v_{q2} = -v_{q3}$$

$$i_{d2} = -i_{d3} \quad \text{and} \quad i_{q2} = i_{q3}$$

Therefore the rotor voltage space vectors and the rotor current space vectors are connected in a conjugated manner

$$\bar{v}_2 = conj(\bar{v}_3) \quad \text{and} \quad \bar{i}_2 = -conj(\bar{i}_3) \tag{4.1.4}$$

Reference Frames

Compared to the SDFM the CDFM has four different reference frames. One attached to each machine side. The reference frames for machine A are straight forward to obtain since machine A basically forms a SDFM on its own. If the view onto machine A is taken as indicated then the reference frame system can be seen in figure 4.4, including the 3-phase and the 2-phase system of the machine. Reference frame "a" is stationary and reference frame "b" is moving in positive direction relative to frame "a" with the mechanical rotor speed ω_{rA} in electrical radians per second of machine A.

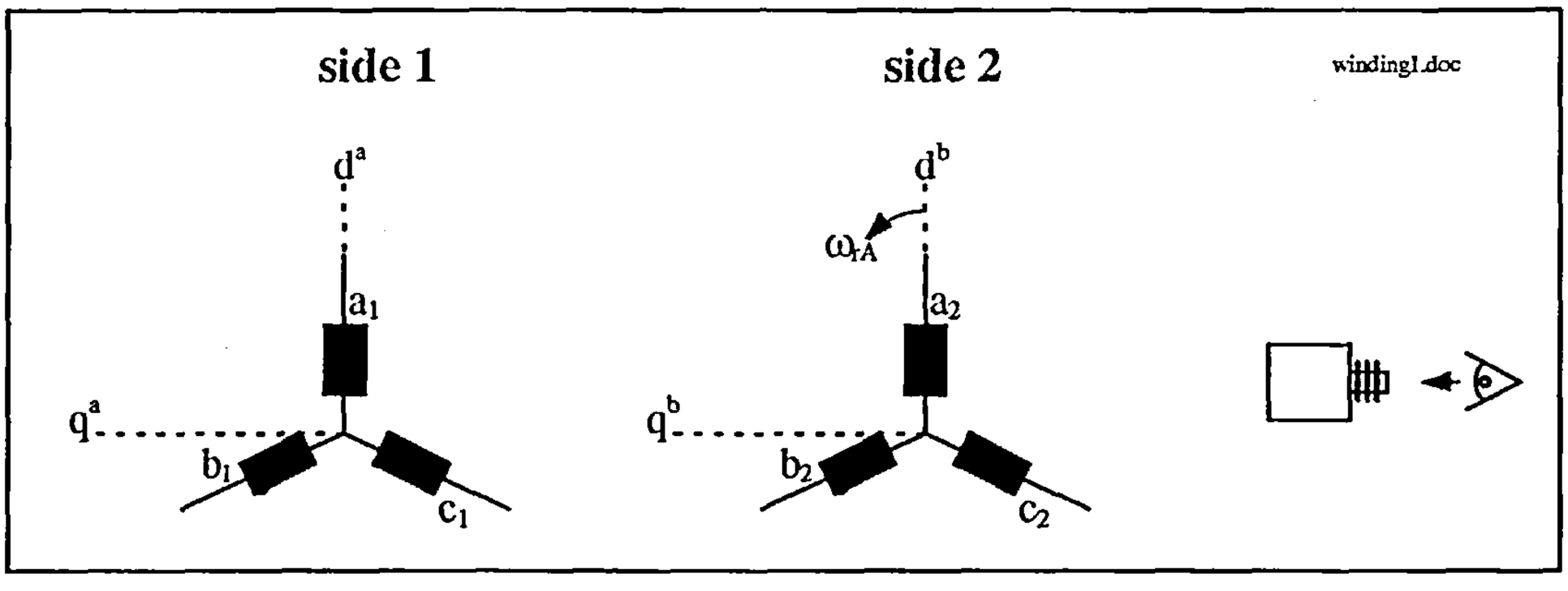

Figure 4.4: Windings and reference frames for machine A of the CDFM

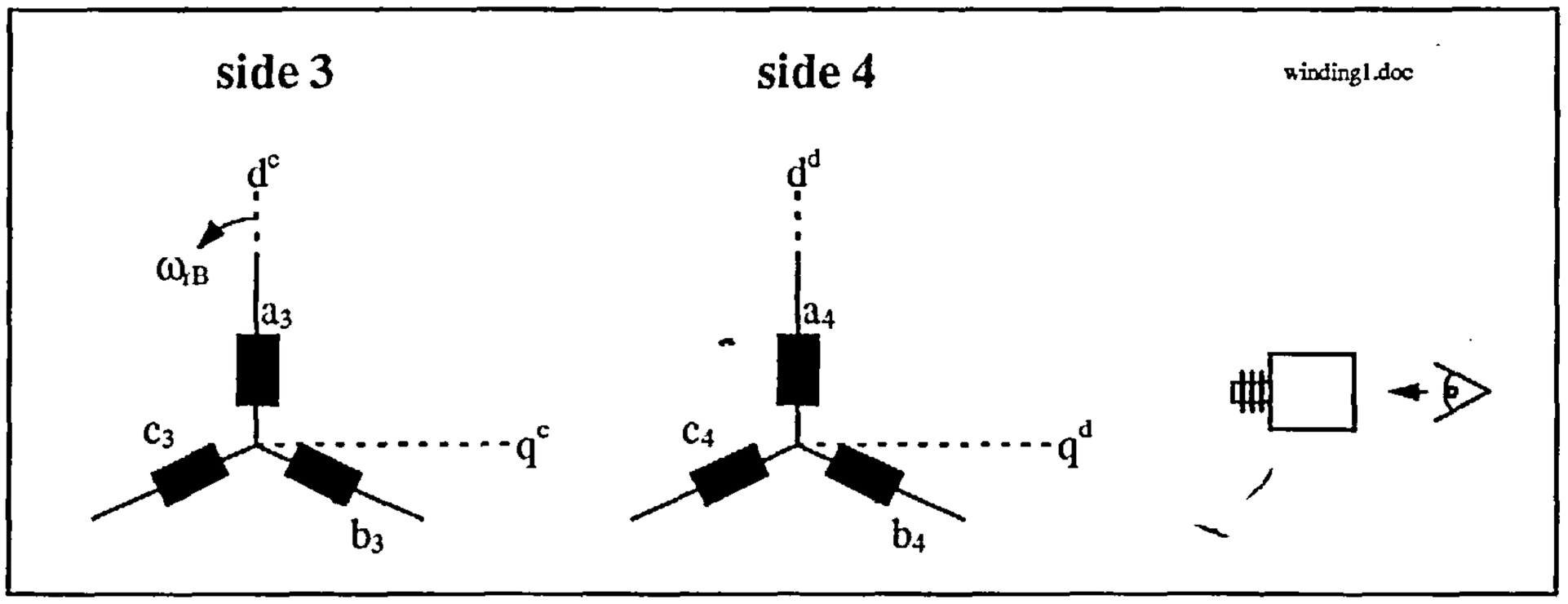

Figure 4.5: Windings and reference frames for machine B of the CDFM - view method I

Taking now a look at machine B by assuming initially to have two identical machines with the same number of pole pairs. The machines in figure 4.1 take a back-to-back positioning. Viewing machine B as indicated in figure 4.5, then the windings and reference frames for machine B take the situation as illustrated in figure 4.5. Here the reference frame for side 4, denoted as "d", is stationary and the reference frame of side 3, denoted as "c", is rotating relative to side 4 with the rotor speed ω_B of machine B.

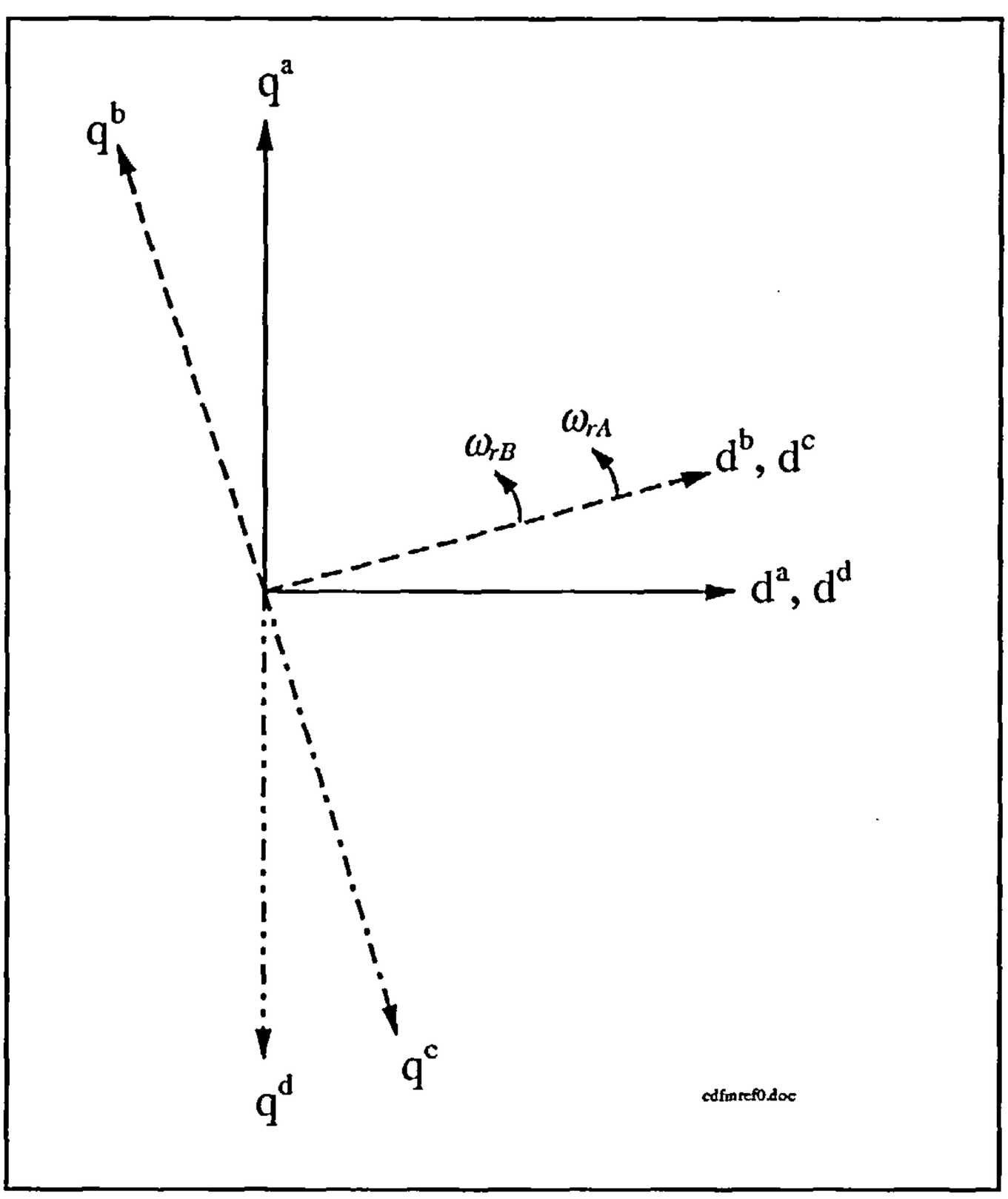

Figure 4.6: Reference frames for the CDFM - view method I

If the rotor phases "a_2" and "a_3" are aligned or in other words the d-axis of the reference frame "b" is aligned with the d-axis of the reference frame "c", then the combined reference frame system for the CDFM can be seen in figure 4.6. As can be seen both stator reference frames "a" and "d" are stationary. Due to the back-to-back arrangement the q-axes of both stator reference frames are pointing in opposite directions. That is also the case for the q-axes of the rotors. As already mentioned the mechanical rotor speed of machine A ω_A in electrical radians per second is relative to reference frame "a" and the rotor speed of machine B ω_B in electrical radians per second is relative to reference frame "d". This reference frame system corresponds to the proper physical "viewing" of the CDFM, where both stator reference frames are stationary. It is for example used in control developments for the BDFM [c27]. However, it makes the whole machine system initially complicated to grasp, since the machine is "viewed" from two sides, or both stator terminals. In case of the

SDFM the machine is regarded only from one terminal, rather than from two. The "view" of the SDFM goes into the stator and from the stator onto the rotor. This way makes it necessary to define all the machine quantities relative to only the stationary stator reference frame. That is different if the reference frame system of figure 4.6 is adopted for the CDFM, since there are now two stationary reference frames.

To simplify the system of figure 4.6 machine B must be seen from a different point of view as indicated in figure 4.7. In comparison to figure 4.5 machine B is viewed from the other side. If it is assumed that the viewer sits on side 3 and looks towards side 4, then side 4 is rotating relative to side 3 with the rotor speed ω_B in the direction as shown in figure 4.7. Again, aligning the d-axes of side 2 and side 3 the complete reference frame system for the CDFM takes now the relation as displayed in figure 4.8. In contrast to the reference frame system in figure 4.6 the q-axes of all four sides take the same position relative to their d-axes. The reference frame "d" of side 4 is no longer stationary, but is now rotating with the angular frequency ω_{AB} relative to the stationary reference frame "a".

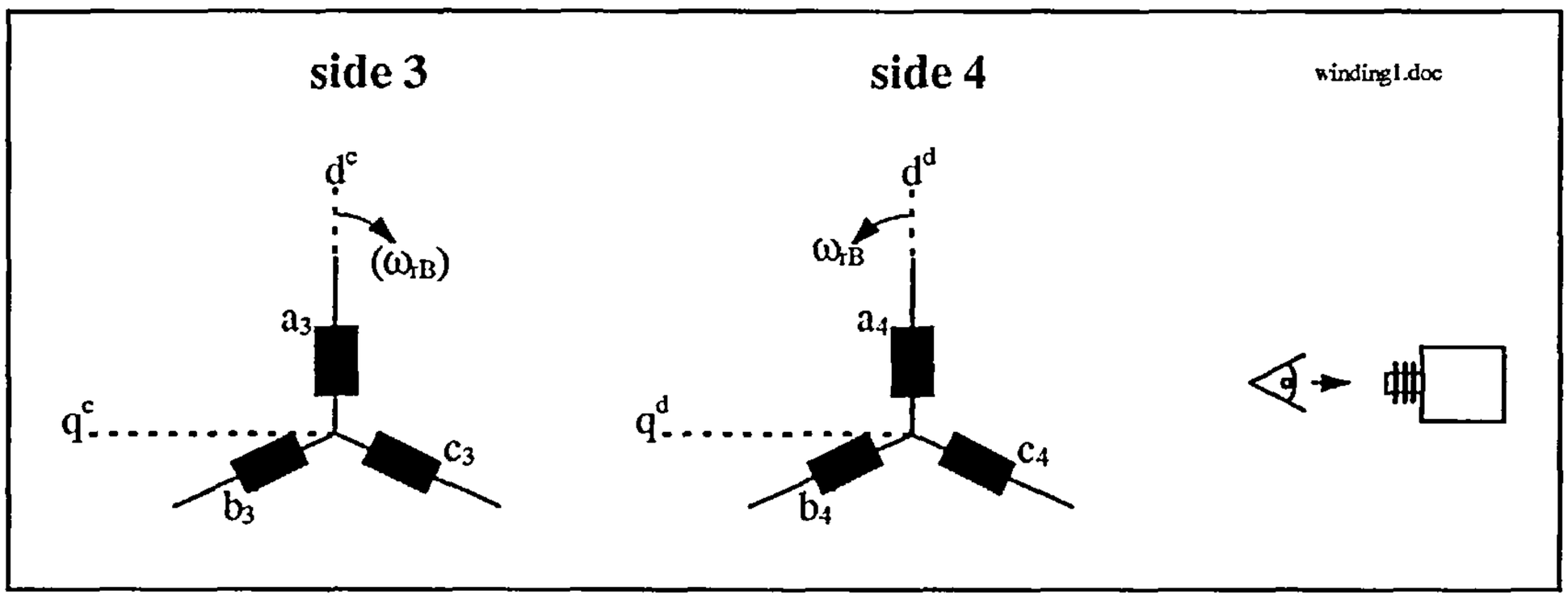

Figure 4.7: Windings and reference frames for machine B of the CDFM - view method II

For positive phase sequence connection

$$\omega_{rAB} = \omega_{rA} + \omega_{rB} \tag{4.1.5}$$

and for negative phase sequence connection

$$\omega_{rAB} = \omega_{rA} - \omega_{rB} \tag{4.1.6}$$

That may seem to be physically not quite correct, but for the matter of developing the control of the CDFM it is easier to deal with, than the system of figure 4.6. Similar to the SDFM, the CDFM can now be regarded only from one stationary reference frame and the view through the CDFM goes from side 1 onto side 2, which is identical with side 3. Side 4 is then viewed relative to side 3. This view of the CDFM will be adopted for all the following considerations.

In order to derive the reference frame system for the CDFM it was assumed initially that the CDFM was composed of two identical machines with the same number of pole pairs. Since all defined rotor angular speeds are so far defined in electrical radians per second, with

$$\omega_{rA} = p_A \omega_m \quad \text{and} \quad \omega_{rB} = p_B \omega_m \tag{4.1.7}$$

the reference frame system in figure 4.8 is valid for any type of pole pair combination and for any type of rotor winding connection as long as the appropriate angular speed relations are used for the respective rotor connection. p_A and p_B are the individual pole pair numbers and ω_m the rotor speed in mechanical radians per second

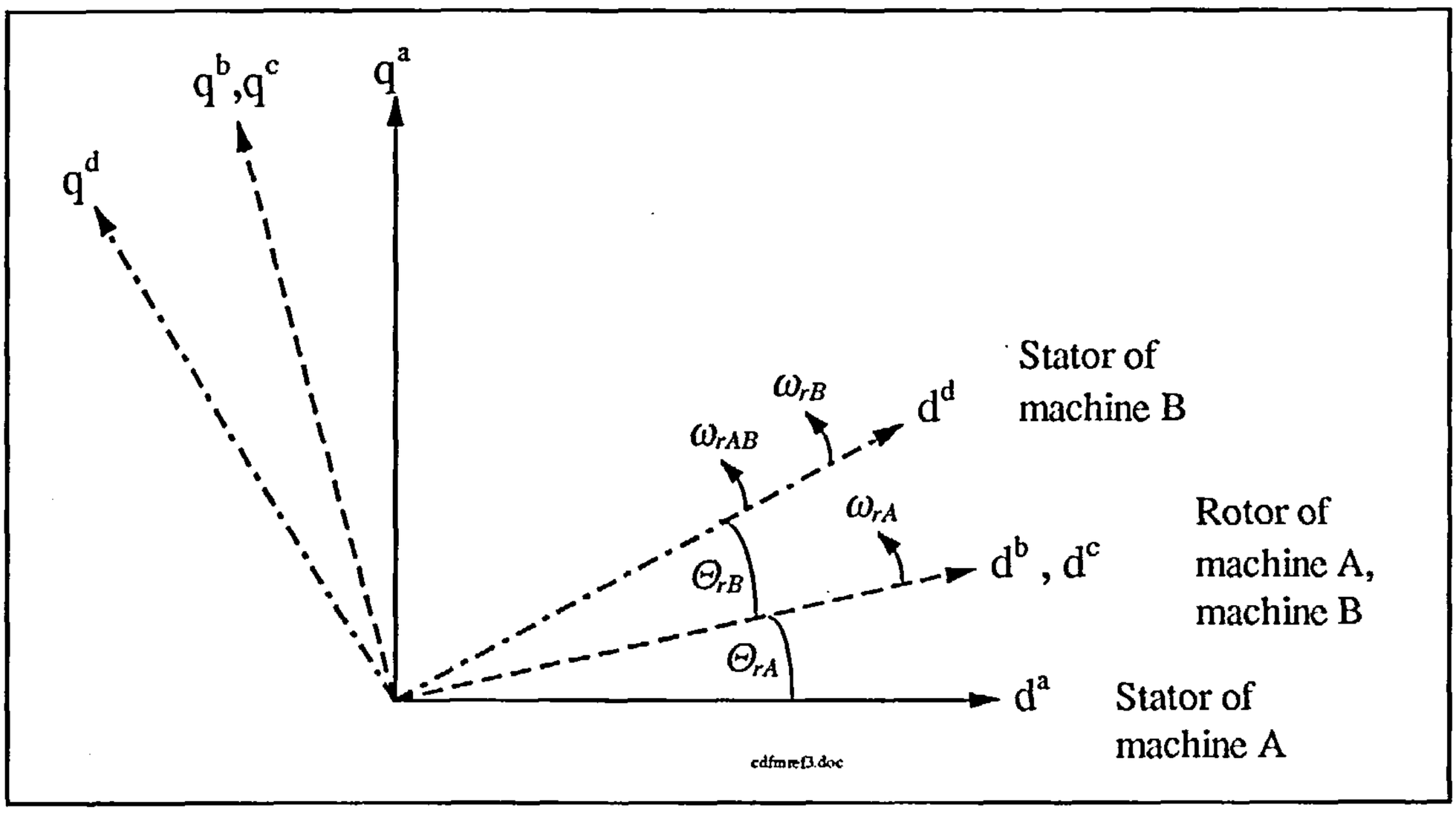

Figure 4.8: Reference frames for the CDFM - view method II

4.1.2 Torque Production

Each single machine of the CDFM produces an independent torque, which is then combined with the relationship of

$$T_{eAB} = T_{eA} + T_{eB} \tag{4.1.8}$$

to give the complete torque for the CDFM. The torque for machine A can be defined as a cross product of both machine currents in a general reference frame "g" [f3]

$$T_{eA} = -\frac{3}{2} p_A L_{mA} (\bar{i}_1^g \times \bar{i}_2^g) \tag{4.1.9}$$

and for machine B in terms of both machine currents

$$T_{eB} = \frac{3}{2} p_B L_{mB} (\bar{i}_4^g \times \bar{i}_3^g) \tag{4.1.10}$$

where L_{mA} is the mutual inductance of machine A and L_{mB} is the mutual inductance of machine B.

The combined torque for *positive phase sequence connection* together with the connection constraint of equation (4.1.2) can be written in the form of

$$T_{eAB} = -\frac{3}{2}[(\, p_A L_{mA} \bar{i}_1^g + p_B L_{mB} \bar{i}_4^g \,) \times \bar{i}_2^g \,] \tag{4.1.11}$$

and in the case of *negative phase sequence rotor connection* together with equation (4.1.4)

$$T_{eAB} = -\frac{3}{2}[(\, p_A L_{mA} \bar{i}_1^g + p_B L_{mB} conj(\bar{i}_4^g \,)) \times \bar{i}_2^g \,] \tag{4.1.12}$$

The equations of motion for the CDFM are as

$$T_{eAB} - T_L = J \frac{d\omega_m}{dt} \tag{4.1.13}$$

and

$$\frac{d\Theta_m}{dt} = \omega_m \tag{4.1.14}$$

where

ω_m is the mechanical rotor speed in mechanical rad/s

Θ_m is the rotor position in mechanical rad

The reference frame position angles in electrical radians, depicted in figure 4.8, take following relationship

$$\Theta_{rA} = p_A \Theta_m \quad \text{and} \quad \Theta_{rB} = p_B \Theta_m \tag{4.1.15}$$

4.1.3 Dynamic Model

The individual machine side quantities expressed at their respective machine side as space vectors are

$$\bar{v}_1^a = R_1 \bar{i}_1^a + \frac{d\bar{\Psi}_1^a}{dt} \quad \text{and} \quad \bar{\Psi}_1^a = L_1 \bar{i}_1^a + L_{mA} \bar{i}_2^a \tag{4.1.16}$$

$$\bar{v}_2^b = R_2 \bar{i}_2^b + \frac{d\bar{\Psi}_2^b}{dt} \quad \text{and} \quad \bar{\Psi}_2^b = L_2 \bar{i}_2^b + L_{mA} \bar{i}_1^b \tag{4.1.17}$$

$$\bar{v}_3^c = R_3 \bar{i}_3^c + \frac{d\bar{\Psi}_3^c}{dt} \quad \text{and} \quad \bar{\Psi}_3^c = L_3 \bar{i}_3^c + L_{mB} \bar{i}_4^c \tag{4.1.18}$$

$$\bar{v}_4^d = R_4 \bar{i}_4^d + \frac{d\bar{\Psi}_4^d}{dt} \quad \text{and} \quad \bar{\Psi}_4^d = L_4 \bar{i}_4^d + L_{mB} \bar{i}_3^d \tag{4.1.19}$$

In order to format the complete CDFM machine model in a general reference frame, as it was done for the SDFM, the space vectors of the individual machine sides have to be transformed onto a common general reference frame as indicated in figure 4.9, in which all angular frequencies are relative to the stationary reference frame "a". Based on the angles in figure 4.9 the side 1 quantities are rotated as

$$\bar{v}_1^g = \bar{v}_1^a e^{-j\Theta_g} \qquad \bar{i}_1^g = \bar{i}_1^a e^{-j\Theta_g} \qquad \bar{\Psi}_1^g = \bar{\Psi}_1^a e^{-j\Theta_g} \tag{4.1.20}$$

those for side 2 and side 3 as

$$\bar{v}_2^g = \bar{v}_2^b e^{-j(\Theta_g - \Theta_{rA})} \quad \bar{i}_2^g = \bar{i}_2^b e^{-j(\Theta_g - \Theta_{rA})} \quad \bar{\Psi}_2^g = \bar{\Psi}_2^b e^{-j(\Theta_g - \Theta_{rA})} \tag{4.1.21}$$

$$\bar{v}_3^g = \bar{v}_3^c e^{-j(\Theta_g - \Theta_{rA})} \quad \bar{i}_3^g = \bar{i}_3^c e^{-j(\Theta_g - \Theta_{rA})} \quad \bar{\Psi}_3^g = \bar{\Psi}_3^c e^{-j(\Theta_g - \Theta_{rA})} \tag{4.1.22}$$

and those for side 4 as

$$\bar{v}_4^g = \bar{v}_4^d e^{-j(\Theta_g - \Theta_{rAB})} \quad \bar{i}_4^g = \bar{i}_4^d e^{-j(\Theta_g - \Theta_{rAB})} \quad \bar{\Psi}_4^g = \bar{\Psi}_4^d e^{-j(\Theta_g - \Theta_{rAB})} \tag{4.1.23}$$

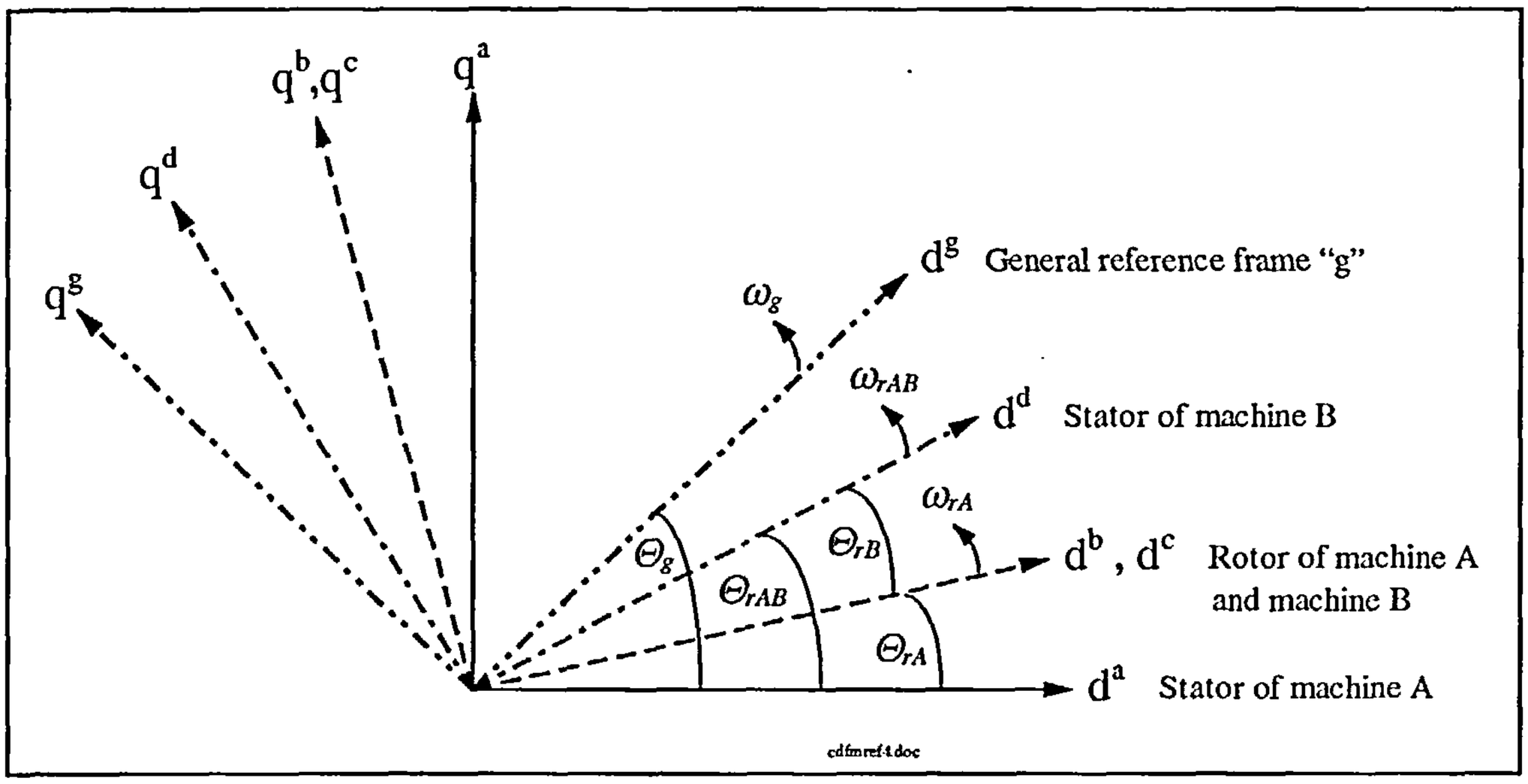

Figure 4.9: Reference frames and angles for the CDFM

It should again be noted that the reference frame "b" is identical to the reference frame "c", so it would not matter whether the side 2 or the side 3 quantities are expressed in the reference frame "b" or "c".

Substituting equations (4.1.20) - (4.1.23) into (4.1.16) - (4.1.19) and carrying out the involved differentiations with the help of

$$\frac{d\Theta_{rA}}{dt} = \omega_{rA}, \quad \frac{d\Theta_{rAB}}{dt} = \omega_{rAB} \quad \text{and} \quad \frac{d\Theta_g}{dt} = \omega_g \tag{4.1.24}$$

yields the following voltage space vectors for each of the machine sides

$$\bar{v}_1^g = R_1 \bar{i}_1^g + \frac{d\bar{\Psi}_1^g}{dt} + j\omega_g \bar{\Psi}_1^g \tag{4.1.25}$$

$$\bar{v}_2^g = R_2 \bar{i}_2^g + \frac{d\bar{\Psi}_2^g}{dt} + j(\omega_g - \omega_{rA})\bar{\Psi}_2^g \tag{4.1.26}$$

$$\bar{v}_3^g = R_3 \bar{i}_3^g + \frac{d\bar{\Psi}_3^g}{dt} + j(\omega_g - \omega_{rA})\bar{\Psi}_3^g \tag{4.1.27}$$

$$\bar{v}_4^g = R_4 \bar{i}_4^g + \frac{d\bar{\Psi}_4^g}{dt} + j(\omega_g - \omega_{rAB})\bar{\Psi}_4^g \tag{4.1.28}$$

The flux linkages in the general reference frame "g" can be expressed in terms of currents as

$$\bar{\Psi}_1^g = L_1 \bar{i}_1^g + L_{mA} \bar{i}_2^g \tag{4.1.29}$$

$$\overline{\Psi}_2^g = L_2\bar{i}_2^g + L_{mA}\bar{i}_1^g \tag{4.1.30}$$

$$\overline{\Psi}_3^g = L_3\bar{i}_3^g + L_{mB}\bar{i}_4^g \tag{4.1.31}$$

$$\overline{\Psi}_4^g = L_4\bar{i}_4^g + L_{mB}\bar{i}_3^g \tag{4.1.32}$$

Looking back at figures 4.2 and 4.3 it can be seen that the rotor quantities, side 2 and side 3, form a closed circuit independent from side 1 and side 4. It is therefore possible to combine the side 2 and the side 3 machine equations, but it is necessary to distinguish between positive and negative phase sequence connection.

General machine model for *positive phase sequence rotor connection*

Combining equation (4.1.26) and (4.1.27) with the connection constraints of (4.1.2) then a rotor voltage equation can be written as

$$0 = (R_2 + R_3)\bar{i}_2^g + \frac{d\overline{\Psi}_2^g}{dt} - \frac{d\overline{\Psi}_3^g}{dt} + j(\omega_g - \omega_{rA})(\overline{\Psi}_2^g - \overline{\Psi}_3^g) \tag{4.1.33}$$

By creating a fictitious rotor flux linkage vector combination in the form of

$$\overline{\Psi}_R^g = \overline{\Psi}_2^g - \overline{\Psi}_3^g \tag{4.1.34}$$

and adding the resistances to give a common rotor resistance

$$R_R = R_2 + R_3 \tag{4.1.35}$$

then (4.1.33) can be rewritten in the form of

$$0 = R_R\bar{i}_2^g + \frac{d\overline{\Psi}_R^g}{dt} + j(\omega_g - \omega_{rA})\overline{\Psi}_R^g \tag{4.1.36}$$

The newly created rotor flux linkage can be expressed together with a combined rotor inductance of

$$L_R = L_2 + L_3 \tag{4.1.37}$$

as

$$\overline{\Psi}_R^g = L_{mA}\bar{i}_1^g + L_R\bar{i}_2^g - L_{mB}\bar{i}_4^g \tag{4.1.38}$$

Combining above equations in the appropriate matter leads to the machine voltage equations in the form of

$$\bar{v}_1^g = R_1\bar{i}_1^g + L_1\frac{d\bar{i}_1^g}{dt} + L_{mA}\frac{d\bar{i}_2^g}{dt} + j\omega_g(L_1\bar{i}_1^g + L_{mA}\bar{i}_2^g) \tag{4.1.39}$$

$$0 = R_R\bar{i}_2^g + L_{mA}\frac{d\bar{i}_1^g}{dt} + L_R\frac{d\bar{i}_2^g}{dt} - L_{mB}\frac{d\bar{i}_4^g}{dt} + j(\omega_g - \omega_{rA})(L_{mA}\bar{i}_1^g + L_R\bar{i}_2^g - L_{mB}\bar{i}_4^g) \tag{4.1.40}$$

$$\bar{v}_4^g = R_4\bar{i}_4^g + L_4\frac{d\bar{i}_4^g}{dt} - L_{mB}\frac{d\bar{i}_2^g}{dt} + j(\omega_g - \omega_{rAB})(L_4\bar{i}_4^g - L_{mB}\bar{i}_2^g) \tag{4.1.41}$$

Separating equation (4.1.39) - (4.1.41) into its 2-dimensional components and using matrix

formation then the electrical model of the CDFM for positive phase sequence rotor connection expressed in the general reference frame can be written as seen in equation (4.1.42).

General machine model for *negative phase sequence rotor connection*

Combining equation (4.1.26) and (4.1.27) with the connection constraints of (4.1.4) then a rotor voltage equation can be written as

$$0 = R_R \bar{i}_2^g + \frac{d\overline{\Psi}_R^g}{dt} j(\omega_g - \omega_{rA})\overline{\Psi}_R^g \tag{4.1.43}$$

where

$$\overline{\Psi}_R^g = \overline{\Psi}_2^g - conj(\overline{\Psi}_3^g) \tag{4.1.44}$$

is the fictitious rotor flux linkage combination, which can also be written in the form

$$\overline{\Psi}_R^g = L_{mA}\bar{i}_1^g + L_R\bar{i}_2^g - L_{mB}conj(\bar{i}_4^g) \tag{4.1.45}$$

Again, combining above equations leads to the machine voltage equations for side 2 and side 4 as

$$0 = R_R\bar{i}_2^g + L_{mA}\frac{d\bar{i}_1^g}{dt} + L_R\frac{d\bar{i}_2^g}{dt} - L_{mB}conj\frac{d\bar{i}_4^g}{dt} + j(\omega_g - \omega_{rA})(L_{mA}\bar{i}_1^g + L_R\bar{i}_2^g - L_{mB}conj(\bar{i}_4^g)) \tag{4.1.46}$$

$$\bar{v}_4^g = R_4\bar{i}_4^g + L_4\frac{d\bar{i}_4^g}{dt} - L_{mB}conj\frac{d\bar{i}_2^g}{dt} + j(\omega_g - \omega_{rAB})(L_4\bar{i}_4^g - L_{mB}conj(\bar{i}_2^g)) \tag{4.1.47}$$

Separating equation (4.1.39), (4.1.46) and (4.1.47) into d-q-components and using matrix formation then the electrical model of the CDFM for negative phase sequence rotor connection expressed in the general reference frame can be written as seen in equation (4.1.48).

The equations (4.1.42) and (4.1.48) together with the equations of motion form the complete dynamic model of the CDFM expressed in a general reference frame for the specific rotor sequence connection.

$$\begin{bmatrix} v_{d1}^{g} \\ v_{q1}^{g} \\ 0 \\ 0 \\ v_{d4}^{g} \\ v_{q4}^{g} \end{bmatrix} = \begin{bmatrix} R_1 + pL_1 & -\omega_g L_1 & pL_{mA} & -\omega_g L_{mA} & 0 & 0 \\ \omega_g L_1 & R_1 + pL_1 & \omega_g L_{mA} & pL_{mA} & 0 & 0 \\ pL_{mA} & -(\omega_g - \omega_{rA})L_{mA} & R_R + pL_R & -(\omega_g - \omega_{rA})L_R & -pL_{mB} & (\omega_g - \omega_{rA})L_{mB} \\ (\omega_g - \omega_{rA})L_{mA} & pL_{mA} & (\omega_g - \omega_{rA})L_R & R_R + pL_R & -(\omega_g - \omega_{rA})L_{mB} & -pL_{mB} \\ 0 & 0 & -pL_{mB} & (\omega_g - \omega_{rAB})L_{mB} & R_4 + pL_4 & -(\omega_g - \omega_{rAB})L_4 \\ 0 & 0 & -(\omega_g - \omega_{rAB})L_{mB} & -pL_{mB} & (\omega_g - \omega_{rAB})L_4 & R_4 + pL_4 \end{bmatrix} \begin{bmatrix} i_{d1}^{g} \\ i_{q1}^{g} \\ i_{d2}^{g} \\ i_{q2}^{g} \\ i_{d4}^{g} \\ i_{q4}^{g} \end{bmatrix}$$

(4.1.42)

$$\begin{bmatrix} v_{d1}^{g} \\ v_{q1}^{g} \\ 0 \\ 0 \\ v_{d4}^{g} \\ v_{q4}^{g} \end{bmatrix} = \begin{bmatrix} R_1 + pL_1 & -\omega_g L_1 & pL_{mA} & -\omega_g L_{mA} & 0 & 0 \\ \omega_g L_1 & R_1 + pL_1 & \omega_g L_{mA} & pL_{mA} & 0 & 0 \\ pL_{mA} & -(\omega_g - \omega_{rA})L_{mA} & R_R + pL_R & -(\omega_g - \omega_{rA})L_R & -pL_{mB} & -(\omega_g - \omega_{rA})L_{mB} \\ (\omega_g - \omega_{rA})L_{mA} & pL_{mA} & (\omega_g - \omega_{rA})L_R & R_R + pL_R & (\omega_g - \omega_{rA})L_{mB} & pL_{mB} \\ 0 & 0 & -pL_{mB} & -(\omega_g - \omega_{rAB})L_{mB} & R_4 + pL_4 & -(\omega_g - \omega_{rAB})L_4 \\ 0 & 0 & (\omega_g - \omega_{rAB})L_{mB} & pL_{mB} & (\omega_g - \omega_{rAB})L_4 & R_4 + pL_4 \end{bmatrix} \begin{bmatrix} i_{d1}^{g} \\ i_{q1}^{g} \\ i_{d2}^{g} \\ i_{q2}^{g} \\ i_{d4}^{g} \\ i_{q4}^{g} \end{bmatrix}$$

(4.1.48)

4.2 Steady State

Steady state investigation of the CDFM is structured in the same manner as for the SDFM to keep coherence and to emphasis similarities. First, however, it is necessary to include a section dealing with the frequency relationships of the CDFM for the two rotor connection possibilities, before deriving a per-phase equivalent circuit. Steady state simulations are then carried out for positive phase rotor connection to show the influence of current control on side 4 and to study the behaviour of internal machine quantities depending on speed. A simplified power flow diagram is developed. Finally, the effect of various pole pair combinations on the internal CDFM power flow is discussed.

4.2.1 Frequency Relations and Slip Definitions

The frequency relation for machine A is as

$$\omega_1 = p_A \omega_m + \omega_2 \tag{4.2.1}$$

and the definition for machine B is [c6]

$$\omega_3 = p_B \omega_m + \omega_4 \tag{4.2.2}$$

For machine B the role of stator and rotor frequency has interchanged, which stems from the fact that side 4, the stator, is viewed from side 3, the rotor. For machine B side 3 can therefore be regarded as its primary side and side 4 as its secondary side.

For *positive sequence rotor connection*, where $\omega_2=\omega_3$, the combined frequency relation of the CDFM can be written in the form

$$\omega_1 = (p_A + p_B)\omega_m + \omega_4 \tag{4.2.3}$$

where, with equation (4.1.7),

$$(p_A + p_B)\omega_m = \omega_{rAB} = \omega_{rA} + \omega_{rB} \tag{4.2.4}$$

which was already introduced in equation (4.1.5) without further explanation. As equation (4.2.3) indicates, the frequency association between the two accessible machine sides, side 1 and side 4, is the same as for a SDFM with the equivalent pole pair number p_A+p_B.

In contrast, for the *negative sequence rotor connection*, where $\omega_2=-\omega_3$, the combined frequency relation of the CDFM can be written in the form

$$\omega_1 = (p_A - p_B)\omega_m - \omega_4 \tag{4.2.5}$$

where, with equation (4.1.7),

$$(p_A - p_B)\omega_m = \omega_{rAB} = \omega_{rA} - \omega_{rB} \tag{4.2.6}$$

which was introduced in equation (4.1.6). Now the frequency relation between side 1 and side 4, equation (4.2.5), follows that of a SDFM with a pole pair number made up from the difference of the individual pole pair numbers, p_A-p_B.

Figure 4.10 shows the frequency relations for the laboratory CDFM machine set with $p_A=4$ and $p_B=2$ for positive and negative phase sequence rotor connection. It can be seen that at standstill and for positive phase sequence connection both stator windings, side 1 and side 4, have positive phase sequence, indicated by the positive value of the frequencies. For negative sequence connection, side 4 phase sequence starts with a negative value, meaning a reversed phase sequence on side 4, caused by the rotor connection.

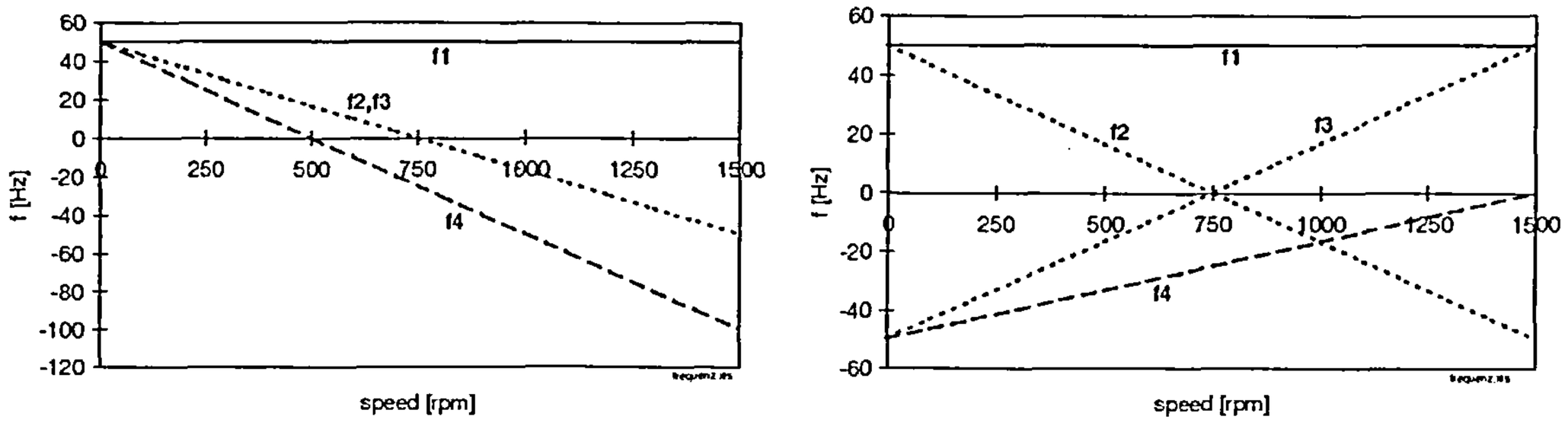

Figure 4.10: Frequencies for the experimental machine set with $p_A=4$ and $p_B=2$

The slip for machine A is defined in the standard manner of

$$s_A = \frac{\omega_2}{\omega_1} = \frac{f_2}{f_1} \tag{4.2.7}$$

and for machine B by "viewing" side 4 from side 3

$$s_B = \frac{\omega_4}{\omega_3} = \frac{f_4}{f_3} \tag{4.2.8}$$

Combining equation (4.2.7) and (4.2.8) for *positive phase sequence rotor connection* gives for a combined equivalent slip, relating side 1 and side 4,

$$s_E = s_A s_B = \frac{\omega_4}{\omega_1} = \frac{f_4}{f_1} \tag{4.2.9}$$

Doing so for *negative phase sequence rotor connection* gives

$$s_E = s_A s_B = -\frac{\omega_4}{\omega_1} = -\frac{f_4}{f_1} \tag{4.2.10}$$

for the equivalent slip. In equation (4.2.10) the negative sign is due to the negative sequence on side 4. The equivalent slip has the positive value 1 at standstill, as it is the case for positive rotor connection.

In figure 4.10 it can be seen that the synchronous speed of machine A ($f_2 = 0Hz$) with 4 pole pairs is at 750 rpm. At this point there is no voltage induced onto side 2 and both machines loose coupling [b5, b15]. This is illustrated in figure 4.11, where experimental steady state measurements on the laboratory CDFM show a collapse of side 4 voltage V_4,

when the CDFM goes through that point.

Considering figure 4.10 for *positive phase sequence rotor connection* shows that f_4 reaches d.c. value at 500 rpm for the experimental machine set. This point can be seen as cascaded synchronous speed and is related to the sum of the pole pair numbers as

$$pos.\ casc.\ sync. = \frac{60 * f_1}{p_A + p_B} \tag{4.2.11}$$

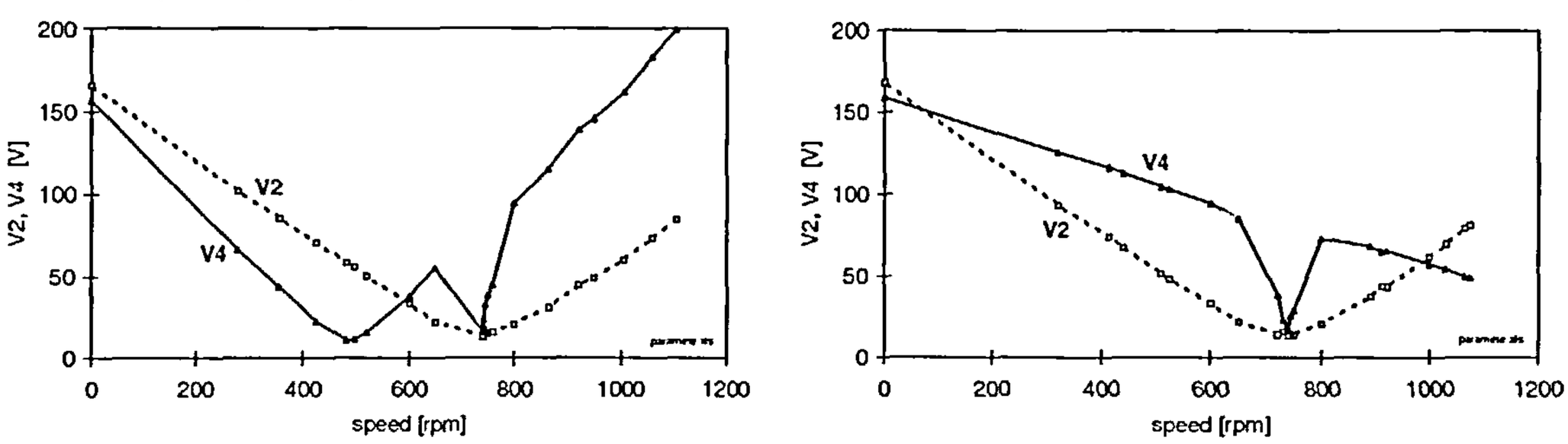

Figure 4.11: Experimental CDFM steady state voltage measurements

(Side 4 open circuited, V_1=70V)

For *negative phase sequence rotor connection* this point lies at 1500 rpm and can be calculated with the difference of both pole pair numbers as

$$neg.\ casc.\ sync. = \frac{60 * f_1}{p_A - p_B} \tag{4.2.12}$$

It can be concluded that in terms of the frequency relationship between the two supply terminals, side 1 and side 4, the CDFM can be considered as a SDFM with the equivalent pole pair number made up of the sum or difference of the individual pole pair numbers depending on positive or negative phase sequence rotor connection.

Consideration of figure 4.11 shows that the voltage on side 4 has a "V-form" similar to the rotor voltage of the SDFM. The "V-form" is symmetrical to the cascaded synchronous speed. The left graph shows measurements for positive rotor connection with the cascaded synchronous speed at 500 rpm. The right for negative rotor connection and 1500 rpm as the cascaded synchronous speed. However, in both cases side 4 voltage has a "break-in" at the synchronous speed of machine A, which is 750 rpm for this particular CDFM set. As mentioned before, both machines lose coupling in the vicinity of this operational point. The CDFM can then no longer be regarded as one unit. In motoring mode it is therefore impossible to drive the CDFM through that point. Operational speed is limited to the subsynchronous range of machine A. In generating mode, however, it would theoretically

be possible to let the CDFM accelerate through that crucial speed range and operation could be resumed at supersynchronous speed of machine A.

4.2.2 Per-Phase Equivalent Circuit

After developing the frequency relations for all four machine sides of the CDFM a per-phase equivalent circuit including iron loss resistance and turns-ratio can be developed.

With the assumption of sinusoidal quantities in the CDFM, the voltage equations for the four sides can be written in phasor form as

$$\bar{V}_1 = R_1\bar{I}_1 + j\omega_1 L_{\sigma 1}\bar{I}_1 + \bar{E}_{1ag} \tag{4.2.13}$$

$$\bar{V}_2 = R_2\bar{I}_2 + j\omega_2 L_{\sigma 2}\bar{I}_2 + \bar{E}_{2ag} \tag{4.2.14}$$

$$\bar{V}_3 = R_3\bar{I}_3 + j\omega_3 L_{\sigma 3}\bar{I}_3 + \bar{E}_{3ag} \tag{4.2.15}$$

$$\bar{V}_4 = R_4\bar{I}_4 + j\omega_4 L_{\sigma 4}\bar{I}_4 + \bar{E}_{4ag} \tag{4.2.16}$$

where

$L_{\sigma 1}$, $L_{\sigma 2}$, $L_{\sigma 3}$ and $L_{\sigma 4}$ are the leakage inductances of the respective machine sides

E_{1ag}, E_{2ag}, E_{3ag} and E_{4ag} are the respective e.m.f.'s due to mutual air-gap flux

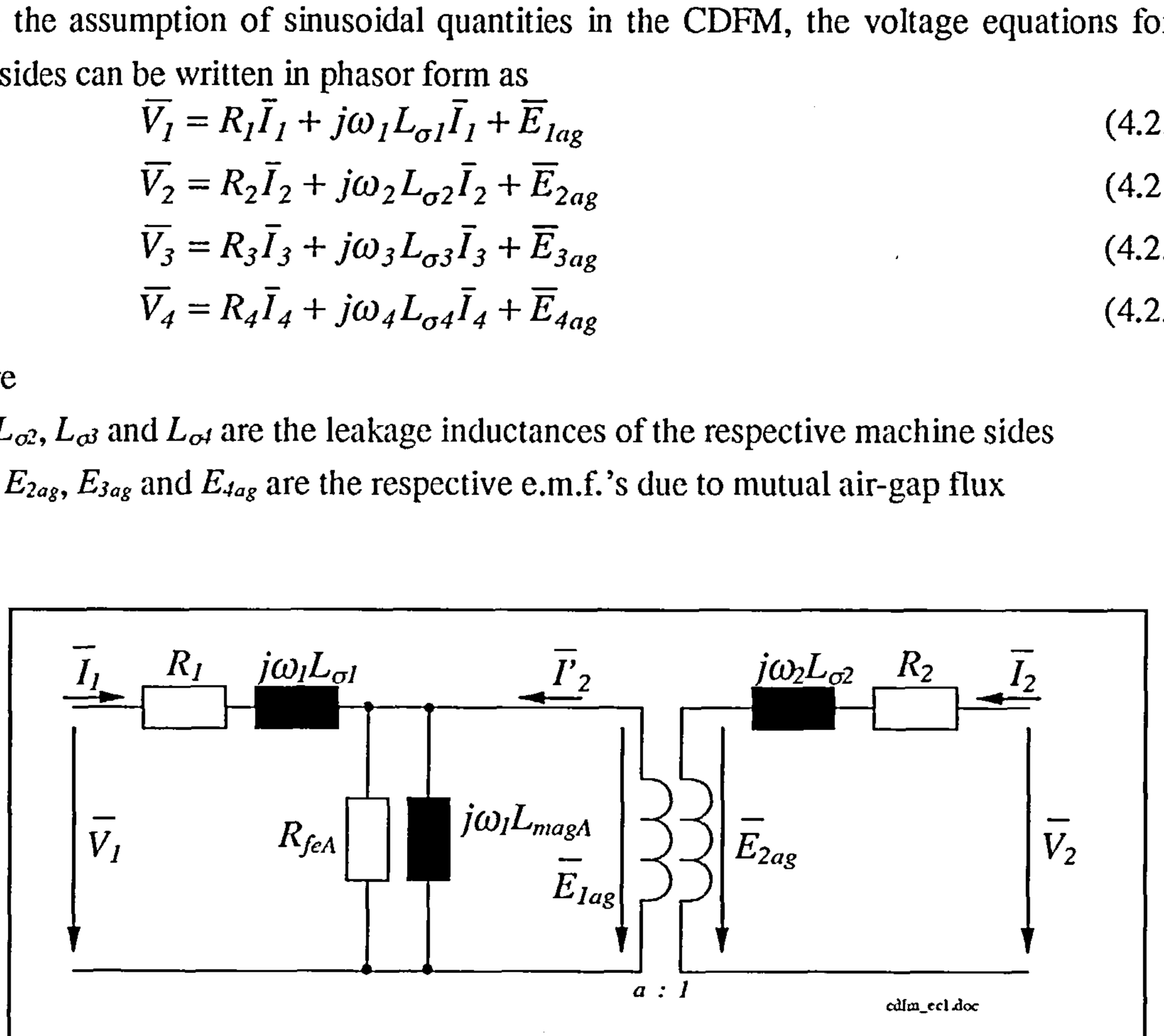

Figure 4.12: Per-phase equivalent circuit of the individual machines of the CDFM

The individual per-phase equivalent circuits for machine A and machine B of the CDFM are exhibited in figure 4.12. The equivalent circuit of machine B shows the magnetising inductance and the iron loss resistance on side 3, rather than on side 4. Side 3 corresponds to the rotor of machine B. This may seem unfamiliar, because in cage induction machine theory these quantities are referred onto the stator side. However, since the electrical machine behaviour for a wound rotor induction machine doesn't change when the role of the rotor and stator is interchanged, the representation of figure 4.12 is preferred. This helps to transfer the "viewing" of the CDFM as introduced for the dynamic model, into the steady state theory. Side 4 is "seen" from side 3 instead the other way round. This is also reflected in the definition of the turns-ratios for the individual machines. The ratio for machine A and machine B is defined as

$$a = \frac{N_1}{N_2} \quad \text{and} \quad b = \frac{N_3}{N_4} \tag{4.2.17}$$

Similar to the relationships for the SDFM the e.m.f.'s can be written in the form of

$$\overline{E}_{1ag} = \frac{\bar{I}_1 + \bar{I}'_2}{\overline{Y}_{magA}} \tag{4.2.18}$$

$$\overline{E}_{3ag} = \frac{\bar{I}_3 + \bar{I}'_4}{\overline{Y}_{magB}} \tag{4.2.19}$$

and with the slip definitions

$$\overline{E}_{2ag} = \overline{E}_{1ag} \frac{s_A}{a} \tag{4.2.20}$$

$$\overline{E}_{4ag} = \overline{E}_{3ag} \frac{s_B}{b} \tag{4.2.21}$$

The magnetising admittances are

$$\overline{Y}_{magA} = \frac{1}{R_{feA}} + \frac{1}{j\omega_1 L_{magA}} \tag{4.2.22}$$

$$\overline{Y}_{magB} = \frac{1}{R_{feB}} + \frac{1}{j\omega_3 L_{magB}} \tag{4.2.23}$$

It has to be noted at this point that despite large frequency variation depending on speed on all four sides of the machine the iron loss resistors keep a constant value and it is assumed that the iron losses for machine A are concentrated on side 1 and those for machine B are concentrated on side 3.

The per-phase equivalent circuits of figure 4.12 consist of four subnetworks representing the individual machine sides. Since the rotor windings are connected it is possible to form a common rotor circuit.
For *positive phase sequence rotor connection* and the constraints of $\omega_2=\omega_3$, $\overline{V}_2 = \overline{V}_3$ and $\bar{I}_2 = -\bar{I}_3$ the equations (4.2.14) and (4.2.15) give a combined rotor voltage equation of

$$0 = (R_2 + R_3)\bar{I}_2 + j\omega_2(L_{\sigma 2} + L_{\sigma 3})\bar{I}_2 + \overline{E}_{2ag} - \overline{E}_{3ag} \qquad (4.2.24)$$

which is the straight forward connection of the rotor subnetworks. A non-referred per-phase equivalent circuit representing the positive phase sequence connection is shown in figure 4.13, where all machine quantities remain on their original machine side. The mathematical connection between the networks is accomplished with equations (4.2.20) and (4.2.21).

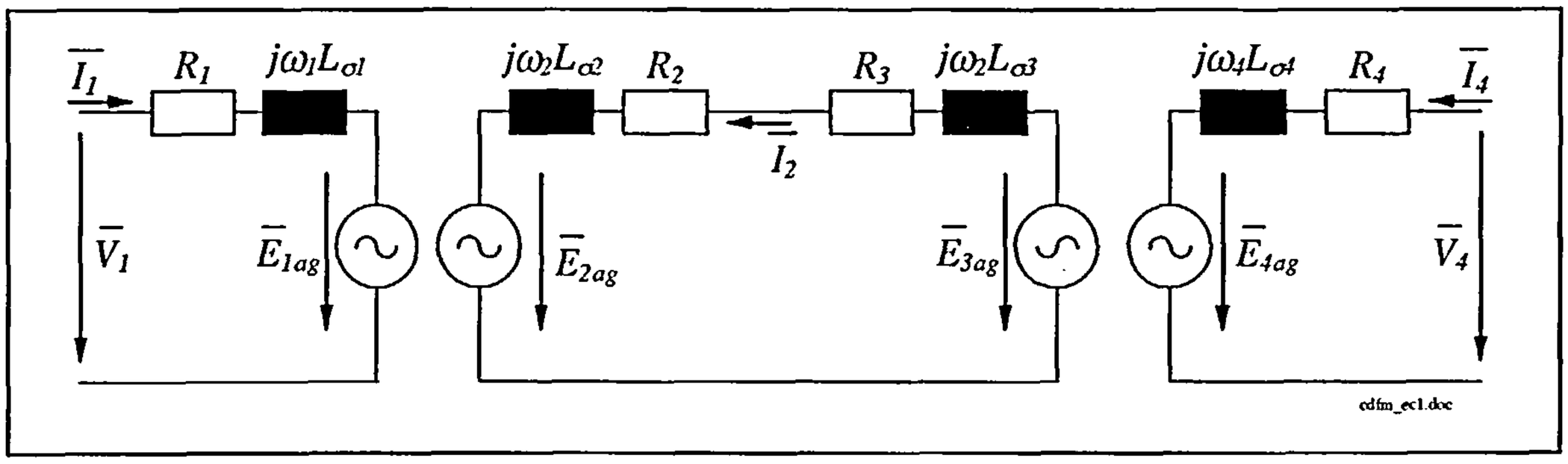

Figure 4.13: Non-referred per-phase equivalent circuit of the CDFM for positive phase sequence rotor connection

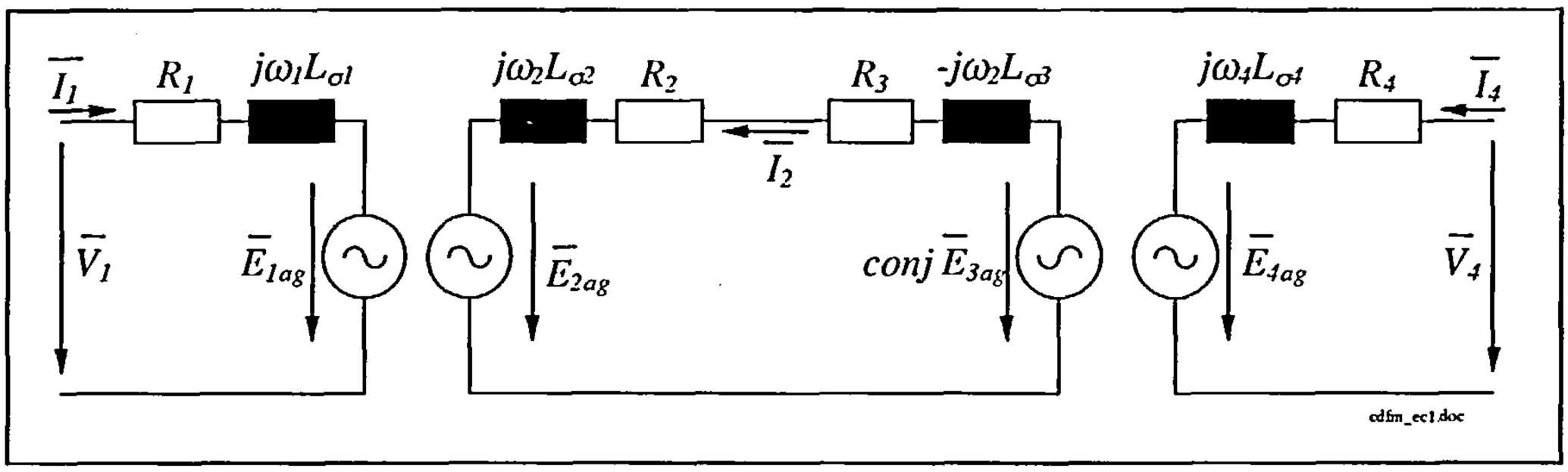

Figure 4.14: Non-referred per-phase equivalent circuit of the CDFM for negative phase sequence rotor connection

For *negative phase sequence rotor connection* and the constraints of $\omega_2 = -\omega_3$, $\overline{V}_2 = conj(\overline{V}_3)$ and $\bar{I}_2 = -conj(\bar{I}_3)$ the equations (4.2.14) and (4.2.15) give a combined rotor voltage equation of

$$0 = (R_2 + R_3)\bar{I}_2 + j\omega_2(L_{\sigma 2} - L_{\sigma 3})\bar{I}_2 + \overline{E}_{2ag} - conj(\overline{E}_{3ag}) \qquad (4.2.25)$$

The conjugation of $\overline{E}_{3ag}$ is due to the negative frequency on side 3 relative to side 2. Since the side 2 rotor current $\bar{I}_2$ flows in the combined rotor loop the negative frequency on side 3 is expressed by the conjugation. In other words, the negative frequency causes a conjugation of the imaginary part of the magnetising admittance (4.2.23). For the same reason there is a negative sign in front of the leakage reactance of side 3, "$-j\omega_2 L_{\sigma 3}$". The mathematical connection between the subnetworks in figure 4.14 is also realised by equation (4.2.20) and (4.2.21) with the mentioned note of taking the conjugated value of (4.2.19).

As it was the case for the SDFM the voltage arrows are pointing from the higher to the lower potential.

Power calculation equations and further steady state treatment of the CDFM are presented in Appendix E.

At the rotor connection point follows, independent of connection sequence,

$$P_2 = -P_3 \quad \text{and} \quad Q_2 = -Q_3 \tag{4.2.26}$$

The definition for the electromagnetic torque of the individual machines is given by

$$T_{eA} = -3 * p_A L_{magA} * (\bar{I}_{mag1} \times \frac{\bar{I}_2}{a}) \tag{4.2.27}$$

$$T_{eB} = -3 * p_B L_{magB} * (\bar{I}_{mag3} \times \frac{\bar{I}_4}{b}) \tag{4.2.28}$$

where

$$\bar{I}_{mag1} = \frac{\overline{E}_{1ag}}{j\omega_1 L_{magA}} \tag{4.2.29}$$

$$\bar{I}_{mag3} = \frac{\overline{E}_{3ag}}{j\omega_3 L_{magB}} \tag{4.2.30}$$

are the magnetising currents flowing through the magnetising inductance. The combined torque for the CDFM is given by

$$T_{eAB} = T_{eA} + T_{eB} \tag{4.2.31}$$

4.2.3 Steady State Simulations

The following simulations are performed in the same way as it was the case for the SDFM to show similarities of both systems.

The SDFM was fed by a voltage source on side 1 and by a current source on side 2. Steady state simulations clearly support the fact, that for stator flux orientation and rotor current control, independent manipulation of stator active and reactive power is possible.

A similar approach is now taken for the CDFM. Side 1 is supplied by a fixed voltage source and side 4 is connected to a bi-directional converter, which acts as a perfect current source, as shown in figure 4.15. The rotor windings are connected in positive phase sequence only. Negative phase sequence is not investigated in this section, since due to the opposing torques its use is not applicable to high power applications.

All simulation results are based on the per-phase equivalent circuit equations. The parameters (Appendix A) used in the simulations are taken from the experimental machines.

Machine A is a 4 pole pair 2.25 kW and machine B is a 2 pole pair 2.25 kW machine. It has to be mentioned that in the simulations a multiplication factor with the calculated iron loss resistances is used. As pointed out for the SDFM this is common practice to get a better agreement between simulations and measurements [f20]. The iron loss resistances keep a constant value and are concentrated on side 1 and on side 3. The factor used for machine A is 4 and for machine B is 1.8. All other parameters are taken with the value as calculated from the tests.

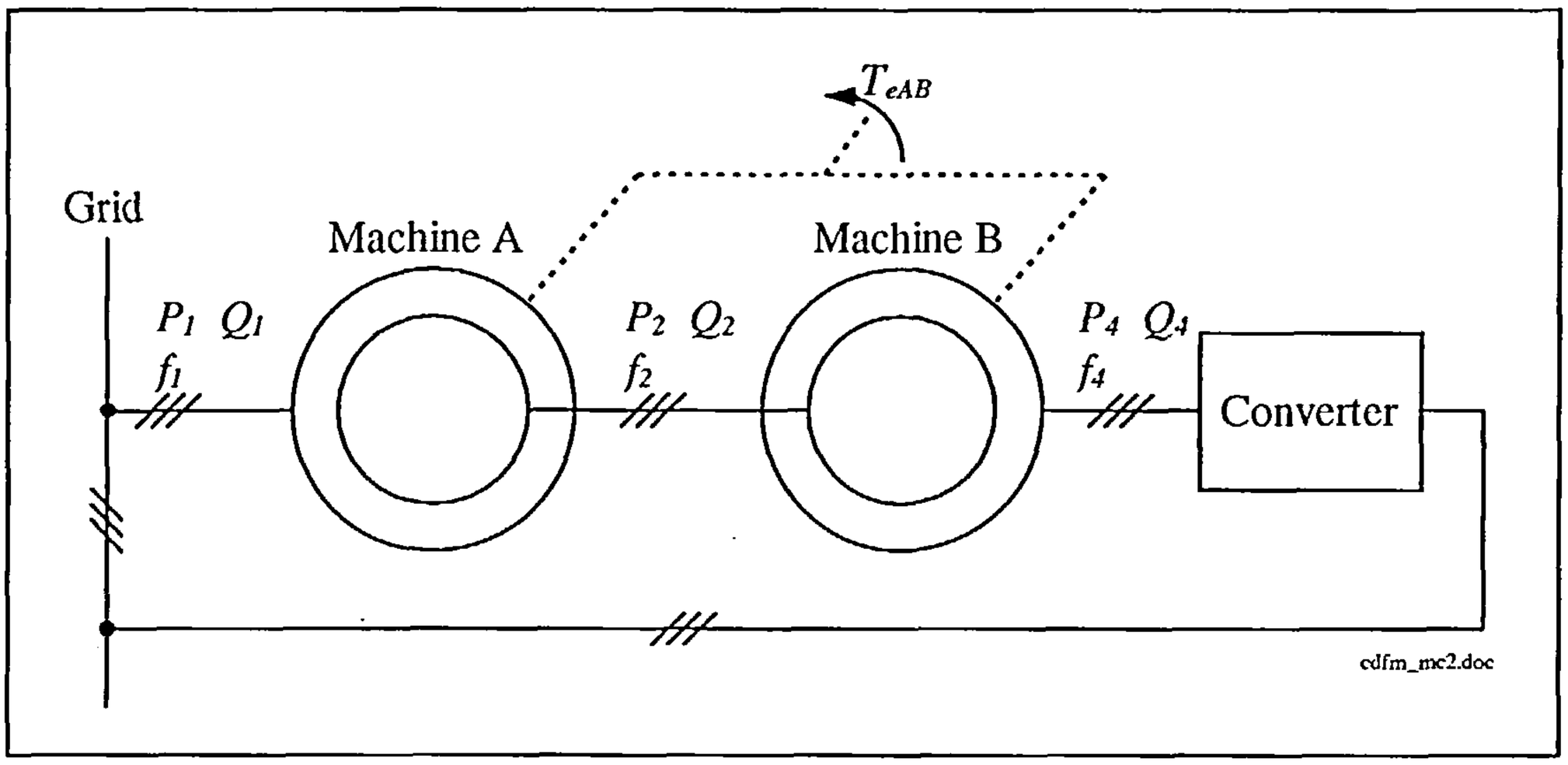

Figure 4.15: Connection of the CDFM

The first set of simulations are performed at a constant speed of 400 rpm, which is subsynchronous of machine A and subsynchronous for the CDFM. The current phasor of side 4 is rotated with a constant magnitude relative to the side 1 voltage phasor as depicted in figure 4.16.

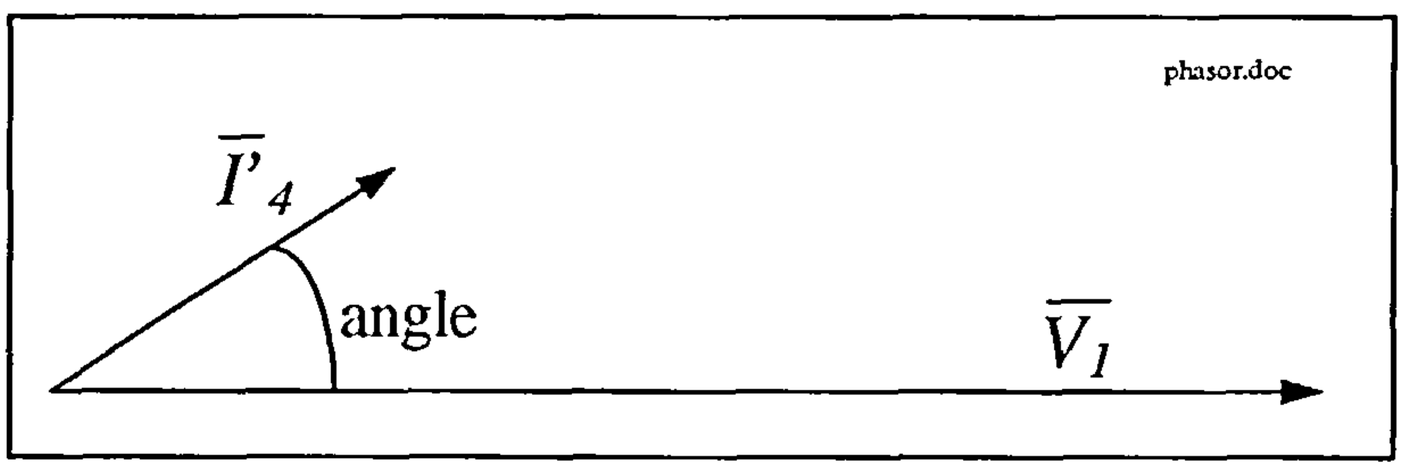

Figure 4.16: Phasor diagram of side 1 voltage and referred side 4 current

Simulation results are shown in figures 4.17 - 4.19. It can immediately be seen, that the shape of the different curves is very similar to the results of the SDFM.

Figure 4.17 shows the results for active side 1 and side 4 power. At around 180° P_1 is at its maximum positive value and the CDFM is in motoring mode, since power is delivered to terminal 1 and positive maximum torque is developed, figure 4.19. At around 0° the CDFM

is in generating mode, having maximum negative values for P_1 and T_{eAB}. The dashed lines in figure 4.17 and 4.19 indicate simulation results where all losses are neglected. Compared to the results of the SDFM the discrepancy between lossed and lossless results for the CDFM is slightly larger. This is due to the relatively high resistance and iron loss values of the experimental machines. This discrepancy should be lower when using larger machines.
The crossover for the dashed lines occurs at 90° and 270° as was the case for the SDFM. This result indicates that the power flow in the cascaded machine must be similar to that of the SDFM.

Figure 4.18 exhibits results for the reactive power of terminal 1 and 4. Again, the curves are similar shaped as the curves for the SDFM. The combined reactive power demand for the CDFM can be written in agreement to the SDFM as

$$Q_{14} = Q_1 + \frac{Q_4}{|s_A s_B|} \tag{4.2.32}$$

where Q_{14} is the sum of the reactive power needed to establish leakage and magnetising flux in the individual machines. Alternatively,

$$Q_{14} = Q_A + Q_B$$

with

$$Q_A = \left|\bar{I}_1\right|^2 X_{\sigma 1} + \left|\bar{I}_2\right|^2 X_{\sigma 2} + \left|\bar{I}_{mag1}\right|^2 X_{magA}$$

and

$$Q_B = \left|\bar{I}_3\right|^2 X_{\sigma 3} + \left|\bar{I}_4\right|^2 X_{\sigma 4} + \left|\bar{I}_{mag3}\right|^2 X_{magB}$$

where

$X_{\sigma 1}$, $X_{\sigma 2}$, $X_{\sigma 3}$ and $X_{\sigma 4}$ are the leakage reactances for the individual machine sides calculated at side 1 frequency f_1

X_{magA} and X_{magB} are the magnetising reactances of machine A and B calculated at side 1 frequency f_1

Q_{14} is shown in figure 4.18 for full parameterised simulations and lossless simulations. The value of Q_{14} for the full parameterised case varies slightly over the whole angle range. This is due to the influence of the resistances on the magnitudes of the different side current phasors and thus affecting Q_A and Q_B. Again, the experimental machines have a high resistance relative to the reactances. Ignoring the winding and iron loss resistance in the equivalent circuit, figure 4.18 shows Q_{14} (dashed line) as a straight line. It represents an average value for Q_{14} calculated with all parameters (solid line).

Experimental data points for P_1 and Q_1, taken from the laboratory machine set, are added to the figures 4.17 and 4.18. The close agreement between simulation and measurements support the use of the per-phase equivalent circuit as steady state model for studies on the CDFM.

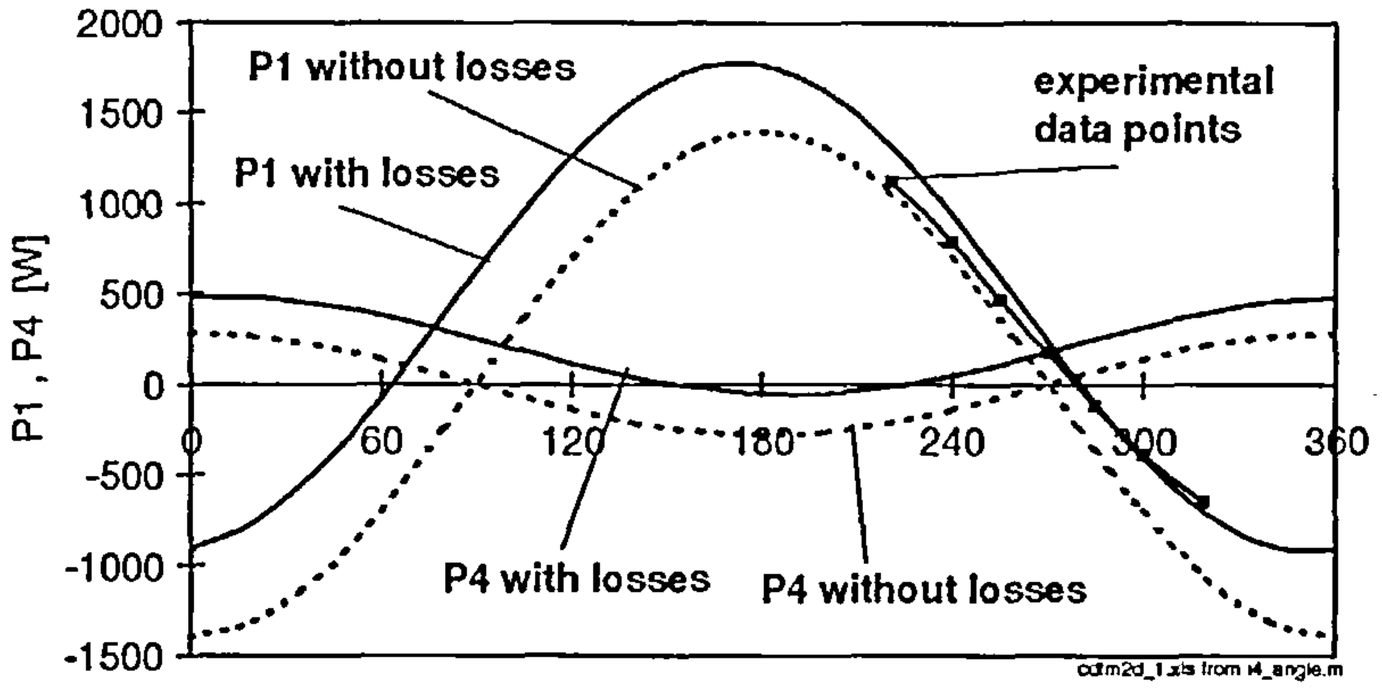

Figure 4.17: Simulated steady state values of P_1 and P_4 with and without losses together with experimental data points ($V_{1rms} = 115V$, $|I_{4peak}| = 4$ A, $n_m = 400$ rpm)

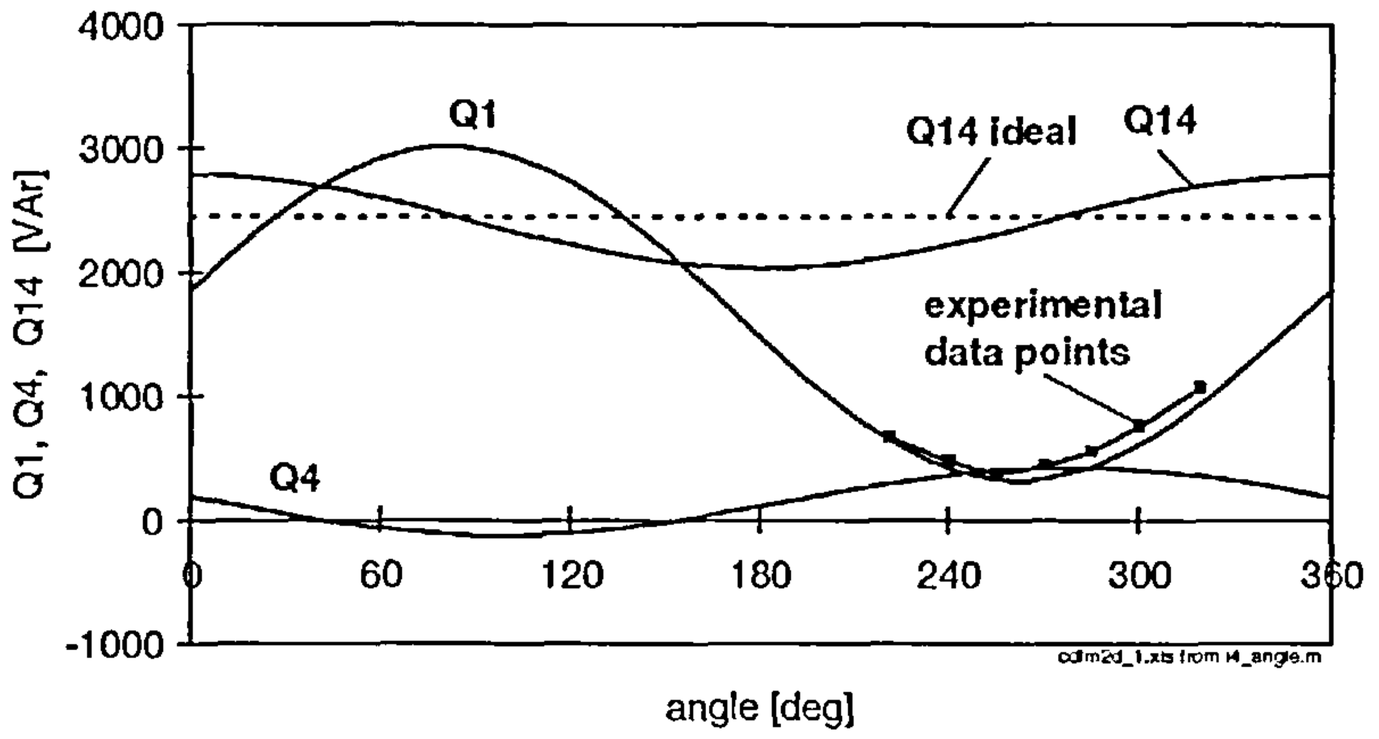

Figure 4.18: Simulated steady state values of Q_1, Q_4 and Q_{14} with and without losses together with experimental data points ($V_{1rms} = 115V$, $|I_{4peak}| = 4$ A, $n_m = 400$ rpm)

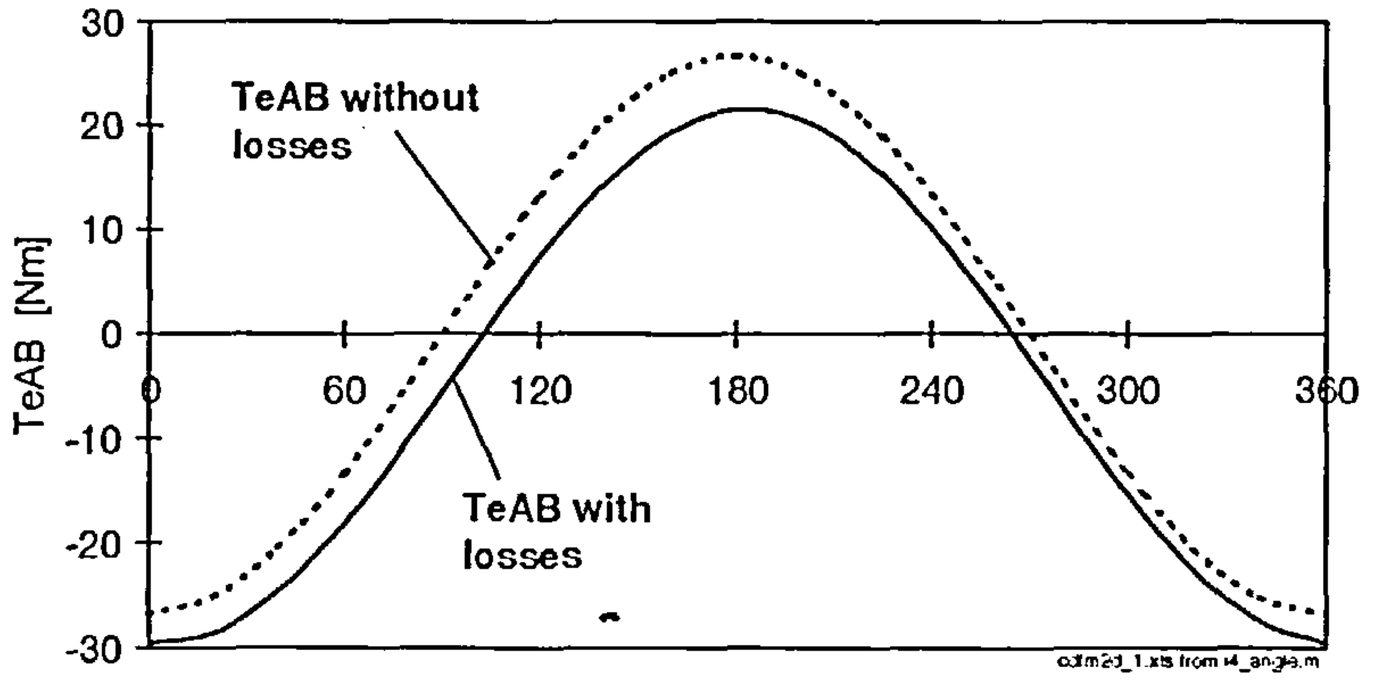

Figure 4.19: Simulated steady state values of T_{eAB} with and without losses ($V_{1rms} = 115V$, $|I_{4peak}| = 4$ A, $n_m = 400$ rpm)

Figure 4.17 and 4.19 show that the solid lines are slightly shifted relative to the dashed lines. This was not the case for the SDFM. The reason lies in the additional rotor circuit loop of the CDFM compared to the SDFM.

To investigate the influence of speed on the performance of the CDFM, when fed by a voltage and a current source, further simulations are carried out. This in the same manner as for the SDFM. On top of the relative position variation between the side 1 voltage phasor and the side 4 current phasor the speed was changed in the range 0 - 750 rpm. That corresponds to the subsynchronous speed range of machine A. In that range lies the main interest for CDFM machine operation, since it is impossible in motoring mode to go beyond that limit imposed by machine A.
In the simulations only positive rotor connection is assumed and the full parameterised equivalent circuit is used for calculations. Side 4 current phasor is rotated with a constant value over the whole angle range as depicted in figure 4.16.

Figure 4.20 shows the results for side 1 active power P_1. In accordance to the SDFM simulations, side 1 active power keeps a constant value for a fixed angle over the whole speed range. Disturbances occur only in the vicinity of the synchronous speed of machine A. This can also be observed in figure 4.21, where the results for side 4 active power are presented. As for the SDFM the active power fed by the converter, varies along the speed axis reaching its minimum value at the cascaded synchronous speed of 500 rpm. At this point the power flow direction is also reversed.

Reactive power results for side 1 and side 4 are displayed in figure 4.22 and figure 4.23. Once more, the similarity to the SDFM is quite obvious. Side 1 reactive power is independent of speed. Side 4 reactive power changes in magnitude along the speed axis according to equation (4.2.32), having the minimum value at the cascaded synchronous speed.

All the simulation results imply that the CDFM can be regarded as a SDFM with the equivalent pole pair number of p_A+p_B not only for the frequency relationships, but also for the power relationships. Furthermore, the similarity of the results suggest that side 1 active and reactive power can be controlled by side 4 current in the same manner as for the SDFM. The field oriented control strategy of the SDFM should therefore be applicable to the CDFM, and is investigated in chapter 5.

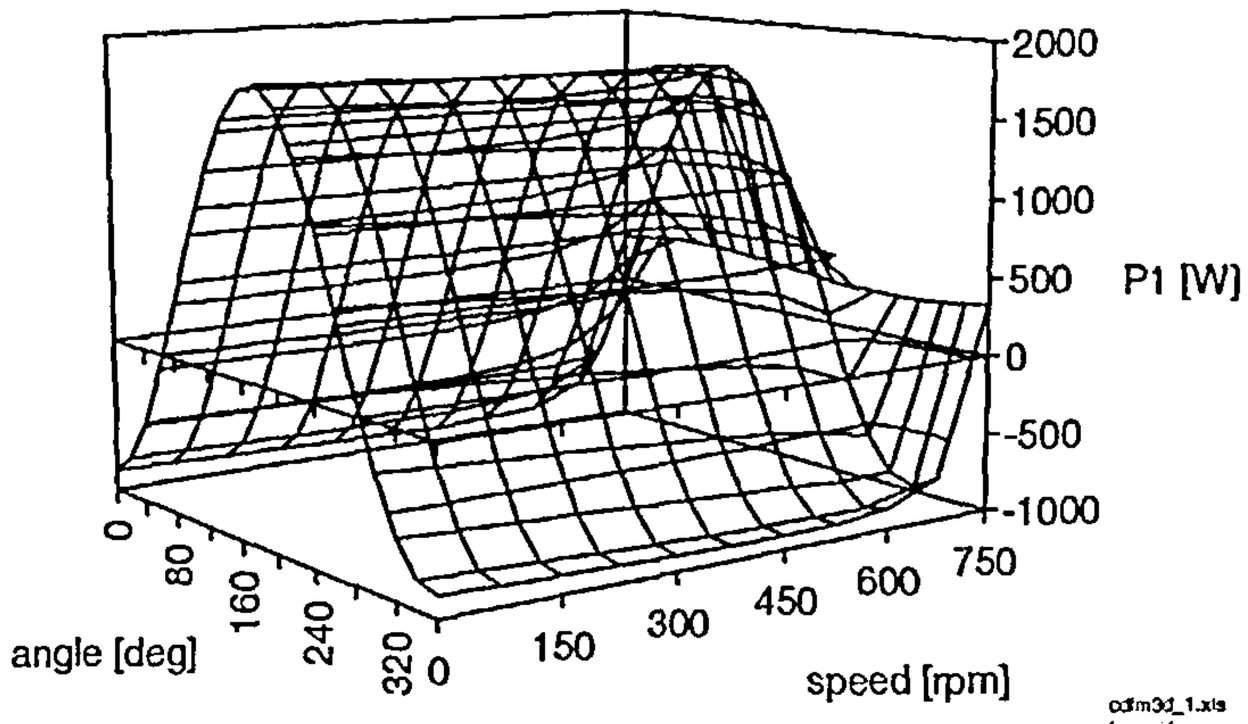

Figure 4.20: Simulated steady state values of P_1 as a function of angle and speed

($V_{1rms} = 115V$, $|I_{4peak}| = 4$ A)

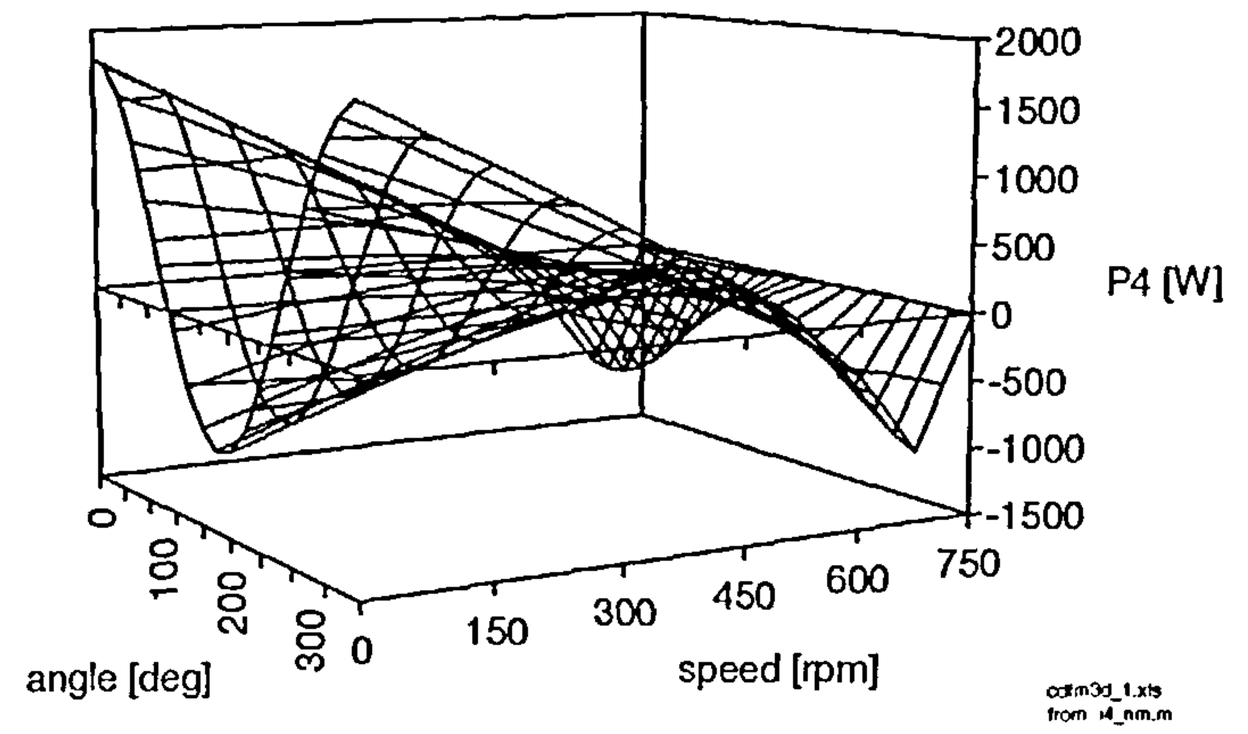

Figure 4.21: Simulated steady state values of P_4 as a function of angle and speed

($V_{1rms} = 115V$, $|I_{4peak}| = 4$ A)

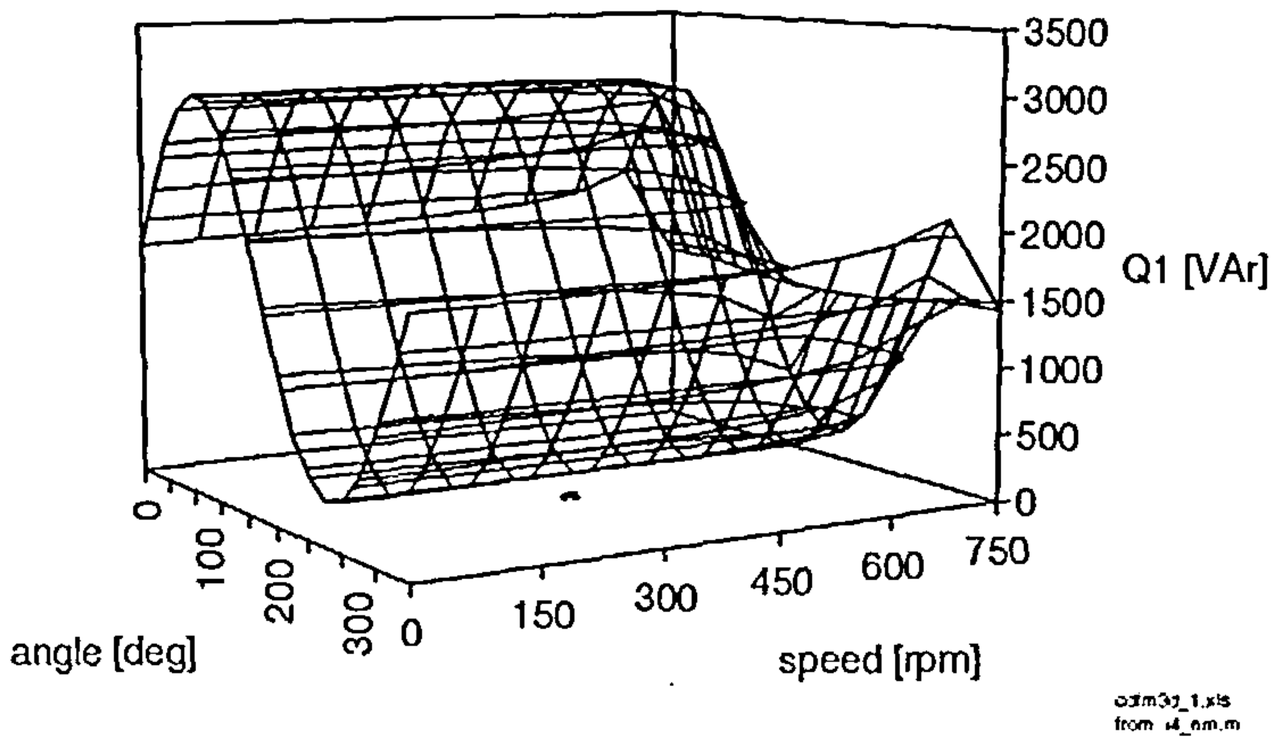

Figure 4.22: Simulated steady state values of Q_1 as a function of angle and speed

($V_{1rms} = 115V$, $|I_{4peak}| = 4$ A)

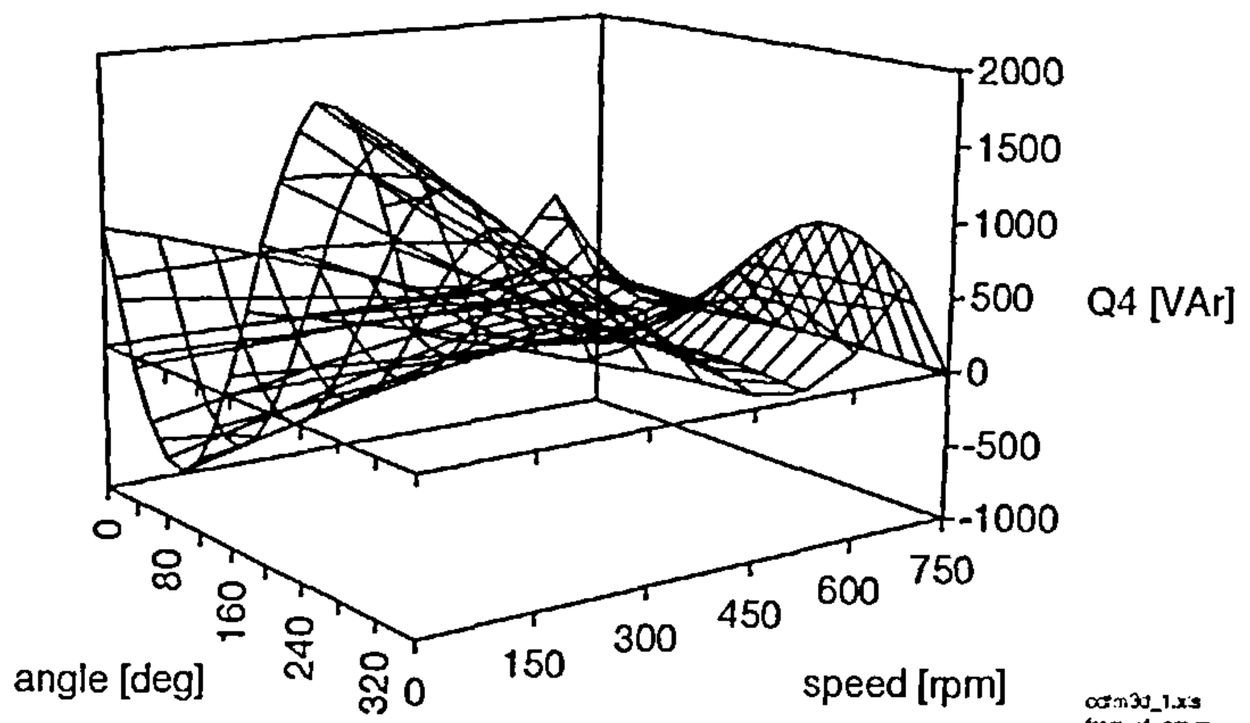

Figure 4.23: Simulated steady state values of Q_4 as a function of angle and speed

($V_{1rms} = 115V$, $|I_{4peak}| = 4$ A)

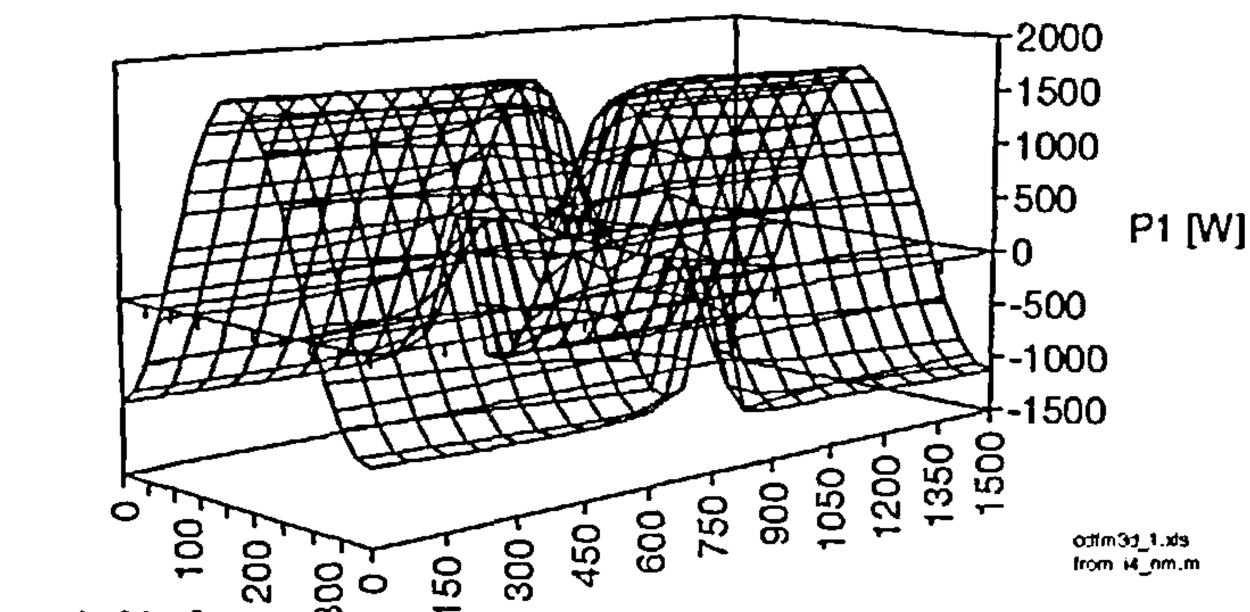

Figure 4.24: Simulated steady state values of P_1 in extended speed range

($V_{1rms} = 115V$, $|I_{4peak}| = 4$ A)

Figure 4.24 gives the simulation results for side 1 active power for an extended speed range of 0-1500 rpm of the CDFM. It shows that the independence of speed upon the side 1 active power in current fed mode is not only limited to subsynchronous speed of machine A, but is also valid in supersynchronous speed. The clear effect of machine A synchronous speed can be seen as disturbance in the shape.

Generating mode of the CDFM could be extended above synchronous speed of machine A. For that it would be possible to stop operation before synchronous speed of machine A is reached, let the machine accelerate and resume operation at a certain point above synchronous speed of machine A. Unfortunately, indicated by figure 4.21 and 4.23, the power handling of the converter on side 4 increases linearly with increasing values of the cascaded equivalent slip. The further away from the cascaded synchronous point the more power has to be processed on side 4. The extension of the speed range has therefore little use in reality.

4.2.4 Power Flow

The steady state simulation results support the idea that the CDFM can be regarded in the same manner as a SDFM concerning its accessible terminals, side 1 and side 4. In section 4.2.1, this was already shown for the frequency and slip relations. Now a simplified power flow model for the CDFM by neglecting losses is developed in analytical form as it was the case for the SDFM.

Although the steady state simulations for the experimental machine set show that the losses have a certain effect on the results, it can be assumed that for machines with higher rating this influence reduces, so that in a first order approach a lossless system can be assumed.

The condensed power and frequency equations for machine A are given as

$$P_2 = -s_A P_1 \tag{4.2.33}$$

$$P_{mA} = -(1 - s_A) P_1 \tag{4.2.34}$$

$$P_{mA} = -2\pi f_m T_{eA} \tag{4.2.35}$$

$$s_A = \frac{f_2}{f_1} \tag{4.2.36}$$

$$f_1 = p_A f_m + f_2 \tag{4.2.37}$$

$$f_{rA} = p_A f_m \tag{4.2.38}$$

They are the same as for a normal SDFM.

By viewing machine B from side 3 and regarding side 3 as the primary side and side 4 as the secondary side, then the condensed power and frequency equations for machine B are

$$P_4 = -s_B P_3 \tag{4.2.39}$$

$$P_{mB} = -(1 - s_B) P_3 \tag{4.2.40}$$

$$P_{mB} = -2\pi f_m T_{eB} \tag{4.2.41}$$

$$s_B = \frac{f_4}{f_3} \tag{4.2.42}$$

$$f_3 = p_B f_m + f_4 \tag{4.2.43}$$

$$f_{rB} = p_B f_m \tag{4.2.44}$$

Due to the connection of two machines follows generally, independent of connection sequence,

$$P_2 = -P_3 \tag{4.2.26 repeated}$$

and

$$P_{mAB} = P_{mA} + P_{mB} \tag{4.2.45}$$

which is the sum of the mechanical powers from both machines, not indicating whether the individual mechanical power flows have same or opposite direction.

By combining the power equations of machine A and machine B with (4.2.26), then the

power of side 1 and side 4 take the form

$$P_4 = -s_A s_B P_1 = -s_E P_1 \tag{4.2.46}$$

Side 1 power multiplied by the equivalent slip value of the CDFM gives the side 4 power.

Doing so for the mechanical power equations for the individual machines delivers a combined CDFM mechanical power equation of

$$P_{mAB} = -(1 - s_A s_B) P_1 = -(1 - s_E) P_1 \tag{4.2.47}$$

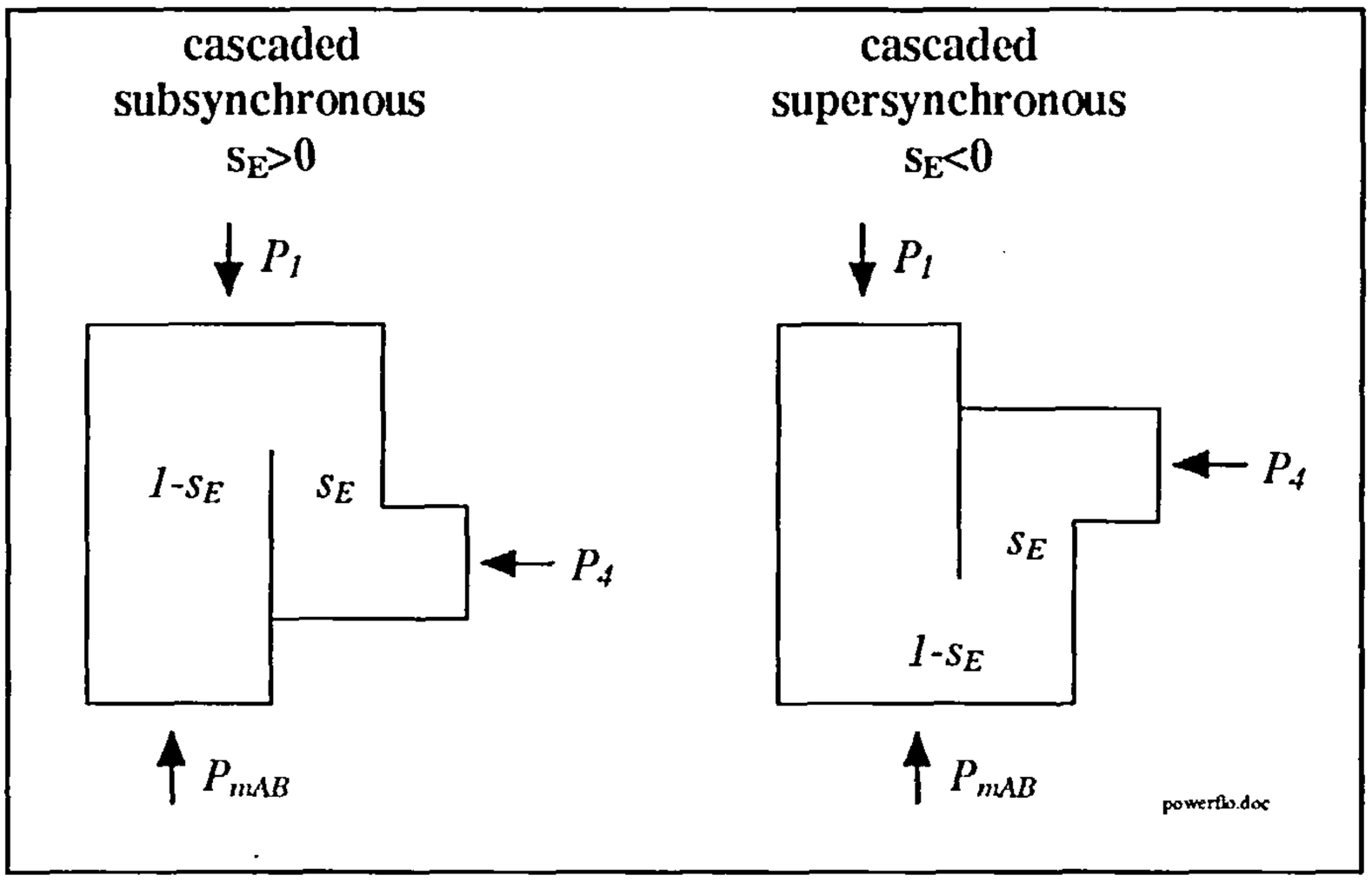

Figure 4.25: Power flow diagram for the CDFM neglecting losses

The last two equations give the relationship between side 1 terminal, side 4 terminal and the combined shaft power of the CDFM. It shows that with the defined cascaded equivalent slip the CDFM behaves like a SDFM in terms of power flow relations. The power flow diagram of the SDFM in figure 3.20 can therefore be applied to the CDFM by replacing P_2 with P_4 and P_m with P_{mAB} as depicted in figure 4.25, where the power flow diagram of the CDFM is drawn for cascaded subsynchronous range and cascaded supersynchronous speed range.

In cascaded subsynchronous speed range and for motoring mode side 4 power can be extracted from the CDFM and fed back to the mains and mechanical power takes a negative value flowing out of the machine. Side 1 has to supply both powers, side 4 and the mechanical power. For generating mode the power flow directions are reversed. Power flows into the system on side 4 and the shaft and can be extracted on side 1.

For cascaded supersynchronous speed the mechanical shaft power is the sum of side 1 and side 4 power. That is identical to the SDFM, where for supersynchronous speed and generating mode for example, power extraction takes place from the stator and the rotor.

The above power flow diagram is valid for positive and negative rotor connection and

depends only on the value of the cascaded equivalent slip. A further breakdown of the power flow diagram for the cascaded subsynchronous and supersynchronous case is displayed in figure 4.26. It clarifies the "internal" connection power flow behaviour of the CDFM.

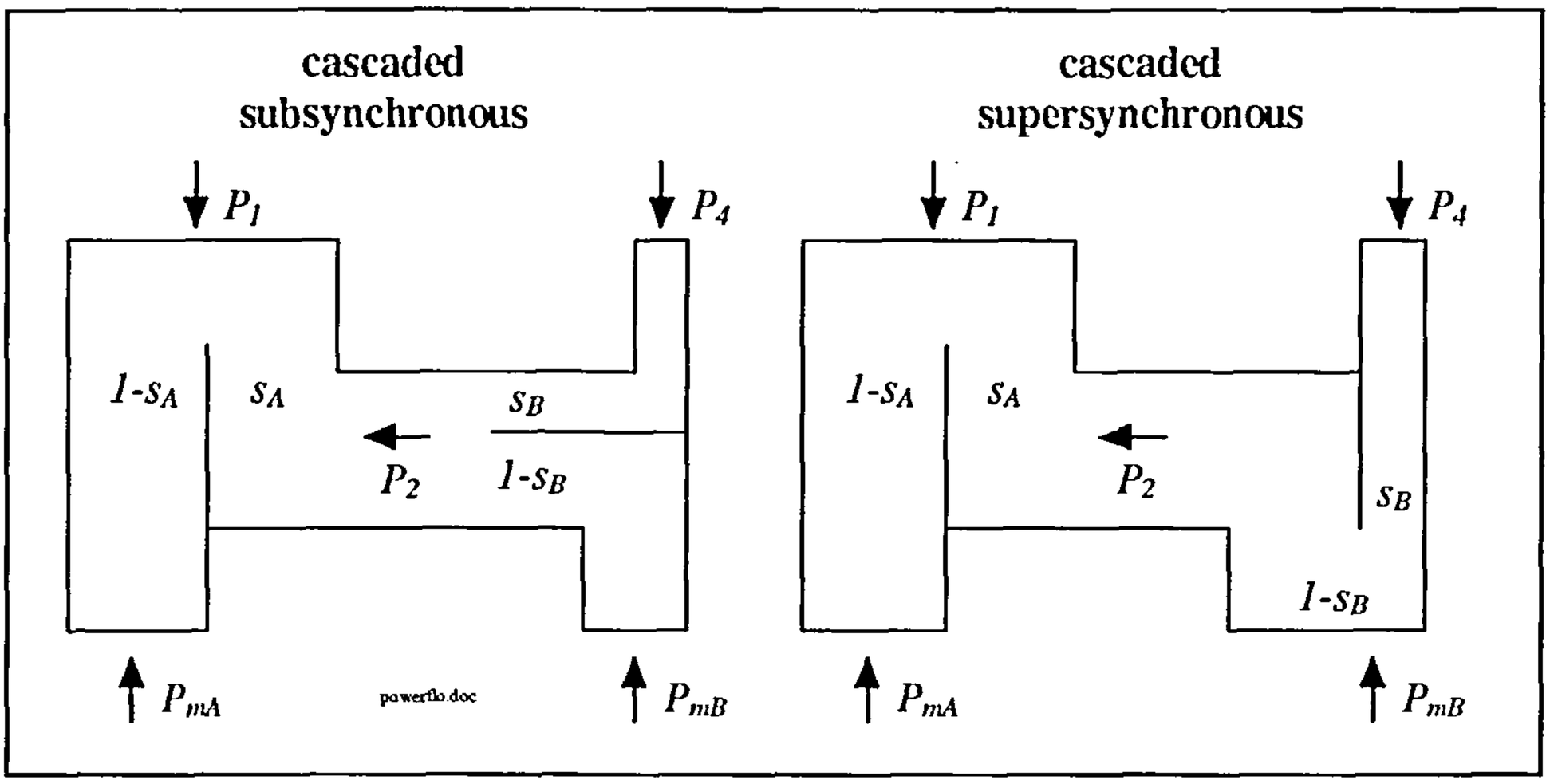

Figure 4.26: Power flow diagram of the CDFM with "internal" power flow neglecting losses

Figure 4.26 shows also that, for a fixed value of slip s_A of machine A, the power conversion from side 1 power into mechanical power can be increased by cascading, since part of the slip power is converted into mechanical power of machine B. For a single SDFM the whole slip power P_2 would be fed back to the supply. That should however not lead to a wrong conclusion, because the slip value s_A of a SDFM must be related to the equivalent slip value s_E of the CDFM and then the power conversion properties are identical for given input values.

$P_{mAB}=P_{mA}+P_{mB}$ $P_2=-P_3$	***Motoring*** $P_{mAB} < 0$	***Generating*** $P_{mAB} > 0$
Cascaded ***Subsynchronous*** $P_1 = -(P_{mAB} + P_4)$	$P_1 > 0$ $P_2 < 0$ $P_4 < 0$	$P_1 < 0$ $P_2 > 0$ $P_4 > 0$
Cascaded ***Supersynchronous*** $P_{mAB} = -(P_1 + P_4)$	$P_1 > 0$ $P_2 < 0$ $P_4 > 0$	$P_1 < 0$ $P_2 > 0$ $P_4 < 0$

table.doc

Table 4.1: Power flow directions of the CDFM neglecting losses

Table 4.1 gives the power flow directions of a CDFM for sub- and supersynchronous speed and motoring and generating mode.

4.2.5 Pole Pair Combinations

So far, the pole pair combination of the two machines in the CDFM was not considered. In this section the influence of the pole pair ratio upon the power flow is derived. For positive and also for the less important negative rotor connection.
Finally, a decision on an optimal pole pair ratio is made based on practical machine utilisation arguments.

Generally, there are six different machine combination possibilities depending on the rotor connection, which are:

Positive phase sequence rotor connection

$p_A > p_B$ $\quad$ $p_A = p_B$ $\quad$ $p_A < p_B$

Negative phase sequence rotor connection

$p_A > p_B$ $\quad$ $p_A = p_B$ $\quad$ $p_A < p_B$

To the case for *positive phase sequence rotor connection:*
Combining above frequency equations of the individual machines with the constraint of $f_2 = f_3$, then the cascaded frequency relation results as

$$f_1 = (p_A + p_B) f_m + f_4 \tag{4.2.48}$$

which was already introduced in section 4.2.1. By using the slip equation of machine A and machine B and combining them, gives the slip values for the individual machines as a function of each other and the pole pairs as [c6]

$$s_A = \frac{p_B}{p_A(1 - s_B) + p_B} \qquad s_B = \frac{s_A(p_A + p_B) - p_B}{s_A p_A} \tag{4.2.49}$$

For a better interpretation it is useful to derive the power ratio between side 1 and side 4 dependent on the pole pair ratio

$$\frac{P_4}{P_1} = -s_E = \frac{p_B}{p_A} - s_A\left(1 + \frac{p_B}{p_A}\right) \tag{4.2.50}$$

As explained, the speed range of the CDFM is limited to the subsynchronous speed of machine A and would therefore have its maximum power output close to the slip value $s_A = 0$. Equation (4.2.50) points out that a small ratio p_B/p_A is favourable, when the power output on side 4 and consequently the converter power should be minimised. Figure 4.27 shows the power relations for the machine set with $p_A = 4$ and $p_B = 2$.

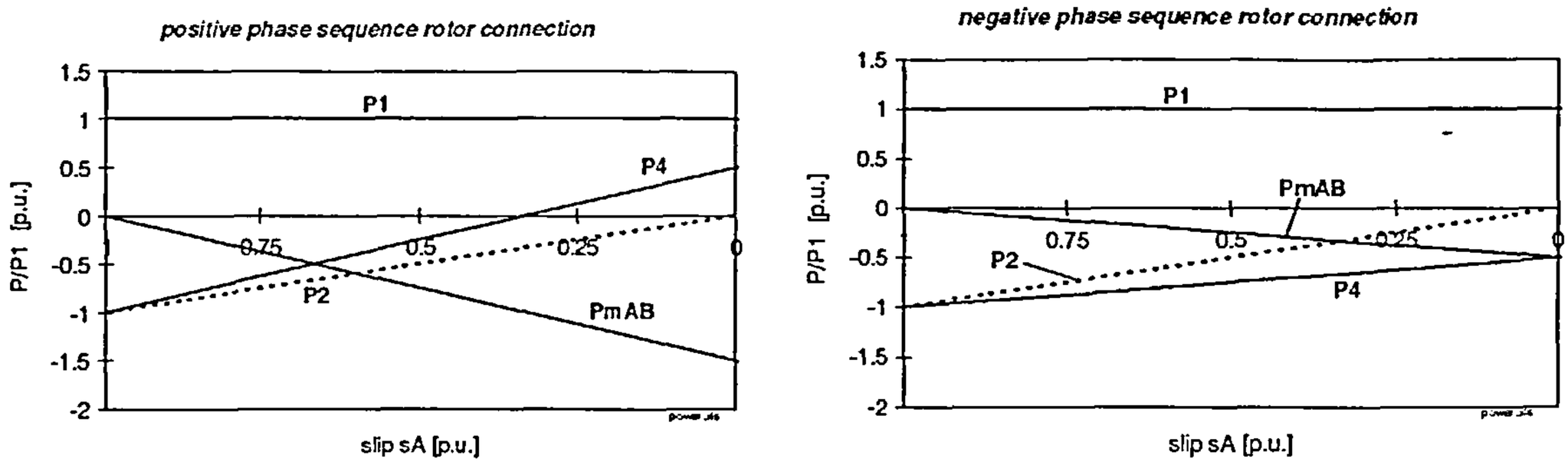

Figure 4.27: Power relations of the CDFM set with $p_A=4$ and $p_B=2$ neglecting losses in subsynchronous speed range of machine A

(constant T_{eA})

As equation (4.2.50) shows, the output on side 4 at maximum speed is half the value of side 1 power. The graphs are per-unitised for constant rated torque of machine A.

The relation between the mechanical powers of the two machines can be found by combining above mechanical power equations with the derived slip equations and leads to

$$\frac{P_{mA}}{P_{mB}} = \frac{p_A}{p_B} \tag{4.2.51}$$

Neglecting losses in the CDFM, the mechanical output of each individual machine is proportional to the number of pole pairs [c6]. Accordingly, the torque produced by each machine is proportional to the ratio of the pole pairs. In figure 4.27 the sum of the mechanical power has the per unit value of 1.5 at $s_A=0$, because the powers are per-unitised to machine A. Machine B, in accordance to equation (4.2.51), produces only half the mechanical power of machine A due to the pole pair ratio.

It can also be seen in figure 4.27 that at standstill ($s_A=1$) the rotor power P_2 and side 4 power P_4 have the same magnitude as side 1 power indicating that the power flow takes place only between the terminals 1 and 4 and no mechanical power is involved, which is expected of course. With increasing speed the rotor power P_2 decreases until it reaches the value zero at slip $s_A=0$. For the CDFM under consideration the cascaded synchronous speed occurs at 500 rpm or at slip $s_A=0.33$. At this point there is no power at terminal 4.

Considering the *negative phase sequence rotor connection* and giving the related equations in a condensed form

$$f_1 = (p_A - p_B) f_m - f_4 \tag{4.2.52}$$

$$s_A = \frac{p_B}{p_A(s_B - 1) + p_B} \qquad s_B = \frac{s_A(p_A - p_B) + p_B}{s_A p_A} \tag{4.2.53}$$

$$\frac{P_4}{P_1} = -s_E = -\frac{p_B}{p_A} - s_A\left(1 - \frac{p_B}{p_A}\right) \tag{4.2.54}$$

$$\frac{P_{mA}}{P_{mB}} = -\frac{p_A}{p_B} \tag{4.2.55}$$

reveals two facts straight away. The mechanical powers, in the ratio of the pole pairs, are counter flowing and the developed machine torques are counter acting, equation (4.2.55). This was already mentioned at the beginning of this chapter and makes this rotor connection unattractive for power applications. As a consequence, for a CDFM with equal pole pairs the power relation between side 1 and side 4 always assumes a unity value regardless of speed, equation (4.2.54). In this case the power flow is from terminal 1 to terminal 4 or vice versa, because the mechanical powers are canceling each other. The power lines for this rotor connection and the used pole pair number are shown in figure 4.27, for completeness.

What is the best machine combination for a CDFM ?

This subject has found only limited attention in the literature and there are no firm conclusions on a best machine combination. In [b5] the main attention was on the power ratio between side 1 and side 4 power. Depending on the required speed range and rotor connection a pole pair number could be chosen to limit the power handling of the converter on side 4. This method of thinking can only be applied to low power machine connections, because excessive power flows would result for some combinations. In generator mode, [b5] favours positive phase sequence rotor connection for subsynchronous speed of machine A and negative phase sequence rotor connection for supersynchronous speed of machine A.
For medium and high power applications, where losses due to power flow and machine utilisation plays an important role, a different solution has to be found for making a decision on the pole pair combination and rating of the individual machines.

Analysis so far showed, that operational speed range is limited to subsynchronous range of machine A and that only positive phase sequence rotor connection is useful.

As established, the two machines develop torques in the ratio of the pole pair number or that the mechanical power produced by the individual machine is in the ratio of their pole pair number. Although for the above power equations losses are neglected, this fact applies approximately to a real machine set.
Consequently, it could be argued that a high pole pair number for machine A should be used and a small pole pair number for machine B, so that the majority of the power is processed by machine A and machine B could therefore be smaller rated than machine A.

Assuming, that the rating of machine A is based on the rated torque multiplied by the

machine synchronous speed leads to the statement

$$P_{mArating} \approx f_{mAsync} T_{eArated} \tag{4.2.56}$$

Since the rated name plate speed of the machine is close to the machine synchronous speed

$$f_{mAsync} = \frac{f_1}{p_A} \tag{4.2.57}$$

the above statement is valid for first order approximation. Doing so for machine B with

$$P_{mBrating} \approx f_{mBsync} T_{eBrated} \tag{4.2.58}$$

$$f_{mBsync} = \frac{f_1}{p_B} \tag{4.2.59}$$

gives four equations for two off-the-shelf wound rotor induction machines, which shall be put together to form a CDFM.

Replacing $P_{mA\,rating}$ in (4.2.56) with

$$P_{mArating} = \frac{p_A}{p_B} P_{mBrating} \tag{4.2.60}$$

which follows from (4.2.51), then (4.2.56) can be rewritten with $P_{mB\,rating}$ as

$$P_{mBrating} = \frac{p_B}{p_A} f_{mAsync} T_{eArating} \tag{4.2.61}$$

From (4.2.57) and (4.2.59), the two machine synchronous speeds take a ratio of

$$f_{mBsync} = \frac{p_B}{p_A} f_{mAsync} \tag{4.2.62}$$

to each other. Substituting (4.2.62) into (4.2.58) leads to the expression

$$P_{mBrating} = \frac{p_B}{p_A} f_{mAsync} T_{eBrating} \tag{4.2.63}$$

Equating (4.2.63) with (4.2.61) gives a final torque rating ratio and therefore machine rating ratio of the individual machines for a CDFM of

$$T_{eArating} = T_{eBrating} \tag{4.2.64}$$

It suggests, that the two machines for a CDFM have to be of the same rating and that means with equation (4.2.51), that both machines must have the same pole pair number. Consequently, two identical machines must be used for the CDFM, when maximum machine efficiency and machine utilisation is a priority as it is in higher power ranges.

To describe it in a different way it will be assumed, that it is possible to drive the CDFM up to the synchronous speed of machine A. Machine A is only fully utilised if it is used close to its synchronous speed. That is also the case for machine B. Since the machines are mechanically connected the machines must have same pole pair numbers so that both machines can be used close to their synchronous speed to get maximum utilisation from the machines. With the rating depending on the pole pair combination two equally rated machines must thus be used.

Due to the loss of machine coupling in the vicinity of the synchronous speed of machine A it

is not possible to drive the CDFM entirely up to that speed, but even the approximation still justifies the argument.
The work of [b15] deals with two identical machines, but no reasoning is given for that.

Power lines for a CDFM with equal pole pairs are depicted in figure 4.28. At $s_A=0.2$ a maximum speed limit line helps to identify the power values at that point, which corresponds to 80% of the subsynchronous speed of machine A. Results in chapter 5 show that close to the synchronous point of machine A the side 4 currents increase rapidly in an uncontrolled manner. It is therefore advisable to keep a certain distance to that operational point. In [b17] further investigations are carried out to determine a maximum speed envelope for motoring and generating mode of the CDFM. For generating mode the maximum speed limit tends to be slightly higher than for motoring mode. But generally speaking, to set the maximum limit at around 80% can be seen as a good compromise. This was also found for the experimental machine set, where at 600 rpm (80% of 750 rpm) the CDFM was still within a "safe" controlling area.

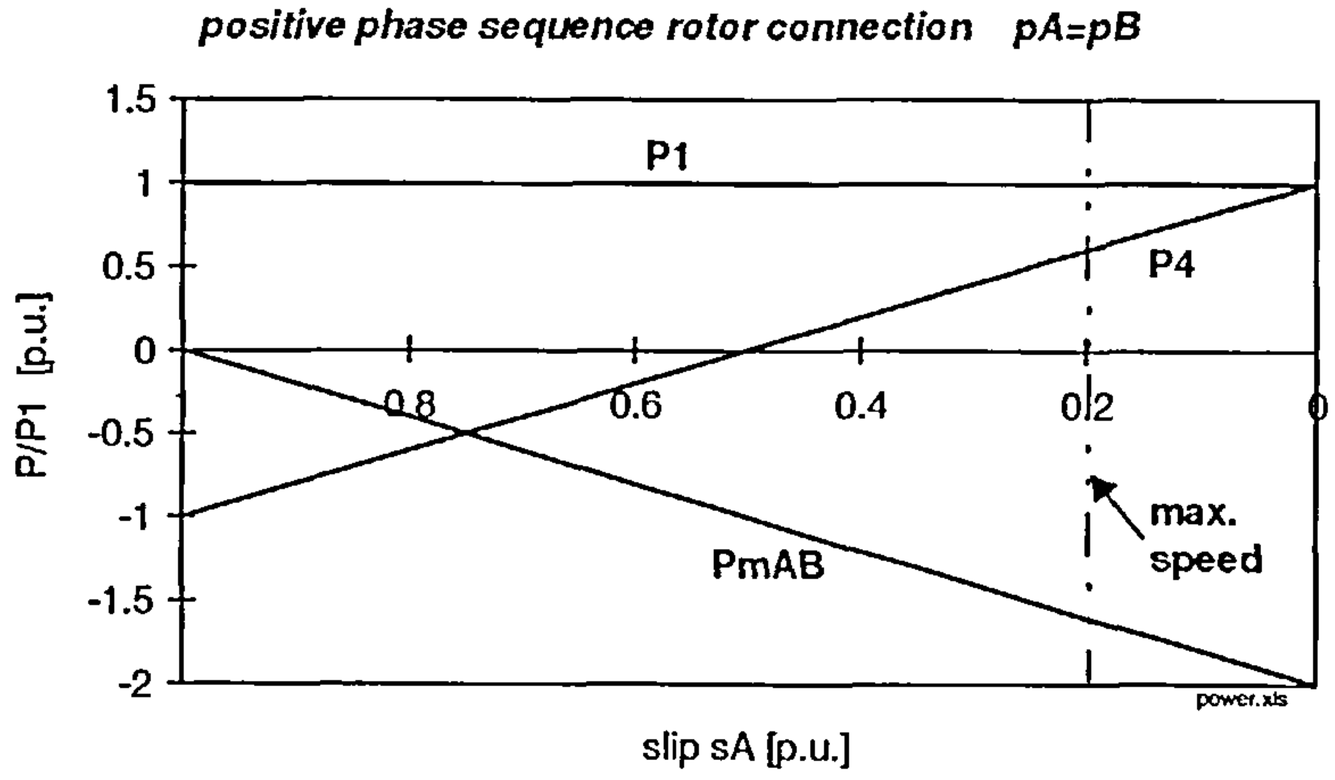

Figure 4.28: Power relations of the CDFM set with $p_A=p_B$ neglecting losses in subsynchronous speed range of machine A (constant T_{eA})

At 80% of their rated speed the individual machines produce only 80% of their rated mechanical power output for rated torque and so the CDFM produces 1.6 times the mechanical power of machine A, as indicated in figure 4.28. At this point, side 1 delivers full output, whereas side 4 delivers only 60% of the normalised power. The power converter on side 4 processes less than 50% of the overall mechanical power. But if full rated torque is needed for start-up a 50% rated converter must be used, to provide the full power on side 4.

4.3 Summary and Conclusions

In this chapter the dynamic CDFM machine model for positive and negative rotor connection is derived. Furthermore, extensive steady state treatment with simulations lead to the following features of the CDFM, which are summarised at this point:

- Rotor Connection

Only positive phase sequence rotor connection is useful, because both machines develop torque in the same direction. In this case the air-gap fields of the machines are counter rotational relative to the rotor.

- Per-Phase Equivalent Circuit

The per-phase equivalent circuit for the CDFM is a straight forward connection of two wound rotor induction machine equivalent circuits.

- Power, Frequency and Slip

The introduction of an equivalent slip for the CDFM, simplifies the two-machine combination and the set can be considered like a SDFM with a pole pair number made up from the sum of the individual pole pair numbers. Valid for frequency, slip and power relations.

- Machine Combination

Based on simple machine utilisation principles, it can be concluded that a CDFM, composed of two wound rotor induction machines, has to consist of two identical rated machines with the same pole pair number for maximum efficiency.

- Speed Range and Converter Rating

The operational range for a CDFM lies in the subsynchronous speed range of machine A. The maximum speed limit is around 80% of the complete range. For that speed range a 50% rated converter must be used.

Based on the steady state simulations, which show similar behaviour as for the SDFM, the stator flux (side 1 flux) oriented control of the CDFM is investigated in the second section of next chapter.

Chapter 5

Field Oriented Control of CDFM

Different control methods and investigations for the CDFM have already been summarised in the introduction. Open-loop V/Hz-control and open-loop current control on side 4 leads to poor performance due mainly to dynamic instabilities [b15]. Improved, high dynamic control performance of the CDFM can be achieved with a field oriented control method of Bauer [b15]. A reference frame, created by the summation of the two stator currents, side 1 and side 4, is used for orientation of an unmeasureable rotor current component to perform torque control. Speed control on two identical 1 kW wound rotor induction machines was carried out and good dynamic performance was achieved. Krebs [b17] extended that work with a state observer for the machine currents and controlled the machine in the state space to ensure good stable performance up to high speeds. The method was implemented on a drive with a 30 kW SF-CDFM and speed control results confirmed the improved effect.
Concerning the control method of [b15], which is only applicable to two identical machines, this thesis investigates whether it is possible to modify the method so that it can be used for unequal machines. Further, the method is largely simplified by removing a mathematical control extension and the so derived method is analysed for power and speed control purposes.
Supported by the steady state results of the CDFM, in the second section of this chapter the stator flux control scheme of the SDFM is applied to the CDFM and its performance regarding decoupled active and reactive power control and speed control is explored.

The following field oriented control methods for the CDFM considers only positive phase sequence rotor connection and the operational speed range is in the subsynchronous speed of machine A.

5.1 Field Oriented Control with Combined Flux Linkage

Starting with the torque equation, as derived earlier,

$$T_{eAB} = -\frac{3}{2}[(\, p_A L_{mA} \bar{i}_1^g + p_B L_{mB} \bar{i}_4^g \,) \times \bar{i}_2^g \,] \qquad (5.1.1)$$

it can be seen, that the expression in the brackets can be replaced by a flux quantity and the

torque equation reduces to

$$T_{e\Lambda B} = -\frac{3}{2}[\overline{\Psi}^{g}_{\mu AB} \times \bar{i}^{g}_{2}] \qquad (5.1.2)$$

where

$$\overline{\Psi}^{g}_{\mu AB} = p_A L_{mA} \bar{i}^{g}_{1} + p_B L_{mB} \bar{i}^{g}_{4} \qquad (5.1.3)$$

is a mathematical combination of the stator currents creating a combined flux linkage vector. This combined magnetising flux vector is a non-physical quantity and therefore does not exist in the machine. It is, however, a useful control variable.

If orientation takes place on that combined flux vector and thus creating the constraints of

$$|\overline{\Psi}^{g}_{\mu AB}| = \Psi^{e}_{\mu AB} = \Psi^{e}_{d\mu AB} \quad \text{and} \quad \Psi^{e}_{q\mu AB} = 0 \qquad (5.1.4)$$

the torque equation (5.1.2) simplifies to the term

$$T_{e\Lambda B} = -\frac{3}{2}\Psi^{e}_{d\mu AB} i^{e}_{q2} \qquad (5.1.5)$$

It shows that in a reference frame attached to the combined flux vector and by keeping the amplitude of the flux vector constant, the torque can be controlled with the q-component of the rotor current in the "e"-reference frame.

The amplitude of the combined magnetising flux vector can be calculated from the side 1 and side 4 current, together with the individual number of pole pairs and the magnetising inductances, in the "a"-frame as

$$\Psi^{e}_{d\mu AB} = |\overline{\Psi}^{a}_{\mu AB}| = |p_A L_{mA} i^{a}_{d1} + p_B L_{mB} i^{a}_{d4}| \qquad (5.1.6)$$

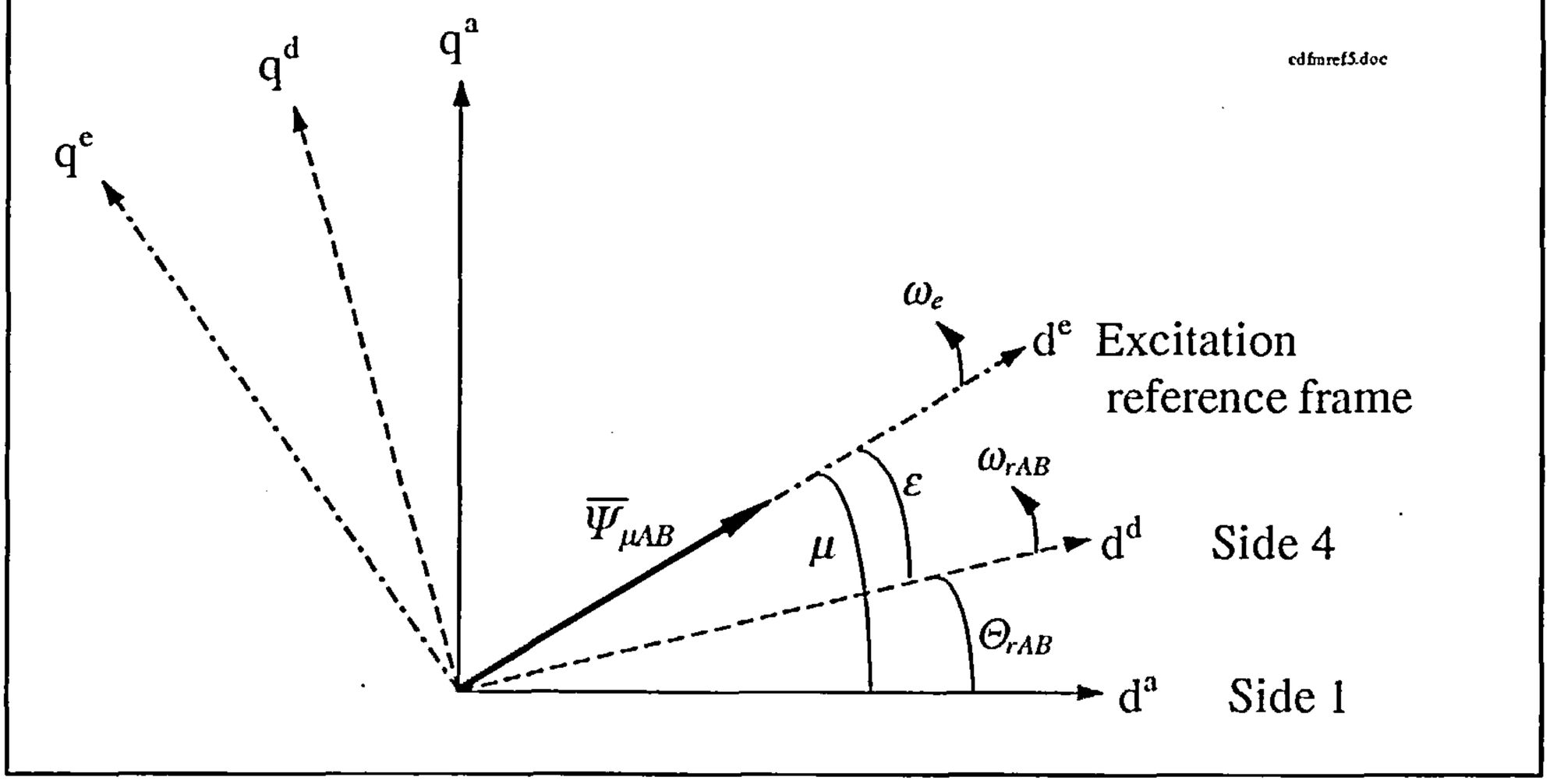

Figure 5.1: Reference frames and angles for the CDFM with combined flux control

In order to do so, the side 4 current has first to be rotated from the "d"-frame onto the stationary reference frame "a". With the signals from an incremental encoder and the use of equation (4.1.15) the required angle between "a" and "d"-frame is

$$\Theta_{rAB} = (p_A + p_B)\Theta_m \tag{5.1.7}$$

with Θ_m as the rotor position angle in mechanical radians per second and Θ_{rAB} is expressed in electrical radians per second.

The angle μ between the stationary reference frame and the field frame can be obtained with the help of the q-component of the combined flux in the "a"-frame divided by the d-component and leads to

$$\mu = arctan\frac{\Psi^a_{q\mu AB}}{\Psi^a_{d\mu AB}} \tag{5.1.8}$$

All angle definitions and reference frames are depicted in figure 5.1. For the sake of clarity the reference frame for the rotor, side 2 and side 3, has been dropped in figure 5.1. Only side 1 and side 4 of the CDFM are shown. As already introduced, the reference frame attached to the combined magnetising flux is denoted as "e"-frame or excitation reference frame to keep similarities to the SDFM expressions.

5.1.1 Speed Control after Previous Method with Modifications

Bauer [b15] developed the field oriented control of the CDFM based on the assumption that two identical machines with same machine parameters are available. In that case, equation (5.1.6) in the "e"-frame would simplify to

$$\Psi^e_{d\mu AB} = p_A L_{mA}(i^e_{d1} + i^e_{d4}) \tag{5.1.9}$$

and the orientation can take place on the simple sum of both stator currents. For the time being it is assumed that the two machines are identical.

As equation (5.1.5) shows, the rotor current component must be manipulated to control the torque. Since the rotor current is not accessible a way must be found to indirectly access the rotor current component.

The defined machine A and machine B magnetising currents expressed in a general reference frame

$$\bar{i}^g_{\mu A} = \bar{i}^g_1 + \bar{i}^g_2 \tag{5.1.10}$$

$$\bar{i}^g_{\mu B} = \bar{i}^g_3 + \bar{i}^g_4 = -\bar{i}^g_2 + \bar{i}^g_4 \tag{5.1.11}$$

can be combined to give an overall artificial magnetising current vector in the form of

$$\bar{i}^g_{\mu AB} = \bar{i}^g_{\mu A} + \bar{i}^g_{\mu B} = \bar{i}^g_1 + \bar{i}^g_4 \tag{5.1.12}$$

For two identical machines this combined magnetising current is aligned with the combined flux linkage vector, as equation (5.1.9) proves, and therefore the q-component of (5.1.12) takes the value zero in the "e"-frame so that

$$i^e_{q\mu A} = -i^e_{q\mu B} \tag{5.1.13}$$

The q-components of the individual machine magnetising currents have an opposing direction to each other in the "e"-frame. With the rotation of equation (5.1.11) into the "e"-frame follows

$$i^e_{q\mu B} = -i^e_{q2} + i^e_{q4} \tag{5.1.14}$$

Substituting (5.1.13) into (5.1.14) yields

$$-i^e_{q\mu A} = -i^e_{q2} + i^e_{q4} \tag{5.1.15}$$

This equation implies, that the rotor current component for controlling the torque can be directed by the accessible side 4 current component, if the machine A magnetising current component is known. With the help of side 1 voltage and flux linkage equations, defined in section 4.1.3, and by using (5.1.10) the machine A magnetising current can be calculated in the stationary reference frame as

$$\bar{i}^a_{\mu A} = \frac{1}{L_{mA}} \int (\bar{v}^a_1 - R_1 \bar{i}^a_1)dt - \sigma_1 \bar{i}^a_1 \tag{5.1.16}$$

with

σ_1 as the side 1 leakage factor.

Side 1 voltage and current are measured quantities. The calculated machine A magnetising current vector has only to be rotated into the "e"-frame to assist with equation (5.1.15) in accessing the rotor current q-component in an indirect way through side 4 current.

The so derived control structure, as used in [b15], is shown in figure 5.2. An inner current control loop is already included in figure 5.2, for providing the demanded side 4 currents in the CDFM

As displayed, the input on the q-axis is the torque demand value, which by division with the magnitude of the combined magnetising flux linkage vector yields the desired rotor current component, in accordance to equation (5.1.5). Subtracting the calculated machine A magnetising q-component gives the value for the side 4 current value, equation (5.1.15).

As derived in equation (5.1.5) the control of the torque of the CDFM is governed by the q-component of the rotor current in the "e"-frame, when the magnitude of the combined magnetising flux stays constant. This, however, cannot be assumed, since the magnitude depends on side 1 and side 4 current and only the side 4 current component is controllable. Four different possibilities on how to control the combined flux of the CDFM via $i_{d4}{}^e$ has been investigated in [b15] and those are:

- control of $i_{d4}{}^e$ for minimum rotor current ($i_{d2}{}^e = 0$)
- control of $i_{d4}{}^e$ to have a constant amplitude of $\Psi_{d\mu AB}{}^e$
- control of $i_{d4}{}^e$ to achieve equal reactive current loading on both machines
- control of $i_{d4}{}^e$ to give minimum inverter rating ($i_{d4}{}^e = 0$)

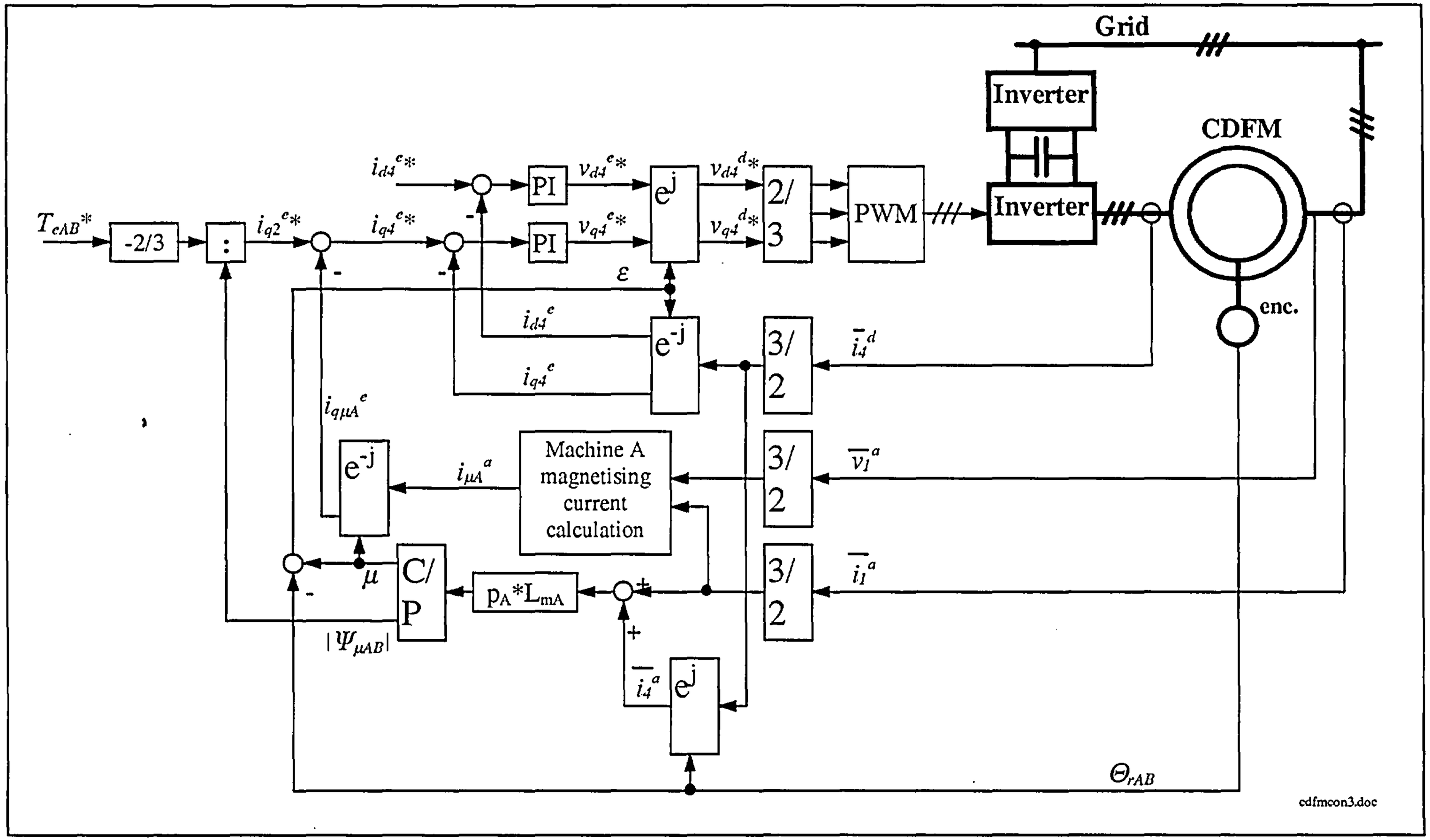

Figure 5.2: Control structure for combined flux control of CDFM [b15]

For all four cases steady state performance and dynamic stability behaviour of the CDFM has been investigated with following results [b15]:
The first method, with no reactive rotor current and thus no reactive power transfer via the rotor, proved to be unstable over the whole operational range and therefore can be ignored.
In the second case a small stable operation area exists, but the steady state reactive machine currents have fairly large amplitudes so that the machine current loading can reach not permissible values and consequently rules out this method of controlling i_{d4}^{e}.
More advantageous is the third method, where the currents i_{d1}^{e} and i_{d4}^{e} are controlled to equal values. In comparison to the first method small reactive rotor currents occur. A large stable operation area exists, but within that area the system damping is relatively weak. Generating mode has positive influence on the damping, in contrast to a motoring mode.
In the last method the bulk of machine magnetisation is provided from side 1. The same stable operation area as for method three exists, but with improved system damping. This way of controlling $i_{d4}^{e} = 0$ is favoured in [b15] and [b17]. An appropriate steady state current vector diagram is drawn in figure 5.3, where the individual machine currents are expressed in the field oriented frame "e".

As displayed, the vectorial summation of side 1 and side 4 currents gives the combined magnetising current vector. The side 4 current is parallel to the q-axis, showing that the d-component is set to zero. Combining the individual machine magnetising current components produces likewise the combined magnetising current vector, equation (5.1.12).

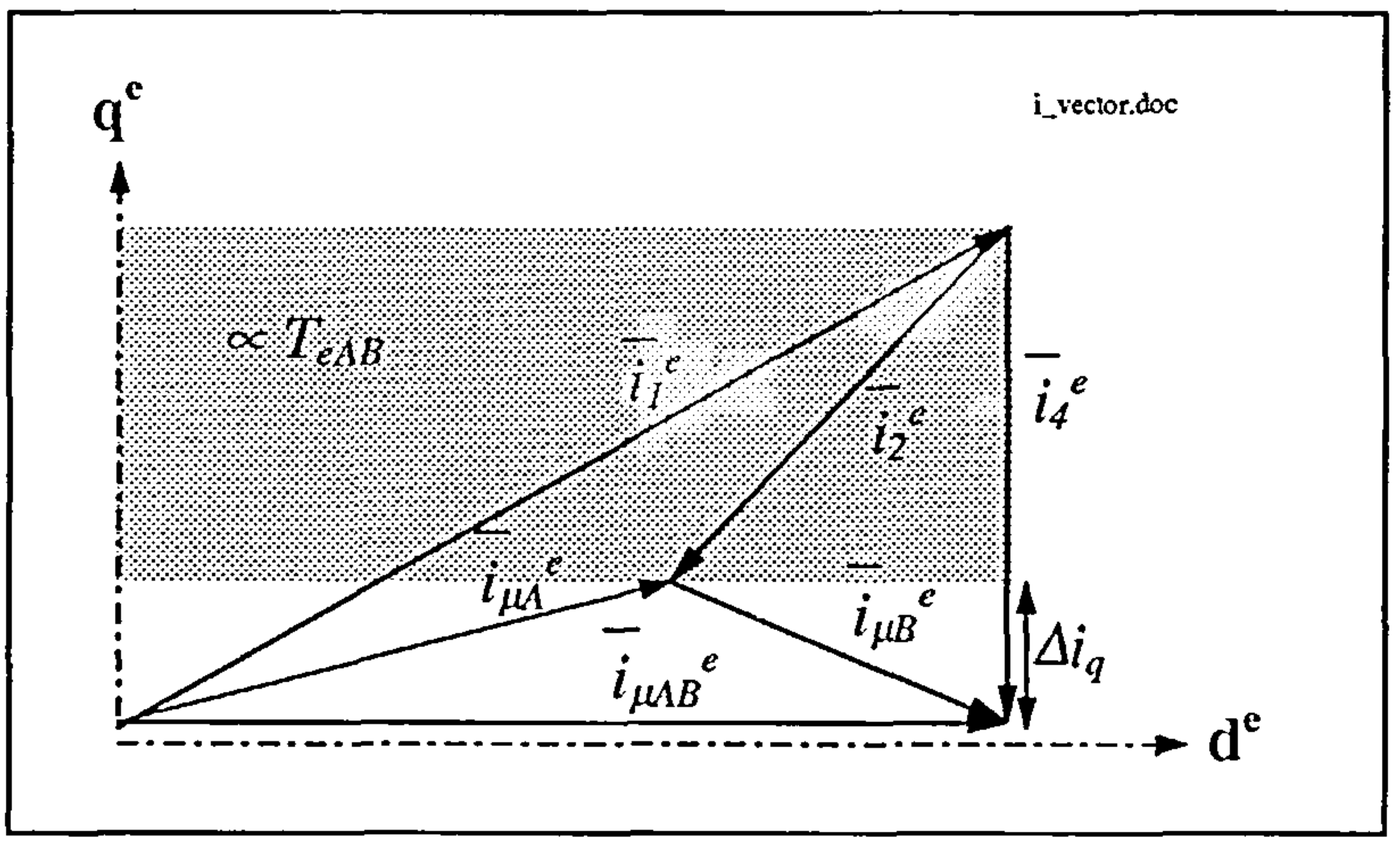

Figure 5.3: Current vector diagram in "e"-frame [b15]

Concerning the losses in the machines, due to the reactive current loading, would suggest, that the machine A current loading is much larger than that of machine B with $i_{d4}^{e} = 0$. In figure 5.3, the side 1 machine current constitutes always the hypotenuse in the triangle with side 4 and the defined overall magnetising current. The current loading in machine A is consequently always higher than in machine B. However, the differences between side 1 and side 4 current magnitude is in reality not as significant as indicated in figure 5.3 [b17].

The shaded area in figure 5.3 is proportional to the developed torque of the CDFM.

By adopting method four of the combined magnetising flux control with $i_{d4}^{e}=0$, the magnitude of $\Psi_{\mu AB}$ is not constant, but depends on the operational point of the machine. Over the speed range the variation in the magnitude is limited and this marginal influence can be compensated by the PI-controller in the q-axis to ensure demanded torque values [b17].

The combined magnetising current vector expressed in the "e"-frame is the sum of the stator current components as mentioned earlier. From equation (5.1.12) follows

$$\bar{i}_{d\mu AB}^{e} = \bar{i}_{d1}^{e} + \bar{i}_{d4}^{e} \tag{5.1.17}$$

This magnetising vector is only aligned to the combined flux vector expressed in the "e"-frame

$$\Psi_{d\mu AB}^{e} = p_A L_{mA} i_{d1}^{e} + p_B L_{mB} i_{d4}^{e} \tag{5.1.18}$$

when both machines are identical and therefore have the same machine parameters and (5.1.18) can thus be written as (5.1.9). Or if the side 4 current d-component is controlled to zero, as it is the case in the last described control method, because then the influence of i_{d4}^{e} drops out in equation (5.1.17) and (5.1.18). Only then, both magnetising quantities point in the same direction. If the side 4 current component is not controlled to zero, then it is not possible to apply the control structure of [b15] to a CDFM, which is composed of different individual machines, as is the case with the experimental machines.
It should be mentioned, that the control method of Krebs [b17] is independent of machine combination used. His state space control structure involves the complete dynamic model of the machine, and therefore parameters. The actual current control takes place in the stationary reference frame, rather than the field oriented frame "e".

If the control method of Bauer [b15] has to be implemented for unequal machines, then a modification is necessary on the control structure shown in figure 5.2.

Modified control

The torque of the CDFM, equation (5.1.5), is manipulated with the q-component of the rotor current in the "e"-frame. A relationship between side 4 q-component and the rotor component has to be established to gain indirect access to the rotor current component. As described above, with support of the magnetising current of machine A delivers the required relationship, but only for identical machines. A novel way must therefore be found to construct the connection for unequal machines.

Substituting the side 1 flux linkage equation (4.1.16) into the combined flux linkage equation (5.1.3) yields

$$\Psi^a_{\mu AB} = \frac{p_A L_{mA}}{L_1}\overline{\Psi}^a_1 + p_B L_{mB}\bar{i}^a_4 - \frac{p_A L_{mA}^2}{L_1}\bar{i}^a_2$$

Rotation into the "e"-frame and splitting into d-q-components together with the constraints of (5.1.4) then

$$i^e_{d4} = \frac{1}{p_B L_{mB}}\Psi^e_{d\mu AB} + \frac{p_A L_{mA}^2}{p_B L_{mB} L_1} i^e_{d2} - \frac{p_A L_{mA}}{p_B L_{mB} L_1}\Psi^e_{d1} \qquad (5.1.19)$$

$$i^e_{q4} = 0 + \frac{p_A L_{mA}^2}{p_B L_{mB} L_1} i^e_{q2} - \frac{p_A L_{mA}}{p_B L_{mB} L_1}\Psi^e_{q1} \qquad (5.1.20)$$

From equation (5.1.20) it can be seen, that the q-component of the rotor current can be directed by the q-component of the side 4 current if the side 1 q-component of the flux in the "e"-frame is known.

From chapter 3, where the field oriented control of the SDFM is explained, it is known that for neglected stator resistance the stator flux has a perpendicular relation to the stator voltage vector and an amplitude relation of

$$|\overline{\Psi}^a_1| \approx \frac{|\bar{v}^a_1|}{\omega_1} \qquad (5.1.21)$$

With the neglect of side 1 resistance, the measured side 1 voltage vector transferred into the combined flux reference frame "e" delivers the required side 1 flux components in the "e"-frame in the form of

$$\Psi^e_{d1} = \frac{v^e_{q1}}{\omega_1} \quad \text{and} \quad \Psi^e_{q1} = -\frac{v^e_{d1}}{\omega_1} \qquad (5.1.22)$$

ω_1 is the constant supply frequency.

From (5.1.22) and (5.1.20) the necessary relation between side 4 and rotor current q-component is given by

$$i^e_{q4} = \frac{p_A L_{mA}^2}{p_B L_{mB} L_1} i^e_{q2} + \frac{p_A L_{mA}}{p_B L_{mB} L_1}\frac{v^e_{d1}}{\omega_1} \qquad (5.1.23)$$

In comparison to the field oriented control of the SDFM, the side 1 voltage in the "e"-frame in (5.1.23) does not necessarily have a constant value, it rather depends on the voltage vector position within the combined flux reference frame "e".

In a way, this method of relating side 4 current to side 2 current is not so different to the method in [b15], because equation (5.1.21) constitutes a hidden integration of side 1 voltage similar to equation (5.1.16).
It can be seen that equation (5.1.23) involves the number of pole pairs and various

inductance values of the two machines and so underlines its independence of machine combination for the CDFM. For equal machines the equation would of course simplify.
The modification of the CDFM control structure with the new relationship is shown in figure 5.4.

In the field oriented control of the SDFM, a counteracting e.m.f. exists in the q-axis within the current control loop. By calculating this slip proportional e.m.f. and adding it to the output of the PI-controller of the q-axis the steady state accuracy can be improved [f2]. This has been shown in the results of figure 3.31 for the SDFM control.
There is no mention of such a fact in [b15] or [b17], and thus it is investigated in the following.

The side 4 voltage and flux linkage equations expressed in the "e"-frame are

$$\bar{v}_4^e = R_4\bar{i}_1^e + \frac{d\Psi_4^e}{dt} + j(\omega_e - \omega_{rAB})\overline{\Psi}_4^e \qquad (5.1.24)$$

$$\overline{\Psi}_4^e = L_4\bar{i}_4^e - L_{mB}\bar{i}_2^e \qquad (5.1.25)$$

Resolving the side 1 flux linkage equation in the "e"-frame

$$\overline{\Psi}_1^e = L_1\bar{i}_1^e + L_{mA}\bar{i}_2^e$$

after the side 2 current and substituting it into (5.1.25) obtains

$$\overline{\Psi}_4^e = L_4\bar{i}_4^e - \frac{L_{mB}}{L_{mA}}\overline{\Psi}_1^e + \frac{L_{mB}L_1}{L_{mA}}\bar{i}_1^e \qquad (5.1.26)$$

From equation (5.1.3) follows in the "e"-frame

$$\bar{i}_1^e = \frac{1}{p_A L_{mA}}\overline{\Psi}_{\mu AB}^e - \frac{p_B L_{mB}}{p_A L_{mA}}\bar{i}_4^e$$

and by implementing it in (5.1.26) gives for the side 4 flux linkage equation in the "e"-frame

$$\overline{\Psi}_4^e = (L_4 - m_1)\bar{i}_4^e - \frac{L_{mB}}{L_{mA}}\overline{\Psi}_1^e + m_2\overline{\Psi}_{\mu AB}^e \qquad (5.1.27)$$

with the abbreviations

$$m_1 = \frac{L_{mB}L_1}{L_{mA}}\frac{p_B L_{mB}}{p_A L_{mA}} \quad \text{and} \quad m_2 = \frac{L_{mB}L_1}{L_{mA}p_A L_{mA}}$$

Replacing (5.1.27) in the side 4 voltage equation (5.1.24), considering only steady state ($\frac{d}{dt} = 0$), splitting into d-q-components and taking account of the constraints (5.1.4) delivers

$$v_{d4}^e = R_4 i_{d4}^e - (\omega_e - \omega_{rAB})[(L_4 - m_1)i_{q4}^e - \frac{L_{mB}}{L_{mA}}\Psi_{q1}^e] \qquad (5.1.28)$$

$$v_{q4}^e = R_4 i_{q4}^e + (\omega_e - \omega_{rAB})[(L_4 - m_1)i_{d4}^e - \frac{L_{mB}}{L_{mA}}\Psi_{d1}^e] + (\omega_e - \omega_{rAB})m_2\Psi_{\mu AB} \qquad (5.1.29)$$

Similar to the SDFM rotor voltage equations, the equations for the CDFM contain a cross coupling term, second terms in (5.1.28) and (5.1.29), and equation (5.1.29) additionally contains a slip proportional e.m.f. part due to the combined magnetising flux. Again, these equations would largely simplify for identical machines.

The slight influence of the cross coupling terms can be ignored, but the e.m.f. part has to be included in the control structure for improved performance. The feed forward term

$$feed\ \ forward = (\omega_e - \omega_{rAB}) \frac{L_{mB} L_1}{L_{mA} p_A L_{mA}} \Psi_{\mu AB} \qquad (5.1.30)$$

is added in the q-axis of the current control loop as contained in figure 5.4. The angular frequency ω_e of the reference frame "e" is in the steady state equal to the side 1 angular frequency ω_1. Dynamically, at step changes in i_4^e, the angular speed of the combined reference frame varies momentarily to ω_1, but since only steady state is considered for equation (5.1.30), ω_e can be replaced by ω_1.

The modified field oriented control for the CDFM in the combined flux reference frame, as described above, has been implemented in the laboratory set-up. To show the feasibility a speed control was performed. The speed controller extension to the q-axis torque demand value is identical to the SDFM extension in figure 3.35. The error signal between actual and demanded speed is fed into an PI-controller and the output delivers the torque demand value. As it is the case for the SDFM control, classical PI-controllersare sufficient, since the controlled variables have d.c.-values in steady state in the field oriented frame "e".

The hardware set-up is identical to the way it was for the SDFM control, with a switching frequency of 2.5 kHz. Only the tasks for the individual microcontrollers are slightly different to the SDFM implementation and the main tasks are listed below:

μC1 sampling and A/D of i_4
complete inner current control loop including PWM
calculation of rotor position and speed form encoder signals
calculation of feed-forward term
calculation of field angle μ
speed loop

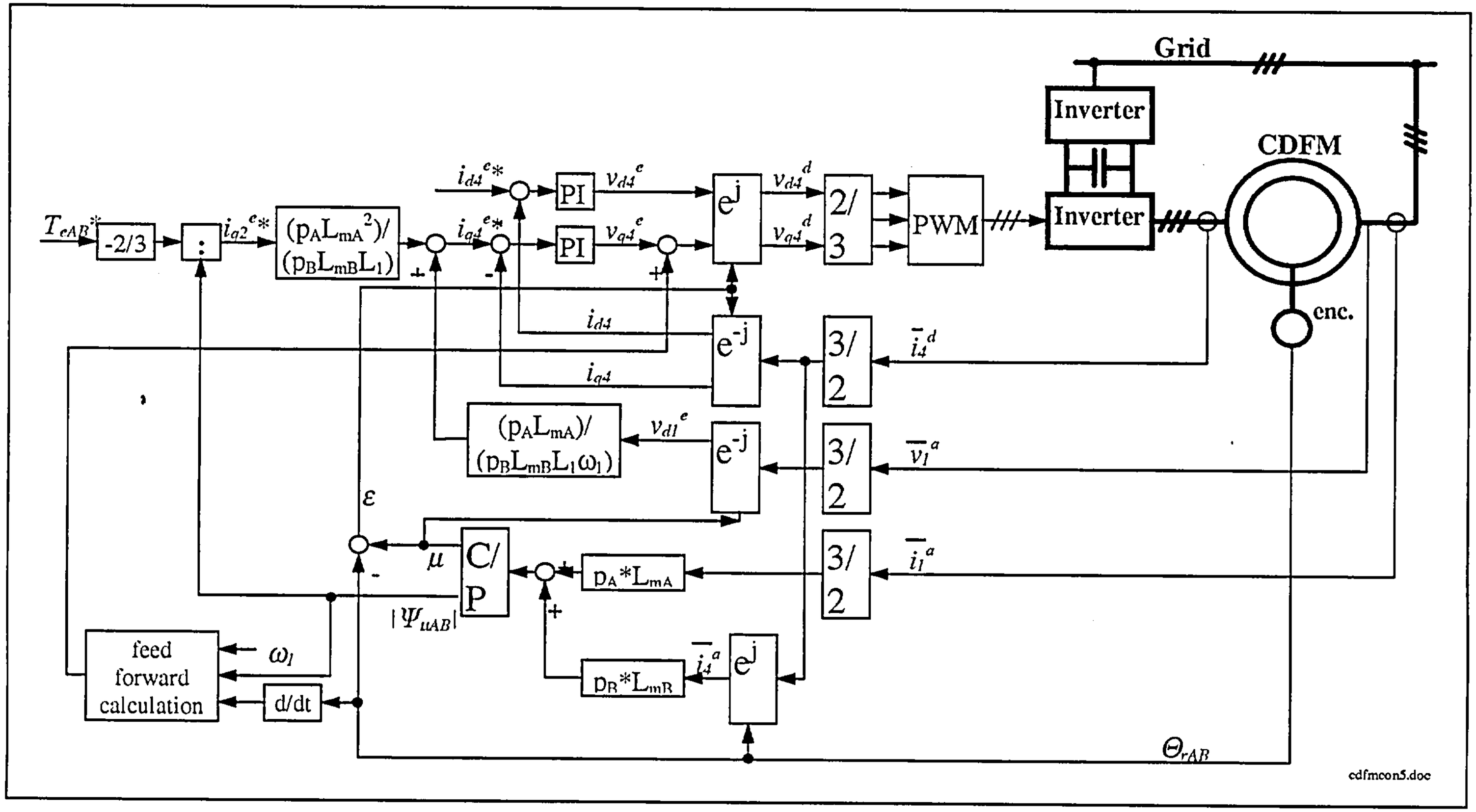

Figure 5.4: Modified control structure for combined flux control of CDFM

µC2	sampling and A/D conversion of v_l
	sampling and A/D conversion of i_l

Data transfer form µC1 to µC2 takes place at the end of the interrupt routine.

Experimental results for a speed ramp demand are shown in figure 5.5. Tests were carried out for two different settings of i_{d4}^{e}*.

In the middle graph of figure 5.5 the value for the d-axis current is at zero level and the q-axis current changes depending on the torque command to follow the desired speed value. It can be seen, that at the speed of 630 rpm the q-axis side 4 current in the "e"-frame exhibits oscillations, which only die out when the speed comes down. This indicates that there may be stability problems associated with the control structure, particularly at higher speeds. This effect has been mentioned [b16].
In the bottom graph of figure 5.5 the d-axis current is set to 1.05 A. For this current level the rotor reactive current is zero for the experimental CDFM. As pointed out [b15], for this current setting the control is largely unstable over a wide speed range. The oscillations in the q-axis current appear again, with the tendency to increase in amplitude. Additionally, the d-axis current starts to oscillate and this is only interrupted when the speed reduces to a low level. Although the oscillations in both cases do not occur over the whole speed range, there have to be stability investigations to find stable operation areas. The oscillations have a frequency of around 7-8 Hz. That corresponds to the rotor frequency of the CDFM at that speed.
It has to be remembered that close to the synchronous speed of machine A, which in this case is 750 rpm, the machines start to lose coupling and control in that area is increasingly difficult.

It is evident, that the magnitude of the q-axis current i_{q4}^{e} in the bottom graph is less than in the graph for i_{d4}^{e}*=0 (middle graph). That is in accordance to equation (5.1.5). For increased i_{d4}^{e} value the magnitude of the combined flux vector increases. Consequently, to produce the same amount of torque the magnitude of the q-axis rotor current and therefore the q-axis side 4 current reduces.

Although the modifications, described above, allow the implementation of the combined flux control of [b15] on unequal machines, there are still stability problems associated with it. Stability investigations are not carried out during this work. A possible reason for the performance degradation in the control and the consequent oscillations may be due to the complicated extension with a summation point and a division in the q-axis of the control to get the side 4 current from a demanded torque value.

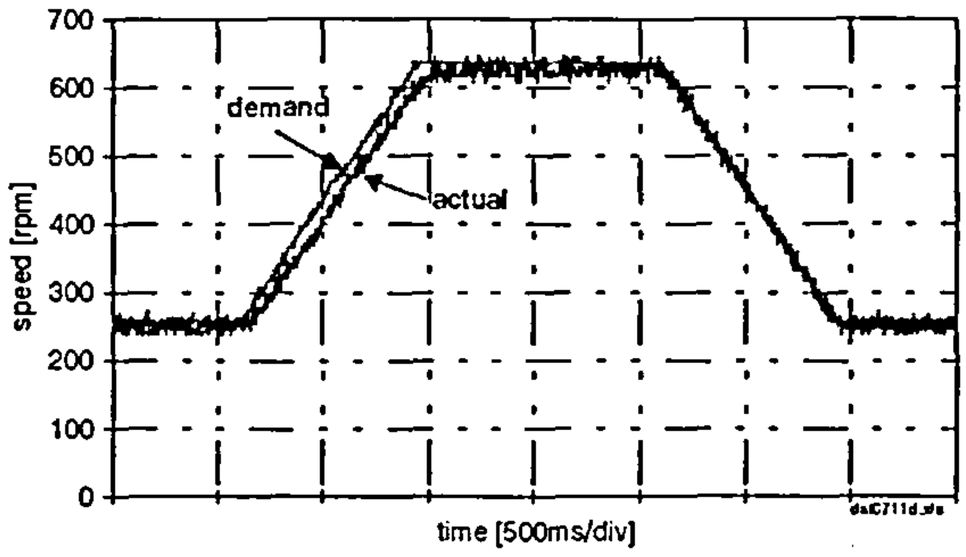

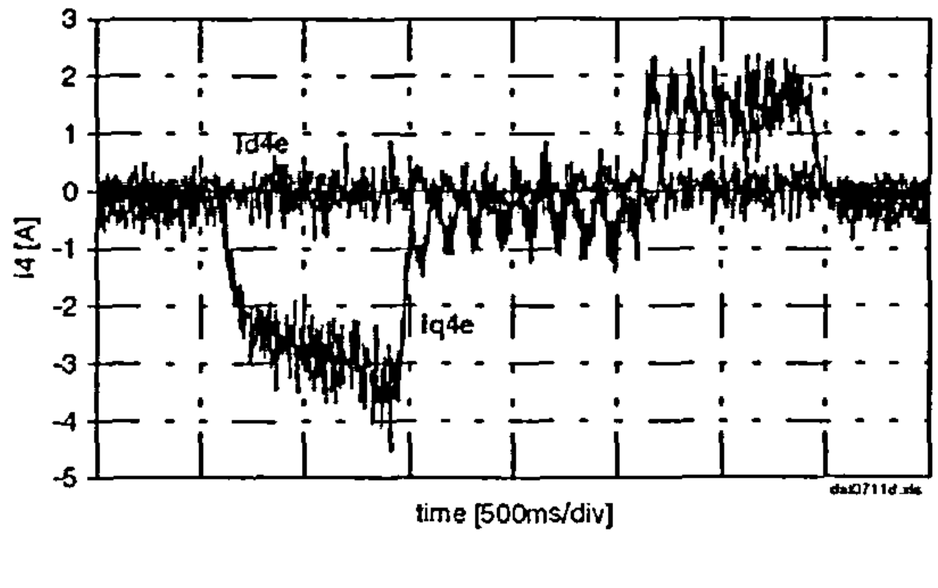

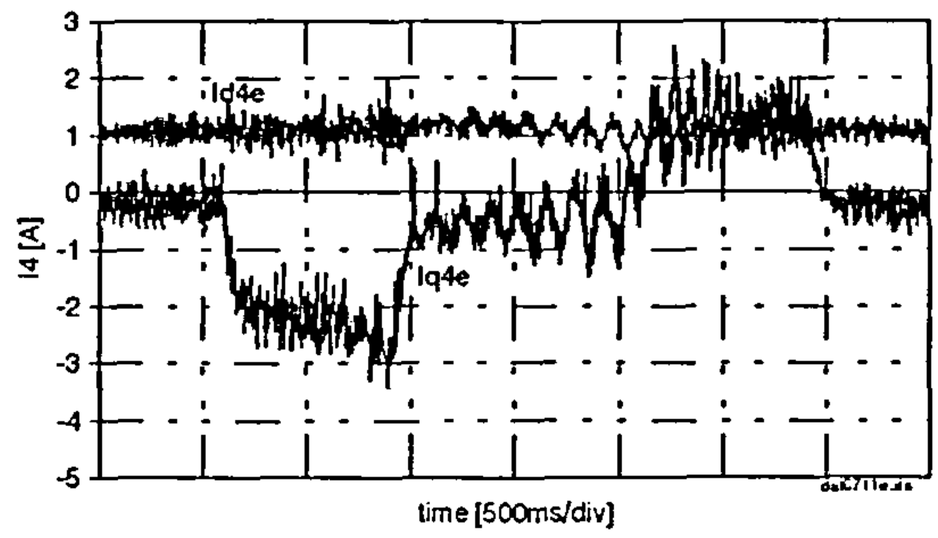

Figure 5.5: Experimental CDFM dynamics for modified combined flux orientation at no-load - modified speed control loop
($n_m^* = 250 - 630$ rpm , $i_{d4}^{e*} = 0$ A and $i_{d4}^{e*} = 1.05$ A)

Would it not be possible to omit that extension and give a direct command value for the q-axis current of side 4 ? This is investigated in the following section.

5.1.1.2 Inner Current Control Loop - Simplified Control

To the question, whether it is practical to remove the q-axis extension and thus simplify the complete control structure, there is also a focus on the point of side 1 active and reactive power control. Or stating it in a different way, does the independent control of side 4 d-component and q-component in the combined flux reference frame lead to a natural decoupled control of machine A active and reactive power as it is the case for the SDFM.

First to the removal of the q-axis extension:

The exact expression for the torque in the combined flux reference frame is given in equation (5.1.5). For a constant value of the combined flux the torque is governed by the q-component of the rotor current in the "e"-frame. In the previous section a relationship between the non-accessible rotor current and the accessible side 4 current q-component was derived. The diagram in figure 5.3 shows that both currents differ with the value denoted as Δi_q. In reality Δi_q is not as critical as figure 5.3 would suggest, certainly this is with identical machines [b17]. Controlling the torque in (5.1.5) with the q-component of side 4 current would therefore only result in a small error.
Keeping the d-component of i_4^e constant and so enabling the magnitude of the combined flux vector to stay constant, only dependent on the d-component of the side 1 current, should allow the torque to be controlled mainly with i_{q4}^e.

The simplified control structure, including the previously described feed-forward term is illustrated in figure 5.6.
Figure 5.7 presents control dynamics of the CDFM in the combined flux frame for a step change in the q-component of the side 4 current. The d-component is set to the critical value 1.05 A, where stability problems arose in the last section.
The torque of the load DC-machine (acting as a prime mover in this case) is set to a fixed value.
Speed variations in figure 5.7 clearly show the influence of i_{q4}^e on the torque of the CDFM. Depending on the torque balance the machine-set is accelerating or decelerating, indicating torque manipulation via i_{q4}^e.

Current waveforms of side 1, side 2 and side 4 in their natural reference frame are also displayed in figure 5.7. In the graph for i_4 in the "d"-frame the phase reversal can clearly be

observed when the CDFM goes through the cascaded synchronous speed of 500 rpm. Although the rotor quantities are normally not measurable in a CDFM and SF-CDFM, the experimental set-up still uses slip-rings and brushes to connect the two machines of the CDFM as described in chapter 2, and allows the measurement of the rotor current waveform. It can be seen that there is no rotor current when $i_{q4}^{e}=0\ A$. This demonstrates that for the setting of $i_{d4}^{e}=1.05\ A$ there is no reactive power transfer across the rotor windings. Only active power transfer takes place, during the period when $i_{q4}^{e}=3\ A$. The magnetisation for machine B is now provided via side 4 and not through machine A. For this state the control of [b15] proved to be unstable. This was also partly observed in figure 5.5 at higher speeds, where oscillations start to build up. No oscillations occur in figure 5.7, but a proper comparison can only be made when a speed control loop is applied to the simplified control as is done later.

The relation between side 1 and side 4 currents in the "e"-frame follows from equation (5.1.3) together with the constraints of (5.1.4) to give

$$i_{d1}^{e}=\frac{1}{p_A L_{mA}}\Psi_{d\mu AB}^{e}-\frac{p_B L_{mB}}{p_A L_{mA}}i_{d4}^{e} \tag{5.1.31}$$

and

$$i_{q1}^{e}=-\frac{p_B L_{mB}}{p_A L_{mA}}i_{q4}^{e} \tag{5.1.32}$$

The relationship can be seen in figure 5.7. The q-component of side 1 current is proportional to the q-component of the side 4 current in the "e"-frame and makes a step change in agreement with equation (5.1.32). For a constant combined flux magnitude the d-components of side 1 and side 4 currents are proportional to each other. The d-component of i_1^{e} keeps a constant value during the transient, since $\Psi_{\mu AB}$ (denoted as "flux mAB" in the graphs) remains basically unaffected from the step change in i_{q4}^{e}. The magnitude and the waveform of $\Psi_{\mu AB}$ are shown in the graphs.

Experimental results for a step in the d-component of side 4 current in the "e"-frame are presented in figure 5.8.

It can be seen that there is a speed variation caused by the step, however to reduced extent compared to the case of a step change in the q-component. The torque variations are due to the changes in the magnitude in $\Psi_{\mu AB}$, in accordance to equation (5.1.5). As displayed in figure 5.8 the magnitude of the artificial combined flux linkage vector changes from about 3 to 5 Wb. That produces a step in i_{d1}^{e}, equation (5.1.31), and i_{q1}^{e} remains unchanged, proportional to the q-component in i_4^{e}.

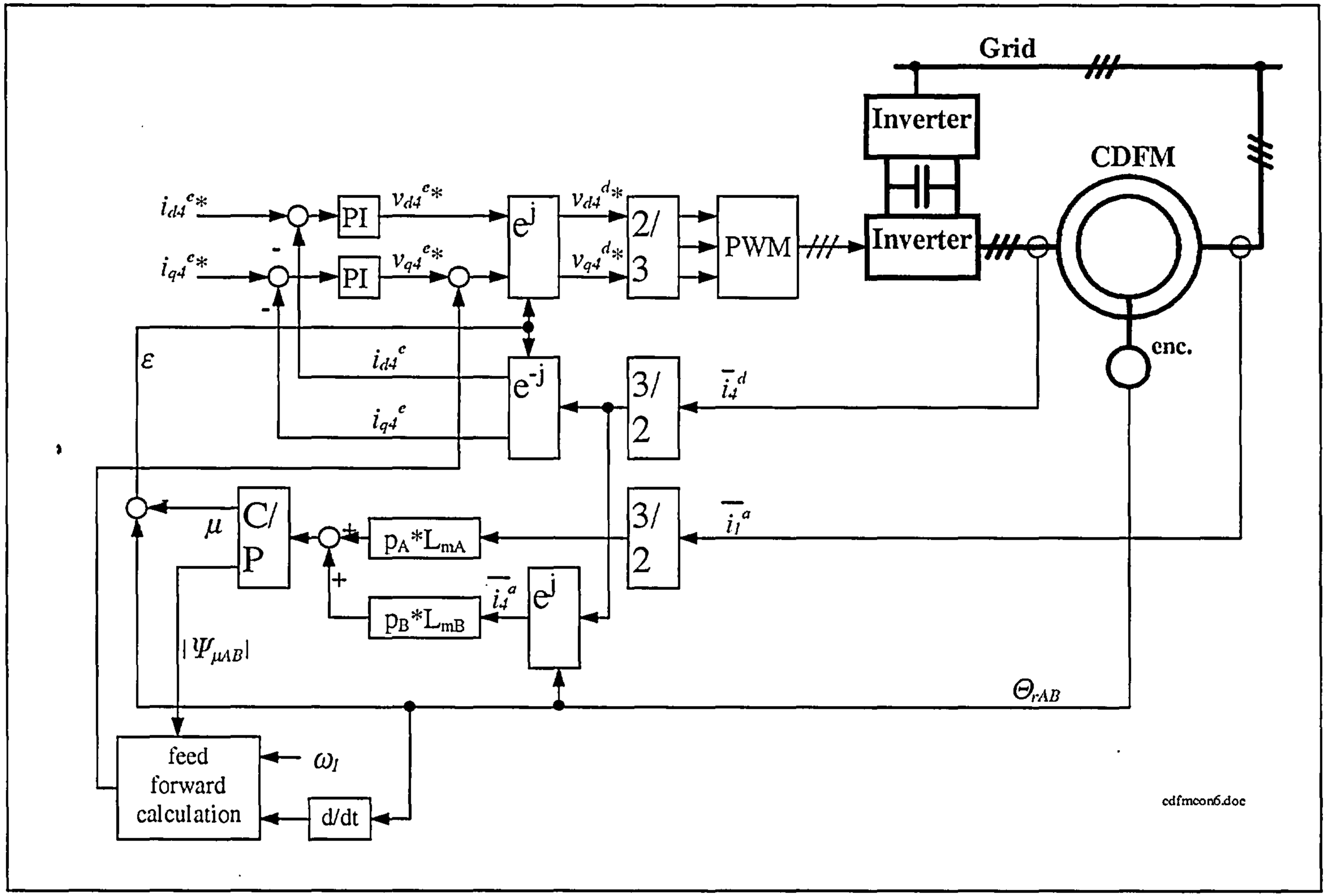

Figure 5.6: Simplified control structure for combined flux control of CDFM

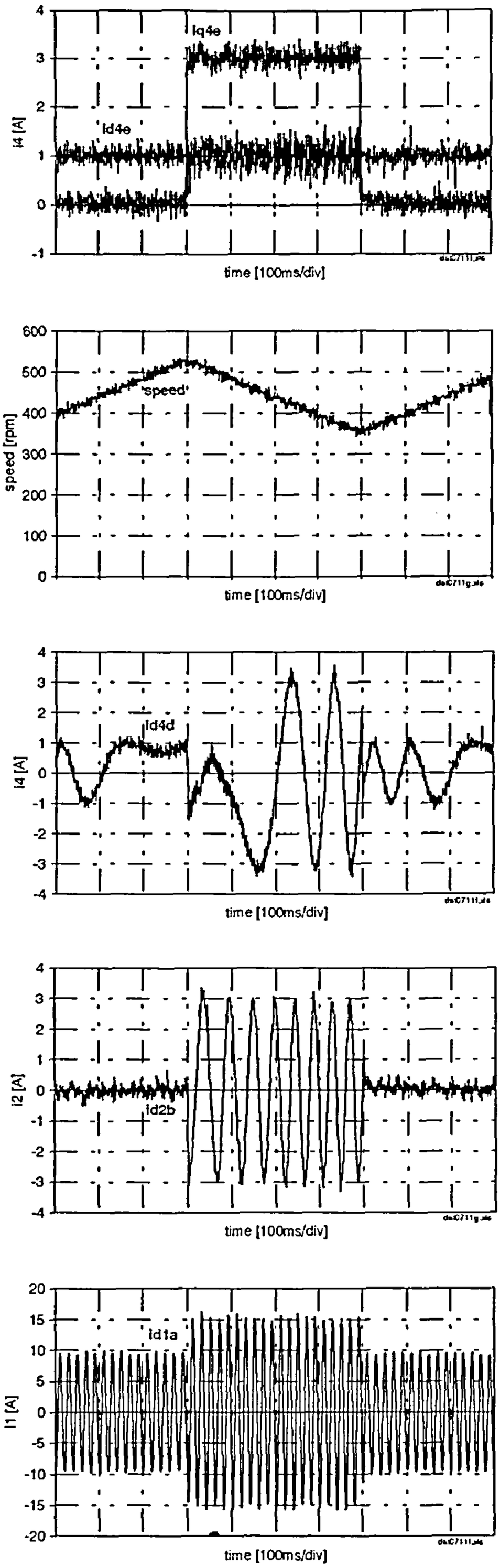

Figure 5.7: Experimental CDFM dynamics for a step change in $i_{q4}^{e}*$ for combined flux linkage orientation - simplified current control loop

(step in $i_{q4}^{e}* = 0$ to 3 A , $i_{d4}^{e}* = 1.05$ A)

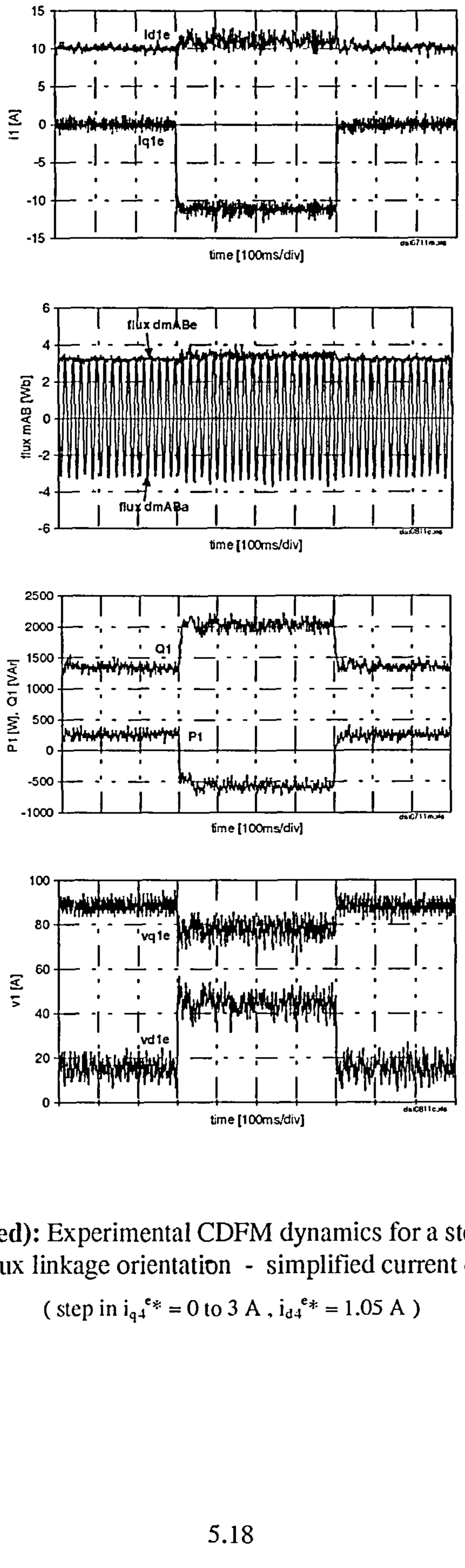

Figure 5.7 (continued): Experimental CDFM dynamics for a step change in i_{q4}^{e*} for combined flux linkage orientation - simplified current control loop

(step in $i_{q4}^{e*} = 0$ to 3 A , $i_{d4}^{e*} = 1.05$ A)

From the results presented to this point the simplified control structure appears to be justified in that the speed control can be performed without the complicated need for relating the rotor current and side 4 current q-component as it is the case in figure 5.2 or 5.4.

As mentioned, it shall also be investigated whether the control of the individual components of side 4 current leads to a natural decoupled active and reactive power control on side 1, similar to the SDFM control. So far this matter has not been considered.

The active and reactive power of side 1 is calculated, already introduced in equation (3.3.20), as

$$P_1 = \frac{3}{2}(v_{d1}^g i_{d1}^g + v_{q1}^g i_{q1}^g) \quad \text{and} \quad Q_1 = \frac{3}{2}(v_{q1}^g i_{d1}^g - v_{d1}^g i_{q1}^g)$$

In the "e"-frame together with (5.1.31) and (5.1.32) the power equations can be written in the form

$$P_1 = \frac{3}{2}[-v_{q1}^e \frac{p_B L_{mB}}{p_A L_{mA}} i_{q4}^e + v_{d1}^e (\frac{1}{p_A L_{mA}} \Psi_{d\mu AB}^e - \frac{p_B L_{mB}}{p_A L_{mA}} i_{d4}^e)] \qquad (5.1.33)$$

and

$$Q_1 = \frac{3}{2}[v_{q1}^e (\frac{1}{p_A L_{mA}} \Psi_{d\mu AB}^e - \frac{p_B L_{mB}}{p_A L_{mA}} i_{d4}^e) + v_{d1}^e \frac{p_B L_{mB}}{p_A L_{mA}} i_{q4}^e] \qquad (5.1.34)$$

Considering equation (5.1.33) first, shows that both components of i_4^e appear in the equation indicating, that side 1 active power is affected by a step in either component. The term in the brackets associated with v_{d1}^e is dependent on variations in i_{d4}^e. If v_{d1}^e would have the value zero, then side 1 active power would only be governed by i_{q4}^e.
In other words, if the side 1 voltage vector would have a position within the "e"-frame so that the d-component is zero, then P_1 is only dependent on i_{q4}^e. For this condition to occur v_1^e would have to be perpendicular to the combined flux vector, but that is not the case. The vector of v_1^e rather varies in position within the "e"-frame, depending on the operational point, but never takes a complete perpendicular position to the combined flux vector. As illustrated in figure 5.7 and 5.8, where the components of side 1 voltage in the "e"-frame are shown, the values change depending on a step in i_{d4}^e or i_{q4}^e. For a step in the d-component of i_4 the d-component of v_1 reduces and for a step in i_{q4}^e the d-component of v_1 increases for the experimental CDFM. The effect in P_1 with a step in i_{d4}^e is also shown in figure 5.8.

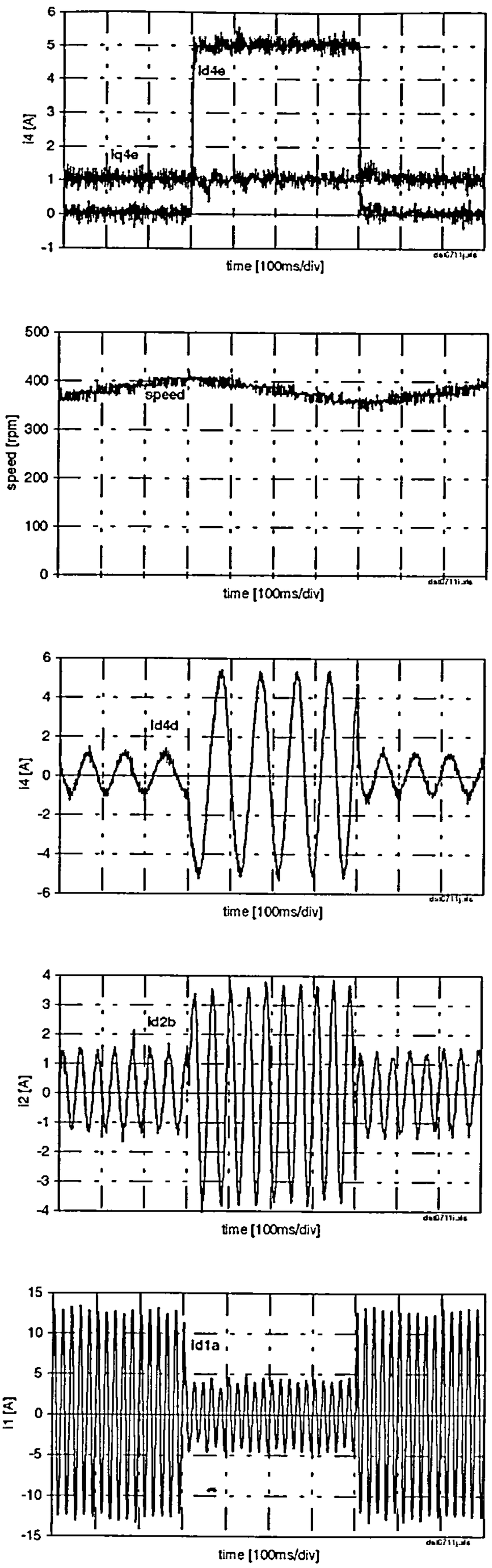

Figure 5.8: Experimental CDFM dynamics for a step change in $i_{d4}^{e}*$ for simplified combined flux linkage control

(step in $i_{d4}^{e}* = 0$ to 5 A , $i_{q4}^{e}* = 1$ A)

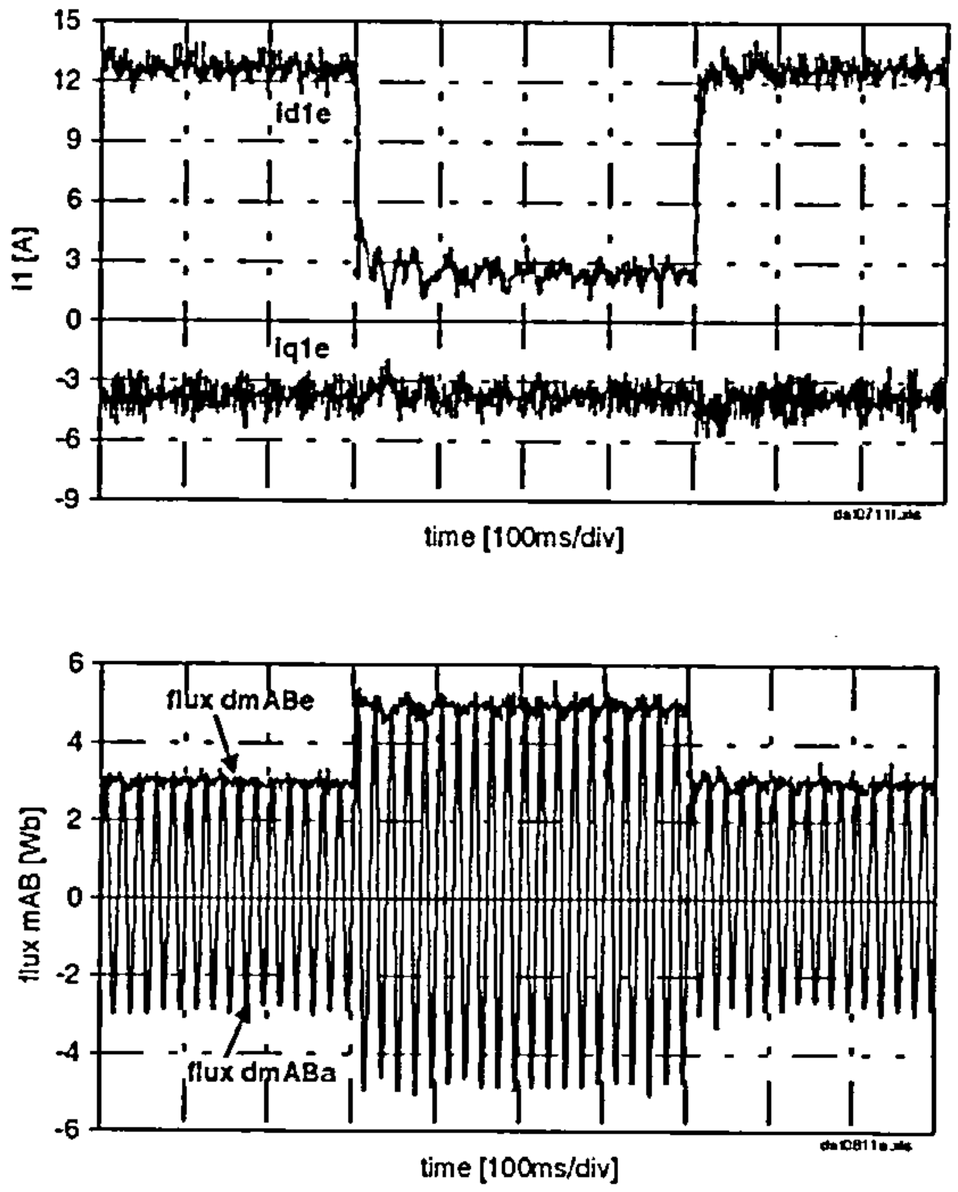

Figure 5.8 (continued): Experimental CDFM dynamics for a step change in $i_{d1}^{e}*$ for simplified combined flux linkage control

(step in $i_{d1}^{e}* = 0$ to 5 A , $i_{q1}^{e}* = 1$ A)

Another reasoning why v_1^e can never take a complete perpendicular relationship towards the combined flux vector and thus cannot eliminate the term v_{d1}^e in equation (5.1.33) can be seen by regarding the torque equation in the "e"-frame for the CDFM. The torque is always affected by both components of side 4 current. Either directly with the q-component of i_4^e or indirectly with the magnitude of the combined flux vector, which is controlled with the d-component of i_4^e. Since for a torque change the mechanical power and therefore the side 1 power is affected no decoupled power control can take place within the combined flux reference frame.

Considering equation (5.1.34) for the reactive power of side 1. There is also a cross-coupling term involved and again associated with v_{d1}^e. For a step in i_{q4}^e the reactive power is influenced, depending on the magnitude of v_{d1}^e. Results are shown in foregoing figures.

Although the d-component of the side 1 voltage in the power equations of (5.1.33) and (5.1.34) may take small values for certain operational points, it can never be completely eliminated. Consequently, the reference frame attached to the combined flux is not suitable for natural decoupled active and reactive power control on side 1.

Despite cross coupling in the power equations, a power control loop was implemented on the laboratory set-up and the results are shown later. But first, other experimental results for the inner current control loop are display in figure 5.9 for different settings of i_{d4}^e and i_{q4}^e over a speed variation. These results demonstrate that the control is not affected from speed changes.

5.1.3 Outer Power Control Loop - Simplified Control

As previously explained, the combined flux reference frame is not appropriate for natural decoupled active and reactive power control, which is achievable with the SDFM. Nevertheless, a power control loop extension to the inner simplified current control loop of figure 5.6 was applied. The extension to the inner loop is the same as for the SDFM extension in figure 3.25. In this case the PI-controller produces demand values for the side 4 currents. The power is calculated from the side 1 current and voltage in the stationary reference frame "a". The complete power control is carried out in µC 2.

Results are presented in figure 5.10. In the left column a step response for a change in the demand value of side 1 active power is shown. Side 1 reactive power is kept at a constant value. It can be seen, that the power loop produces a decoupled control for P_1 and Q_1. But that is only possible, because the inner currents are "forced" by the outer loop in such a way, that they take appropriate values to yield the demanded power values.

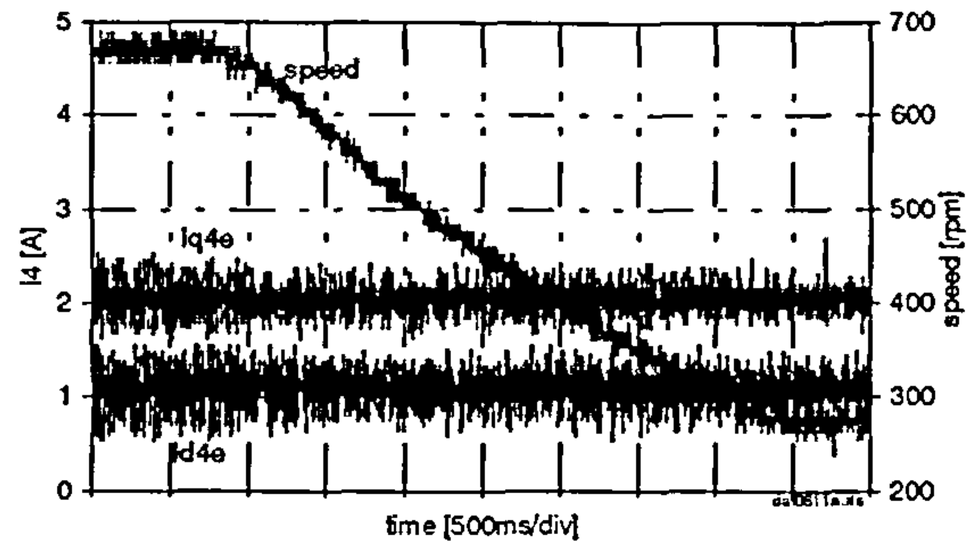

Figure 5.9: Experimental CDFM dynamics of the over speed range with constant demand values $i_{d4}^{e}*$ and $i_{q4}^{e}*$ for combined flux orientation
- simplified current control loop

(top: $i_{d4}^{e}* = 1.05$ A , $i_{q4}^{e}* = 2$ A

bottom: $i_{d4}^{e}* = 4$ A , $i_{q4}^{e}* = 1$ A)

That again proves that no natural decoupled control takes place, where one control variable is proportional to the active power and the other to the reactive power of side 1.
The speed is changing depending on the torque balance of the CDFM to the prime mover, caused by the step in side 1 active power.

The right column of figure 5.10 shows results for a step in the reactive power demand of the power control loop showing a similar outcome. The outer power control loop ensures decoupled active and reactive power control, but this takes place through feedback principles, "forcing" the inner currents to have suitable values. The speed remains almost constant, demonstrating that the torque is not affected by the step variation in Q_1. In this case the controller for Q_1 generates a demand step in i_{d4}^{e} and thus in the magnitude of the combined flux, which in turn affects the torque of the CDFM. The so caused torque variation has to be canceled by an appropriate value of i_{q4}^{e}.

Figure 5.11 shows results of the power control loop for constant demand values in P_1 and Q_1 over a wide speed range. The side 1 active and reactive power is not affected of speed.

It has to be mentioned that the laboratory machines used to compose the CDFM form an unfortunate combination due to their pole pair numbers and their relatively high proportionate losses, particularly machine A. Therefore the values reached for P_1 are comparatively small in figure 5.10.
Looking at the active power equation (5.1.33) shows, that for zero currents on side 4 the active power P_1 takes a positive value, since the involved combined flux linkage quantity is composed of side 1 and side 4 current components and the side 1 component is present as soon as side 1 is connected to a supply, even if side 4 is open circuited. The CDFM seen from side 1, with open circuit on side 4, looks like a cage induction machine, when the rotor windings of both machines are connected and constitute a closed circuit. Thus normal induction machine action takes already place by only connecting side 1 to a supply network. Rotor current is flowing and torque is already produced, equation (5.1.5), although the machine is not very efficient. If this torque overcomes the friction torque at standstill, then the CDFM starts slowly to accelerate until the produced torque is counteracted by friction and windage torque. All losses have to be supplied from side 1 and therefore P_1 takes a positive value. Before extracting power on side 1, those losses have to be overcome or fed from another source, mechanical shaft or side 4. Therefore the magnitude of P_1 does not take a large value in the experimental set-up.
The same argument is applicable to the reactive power of side 1. With side 4 open circuited all excitation power flows via terminal 1. Thus before creating leading power factor on side 1, all reactive power for the CDFM has to be supplied by side 4, as pointed out in the steady state analysis of the CDFM.

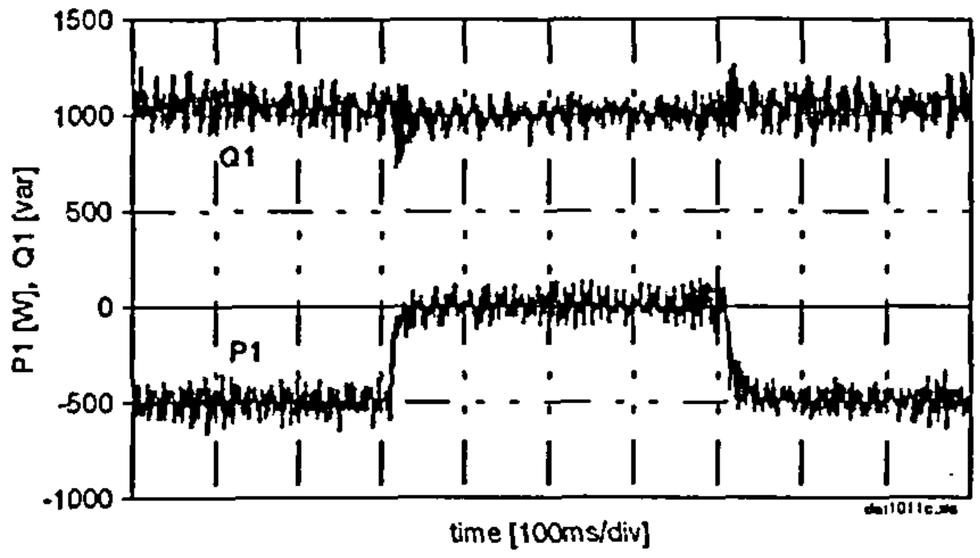

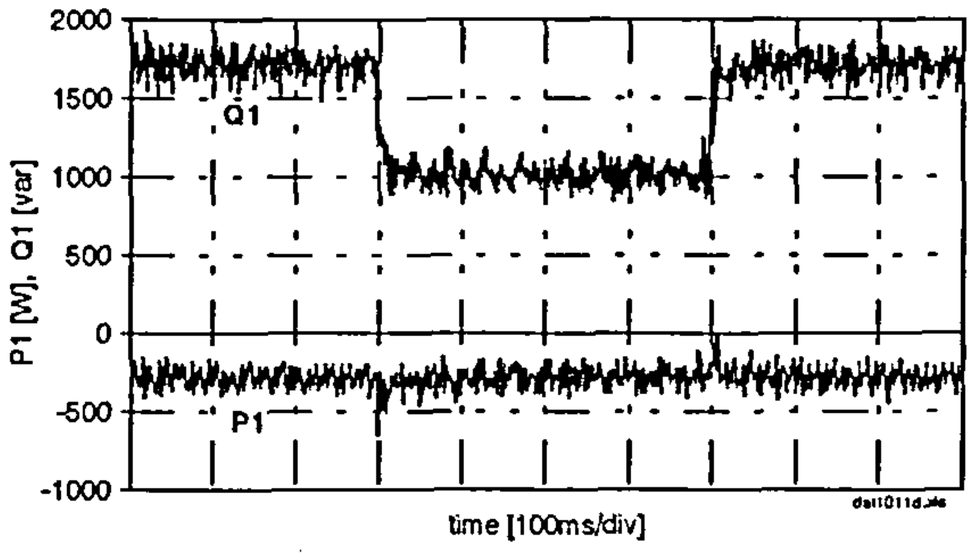

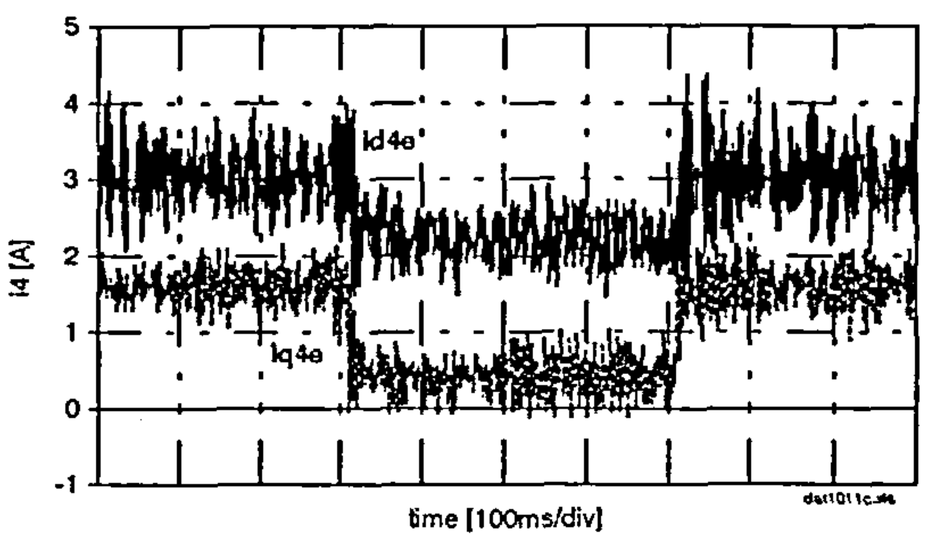

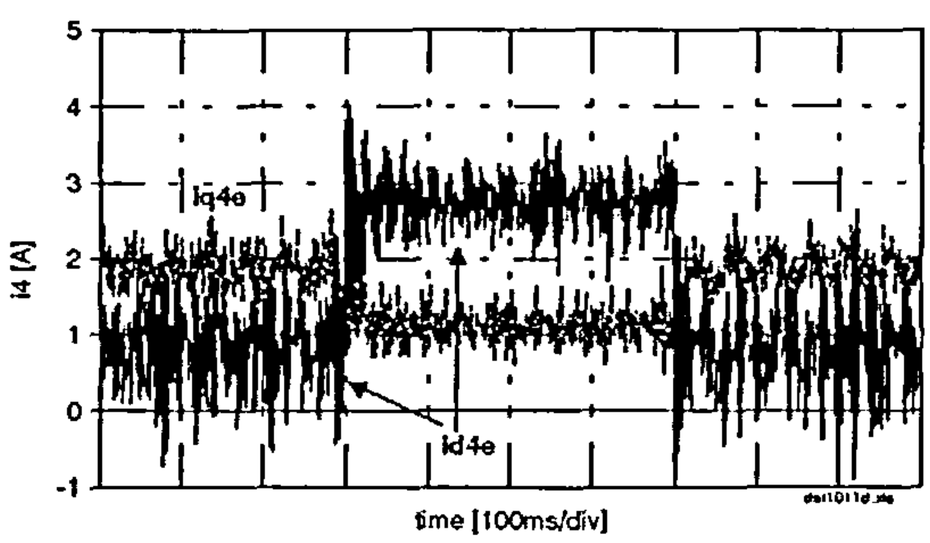

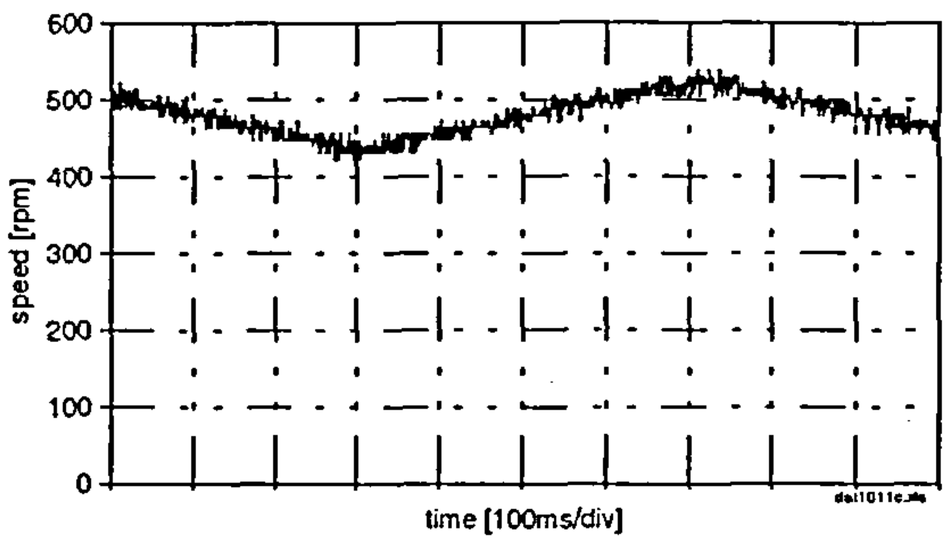

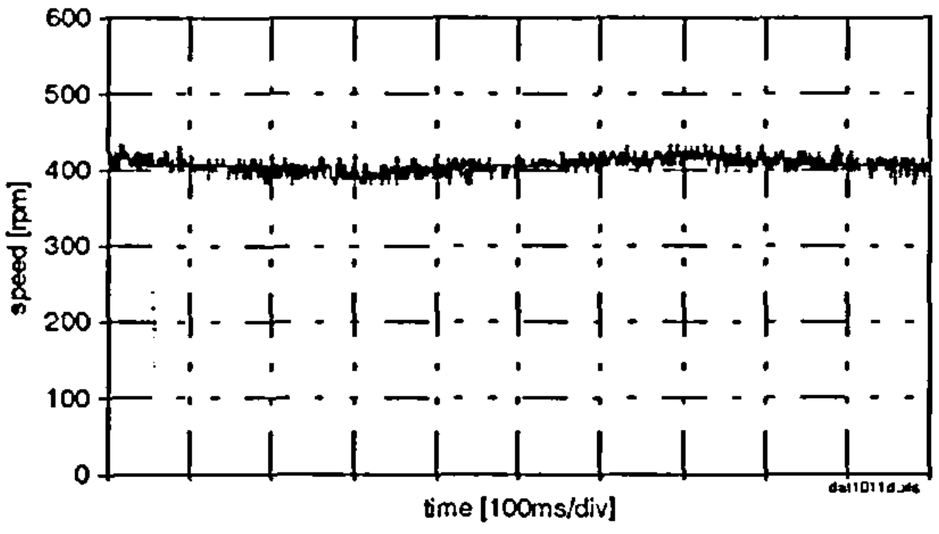

Figure 5.10: Experimental CDFM dynamics for combined flux orientation for step changes in P_1^* and Q_1^*
- simplified power control loop

(left column: step in P_1^* = -500 to 0 W , Q_1^* = 1000 VAr

right column: step in Q_1^* = 1700 to 1000 VAr , P_1^* = -300 W)

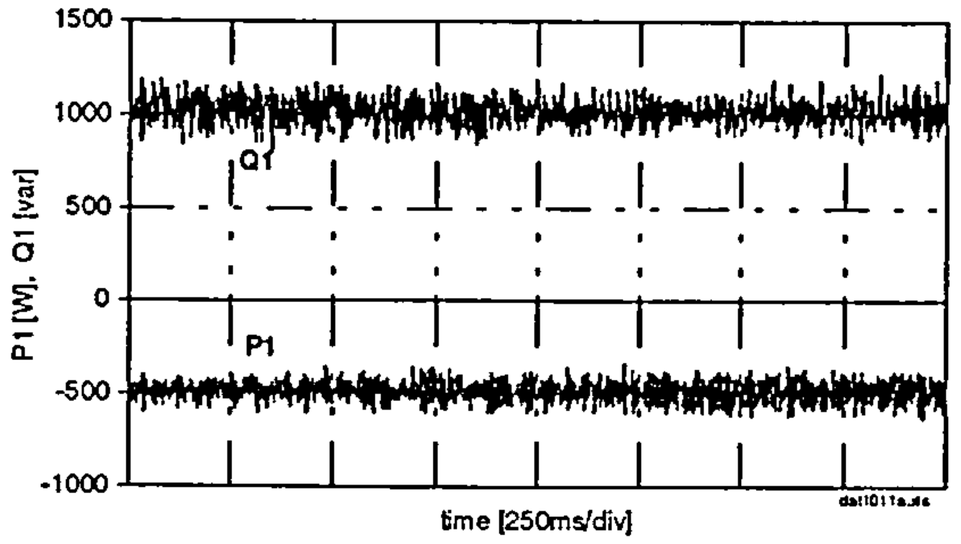

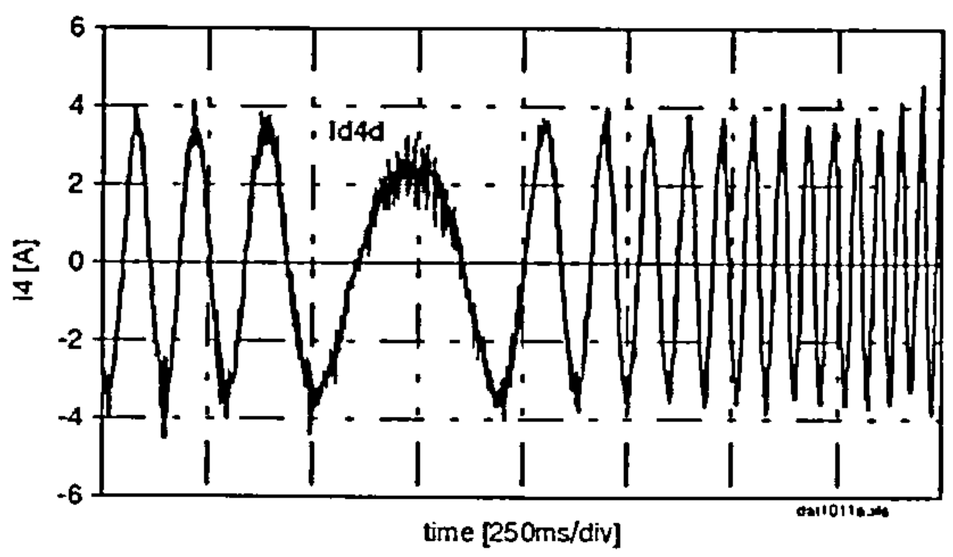

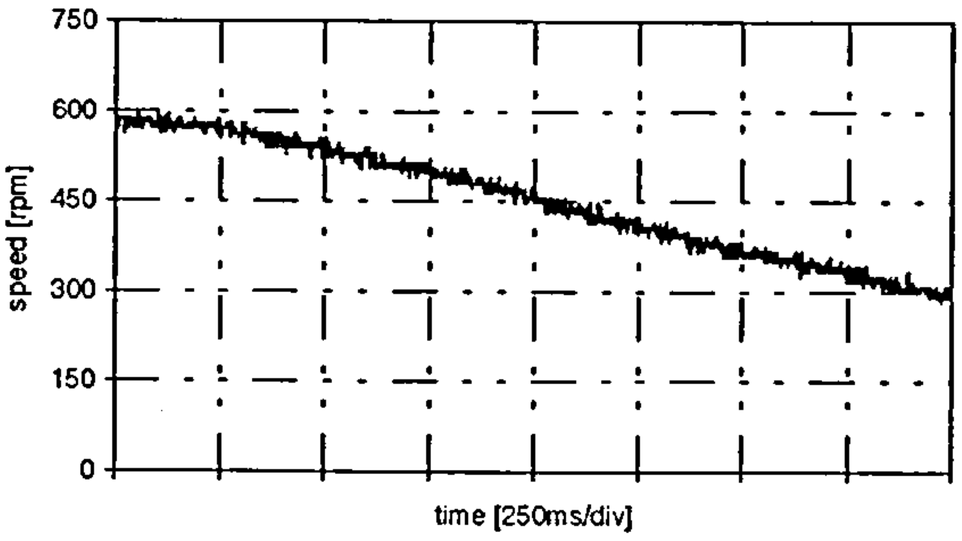

Figure 5.11: Experimental CDFM dynamics for combined flux orientation over speed range with constant demand values for P_1* and Q_1*
- simplified power control loop
(P_1* = -500 , Q_1* = 1000 VAr)

5.1.4 Speed Control Loop - Simplified Control

The results from the simplified inner current control loop are encouraging for the removal of the complicated extension on the q-axis. They show, that despite the simplification, torque is largely controlled by the q-component of i_4^e. To further compare the simplified scheme to the modified scheme of figure 5.4 a speed control loop was implemented for the simplified control structure.
Again, a PI-controller fed by the error between actual and desired speed produces the demand value for the q-axis current component of i_4^e.

Experimental results are shown in figure 5.12. The speed response is as good as for the modified control, despite the difference Δi_q between rotor current and side 4 current, which was necessary to perform the "exact" torque control. That small error caused by Δi_q is compensated by the PI-controller in the speed loop. This controller makes sure, that the value for i_{q4}^e is large enough to produce the desired torque to follow the speed demand.

In figure 5.12 different settings for i_{d4}^e are prescribed. It can be seen that compared to the results of figure 5.5, there are no oscillations present in the results shown in figure 5.12. Not even for the critical value of $i_{d4}^e = 1.05\ A$. The small low frequency overshoot in figure 5.12 is due to the fact, that at the speed 630 rpm the control of the CDFM starts to become difficult, since it is in the vicinity of the machine A synchronous speed.
It is even possible to set the d-component of the side 4 current to any value, without affecting the speed control performance, as long as side 4 is not saturated. Depending on the value of i_{d4}^e the magnitude of i_{q4}^e varies, as was the case in figure 5.5. The larger the value for i_{d4}^e the less magnitude in i_{q4}^e is needed to produce the same amount of torque. That is clearly visible in figure 5.12, where the magnitude of i_{q4}^e decreases for higher values in i_{d4}^e.

As shown the simplified speed loop not only produces an equally good response in speed control, but also removes instability problems associated with the modified combined flux control of the CDFM.

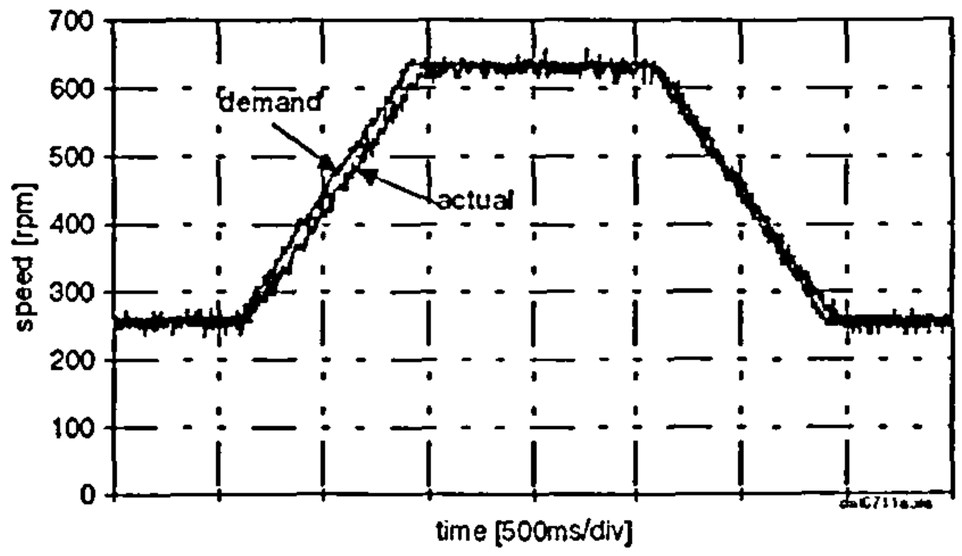

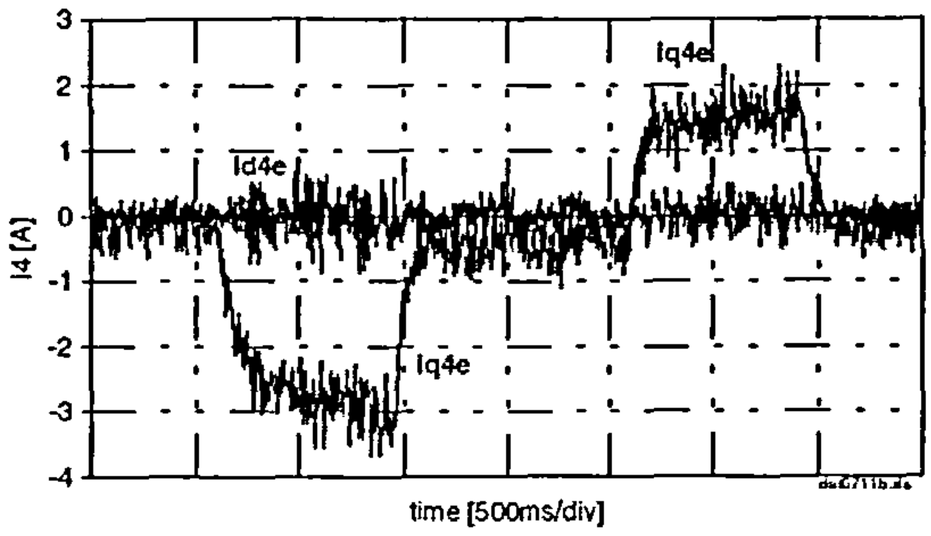

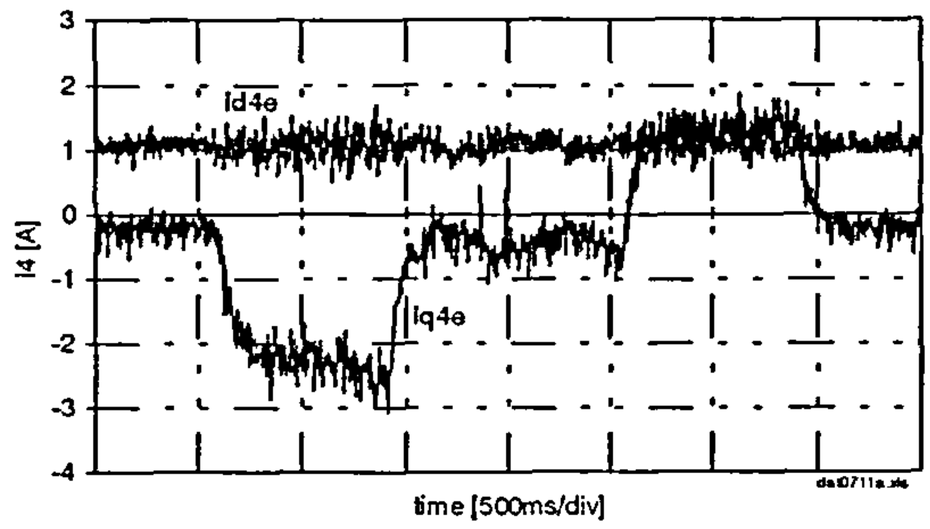

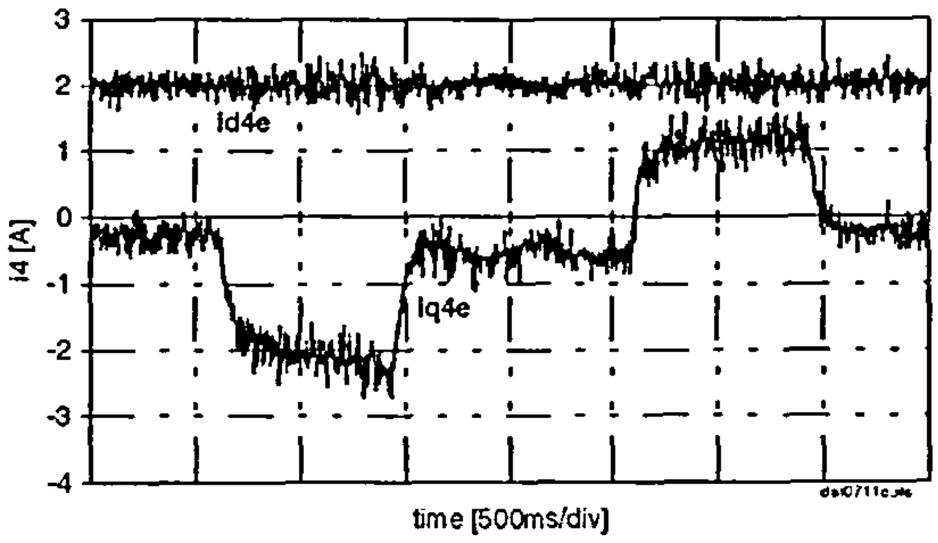

Figure 5.12: Experimental CDFM dynamics for combined flux orientation at no-load with different settings for $i_{d4}^{e}*$ - simplified speed control loop

(n_m* = 250 to 630 rpm , $i_{d4}^{e}*$ = 0 A, $i_{d4}^{e}*$ = 1.05 A and $i_{d4}^{e}*$ = 2 A)

5.1.5 Summary

The combined flux control of Bauer [b15] is only applicable to identical machines for a CDFM. Modifications were necessary to apply the combined flux control to an unequal machine-set. Results of an implemented speed control proved the feasibility of the modified method, but there are still associated stability problems as mentioned in [b16].

After the introduction of a feed-forward term in the q-axis within the inner current control loop, the whole control structure was simplified by removing the mathematical extension in the q-axis. This mathematical constructed extension is necessary to ensure "correct" control according to the machine equations.
Results from the simplified inner current control loop showed the performance of this simple method.

Investigations, into whether the combined flux reference frame is suitable for natural decoupled side 1 active and reactive power, indicated that there is no straight forward connection between side 4 current component and side 1 power equations. Cross coupling terms are present, which are obviously inherent to this particular reference frame.
Despite the cross coupling, independent active and reactive power control by an outer power control loop is still possible. The inner current components are "forced" to take a value to produce the desired power values.

Speed control results on the simplified method showed, that the speed performance is not inferior to the modified speed control. On the contrary, oscillations present in the modified control are not present with the simplified method.

The simplified method of the combined flux reference frame control can therefore be used for speed control applications of the CDFM.

Dynamic simulation results (Appendix E, figures E.20-E.22) illustrate the behaviour of a number of variables within the control loop. The parameter set of a 30 kW SF-CDFM is used for simulations to study the performance of the control on a higher rated machine.
Three different cases are simulated:
- control as introduced by Bauer [b15]
- simplified current loop
- simplified power control loop

The demand values are set in order to get similar magnitudes for the different quantities. The simulations show, that there is hardly any difference between the Bauer-control [b15] and the simplified current loop control. In both cases there is a cross coupling in P_1 and Q_1. The simulation for the power control loop shows the effect on the inner currents so that

they yield the desired power values.

Comparison of experimental and simulation results show much agreement in the basic behaviour of the machine although different machines are considered.

5.2 Field Oriented Control with Stator Flux Linkage

Steady state results of the CDFM showed, that the performance is very similar to the single doubly-fed induction machine. Depending on the positioning of the side 4 current phasor relative to the side 1 voltage phasor, the side 1 active and reactive power changes in magnitude. This suggests that the field oriented control method of the SDFM is applicable to the CDFM to achieve natural decoupled side 1 active and reactive power control as it is with the SDFM.
CDFM frequency, slip and power relations proved to have the identical structure as for the SDFM. However, compared to the SDFM the dynamic model of the CDFM contains an additional voltage equation, caused by the closed rotor winding circuit. This rotor circuit could have an effect on a stator flux oriented control for the CDFM.

This section describes the application of the stator flux field oriented control method as used for the SDFM on the CDFM.
It should be noted that the term "stator flux" is ambiguous when used with the CDFM, since there are two stators involved, but this term shall be used throughout the thesis to keep expression similarities to the SDFM control. The term "stator flux" is solely related to the machine A stator, side 1, flux linkage.

As mentioned in the introduction, stator flux oriented control was successfully applied to the doubly-fed reluctance machine [d3]. This, however, is no surprise, because the SDFM steady state and dynamic model completely describes the DFRM. Concerning the BDFM, there has been no investigation as to whether this type of control could be used.
Even for the CDFM, this topic has found little attention to date. The only reported work in this area is by Sathiakumar and Koczara [b12, b13]. In [b12] a dynamic machine model of the CDFM in the reference frame attached to the stator flux is derived and the companion paper [b13] presents simulation results for the control with impressed side 4 currents. It is concluded, that it is possible to control side 1 active power with the q-component of the side 4 current in the "e"-frame and to manipulate side 1 reactive power with the d-component of side 4 current. No experimental results are shown and it is not made clear to what extent the rotor circuit plays a role. This scheme is analysed in the following section.

The dynamic machine model of the CDFM in a general reference frame is described by equations (4.1.39) - (4.1.41). By transferring the combined rotor flux equation (4.1.38) onto a reference frame attached to the stator flux yields

$$\overline{\Psi}_R^e = L_{mA}\bar{i}_1^e + L_R\bar{i}_2^e - L_{mB}\bar{i}_4^e \qquad (5.2.1)$$

Again, this "rotor flux" quantity is only fictitious and does not exist in the machine. It is created with Kirchhoff's law applied to the flux linkages in the rotor loop and is composed of the individual rotor flux linkages as introduced in equation (4.1.34)

$$\overline{\Psi}_R^e = \overline{\Psi}_2^e - \overline{\Psi}_3^e$$

The combined rotor flux should not be confused with the combined overall magnetising flux as used in the last section for the field oriented control. $\Psi_{\mu AB}$, in the previous section is a vectorial summation, whereas the combined rotor flux is a subtraction. The magnitude of the combined rotor flux has a small value as will be shown later by simulations, since side 2 and side 3 flux linkages do not differ in a great deal.

It is useful for further analysis to derive the combined rotor flux linkage as a function of different quantities.

Involving the side 1 flux linkage equation (4.1.16), transferring it into the "e"-frame and substituting the side 1 current in (5.2.1) obtains

$$\overline{\Psi}_R^e = k_1 \bar{i}_2^e + \frac{L_{mA}}{L_1}\overline{\Psi}_1^e - L_{mB}\bar{i}_4^e \qquad (5.2.2)$$

In the same way by substituting the rotor current leads to

$$\overline{\Psi}_R^e = k_2 \bar{i}_1^e + \frac{L_R}{L_{mA}}\overline{\Psi}_1^e - L_{mB}\bar{i}_4^e \qquad (5.2.3)$$

k_1 and k_2 are constants with the value of

$$k_1 = L_R - \frac{{L_{mA}}^2}{L_1} \quad \text{and} \quad k_2 = L_{mA} - \frac{L_R L_1}{L_{mA}}$$

It can be seen that in (5.2.2) and (5.2.3) the stator flux is already contained, which in the stator flux reference frame is subject to the constraints of equation (3.3.3)

$$\Psi_{q1}^e = 0 \quad \text{and} \quad \Psi_{d1}^e = |\overline{\Psi}_1^a| = \Psi_1^e \qquad (3.3.3 \text{ repeated})$$

Reference frames for the CDFM in stator flux oriented control are depicted in figure 5.13. For clarity the rotor reference frame is omitted and it can be seen that the CDFM reference frame system containing only the accessible sides, side 1 and side 4, is identical to the SDFM system in figure 3.21.

Deriving a model for the CDFM in the "e"-frame in dependence of the stator flux with the help of the side 1 voltage equation (4.1.25) transferred into the stator flux frame

$$\bar{v}_1^e = R_1 \bar{i}_1^e + \frac{d\overline{\Psi}_1^e}{dt} + j\omega_e \overline{\Psi}_1^e$$

and by using (5.2.3) gives for the d-q-components

$$\frac{d\Psi_{d1}^{e}}{dt} - \frac{R_1 L_R}{k_2 L_{mA}}\Psi_{d1}^{e} = -\frac{R_1}{k_2}\Psi_{dR}^{e} - \frac{R_1 L_{mB}}{k_2} i_{d4}^{e} + v_{d1}^{e} \qquad (5.2.4)$$

$$\frac{d\mu}{dt} = \omega_e = -\frac{R_1}{k_2}\frac{\Psi_{qR}^{e}}{\Psi_{d1}^{e}} - \frac{R_1 L_{mB}}{k_2}\frac{i_{q4}^{e}}{\Psi_{d1}^{e}} + \frac{v_{q1}^{e}}{\Psi_{d1}^{e}} \qquad (5.2.5)$$

μ is the angle between frame "a" and frame "e", figure 5.13. The angular speed ω_e is relative to the stationary frame and can be replaced by the side 1 angular speed ω_1, as shown for the SDFM, since the reference frame attached to the stator flux rotates with the synchronous frequency of the supply, equation (3.3.15).

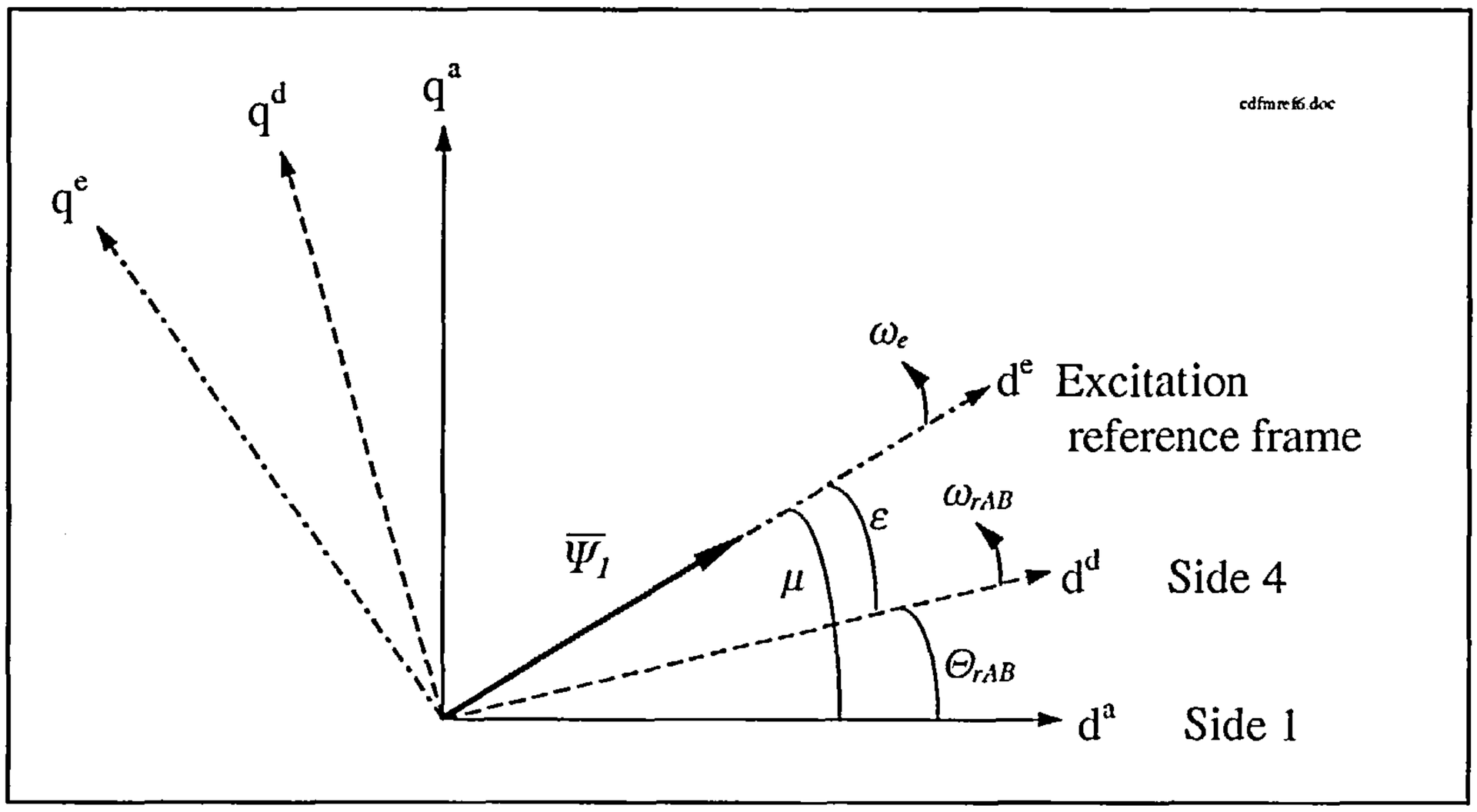

Figure 5.13: Reference frames and angles for the CDFM with stator flux control

Equations (5.2.4) and (5.2.5) contain an additional term associated with the combined rotor flux, compared to the equations (3.3.8) and (3.3.9) of the SDFM. Despite assuming perfect impressed currents on side 4, the equations (5.2.4) and (5.2.5) do not describe the CDFM fully as it is the case for the SDFM equations. Additionally, there is equation (4.1.16) needed to entirely describe the machine dynamics in the "e"-frame.

In order to calculate the angle ε between side 4 and the "e"-frame, the same angle construction method can be used as exhibited in figure 3.22. For neglected side 1 resistance ($R_1=0$) the stator flux is $\pi/2$ lagging behind the side 1 voltage and so the side 1 voltage components take the values, equation (3.3.17),

$$v_{d1}^{e} = 0 \quad \text{and} \quad v_{q1}^{e} = \omega_1 \Psi_1^{e} = \sqrt{2} V_1 = const. \qquad (3.3.17 \text{ repeated})$$

SDFM analysis proved that the stator flux is impressed by the stiff supply voltage on side 1 and that therefore the rotor currents manipulate the stator currents as shown in equation (3.3.18) and (3.3.19). Relating the side 4 currents to the side 1 currents in the "e"-frame for

the CDFM with the help of equation (5.2.3) gives

$$i_{d1}^{e} = \frac{1}{k_2}\Psi_{dR}^{e} - \frac{L_R}{k_2 L_{mA}}\Psi_{d1}^{e} + \frac{L_{mB}}{k_2} i_{d4}^{e} \tag{5.2.6}$$

$$i_{q1}^{e} = \frac{1}{k_2}\Psi_{qR}^{e} + \frac{L_{mB}}{k_2} i_{q4}^{e} \tag{5.2.7}$$

Again, a similar pattern as for the SDFM, but with the additional term related to the combined rotor flux. In the SDFM analysis for neglected side 1 resistance the rotor current components in the "e"-frame are directly linked to the respective stator current components. Now, the relation between side 1 and side 4 current components depends on the d-q-components of the combined rotor flux in the "e"-frame.

A direct and decoupled connection between side 1 and side 4 currents is only secured if the individual side 1 current d-q-components are proportional to the respective side 4 current d-q-components.

Having a look at the rotor loop voltage equation (4.1.36) in the general reference frame and stating it in the excitation reference frame "e" then

$$0 = R_R \bar{i}_2^{e} + \frac{d\bar{\Psi}_R^{e}}{dt} + j\omega_\Omega \bar{\Psi}_R^{e} \tag{5.2.8}$$

where

R_R is the combined rotor loop resistance R_2+R_3 and

$\frac{d\Omega}{dt} = \omega_\Omega$ with Ω as the angle between the rotor reference frame "b" and the excitation reference frame "e".

Splitting (5.2.8) into d-q-components and regarding only steady state yields

$$\Psi_{qR}^{e} = \frac{R_R}{\omega_\Omega} i_{d2}^{e} \tag{5.2.9}$$

$$\Psi_{dR}^{e} = -\frac{R_R}{\omega_\Omega} i_{q2}^{e} \tag{5.2.10}$$

The rotor current components are linked with the side 4 current via the side 4 flux linkage equation as

$$i_{d2}^{e} = \frac{L_4}{L_{mB}} i_{d4}^{e} - \frac{1}{L_{mB}}\Psi_{d4}^{e} \tag{5.2.11}$$

$$i_{q2}^{e} = \frac{L_4}{L_{mB}} i_{q4}^{e} - \frac{1}{L_{mB}}\Psi_{q4}^{e} \tag{5.2.12}$$

Respective components of side 2 and side 4 currents are directly related. Consequently, equations (5.2.9) and (5.2.10) constitute a cross coupling between the d-axis and the q-axis in the "e"-frame due to the rotor circuit. The degree of cross coupling depends on two parameters, the combined rotor resistance and the rotor speed relative to the angular speed of the excitation frame.

The smaller the combined rotor resistance, the smaller is the cross coupling effect. The second parameter, ω_Ω, can vary between two extremes in the operational speed range of the CDFM. At standstill $\omega_\Omega=2\pi f_1$, since the rotor is stationary and "sees" the excitation reference frame rotating with synchronous speed. When the rotor reaches synchronous speed of machine A, $\omega_\Omega=0$. The closer the rotor speed approaches synchronous speed, the larger is the effect of the cross coupling in above equations. At 80 % of the subsynchronous speed of machine A, the influence of the speed on the cross coupling is five times that at standstill.

Simulation results, showing the influence on the cross coupling, are presented in figure 5.14. Three different cases of the combined rotor flux linkage in the "e"-frame are displayed for step changes in the components of the side 4 current.

The first set, with normal rotor resistance values at a speed of 200 rpm clearly shows the cross coupling effect in the q-component of Ψ_R^e (denoted as "flux R" in the graphs) caused by a step in i_{d4}^e and the effect in the d-component of Ψ_R^e caused by i_{q4}^e. The second set shows the case for 600 rpm with normal resistance values. Compared to the simulation results at 200 rpm, there is an increase in the magnitude of the combined rotor flux linkage and its cross coupling. A significant change can be seen in the third set. There the resistance values are halved at a speed of 600 rpm. The rotor flux linkage and the cross coupling effect have halved as well, compared to the normal resistance case.

These results show that a cross coupling in the combined rotor flux linkage exists, but can be kept small with small rotor resistance values. It can be assumed, that the side 4 currents mainly manipulate directly the side 1 currents as equations (5.2.6) and (5.2.7) show.

Employing equations (5.2.6) and (5.2.7) in the side 1 active and reactive power equations of (3.3.20) leads with the stator voltage constraints of (3.3.17) to the power equations of the CDFM in stator flux orientation as

$$P_1 = \frac{3}{2}\sqrt{2}V_1\left(\frac{1}{k_2}\Psi_{qR}^e + \frac{L_{mB}}{k_2}i_{q4}^e\right) \tag{5.2.13}$$

and

$$Q_1 = \frac{3}{2}\sqrt{2}V_1\left(\frac{1}{k_2}\Psi_{dR}^e - \frac{L_R}{k_2 L_{mA}}\Psi_{d1}^e + \frac{L_{mB}}{k_2}i_{d4}^e\right) \tag{5.2.14}$$

The structure of (5.2.13) and (5.2.14) is similar to the respective equations for the SDFM, but the CDFM power equations include the rotor flux term. As shown, the rotor flux term is subject to cross coupling, depending on the rotor resistance and speed. If the cross coupling effect is minimised, then the side 4 q-component controls the stator active power and the d-component controls the stator reactive power, accordingly to the control of the SDFM.

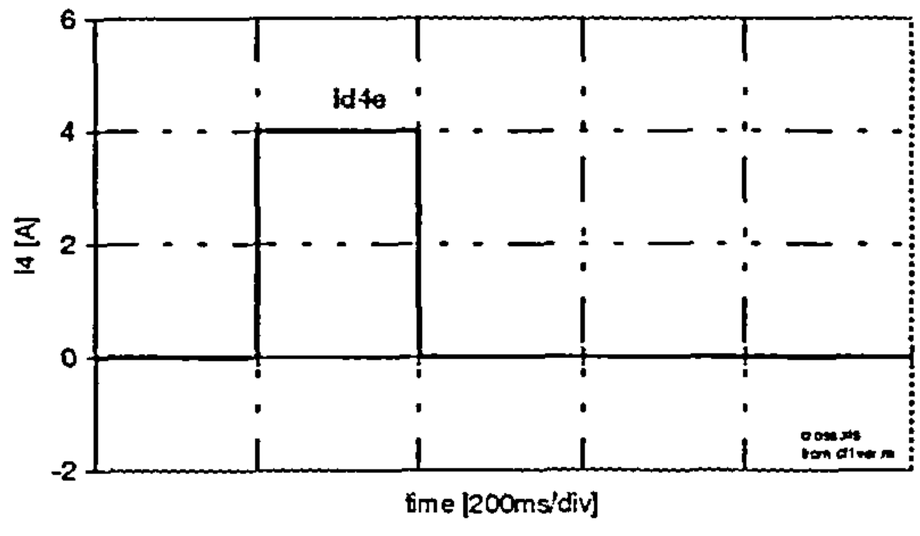

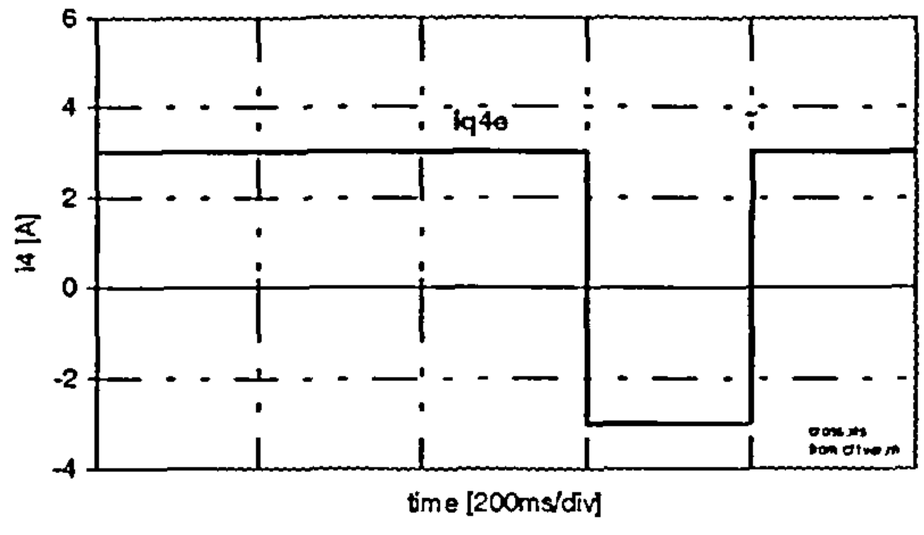

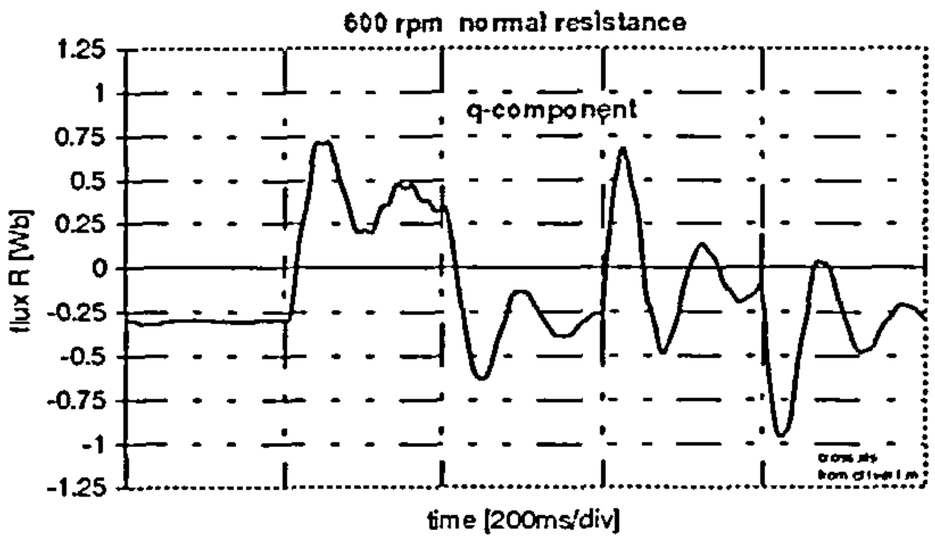

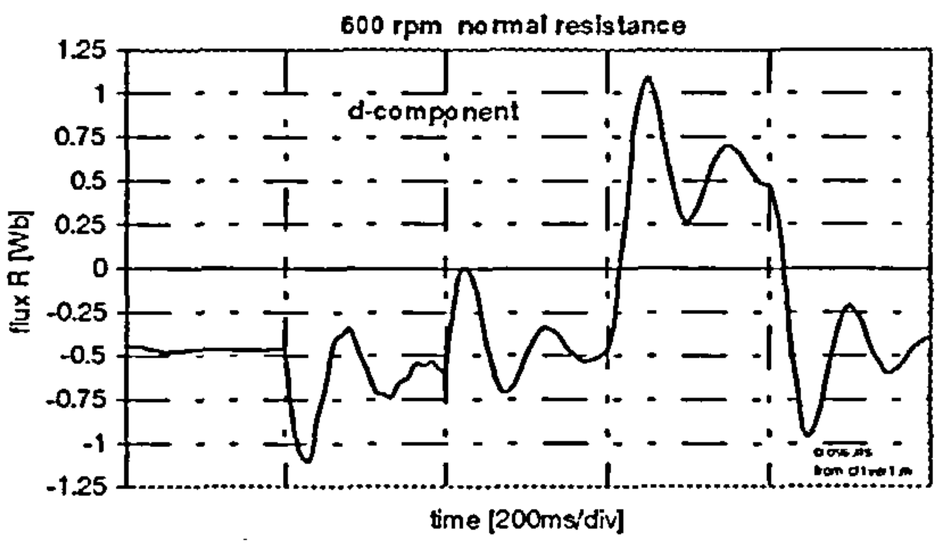

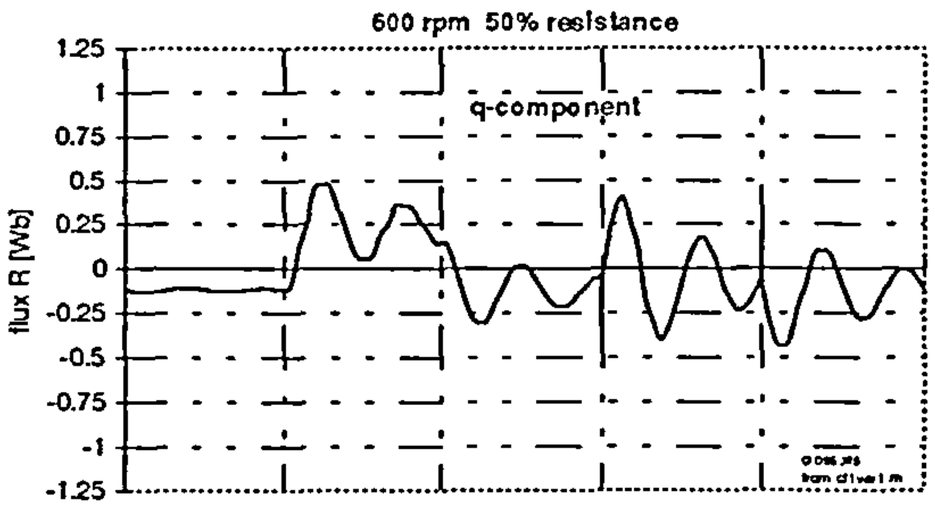

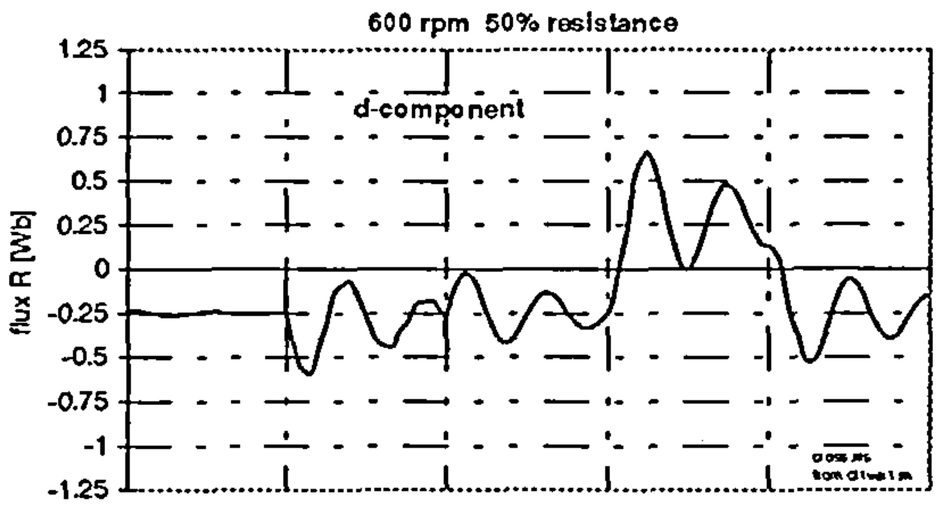

Figure 5.14: Simulation of cross coupling influence in Ψ_R^e

(step in i_{d4}^{e*} = 4 to 0 to 4 A

step in i_{q4}^{e*} = 3 to -3 to 3 A)

5.2.1 Inner Current Control Loop

For finalising stator flux control of the CDFM it is necessary to investigate whether there is a feed-forward term within the inner current control loop.

Substituting (5.2.2) in the side 4 flux linkage equation in the "e"-frame gives

$$\overline{\Psi}_4^e = -\frac{L_{mB}}{k_1}\overline{\Psi}_R^e + \frac{L_{mA}L_{mB}}{k_1 L_1}\overline{\Psi}_1^e + k_3\bar{i}_4^e \qquad (5.2.15)$$

with the constant

$$k_3 = L_4 - \frac{L_{mB}^{\ 2}}{k_1}$$

Replacing (5.2.15) in the side 4 voltage equation in the excitation reference frame and considering only steady state yields

$$v_{d4}^e = R_4 i_{d4}^e + (\omega_e - \omega_{rAB})[\frac{L_{mB}}{k_1}\Psi_{qR}^e - k_3 i_{q4}^e] \qquad (5.2.16)$$

$$v_{q4}^e = R_4 i_{q4}^e - (\omega_e - \omega_{rAB})[\frac{L_{mB}}{k_1}\Psi_{dR}^e - k_3 i_{d4}^e] + (\omega_e - \omega_{rAB})\frac{L_{mA}L_{mB}}{k_1 L_1}\Psi_{d1}^e \qquad (5.2.17)$$

The second terms constitute slight cross coupling effects in the voltage equations and the third term of equation (5.2.17) is a slip proportional term

$$feed\ \ forward = (\omega_1 - \omega_{rAB})\frac{L_{mA}L_{mB}}{k_1 L_1}\Psi_{d1}^e \qquad (5.2.18)$$

which has to be included as a feed forward term in the inner current control loop to increase steady state accuracy as was the case for the SDFM and for the combined flux control of the CDFM.

The inner current control structure for the CDFM in stator flux oriented control is shown in figure 5.15. The complete control structure is identical to the one for the SDFM in figure 3.24.

Experimental results for the inner current control loop are presented in figures 5.16 - 5.19. Figure 5.16 shows dynamics for a step change in the d-component of i_4^e. It can be seen, that the influence of the cross coupling in the combined rotor flux has only a marginal effect on the results. The side 4 current components manipulate the components of the side 1 currents in an almost completely direct manner. That is reflected as well in the graph for the active and reactive power, which are independently controlled by the individual current components of i_4^e.

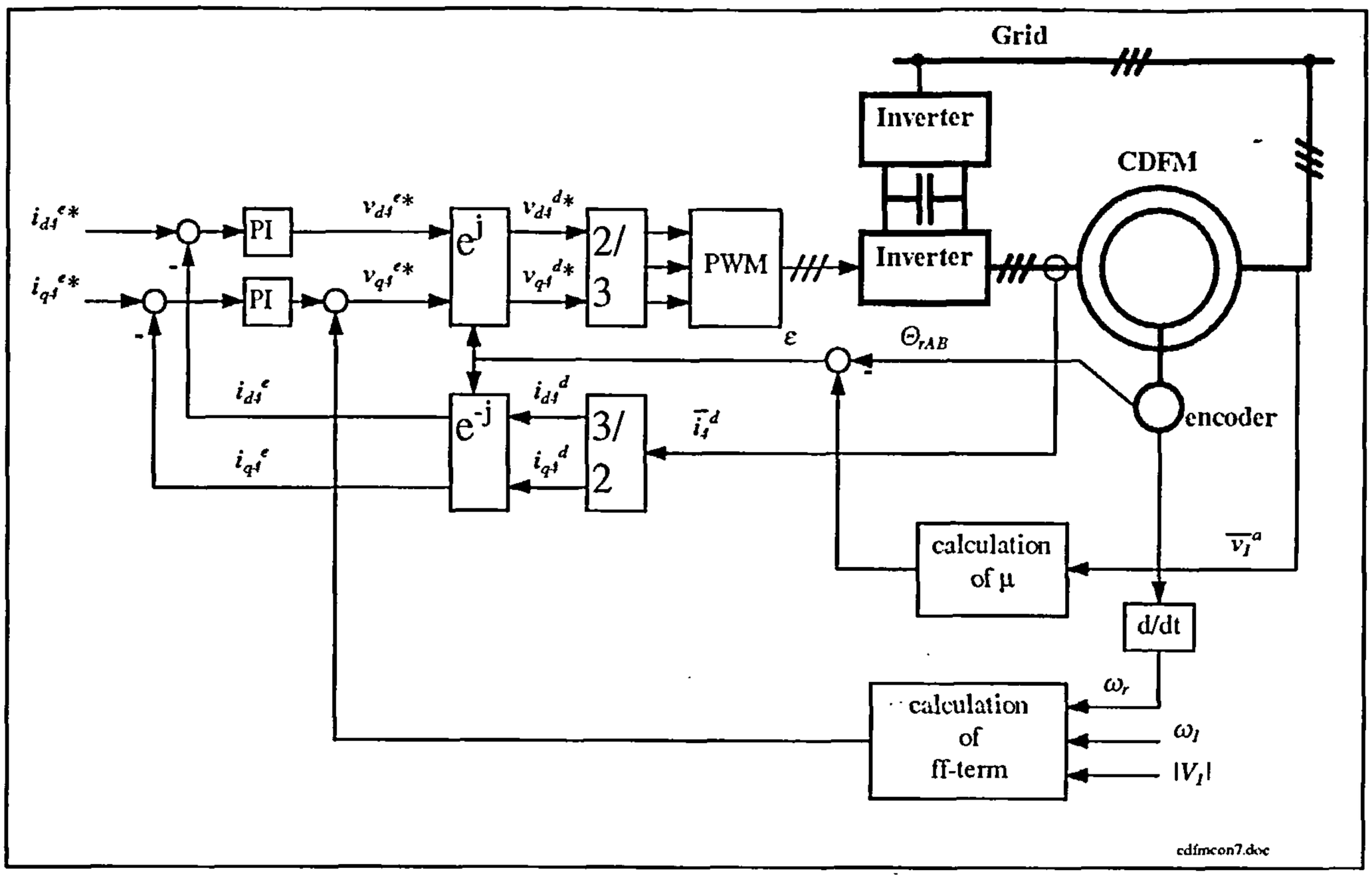

Figure 5.15: Stator flux control structure of the CDFM - inner current control loop

Figure 5.17 shows the same step response in the d-axis current component together with the side 1 phase voltage and phase current in the "a"-frame. The sudden phase change in the current and its sudden magnitude change at the step shows the rapid transition from one steady state to another without any oscillatory transients. This can also be seen in figure 5.18 for a step change in the q-component of the side 4 current.

A second set of graphs for a step in i_{q4}^{e} are displayed in figure 5.19. It can be seen, that the q-axis component of i_4^e directs side 1 current q-component and therefore the active power on side 1. The d-component of i_4^e controls the side 1 current d-component and therefore the side 1 reactive power. Compared to the step change in the d-axis, shown in figure 5.16, the decoupling is less pronounced. There are two reasons for this:

Firstly, as is known from the stator flux control of the SDFM in chapter 3, the actual orientation takes place in a reference frame fixed to the stator voltage (see figure 3.23). Therefore the q-component of the stator flux is not entirely zero and would appear in equation (5.2.7). In the reference frame fixed to the side 1 voltage vector (denoted as "e+" in chapter 3) equations (5.2.6) and (5.2.7) change to

$$i_{d1}^{e+} = \frac{1}{k_2}\Psi_{dR}^{e+} - \frac{L_R}{k_2 L_{mA}}\Psi_{d1}^{e+} + \frac{L_{mB}}{k_2} i_{d4}^{e+}$$

$$i_{q1}^{e+} = \frac{1}{k_2}\Psi_{qR}^{e+} - \frac{L_R}{k_2 L_{mA}}\Psi_{q1}^{e+} + \frac{L_{mB}}{k_2} i_{q4}^{e+}$$

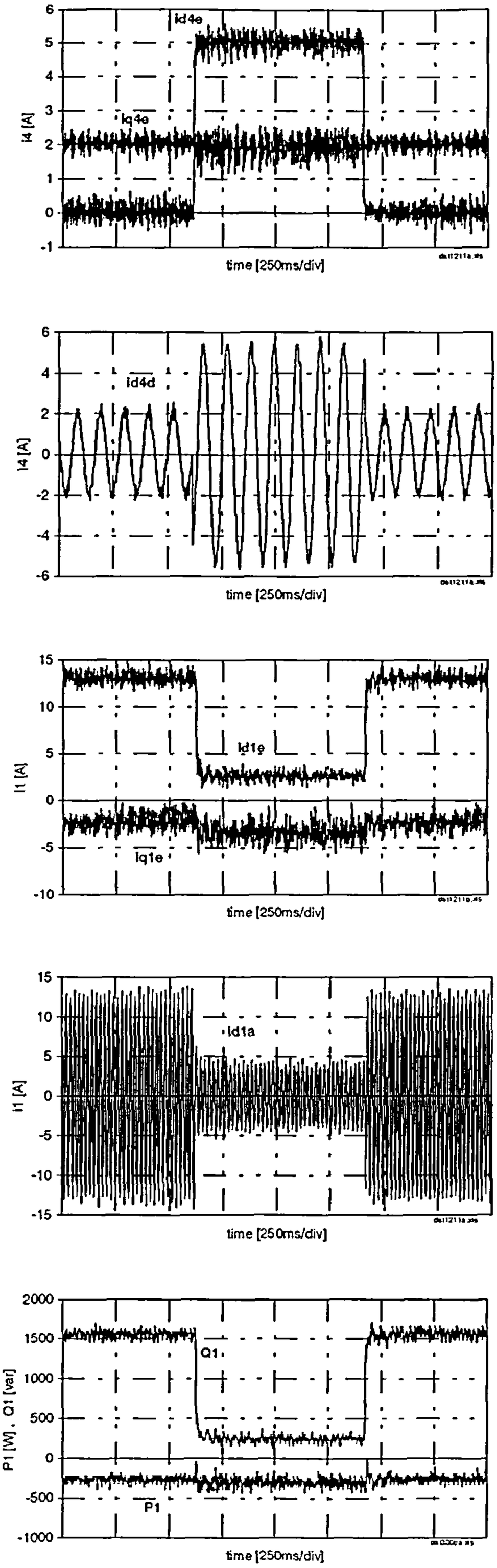

Figure 5.16: Experimental CDFM dynamics I for stator flux orientation - current control loop

($i_{d4}^{e*} = 0$ to 5 A , $i_{q4}^{e*} = 2$ A , $n_m = 400$ rpm)

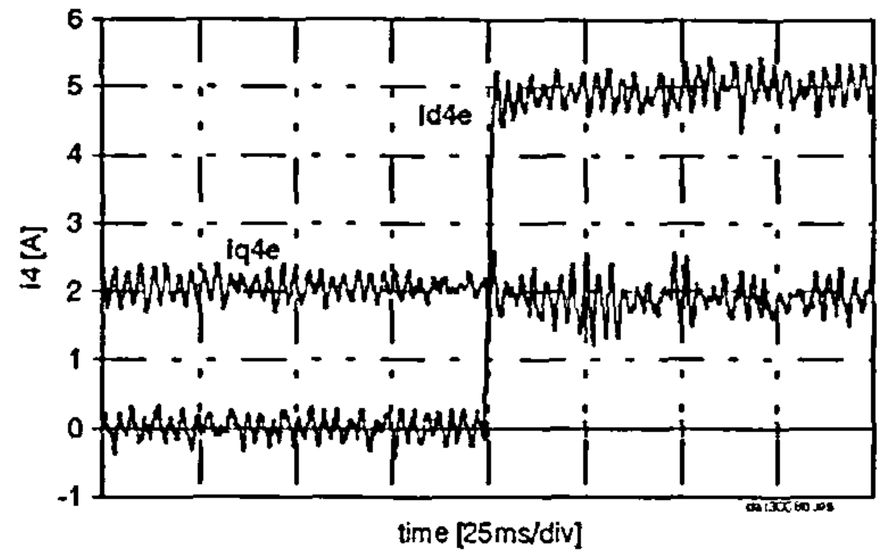

Figure 5.17: Experimental CDFM dynamics II for stator flux orientation - current control loop

($i_{d4}^{e*} = 0$ to 5 A , $i_{q4}^{e*} = 2$ A , $n_m = 400$ rpm)

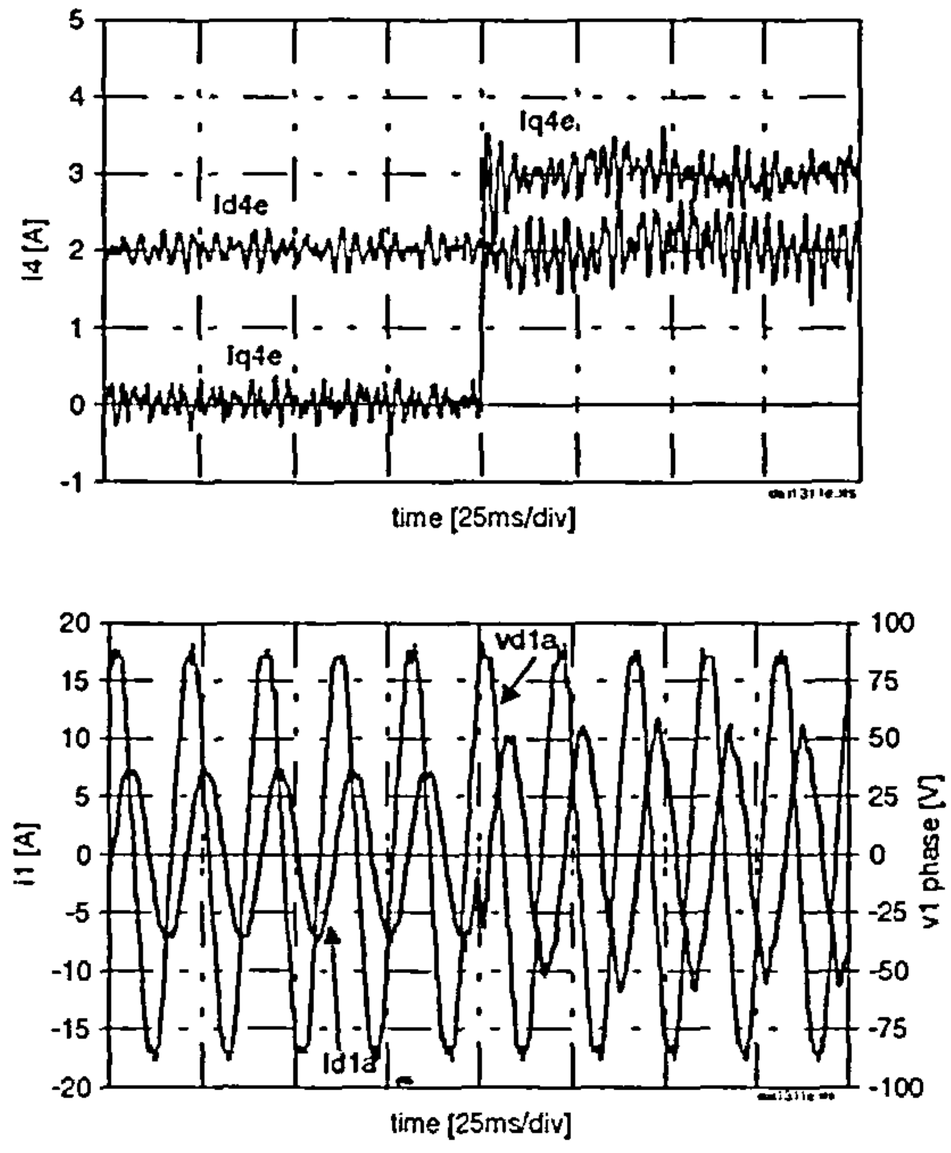

Figure 5.18: Experimental CDFM dynamics III for stator flux orientation - current control loop

($i_{d4}^{e*} = 2$ A , $i_{q4}^{e*} = 0$ to 3 A , $n_m = 400$ rpm)

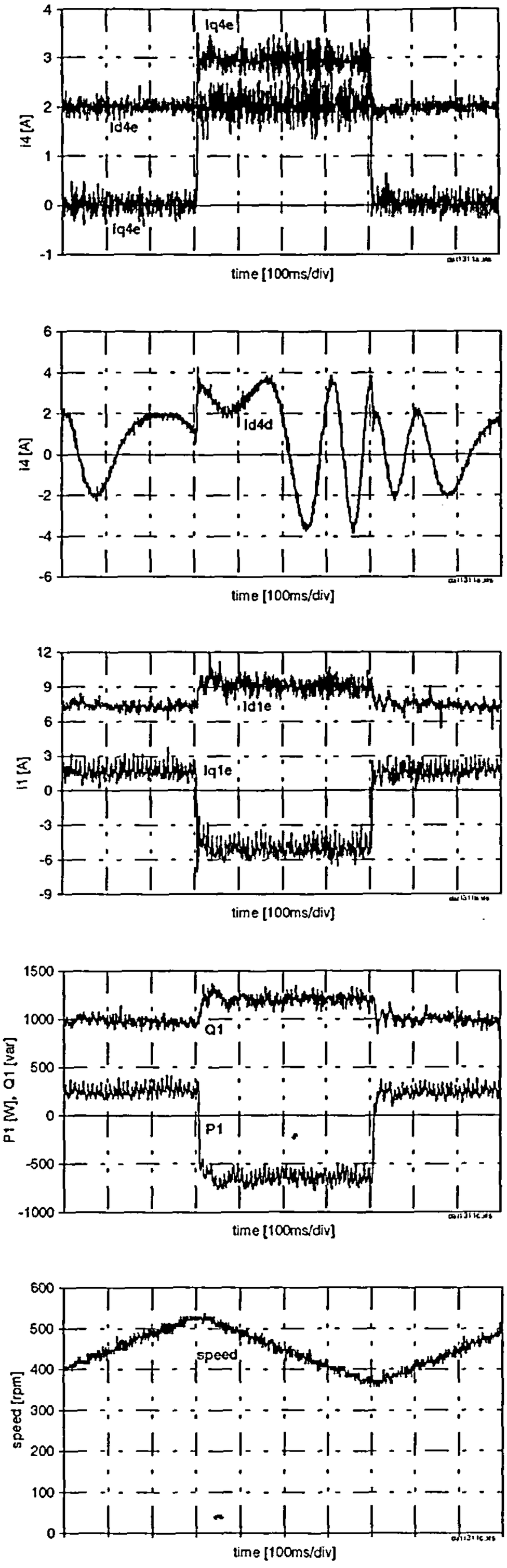

Figure 5.19: Experimental CDFM dynamics IV for stator flux orientation - current control loop

($i_{d4}^{e*} = 2$ A , $i_{q4}^{e*} = 0$ to 3 A)

The d-q-components of Ψ_1^{e+}, can vary slightly, depending on the positioning of the stator flux vector within the reference frame "e+". A step in i_{d4}^{e+} or i_{q4}^{e+} would have an effect on the values of Ψ_1^{e+} and would cause a "cross coupling disturbance" as explained in chapter 3 for the SDFM. The indication, that orientation takes actually place in the "e+"-frame is that i_{d1}^{e+} is directly proportional to the reactive power and i_{q1}^{e+} to the active power. This follows from the power equations together with the constraint of $v_{d1}^{e+} = 0$ as mentioned already in chapter 3 for the SDFM.

The second and obviously far more significant reason for the cross coupling is due the rotor circuit effects as derived earlier. As the simulations in figure 5.14 show, the d-component and the q-component of the combined rotor flux linkage in the "e"-frame do not have to have necessarily equal values, they rather depend on the positioning of Ψ_R^e within the excitation reference frame. It can be seen that the magnitude of Ψ_{qR}^e and therefore the cross coupling in Ψ_{qR}^e in figure 5.14 has a smaller value than Ψ_{dR}^e. The cross coupling effect in Ψ_{qR}^e caused by a step in i_{d4}^e, as shown in figure 5.16, has a far less impact than the cross coupling in Ψ_{dR}^e caused by a step in i_{q4}^e, as shown in figure 5.19.

The "cross coupling disturbance" caused by the orientation in the "e+"-frame rather than the "e"-frame can generally be neglected, because its influence is very small. The main reason for the cross coupling effect in figure 5.19 is caused by the rotor flux linkage. But basically both effects can act together or they can counteract each other and therefore compensate slightly.

Despite the cross coupling in figure 5.19, it can still be said that the individual side 4 current component manipulate the respective side 1 current components and therefore mainly controls side 1 active and reactive power in a natural decoupled manner. Dynamic simulation results (Appendix E, figures E.23 and E.24) for a 30 kW SF-CDFM as described by Krebs [b17] show that the cross coupling effect is not so severe on larger machines.

Figure 5.20 shows experimental results of the inner current control loop with constant demand values for the individual current component over a changing speed range, indicating the independence of speed on the inner current control loop.

The side 4 current q-component in figure 5.19 exhibits a slight over- and undershoot at the step from 0 to 3 A, which is also visible in i_{d1}^e and Q_1. This overshooting is not present at the step from 3 to 0 A. The "over shoot tendency" increases the closer the speed approaches machine A synchronous speed at 750 rpm. As mentioned, in the vicinity of machine A synchronous speed the CDFM is more difficult to control, since the electromagnetic coupling between the two machines reduces [b17].

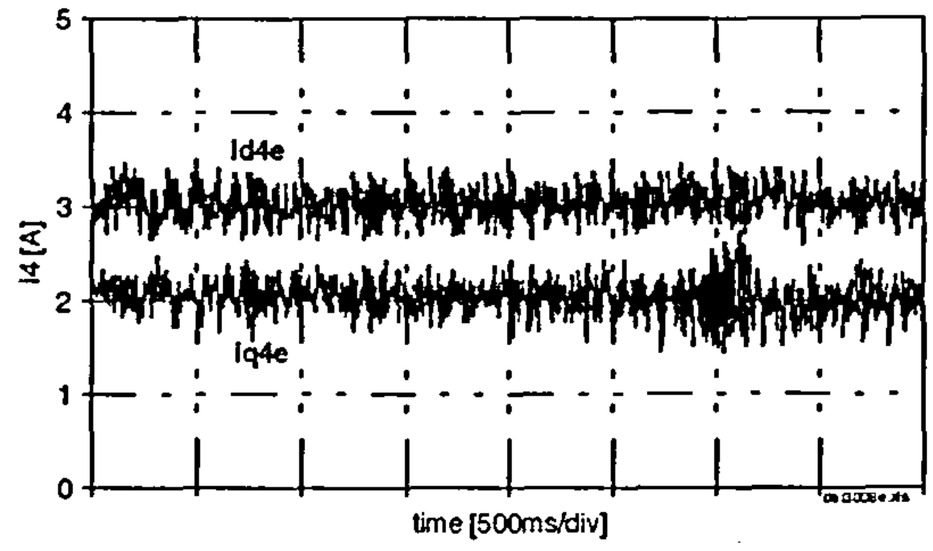

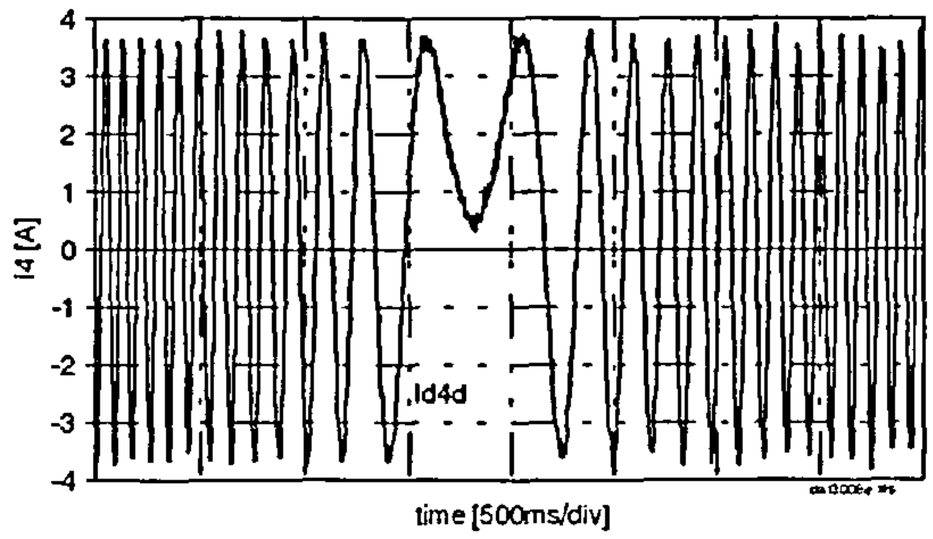

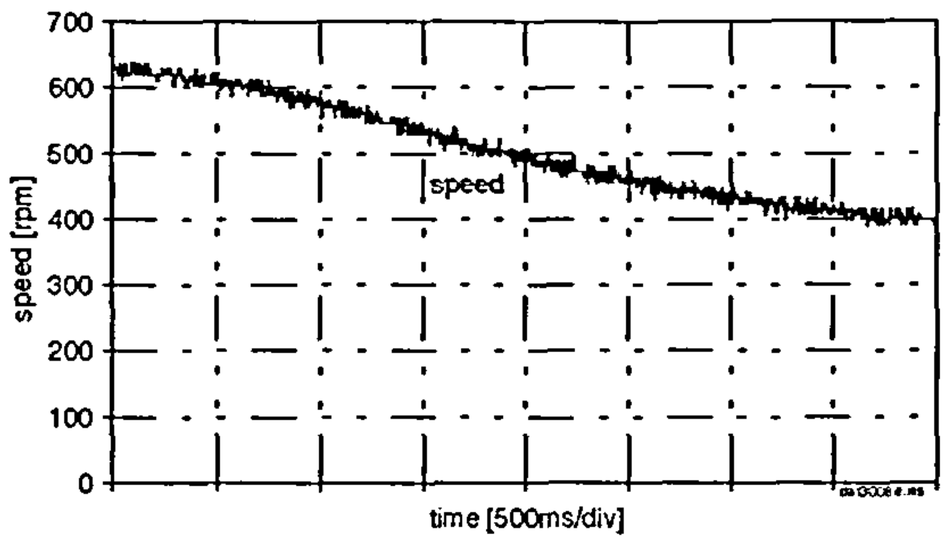

Figure 5.20: Experimental CDFM dynamics of the stator flux orientation with constant demand values for i_{d4}^{e} and i_{q4}^{e} over speed range
- current control loop
($i_{d4}^{e*} = 3$ A , $i_{q4}^{e*} = 2$ A)

5.2.2 Outer Power Control Loop

Figure 5.21 and figure 5.22 show steady state simulation results of i_{d4}^e and i_{q4}^e for different values of side 1 active and reactive power. In order to keep the same power values over the speed range the current values have to increase rapidly close to machine A synchronous speed, thus complicating the control.

Figure 5.21 shows results for various side 1 active power values and a constant side 1 reactive value. It can be seen that i_{q4}^e changes for different active power values and i_{d4}^e remains almost unchanged for the different cases, indicating that P_1 is controlled by i_{q4}^e, as seen in the forgoing experimental results. Experimental data points for the case where the side 1 active power P_1=*-500 W* and the reactive power Q_1=*1000 VAr* are depicted in the graphs. The experimental data points are very close to the simulated values (thickened line), especially for the q-component of side 4 current.

Figure 5.22 has the results for a constant value in P_1=*-500 W* and for different values in Q_1. Now the d-component of i_4^e varies, depending on the set reactive power. The q-component remains largely unchanged. Again here, the depicted experimental data points are in very close agreement to the respective simulation results.

The simulations show, that the values of i_4^e remain largely constant up to 600 rpm and then starts to increase above 600 rpm. As long as the speed stays within a "safe" operation area, which is about up to 600 rpm for the experimental CDFM (80% of speed range), the CDFM can be properly controlled.

Experimental results of an outer power control loop extended onto the inner current control loop are shown in figure 5.23 and 5.24.

Figure 5.23 shows the dynamics for a step in the reactive power demand value. Active and reactive power are controlled totally independent of each other. The side 4 current component i_{d4}^e of the inner loop, shown in figure 5.23, changes according to equation (5.2.14) and i_{q4}^e remains almost perfectly unaffected from the step change.

Figure 5.24 displays the results for a step in the active power demand value. Again, active and reactive power show no sign of cross coupling. Now i_{q4}^e performs a step change to justify equation (5.2.13). As seen already in figure 5.19, the cross coupling effect due to the rotor circuit is more pronounced in the d-axis of the "e"-frame. The d-component of i_4^e shows a slight change at the step in figure 5.24.

Although, there is a degree of cross coupling present, the overall power control can nevertheless be described as basically decoupled, where one current component controls active power and the other component reactive stator power.

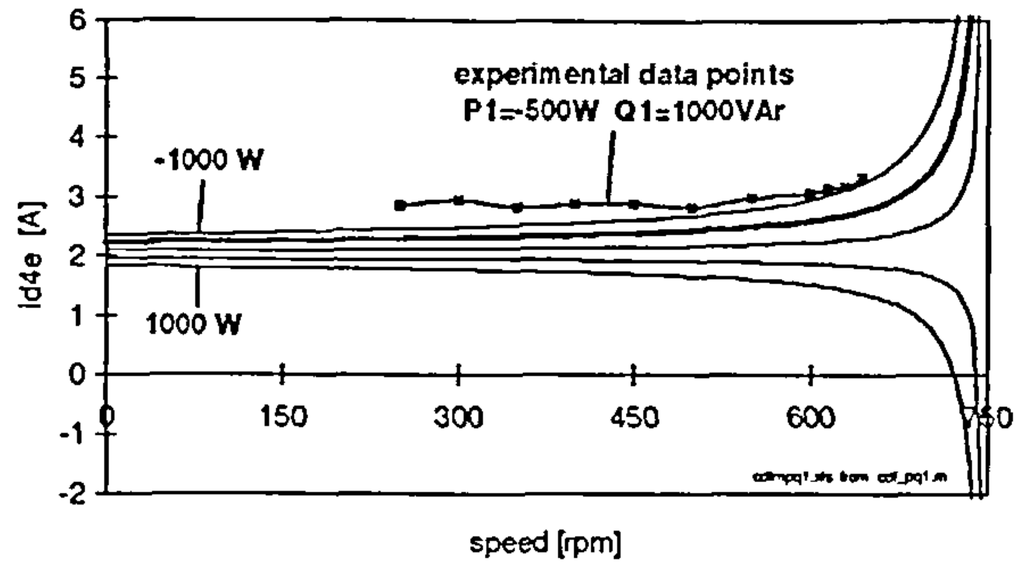

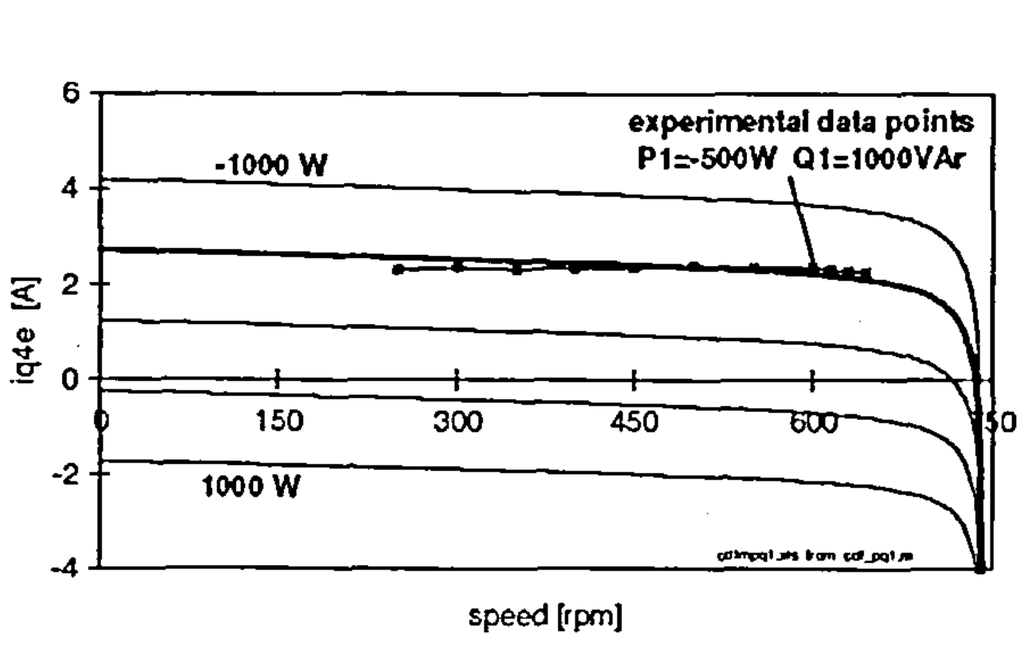

Figure 5.21: Simulated CDFM steady state curves together with experimental data points for i_{d4}^{e} and i_{q4}^{e} for different active power demand values

(Q_1^* = 1000 VAr , P_1^* = -1000 to 1000 W in steps of 500 W)

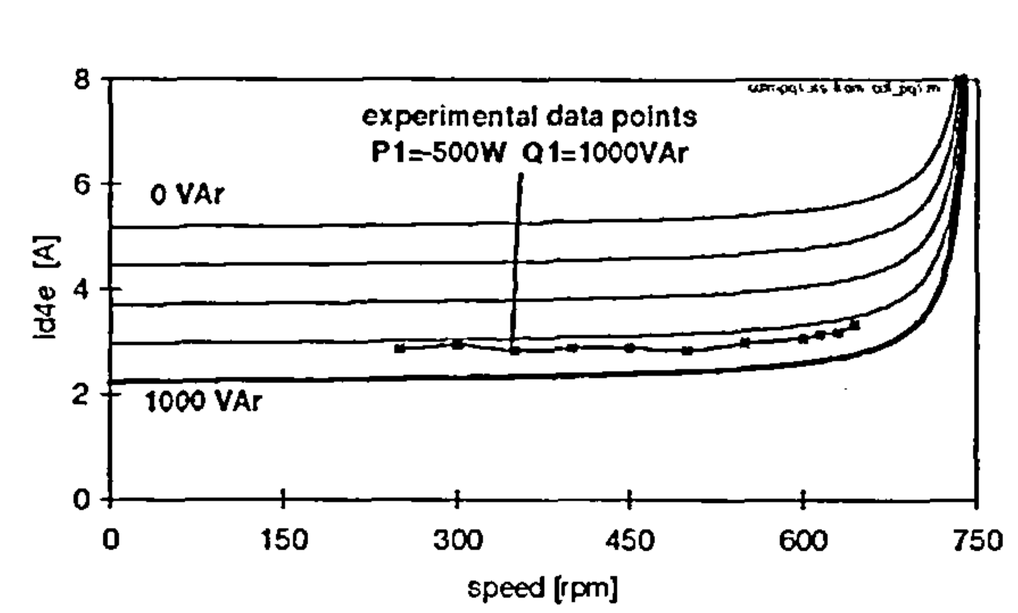

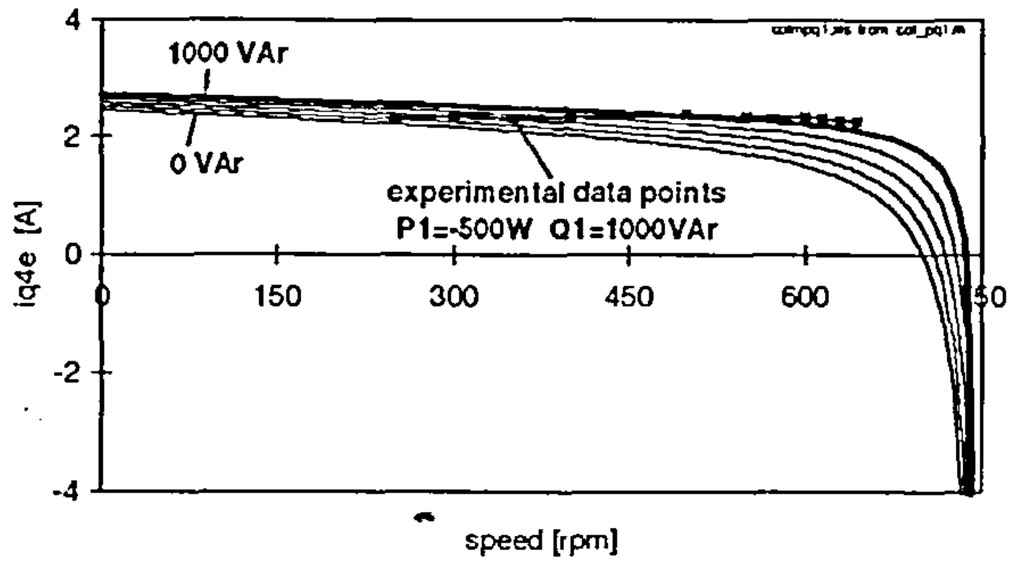

Figure 5.22: Simulated CDFM steady state curves together with experimental data points for i_{d4}^{e} and i_{q4}^{e} for different reactive power demand values

(Q_1^* = 1000 to 0 VAr in steps of 250 VAr , P_1^* = -500 W)

Figure 5.25 illustrates results for a speed variation with constant demand values for the active and reactive power, underlining the independence of the power control loop of speed.

5.2.3 Speed Control Loop

During consideration of speed control of the SDFM it was seen that the q-component of the rotor current is proportional to the developed torque. With the addition of a PI-controller in the q-axis of the inner current control loop, it was possible to create an outer speed control loop. This approach is now considered for the stator flux oriented control of the CDFM.

The torque of machine A of the CDFM, involving the stator flux linkage can be written in a general reference frame as

$$T_{eA} = -\frac{3}{2} p_A \frac{L_{mA}}{L_1} (\overline{\Psi}_1^g \times \bar{i}_2^g) \tag{5.2.19}$$

and the torque for machine B as

$$T_{eB} = -\frac{3}{2} p_B L_{mB} (\bar{i}_4^g \times \bar{i}_2^g) \tag{5.2.20}$$

Combining both torque equations gives for the CDFM torque

$$T_{eAB} = -\frac{3}{2} (p_A \frac{L_{mA}}{L_1} \overline{\Psi}_1^g + p_B L_{mB} \bar{i}_4^g) \times \bar{i}_2^g \tag{5.2.21}$$

This equation is similar to equation (5.1.1), which was the basis for the CDFM control oriented on an artificial combined flux linkage vector. The term in the brackets of (5.2.21) constitutes such an artificial combined flux linkage. Furthermore, it can be seen that for open circuited side 4 the CDFM develops a torque component

$$T_{eAB} = -\frac{3}{2} p_A \frac{L_{mA}}{L_1} \overline{\Psi}_1^g \times \bar{i}_2^g$$

As explained earlier, by creating a closed rotor circuit the CDFM starts to function as a simple cage induction machine. Albeit a low efficiently machine.

To obtain the developed torque of the CDFM for stator flux orientation, the torque equation has to be developed as a function of the stator flux linkage and the side 4 current vector. Resolving equation (5.2.2) after the rotor current and substituting it in (5.2.21) yields

$$T_{eAB} = -\frac{3}{2} (p_A \frac{L_{mA}}{L_1} \overline{\Psi}_1^g + p_B L_{mB} \bar{i}_4^g) \times (\frac{1}{k_1} \overline{\Psi}_R^g - \frac{L_{mA}}{k_1 L_1} \overline{\Psi}_1^g + \frac{L_{mB}}{k_1} \bar{i}_4^g)$$

Stating it in the "e"-frame together with the stator flux constraint of $\Psi_{q1}^e = 0$ obtains for the torque equation

$$T_{eAB} = -\frac{3}{2}\{(p_A \frac{L_{mA}}{L_1 k_1}\Psi^e_{d1} + p_B \frac{L_{mB}}{k_1} i^e_{d4})\Psi^e_{qR} + [(p_A + p_B)\frac{L_{mA}L_{mB}}{k_1 L_1}\Psi^e_{d1} - p_B \frac{L_{mB}}{k_1}\Psi^e_{dR}]i^e_{q4}\} \quad (5.2.22)$$

This equation looks rather complicated and does not give a straight forward connection of i_{q4}^e and the torque at first sight. Both side 4 current components appear in equation (5.2.22) which indicates, that the torque is affected by either a change in i_{d4}^e or i_{q4}^e. As simulation results have shown the influence of i_{d4}^e is far less than of i_{q4}^e. However, if i_{d4}^e is kept at a constant value, then the term

$$(p_A \frac{L_{mA}}{L_1 k_1}\Psi^e_{d1} + p_B \frac{L_{mB}}{k_1} i^e_{d4})\Psi^e_{qR}$$

remains constant. No cross coupling is involved, since Ψ_{qR}^e would only be affected by a change in i_{d4}^e.

The remaining term in equation (5.2.22) is governed by i_{q4}^e, but the d-component of the combined rotor flux is present, which is subject to cross coupling caused by i_{q4}^e. This cross coupling has no influence in this case, because i_{q4}^e would take a certain value to give a set torque despite the effect in Ψ_{dR}^e. Consequently, for a fixed value in i_{d4}^e, the torque developed by the CDFM in the stator flux reference frame is directly proportional to the q-component of i_4^e, despite cross coupling caused by the rotor circuit. The larger the set value for i_{d4}^e, the more reactive power is supplied by terminal 4 and the less magnitude of i_{q4}^e is necessary to develop a certain torque value.

Experimental results of a speed control loop are shown in figure 5.26. It can be seen that the q-component of i_4^e varies, depending on the torque demand value set by the outer speed loop controller to follow the desired speed ramp. The d-component remains unaffected.

Additionally, a graph displaying the rotor voltage shows very clearly the change in frequency and magnitude of the rotor voltage for varying speed. The closer the speed approaches machine A synchronous speed, the more the rotor voltage magnitude and frequency reduces.

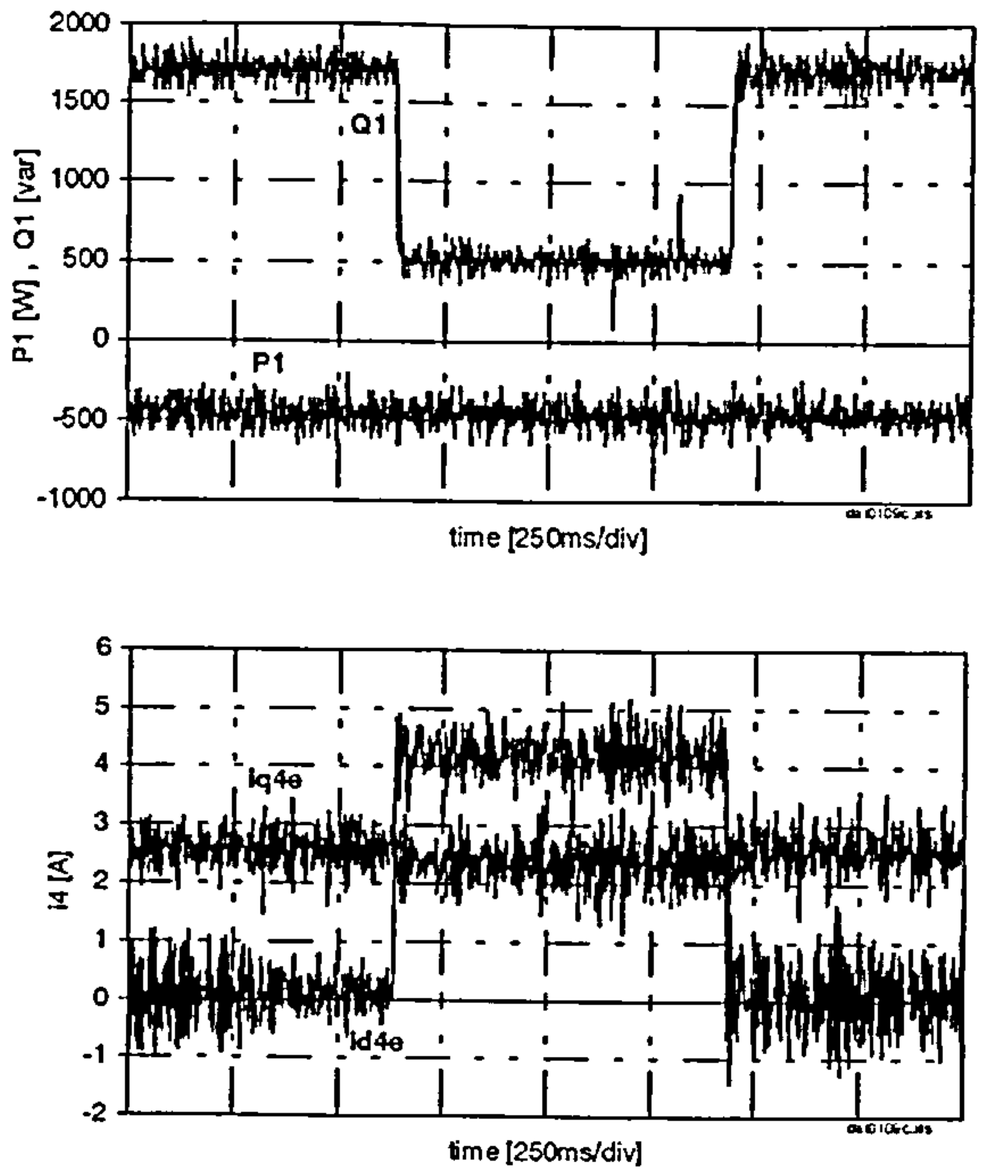

Figure 5.23: Experimental CDFM dynamics I for stator flux orientation - power control loop

(Q_1^* = 1700 to 500 VAr , P_1^* = -500 W)

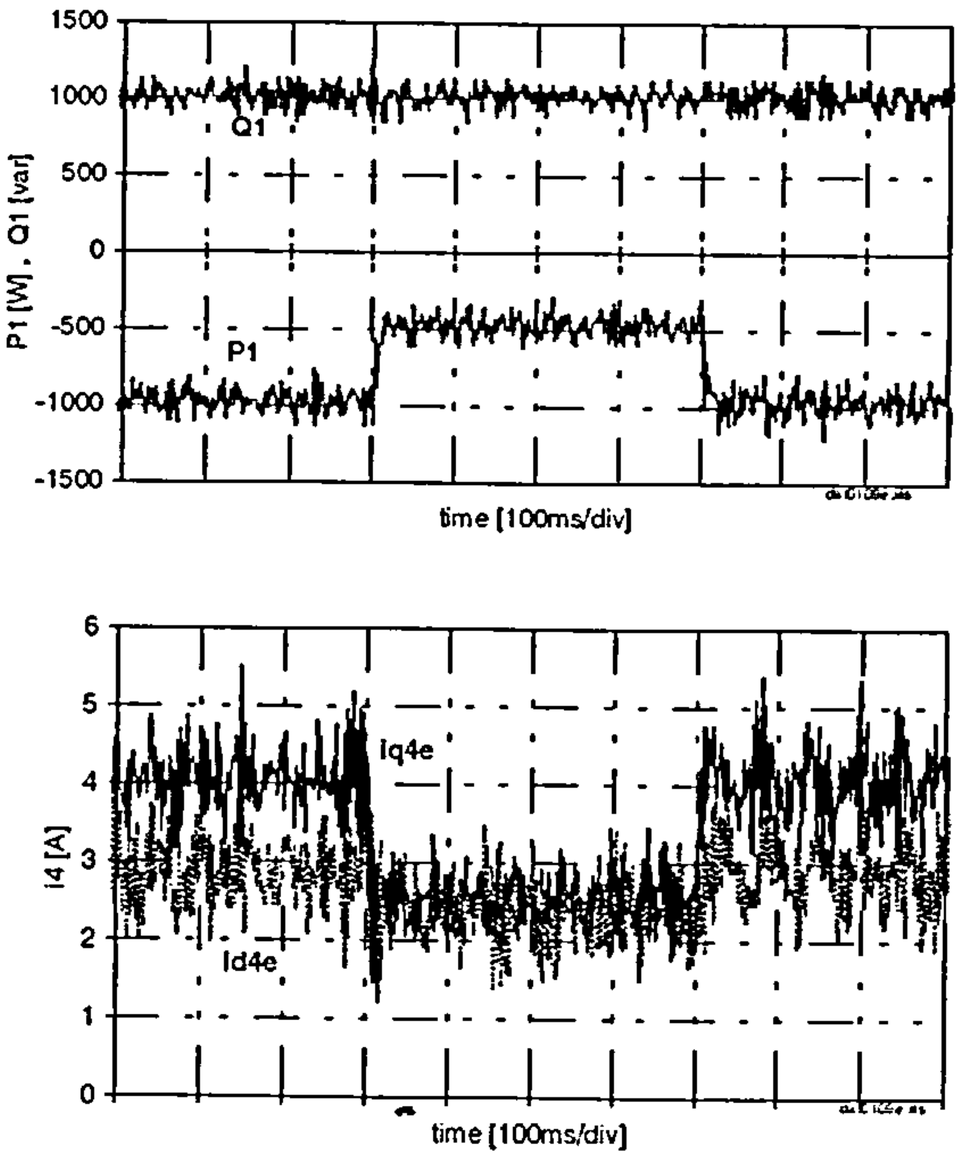

Figure 5.24: Experimental CDFM dynamics II for stator flux orientation - power control loop

(Q_1^* = 1000 VAr , P_1^* = -1000 to -500 W)

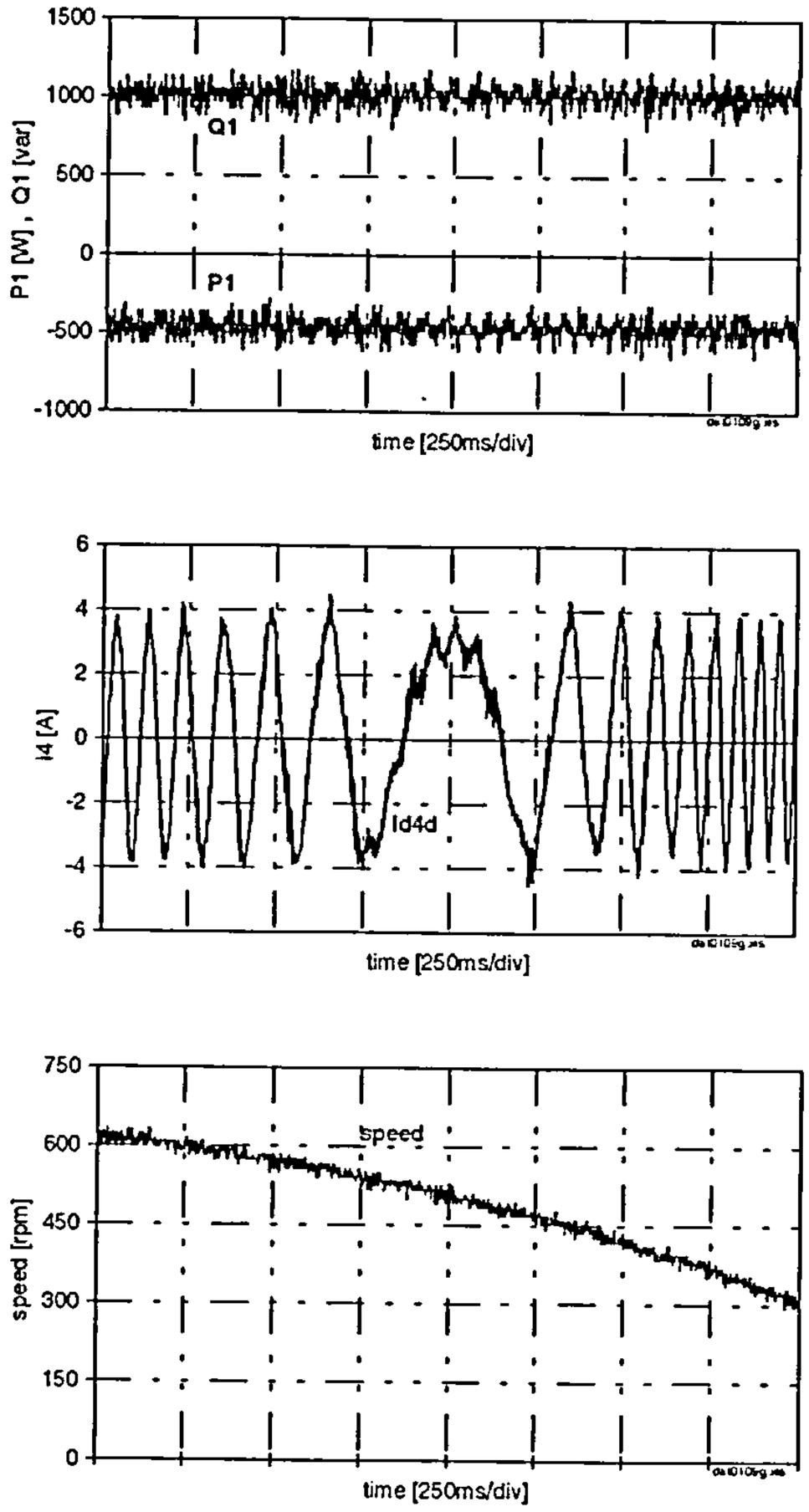

Figure 5.25: Experimental CDFM dynamics III for stator flux orientation - power control loop

($Q_1^* = 1000$ VAr , $P_1^* = -500$ W)

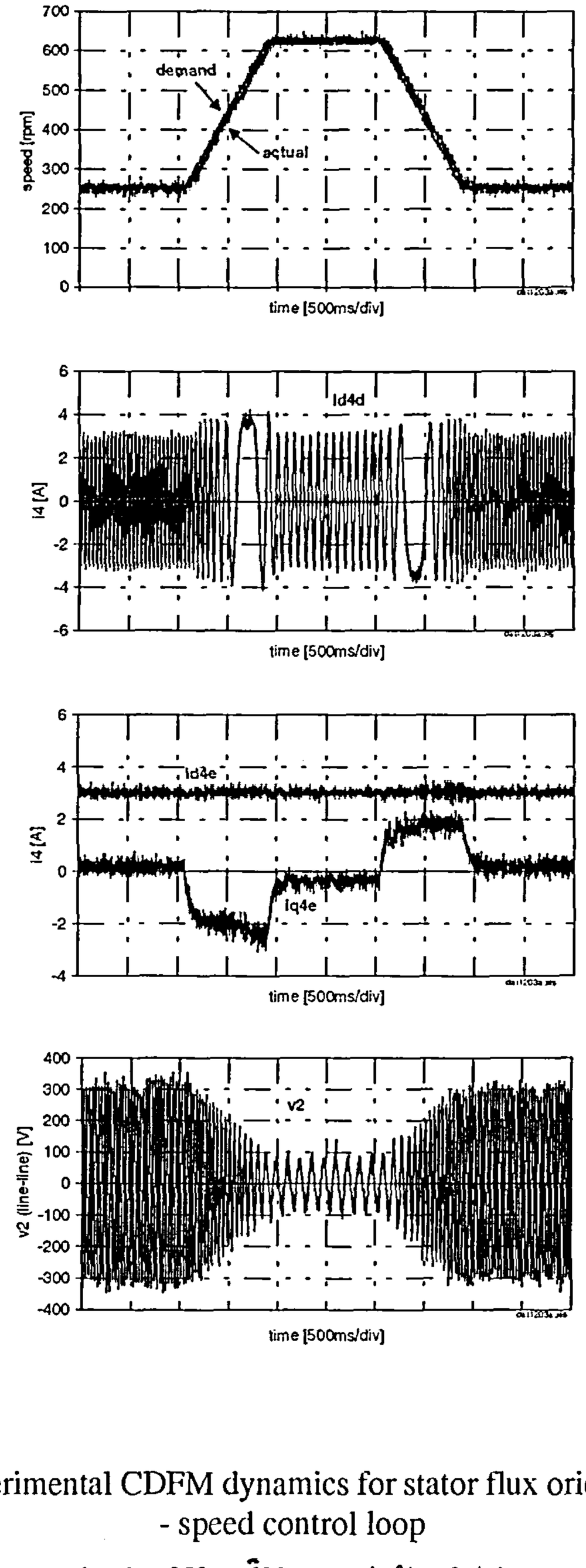

Figure 5.26: Experimental CDFM dynamics for stator flux orientation at no-load - speed control loop

($n_m^* = 250$ to 630 rpm , $i_{d4}^{e*} = 3$ A)

5.2.4 Summary

The investigation of the stator flux oriented control initially applied to the SDFM and now applied to the CDFM, shows that in general the developed CDFM equations have similar structure as the corresponding SDFM equations. However, there is always a term associated with the combined rotor flux linkage present in the CDFM equations.

It turns out that this combined rotor flux linkage is subject to cross coupling between the d-axis and q-axis in the "e"-frame. The cross coupling intensity depends on the combined rotor resistance value and the rotor speed. With low rotor resistance values, this cross coupling can be kept small.

Despite the cross coupling effect, it can still be said, that a "natural decoupled" active and reactive power control of side 1 can be performed on the CDFM as is the case for the SDFM.

For constant values of the d-component of the side 4 current in the "e"-frame the torque developed by the CDFM is directly proportional to the q-component of i_4^e and proper speed control can be performed with the CDFM.

5.3 Comparison of Field Oriented Control Schemes of the CDFM

In section 5.1 the field oriented control of the CDFM in a reference frame fixed to an artificial magnetising flux linkage has been presented. The control, developed in [b15], is only applicable to identical machines and therefore a method has been developed to apply the control to unequal machines. This control method can be largely simplified if the mathematical extension in the q-axis is removed. Inner current control loop, outer power control loop and speed control loop results show the behaviour of the system.

In the previous section 5.2 the field oriented control based on the stator flux linkage of the CDFM has been investigated. It has been shown that an artificial combined rotor flux linkage term is present in all equations for this particular reference frame. This term introduces a cross coupling between d-axis and q-axis.

After focusing on the basic feature, the comparison of both field oriented control methods is divided into three topics. Inner current control loop, outer power control loop and speed loop. Only the simplified combined magnetising flux control of the CDFM is compared to the stator flux control.

General Features of the Control Approach

Simplified overall magnetising flux linkage control

The important variable is the artificially created combined overall magnetising flux vector. It is a combination of both sets of stator currents of the CDFM.

Stator flux linkage control

The important variable in this case is a combined rotor flux linkage vector. This vector results from the subtraction of side 2 and side 3 flux linkages. This term causes a cross coupling for this reference frame.

Inner Current Control Loop

Simplified overall magnetising flux linkage control

A slip proportional feed forward term associated with the overall magnetising flux has to be included in the q-axis for better steady state accuracy.

The individual side 4 current components directly manipulate the respective side 1 current components. This, however, does not lead to a direct natural manipulation of side 1 active and reactive power. Cross coupling is present in the power equations. This cross coupling depends on the positioning of the side 1 voltage vector within the reference frame attached to the combined magnetising vector. It is not possible to remove this cross coupling effect.

Stator flux linkage control

Here also, a slip proportional feed forward term appears in the q-axis. It is related to the stator flux linkage of the CDFM.

Compared to the overall magnetising flux control, the relation between side 4 and side 1 current components is not completely decoupled. A cross coupling due to the combined rotor flux is involved. Although, the cross coupling effect is clearly visible in the results it is still small enough to allow a claim of mainly direct connection between side 1 and side 4 current components. Side 1 active and reactive power is related in the same manner to the side 4 current components as the side 1 current components to the side 4 currents. Consequently, cross coupling is also present, but still within a limit so that a "natural decoupled" active and reactive power manipulation can be claimed.

In the reference frame attached to the stator flux (actually attached to the stator voltage) the components of the stator voltage take the values

$$v_{d1}^{e} = 0 \quad \text{and} \quad v_{q1}^{e} = \sqrt{2}V_1$$

A look at the results of the combined magnetising flux current control in figures 5.7 and 5.8 shows, that the magnitude of v_{d1}^{e} is mostly smaller than that of v_{q1}^{e} in the combined flux reference frame. Both components are subject to variations, depending on the components of i_4^{e} in the combined flux reference frame. Especially in figure 5.8, the magnitude of v_{d1}^{e} is small compared to the value of v_{q1}^{e}. The ratio between the d-axis component to the q-axis component of the side 1 voltage in the "e"-frame of the combined flux orientation suggests, that the reference frame angle in this case is not far away from a stator flux reference frame angle.

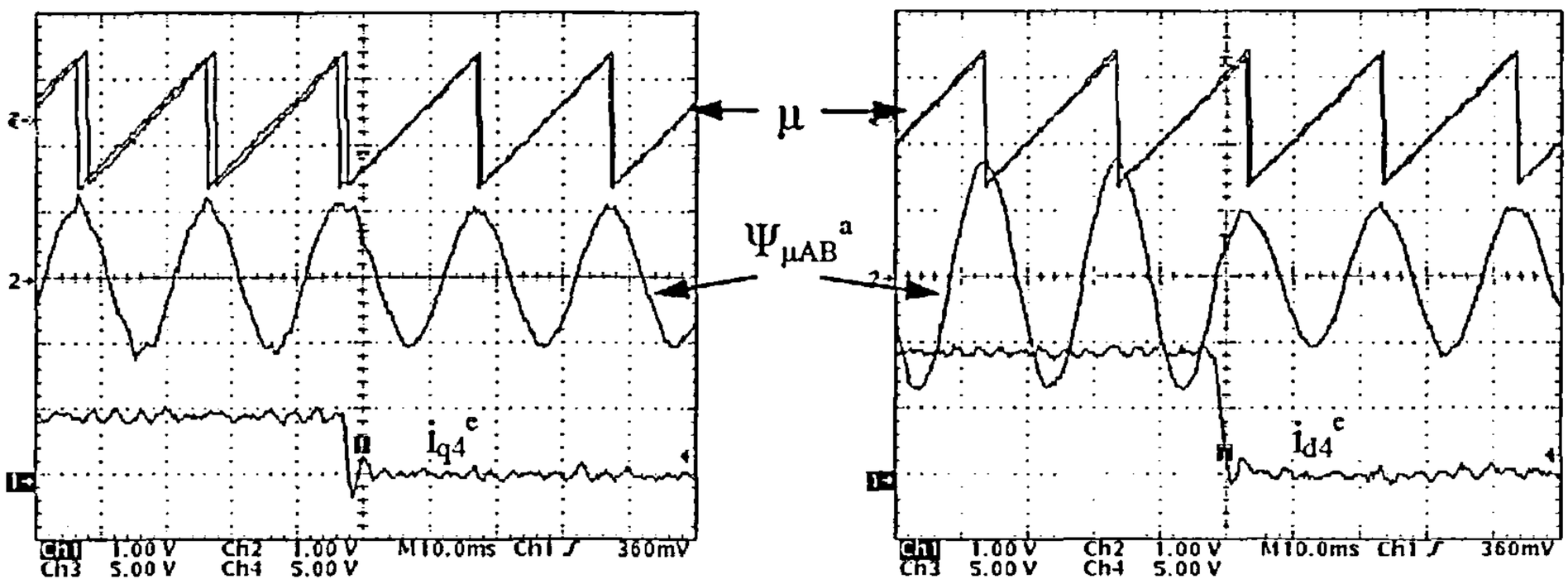

Figure 5.27: Angle μ , $\Psi_{\mu AB}^{a}$ and i_4^{e} components of the combined flux control of the CDFM in addition to a reference angle μ for stator flux orientation

(left: step in $i_{q4}^{e} = 2.5$ to 0 A right: step in $i_{d4}^{e} = 5$ to 0 A)

The plots in figure 5.27 show results of the current control for the combined flux linkage orientation, displaying the angle μ (top) the combined flux linkage in the "a"-frame $\Psi_{\mu AB}^{a}$ (middle) and the respective step current component of i_4^{e} (bottom). As a reference to the angle μ of the combined flux orientation the angle μ of the stator flux orientation is also shown in figure 5.27 (both angles μ are overlaid).

For a step in i_{q4}^{e} in the combined reference frame this reference frame moves relative to the stator flux reference frame (left plot). For a step in i_{d4}^{e} in the combined reference frame there is hardly any positional change between the two reference frames (right plot).

Generally, it can be seen that the two reference frames are close together, but they are never totally aligned.

Outer Power Control Loop

Simplified overall magnetising flux linkage control

It is possible to achieve independent active and reactive power control with a power control loop. The inner currents are forced to a value to so that they allow the desired active and

reactive power to be created. The control is not decoupled in the sense, that a current component independently controls a power component. As figure 5.10 indicates a step change on one of the power components results in a notch at the other component.

Stator flux linkage control

Despite the cross coupling introduced with the rotor winding, the active and reactive power control can be mainly regarded as naturally decoupled as it is the case for the SDFM.

For active and reactive power control the reference frame attached to the combined magnetising flux is suitable, but not in a straight forward manner as the control in the reference frame attached to the stator flux linkage. The stator flux reference frame is therefore the preferred choice for active and reactive power control.

Speed Control Loop

Simplified overall magnetising flux linkage control

The omission of the extension in the q-axis causes a small error in the torque control of the CDFM. However, if the d-component of i_4^e is kept constant than this error is of no concern and the torque is directly proportional to the q-component of i_4^e. The higher the d-component value the smaller is the q-component value for the same torque.

Stator flux linkage control

Here it is a similar case. For fixed values of the d-component of i_4^e the torque is directly proportional to the q-component of i_4^e. For higher values of i_{d4}^e the q-component takes a smaller value in order to develop the same torque.

Generally, speed control can be performed with both reference frames. The advantage of the stator flux reference frame in this case is that the side 1 reactive power remains mainly fixed only subject to a small cross coupling effect in the combined rotor flux linkage, whereas the reactive power for the combined magnetising flux reference frame is subject to larger variations, depending on the position of the side 1 voltage vector within the combined flux reference frame.

Overall Result

The control in the reference frame attached to the artificial combined flux linkage is suitable for torque and speed control.

The control in the reference frame attached to the stator flux linkage is suitable for torque and speed control and additionally for decoupled active and reactive power control.

5.4 Summary

This chapter deals with two different field oriented control principles for the CDFM.

Firstly, the combined flux linkage oriented control, introduced by Bauer [b15] is modified so that it can be applied to a CDFM composed of two unequal machines. Further simplifications of that method, by removing a mathematical control extension, show good performance and a more stable control behaviour than the control described in [b15]. However, this method is not suitable for natural decoupled active and reactive power control.

Secondly, based on the steady state simulation results a stator flux linkage field oriented control is studied with the conclusion, that it is applicable to a CDFM almost in the same effective manner as it is to the SDFM.

Chapter 6

Sensorless Control of SDFM and CDFM

In chapter 3 and chapter 5, the field oriented control of the SDFM and CDFM has been developed with the assumption that a shaft sensor is available to deliver the necessary rotor position angle and the speed of the machine. For the experimental laboratory set-up an incremental encoder is used.

A sensor mounted on a machine or implemented within the machine design adds cost and complexity to the system and constitutes a potential source of failure, which could bring the whole drive system to a halt.

In recent years extensive research has been taken place in order to develop sensorless control methods, particularly for cage induction machine drives, to minimise costs and to increase the robustness of the system. Various different control methods such as model reference adaptive system or extended Kalman filter techniques were investigated [f15] and applied to cage induction machines.

By comparison, little effort has been invested on doubly-fed machines. This was mainly due to the limited use of such machines. However, more recently the doubly-fed machines have been receiving renewed interest.

This chapter describes a sensorless control method for the SDFM introduced by Arsudis [a7]. It is then extended to be applicable to a speed loop and a variation of this method is introduced. Additionally, it is investigated as to whether this sensorless method can be applied to the stator flux oriented CDFM control.

6.1 Sensorless Control of SDFM

The reference frames including the rotor current vector for the stator flux field oriented control of the SDFM are depicted in figure 6.1. For neglected stator resistance ($R_1=0$) the angle μ between the stationary reference frame and the excitation reference frame is obtained from the stator voltage vector. In order to rotate the rotor current vector into the excitation reference frame for control the angle ε is required. In chapter 3 this angle was obtained by a simple subtraction of $\varepsilon=\mu-\Theta_r$. This angle construction method is illustrated in figure 3.22.

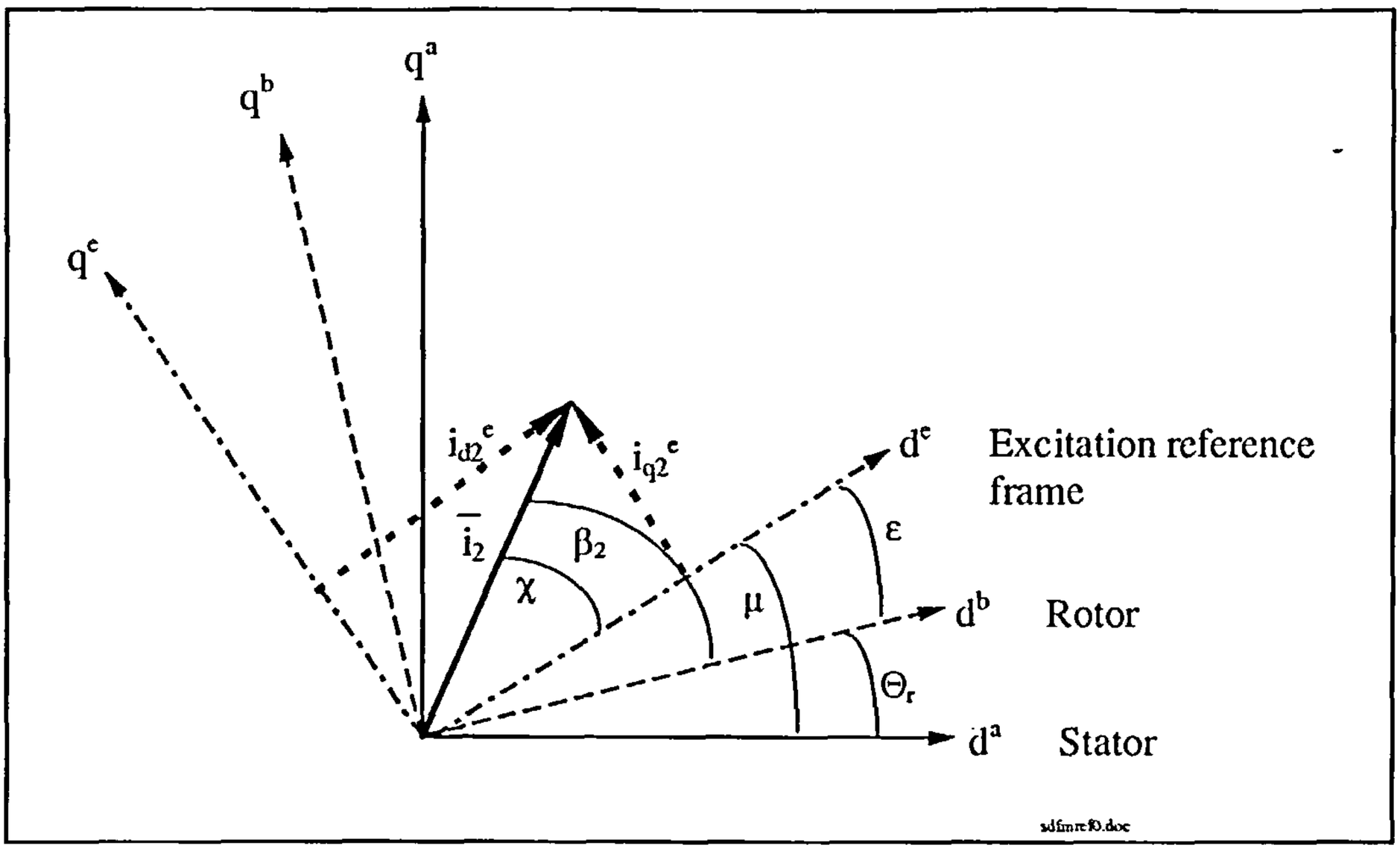

Figure 6.1: Reference frames and angles for the sensorless SDFM control

In a sensorless scheme the rotor position angle is not available and an alternative way must be found to construct the angle ε. In [a7], where a SDFM stator flux oriented control with decoupled active and reactive power control is presented, this is solved in the following way:

The relation between the rotor current and the stator current in the "e"-frame is given by equations (3.3.18) and (3.3.19) in chapter 3. By rearranging these equations, the individual rotor current components in the "e"-frame can be calculated from the stator current components in the form of

$$i^e_{d2\,calc} = \frac{1}{L_m}\Psi^e_{d1} - \frac{L_1}{L_m} i^e_{d1} \tag{6.1.1}$$

$$i^e_{q2\,calc} = -\frac{L_1}{L_m} i^e_{q1} \tag{6.1.2}$$

Equation (6.1.1) and (6.1.2) imply, that with a transformation of the measured stator current into the "e"-frame the rotor current components in the "e"-frame can be calculated. As is known from chapter 3 the stator flux d-component is constant and the stator current is measured in the stationary reference frame "a". With the given knowledge of μ this stator current can easily be transformed into the "e"-frame. A C/P- transformation of the estimated current $i_2{}^e{}_{calc}$ yields the angle χ as displayed in figure 6.1. χ is the angle between the rotor current space vector and the d-axis of the "e"-reference frame.

The measured rotor current in its natural reference frame "b" delivers the angle β_2 after a cartesian-to-polar transformation. The rotor current is measured anyway to apply the inner current control loop and therefore no additional effort is required apart from the C/P-transformation.

With the estimated angle χ and β_2 the angle ε follows as $\varepsilon=\beta_2-\chi$. This angle construction method (denoted as "Method A") is shown in figure 6.2, where the 3-to-2 calculation of the measured currents is omitted.

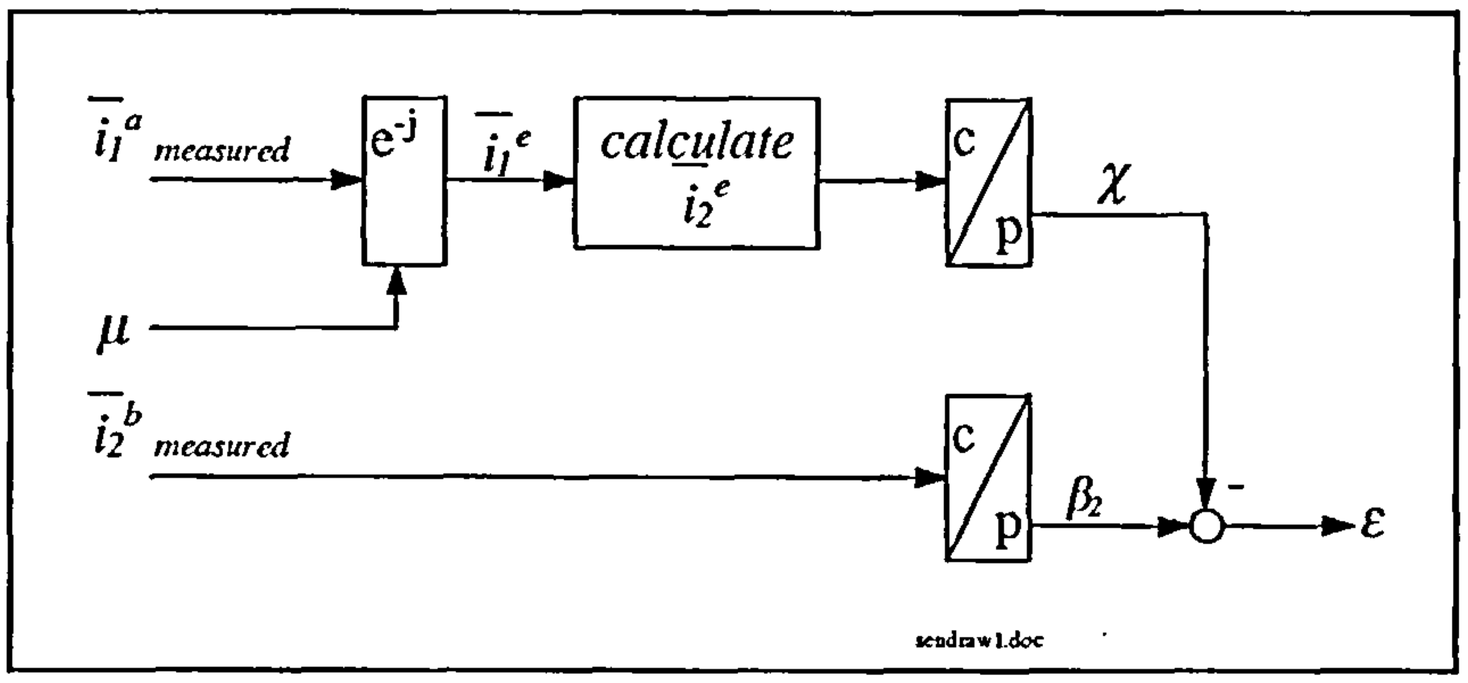

Figure 6.2: Angle construction method of the sensorless SDFM after [a7] ("Method A")

Figure 6.3 shows three different cases for the actual and the estimated angle ε, while having the position sensor still in place. A step is applied to the q-axis current of i_2^e and i_{d2}^e is set for three different values. In the left picture i_{d2}^e is set to 0 A and i_{q2}^e makes a step from 0 to 2 to 0 A. It can be seen, that during the time when i_{q2}^e is at 0 A the angle ε cannot be properly estimated, but it is possible during the time when i_{q2}^e is at 2 A. That is because the angle β_2 can only be obtained from the cartesian-to-polar transformation for a sufficiently large magnitude in i_2^b. In the middle graph, where i_{d2}^e is set to 1 A, there are still disturbances in the estimated ε, which are due to the ripple on both rotor current components. The right picture, with i_{d2}^e at 3 A, shows that the angle ε can now be estimated without problems, when $i_{q2}^e = 0$ A.

As a consequence, it has to be ensured that rotor current amplitude $|i_2^b|$ is always large enough to identify the angle β_2 properly. In [a7] this problem is not discussed. The best way to achieve a "safe" angle estimation is probably by setting i_{d2}^e to a certain current level and leave i_{q2}^e free for control purposes. In that way it is not possible to control the stator reactive power any more, since it is set to a constant level, but it is ensured that the rotor current is always large enough. The d-component current i_{d2}^e is set to 4 A in the following experimental implementation, which gives a capacitive stator reactive power of about Q_1=-*1.3 kVAr*.

The sample and switching frequency for the sensorless SDFM experimental implementation is set to 2.5 kHz to allow 400µs for software execution. This is the same frequency as was used for the speed control of the SDFM in chapter 3. The inner current control loop, angle calculation, power-loop and speed-loop are performed by µC1, whereas µC2 handles power calculation and the sampling of stator quantities.

$i_{d2}^{e} = 0\ A$ $i_{d2}^{e} = 1\ A$ $i_{d2}^{e} = 3\ A$

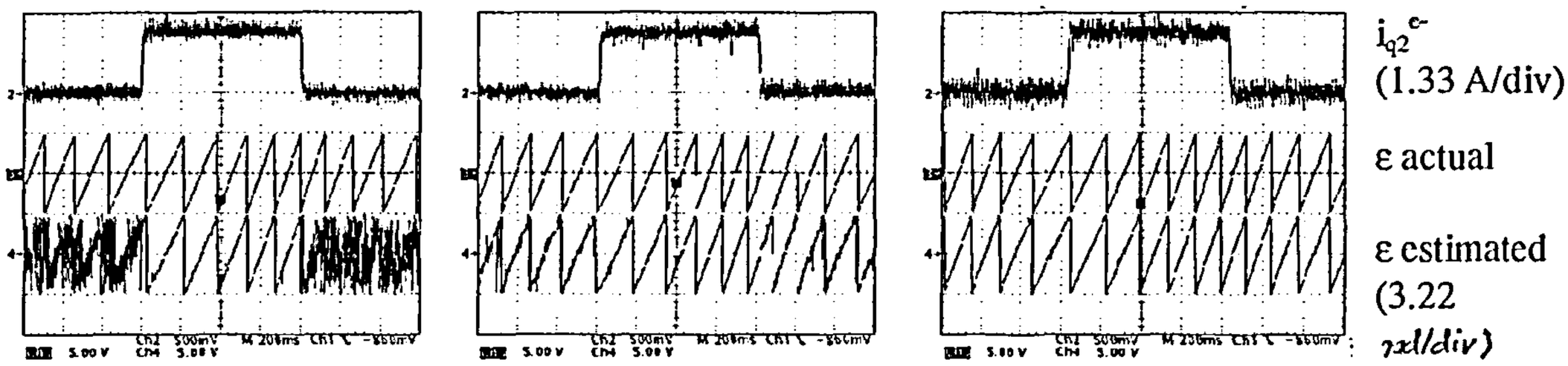

Figure 6.3: Experimental actual and estimated angle ε for three different values of i_{d2}^{e} with a step in i_{q2}^{e}

(step in i_{q2}^{e*} = 0 to 2 to 0 A)

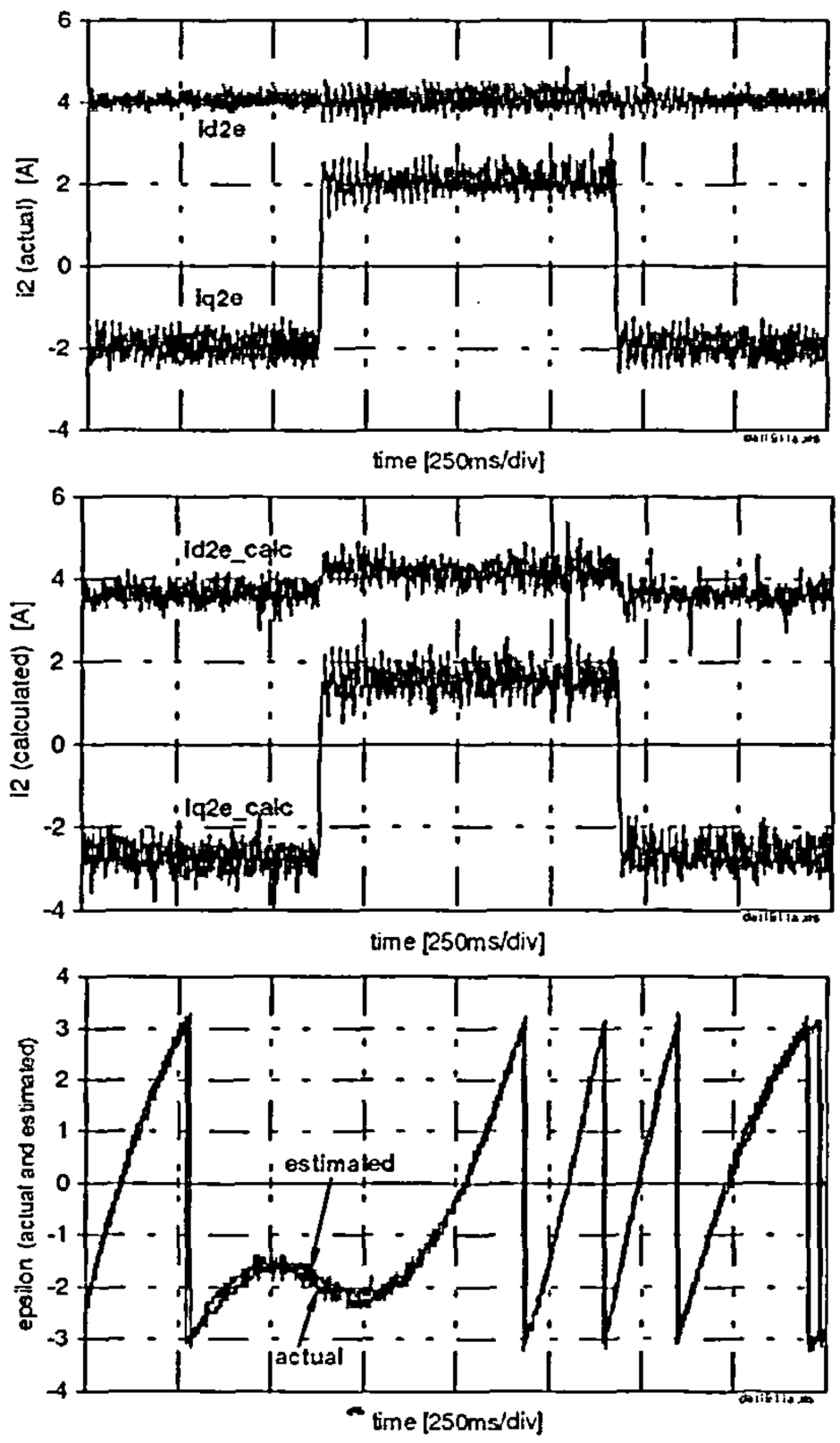

Figure 6.4: Experimental SDFM dynamics of actual and estimated i_2^{e} with sensor in use - current control loop

(i_{d2}^{e*} = 4 A , i_{q2}^{e*} = -2 to 2 A)

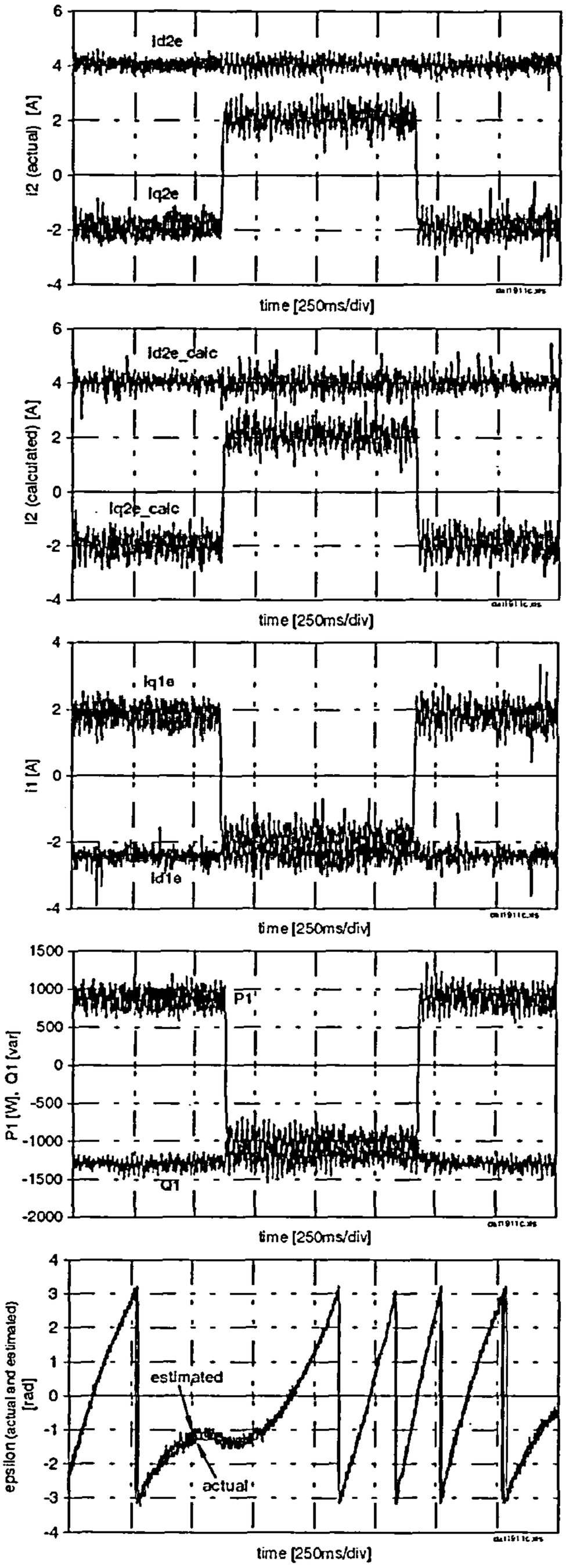

Figure 6.5: Sensorless experimental SDFM dynamics - current control loop

($i_{d2}^{e*} = 4$ A , $i_{q2}^{e*} = -2$ to 2 A)

Figure 6.4 displays results for the inner current control loop of the actual and the calculated rotor current in the "e"-frame and estimated angle ε, with having the position sensor still in place. It can be seen, that the calculated rotor current, necessary to give the angle $\bar{\chi}$, shows the same slight cross coupling, caused by $R_1 \neq 0\ \Omega$, as known from figure 3.29 for the stator current components in the "e"-frame. Despite this, the actual and the estimated ε are almost identical.
This cross coupling in the calculated rotor current disappears within the inner current loop, when the sensorless control is in place as seen in figure 6.5. The actual and the calculated rotor current components show similar values, with $i_2{}^e{}_{calc}$ having a slightly higher ripple content. The estimated and the actual angle ε are in very close agreement and the sensorless current control loop shows no detrimental performance in comparison to the current control loop with position sensor apart from a marginally higher ripple content in various quantities.

Experimental results for a stator power control loop, with position sensor, are shown in figure 6.6. A PI-controller for the stator active power is cascaded in the q-axis of the inner current control loop to deliver the demand q-axis rotor current. Again, $i_{d2}{}^{e}{}^{*}$ is kept at 4 A. As known from chapter 3, decoupled active and reactive power control is achieved.
In comparison, sensorless control results for the stator active power control are illustrated in figure 6.7. The sensorless power control introduces a marked ripple content in P_1 and $i_{q2}{}^e$, whereas this is not the case in the d-axis. Despite the increased ripple, the control is still useable.

Sensorless control in this chapter and [a7] has so far only dealt with the application of the control for a power loop. However, by further developing the applied principle a novel way for a sensorless speed control loop can be derived.
Considering the angles in figure 6.1, it can be seen, that the rotor position angle Θ_r can be estimated in the way $\Theta_r = \mu - \varepsilon$. The angle μ is known from the stator voltage measurement and the angle ε can be constructed as displayed in figure 6.2. Differentiating the acquired rotor position angle delivers the rotor speed in electrical rad/s as

$$\omega_r = \frac{d\Theta_r}{dt}$$

This signal can be used to form a speed feed-back and thus apply a sensorless speed control to the SDFM.

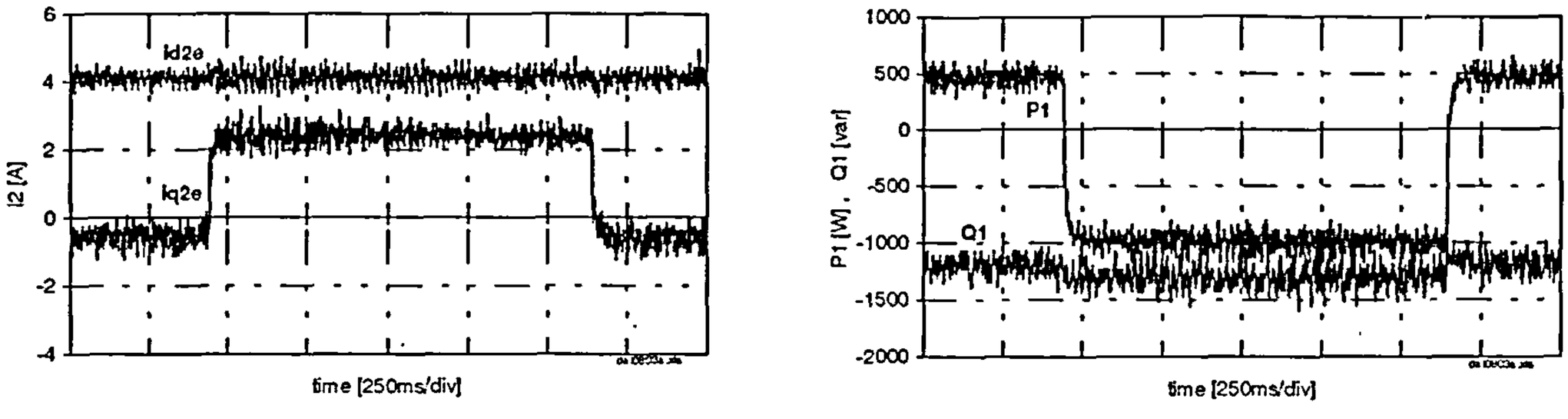

Figure 6.6: Experimental SDFM dynamics for P_1-control with position sensor

($i_{d2}^{e}* = 4$ A, $P_1* = 500$ to -1000 W)

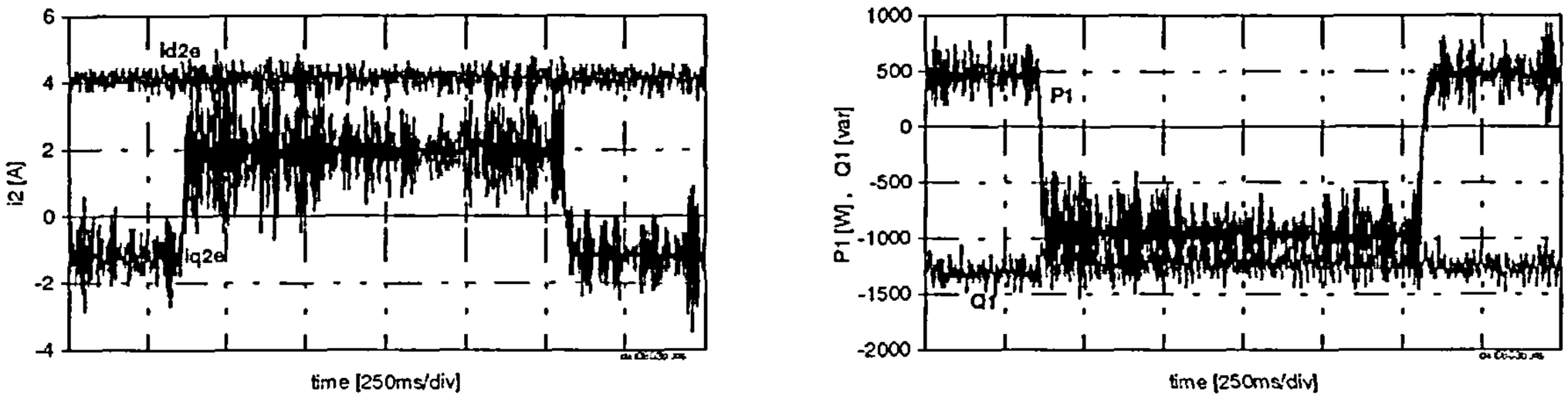

Figure 6.7: Sensorless experimental SDFM dynamics for P_1-control

Method A

($i_{d2}^{e}* = 4$ A, $P_1* = 500$ to -1000 W)

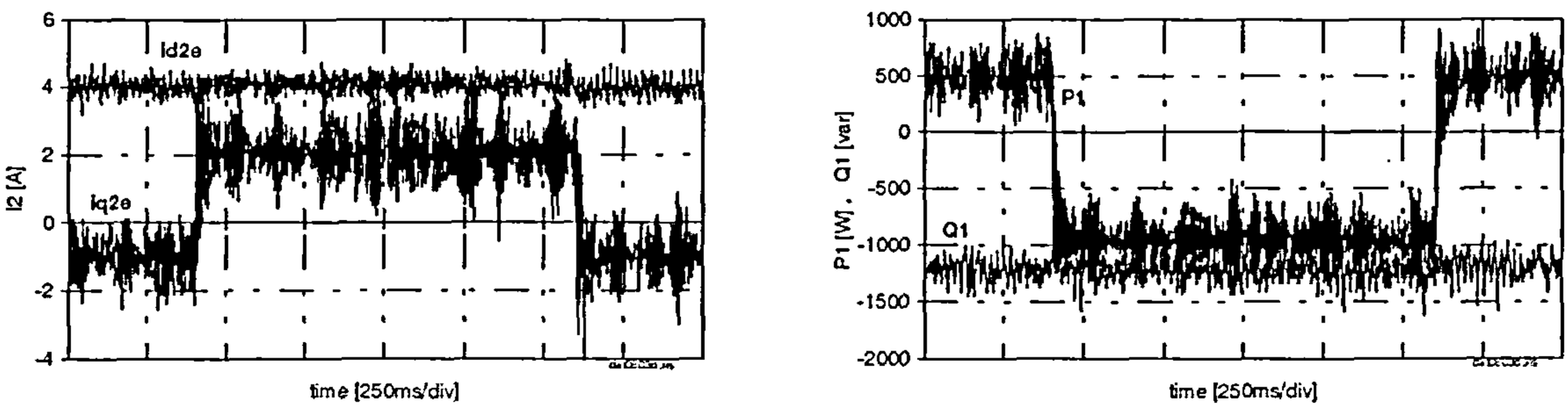

Figure 6.8: Sensorless experimental SDFM dynamics for P_1-control

Method B

($i_{d2}^{e}* = 4$ A, $P_1* = 500$ to -1000 W)

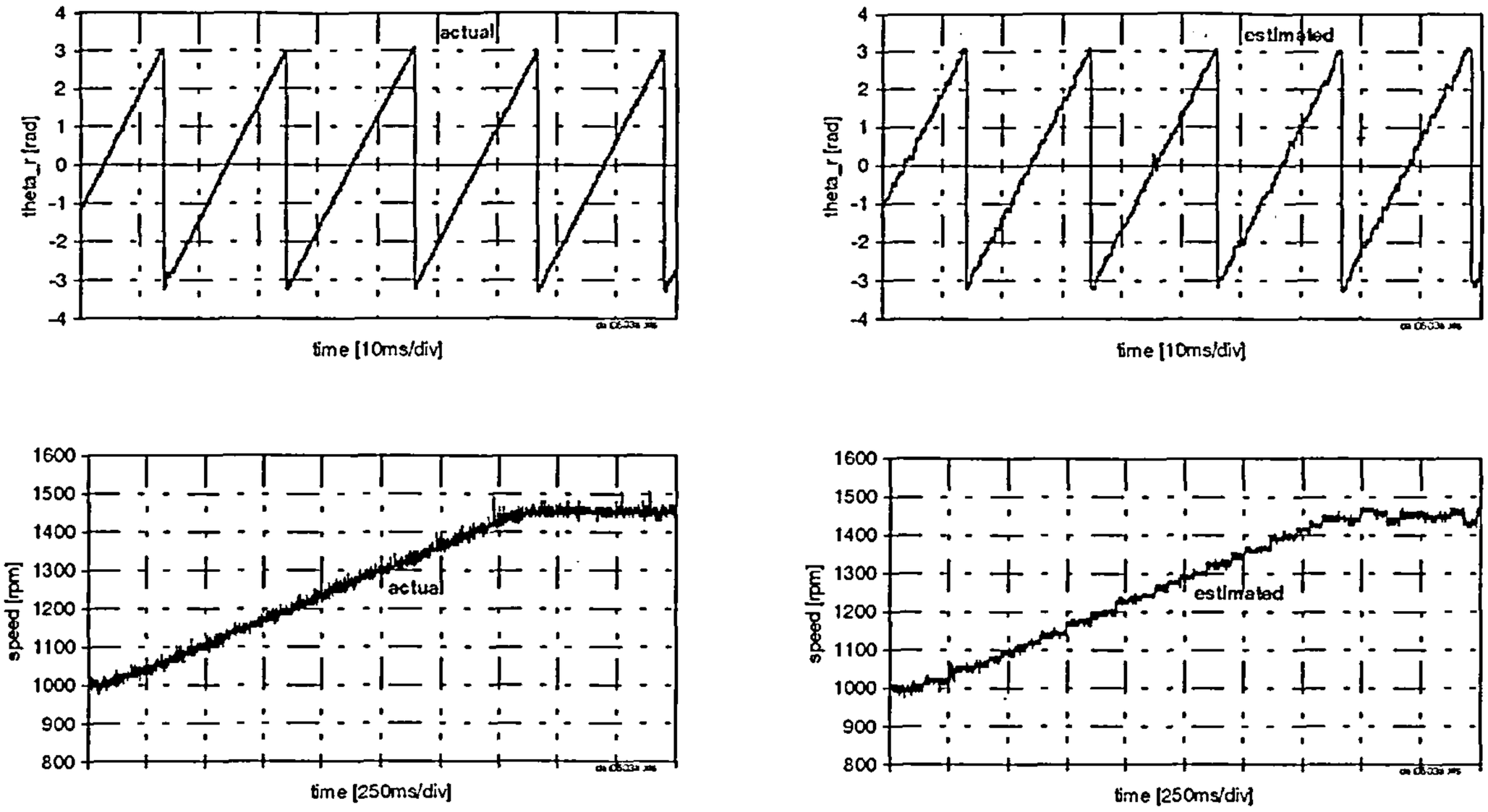

Figure 6.9: Actual and estimated rotor position angle Θ_r and rotor speed ω_r

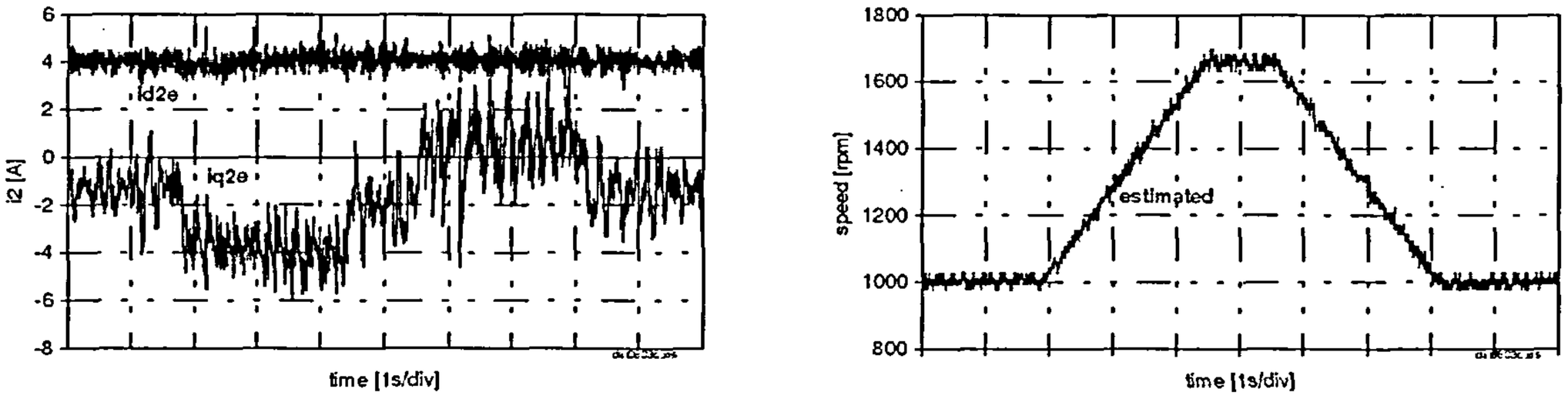

Figure 6.10: Sensorless experimental SDFM dynamics for speed control

Method A ($i_{d2}^{e*} = 4$ A, $n_m^* = 1000$ to 1650 rpm, no-load)

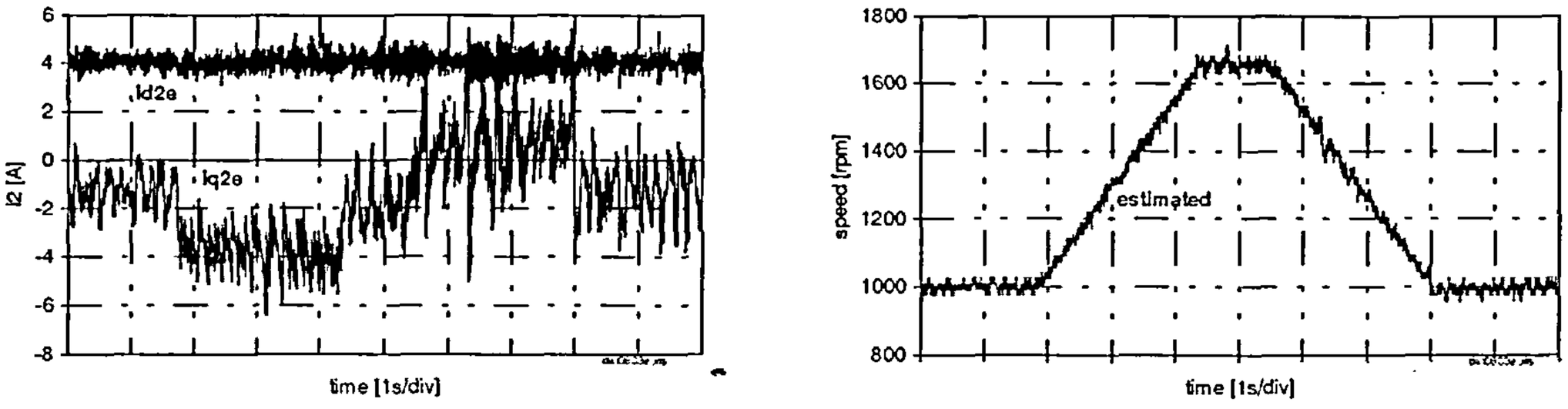

Figure 6.11: Sensorless experimental SDFM dynamics for speed control

Method B ($i_{d2}^{e*} = 4$ A, $n_m^* = 1000$ to 1650 rpm, no-load)

It has to be mentioned that a sensorless speed and reactive power control for a SDFM is described in [a9]. However, the method used is different. A "torque angle" signal is introduced from which a speed feed back signal can be derived.

Figure 6.9 shows the actual and the estimated rotor position angle ("theta_r" in the graphs). Both angles are in very close agreement. However, the estimated Θ_r displays a more coarse wave form compared to the actual signal.
The actual and the estimated speed signal for a speed ramp from 1000 to 1460 rpm is also displayed in figure 6.9. Here, the estimated speed signal shows a more "stepwise" speed variation compared to the actual signal, due to the following reason. The differentiation of the estimated rotor position angle for every switching cycle yields a very spiky speed signal with the mean value of the actual speed. That is because the gradient of the estimated rotor position angle is not monotonic as is the case with the actual rotor position angle obtained from the encoder signals. In other words, the successive rotor position values for every cycle may not increase in a steady manner. The time for differentiation is therefore increased to 18 cycle times to reduce this problem. The calculated speed signal therefore remains constant for 18 cycle times and allows only a stepwise variation.
An increased angle resolution may improve the speed signal. The implemented code has an angle resolution of 0.9° defining 400 values for the angle range 0-2π.

Nevertheless, sensorless speed control results are shown in figure 6.10. The speed demand performs a speed ramp from 1000 to 1650 rpm and back covering sub- and supersynchronous speed. The estimated speed signal in figure 6.10 is used as a feed-back for the PI-controller in the q-axis. It can be seen that the q-axis current i_{q2}^e contains "spike-blocks" over the 18 cycle times used for the speed calculation. The d-axis current remains unaffected. Despite the stepwise speed values the SDFM follows the desired speed ramp surprisingly well. Compared to the speed loop results of the SDFM with sensor, in figure 3.34, the dynamic speed variation had to be reduced for the sensorless case to cater for the averaging 18 cycle calculation.

The method so far ("Method A") uses the stator currents for the calculation of the rotor current and hence the angle χ. Analysis in chapter 3 has shown that the rotor current components are proportional to the stator active and reactive power. Consequently, instead of stator current the stator active and reactive power could be used to calculate the rotor current in the form

$$i_{d2\,calc}^e = \frac{1}{L_m}\Psi_{d1}^e - \frac{2}{3}\frac{L_1}{\sqrt{2}V_1 L_m}Q_1 \qquad (6.1.3)$$

$$i_{q2\,calc}^e = -\frac{2}{3}\frac{L_1}{\sqrt{2}V_1 L_m}P_1 \qquad (6.1.4)$$

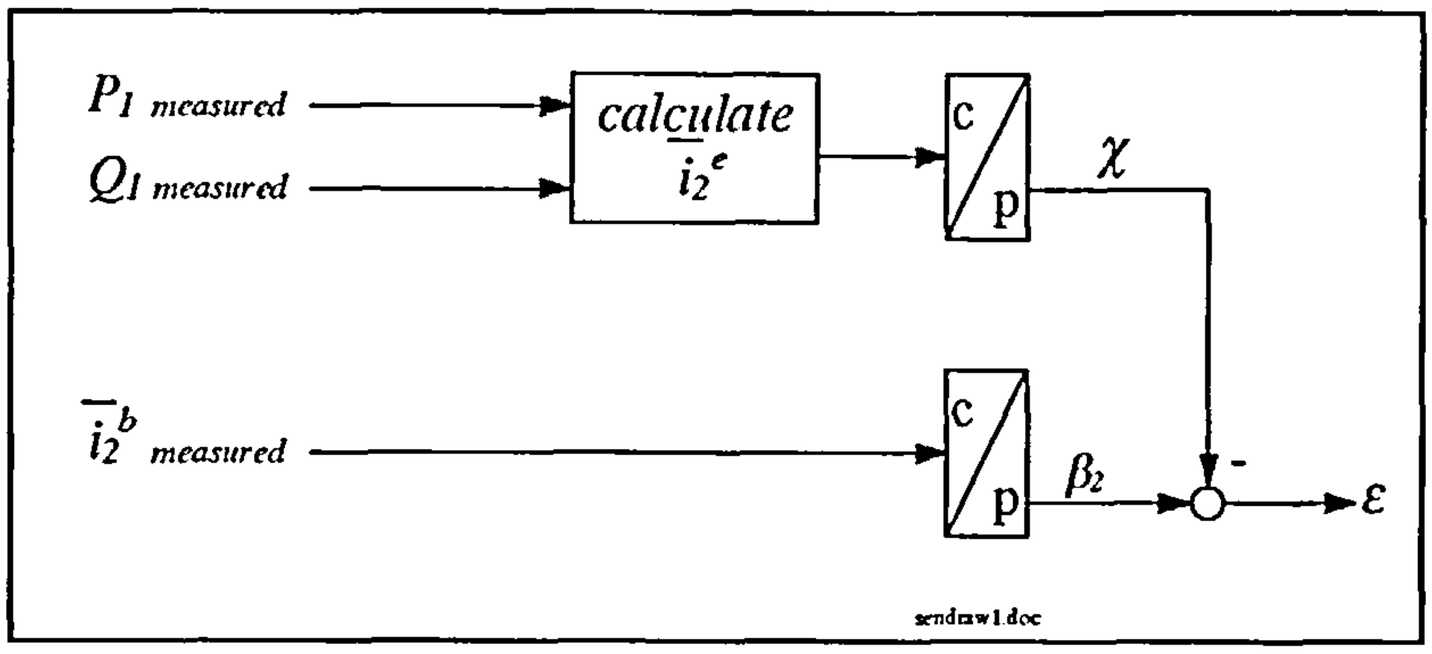

Figure 6.12: Angle construction method of the sensorless SDFM from power measurements ("Method B")

The resulting angle construction method ("Method B") is illustrated in figure 6.12.

In comparison to Method A, the angle construction method in figure 6.12 does not contain the transformation block, necessary for the stator current, and so can be seen as a simpler method, as long as the SDFM is used for power control, since Method B makes it necessary to calculate P_1 and Q_1 in real time.

Simulation results of a position sensorless SDFM control are presented in [a8]. In this paper the power measurements are also utilised to calculate the rotor current in the "e"-frame. The power control method however is different. A so called "angle controller", comparing to angle signals, delivers the demand value for the current loop.

The same power control and speed control as for Method A are performed with the angle construction Method B and results are displayed in figure 6.8 and 6.11, respectively.
Perfectly decoupled power control is accomplished as can be seen in figure 6.8, and the ripple content in the q-axis is still as high as it is in figure 6.7.
The speed loop results, in figure 6.11, show no significantly different wave forms in comparison to figure 6.10, and the SDFM machine set follows the demanded speed with a good response. Although, there is no visual difference in the calculated speed waveforms, the speed control with Method B was acoustically inferior to Method A.

Comparing Method A with Method B, it can be said that both methods are equally applicable for power and speed control of the SDFM. This should be no surprise, since in the "e"-frame the active power is directly proportional to i_{q1}^e and the stator reactive power to i_{d1}^e.

The complete sensorless control structure for the SDFM is displayed in figure 6.13.

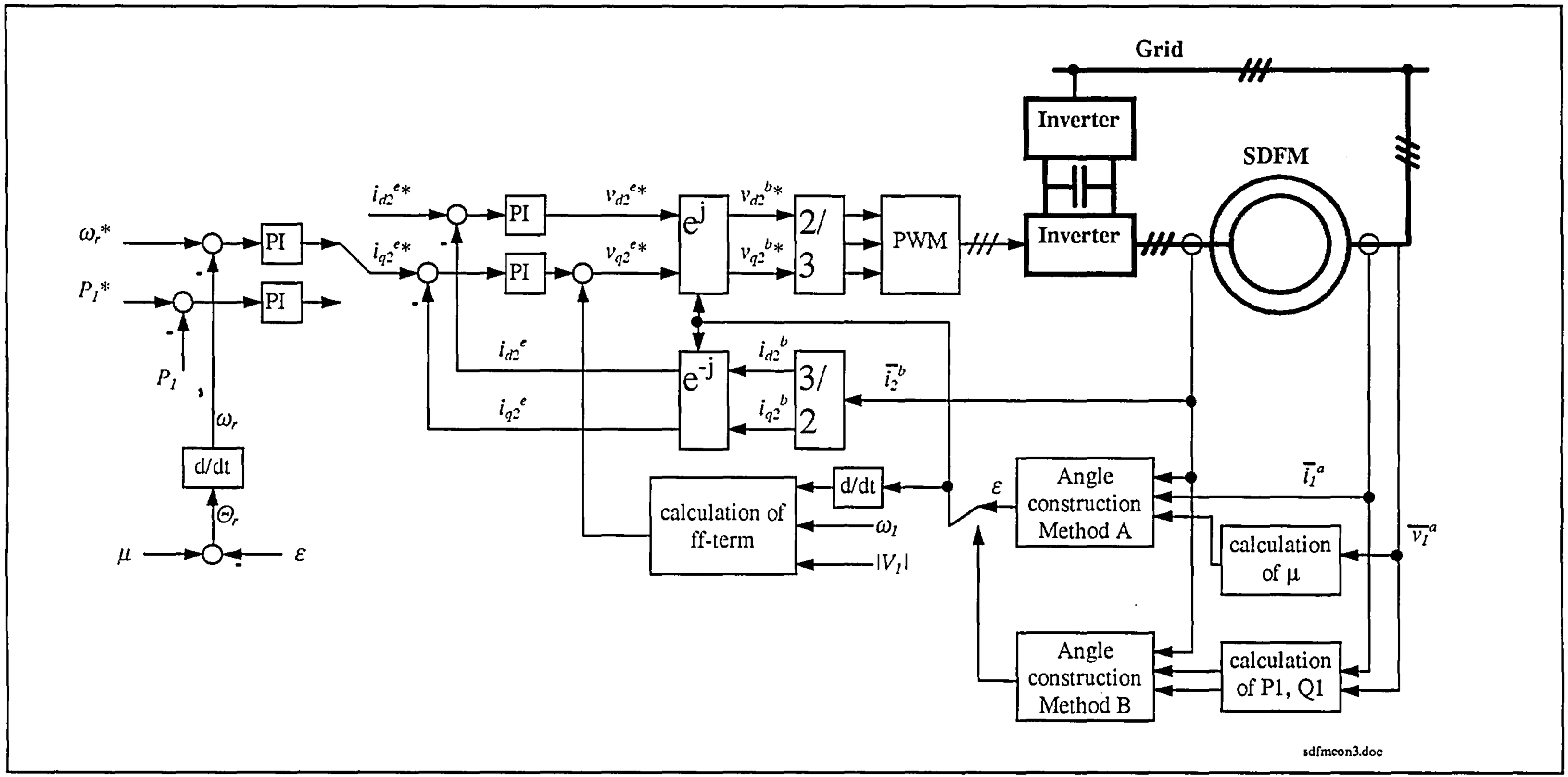

Figure 6.13: Sensorless SDFM control structure - Method A and Method B

The feed forward term included in figure 6.13 requires the slip frequency for calculation as equation (3.3.27) shows. For the sensorless control this can be obtained by differentiating the estimated angle ε in the same way as Θ_r is differentiated.

6.2 Sensorless Control of CDFM

Analysis of the CDFM field oriented control for the stator flux reference frame has shown, that the control behaviour of the CDFM is similar to the SDFM, except for a cross coupling caused by the rotor circuit loop in the CDFM. Experimental results indicated that the cross coupling has a certain effect on the control, but the influence remains limited within the overall control concept. This would suggest, that the SDFM sensorless methods may be applicable to the CDFM. In the following the sensorless Method B of the SDFM is applied to the stator flux oriented CDFM control.

The sensorless Method B used for the CDFM gives an angle construction method as shown in figure 6.14. The angles considered are illustrated in figure 6.15.

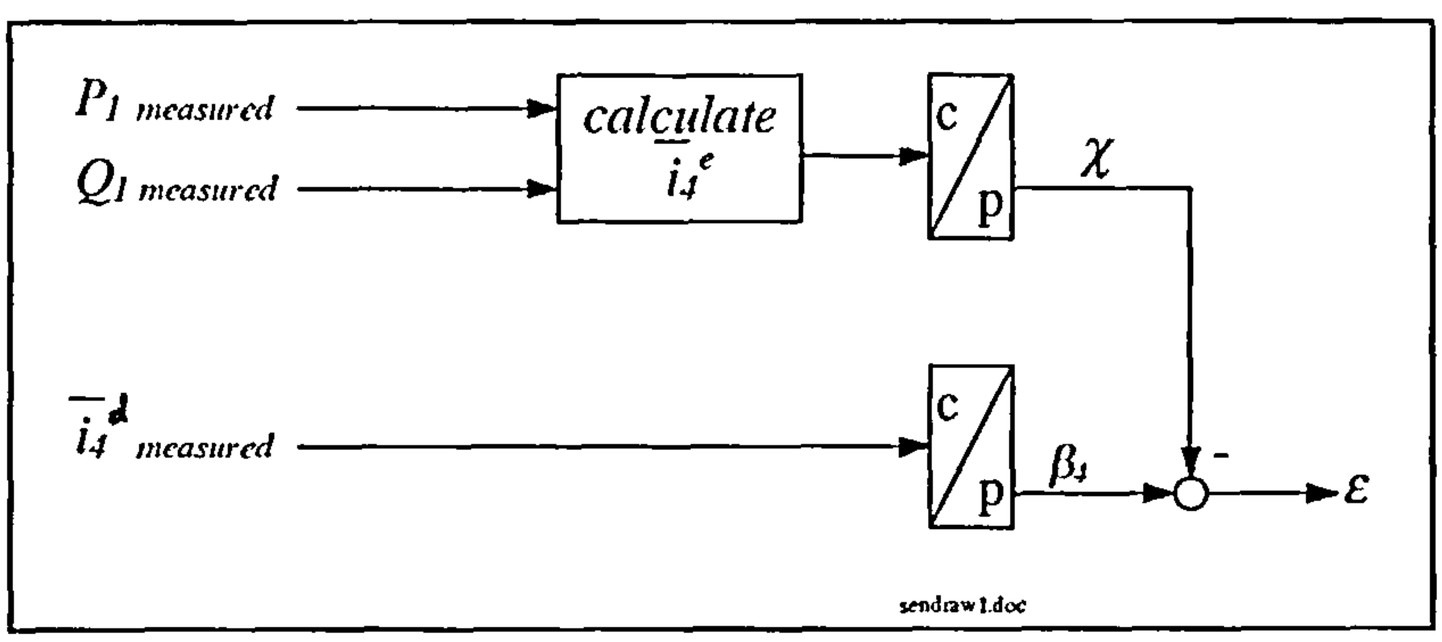

Figure 6.14: Angle construction method of the sensorless CDFM from power measurements ("Method B")

Utilising the power equation for the stator flux oriented CDFM, the side 4 current components in the "e"-frame can be calculated from the power measurements in the form of

$$i^e_{d4calc} = -\frac{1}{L_{mB}}\Psi^e_{dR} + \frac{L_R}{L_{mA}L_{mB}}\Psi^e_{d1} + \frac{2}{3}\frac{k_2}{\sqrt{2}V_1 L_{mB}}Q_1 \qquad (6.2.1)$$

$$i^e_{q4calc} = -\frac{1}{L_{mB}}\Psi^e_{qR} + \frac{2}{3}\frac{k_2}{\sqrt{2}V_1 L_{mB}}P_1 \qquad (6.2.2)$$

It can be seen that the cross coupling due to Ψ_R^e effects the angle χ in the angle construction method as displayed in figure 6.14. Thus, the effect would be seen in the angle ε, needed for the transformation of the side 4 current into the "e"-frame and back.

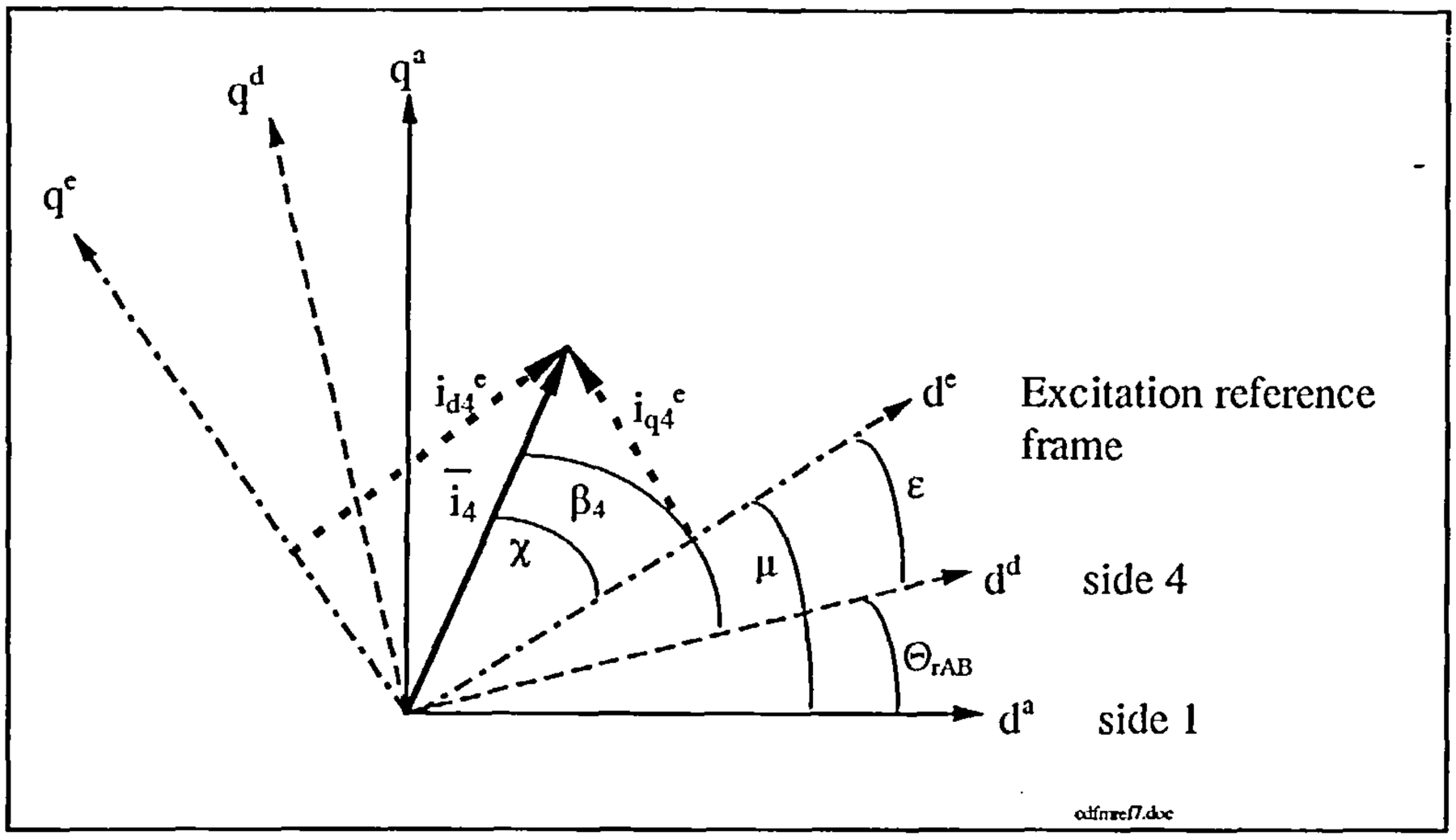

Figure 6.15: Reference frames and angles for the sensorless CDFM control

Experimental results in figure 6.16 show, that the influence of the cross coupling in equation (6.2.1) and (6.2.2) is not very severe so that the actual and the estimated angle ε are still in very close agreement. The left column of figure 6.16 shows results for the inner current control loop with the position sensor in place and the right column gives the results for the sensorless case.

The cross coupling as visible in the sensored calculated i_4^e current is stronger in $i_4^e{}_{calc}$ for the sensorless case. Also, the ripple content for the sensorless method is higher than it is for the sensored method.

Considering figure 6.17 and figure 6.18, where the power control results for sensored and sensorless case are presented, it can be seen that the cross coupling effect in Q_1 increases slightly with the sensorless method. This is an amplified effect of the cross coupling in the first place. The angle ε for the sensorless case differs slightly from the actual angle ε. As a consequence the field orientation performance is reduced which causes an increased cross coupling effect. Despite that, sensorless control is still applicable to the CDFM as displayed in figure 6.18, There is, however, a higher ripple content in i_{q4}^e and P_1.

Regarding a sensorless speed control application for the CDFM, the angle between side 1 and side 4 can also be calculated from the acquired angle ε by a subtraction of $\Theta_{rAB}=\mu-\varepsilon$. The rotor angle follows as

$$\Theta_{rA} = \frac{p_A}{p_A + p_B}\Theta_{rAB}$$

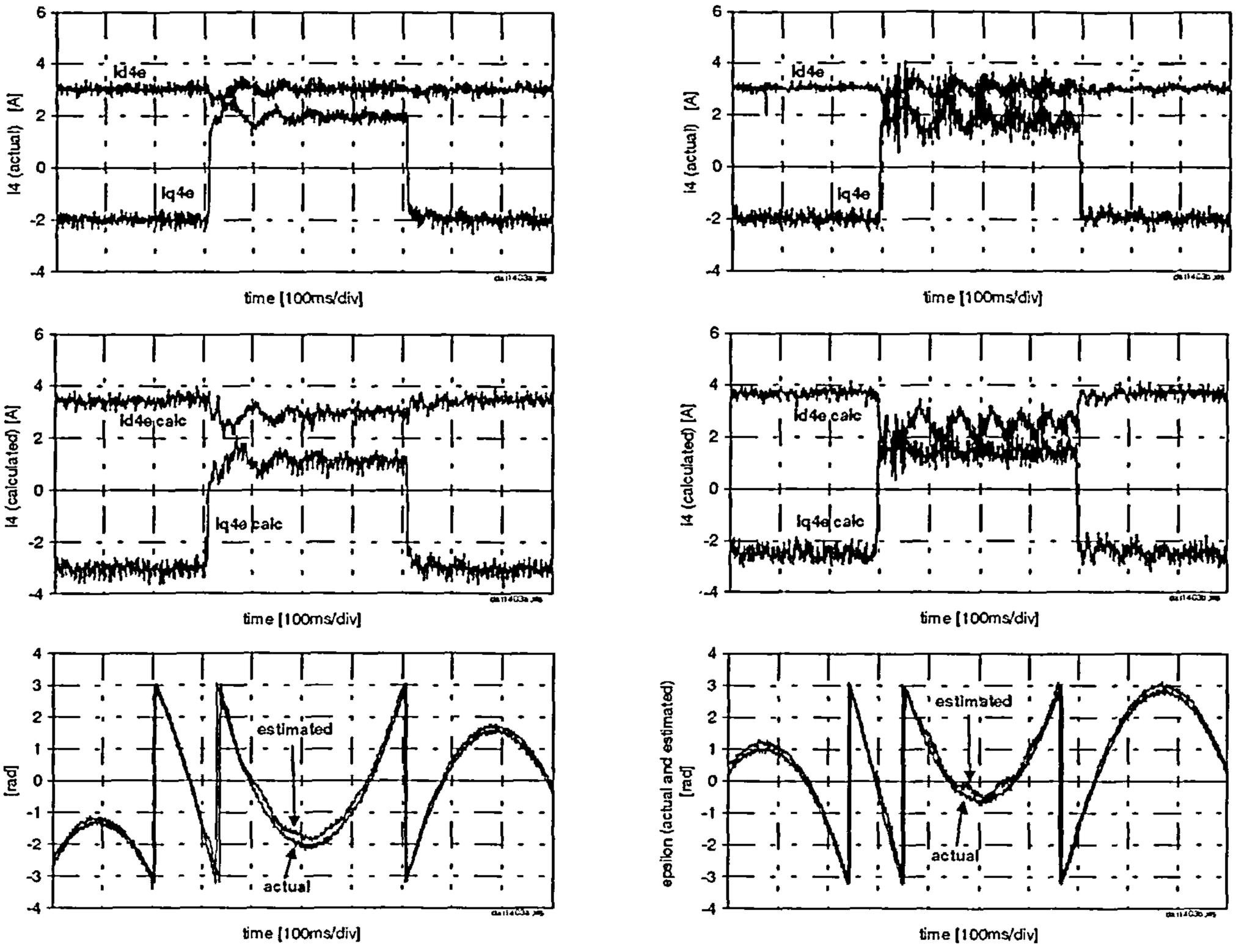

Figure 6.16: Experimental CDFM dynamics - current control loop
left column: with sensor right column: sensorless
($i_{d4}^{e*} = 3$ A , $i_{q4}^{e*} = -2$ to 2 A)

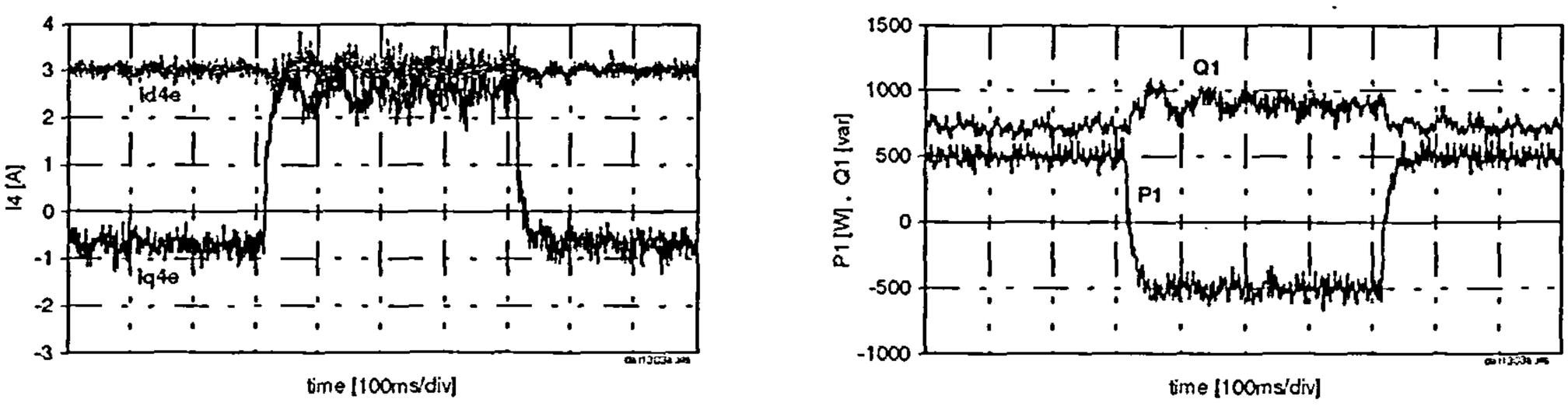

Figure 6.17: Experimental CDFM dynamics for P_1-control with position sensor
($i_{d4}^{e*} = 3$ A , $P_1^* = 500$ to -500 W)

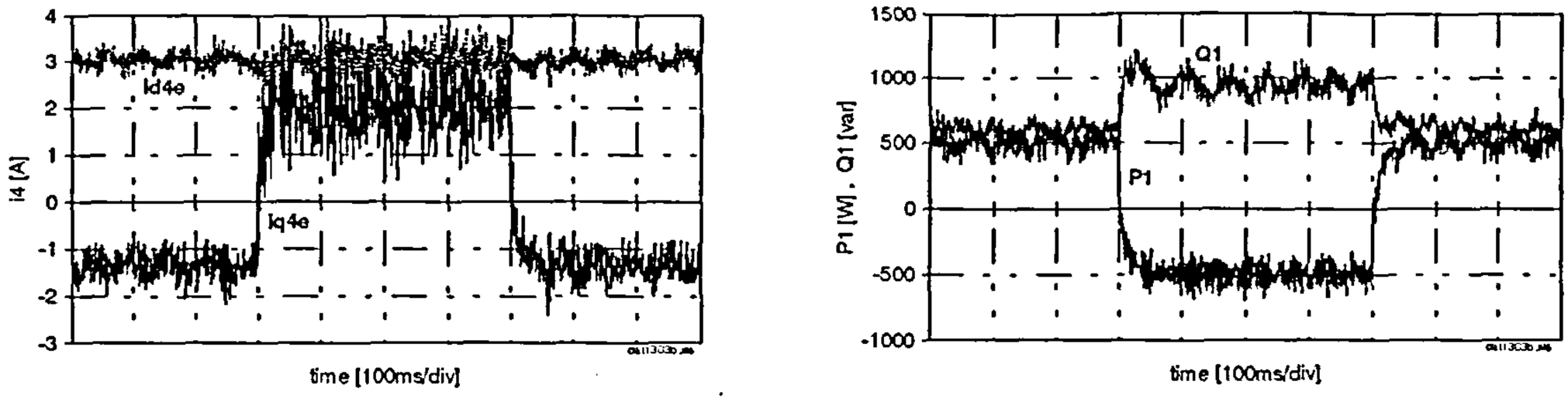

Figure 6.18: Sensorless experimental CDFM dynamics for P_1-control

(i_{d4}^{e}* = 3 A , P_1* = 500 to -500 W)

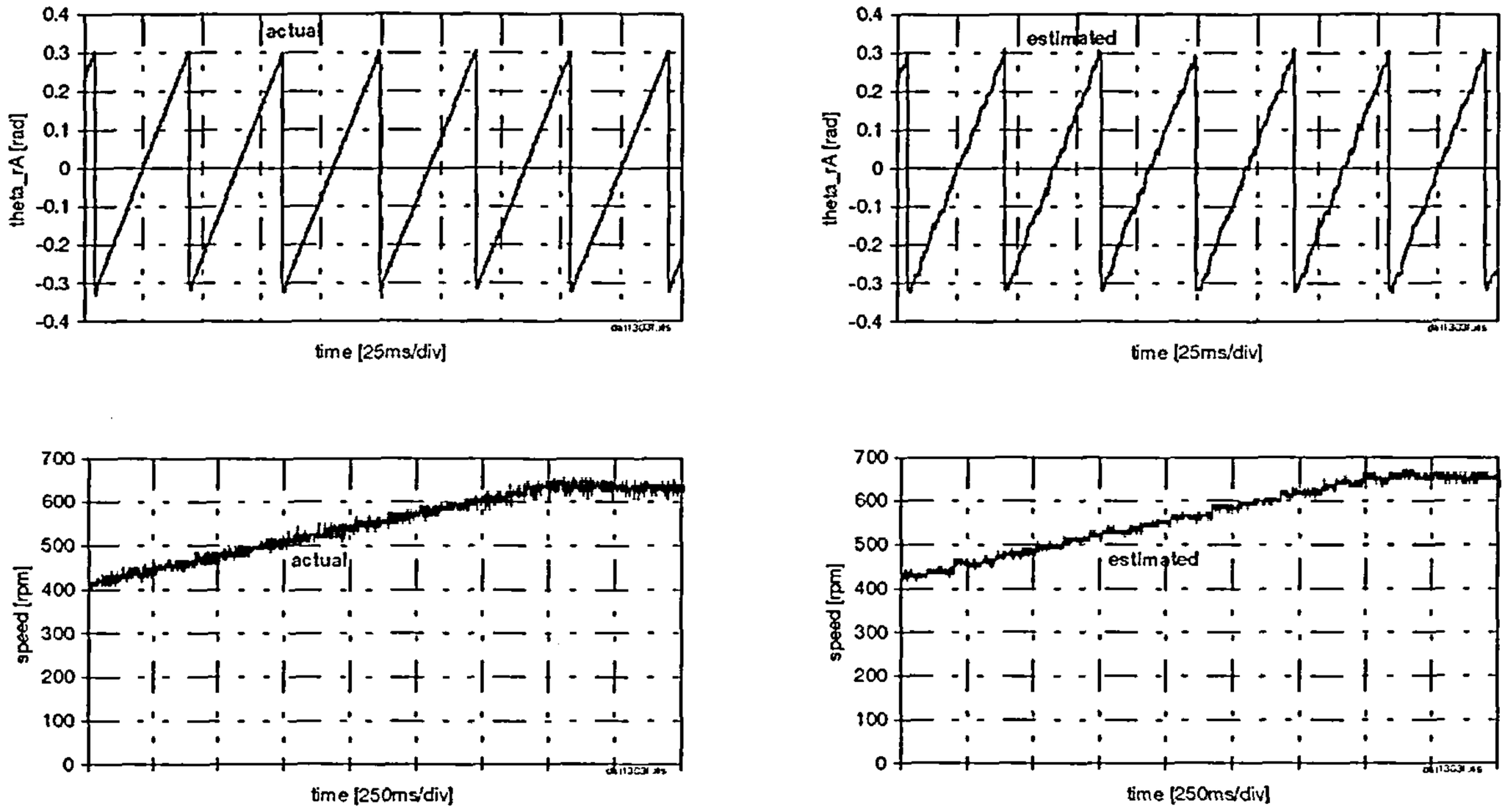

Figure 6.19: Actual and estimated rotor position angle Θ_{rA} and rotor speed ω_{rA}

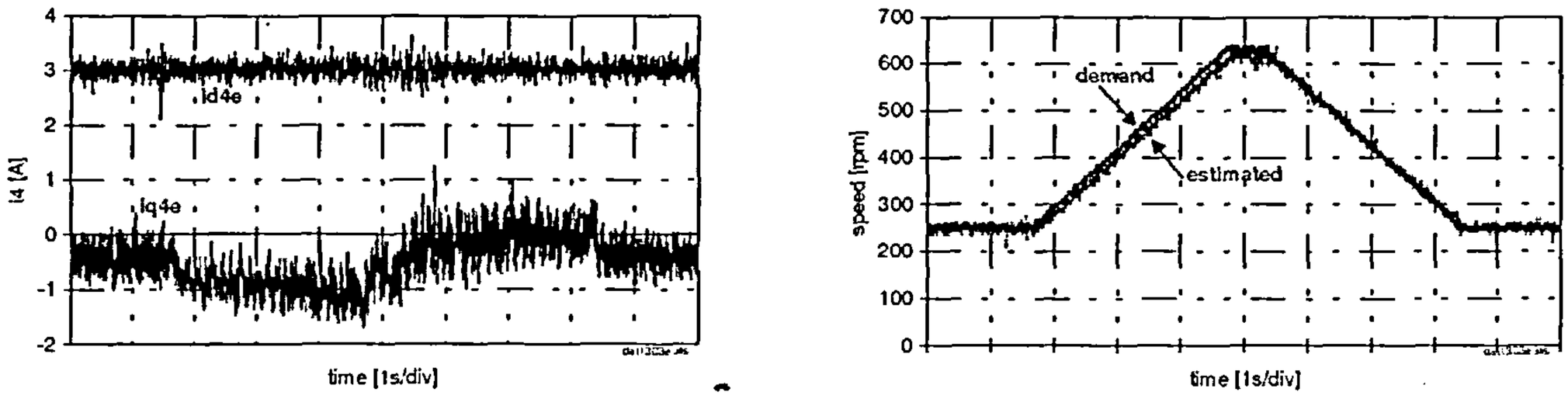

Figure 6.20: Sensorless experimental CDFM dynamics for speed control

(i_{d4}^{e}* = 3 A , n_m* = 250 to 630 rpm)

The differentiation of this angle can be used to form a speed control loop as for the sensorless SDFM. Angle and speed results for sensored and sensorless current control loop are displayed in figure 6.19.

Similar to the SDFM case the calculated angle Θ_{rA} contains notches and the calculated speed graph has a step wise shape due to the differentiation over more than one cycle. Apart from that, the actual and the calculated angle and speed values show a good coincidence.

Sensorless speed control results are given in figure 6.20. The ripple content is higher in i_{q4}^{e} and the dynamic speed demand ramp had to be lowered in comparison to the sensored case in figure 5.26, but sensorless speed control is still feasible.

As a conclusion it can be said that the sensorless method for the SDFM can also be applied to the CDFM, despite the inherent cross coupling caused by the rotor circuit loop.

6.3 Summary

This chapter presents sensorless control results for the SDFM and the CDFM. A sensorless control principle described in [a7] is applied to the SDFM and an alternative calculation method for the required angle is shown, which leads to similar results.

Extending the sensorless control methods and differentiating the acquired angles forms the basis for a novel sensorless speed control method for the SDFM.

It is shown that a sensorless control method developed for the SDFM can be applied to the stator flux oriented CDFM control.

For SDFM and CDFM, the sensorless control leads to proper stator active power control and speed control, with the drawback of an increased ripple contents in various quantities and a reduced dynamic performance for the speed control.

Chapter 7

Harmonic Analysis , Simulation and Modeling

Field Oriented Control of the SDFM and the CDFM is based only on the fundamental waveforms of the different machine quantities. All other harmonic waveforms are ignored. However, the experimental laboratory set-up is exposed to various harmonic producing sources, which are dissected in the following.

A detailed analysis of the distribution and transmission of the current harmonics within the SDFM and CDFM is one aspect of this chapter. In addition an investigation into whether a steady state model can be used to model the harmonic machine current distribution in the system, as a result of the inverter voltage harmonics. If correct then the model could be employed as a tool for theoretical harmonic analysis.

7.1 Sources and Effects of Harmonics

The stator of the SDFM is connected to the supply network and the rotor is fed by a voltage source inverter, as shown in figure 7.4. Similarly, the CDFM is connected to the supply on side 1 and side 4 is supplied by an inverter, as depicted in figure 7.9. Therefore, the complete drive system offers three different sources of supply harmonics. The supply network, the machine-side inverter and the line-side inverter. Additionally, the machine itself can be a source of various harmonics. All of these harmonic sources have certain effects on the system as discussed later.

Before that, the sampling and harmonic calculation process is briefly described: Integer multiples of the respective fundamental of the various waveforms of voltages and currents (see Appendix G for waveform plots) are sampled with a digital oscilloscope giving a value-over-time series. That time series is processed by the digital computer with the help of the FFT capabilities of MATLAB creating the frequency spectrum of the sampled quantity (further information on FFT *is* in Appendix F). Sample frequency and frequency resolution for each frequency spectrum are noted next to the figures.
All frequency spectrum graphs are presented in percentage form of the fundamental, giving a normalised view of the harmonic amplitudes. Only figure 7.2 and 7.3, where the FFT is carried out by the digital oscilloscope, give the absolute value of the harmonics.

7.1.1 Harmonic Sources

Supply network

The line-line and the phase voltage harmonics of the supply voltage are measured and displayed in figure 7.1. It can be seen, that harmonics of the order $(m6\pm1)f_1$ with m=1,2,3,.. are present in the line-to-line and the phase voltage. The phase voltage spectrum contains also triplen harmonics, which will not appear in the line-line voltage.

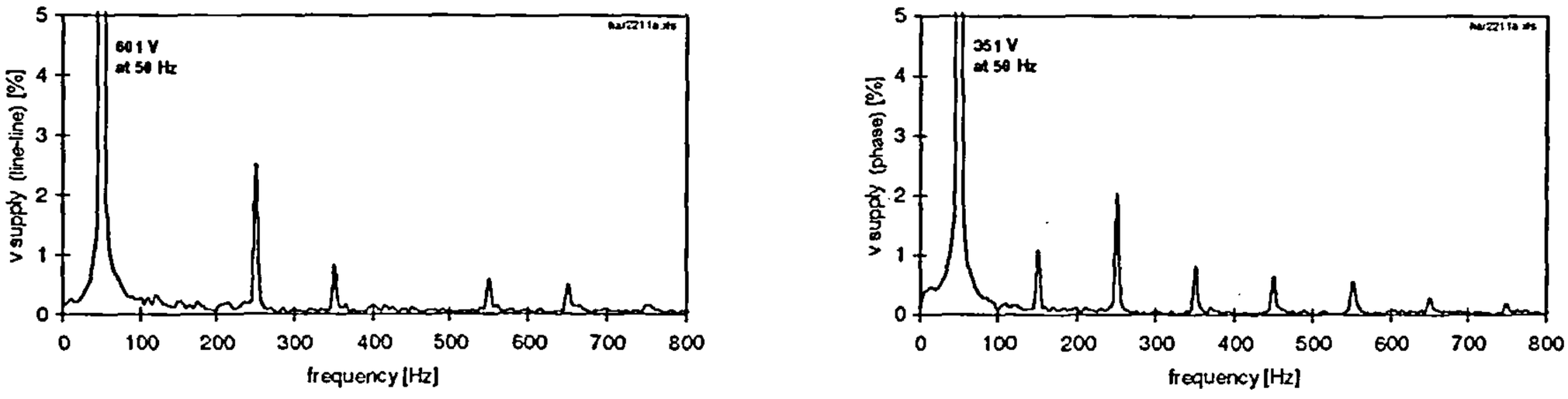

Figure 7.1: Harmonics of the supply network voltage (left: line-line , right: phase)

($\Delta f = 5$ Hz , 5 kS/s)

The fundamental, the 7th and the 13th harmonic of the line-line voltage are of positive phase sequence and the -5th and the -11th are of negative phase sequence [f4].

Line-Side Inverter

The line-side inverter of the bi-directional converter has a carrier or switching frequency of

$$f_{c\_y} = 7.45\ kHz.$$

As exemplified in figure 7.4, the line-side inverter is connected via inductors with the supply network to reduce the high frequency ripple on the current. As a controlled front-end, which produces unity power factor at its connection point, the inverter controls the d.c.-link voltage to 650 V.

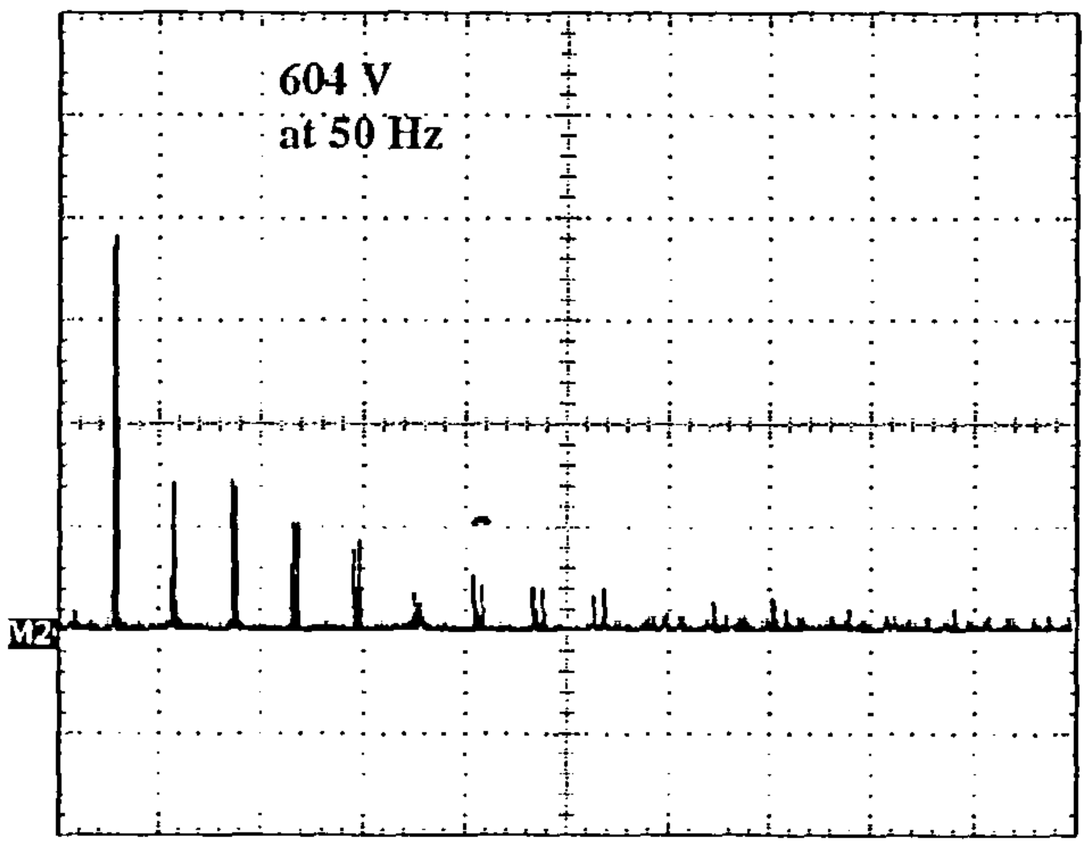

Figure 7.2: Harmonics of the line-line voltage v_y of the line-side inverter

(x-axis: 12.5 kHz/div y-axis: 10V/div , $\Delta f = 5$ Hz , 250 kS/s)

Figure 7.2 shows the frequency spectrum of the line-line voltage at the output terminals of the inverter with the typical spectrum of a PWM inverter producing harmonic side-bands centered around the multiples of the switching frequency [f16].

Machine-Side Inverter

Another source of voltage harmonics is the machine-side inverter, which has a switching frequency of

$$f_{c\_m} = 2.5\ kHz.$$

The harmonics of the line-line voltage v_2 are displayed in figure 7.3. (see section 7.2.1 for operational point details). The modulation index for the machine-side inverter at the operational point is small (≈0.24) and as elaborated in [f17], this causes the harmonic side-bands centered around the even multiples of the switching frequency to be more dominant than those centered around the odd multiples.

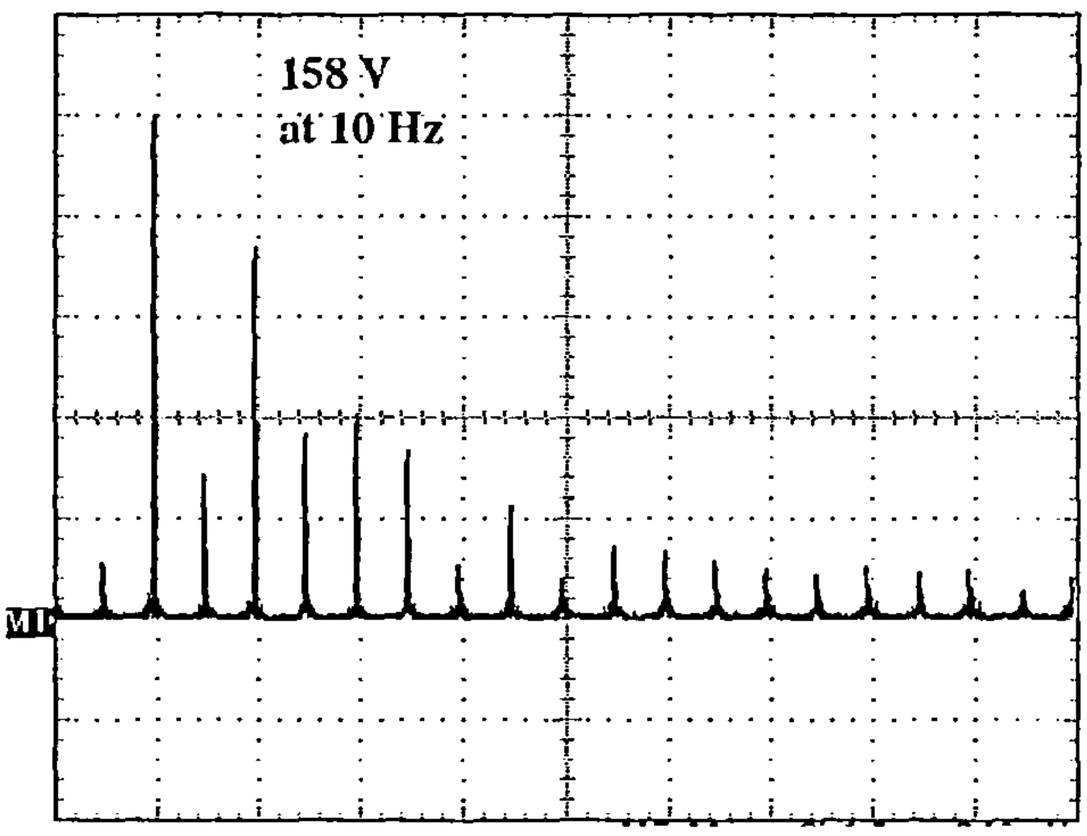

Figure 7.3: Harmonics of the line-line voltage v_2 of the machine-side inverter at 1200 rpm for the SDFM (x-axis: 5 kHz/div y-axis: 20V/div , Δf = 2 Hz , 100 kS/s)

The space vector PWM scheme for the machine-side inverter switches two voltage vectors within one switching period and therefore has an effective switching frequency of the line-line voltage of double the phase leg switching frequency. With increasing modulation index the dominant appearance of the side-band harmonics around the even multiples reduces and the odd multiple side-bands increase in amplitude [f17] (see also Appendix G for simulation studies and switching waveforms).

Electrical Machine

Harmonics created by an electrical machine are mainly due to constructional constraints on the machine design. Important ones are the slot harmonics, the effects of which can be mitigated by skewed rotor bars, and harmonics caused by the stepwise shape of the resultant m.m.f. wave in the machine. Those harmonics are in the order of $(m6\pm1)f_1$ with m=1,2,3,... Their influence on the 3-phase voltages can be reduced by pitching [f8].

Other Harmonic Sources

Other harmonics can be created by saturation effects in electrical machines and transformers connected to the supply network. Also p-pulse rectifier circuits connected to the supply network produce harmonics of the order (*m*p-pulse±1*) with m=1,2,3,.. [f27].

7.1.2 Effects of Harmonics

Harmonic currents in general cause additional copper losses in the machine, whereas low-order harmonics are responsible for undesirable torque ripples in the machine. Although the torque harmonics are produced by the harmonic currents, there is no stringent relationship between both of them [f16].
The high-order harmonics produced by the inverters can also cause EMC problems in the surrounding control equipment.

7.2 Harmonic Analysis

The harmonic analysis of the laboratory set-up determines the distribution of the harmonic currents and shows the transmission through the air-gap of the electrical machine. This section is divided into the analysis for the SDFM and a separate analysis for the CDFM.
The analysis is focused on harmonics produced by the power converter.

7.2.1 Harmonic Analysis of the SDFM

The operational point at which the current and voltage harmonics are analysed is:

speed = 1200 rpm , $f_1 = 50$ Hz, $f_2 = 10$ Hz

$V_1 = 420$ V

$i_{d2}^{c}* = 4$ A, $i_{q2}^{c}* = 2$ A

$P_1 \approx -730$ W, $Q_1 \approx -1300$ VAr

modulation index at rotor side = $0.244 = V_{2peak\ line\text{-}line} / V_{DC}$

The complete circuit for the SDFM connection including inductances and resistances is displayed in figure 7.4.

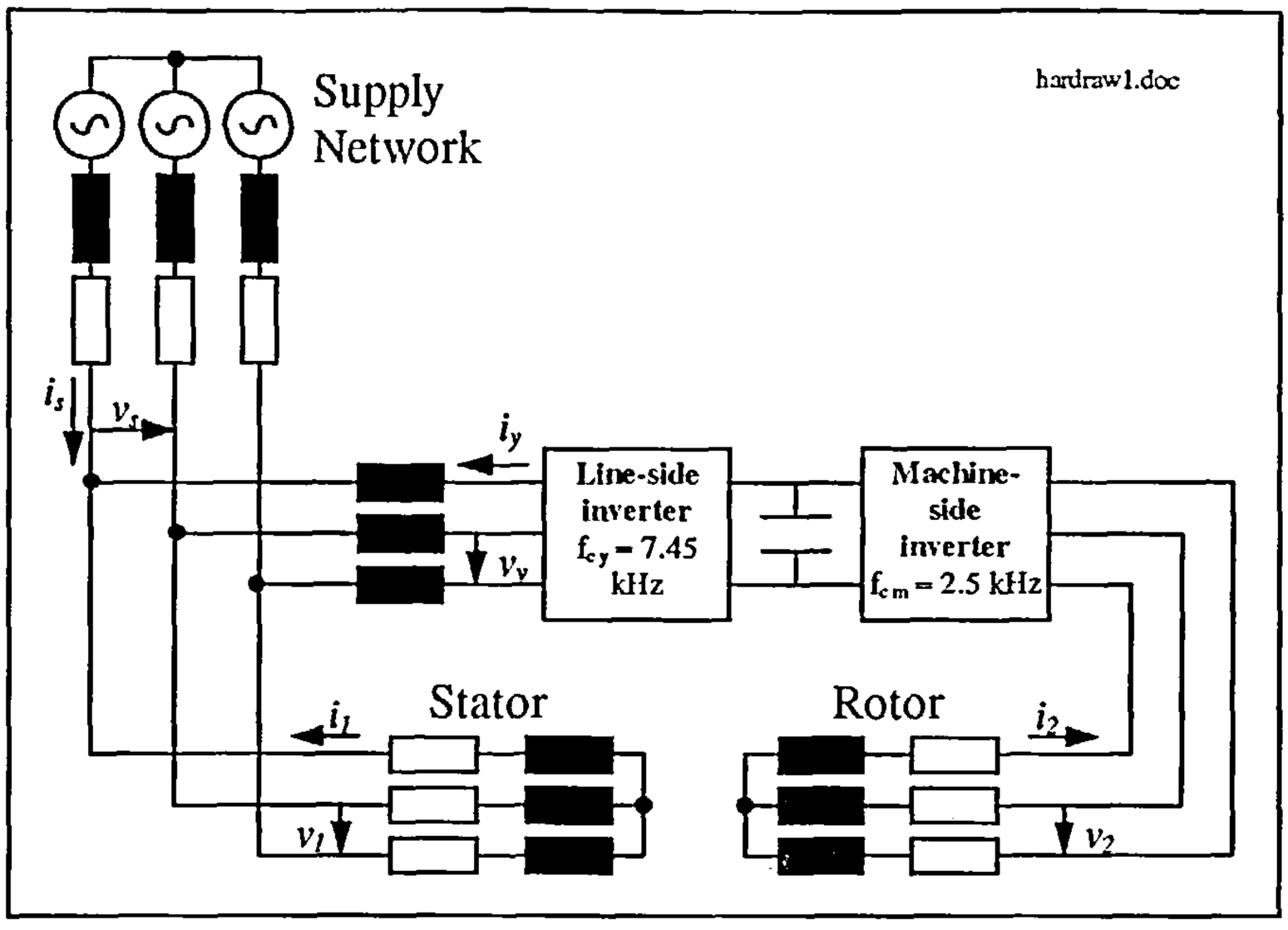

Figure 7.4: SDFM connection circuit

Harmonic spectra at 1200 rpm for the different system quantities as marked in figure 7.4 are shown in figures 7.5 and 7.7. The left column contains the spectrum up to 17.5 kHz and the right column gives the low-frequency range of the respective quantity.

Harmonics due to the machine-side inverter

The machine-side inverter is responsible together with the current control loop to impress the desired rotor current fundamental. As a voltage-source inverter, switching voltage blocks onto the rotor windings, it can be seen that the inverter creates voltage harmonics, v_2 in figure 7.7, and therefore current harmonics, i_2 in figure 7.5, in the rotor circuit with the frequency of $-2f_2 \pm c_1 f_{c\_m}$ with c_1=1,3,5,... producing harmonic side-bands around odd multiples of the switching frequency (2480 Hz, -2520 Hz, 7480 Hz, -7520 Hz, ..) and harmonics of the order $f_2 \pm c_2 f_{c\_m}$ with c_2=2,4,6,... producing harmonic side-bands centered around even multiples of f_{c_m} (-4990 Hz, 5010 Hz, -9990 Hz, 10010 Hz, ..).

The current harmonics present on the rotor side are transformed via the air-gap onto the stator side. At the same time they experience a frequency shift caused by the rotational speed of the rotor, which gives a frequency relation of

$$f_{1v} = f_{2v} + f_{shift} \tag{7.2.1}$$

f_{1v} and f_{2v} are the harmonic frequencies and $f_{shift} = pf_m$ is the mechanical rotor frequency multiplied by the pole pair number. For 1200 rpm $f_{shift} = 40\ Hz$.

The rotor current harmonics act in a first order approximation as a harmonic current source for the stator current harmonics so that the harmonic current magnitude relationship takes the simple form of

$$|i_{1v}| \approx \frac{1}{a}|i_{2v}|$$

with

a as the turns-ratio [f19].

As displayed in figure 7.5 the rotor current harmonics transferred onto the stator side cause a considerable harmonic content in i_1. The frequencies of the stator current harmonics are $(f_{shift}-2f_2)\pm c_1 f_{c\_m}$ with c_1=1,3,5,... (-2480 Hz, 2520 Hz, -7480 Hz, 7520 Hz, ..) and $f_1 \pm c_2 f_{c\_m}$ with c_2=2,4,6,... (-4950 Hz, 5050 Hz, -9950 Hz, 10050 Hz, ..).

The frequency relationship of the current harmonics between rotor and stator for the machine-side inverter produced harmonics can generally be written as:

Rotor	$\Rightarrow$	*Stator*	
$-2f_2 \pm c_1 f_{c\_m}$		$(f_{shift}-2f_2)\pm c_1 f_{c\_m}$	with c_1=1,3,5,...
$f_2 \pm c_2 f_{c\_m}$		$f_1 \pm c_2 f_{c\_m}$	with c_2=2,4,6,...

It has to be mentioned that the harmonic side-bands on the rotor consists not only of one pair centered around the multiple switching frequency, but continuous in the order as described above. However, the amplitude of those is much lower compared to the "first side-band", so that they are not included in this analysis. This applies also to the harmonic side-bands produced by the line-side inverter.

Harmonics due to the supply network

As a second harmonic source the supply network contains low-order voltage harmonics in v_1 (v_s) of the order $(m6\pm 1)f_1$ with m=1,2,3,.. as displayed in figure 7.7 and figure 7.1. These create harmonics with the same frequency in the stator current i_1 and the supply current i_s, as shown in figure 7.5 and 7.7. The significant one is the -5th harmonic (-250 Hz). This stator current harmonic is transferred onto the rotor side with the help of equation (7.2.1) and causes a rotor current harmonic at -290 Hz, which can be written as f_2-6f_1. It can also be seen in figure 7.5 that there is a significant rotor current harmonic at -90 Hz, which leads to the conclusion that there must be a negative fundamental present in the stator voltage causing a stator current harmonic at $-f_1$. The rotor harmonics at -90 Hz and -290 Hz are the most important low-order harmonics in the rotor current and also in the rotor voltage.

The frequency relation for the stator and rotor for the network produced harmonics can be written as

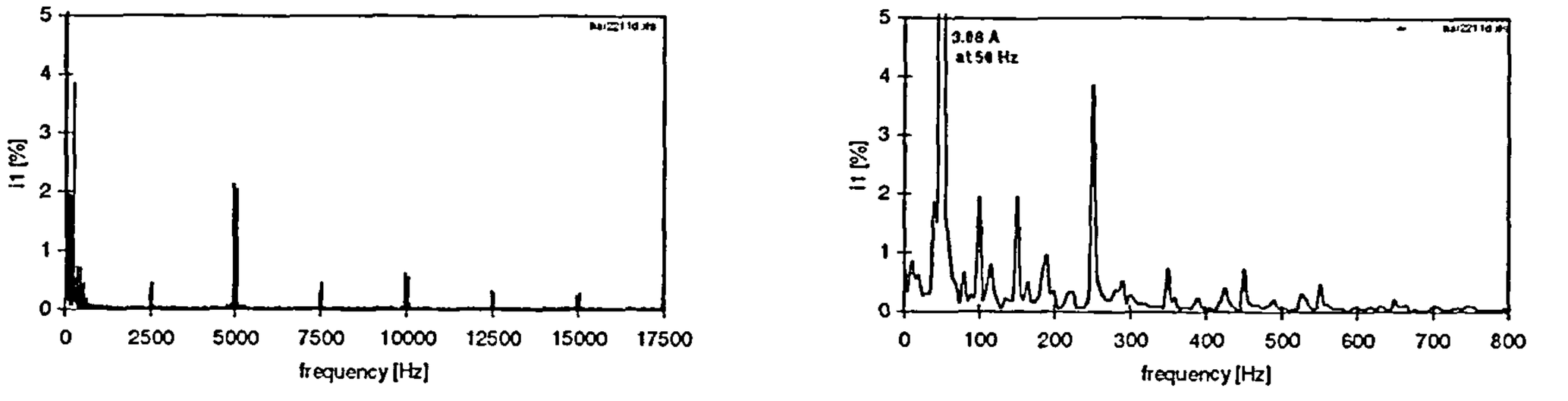

Figure 7.5: SDFM harmonics of stator current i_1 and rotor current i_2 at 1200 rpm

($\Delta f = 5$ Hz , 50 kS/s)

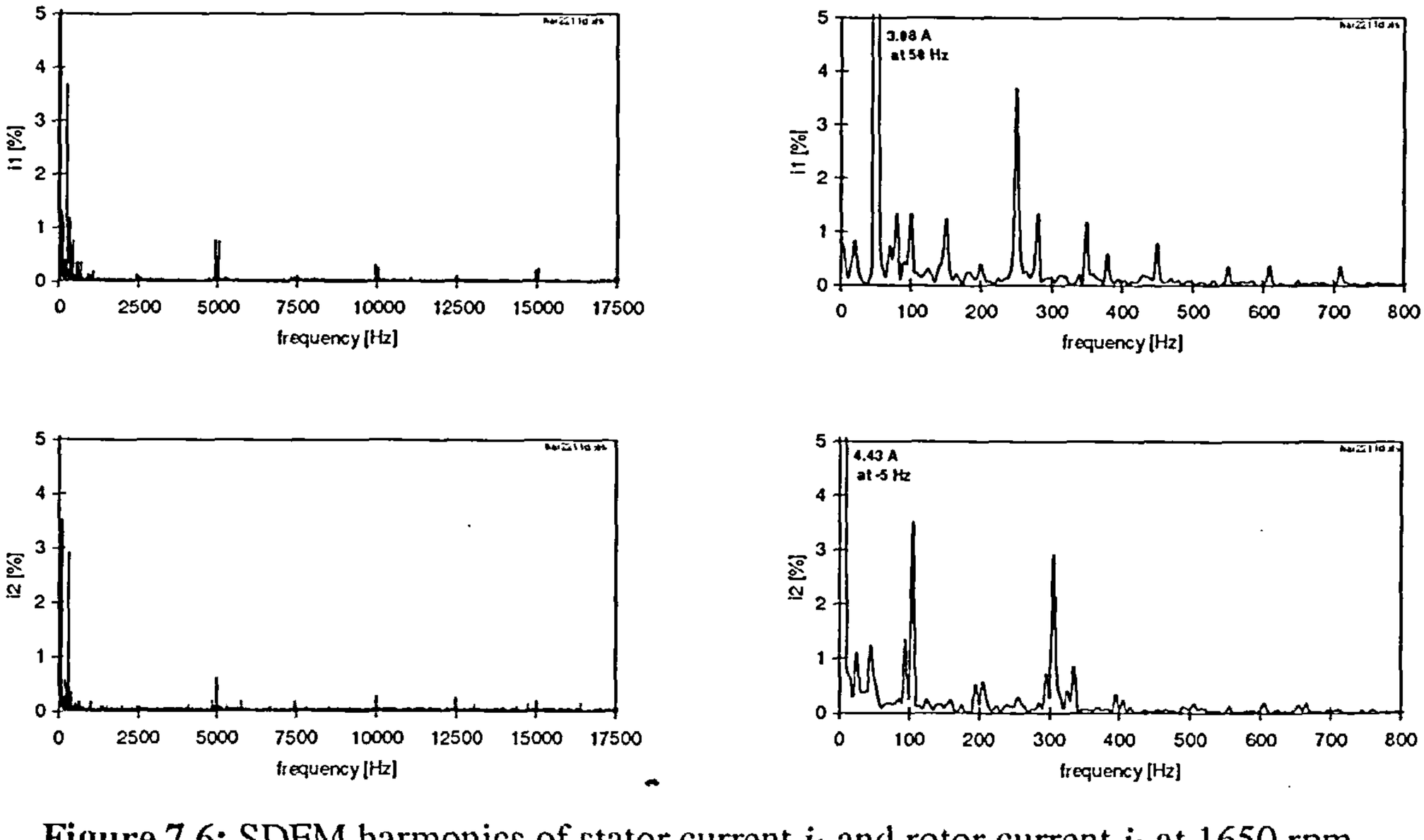

Figure 7.6: SDFM harmonics of stator current i_1 and rotor current i_2 at 1650 rpm

($\Delta f = 5$ Hz , 50 kS/s)

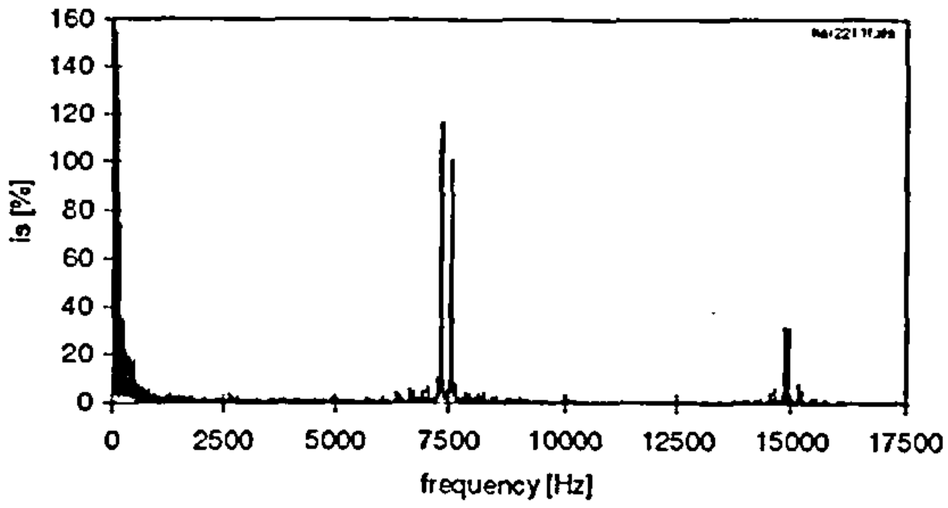

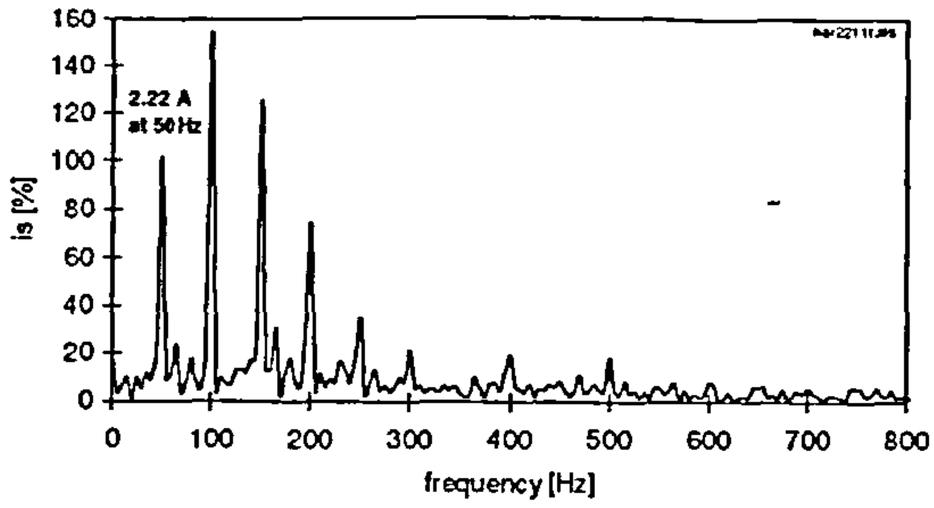

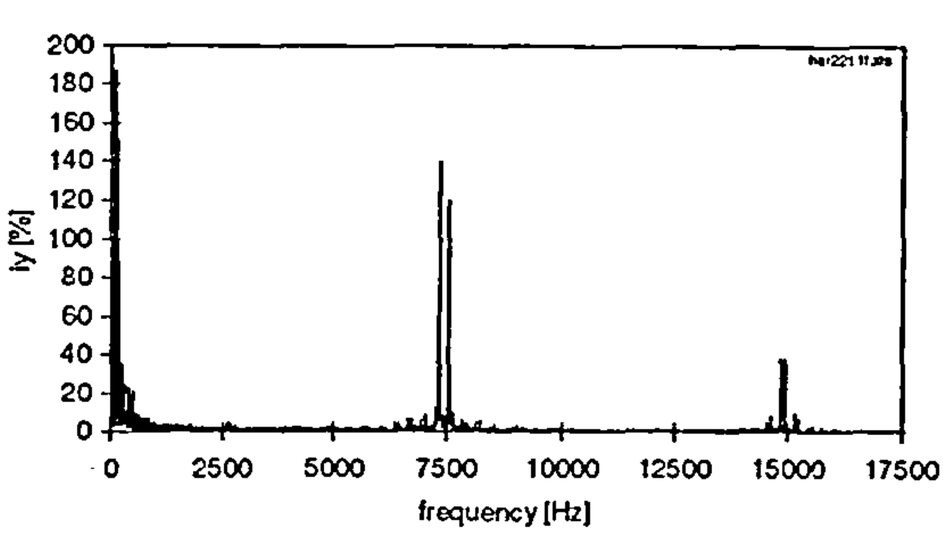

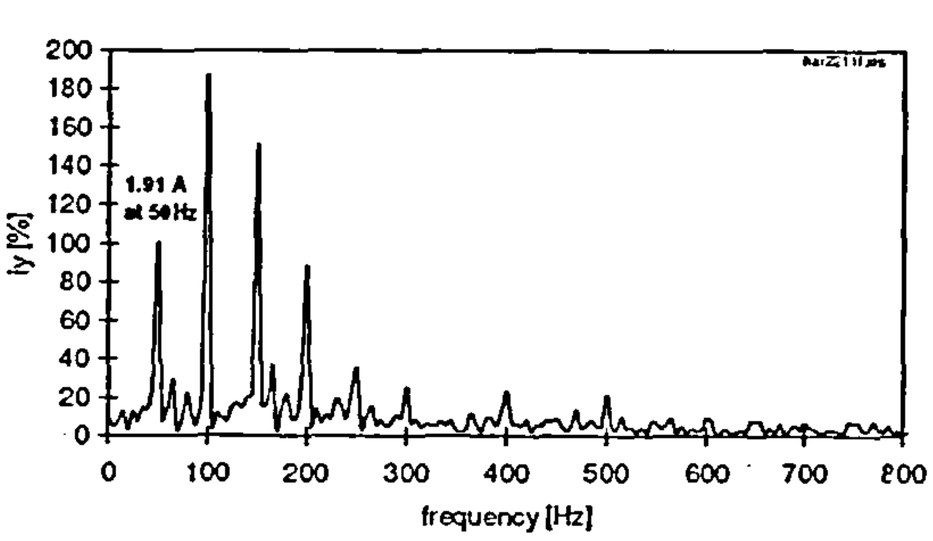

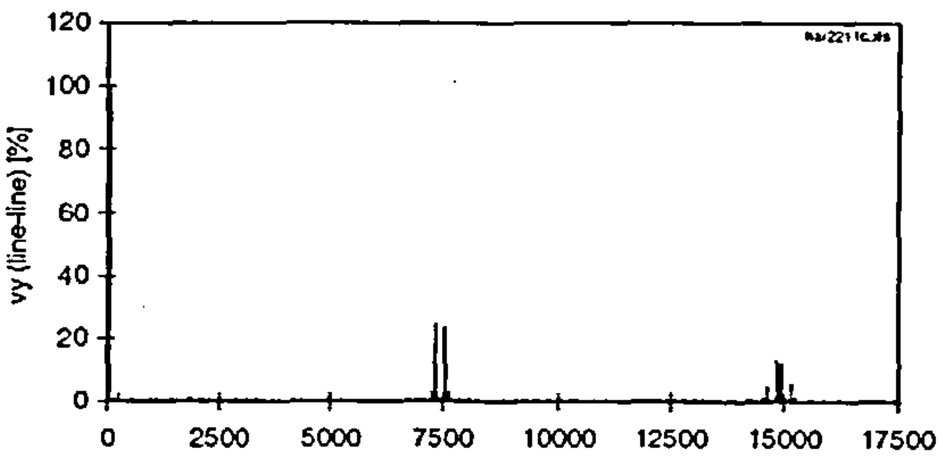

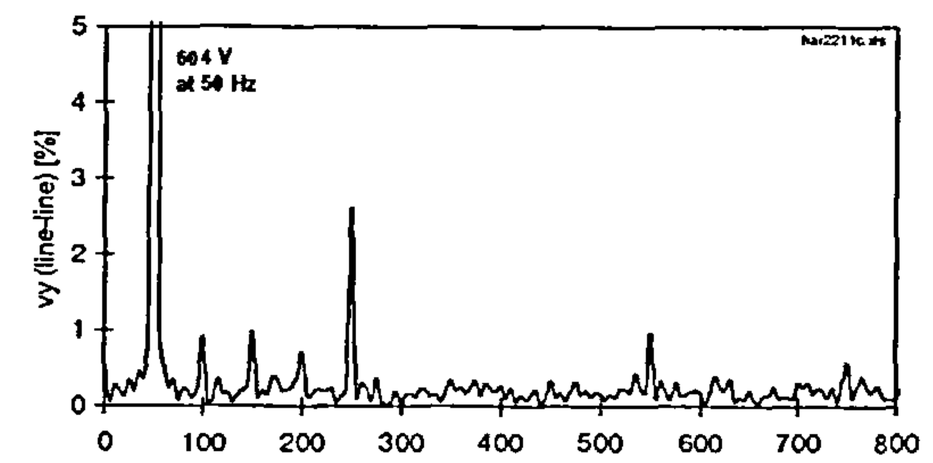

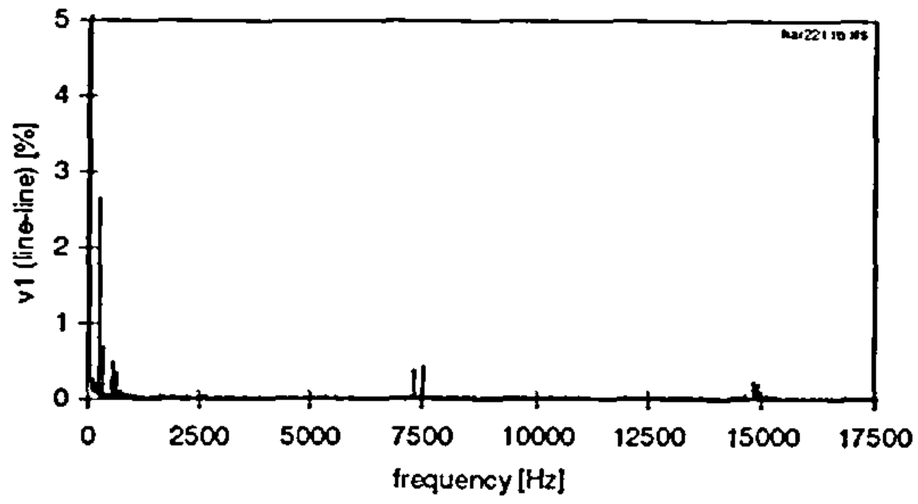

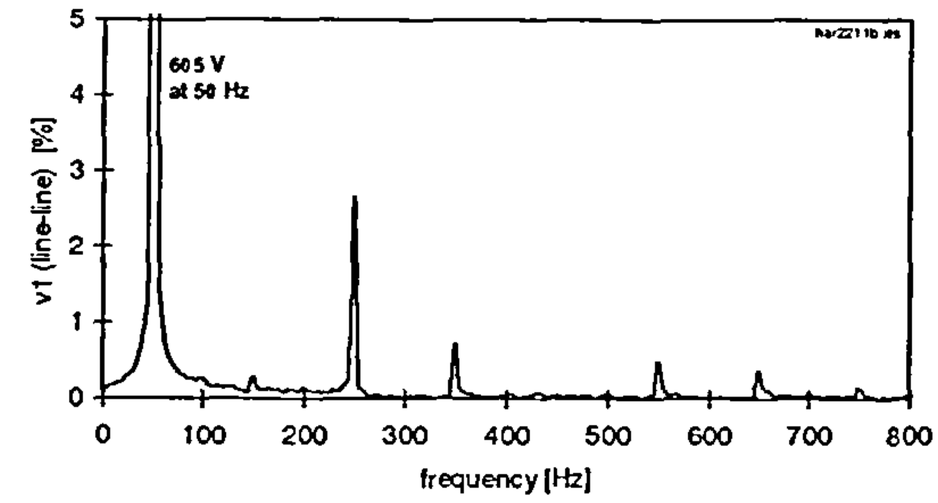

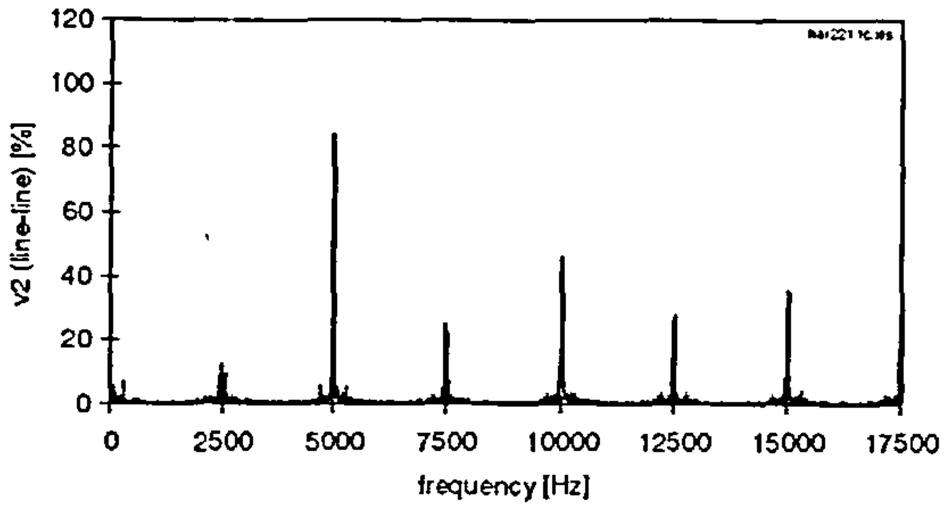

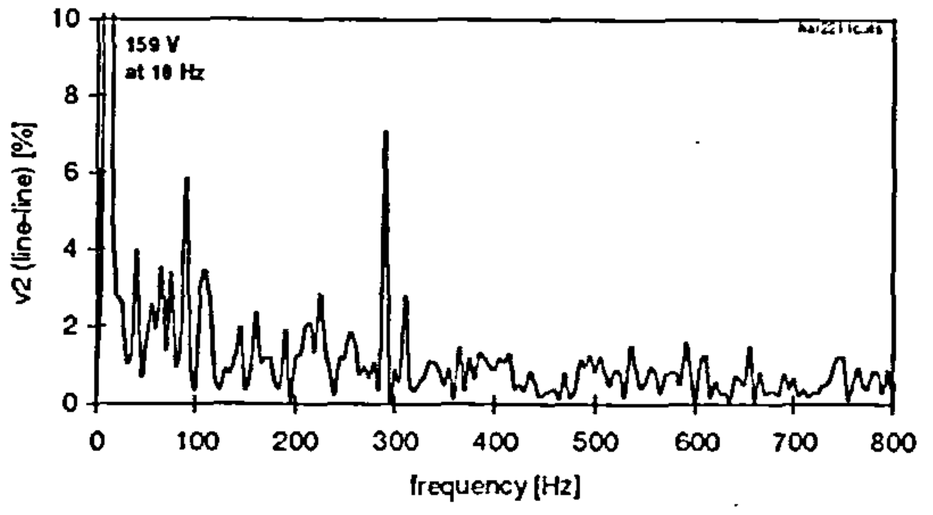

Figure 7.7: SDFM harmonics of i_y , i_s , v_y , v_2 and v_1 (v_s) at 1200 rpm

($\Delta f = 5$ Hz , 50 kS/s)

Stator	⇒	*Rotor*
$-f_1$		f_2-2f_1
$-5f_1$		f_2-6f_1

Harmonics due to the line-side inverter

The remaining important harmonics in the system are created by the line-side inverter. There are low frequency and high frequency harmonics as a result of it. First to the high frequency harmonics.

The side-band voltage harmonics have the same relationship as it is the case for the machine-side harmonics, but this time centered around the multiples of the switching frequency of f_{c_y} = 7.45 kHz, i.e. $-2f_1 \pm c_1 f_{c\_y}$ with c_1=1,3,5,...(7350 Hz, -7550 Hz,..) and $f_1 \pm c_2 f_{c\_y}$ with c_2=2,4,6,...(-14850 Hz, 14950 Hz,..). The influence of those harmonics can be seen in the line-side inverter current i_y and the supply current i_s. In the stator and rotor current those harmonics are negligible compared to the machine-side inverter produced harmonics.

In the low-frequency range the line-side inverter produces dominant current harmonics in the inverter current i_y at the frequencies 100 Hz, 150 Hz and 200 Hz, figure 7.7. The line-side inverter is rated for 47 kW and 68 A. The r.m.s. current i_y at the operational point is with 1.3 A in a magnitude range, which can be considered as a ripple magnitude for the full rated current. The current waveform (Appendix G) shows no dominant 50 Hz waveform. The overemphasising of those particular harmonic currents, relative to the fundamental, is due to the low magnitude of the fundamental current. Those three harmonic currents appear mainly in the machine-side inverter current i_y and the supply current i_s.

A harmonic current at 100 Hz and 150 Hz is also present in the stator, but with a reduced magnitude compared to the -5th harmonic. Both harmonics appear as well on the rotor with the shifted frequency of 60 Hz and 110 Hz, respectively.

In general, for the harmonic current distribution in the experimental laboratory set-up, it can be said that the line-side inverter switching influences the supply current, but has hardly any effect on the stator and rotor current harmonics. In contrast to that, the machine-side inverter produces current harmonics in the rotor and stator, but the supply current remains unaffected. The low-frequency voltage harmonics of the network voltage cause mainly a negative fundamental and -5th current harmonic in the stator and a related current harmonic in the rotor.

However, the laboratory machine has relatively high leakage inductances compared to the line-side inverter inductor and the supply inductance. Figure 7.8 shows the per-phase equivalent circuit of the system illustrating the inductances and the harmonic voltage sources (considering only high frequency harmonics produced by the two inverters).

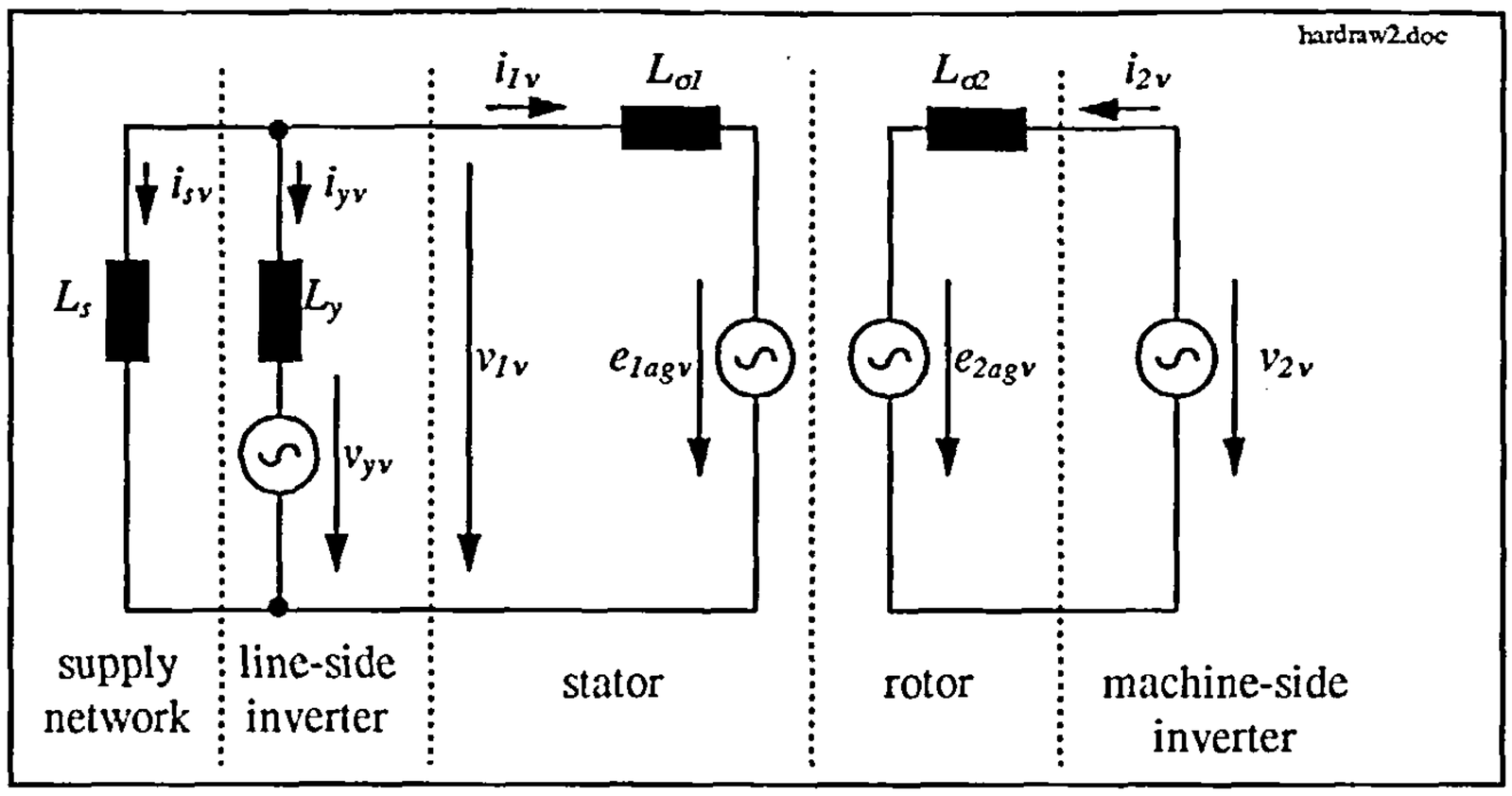

Figure 7.8: Per-phase harmonic equivalent circuit for the SDFM

The values for the different inductances are:

$L_s = 0.004\ H$

$L_y = 0.001\ H$

$L_{\sigma 1} = 0.025\ H$

$L_{\sigma 2} = 0.024\ H$

Resistances are neglected at the high frequency harmonics produced by the inverters, since reactances dominate.

Because of the large ratio of about 6:1 between the stator leakage inductance $L_{\sigma 1}$ and the supply inductance L_s the voltage harmonics of the line-side inverter produce mainly the harmonic currents i_{sv} and i_{yv}. The reactance in the supply network path is far less than in the stator path, so that the line-side inverter voltage harmonics cause negligible harmonic currents in the stator.

The harmonic stator currents due to the machine-side inverter voltage harmonics flows also in the appropriate ratio in the supply and line-side inverter path, but its magnitude is insignificant compared to the line-side inverter produced current harmonics as shown in figure 7.7.

The harmonic current analysis of the experimental system gives a distorted picture as a consequence of the inductance ratios. For a properly matched system, where the SDFM rating is higher than the laboratory machine, the above inductance ratio takes a far less value. The stator inductance of a 22 kW slip-ring induction machine for example [a6] is with 3.5 mH about the same as the supply inductance. In that case, there ought to be also harmonic currents in the supply current, which stem from the machine-side inverter and harmonic currents in the stator produced by the line-side inverter voltage harmonics.

Nevertheless, the harmonic analysis of the experimental SDFM delivers a valuable insight in the harmonic current distribution of the system.

Finally, to show the SDFM current harmonics for a different speed, figure 7.6 gives the stator and rotor current harmonics for a speed of 1650 rpm. At that point $f_2 = -5\ Hz$ and $f_{shift} = 55\ Hz$. The low-order harmonics are much the same as for 1200 rpm with the dominant -5th for the stator current harmonic and the related rotor current harmonic f_2-$6f_1$ at -305 Hz. Also the rotor harmonic f_2-$2f_1$ at -105 Hz caused by the negative stator current fundamental has a dominant magnitude.

The high frequency current harmonics are reduced in magnitude, since the modulation index is lower for 1650 rpm, but they are still present in both, the stator and the rotor.

7.2.2 Harmonic Analysis of CDFM

The operational point details of the CDFM harmonic analysis are:

speed = 450 rpm , $f_1 = 50$ Hz, $f_2 = 20$ Hz, $f_4 = 5$ Hz

$V_1 = 116$ V

$i_{d4}^{e*} = 4$ A, $i_{q4}^{e*} = 2.5$ A

$P_1 \approx -500$ W, $Q_1 \approx 500$ VAr

modulation index on side 4 = 0.108 = $V_{4peak\ line\text{-}line} / V_{DC}$

The connection of the CDFM with the supply network and the converter is illustrated in figure 7.9. A variac (auto transformer) on side 1 is used to bring the supply voltage down to the side 1 voltage level. Side 1 is in delta-connection.

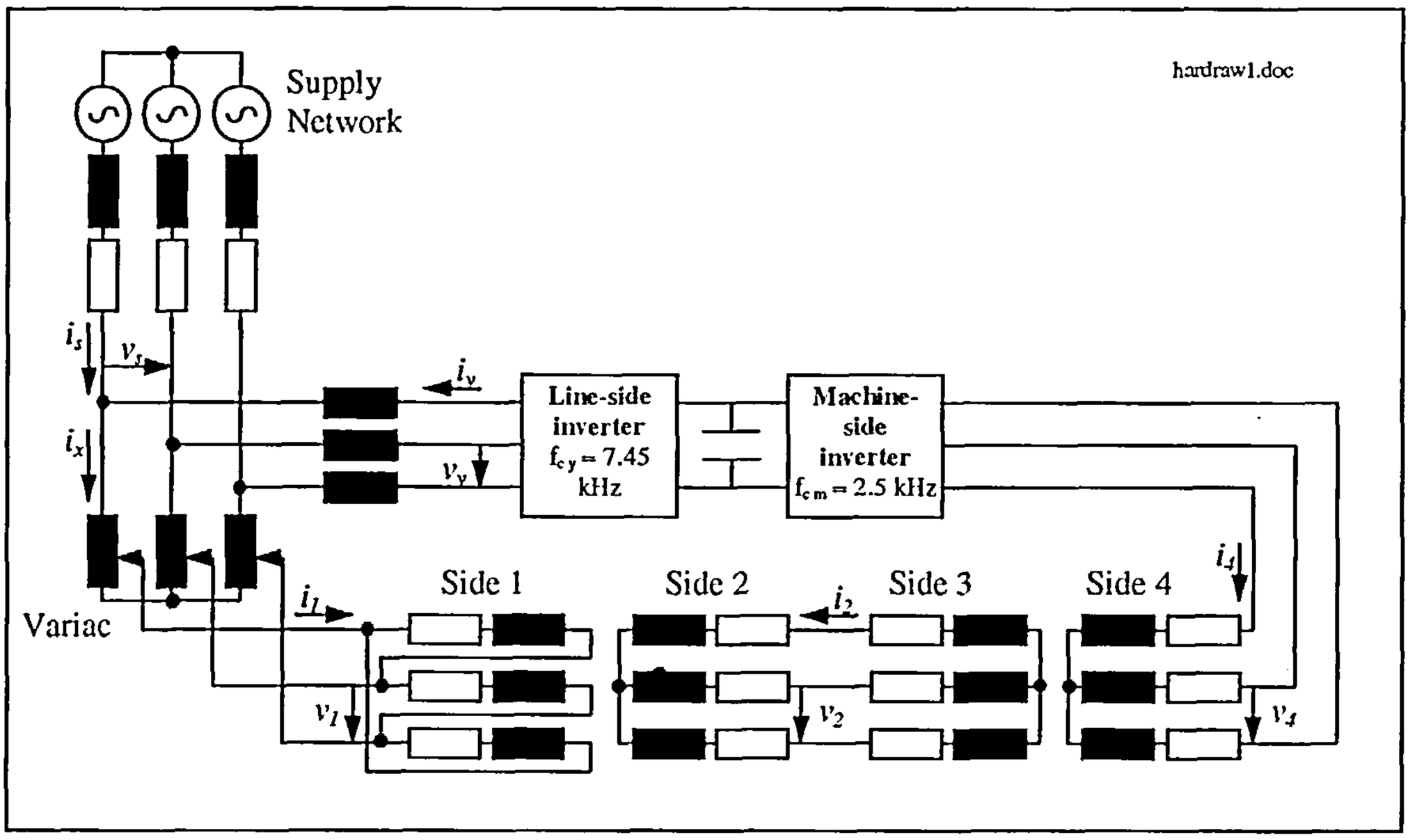

Figure 7.9: CDFM connection circuit

The switching frequency of the line-side inverter and the machine-side inverter is the same as for the SDFM case.

Harmonic frequency spectra for the mentioned operational point are depicted in figure 7.10, 7.12 and 7.13.

Harmonics due to the machine-side inverter

Due to the low modulation index, the machine-side inverter produces dominant voltage harmonic side-bands centered around the even multiples of the switching frequency for the side 4 voltage v_4, as shown in figure 7.12. The side-bands for the odd multiples are much more reduced in comparison to the ones in figure 7.7, where the modulation index is more than double the modulation index as for figure 7.12.

In figure 7.12 it can be seen, that the harmonic voltage side-bands produced by the machine-side inverter show other harmonic side-bands, which are centered around multiples of the switching frequency, but further away from the switching frequency than the "first side-band". Compared to figure 7.7, they are larger in magnitude, but as it is the case for the SDFM harmonic analysis, those "additional side-bands" are not included in the CDFM harmonic analysis and later in the simulations, since their significance is not as important as for the main side-band.

The side-band harmonics produced on side 4 by the machine-side inverter have the frequency of $-2f_4 \pm c_1 f_{c\_m}$ with c_1=1,3,5,.. (2490 Hz, -2510 Hz, 7490 Hz, -7510 Hz, ..) when centered around odd multiples of the switching frequency and $f_4 \pm c_2 f_{c\_m}$ with c_2=2,4,6,.. (-4995 Hz, 5005 Hz, -9995 Hz, 10005 Hz, ..) when centered around even multiples of the switching frequency.

Figure 7.10 shows, that the produced current harmonics on side 4 in i_4 are of low magnitude and only the side-band harmonics around 5000 Hz are of importance. Nevertheless, the side 4 current harmonics are transmitted through the machine B and machine A air-gaps onto side 2 and side 1, respectively. The experienced frequency shift follows the relation of

$$f_{1v} = f_{2v} + f_{shiftA} \tag{7.2.2}$$

$$f_{2v} = f_{4v} + f_{shiftB} \tag{7.2.3}$$

and, considering only side 1 and side 4,

$$f_{1v} = f_{4v} + f_{shiftAB} \tag{7.2.4}$$

where

f_{1v}, f_{2v} and f_{4v} are the respective harmonic frequencies and f_{shiftA}, f_{shiftB} and $f_{shiftAB} = f_{shiftA} + f_{shiftB}$ are the rotor speeds in electrical Hz. For the speed of 450 rpm $f_{shiftA} = 30\ Hz$, $f_{shiftB} = 15\ Hz$ and $f_{shiftAB} = 45\ Hz$.

Normally it is not possible to access the side 2 quantities of a CDFM, but the experimental machine set-up still uses slip-rings for connection and therefore it is possible to sample the rotor quantities for the present case.

The harmonics, due to the machine-side inverter, on side 2 in i_2 have the frequency of $(f_{shiftB}-2f_4)\pm c_1 f_{c\_m}$ with c_1=1,3,5,.. (-2495 Hz, 2505 Hz, -7495 Hz, 7505 Hz, ..) and $f_2\pm c_2 f_{c\_m}$ with c_2=2,4,6,.. (-4980 Hz, 5020 Hz, -9980 Hz, 10020 Hz, ..).

Continuing on side 1, the harmonics produced by the machine-side inverter end up as harmonics on side 1 in i_1 with the frequency of $(f_{shiftAB}-2f_4)\pm c_1 f_{c\_m}$ with c_1=1,3,5,.. (-2465 Hz, 2535 Hz, -7465 Hz, 7535 Hz, ..) and $f_1\pm c_2 f_{c\_m}$ with c_2=2,4,6,.. (-4950 Hz, 5050 Hz, -9950 Hz, 10050 Hz, ..).

In general, the frequency relationship between the different machine sides for the harmonics produced by the machine-side inverter take following form:

side 4	⇒	*side 2*	⇒	*side 1*	
$-2f_4\pm c_1 f_{c\_m}$		$(f_{shiftB}-2f_4)\pm c_1 f_{c\_m}$		$(f_{shiftAB}-2f_4)\pm c_1 f_{c\_m}$	with c_1=1,3,5,...
$f_4\pm c_2 f_{c\_m}$		$f_2\pm c_2 f_{c\_m}$		$f_1\pm c_2 f_{c\_m}$	with c_2=2,4,6,...

Harmonics due to the supply network

The two dominant low-frequency harmonics on side 1, caused by the supply network are the -5th and the 7th harmonic, figure 7.10 and 7.12. The -5th transmits through the CDFM and produces a related current and voltage harmonic at -280 Hz on side 2 and at -295 Hz on side 4. For the 7th, the related harmonics are 320 Hz on side 2 and 305 Hz on side 4. Other harmonics on side 1 such as the -fundamental, 3rd, -9th are present and have related harmonics on side 2 and side 4.

The important low-order harmonics produced by the supply network and distributed in the CDFM can be written as

side 1	⇒	*side 2*	⇒	*side 4*
$-5f_1$		f_2-6f_1		f_4-6f_1
$7f_1$		f_2+6f_1		f_4+6f_1

Harmonics due to the line-side inverter

The high frequency harmonics caused by the line-side inverter are at $-2f_1\pm c_1 f_{c\_y}$ with c_1=1,3,5,... and $f_1\pm c_2 f_{c\_y}$ with c_2=2,4,6,... as already explained in section 7.2.1, and again the resulting current harmonics can only be seen in the line-side current i_y and the supply current i_s, figure 7.13. In the CDFM, those harmonics are of no concern, figure 7.10.

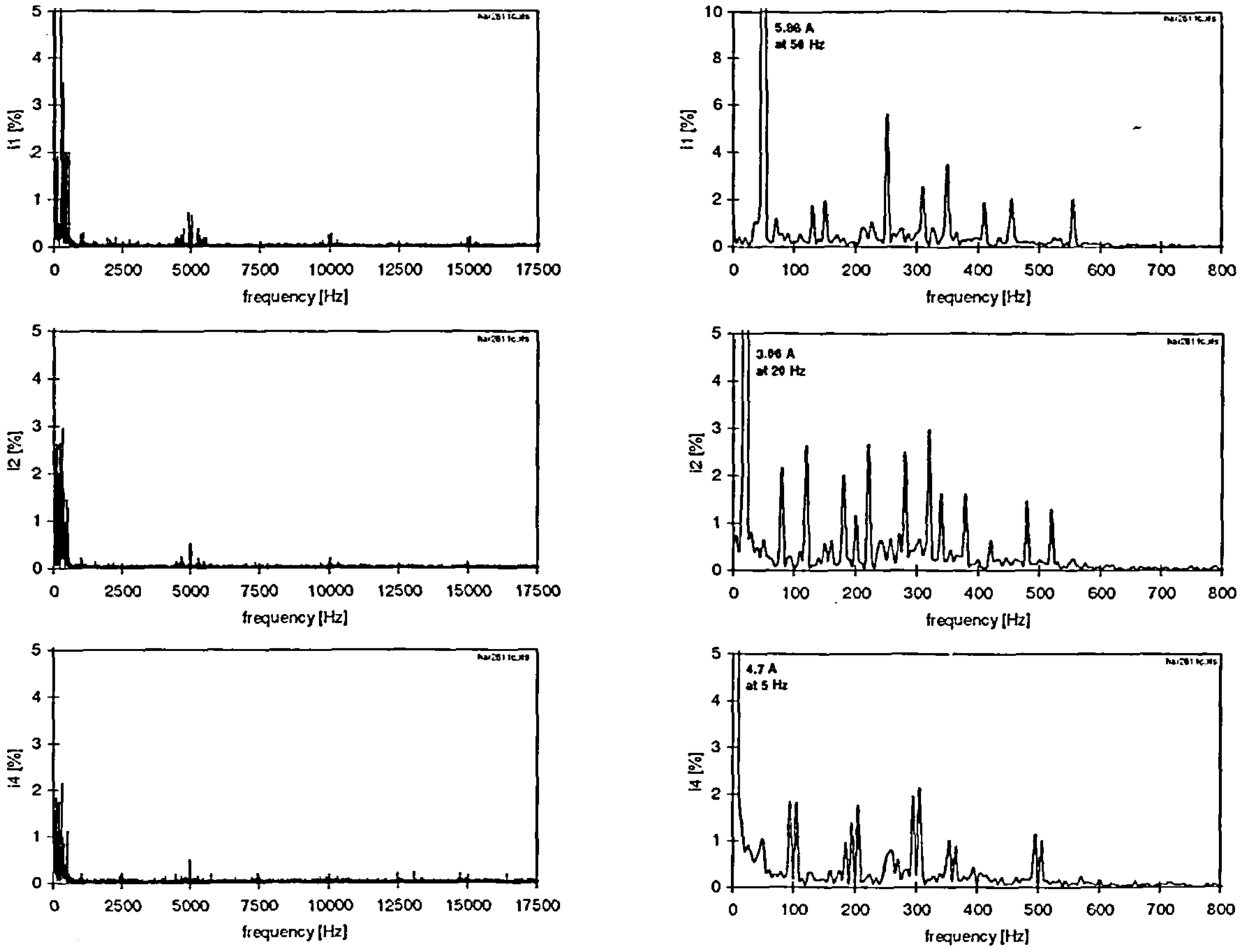

Figure 7.10: CDFM harmonics of i_1, i_2 and i_4 at 450 rpm

($\Delta f = 5$ Hz , 50 kS/s)

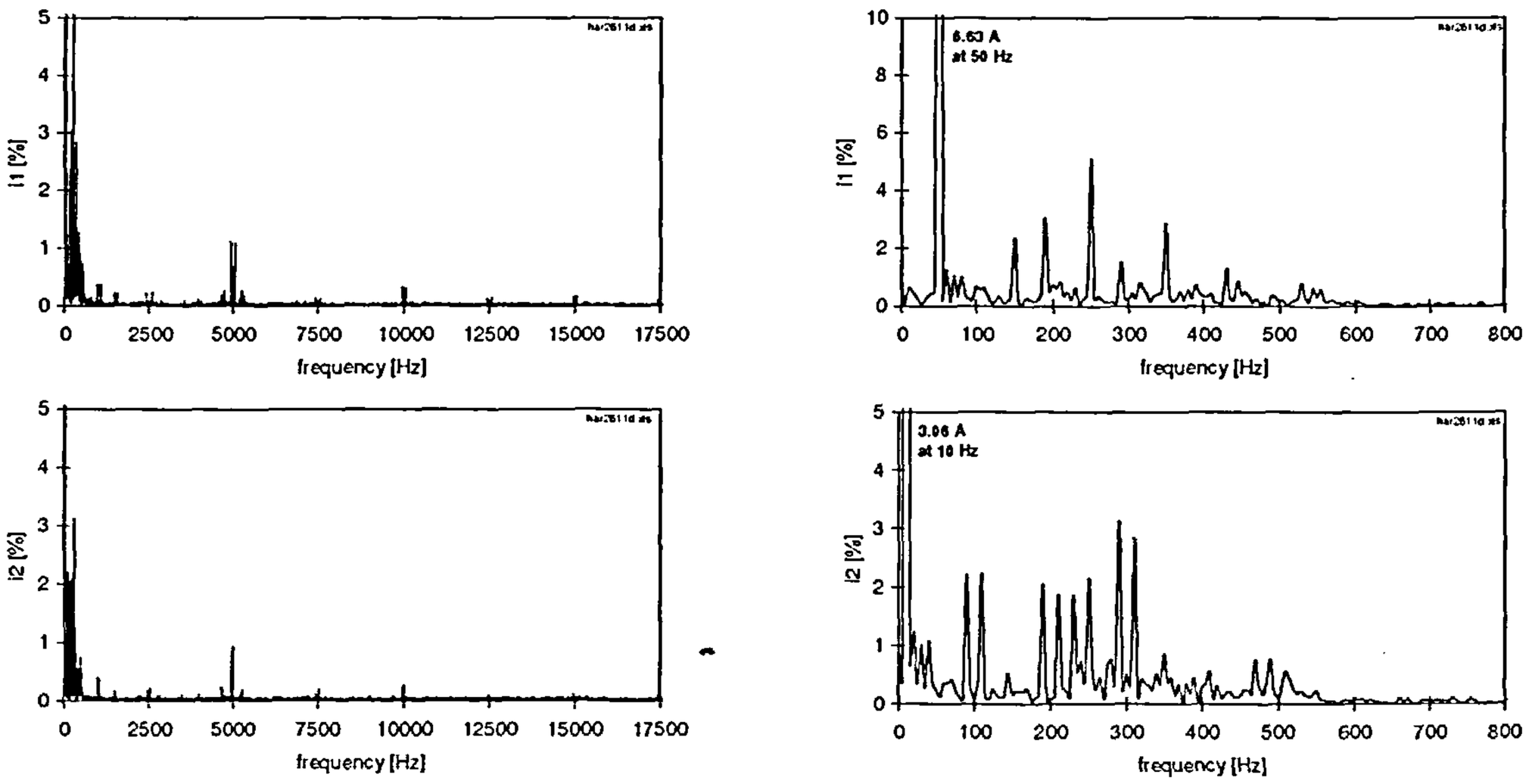

Figure 7.11: CDFM harmonics of i_1, i_2 and i_4 at 600 rpm

($\Delta f = 5$ Hz , 50 kS/s)

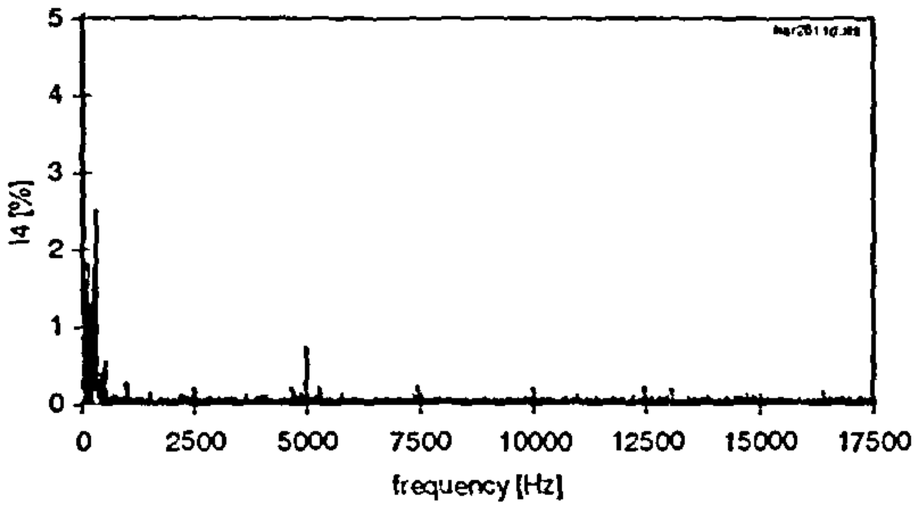

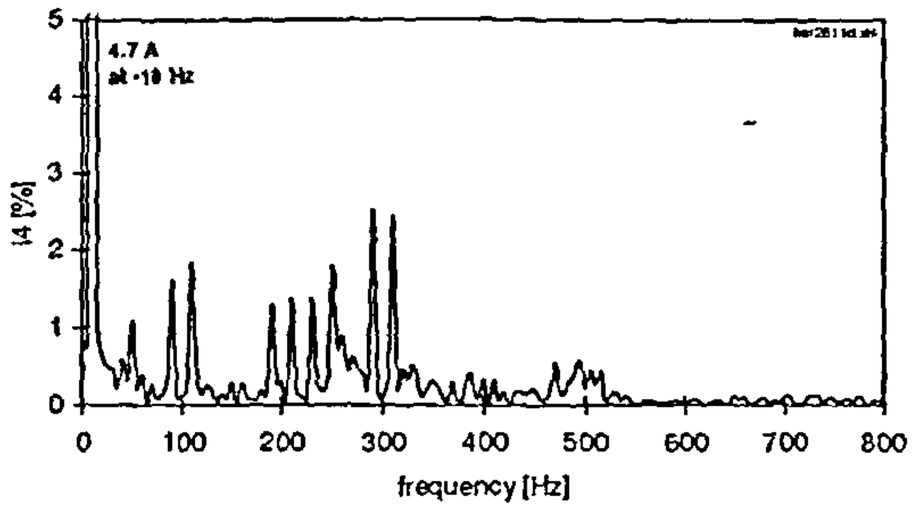

Figure 7.11 (continued): CDFM harmonics of i_1, i_2 and i_4 at 600 rpm

($\Delta f = 5$ Hz , 50 kS/s)

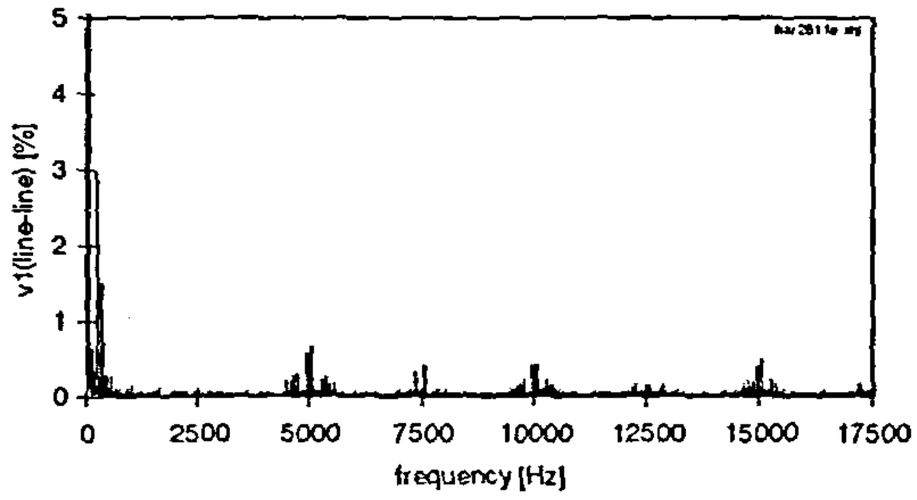

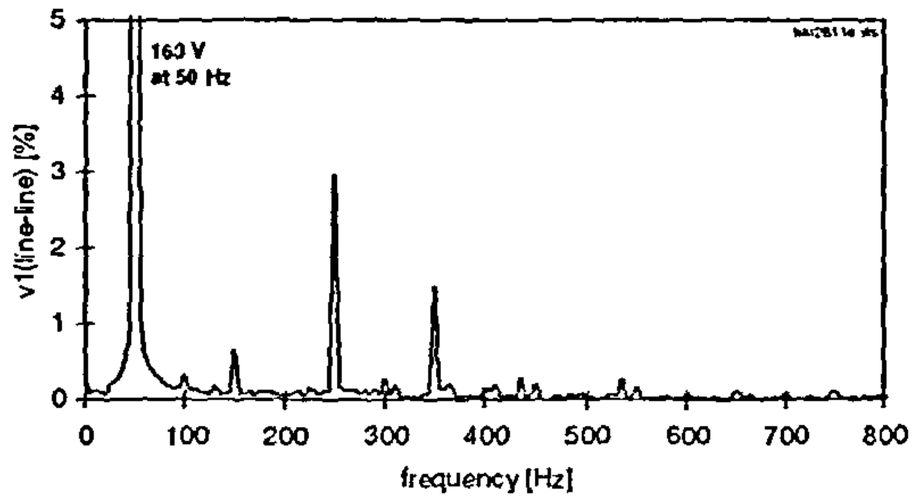

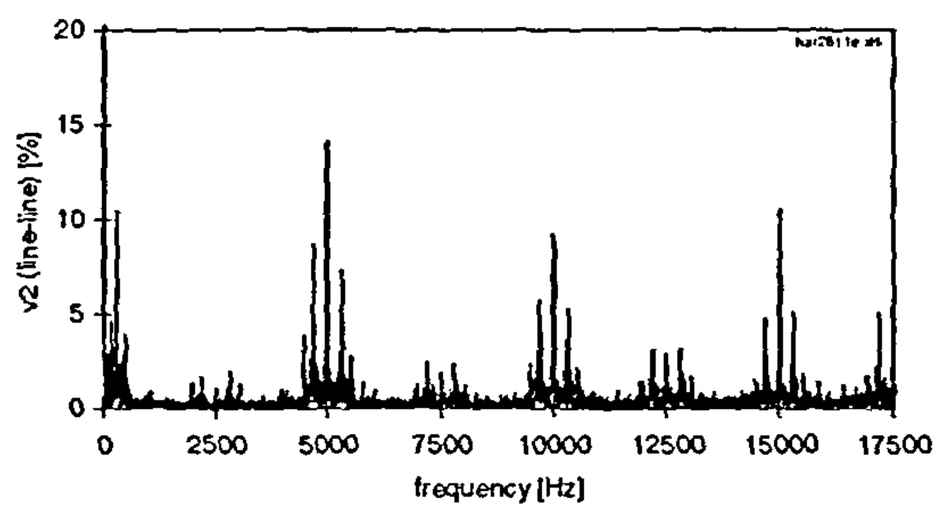

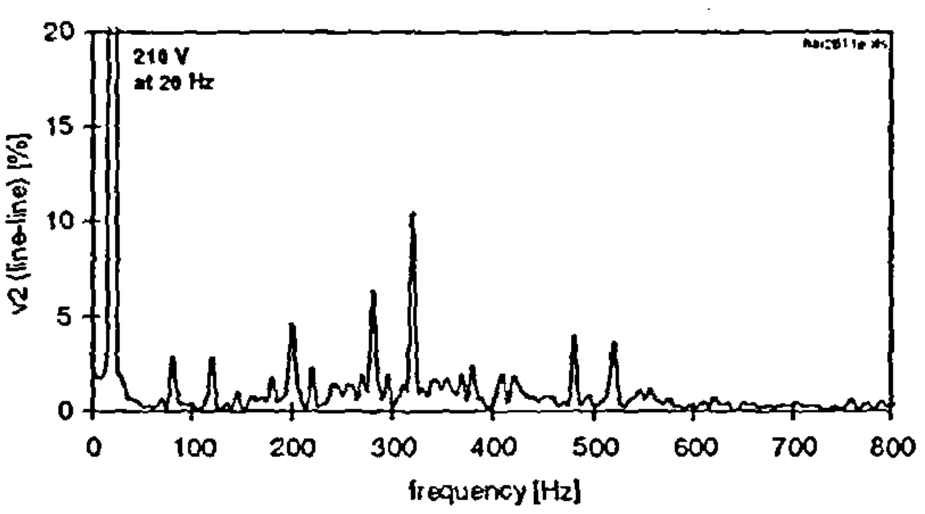

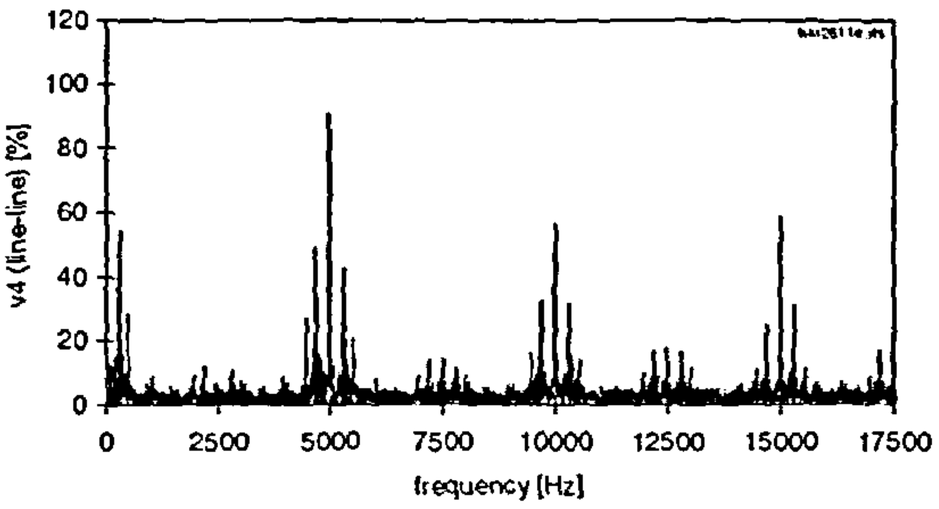

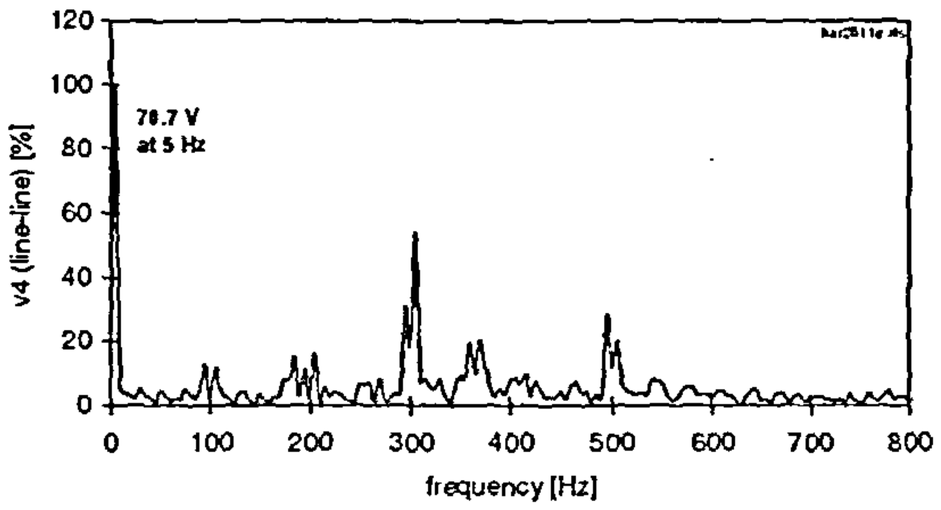

Figure 7.12: CDFM harmonics of v_1, v_2 and v_4 at 450 rpm

($\Delta f = 5$ Hz , 50 kS/s)

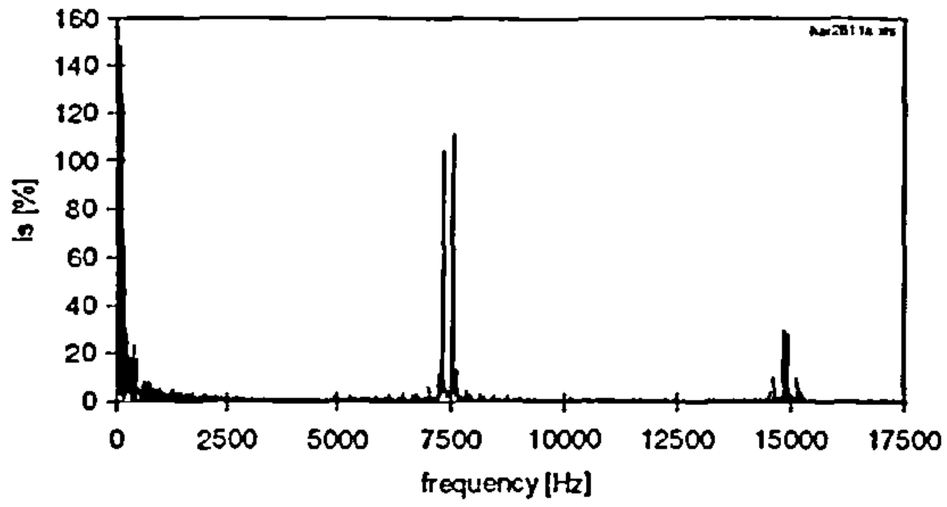

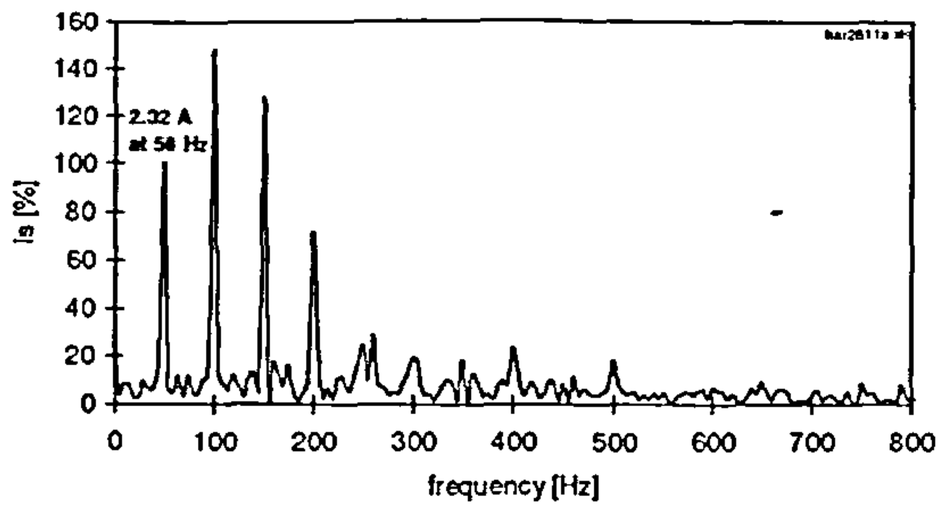

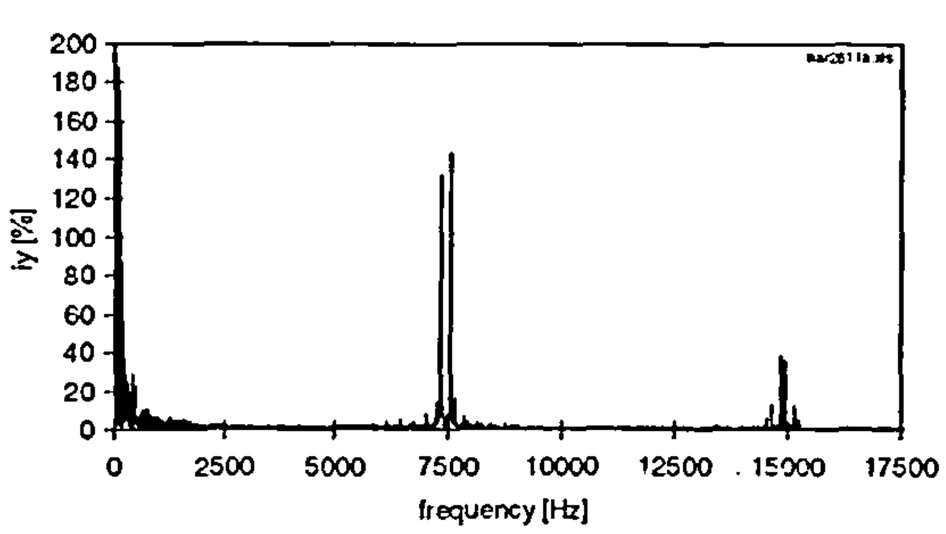

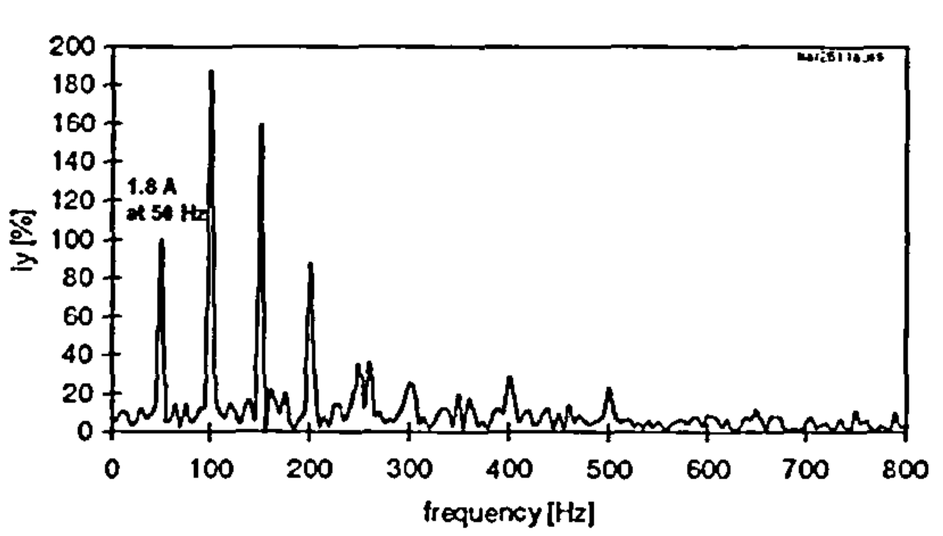

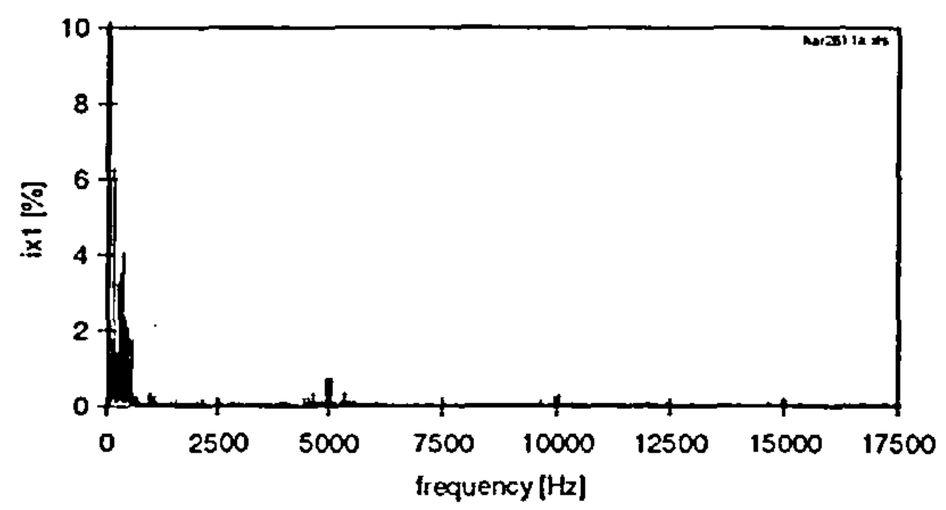

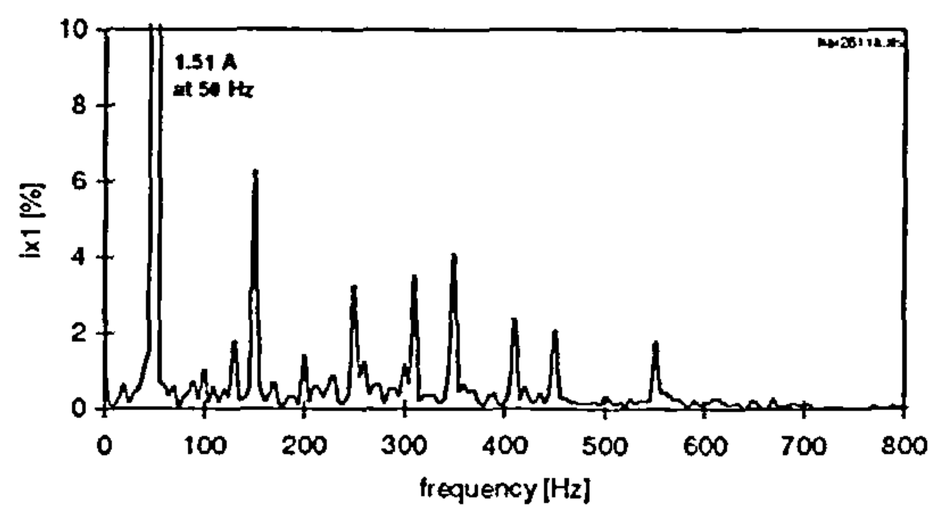

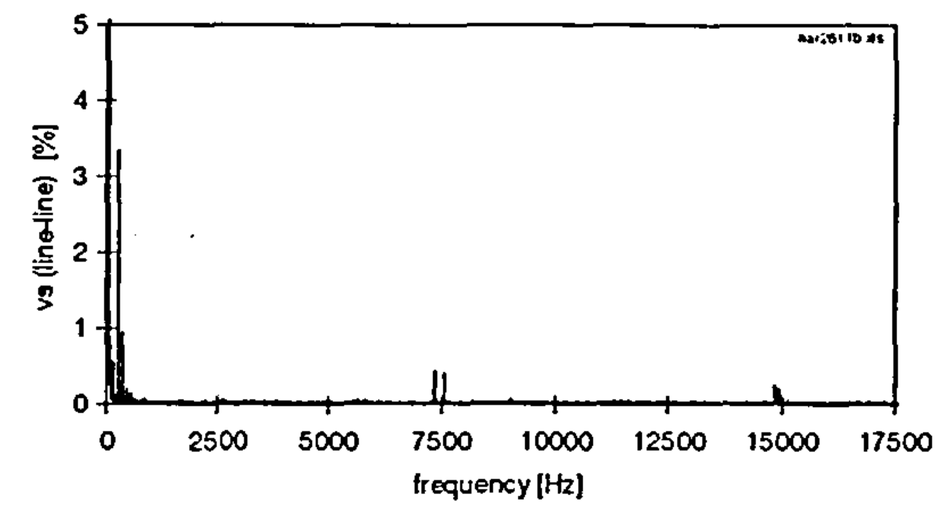

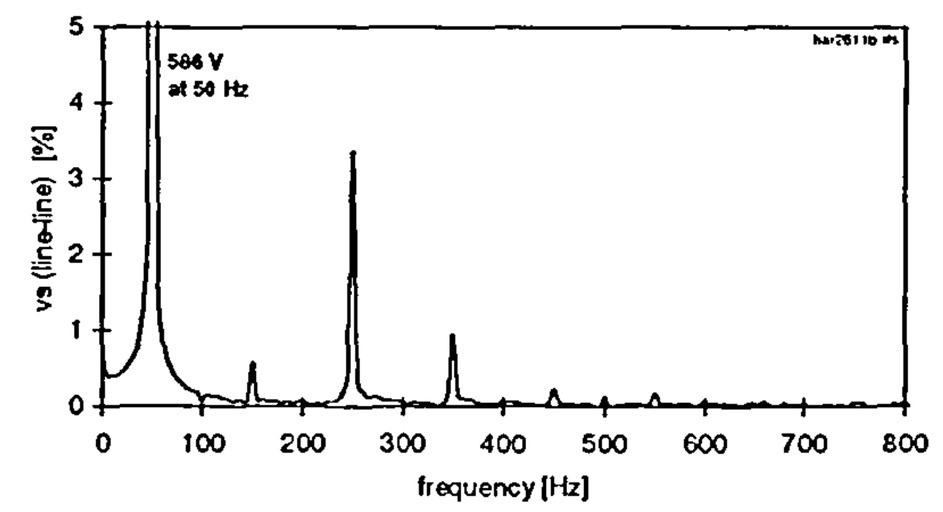

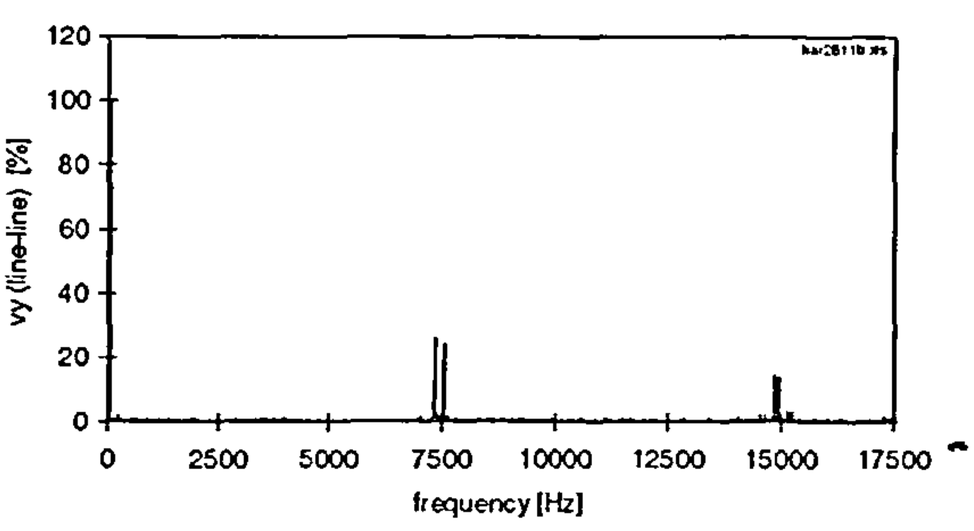

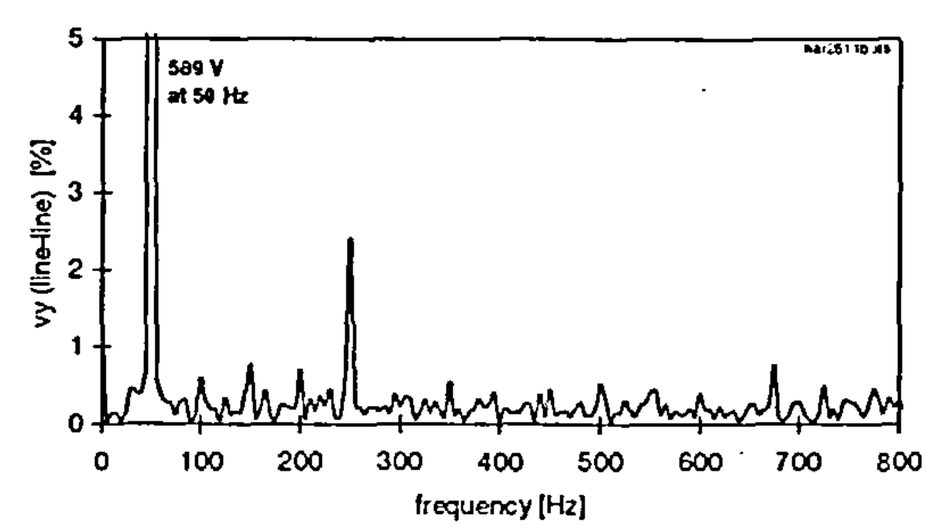

Figure 7.13: CDFM harmonics of i_y, i_{x1}, i_s, v_y, v_s (v_x) at 450 rpm

($\Delta f = 5$ Hz , 50 kS/s)

Similar to section 7.2.1, the line-side inverter current i_y and the supply network current i_s show a strong magnitude for the low-order harmonics at 100 Hz, 150 Hz and 200 Hz, produced by the 68 A rated line-side inverter.

Other harmonics

A set of harmonics around the 200 Hz on side 2 and side 4 are present, which may be caused by the machine itself or by the machine-side inverter, but they shall not be considered.

In agreement with the SDFM harmonic analysis, it can be said that the machine-side inverter causes high-frequency current harmonics in the CDFM, but not in the supply network. The resultant CDFM current harmonics have a small amplitude, largely due to the small modulation index at this operational point. Only the current side-band harmonics at twice the switching frequency show a recognisable amplitude. The switching of the line-side inverter is responsible for harmonics in the line-side inverter current and the supply current, but the CDFM currents remain unaffected. Low-order current harmonics in the CDFM are a result of voltage harmonics in the supply network.

In conclusion, concerning the high frequency harmonics produced by the inverters, the harmonic current distribution of the CDFM system is subject to the somewhat artificial system inductance ratios, where the machine inductances are comparatively large compared to the supply inductance, which is similar to the SDFM system. Additionally, the CDFM connection circuit involves a variac on side 1, which also adds more inductance to the system and thus further limits the harmonic currents.

A per-phase harmonic equivalent circuit containing only inductances is given in figure 7.14. The supply network, the line-side inverter, the variac and only side 1 of the CDFM is illustrated in figure 7.14.

The inductance values are:

$L_s = 0.004\ H$

$L_y = 0.001\ H$

$L_x = 0.006\ H$

$L_{\sigma l} = 0.009\ H$

It can be seen, that the harmonic voltage produced by the line-side inverter is first reduced by the variac reactance ratio before the resulting side 1 terminal harmonic voltage can create harmonic currents across the high reactance side 1 path. Therefore, the effect of the line-side inverter harmonics on the CDFM currents is not visible in figure 7.10 compared to the machine-side inverter created current harmonics.

Also, as a consequence of the large magnitude of the current harmonics due to the line-side inverter in the supply, the harmonic currents due to the machine-side inverter do not show up in figure 7.13.

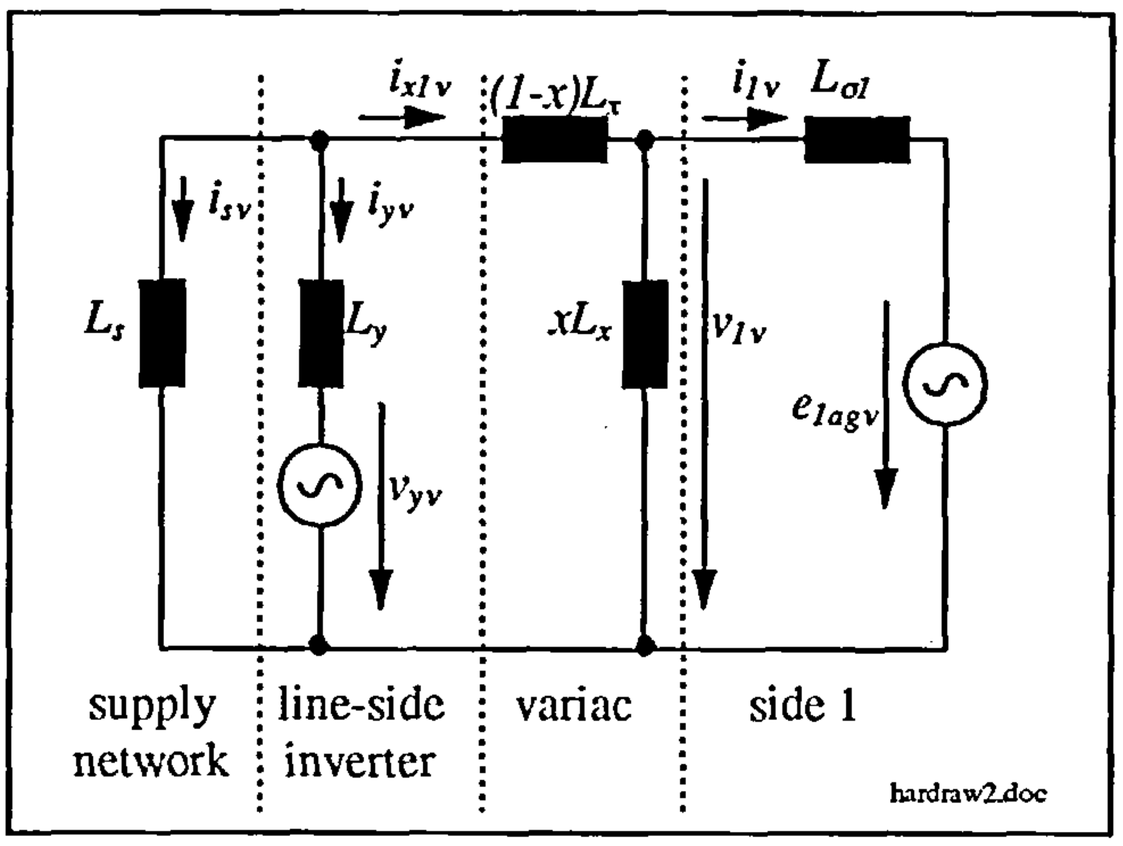

Figure 7.14: Per-phase harmonic equivalent circuit for the CDFM

To show the machine currents for a different speed, figure 7.11 gives the current harmonics of the CDFM for a speed of 600 rpm. The fundamental frequencies of the system in this case are $f_2 = 10\ Hz$, $f_4 = -10\ Hz$, $f_{shiftA} = 40\ Hz$ and $f_{shiftB} = 20\ Hz$. The current magnitudes of the harmonics are not much different to those at 450 rpm in figure 7.10 and the frequency relation is as given above.

7.3 Harmonic Simulation and Modeling

In the previous section, an analysis of the harmonic current distribution of the SFDM and the CDFM system has been presented. In both cases, the current harmonics produced by the machine-side inverter appear in the machines and the current harmonics produced by the line-side inverter appear in the supply current. As explained the harmonic current distribution is largely determined by the inductance ratios of the system.

Harmonic analysis and measurements are time consuming and the complete drive system has to be in place to carry it out. This section presents a simulation and modeling process to predict the harmonic current distribution of a real system with the knowledge of the involved inductances. It focuses on the high frequency harmonics produced by the voltage-source inverters. The low frequency harmonics are not considered, since they can depend on the control strategy involved and also on the supply network harmonics, which may not always be known in the first place. However, the high frequency harmonics of the inverters have a rather predictable pattern for fixed switching frequency and they are present independent of the control mechanism used.

For both cases, the SDFM and the CDFM, the harmonic prediction process is demonstrated by modeling the effect of the current harmonics caused by the machine-side inverter.

A doubly-fed system, SDFM or CDFM, contains two harmonic voltage producing inverters. The first step of the harmonic current distribution process makes it therefore necessary to establish the harmonic voltages of an inverter. This can either be done by harmonic analysis on measured inverter output voltage waveform or by harmonic analysis on time-step simulation of the used space vector PWM of the inverter, which is carried out in this case. FFT, using MATLAB, of the simulated time-series yields the harmonic voltage content giving magnitude and frequency of the particular harmonics.
In the second step, steady state modeling of the whole system based on a per-phase equivalent circuit model for each individual harmonic voltage delivers a series of harmonic currents. Here, only one harmonic is modeled at a time. Repeating the analysis for all the harmonic voltages and using superposition produces the complete harmonic current spectrum.
To normalise the modeled current harmonics, rather than use absolute values, the steady state model for the fundamental power flow is used to obtain the fundamental current values. Alternatively, there is also the possibility to use rated values of a potential systems.

The three steps used for the harmonic current prediction process are in short as follows:

1. Time-step simulation of the inverter switching and FFT of the acquired voltage time-series. (Alternatively, FFT on measured inverter output waveform)
2. Steady state modeling of the system for each individual harmonic voltage. Superposition of the modeled harmonic currents obtains the frequency spectrum of the harmonic currents.
3. If necessary for normalising, the fundamental steady state model can be used for calculation of the fundamental magnitudes.

The described process is carried out for the SDFM and for the CDFM system.

7.3.1 Simulation and Modeling of the SDFM Harmonics

Inverter time-step simulation
The applied space vector PWM (Appendix G) has the advantage of easy real-time processor implementation and also allows a precise digital computer simulation. Once the demand value for the voltage vector is known and the cycle time is fixed, determined by the inverter switching frequency, the individual time sequences within one switching cycle can be calculated. FFT of the obtained time series gives the frequency spectrum of the inverter

voltage. The time-step simulation is carried out by a C program in BORLAND C++. The parameters necessary for simulation are the d.c.-link voltage, the modulation index, the switching frequency and the simulation step width.

Parameters for the time-step simulation of the machine-side inverter:

d.c.-link voltage:	650 V	
modulation index:	0.244	(as in measurements)
switching frequency:	2.5 kHz	
simulation step width:	1 µs	

The sampling frequency is 50 kHz as it was for the measurements.

Parameters for the time-step simulation of the line-side inverter:

d.c.-link voltage:	650 V	
modulation index:	0.9292	(as in measurements)
switching frequency:	7.45 kHz	
simulation step width:	1 µs	

The sampling frequency is 100 kHz.

The simulation takes no account of inverter switching dead time.

Simulated voltage harmonics of the machine-side and the line-side inverter at the particular operational point of the SDFM are presented in figure 7.15. It can be seen that both simulated frequency spectra closely match the measured data in figure 7.7. The main side-band coincides very well with the actual system measurements, however there are slight differences for the additional side-bands, but those are not considered, due to their small magnitude.

The simplification by not simulating the dead time effect is justified when looking at the simulated harmonics.

A comparison of the measured and the simulated voltage harmonics of the machine-side inverter is given in table 7.1.

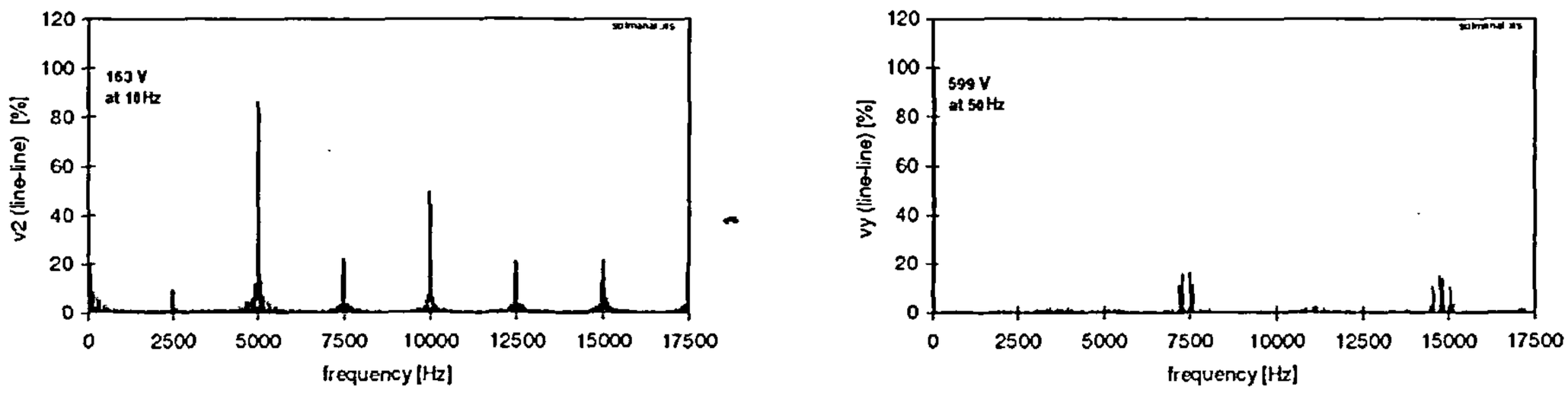

Figure 7.15: Simulated SDFM inverter voltage harmonics

Steady state harmonic modeling

Each harmonic current flowing in the rotor and stator of the SDFM can be represented in vector form by

$$\bar{i}_{2v} = i_{2v} e^{j(\omega_{2v} t + \Phi_2)} \tag{7.3.1}$$

$$\bar{i}_{1v} = i_{1v} e^{j(\omega_{1v} t + \Phi_1)} \tag{7.3.2}$$

with

ω_{2v} and ω_{1v} as the harmonic angular frequencies

The relation of the harmonic angular frequencies between stator and rotor is, in agreement to equation (7.2.1),

$$\omega_{1v} = \omega_{2v} + \omega_{shift} \tag{7.3.3}$$

where

$\omega_{shift} = 2\pi p_A f_m$ is the mechanical rotor angular frequency in electrical rad/s

The harmonic space vectors in (7.3.1) and (7.3.2) can in steady state conditions be presented in phasor form as

$$\bar{i}_{2v} = i_{2v} e^{j\omega_{2v} t} e^{j\Phi_2} = \bar{I}_{2v} e^{j\omega_{2v} t} \tag{7.3.4}$$

$$\bar{i}_{1v} = i_{1v} e^{j\omega_{1v} t} e^{j\Phi_1} = \bar{I}_{1v} e^{j\omega_{1v} t} \tag{7.3.5}$$

The same can be applied to the remaining voltage and current vectors of the SDFM system as illustrated in figure 7.4. Doing so and omitting the redundant terms, the harmonic vector equations of the SDFM can be written in phasor form as

$$\bar{V}_{1v} = j\omega_{1v} L_{\sigma 1} \bar{I}_{1v} + \bar{E}_{1agv} \tag{7.3.6}$$

$$\bar{V}_{2v} = j\omega_{2v} L_{\sigma 2} \bar{I}_{2v} + \bar{E}_{2agv} \tag{7.3.7}$$

$$\bar{E}_{1agv} = (\bar{I}_{1v} + \frac{\bar{I}_{2v}}{a}) j\omega_{1v} L_{mag} \tag{7.3.8}$$

$$\bar{E}_{2agv} = \frac{s_v}{a} \bar{E}_{1agv} \tag{7.3.9}$$

The harmonic slip is defined as

$$s_v = \frac{\omega_{2v}}{\omega_{1v}} \approx 1 \tag{7.3.10}$$

Equations (7.3.6) - (7.3.10) are similar to the steady state model of the SDFM as presented in chapter 3 with the exception, that they represent the SDFM for the individual harmonics (fundamental is one case) and that resistance and the iron loss terms are no longer present. Although the resistances in the system are subject to skin effects and therefore increase in value they can be neglected compared to the reactances, which are linearly increasing with frequency [f5]. The use of an equivalent resistance for the iron losses is not significant to the overall flow of harmonic currents [f6].

The remaining quantities of the SDFM system are

$$\bar{V}_{1v} = \bar{V}_{sv} + j\omega_{1v} L_s \bar{I}_{sv} \tag{7.3.11}$$

$$\bar{V}_{1v} = \bar{V}_{yv} + j\omega_{1v} L_y \bar{I}_{yv} \tag{7.3.12}$$

and

$$\bar{I}_{1v} = -\bar{I}_{sv} - \bar{I}_{yv} \tag{7.3.13}$$

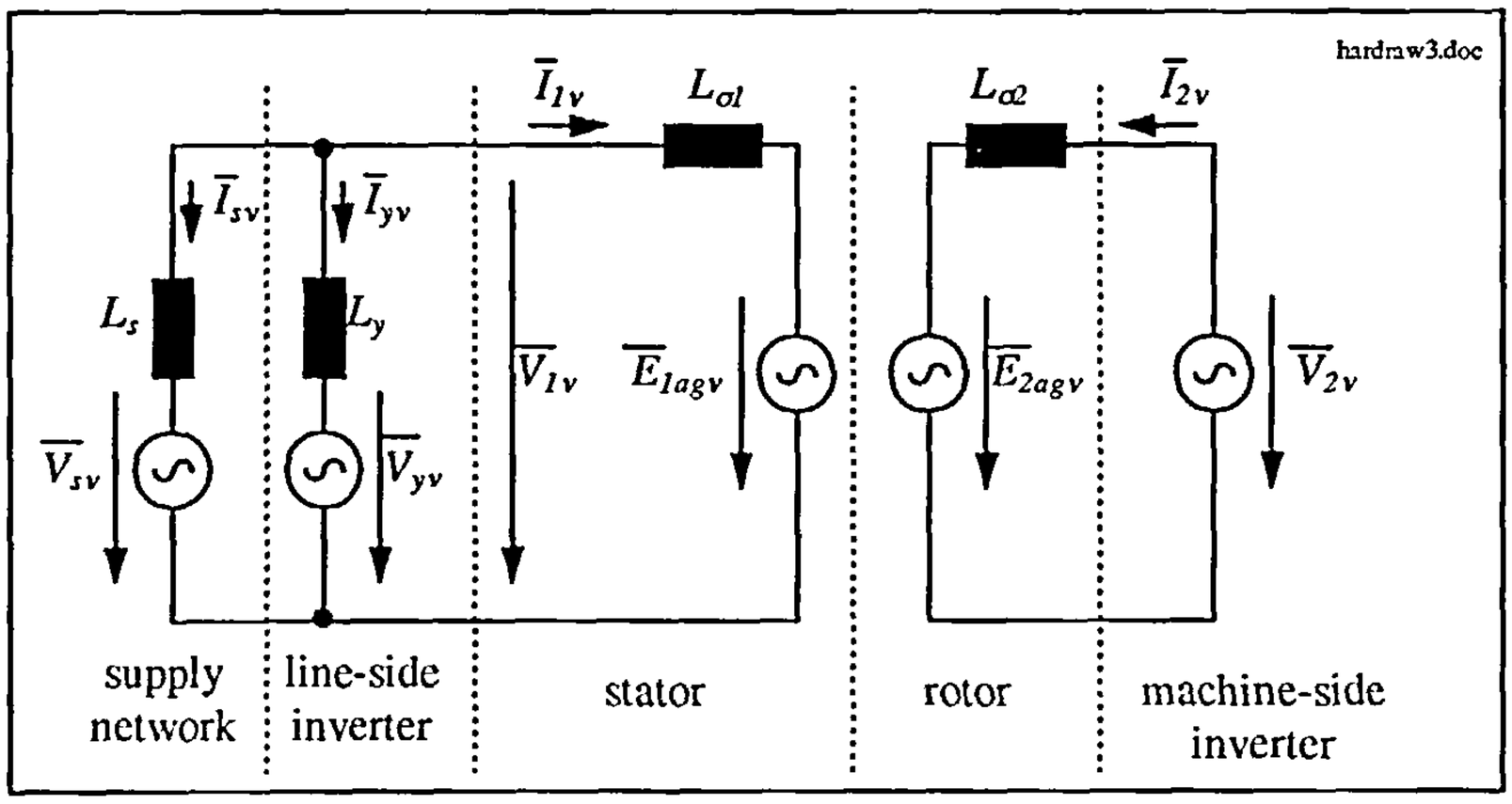

Figure 7.16: Per-phase harmonic steady state equivalent circuit of the SDFM system

V_{sv} and V_{yv} are the phasors for the supply network and the line-side inverter voltages. As mentioned, only the harmonic voltages produced by the two inverters are considered and thus the supply network voltage is of no concern, but it is included in the equations to derive a general harmonic model.

The per-phase equivalent circuit for above equations is displayed in figure 7.16.

The complete system harmonic model of the SDFM is given by equation (7.3.14). The derivation and the impedance definitions can be found in Appendix E.1.3.

$$\begin{bmatrix} \bar{V}_{sv} \\ \bar{V}_{yv} \\ \bar{V}_{2v} \end{bmatrix} = \begin{bmatrix} -(\bar{Z}_{11v} + \bar{Z}_{sv}) & -\bar{Z}_{11v} & \bar{Z}_{magv}\frac{1}{a} \\ -\bar{Z}_{11v} & -(\bar{Z}_{11v} + \bar{Z}_{yv}) & \bar{Z}_{magv}\frac{1}{a} \\ -\bar{Z}_{magv}\frac{s_v}{a} & -\bar{Z}_{magv}\frac{s_v}{a} & \bar{Z}_{22v} \end{bmatrix} \begin{bmatrix} \bar{I}_{sv} \\ \bar{I}_{yv} \\ \bar{I}_{2v} \end{bmatrix} \tag{7.3.14}$$

The harmonic currents are now calculated in following sequence:

1. Determine the harmonic voltage source and the respective voltage harmonic phasor for a particular frequency. All other harmonic voltages phasors take the value zero.
2. Calculate impedances at the harmonic frequency
3. Solve equation (7.3.14), which requires the inverse of the impedance matrix.

f_2 [Hz]	measured $V_{2ll\ peak}$ [V]	simulated $V_{2ll\ peak}$ [V]	$V_{2\ phase}$ [V]	measured $I_{2\ peak}$ [A]	modeled $I_{2\ peak}$ [A]	f_1 [Hz]	measured $I_{1\ peak}$ [A]	modeled $-I_{1\ peak}$ [A]
10	159	163	94.1	4.47	4.47	50	3.08	2.99
2480	19	15	8.7	0.014	0.012	2520	0.014	0.011
-2520	13	15	8.7	0.013	0.012	-2480	0.011	0.011
-4990	133	139	80.3	0.062	0.052	-4950	0.065	0.05
5010	128	132	76.2	0.062	0.05	5050	0.063	0.048
7480	39	35	20.2	0.012	0.009	7520	0.014	0.008
-7520	34	33	19.1	0.008	0.009	-7480	0.007	0.008
-9990	71	79	45.6	0.017	0.015	-9950	0.018	0.014
10010	65	71	41	0.014	0.013	10050	0.017	0.013
12480	33	33	19.1	0.006	0.005	12520	0.008	0.005
-12520	30	20	11.5	0.008	0.003	-12480	0.008	0.003
-14990	48	30	17.3	0.007	0.004	-14950	0.007	0.003
15010	56	34	19.6	0.008	0.004	15050	0.008	0.004

hartable.doc

Table 7.1: Measured and modeled SDFM current harmonics due to the machine-side inverter

This sequence has to be repeated for each individual harmonic voltage. If there are two harmonic voltage sources present at the same frequency, then the sequence has to be carried out twice. Each time setting one voltage source to zero. Superposition of the acquired harmonic currents from each event gives the total harmonic current for the frequency of interest. A program written in MATLAB is used for this purpose.
It has to be borne in mind that the harmonic voltages obtained from the time-step simulations of the inverter switching are line-to-line quantities, but the model represents phase quantities. Correct scaling must therefore be used.

As an example, the simulation and modeling process is applied for calculation of the machine current harmonics of the SDFM, which stem from the machine-side inverter voltage harmonics. Results of the harmonic currents for the stator and the rotor are listed in table 7.1, which also contains the values of the measured current harmonics.
It can be seen that the modulation process delivers results, which are quite close to the measured values.

To complete the modeling process it is necessary to use the per-phase equivalent circuit of the SDFM for calculating the fundamental current components of the stator and the rotor. For that the steady state model as used for simulations on the SDFM in chapter 3 is employed. This model also contains the iron loss resistor as explained in chapter 3. The inputs to the model are the stator voltage and the rotor current fundamental. The output is the fundamental of the stator current. The results are listed in table 7.1.

Finally, the normalised machine current harmonics due to the machine-side inverter are depicted in figure 7.17. As the results in table 7.1 have already shown, the simulation and modeling process delivers very close results to the real system. Comparing figure 7.17 with figure 7.5 underlines the usefulness of the described process in graphical form.

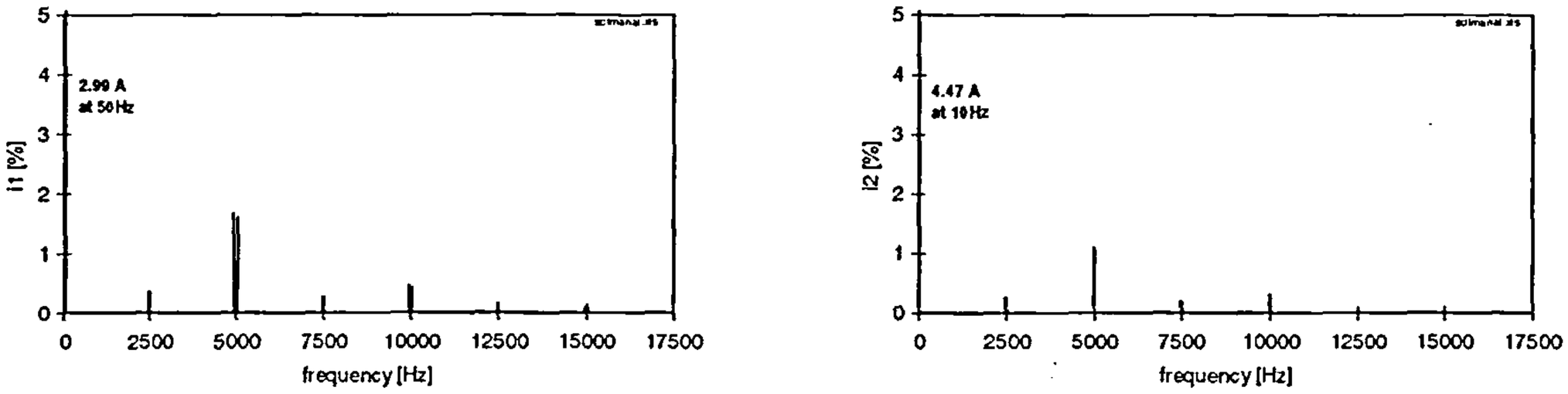

Figure 7.17: Modeled SDFM current harmonics

A main reason to apply the described method to a system is to investigate the harmonic current propagation of the machine-side inverter caused current harmonics through the SDFM into the supply. However, the measured results show, the relevance to this particular laboratory system is rather limited, but it can be expected that the described simulation and modeling process constitutes a helpful tool in investigating theoretically the harmonic current content of an inverter-fed system, as long as the involved inductances are known.

7.3.2 Simulation and Modeling of the CDFM Harmonics

Now the whole harmonic current prediction process is applied to the CDFM system.

Inverter time-step simulation

For simulation of the machine-side inverter following parameters are used:

d.c.-link voltage: 650 V
modulation index: 0.108 (as in measurements)
switching frequency: 2.5 kHz
simulation step width: 1 µs

The sampling frequency of the simulated waveform is 50 kHz.

Parameters for the line-side inverter are the same as used in section 7.3.1.

The acquired frequency spectrum of the line-line voltage of the respective inverters are shown in figure 7.18 and the values for the interesting voltage harmonics of the machine-side inverter are listed in table 7.2 for comparison with the measured values. There is

generally a good agreement between real and simulated harmonics. Only the values for the harmonics at around 15 kHz differ to a larger extend compared to the other values. This may be due to the neglect of the dead-time effects in the simulations, which effects the results more at a small modulation index.

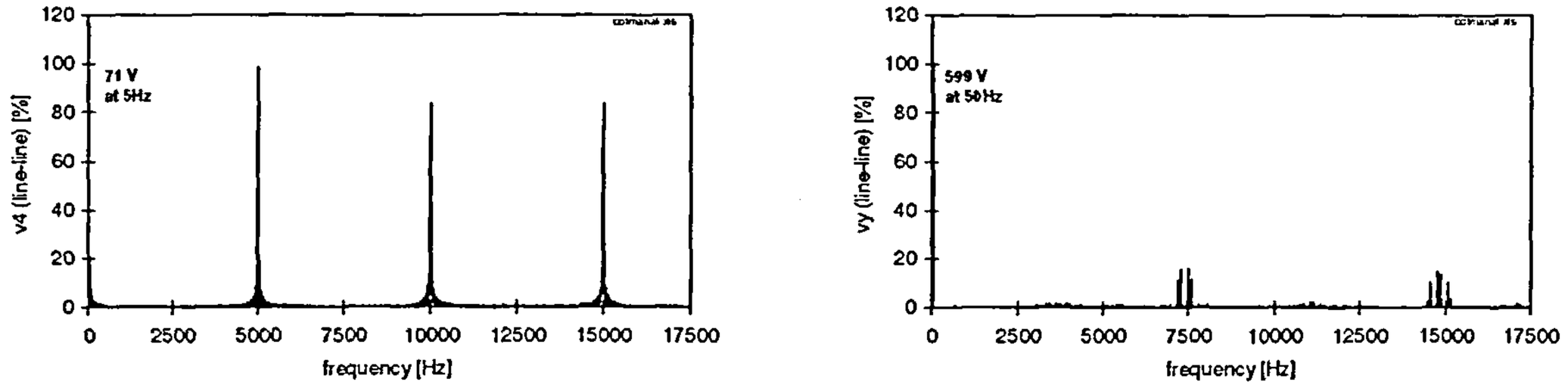

Figure 7.18: Simulated CDFM inverter voltage harmonics

Steady state harmonic modeling

Representing the harmonic currents and voltages already in phasor form as introduced in the previous section delivers the following equations for the CDFM:

$$\overline{V}_{1v} = j\omega_{1v} L_{\sigma 1} \bar{I}_{1v} + \overline{E}_{1agv}$$

$$\overline{V}_{2v} = j\omega_{2v} L_{\sigma 2} \bar{I}_{2v} + \overline{E}_{2agv}$$

$$\overline{V}_{3v} = -j\omega_{2v} L_{\sigma 3} \bar{I}_{2v} + \overline{E}_{3agv}$$

$$V_{4v} = j\omega_{4v} L_{\sigma 4} I_{4v} + E_{4agv}$$

$$\overline{E}_{1agv} = (\bar{I}_{1v} + \frac{\bar{I}_{2v}}{a}) j\omega_{1v} L_{magA}$$

$$\overline{E}_{2agv} = \frac{s_{Av}}{a} \overline{E}_{1agv}$$

$$\overline{E}_{3agv} = (-\bar{I}_{2v} + \frac{\bar{I}_{4v}}{b}) j\omega_{2v} L_{magB}$$

$$\overline{E}_{4agv} = \frac{s_{Bv}}{b} \overline{E}_{3agv}$$

$$s_{Av} = \frac{\omega_{2v}}{\omega_{1v}} \approx 1$$

$$s_{Bv} = \frac{\omega_{4v}}{\omega_{2v}} \approx 1$$

The remaining quantities of the CDFM system, including a variac at side 1, are

$$\overline{V}_{xv} = \overline{V}_{sv} + j\omega_{1v} L_s \bar{I}_{sv}$$

$$\overline{V}_{xv} = \overline{V}_{yv} + j\omega_{1v} L_y \bar{I}_{yv}$$

$$\overline{V}_{xv} = \overline{V}_{1v} + j\omega_{1v} (1-x) L_x \bar{I}_{x1v}$$

$$\overline{V}_{1v} = j\omega_{1v} x L_x \bar{I}_{x2v}$$

and

$$\bar{I}_{x1\nu} = -\bar{I}_{s\nu} - \bar{I}_{y\nu}$$
$$\bar{I}_{1\nu} = -\bar{I}_{x2\nu} - \bar{I}_{s\nu} - \bar{I}_{y\nu}$$

$I_{x1\nu}$ and $I_{x2\nu}$ are the variac harmonic currents and x is the ratio between output and input voltage of the variac as

$$x = \frac{\bar{V}_{1\nu}}{\bar{V}_{x\nu}}$$

which is determined by the fundamental voltage ratio.

The per-phase harmonic equivalent circuit of the CDFM is displayed in figure 7.19. Compared to the SDFM system the circuit in figure 7.19 is much more complicated, especially due to the variac.

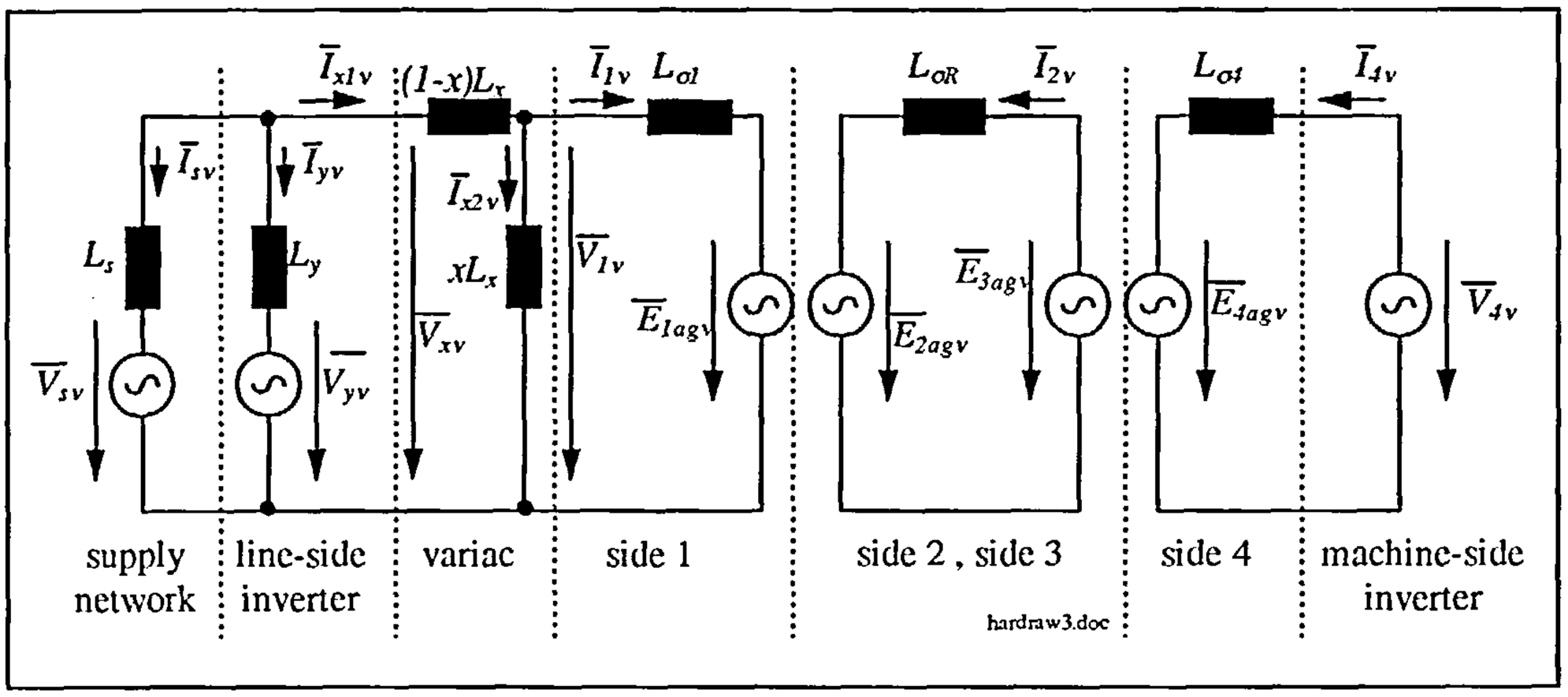

Figure 7.19: Per-phase harmonic steady state equivalent circuit of the CDFM system

Nevertheless, the compact mathematical description of the CDFM system is given with equation (7.3.15). The derivation and the impedance definitions can be found in Appendix E.1.4.

$$\begin{bmatrix} \bar{V}_{s\nu} \\ \bar{V}_{y\nu} \\ \bar{V}_{4\nu} \\ 0 \end{bmatrix} = \begin{bmatrix} \bar{Z}_{c\nu} - \bar{Z}_{x1\nu} - \bar{Z}_{s\nu} & \bar{Z}_{c\nu} - \bar{Z}_{x1\nu} & \bar{Z}_{magA\nu}\frac{1}{a}\bar{Z}_{a\nu} & \bar{Z}_{c\nu} \\ \bar{Z}_{c\nu} - \bar{Z}_{x1\nu} & \bar{Z}_{c\nu} - \bar{Z}_{x1\nu} - \bar{Z}_{s\nu} & \bar{Z}_{magA\nu}\frac{1}{a}\bar{Z}_{a\nu} & \bar{Z}_{c\nu} \\ -\bar{Z}_{magB\nu}\frac{s_{B\nu}}{b}\bar{Z}_{b\nu} & -\bar{Z}_{magB\nu}\frac{s_{B\nu}}{b}\bar{Z}_{b\nu} & \bar{Z}_{44\nu} - \bar{Z}_{magB\nu}\frac{s_{B\nu}}{b}\bar{Z}_{a\nu} & -\bar{Z}_{magB\nu}\frac{s_{B\nu}}{b}\bar{Z}_{b\nu} \\ \bar{Z}_{c\nu} & \bar{Z}_{c\nu} & \bar{Z}_{magA\nu}\frac{1}{a}\bar{Z}_{a\nu} & \bar{Z}_{c\nu} - \bar{Z}_{x2\nu} \end{bmatrix} \begin{bmatrix} \bar{I}_{s\nu} \\ \bar{I}_{y\nu} \\ \bar{I}_{4\nu} \\ \bar{I}_{x2\nu} \end{bmatrix} \tag{7.3.15}$$

As it was the case for the SDFM system, the harmonic modeling is applied to the harmonics created by the machine-side inverter. Due to the low modulation index, the interesting

harmonics are centered around even multiples of the switching frequency. The resulting modeled currents are listed in table 7.2, together with the measured values. Table 7.2 also gives the fundamental values obtained from the fundamental steady state model.

The modeled current harmonics of the CDFM are generally within an acceptable margin of the real values. Discrepancies are largely introduced by the complexity of the system due to the variac connection and the error in the used inductances for modeling compared to actual system inductances.
The graphical representation of the results are given in figure 7.20, which compares well with the graphs in figure 7.10.

f_2 [Hz]	measured $V_{4ll\ peak}$ [V]	simulated $V_{4ll\ peak}$ [V]	$V_{4\ phase}$ [V]	measured $I_{4\ peak}$ [A]	modeled $I_{4\ peak}$ [A]	f_1 [Hz]	measured $I_{1\ peak}$ [A]	modeled $I_{1\ peak}$ [A]
5	70.7	71.6	41.3	4.7	4.71	50	5.88	5.48
-4990	64	70	40.4	0.023	0.013	-4950	0.041	0.031
5010	60	63	36	0.019	0.011	5050	0.039	0.027
-9990	39	59	34	0.009	0.006	-9950	0.012	0.012
10010	37	48	27	0.005	0.004	10050	0.015	0.010
-14990	16	41	24	0.005	0.002	-14950	0.011	0.007
15010	19	59	34	0.005	0.004	15050	0.012	0.008

hartable.doc

Table 7.2: Measured and modeled CDFM current harmonics due to the machine-side inverter

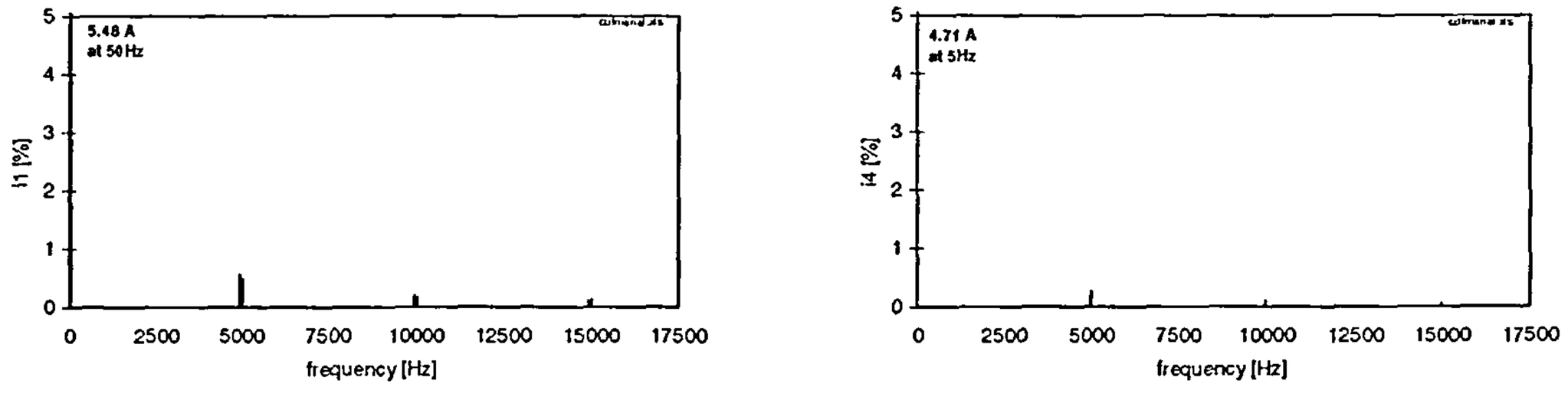

Figure 7.20: Modeled CDFM current harmonics

It can be concluded that the used harmonic current prediction process delivers close realistic results for the current harmonics for both systems, the SDFM and the CDFM. Although the laboratory machine set used gives distorted harmonic current distributions due to the inductance values of the system, the simulated values are confirmed.

7.4 Summary

This chapter deals with the harmonics appearing in the SDFM and the CDFM drive system. Starting with the dissection of the different harmonic creating sources, a thorough analysis of the current and voltage harmonics for the SDFM and the CDFM is given. Harmonics, transmitting through the machine system are related in frequency terms depending on the harmonic producing source and thus create a clear picture of where the harmonics come from and how they propagate through the system.

Finally, a harmonic current prediction, simulation and modeling process for the inverter produced harmonics is described. Based on the time-step simulation of the inverter voltage waveform and with the knowledge of the system inductances, this harmonic current prediction process generates good results allowing it to be used for determining harmonic currents of an inverter fed system, such as the SDFM and the CDFM.

Chapter 8

Conclusions

New conclusions resulting out of this thesis are written in *italic*.

The primary objective of this research has been an investigation into the field oriented control performance of doubly-fed induction machines, for single and cascaded machine arrangements.

Beginning with the space vector theory a dynamic two-axis machine model for the SDFM (single doubly-fed induction machine) is derived in a general reference frame to serve as foundation for the field oriented control.

Steady state treatment with simulations on the per-phase equivalent circuit allows an insight of the power flow behaviour of the doubly-fed machine. It shows that the variation of the rotor current phasor relative to the stator voltage phasor manipulates the active and reactive power flow in the SDFM. Experimental steady state measurements support the steady state simulation results obtained from the per-phase equivalent circuit equations and confirm it as a useful simulation tool.

The field oriented control of the SDFM is based on stator flux orientation. Neglecting the stator resistance, the measurement of the stator voltage vector relates to the position of the stator flux with only a small error. Experimental results of an inner current control loop show the manipulation of the active power by the q-axis rotor current component and the reactive power by the d-axis rotor current component. Adding a slip proportional feed-forward term to the output of the q-axis current controller eases the tuning and improves the steady state accuracy of the control. Extending the inner control loop with an outer power control loop with active and reactive stator power feedback allows an excellent decoupled control of those quantities, which is confirmed by experimental results. Since the q-axis rotor current component in the field oriented reference frame is proportional to the machine torque the inner q-axis current control loop can be extended with an outer speed control loop. Experimental results show the high performance speed control of the system. The d-axis rotor current component in this case is set to a constant value, which keeps the reactive power consumption of the SDFM largely unchanged.

The CDFM (cascaded doubly-fed induction machine) is a connection of two wound rotor induction machines. Both machines can have different machine ratings and parameters and they can be connected in two different ways, with positive and negative rotor sequence connection. In this thesis a two-axis dynamic machine model is derived for either machine connection. The developed reference frame system can be applied to both machine connections and it has the advantage that the "viewing" of the CDFM goes from side 1 towards side 4 of the machine. In this case, the reference frame of the stator of machine B, side 4, is moving relative to side 1 and is not stationary. This helps to ease the understanding of the CDFM.

The extensive steady state description of the CDFM is in parallel to the steady state description of the SDFM to highlight similarities. Starting with the frequency and slip definitions of each individual machine it becomes clear that the CDFM has the same frequency and slip equations as a SDFM with an equivalent pole pair number made up from the sum or difference of the individual machine pole pair number, depending on the rotor phase sequence connection. Neglecting losses, the power conversion properties between its three accessible machine sides of the CDFM are the same as for a SDFM, with the introduction of an equivalent slip, relating side 1 and side 4 of the CDFM. The individual developed electromechanic torque components of the CDFM are in proportion to their pole pair number and they are co-acting for positive phase sequence connection and counter-acting for negative phase sequence connection. Consequently, only the positive phase sequence rotor connection, where both air-gap fields are counter-rotational relative to the rotor, is the useful connection option.

An investigation based on machine utilisation principles leads to the conclusion that two identical machines have to be connected to form a CDFM. In that case the mechanical load is shared in equal terms between the individual machines, ignoring losses. The speed range of a CDFM can be up to about 80% of the subsynchronous speed of machine A. By further nearing the synchronous speed of machine A the coupling between the individual machines decreases and is entirely lost at the synchronous speed of machine A. *In that speed range, the CDFM has the same power relationship between side 1 and side 4 as a SDFM has between the stator and rotor. For full torque capabilities from standstill the bi-directional converter on side 4 has to handle 50% of the full power rating.*

The steady state equivalent circuit of a CDFM is a serial connection of two SDFM equivalent circuits. As with the reference frames, it is advantageous to view the CDFM from side 1 towards side 4. In that case, side 3 acts as the primary side of machine B and side 4 as the secondary machine side. Per-phase equivalent circuit steady state simulations of the CDFM with the variation of the side 4 current phasor relative to the side 1 voltage

phasor shows a similar power flow behaviour in the CDFM as for the SDFM. The steady state simulation results are confirmed by experimental steady state measurements.

A previously developed field orientated control method for the CDFM takes the measurements of the side 1 and side 4 currents to create a so-called artificial combined flux reference frame for orientation of the inaccessible rotor current q-component. This rotor current component is proportional to the CDFM torque in that reference frame. In order to manipulate the rotor current component via side 4 a mathematical extension in the q-axis is necessary. *Since this control method is only applicable to a CDFM composed of equal machines, a modification is developed in this thesis to allow the implementation on a CDFM composed of any machine combination. Experimental speed control results show the performance of the modified combined flux oriented control method. It is shown, that particularly at high speeds instability problems arise, which are also mentioned for the original control implementation. As a likely cause for the control instabilities, the mathematical q-axis extension is removed and the resulting simplified control method is analysed in this work. In comparison to the original control the simplified control introduces a slight error in the torque control equation in the q-axis. However, this is of no concern, since the error is corrected by a closed torque or speed control loop. Experimental results show that the simplified speed control for the combined flux orientation is not inferior to the original control. On the contrary, instability problems are not present with the simplified method.*
An investigation, whether the combined flux control leads to natural decoupled active and reactive power control of the CDFM reveals that this is not the case, because of cross coupling effects.

The steady state simulation study of the CDFM forms the basis and the justification for the SDFM control method to be applied to the CDFM. Implementing the stator (side 1) flux field oriented control for the first time to a CDFM reveals that the additional closed rotor circuit loop of the CDFM in comparison to the SDFM causes cross coupling effects. Those cross coupling effects are related to the rotor resistance and the rotor speed. The smaller the rotor resistance, the smaller is the cross coupling and the closer the speed approaches machine A synchronous speed the higher is the cross coupling. If a CDFM with small rotor resistance values is used and the maximum speed of the CDFM is limited to about 80% of machine A synchronous speed, then it can be said that despite the cross coupling good enough "natural decoupled" active and reactive power control can be achieved as it is known from the SDFM research. An outer power control loop compensates the slight cross coupling effect as confirmed by experimental results. If the d-axis current demand value is set to a constant value, then a speed control loop extension in the q-axis allows the torque to be controlled to follow the demanded speed as shown by experimental work.

A previously developed position sensorless stator flux oriented control method for active and reactive power control of the SDFM is based on the proportionality between stator and rotor current components in the stator flux reference frame. *This proportionality is also valid between active and reactive power and the rotor current components as shown in this thesis. Both sensorless methods lead to the same control results for active power control. However, the ripple content on the active power and current components is larger than for the sensored method. Using the estimated rotor position angle derived from the proportionality between stator (current or power) and rotor (current) quantities and differentiating the estimated angle signal gives a speed signal estimate. This can be employed for a novel speed control technique. Both methods (stator current or stator power based) yield similar sensorless speed control performance of the SDFM. Compared to the sensored speed control method the sensorless scheme results in higher ripples on the q-axis rotor current component and the control bandwidth of the sensorless method is lower than for the sensored scheme.*

The stator (side 1) power based sensorless method is applied to the CDFM. Despite the cross coupling effect, which distorts the proportionality between side 1 and side 4 quantities, the sensorless method is still feasible. The sensorless power control loop results in slightly increased cross coupling and higher ripple on the active power and the q-axis current component of side 4. Similar to the novel sensorless speed control of the SDFM the sensorless speed control applied to the CDFM results in a higher ripple content of the q-axis current component of side 4 and a lower speed control loop bandwidth, compared to the sensored arrangement.

An extensive harmonic analysis of both stator flux oriented control implementations, the SDFM and the CDFM, yields a detailed picture of harmonic sources and harmonic current propagation through the system. A novel harmonic current prediction process generates close realistic results to justify its application as a tool for harmonic current calculation. The process consists of three steps. Firstly, the time-step simulation of PWM inverter voltage waveforms with successive FFT to give harmonic voltage frequencies and magnitudes. In the second step, each single harmonic voltage serves as an input to a harmonic steady state model, which takes account only of the system inductances, and delivers complex harmonic current phasors. If necessary for normalising purposes in a third step, the fundamental steady state model can be used to calculate the current at fundamental frequency.

Commenting generally on the brushless doubly-fed machine arrangements it can be said, that a CDFM composed of two wound rotor induction machines is in reality probably difficult to realise, since the slip rings are mostly within the machine frame. A direct

connection of the slip rings is therefore not possible. It is more advantageous to have a SF-CDFM in terms of compactness. However, the drawback of a SF-CDFM and also of a BDFM are the additional rotor copper losses, which effect the overall efficiency of such a system. This is not the case for a DFRM, which also holds to its benefit that the steady state and field oriented control theory of a SDFM is applicable to it. Nevertheless, it is hard to say at the present time which doubly-fed machine arrangement will find increased commercial application in future.

Further Work

In order to support the experimental results of the CDFM for combined flux oriented control, modified and simplified, it is necessary to carry out stability investigations to establish unstable or slightly damped operating regions. Although there are no stability problems encountered for the stator flux oriented control of the CDFM it is worth to make stability investigations also for this control method.

The stator flux oriented control of a CDFM is subject to slight cross coupling due to the closed rotor circuit loop. It may be worth exploring if there is the possibility of a decoupling circuit.

With the work presented in this thesis there have been investigations on two different reference frames for orientation of the CDFM, i.e. the combined flux and the stator (side 1) flux. Field orientation in terms of rotor flux (side 2 or side 3) of the CDFM has not been considered.

Much research effort has recently been applied to low speed cage induction machine drives to solve the problems associated with low stator voltage and low frequency. A doubly-fed machine arrangement has at standstill the same frequency as on the primary side and the voltage is at its maximum. It may be worth investigating the SDFM / CDFM arrangement for low speed applications. The work presented in the thesis is only focused on a speed range centered around the synchronous speed.

The position sensorless speed control of the SDFM / CDFM introduces a higher ripple content in the q-axis current and the control bandwidth is lower as for the sensored control. It may be possible to increase the control bandwidth and lower the ripple by increasing the angle resolution of the angles involved.

The thesis has concentrated on CDFM's and SF-CDFM's. The stator flux oriented control method has not yet been applied to a BDFM, which leaves room for work in this area.

Appendix A

Experimental Machine Set

A.1 Wound Rotor Induction Machines

Two wound rotor induction machines are used during experimental work. One is used as SDFM and as machine B of the CDFM. The second machine serves as machine A of the CDFM.
Specifications, parameter identification and the electrical connection are described in the following.

A.1.1 Specifications and Parameters

Name plate data and derived rated slip and torque values for the wound rotor induction machines are listed next:

SDFM / machine B: 2.25 kW (3HP) BROOK wound rotor induction machine
1420 rpm , $s_{rated} = 0.0533$, $T_{e\ rated} = 15.1$ Nm
2 pole pairs
stator: 400 - 440 V / 8 A
rotor: 390 V / 6 A

machine A of CDFM: 2.25 kW (3HP) HOMES wound rotor induction machine
670 rpm , $s_{rated} = 0.119$, $T_{e\ rated} = 32.1$ Nm
4 pole pairs
stator: 440 V / 6.4 A
rotor: 135 V / 11 A delta

The parameters of the induction machines are calculated from the standard short circuit and open circuit machine tests as described in the next section.
The per-phase parameters of the individual machines are given below. It is important to note that in case of the SDFM the primary parameters are stator parameters and the secondary rotor parameters. In case of the CDFM that is different. As explained in chapter

4, the "viewing" of the CDFM goes from side 1 towards side 4 through the machine, rather than seeing it from both stationary machine sides. Therefore, side 1 of machine A is considered as it's primary side and is the rotor of the HOMES machine. Side 2 is consequently the stator of the concerning machine. The tertiary side, side 3, of the CDFM is the rotor of machine B. The stator of machine B is then considered as the secondary side of machine B and constitutes side 4. The iron losses are concentrated on side 1 and side 3 only for the respective machines.

SDFM ("1" = stator of BROOK , "2" = rotor of BROOK)

pole pairs:	2
turns-ratio:	$a = 1.013 = N_1/N_2$
resistances:	$R_1 = 4.4\ \Omega$
	$R_2 = 5.9\ \Omega$
leakage ind.:	$L_{\sigma 1} = 0.025$ H
	$L_{\sigma 2} = 0.024$ H
mag. ind.:	$L_{mag} = 0.88$ H
iron res.:	$R_{fe} = 384\ \Omega$

CDFM - machine A ("1" = rotor of HOMES , "2" = stator of HOMES)

pole pairs:	4
turns-ratio:	$a = 0.588 = N_1/N_2$
resistances:	$R_1 = 2.3\ \Omega$
	$R_2 = 3.9\ \Omega$
leakage ind.:	$L_{\sigma 1} = 0.00878$ H
	$L_{\sigma 2} = 0.0254$ H
mag. ind.:	$L_{magA} = 0.08$ H
iron res.:	$R_{feA} = 40\ \Omega$

CDFM - machine B ("3" = rotor of BROOK , "4" = stator of BROOK)

pole pairs:	2
turns-ratio:	$b = 0.987 = N_3/N_4$
resistances:	$R_3 = 5.9\ \Omega$
	$R_4 = 4.4\ \Omega$
leakage ind.:	$L_{\sigma 3} = 0.024$ H
	$L_{\sigma 4} = 0.025$ H
mag. ind.:	$L_{magB} = 0.858$ H
iron res.:	$R_{feB} = 374\ \Omega$

A.1.2 Parameter Identification

In order to determine the parameters of each wound rotor induction machine the standard short-circuit and open-circuit tests [f4, f7] were applied to the machines.

Resistance Test

A wound rotor induction machine allows to have access to the stator and the rotor windings. For a star-connected winding it is possible to calculate the per-phase resistance by applying a d.c. voltage and measuring the voltage drop and current. Doing that for the three phases and averaging the results gives the d.c. resistance. For a delta-connected system it is necessary to make a delta-to-star calculation.

Turns-Ratio Test

The turns ratio of the induction machine is the ratio of stator air-gap voltage to the rotor air-gap voltage

$$a = \frac{N_1}{N_2} = \frac{E_{1ag}}{E_{2ag}}$$

at standstill. However, those voltages are not directly accessible, when making the tests. When applying rated voltage V_1 on the stator side the stator leakage and resistance must be considered and by applying rated voltage V_2 to the rotor side the rotor leakage and resistance must be considered. By doing so the turns ratio can be calculated as [f4]

$$a = \sqrt{\frac{r_1}{r_2}}$$

where

$$r_1 = \frac{V_1}{E_{2ag}} \quad \text{and} \quad r_2 = \frac{V_2}{E_{1ag}}$$

Short Circuit Test (Locked Rotor Test)

This test allows to calculate the per-phase leakage inductances and resistances. The test can be performed twice by either short circuiting the rotor or the stator. Figure A.1 shows the per-phase circuit for a short circuit on the rotor.

In this test the high ohmic magnetising path can be neglected compared to the rotor leakage and resistance. Stator voltage is applied to establish rated phase current. Voltage, current and power is measured with the two-watt-meter method. The individual parameters can be calculated as

$$\cos\varphi = \frac{P_{3\,phase}}{3 * V_{phase} * I_{phase}} \tag{A1}$$

with

$$\bar{I}_1 = I_{phase}(\cos\varphi - j\sin\varphi) \quad \text{and} \quad \bar{V}_1 = V_{phase} \tag{A2}$$

gives for the complete impedance

$$\bar{Z}_1 = \frac{\bar{V}_1}{\bar{I}_1} \tag{A3}$$

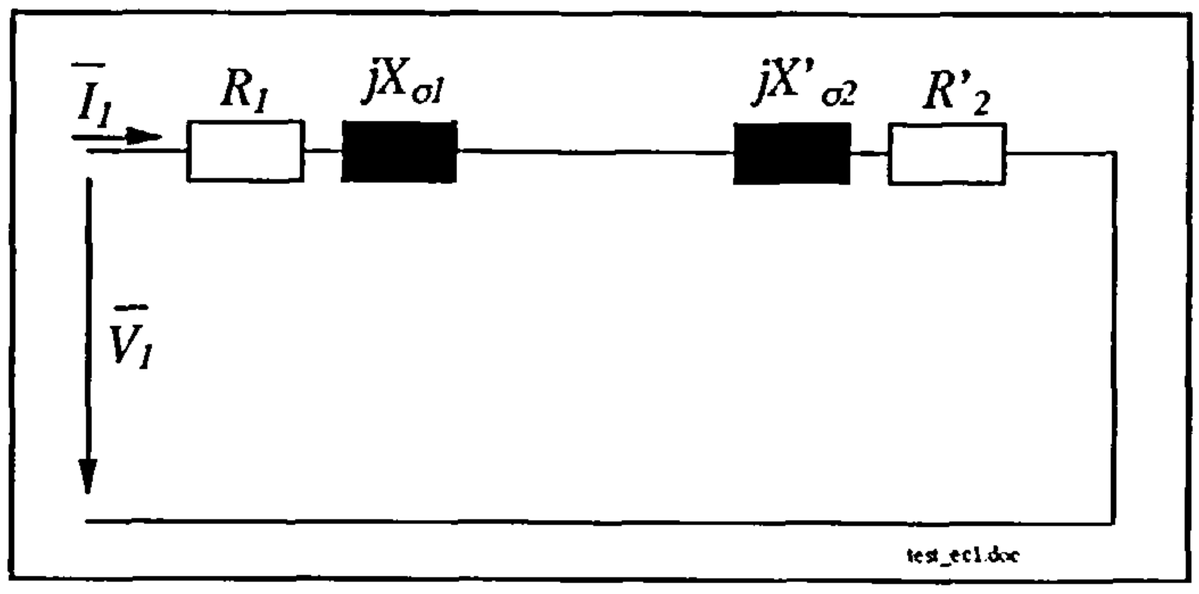

Figure A.1: Short rotor per-phase equivalent circuit

Due to skin effects the resistance for the stator and rotor side will be higher than measured from the d.c. resistance test. The value for 50 Hz can be calculated with

$$R_1 + R'_2 = real(\bar{Z})$$

where the ratio between R_1 and R'_2 ought to be in the ratio given by the d.c. test [f4].
IEEE test procedures recommend the empirical distribution of the leakage reactances in the ratio of $X_1 = X'_2$ for wound rotor induction machines [f7], which then gives

$$X_1 = X'_2 = 0.5 * imag(\bar{Z}_1)$$

Open Circuit Test

At this point it is normally necessary to perform a no-load test when having a cage induction machine. However, that is different and much more convenient with a wound rotor induction machine and a prime mover. With the open circuit test the iron loss resistor and the magnetising inductance can be calculated. Figure A.2 shows the per-phase equivalent circuit for an open circuited rotor.

For cage induction machines it is usually assumed that the iron losses are concentrated on the stator side, because the rotor encounters only small frequencies. Depending on the operational speed range of a wound rotor induction machine the rotor frequency can reach high values, which can even be higher than the stator frequency. Since the iron losses are proportional to the frequency it suggests that the assumption of the cage induction machine iron loss resistor doesn't apply to a wound rotor induction machine. However, tests showed

that the influence of the speed on the iron loss resistor is only marginal and the assumption that all iron losses are concentrated on the stator side can be adopted.

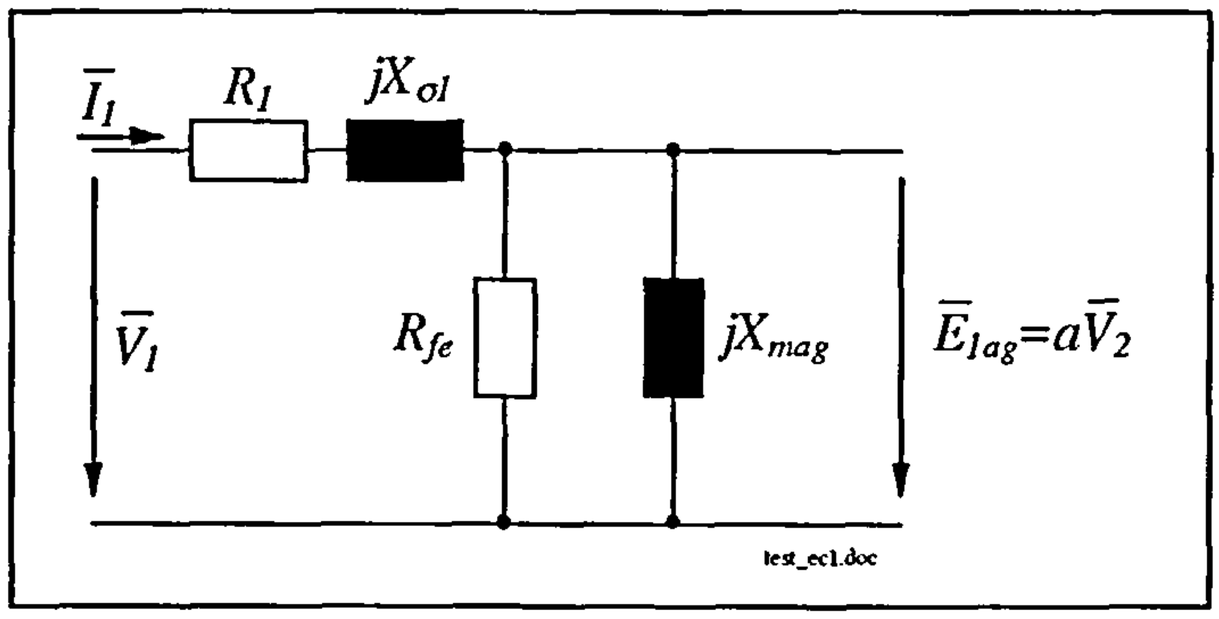

Figure A.2: Open rotor per-phase equivalent circuit

Rated stator voltage is applied and voltage, current and power is measured. The parameters can be calculated together with equations (A1) - (A3) and using results from the short circuit test as

$$\overline{Z}_{mag} = \overline{Z} - (R_1 - jX_{\sigma 1})$$

and

$$R_{fe} = \frac{\left|\overline{Z}_{mag}\right|^2}{real(\overline{Z}_{mag})}$$

$$X_{mag} = \frac{\left|\overline{Z}_{mag}\right|^2}{imag(\overline{Z}_{mag})}$$

Alternatively, at standstill and by measuring rotor voltage the parameters can be calculated with the assumption of

$$\overline{E}_{1ag} = \overline{V}_2 * a \quad \text{and} \quad \overline{Z}_{mag} \approx \frac{\overline{E}_{1ag}}{\overline{I}_1}$$

as

$$R_{fe} = \frac{\overline{Z}_{mag}}{real\overline{I}_1}$$

$$X_{mag} = \frac{\overline{Z}_{mag}}{imag(\overline{I}_1)}$$

A.1.3 Mechanical Set-Up

All three machines, the two wound rotor induction machines and the DC-machine, are arranged on the same bed-plate as shown in figure A.3. The DC-machine has a through shaft, which makes it possible to connect a wound rotor induction machine on either side.

The wound rotor induction machines are mechanically connected so that side 2 and side 3 phases are aligned.
An incremental encoder is mounted on the shaft end of the machine arrangement.

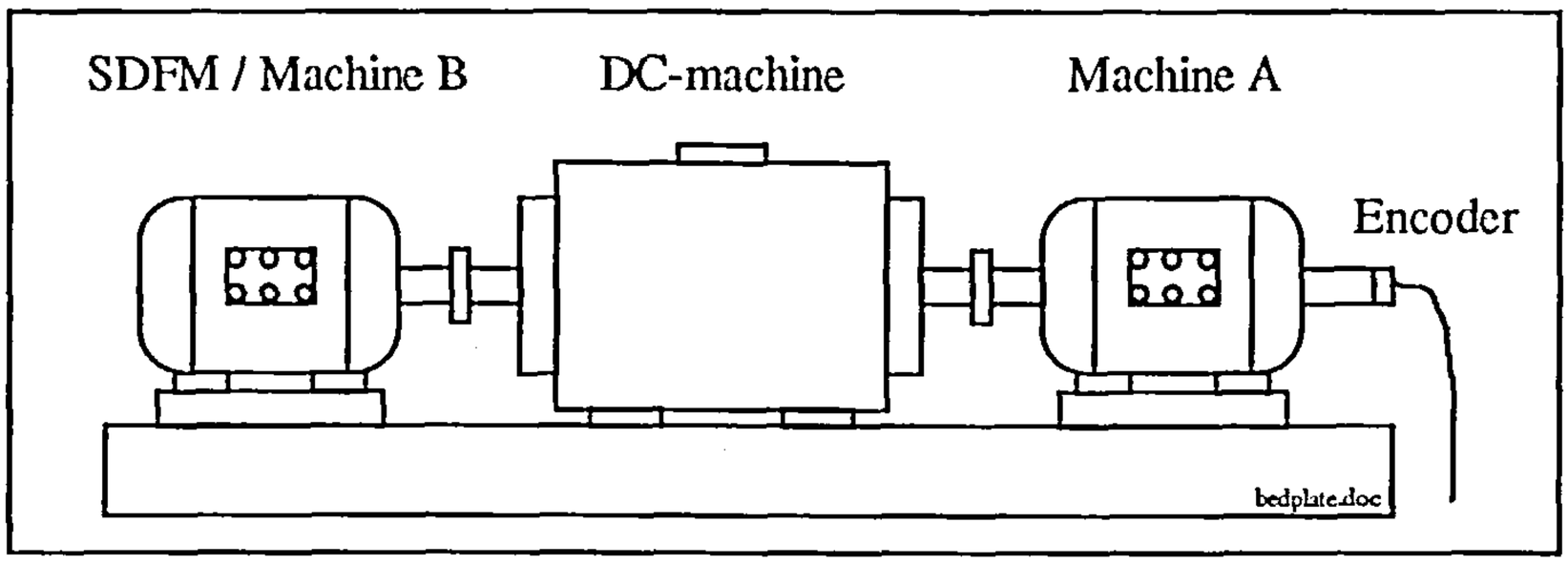

Figure A.3: Bed-plate arrangement of the machines

A.1.4 Electrical Connection Circuits

The electrical 3-phase machine connections of the SDFM and particularly of the CDFM have to be in an appropriate manner so that the resulting fields rotate in the correct direction. Those connections are outlined in the following.

SDFM

The stator of the SDFM is connected via a switch to the supply network and the rotor is directly connected to the inverter. Both, the stator and the rotor of the SDFM are connected in star. The abbreviations "r", "y" and "b" are indicating the three phases connections as red, yellow and blue.

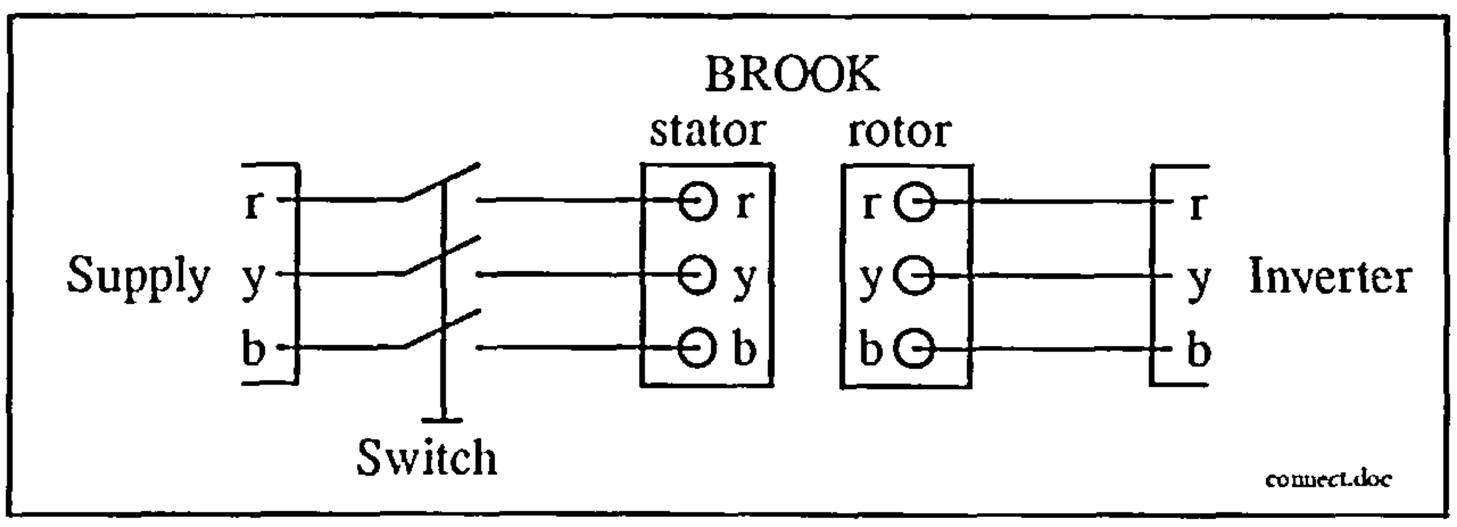

Figure A.3: SDFM connection

CDFM

The connection arrangement of the CDFM is illustrated in figure A.4. The 3-phase windings of the delta connected HOMES rotor are connected with the slip-rings to a variac via a switch. HOMES stator connects to the slip-rings of the BROOK rotor and the BROOK

stator is connected to the machine-side inverter.

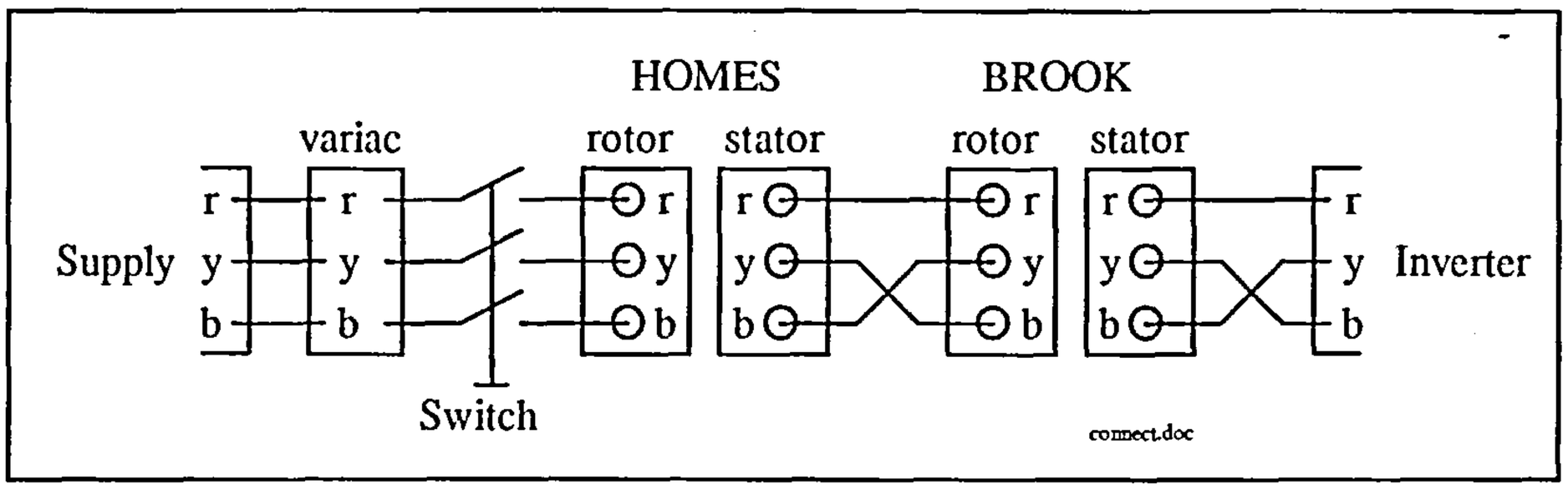

Figure A.4: CDFM connection

A.2 DC-machine

The prime mover of the machine arrangement is a HIGGS DC-machine. As a series wound type it has following specifications:

3.75 kW (5HP)

1000 rpm , $T_{e\ rated} = 35.8$ Nm

100 V / 46.7 A

To allow easier control the DC-machine is connected as a separately excited machine. In order to do so, both the field and the armature low-voltage high-current windings had to be connected with a transformer and variac arrangement as shown in figure A.5 and A.6.
The armature winding current can be controlled by a dc-chopper with a maximum current rating of 42 A. The input of the chopper is a 3-phase 208 V voltage. It is then rectified to produce the internal dc-link. A transformer provides electrical isolation to the grid and the variac is used for the voltage adjustment of the chopper input.

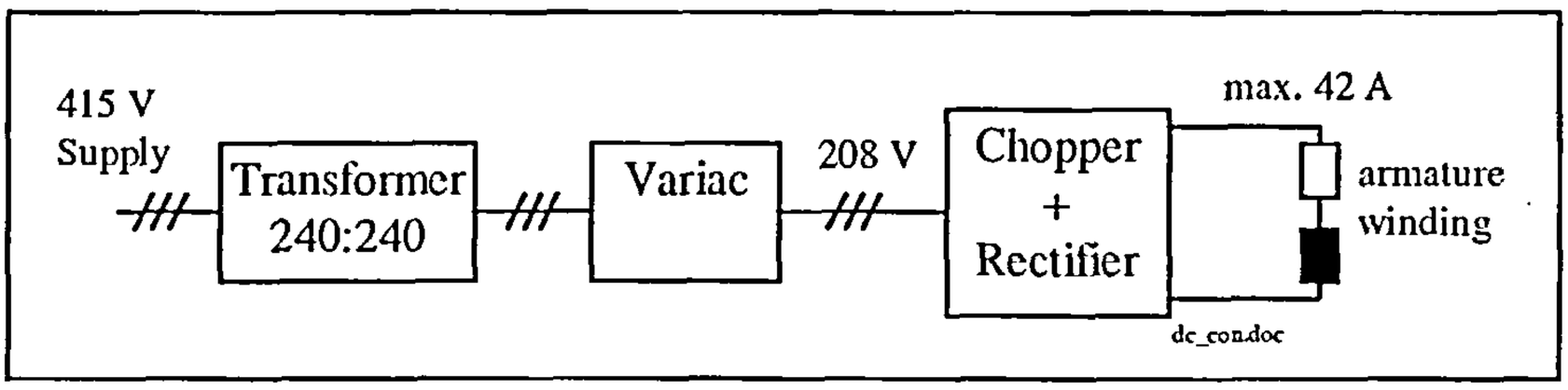

Figure A.5: Armature winding connection of the DC-machine

The field winding is connected to a 3-phase diode rectifier module 6RI75G of FUJI. The input to that is provided by a variac and parallel transformer configuration. They allow to lower the voltage and to transform the current up. The maximum rating of the field current is 32 A, which is imposed by the max. rating of the parallel transformer circuit. Due to the limited field current the max. output torque is reduced to about 70% of its original rating.

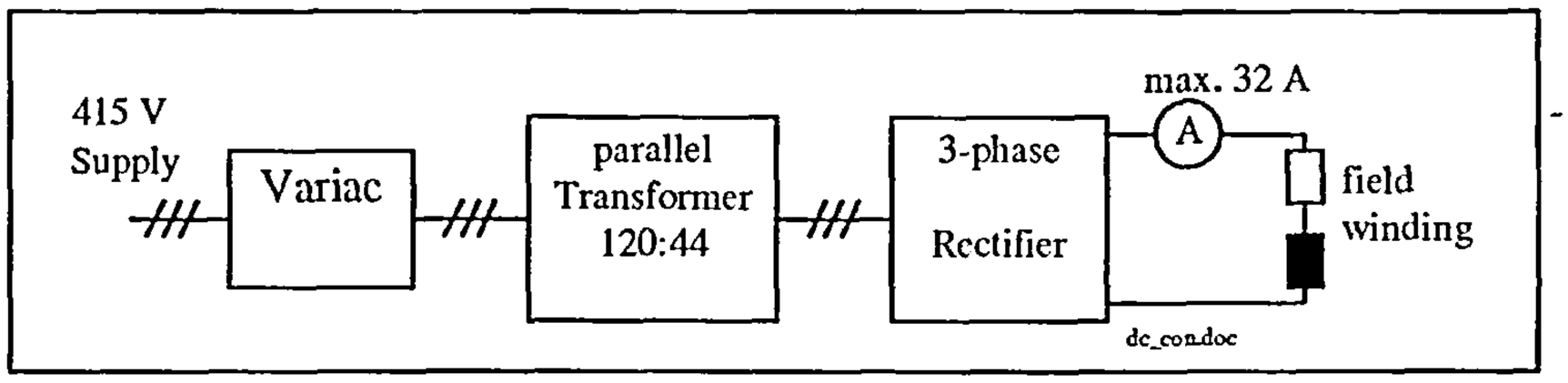

Figure A.6: Field winding connection of the DC-machine

A.3 Determination of Inertia

The determination of the mechanical inertia of the machine set is carried out with the help of the so-called run-out test [f2]. The knowledge of the inertia is not necessariiy important for control purposes on the experimental machine set, but it is needed for simulation purposes and it is generally useful to have a rough idea of the involved inertia of the system.
To get the exact inertia value of a complex mechanical body such as an electrical machine is not straight forward and can in practice only be determined by approximation. The used run-out test has the advantage, that it can be conducted with the complete drive in place, requiring no knowledge about details of the plant and the obtained accuracy (±10 %) is usually acceptable and sufficient for most cases [f2].

The test is performed with electrical measurements on the DC-machine.

The electrical input power to the DC-machine for a constant field current can be calculated as

$$P_{el} = P_{loss} + P_{cu} + J\omega_m \frac{d\omega_m}{dt} \qquad \text{(A.4)}$$

with
P_{el} as the electrical input power
P_{loss} as the power needed to overcome friction and windage losses
P_{cu} as the copper losses
the remaining term is the power needed to accelerate the inertia

Determining the armature resistance from a dc-test allows to calculate the copper losses for a certain armature current as

$$P_{cu} = R_a I_a^2 \qquad \text{(A.5)}$$

The average armature resistance was calculated to $R_a = 0.307\ \Omega$.

Measuring the electrical power of the DC-machine for several steady-state speeds gives a

power-speed relationship with the powers of P_{loss} and P_{cu}, because the last term of equation (A.4) drops out, since only steady-state speeds are considered.

Subtracting the copper losses from the electrical input power allows to calculate the remaining power P_{loss}. As mentioned, this power represents friction and windage losses of the machine set at different speeds. Figure A.7 shows the P_{loss} - *speed* relationship for three different field current settings of the DC-machine. As can be expected the graphs are very close together, since the field of the DC-machine has no relation to the friction and windage losses of the machine set. Averaging the graphs and making a polynomial fit gives the equation of

$$P_{loss} = 0.013\omega_m^2 + 2.588\omega_m + 3.629 \qquad (A.6)$$

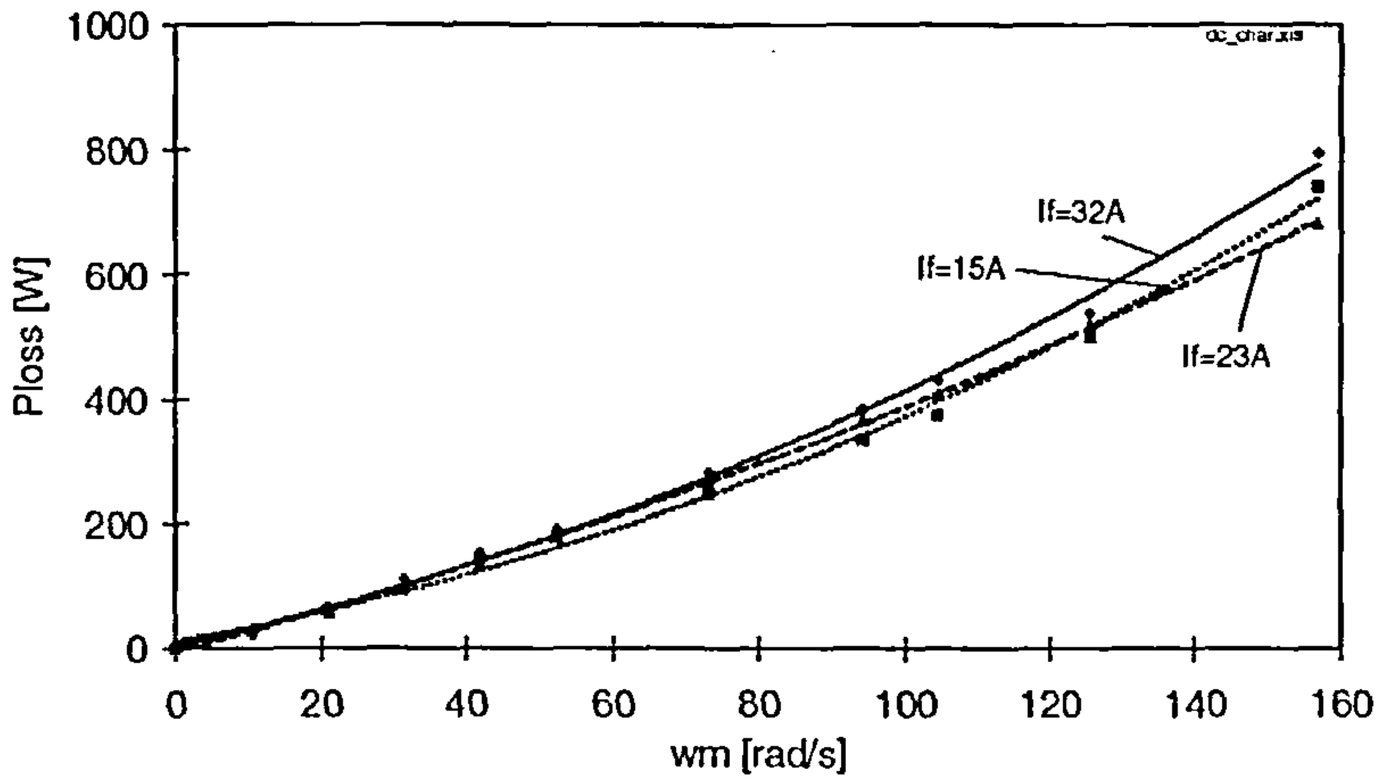

Figure A.7: P_{loss} - *speed* relation

A steady-state loss torque graph can be obtained from the P_{loss} graph with

$$T_{loss} = \frac{P_{loss}}{\omega_m} \qquad (A.7)$$

This loss torque is equal to the torque produced by friction and windage at constant speeds. The loss torque graph is shown in figure A.8. For the run-out test, the drive is now accelerated to some initial speed, where the drive power is switched off, so that the plant is decelerated by the loss torque with the speed sampled as a function of time as shown in figure A.8. Solving the equation of motion for J results in

$$J \approx \frac{-T_{loss}}{\frac{d\omega_m}{dt}} \quad , \qquad T_e = 0 \qquad (A.8)$$

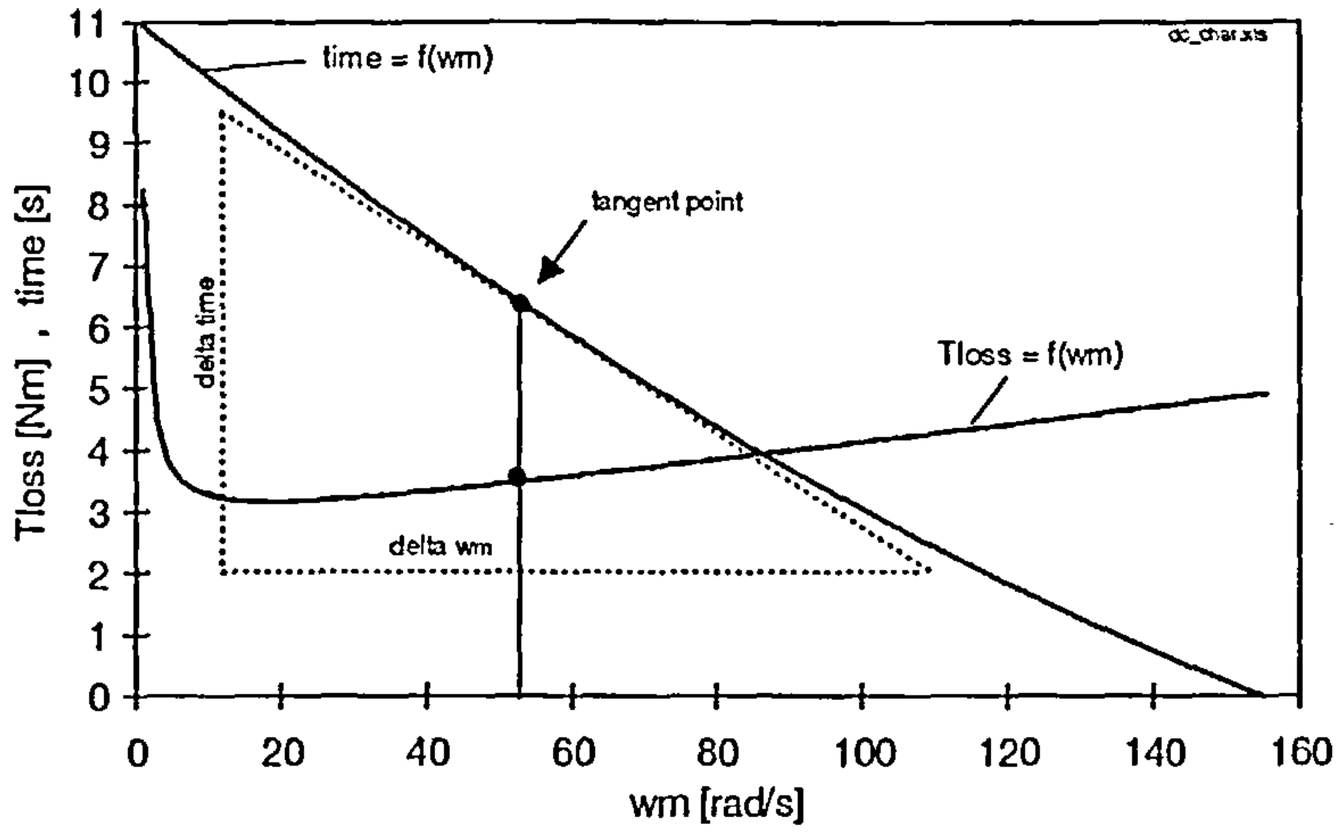

Figure A.8: Graphical determination of inertia

Making a graphical differentiation at various speed points as indicated in figure A.8 and averaging the results gives an inertia of

$$J \approx 0.271\ kgm^2$$

Alternatively, by applying the principle of energy conservation another way can be employed to calculate the inertia in graphical form. At the speed $\omega_{m\,start}$ at which the drive is switch off the mechanical energy of

$$E_m = \frac{1}{2} J \omega_{mstart}^2 \qquad \text{(A.9)}$$

is stored in the rotating masses of the system. This energy is dissipated during the run-out test along the P_{loss} curve of figure A.7 so that the inertia can be calculated from equation A.9 as

$$J = \frac{\sum P_{loss}\, \Delta t}{0.5\, \omega_{mstart}^2} \qquad \text{(A.10)}$$

For the calculation both graphs have to be used. First, using figure A.8, the time axis is split into time intervals. The interval 0,5 s chosen. At each time interval a speed reading is taken and the respective P_{loss} value from figure A.7 is determined. The dissipated energy of

$$P_{loss}\, \Delta t$$

in that interval can be calculated. Doing that for each individual time interval, 22 for the present case, gives the stored mechanical energy and equation (A.10) can be used to calculated the inertia.

The value obtained with this method is close to the previous calculated result with

$$J \approx 0.253\ kgm^2$$

Appendix B

Electrical and Electronic Circuits

This appendix is an extension to chapter 2 and describes in detail the electrical and electronic circuits used for the laboratory implementation of the SDFM / CDFM system. Due to the donation of essential laboratory equipment not all circuits had to be purpose-designed and built. However, some of the donated and pre-designed hardware had to be modified to interface it with the remaining hardware circuits. The purpose-designed circuits are fully explained in functional terms.

B.1 Power Converter

The power converter is a modified BOSCH Servodyn-D [f24] converter unit consisting of following modules: *grid connection module*, *line inductors*, *supply module* and a modified *inverter module*.
A detailed front view of the power converter unit is given with figure B.1 (see pictures in chapter 2 for physical set-up).

The *grid connection module* connects to a 3-phase 380...415 V ±10% supply network and contains fuses and contactors. The contactors allow an automatic soft charge process of the d.c.-link at switch-on. At the same time the connected 3-phase voltages are analysed for the voltage level and correct phase sequence. Any detected error will be indicated on the LED of the *supply module*. The start-up diagnosis is performed by a control circuit in the *supply module*. For that the logic interface connector of the grid connection module must be connected to the X32 connector of the *supply module*.

Three 1 mH *line inductors* are placed between the grid connection module and the supply module to decouple the grid from the dc-link.

The center of the power converter unit is the *supply module* with following specifications:

module name:	VM A70 CR101 -D
d.c.-link voltage:	650 V controlled
rated current:	68 A

rated power: 47 kW
switching frequency: 7.45 kHz

As a controlled front-end it produces unity power factor at the grid connection point. It is autarkic functional, has 4-quadrant operation and controls the d.c.-link to 650 V.
In an industrial drive application this module normally provides the d.c.-link voltage for several inverter modules. All described modules are mounted on a back panel module, which provides the d.c.-link connection to the supply module.

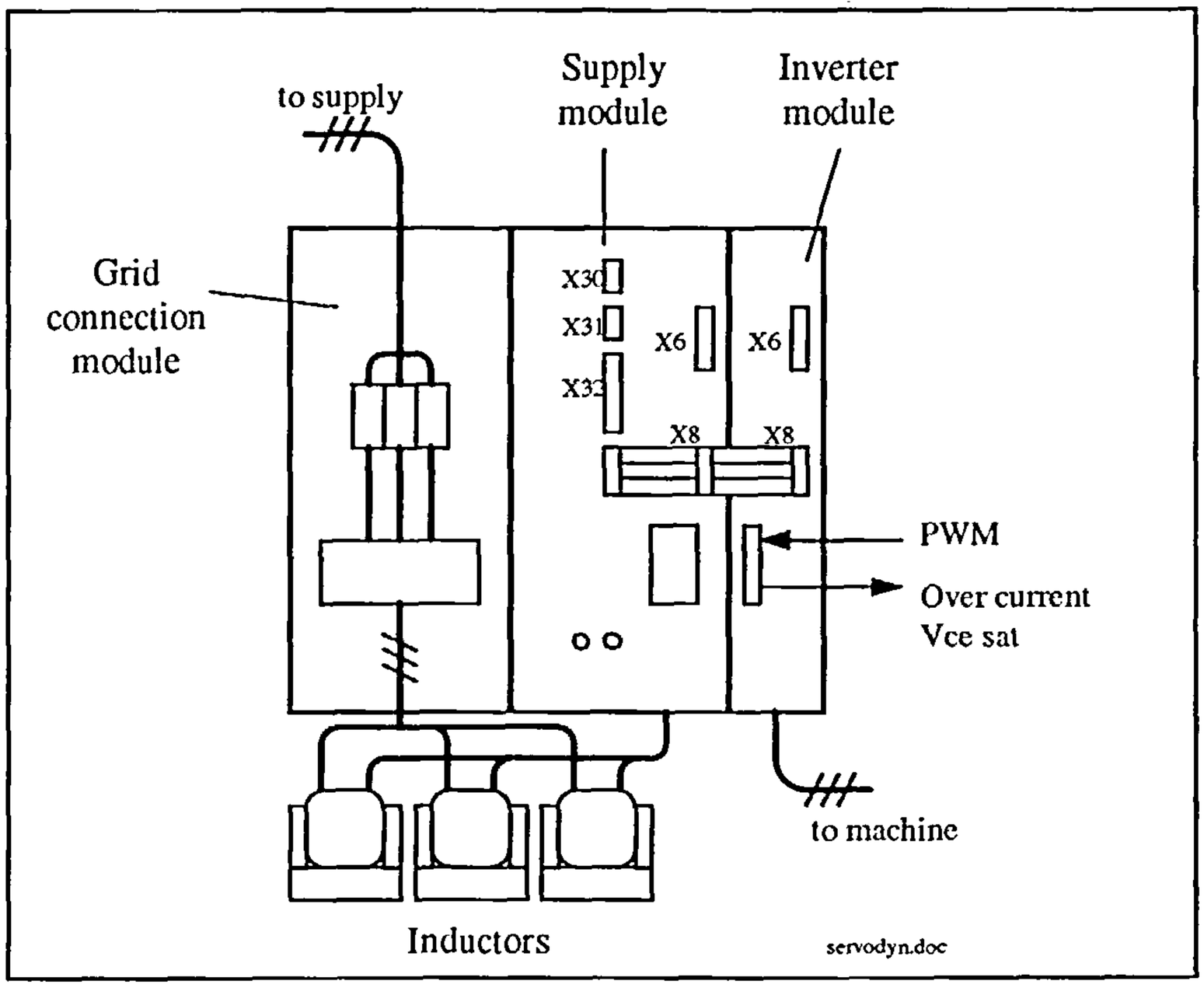

Figure B.1: BOSCH power converter unit

The *inverter module* DMA 15A 1101-D contains the machine-side inverter and is rated for 7 A (maximal 15 A). This module had to be modified in order to interface it with the externally used controller unit. The originally present controller card of the module had to be removed and was replaced by an interface circuit (see section B.2.1) to provide a connection for the PWM signals from the microcontroller board to the module driver circuits.
The module internal driver circuits provide $V_{ce\ sat}$ detection and switch the signal to the IGBT's off at a fault. Additionally, the overcurrent detection circuit of the module produces a TTL signal which is used by the interface circuit to disable the PWM signals coming through to the driver circuits.

B.2 Interface Circuits

B.2.1 Inverter Interface

PWM signal generation is carried out by the PWM unit of the 80C167. Three PWM signals are produced. Electronic circuitry on the µC 1 board inverts the three signals to create the remaining three signals. At the same time a 4 µs dead-time is added.
To interface the six PWM signals to the IGBT driver circuits of the BOSCH inverter module the interface circuit of figure B.2 was designed.
An optocoupler stage is used for electrical isolation between controller and power hardware, before the signals are fed to the low-active driver circuits of the inverter module. The incoming PWM signals can pass the optocoupler stage only, when a second signal is added to the PWM signals. This signal is created by an error latch circuit as displayed in figure B.3.
The error latch circuit latches a signal created by the overcurrent detection circuit of the inverter module. To enable the signal from the error latch circuit to go through to the inverter interface circuit the enable switch has to be closed to AND the signal. In normal operating circumstances the overcurrent detection circuit produces a low signal and causes a high at the output of the error latch circuit.

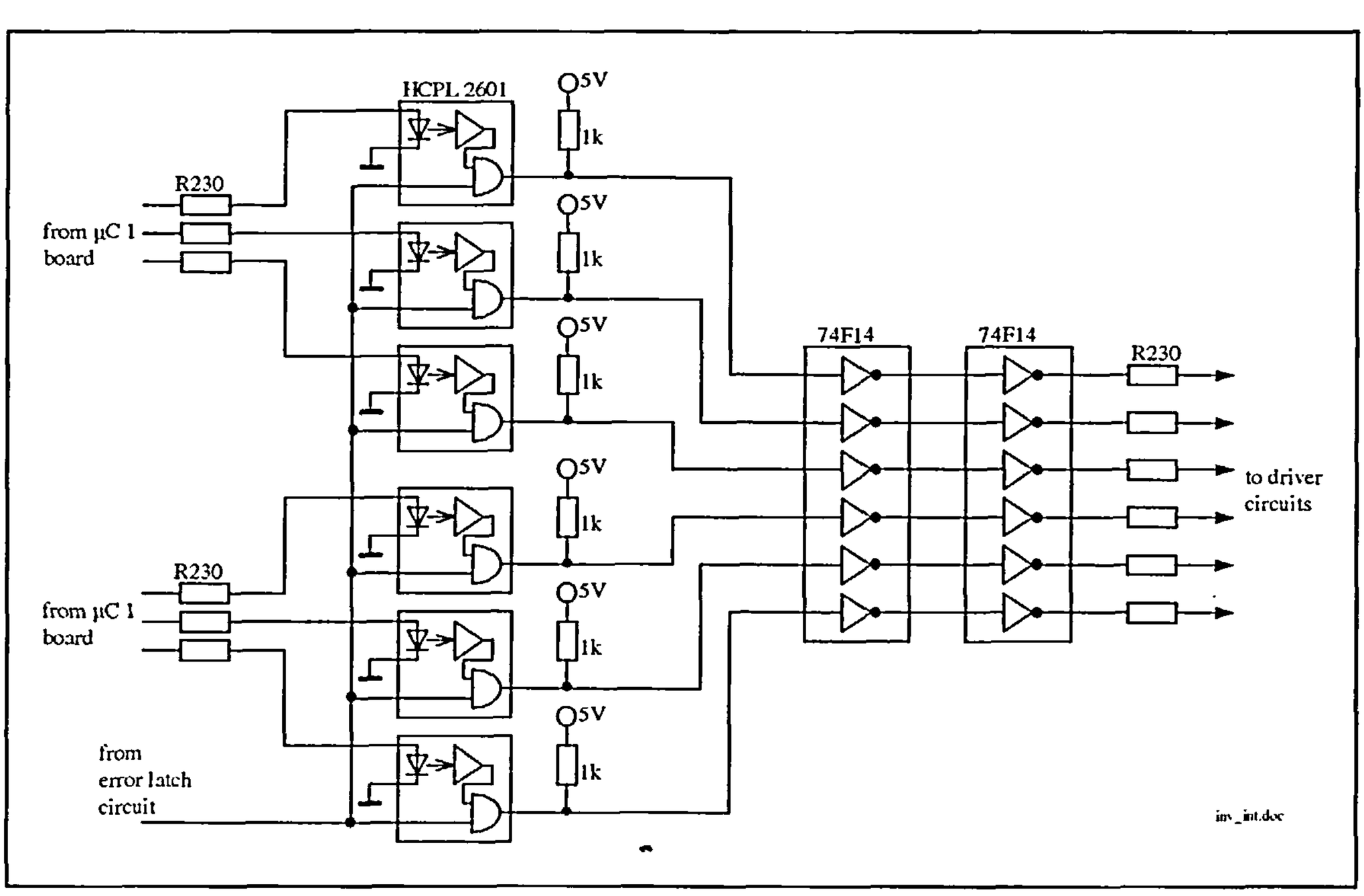

Figure B.2: Inverter interface circuit (interface 1)

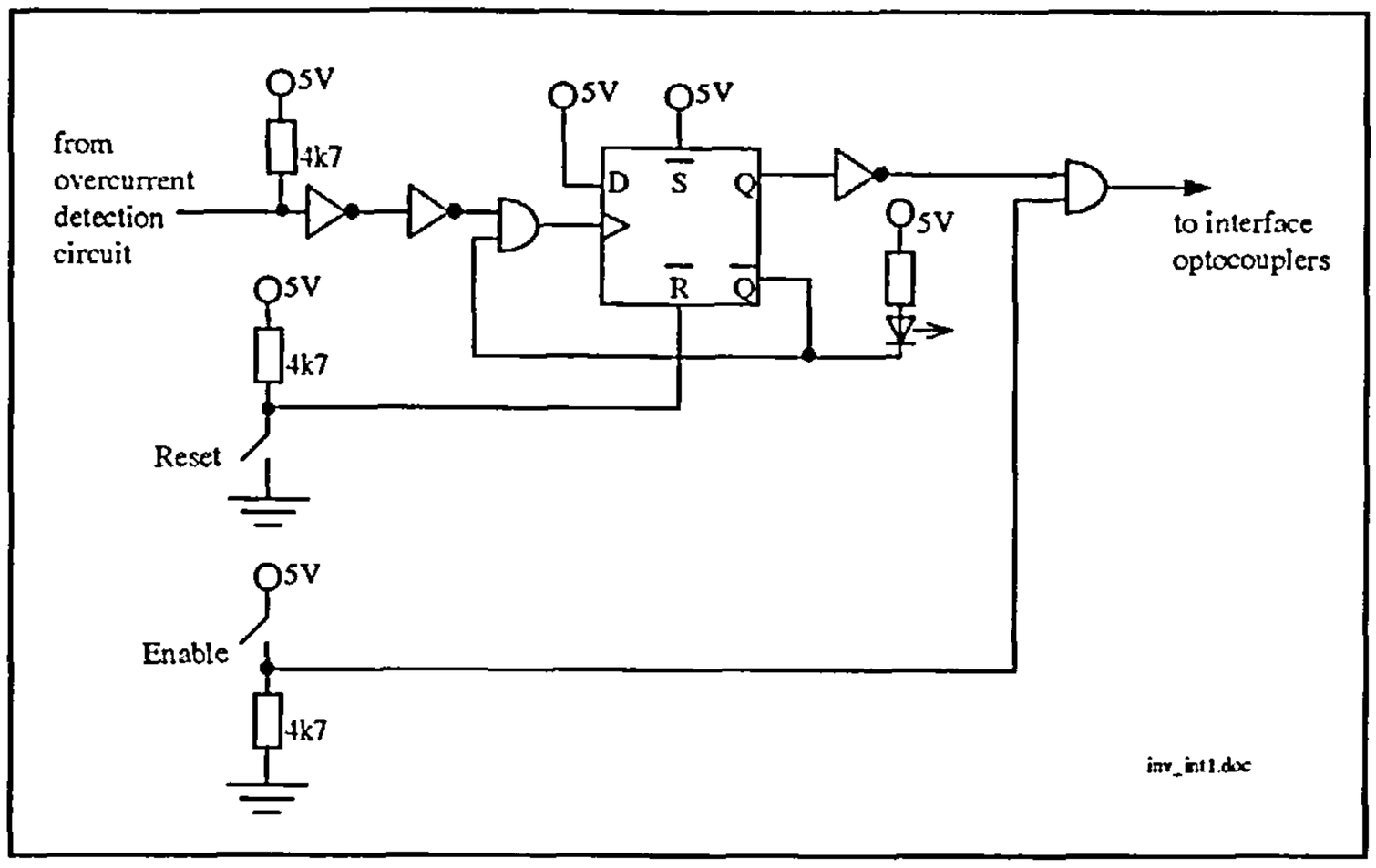

Figure B.3: Error latch circuit

At an overcurrent detection the input signal to the error latch circuit goes high and clocks with the low-to-high transition the D-FF of the circuit. As a consequence, Q goes high and $\overline{Q}$ goes low and blocks any further signal getting through to the clock input of the D-FF. The LED at the $\overline{Q}$ output indicates the overcurrent trip. The signal to the inverter interface circuit is low and blocks the PWM signals at the optocouplers.

Only when the reset button of the error latch circuit is closed and resets the D-FF, the PWM signals are allowed to go through again. At any new overcurrent detection the PWM signals are block once more.

The advantage of this error latch circuit in conjunction with the inverter interface circuit is that at any overcurrent trip, the system can be resetted "on the fly" without restarting the complete hardware. This prevents from going through the whole restarting process of the hardware in case the overcurrent is tripped by a current spike. Of course, if the overcurrent trip comes on several times after resetting, then there must be a fault in the control of the system.

The 5 V circuit supply and the GROUND of the error latch circuit are at inverter circuit level, whereas the input signals to the optocoupler stage of the inverter interface circuit are at controller hardware level.

B.2.2 Current Measurements

The drive implementation of the SDFM 7/ CDFM system requires two current sensing circuits. One for the machine-side inverter current, which is to be controlled, and one for the stator or side 1 current.

First to the machine-side inverter current sensing circuit: The circuit is shown in figure B.4.

A LEM LTA 50P/SP1 current transducer is used for current sensing, based on the Hall effect. The transducer is rated for 50 A rms and has a turns ratio of 1:1000, e.g. the connected current output produces 1 mA per sensed A. With 5 turns through the transducer and the 75 Ω resistor a voltage of *-5 V to 5 V* results at V_{in}. That is for a maximum current of 13.28 A (≈9.4 A rms).

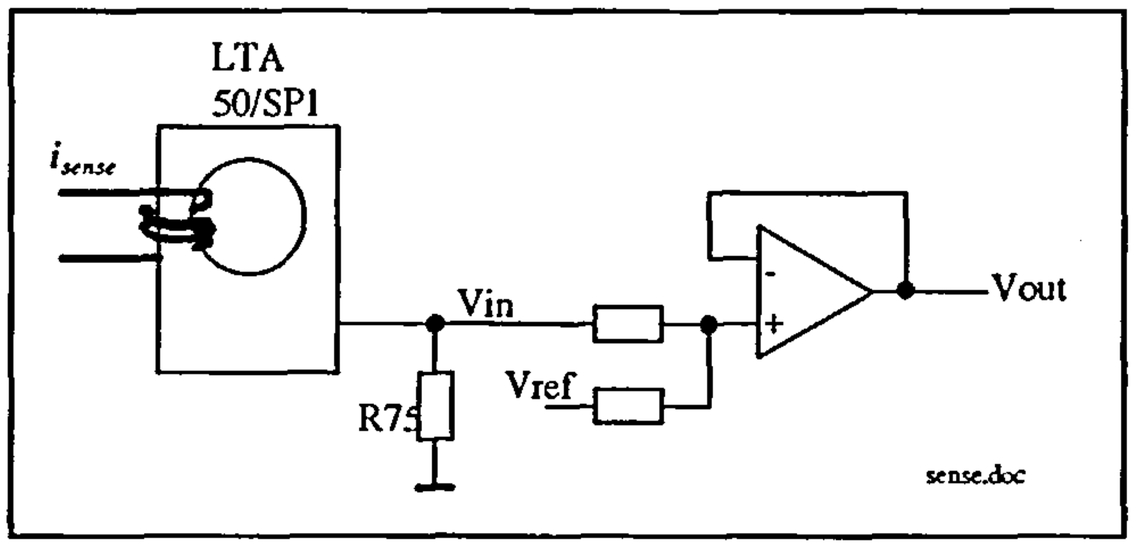

Figure B.4: Current measurement of controlled current (interface 2)

With V_{ref} = *5 V*, the operational amplifier produces a voltage range of *0 - 5 V* at V_{out}. This voltages is fed to the 10-bit ADC of µC 1. The resulting relation between sensed current and V_{out} is

$$V_{out} = \frac{1}{2}(0.375\, i_{sense} + 5)$$

After ADC and converting the 10-bit value to a 16-bit digital number the relation of

$$digital\,value = 2465\, i_{sense}$$

can be written. All three machine-side inverter currents are sensed with circuits as in figure B.4.

A LEM LA 25-NP current transducer is used for sensing of the stator current, figure B.5. The current transducer is connected so that a turns-ratio of 2:1000 results for a rated current of 12 A. The resistance chain at the current output of the transducer is designed that a voltage range of V_{in} =±*2.5 V* for a maximum current of 16.66 A (≈11.8 A rms) is produced. With V_{ref} = *1.25 V* the relation between V_{out} and the sensed current takes the form of

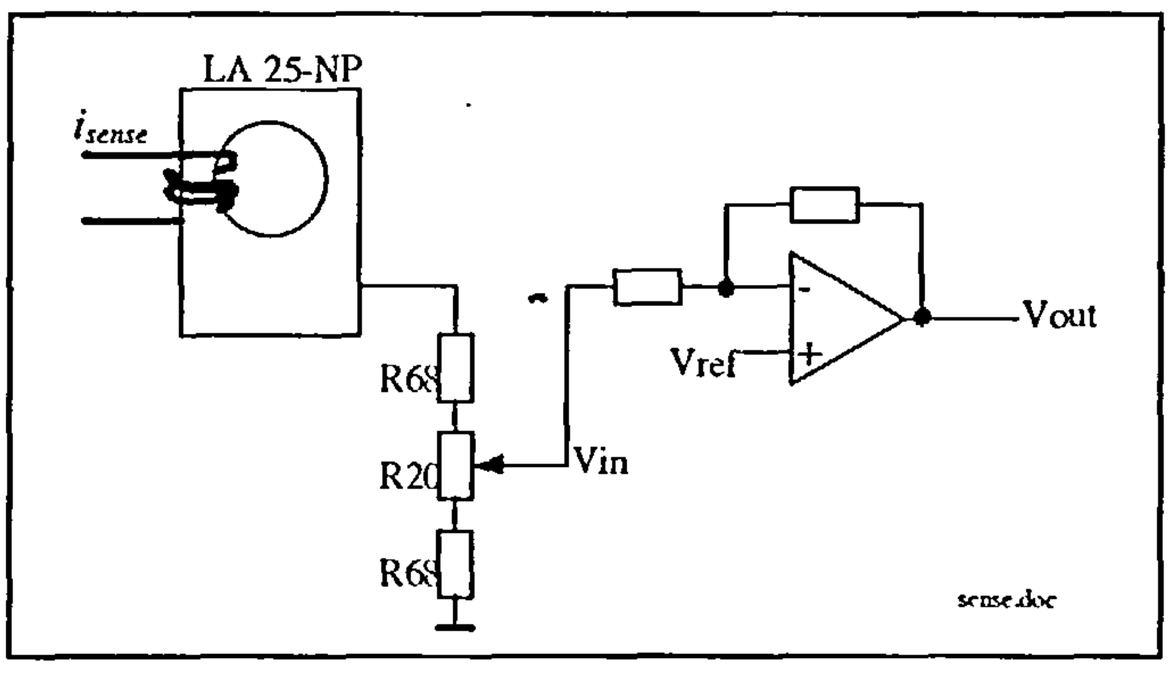

Figure B.5: Stator current measurement (interface 4)

$$V_{out} = 2.5 - 0.15\, i_{sense}$$

where V_{out} has a voltage range of 0 - $5\ V$ at maximum current. After ADC in µC 2 and converting the 10-bit value to a 16-bit digital value following current to digital number relation results

$$digital\,value = -1789\, i_{sense}$$

Two stator line currents are sensed with the circuit of figure 5, the third is calculated internally by µC 2.

B.2.3 Voltage Measurement

The sensing of two *phase* supply voltages is accomplished with the circuit of figure B.6. The 1 MΩ input resistance chain to the differential operational amplifier stage produces a voltage output of $\pm 2.5\ V$ at V_{in} for a maximum input voltage of *367.6 V (≈260 V rms)*. The second stage creates with $V_{ref} = 1.25\ V$ a voltage range of $V_{out} = 0$ - $5\ V$ for ADC in µC 2.

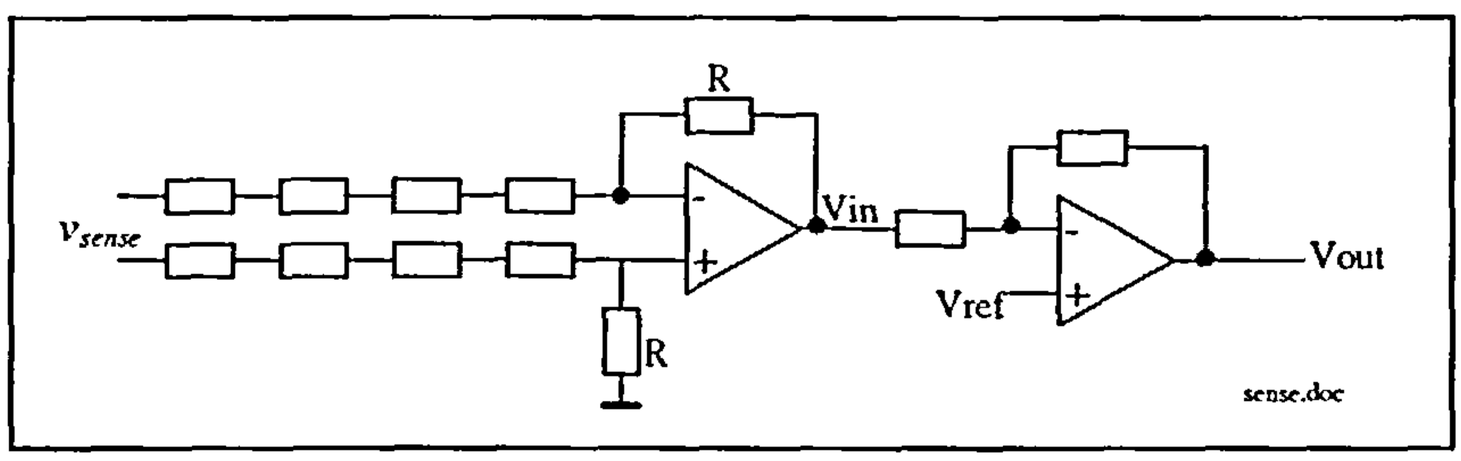

Figure B.6: Stator voltage measurement (interface 4)

With $R = 6.8\ k\Omega$ the relation of

$$V_{out} = 2.5 + \frac{6.8}{1000} v_{sense}$$

results between sensed voltage and the voltage at the ADC input, which gives finally

$$digital\,value = 89\, v_{sense}$$

B.2.4 Encoder Interface

The optical incremental encoder produces the signals *A*, *B* and *H* together with their complements. *A* and *B* are rectangular pulse trains 90° shifted relative to each other. There are 5000 pulses per revolution. *H* is a reference signal once per revolution.
To filter out noise on the cable between the encoder and the interface circuit a differential line receiver 26LS32 connects to the incoming cable signals and produces the three signals *A*, *B* and *H*. To allow a general design of the interface circuit, figure B.7, signal *A* is fed to a counter for frequency reduction purposes if needed. An optocoupler stage provides

isolation between encoder and controller circuit. The resulting signals *A*, *B* and *H* are fed to µC 1 for position and speed calculation.

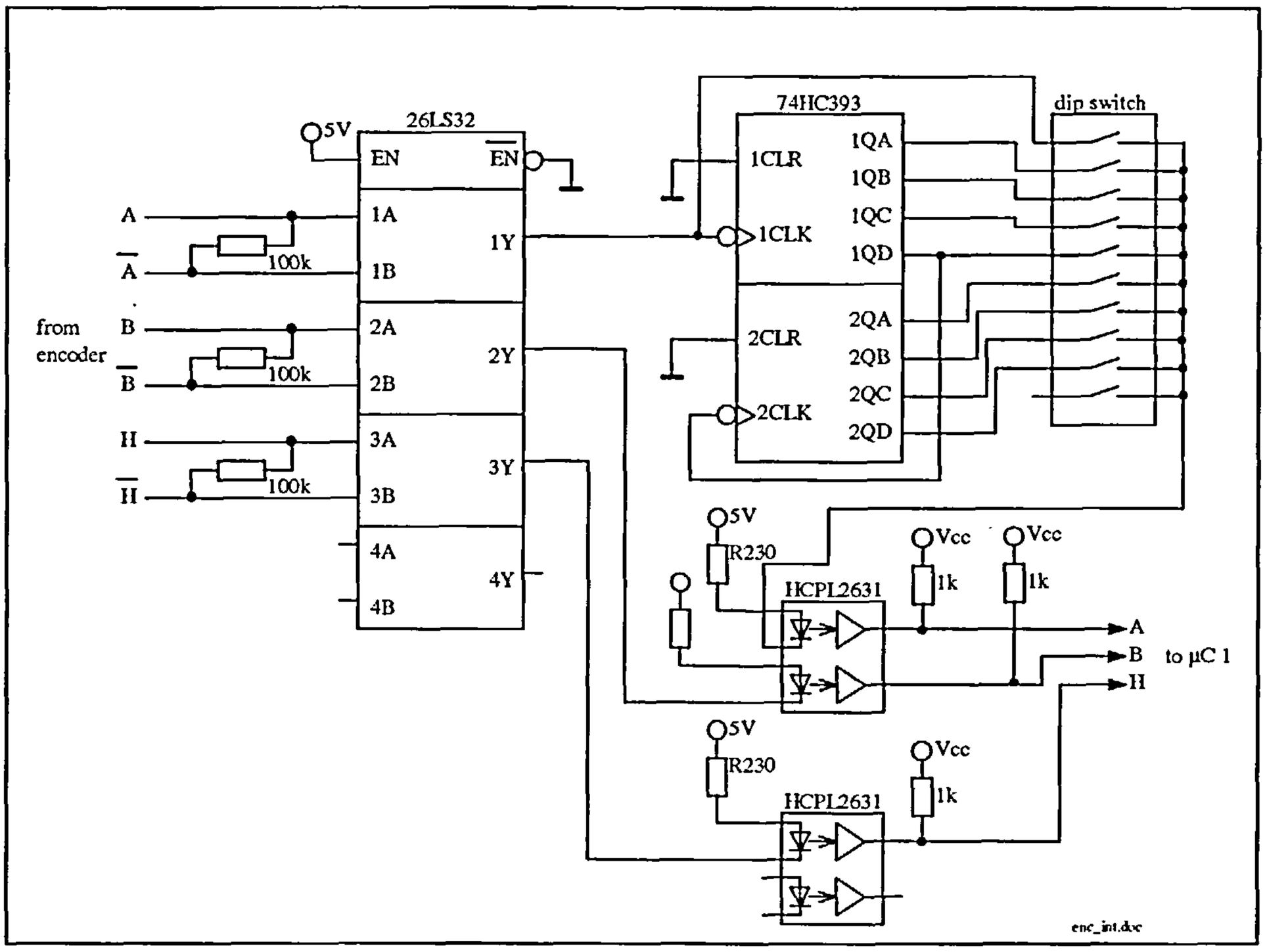

Figure B.7: Encoder interface circuit (interface 3)

B.2.5 Data Storage Card

A 32 k x 16 bit RAM card was designed for data storage purposes. Two parallel 8-bit 32 k RAM's are used as shown in the circuit at the end of this appendix. The card was then extended to 64 k by mounting additional 32 k RAM's on the card. Data is written from µC 1 and read out by the PC via a parallel port.

The data writing sequence is shown in the left half of figure B.8. After initialisation by µC 1 the 16-bit data is outputted on port 2 and the control lines are connected to port 8 of µC 1. The software is set that up to six different variables can be written to the RAM card per PWM cycle. Each writing sequence contains the three steps as indicated in figure B.8, which are:

1. *output 16-bit data on port 2*
2. *write enable signal to RAM*
3. *increase RAM address*

After the writing process is finished µC 1 enables the RAM's to be controlled from the parallel port of the PC.

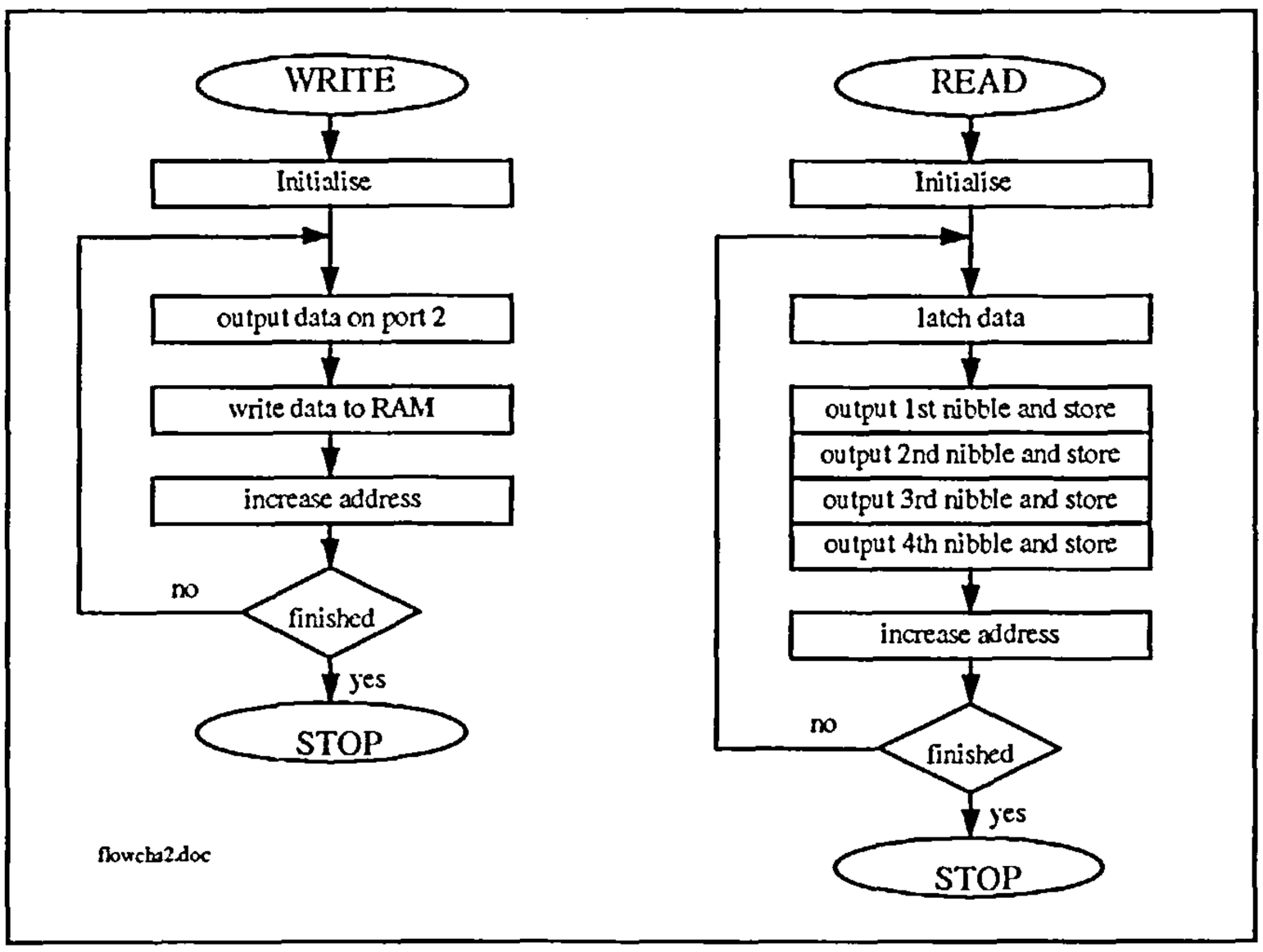

Figure B.8: Write and read sequence of the data storage card

The reading out sequence of the stored data via the parallel port of the PC, as shown in the right half of figure B.8, is implemented in a C program "readdata.c", which is run under BORLAND C++.

The parallel port of the PC allows only 4-bit to be read in at a time, so that the 16-bit data is read as four nibbles in a row. For that, the 16-bit data of the RAM's is latched in four 8-bit latches (uses only 4-bit). After that each latch is read out individually. An address increase finishes the read out sequence.

The read data is written to a file in spreadsheet format by "readdata.c".

B.2.6 Digital-Analog Card

A 12-bit digital-analog card (DAC) allows to output internal variables of µC 1 for display and also for data storage on a digital oscilloscope. Six 12-bit MAX502 DAC's are used, so that six variables can be outputted during one PWM cycle.

The data line for the DAC card are connected to port 2 of µC 1 and the control lines are connected to port 4. The circuit of the DAC card is shown at the end of this appendix.

Before the internal 16-bit variable can be sent to the DAC it has to be truncated to 12-bit.

The variables are then outputted one after the other by µC 1 at the end of the PWM cycle.

The DAC's are configured to bipolar operation to allow a voltage range of *-5 V to + 5 V* for the 12-bit value.

B.2.7 EPROM Emulator

The compiling process of the source-code file creates a file in intel-hex format. This file is used for programming of EPROM's. Two 8-bit EPROM's, containing the programmed software, are needed by µC 1 and µC 2 respectively. The EPROM's are arranged that one has the even-address byte and one the odd-address byte of the 16-bit data, made up from two bytes.

For each software change new EPROM's must be programmed. During the control software development stage this results in a considerable amount of programming processes and time. In order to allow a faster software change process an EPROM emulator has been designed. This emulator is connected to the parallel port of the PC and plugged into the EPROM sockets of one of the microcontroller boards. Only one microcontroller board can be connected to the emulator at the time. The other has to have programmed EPROM's during that time.

The emulator writing process goes in two steps, which is implemented by a C program "ram_fill.c" and run in BORLAND C++. In the first step, the intel-hex file data is read and organised in two data arrays. One for even and one for odd addresses. This is essential, since the intel-hex file does not necessarily list the data bytes in successive address order. Once the data bytes are contained in the arrays, depending on their address, the second step can be employed. In that, the data is written from the arrays to the emulator RAM's, depending on the data address. Even and odd addresses and the respective data bytes are latched in successive order and then a RAM writing signal allows to write the data into the RAM's.

The appropriate flow charts for the data reading and RAM writing process are displayed in figure B.9. The circuit of the emulator card is shown at the end of this appendix.

After the emulator has been written the microcontroller can be resetted to read code from the emulator RAM's.

B.2.8 Connections to the PC

At this point all connections to and from the PC with the drive hardware are summed up. There is one serial connection and two parallel port connections.

Both microcontroller boards have a serial link connection made up with an RS-232 IC, so that a *serial link* to the PC can be established with one of the microcontrollers at a time. During software development it is useful to have insight to certain control variables of either µC 1 or µC 2. The connection can be mechanically swapped between the boards.

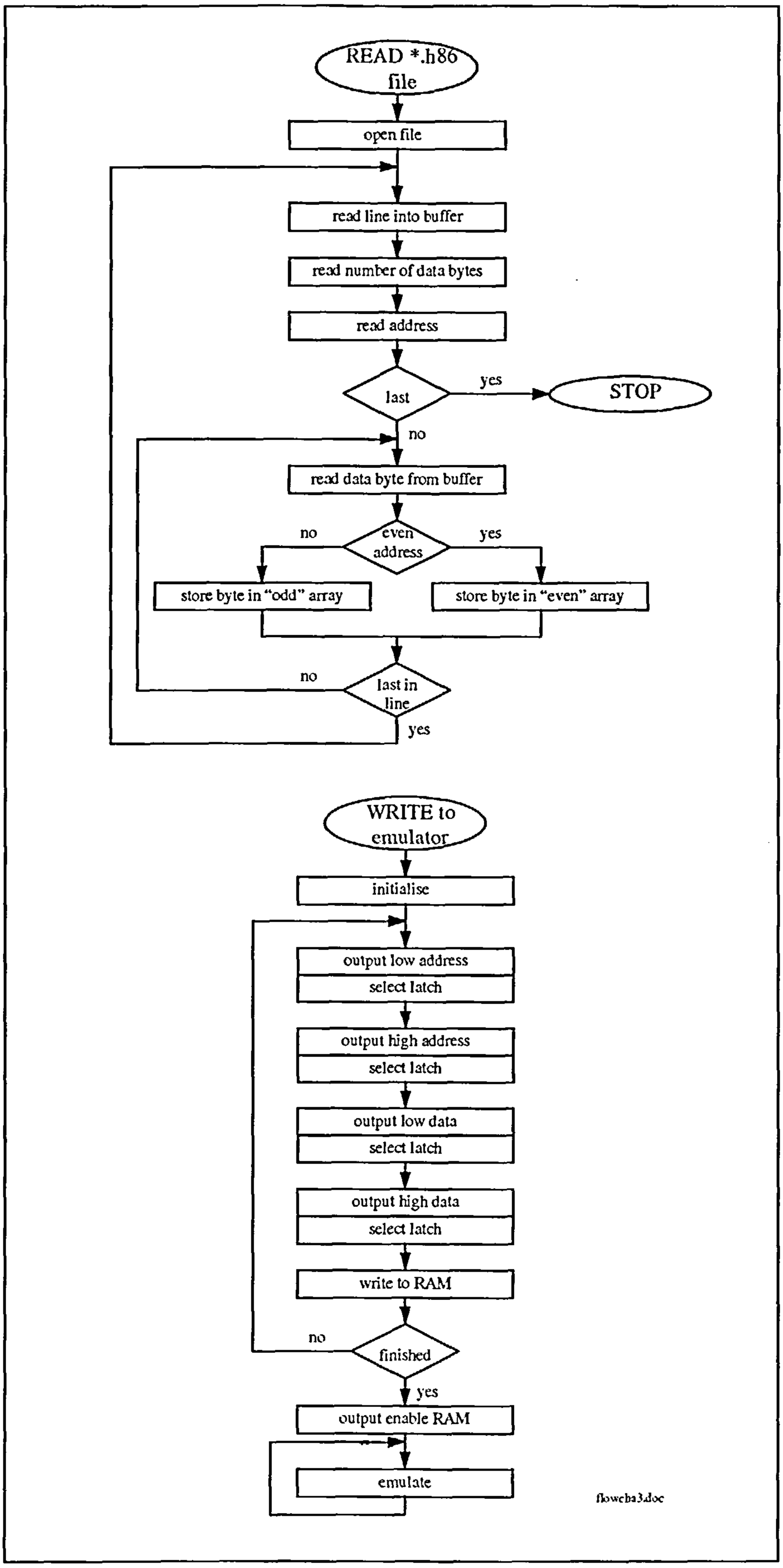

Figure B.9: Flow charts for emulator writing

During normal control operation the serial link connection is continuously made with µC 1. Due to the limited transmission rate of a serial link, only non-time-critical values are sent to the PC for monitoring purposes. Among those are the mechanical speed of the machines, PI-controller parameters and control demand values. The sent data is displayed on the PC screen.

As mentioned in section B.2.5 and B.2.7, two *parallel connections* are necessary with the PC. One for reading data from the data storage card and one for sending data to the EPROM emulator.

B.3 Microcontroller Connections

The controller hardware consists of two pre-designed microcontroller boards, originally designed for laser firing circuit control. Both boards had to be modified, so that they are suitable for a drive control application. This section describes the signal input and output connections of the microcontrollers, µC 1 and µC 2, as used in the hardware implementation, to give a foundation for a potential design of a single board with two controllers.

Only the signal ports are described and listed in succession depending on their pin number.

µC 1 - connections

$\overline{CS0}$ - this chip-select signal enables the data output of the EPROM's

$\overline{CS2}$ - this chip-select signal enables the bus driver IC for the six PWM signals

P8.0-P8.5 - outputs the control signals for data storage card

P8.6 - outputs a signal to EX0IN of µC 2 for external interrupt request generation

POUT0-POUT2 - outputs the three PWM signals. They go to the on-board inverting and dead-time circuitry

P7.3 - outputs a signal to check the timing of the implemented control software

AN0-AN2 - ADC input for the three sensed currents

AN3, AN4 - ADC input of two potentiometer signals to allow manually internal parameter manipulation

P2.0-P2.15 - data storage card and DAC card data outputs

T3IN - timer input of signal B from encoder

T2IN - timer input of signal H from encoder

MRST - connected to MRST of µC 2, but not activated

MTSR - receives communication signals from MTSR of µC 2

TXD0 - transmits data to on-board RS-232

RXD0 - receives data from on-board RS-232

SCLK - receives clocking pulses from SCLK of µC 2 for serial connection

P4.0-P4.5 - control signal outputs for DAC card

AD0-AD15 - on-board EPROM data inputs

A1-A15 - on-board EPROM address outputs

XTAL1, XTAL2 - oscillator connections

$\overline{RSTIN}$ - signal input from on-board reset button and start-up reset circuit

µC 1

$\overline{CS0}$	→	EPROM output enable
$\overline{CS2}$	→	enable bus driver IC for PWM signals
P8.0 - P8.5	→	Data Storage Card - control
P8.6	→	to EX0IN of µC 2
POUT0 - POUT2	→	3 PWM output signals
P7.3	→	signal for timing check with oscilloscope
AN0 - AN2	←	3 current sensor signals
AN3	←	POT 1 (from potentiometer)
AN4	←	POT 2 (from potentiometer)
P2.0 - P2.15	→	DAC + Data Storage Card - data
T3IN	←	B of encoder
T2IN	←	H of encoder
MRST	—	MRST of µC 2 (not used)
MTSR	←	from MTSR of µC 2
TXD0	→	to RS 232
RXD0	←	from RS 232
SCLK	←	from SCLK of µC 2
P4.0 - P4.5	→	DAC - control
AD0 - AD15	←	EPROM - data
A1 - A15	→	EPROM - address
XTAL1, XTAL2	←	Oscillator
$\overline{RSTIN}$	←	reset button and start-up reset circuit

µC 2

$\overline{CS0}$	→	EPROM output enable
P8.0 - P8.4	→	signals for timing check with oscilloscope
AN0 - AN1	←	2 voltage sensor signals
AN2 - AN3	←	2 current sensor signals
AN4	←	POT 3 (from potentiometer)
AN5	←	POT 4 (from potentiometer)
EX0IN	←	external signal from µC 1
MRST	—	MRST of µC 1 (not used)
MTSR	→	to MTSR of µC 1
TXD0	→	to RS 232
RXD0	←	from RS 232
SCLK	→	to SCLK of µC 1
AD0 - AD15	←	EPROM - data
A1 - A15	→	EPROM - address
XTAL1, XTAL2	←	Oscillator

S0C167.doc

Figure B.10: Microcontroller connections

µC 2 - connections

$\overline{CS0}$ - this chip-select signal enables the data output of the EPROM's

P8.0-P8.4 - outputs signals to check the timing of the implemented control software

AN0-AN1 - ADC input for two sensed stator voltages

AN2- AN3 - ADC input of two sensed stator currents

AN4, AN5 - ADC input of two potentiometer signals to allow manually internal parameter manipulation

EX0IN - input of signal from µC 1 for external interrupt request generation

MRST - connected to MRST of µC 1, but not activated

MTSR - transmits communication signals to MTSR of µC 1

TXD0 - transmits data to on-board RS-232

RXD0 - receives data from on-board RS-232

SCLK - sends clocking pulses to SCLK of µC 1 for serial connection

AD0-AD15 - on-board EPROM data inputs

A1-A15 - on-board EPROM address outputs

XTAL1, XTAL2 - oscillator conniptions

Figure B.10 gives a condensed connection overview of both microcontrollers with indication of port input or output.

B.4 User Interface and Start-Up Sequence

B.4.1 User Interface

During operation of the experimental laboratory set-up there are passive and active user interfaces. Passive interfaces in terms of status indicators and parameter monitoring and active interfaces in terms of potentiometer inputs to the microcontrollers.

Passive interfaces

The status of the power converter is displayed on a 7-segment LED. In case of any problem, an error number will be displayed.

The top front-panel of the control rack has three labeled LED's. A green LED comes on, when the enable signal for the error latch circuit of figure B.3 is given. Two red LED's indicate an overcurrent detection signal and an $V_{ce\,sat}$ signal.

In order to check timing sequences and software run time durations of both microcontrollers, they output some signals associated to certain program parts. The signals can be monitored on oscilloscopes.

The main status indicator, parameter indicator and user feedback is provided by the screen

display of internal microcontroller variables and parameters. µC 1 sends data to the PC via a serial link. In that way it is possible to monitor and display mechanical speed values, control parameters and other variables. Due to the limited transmission speed (19.2 kbaũd) of a serial link only slow changing variables are displayed.

Active interfaces

The only means of active manipulation of software during operation is provided by two potentiometer inputs to the ADC of each microcontroller. This feature is mainly used for tuning purposes and demand value settings.

B.4.2 Start-Up Sequence of Hardware

The purpose of a start-up sequence is to avoid excessive inrush currents due to machine magnetisation or d.c.-link charge-up.

The first step of the start-up sequence for the SDFM or CDFM system is to take the DC-machine control into action. First the field current is allowed up to 32 A by turning the appropriate variac. Then the armature current control chopper is switched to the mains. This enables manual control of the machine rig speed.

In the second step the power converter is switched on. An automatic soft charge process by the power converter allows to charge the dc-link of the system.

In the third step it has to be distinguished between SDFM and CDFM system:

In case of the SDFM system, the machine magnetisation is initially provided by the machine-side inverter connected to the rotor; the stator is still open at this point. Having the SDFM at synchronous speed and enabling the control of the machine-side inverter allows to magnetise the SDFM though the rotor. If the resulting stator voltage is in synchronism with the supply network voltage, checked by the 3-lamp-method, the switch connecting the stator to the supply can be closed, resulting in only minor transient currents. At this point the SDFM is properly connected to the system.

In case of the CDFM, that is different. Having the CDFM at its synchronous speed, the supply side variac connected to side 1 of the CDFM can be slowly turned up, so that the machine magnetisation is provided via side 1. The control of the machine-side inverter is still disabled at this point. Having rated voltage at side 1 the machine-side inverter can be taken into action and the CDFM is in full operation conditions.

32K RAM Card

Version 1 March 97

Bernhard Hopfensperger
University of Newcastle

From C167

To parallel port of PC

74F541 IC1
74F541 IC2
74F541 IC3
IC4 RAM 32K
IC5 RAM 32K
74F383 IC6
74F383 IC7
74F573 IC8
74F573 IC9
74F573 IC10
74F573 IC11
IC12 74F541
IC13 74F139
74F14 IC14

CE# RAM H
OE# RAM
WE# RAM

R clk
R clr

R1 4K7
R2 4K7
R3 4K7

Voo
GND

12-bit DAC

Version1 April 97

Bernhard Hopfensperger
Uni Newcastle

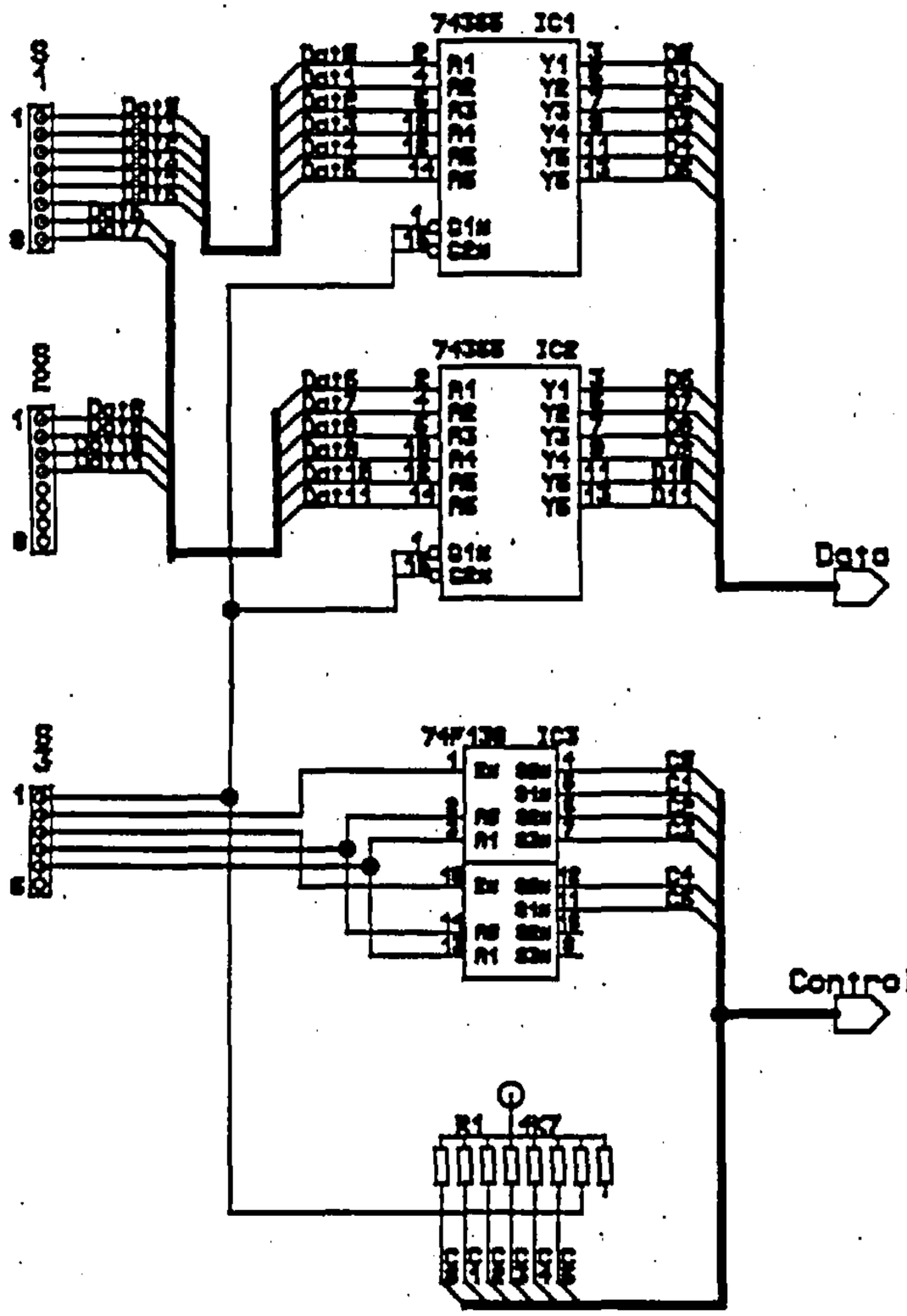

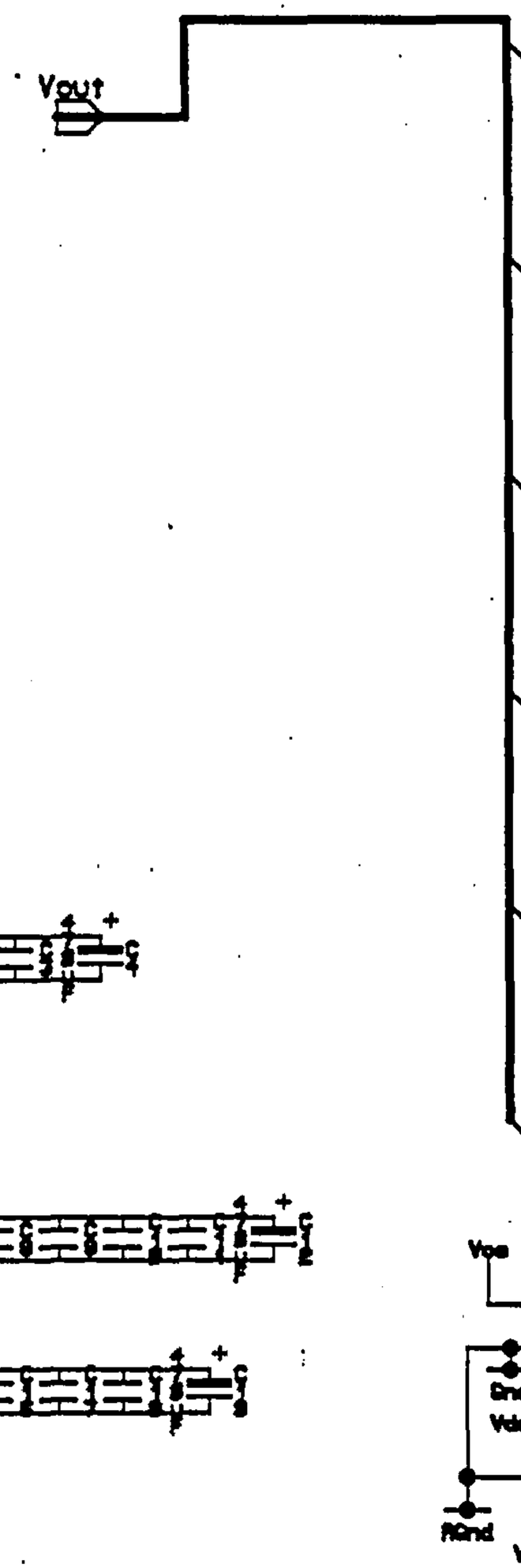

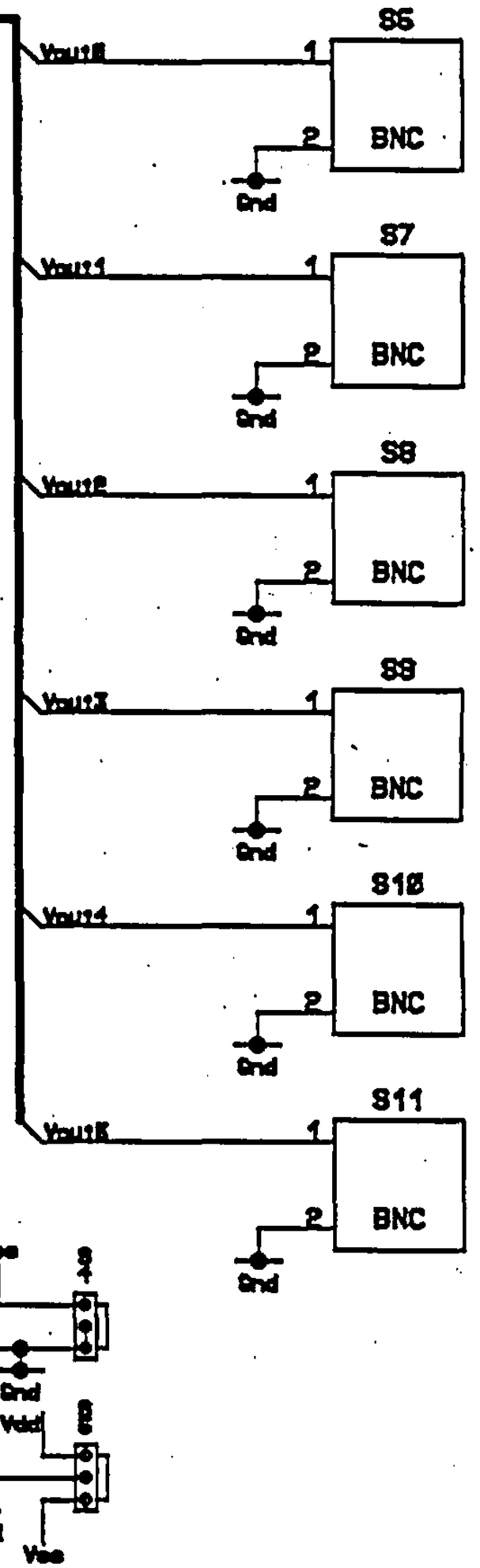

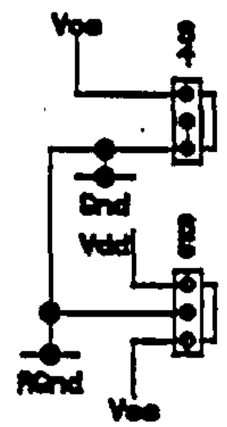

13

Control
Data
MAX502
CS#
WR#
D0
D1
D2
D3
D4
D5
D6
D7
D8
D9
D10
D11
VOUT
VREF
RA
RB
RC
RFB
IC4
IC5
IC6
IC7
IC8
IC9
Vout
REF02CP
VOUT
TRIM TEMP
IC10
AD712
IC11a
R2
R3
R4
10K
0.1%
Gnd

EPROM-Emulator v.1 B.H.

Appendix C

Microcontroller Programming

C.1 In General

The programming of both microcontrollers is carried out in the high level language C. A Keil GmbH compiler set to maximum optimisation is used for compilation and linking purposes.

The 80C167 is a 16-bit fixed point microcontroller. In order to fully utilise the available 16-bit resolution all machine quantities have to be properly scaled. An *integer* data type is used for internal control variable representation. Table C.1 has the maximum range and the scaling factors used for each machine quantity. It also contains the scaling for the value outputted by the DAC-card.

quantity	*max. range*	*scaling for internal digital value (±32767 digits)*	*scaling for DAC output (±5 V)*
i_1	*±16.67 A*	*1789 digit/A*	*0.273 V/A*
v_1	*±367.6 V*	*89 digit/V*	*0.0136 V/V*
i_2 , i_4	*±13.28 A*	*2465 digit/A*	*0.376 V/A*
P_1 , Q_1	*±10100 W(VAr)*	*3244 digit/kW (kVAr)*	*0.495 V/W (VAr)*
v_2	*±375.3 V*	*87 digit/V*	*0.0133 V/V*

Table C.1: Scaling factors

The programming description of various control blocks in following section is given in a principal form without stating the actual program code, since scaling figures and data type conversions may depend on the respective variables. If any scaling is required with the control block this is given by a general "*scale*" factor.

C.2 "3-to-2" and "2-to-3" Transformation

The field oriented control of the SDFM or CDFM takes place in a 2-dimensional d-q-plane.

In order to convert the 3-phase machine quantities to 2-phase control quantities a 3-to-2 non-power invariant transformation is carried out. For the conversion of the 2-dimensional demand values back to 3-phase demand values a 2-to-3 transformation is needed. Both transformations are implemented in the control software as:

```
// 3-to-2 transformation
d = a;
q = scale ( b - c );

// 2-to-3 transformation
a = d;
b = scale ( d + q );
c = scale ( d - q );
```

C.3 Look-Up Tables

The usage of trigonometric functions in the program code results in numerous summations and multiplications, since they are usually represented by their exponential series. As a consequence the implementation of trigonometric functions is very time consuming. This can be a problem in an application, where the time for program execution by the microcontroller should be as little as possible.

In order to avoid the usage of trigonometric functions in the program code, look-up tables are employed. They allow a quick implementation by picking a certain value from a pre-arranged array.

Three look-up tables are used and designated for the functions of *sin*, *cos* and *arctan*. All of the look-up tables are one-dimensional arrays.

The *sin* and *cos* tables have 400 entries each, which results in an angle resolution of 0.9°. The tables return an 16-bit integer number at the demanded angle.

```
// sin look-up table call
value = sin400[ angle ];

// cos look-up table call
value = cos400[ angle ];
```

An *arctan* look-up table has 3666 entries. It returns the angle values of 0..100 representing the first quadrant.

```
//arctan look-up table call
angle = arctan[ value ];
```

C.4 Reference Frame Transformations

Two reference frame transformations are used. One for a "positive" transformation (e^{jangle}) and one for a "negative" transformation ($e^{-jangle}$), between the "new" and the "old" reference frame system.

```
// positive transformation
d_new = d_old * cos400[angle] - q_old * sin400[angle];
q_new = d_old * sin400[angle] + q_old * cos400[angle];
```

```
// negative transformation
d_new = d_old * cos400[angle] + q_old * sin400[angle];
q_new = -d_old * sin400[angle] + q_old * cos400[angle];
```

C.5 Angle Calculation

Field orientation requires the calculation of the angle between the excitation reference frame and the stationary reference frame. With the *arctan* look-up table this is done by:

```
// angle calculation
IF(d==0) d=1;                          // avoid 0 at division
qq = scale*q;                          // scale q
value = qq/d;                          // divide
IF(value>=3666) value = 3666;          // limit
IF(value<=-3666) value = -3666;
IF(value<0) value=-value;              // allow only absolute value
angle = arctan[value];                 // take angle from look-up table
IF(d<0 && q>=0) angle = 200-angle;     // sort out correct quadrant
IF(d<0 && q<0) angle = angle+200;
IF(d>=0 && q<=0) angle = 400-angle;
```

C.6 Position and Speed Measurement

The incremental encoder provides 5000 pulses per revolution for the signals *A* and *B* and one reference pulse per revolution for the signal *H*. Signals *A* and *B* are shifted 90° to each other as displayed in figure C.1.

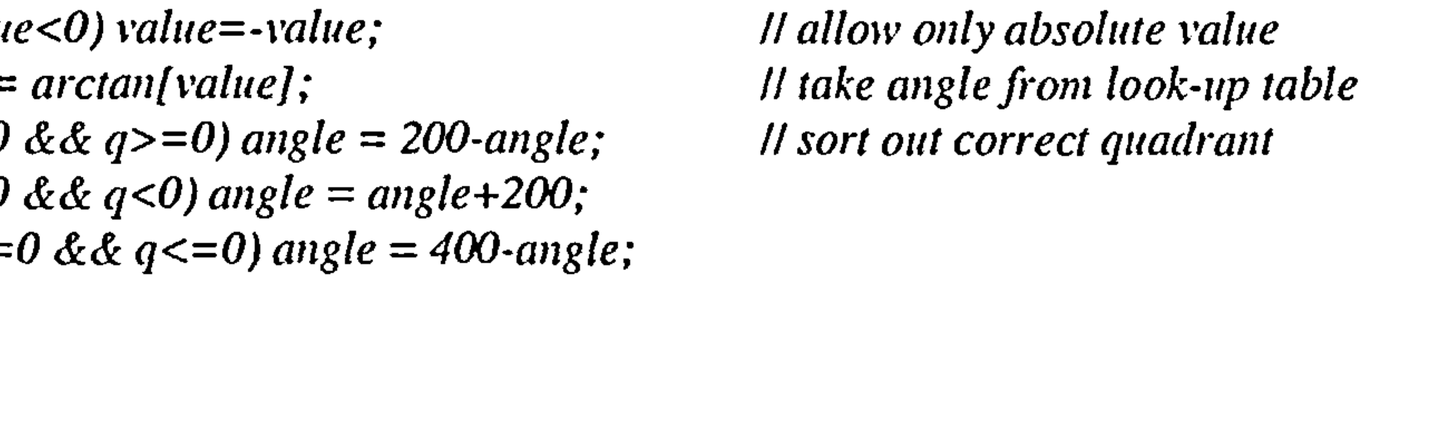

Figure C.1: Encoder pulses

The rotor position of the machine is established by counting pulses from the encoder within one revolution. At the arrival of the reference pulse the count value is set to zero and the counting starts from new. This is carried out by feeding signals *B* and *H* to µC 1 in which the general purpose timer unit 1 "GPT1" is set to perform the desired counting method. This is shown in figure C.2.

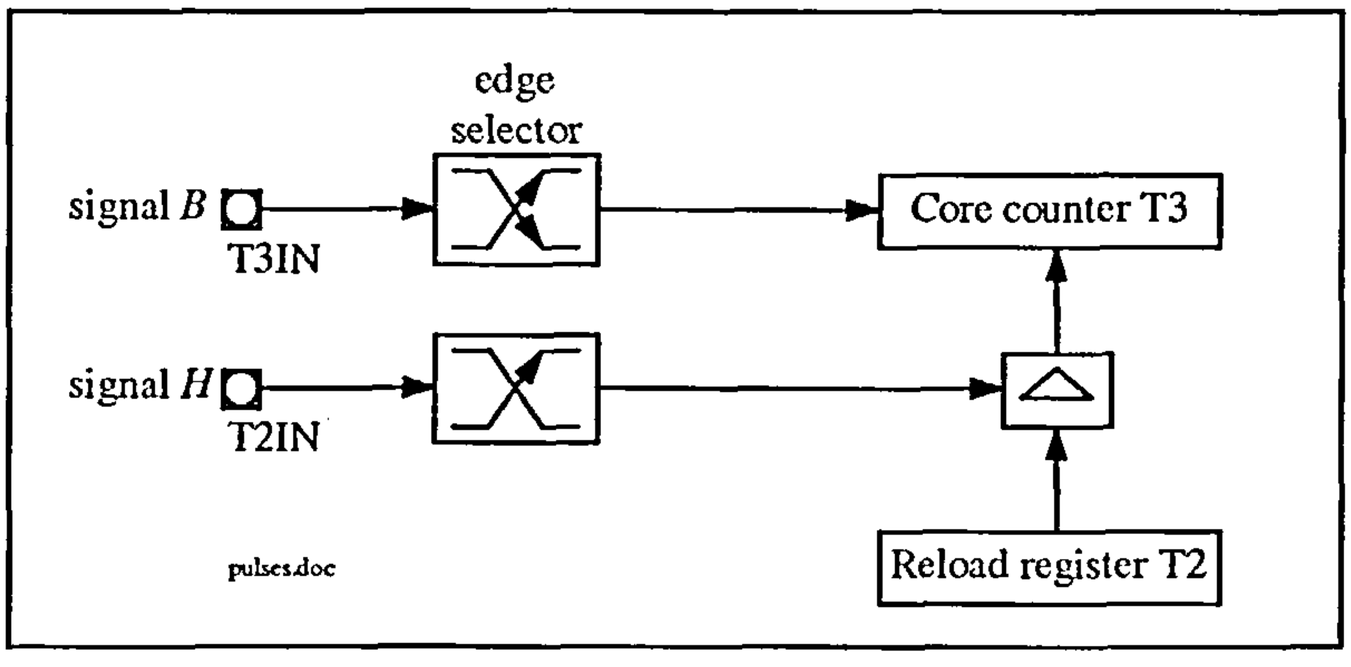

Figure C.2: Position counting with GPT1 of µC 1

The GPT 1 of µC 1 is set that the core counter T3 is in counting mode and the auxiliary timer T2 in reload mode. The edge selector for T3 is set for positive and negative edge transition counting and the edge selector for the reload triggering is set for only positive edge detection. Counter T3 is continuously counting the edges of the incoming signal *B*, which can lead to a counter content of maximal 10000 for one revolution. At an edge detection of the signal H, the counter register T3 is reloaded with the content of the reload register T2, which is constantly set to zero. In that way the counter register T3 always holds the actual position in count values 0..10000.

The internal rotor position angle is scaled that an angle resolution of 0.9° results leading to 0..400 values for 0..360°. The counter register content T3 has to be scaled accordingly.

```
// position measurement with counter T3
position_angle = scale * T3;                    // range of T3 = 0..10000
```

The rotor speed in rpm is calculated with the pulse counting method by numerical differentiation as

$$speed = \frac{60 * n}{N * T_{PWM}}$$

with

n as the number of counted pulses within one PWM period ($n = T3(k) - T3(k-1)$)

N as the maximum count number = 10000

T_{PWM} as the PWM period

The resulting speed resolution with this method for a switching frequency of 2.5 kHz can be calculated as

$$\Delta speed = \frac{60}{N * T_{PWM}} = 15\,rpm$$

For the 4 kHz switching frequency the speed resolution is 24 rpm.

The code for the microcontroller programming is listed next:

```
// speed calculation
new_pos = T3;
IF(old_pos>new_pos) delta_pos = new_pos + ( 10000 - old_pos );
ELSE delta_pos = new_pos - old_pos;
old_pos = new_pos;
nm = scale * delta_pos;
```

C.7 Power Calculation

The active and reactive power of a certain machine side is calculated from the d-components and the q-components of the respective voltage and current in the respective reference frame. This is implemented as:

```
// active and reactive power calculation
P = scale * (v_d*i_d + v_q*i_q);
Q = scale * (v_q*i_d - v_d*i_q);
```

C.8 PI-Controller

The structure of the used PI-controller is displayed in figure C.3, where the proportional and the integral parts are shown separately. The limiter together with the switch at the input to the integral part constitutes an anti-reset-windup method. In case the controller output reaches a set limit, the switch to the integral part will be opened and the integration stops. This prevents the integrator from winding up and allows a quick response at the controller output for a sign change of the error input.

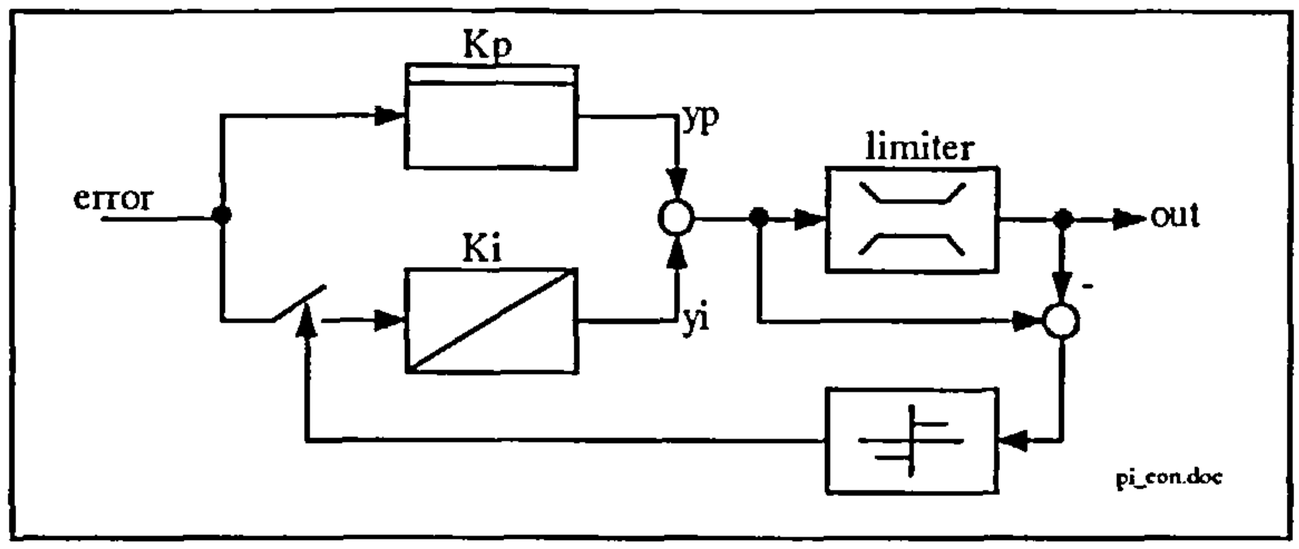

Figure C.3: PI-controller

The respective code for the controller as illustrated in figure C.3 is listed next:

```
error = demand - actual;
IF(error>limit1) error = limit1;          // limit error input
IF(error<-limit1) error = -limit1;

IF(stop==1) stop=0;                       // don't integrate
ELSE
{
  accu = accu_old + error;                // integrate
  IF(accu>limit2) accu = limit2;          // limit accumulator content
  IF(accu<-limit2) accu = -limit2;
  accu_old = accu;
}

yp = Kp * error;
yi = Ki * accu;
out = yp + yi;

IF(out>limit3)                            // output limiter
{
out = limit3;
stop = 1;
}
IF(out<-limit3)
{
out = -limit3;
stop = 1;
}
```

C.9 PWM

The microcontroller 80C167 has its own PWM unit with four independent controllable PWM channels. Three PWM channels are used for the SDFM / CDFM control. An electronic circuit on the same board as µC 1 produces the remaining three PWM signals, including dead-time.

The interrupt generated by PWM0-channel determines the switching frequency and the resulting calculation time for software implementation. A description of the PWM signal production is presented in section G.1.3 of appendix G.

C.10 Two Microcontroller Configuration

Two microcontroller 80C167 are used for software execution. They communicate via a fast serial connection. The data transfer is unidirectional from µC 2 to µC 1, as indicated in figure C.4, which shows a timing diagram of the microcontroller set-up.

Timing of µC 1

The maximum execution time of the implemented code is determined by the PWM cycle of µC 1. PWM0-channel is used for internal interrupt request generation. For the used switching frequency of 2.5 kHz an execution time of 400µs results.

For the initially used 4 kHz switching frequency of the SDFM control the duration of the PWM cycle is 250µs. This time turned out to be too small for experimental purposes, so that is was later extended to 400µs. Figure C.4 gives the timing for the 4 kHz implementation in brackets.

At the beginning of each control cycle is the reading out of "sampled" and "received" variables from the previous cycle. The ADC writes the sampled data into an one-dimensional array with five entries. That "sample" array is read out to have the variables available in the current PWM cycle. After that another array is read out. A one-dimensional "receive" array with nine entries holds the data variables transferred from µC 2 at the end of the previous cycle. Once those two arrays are read out the control algorithm starts and finishes with the PWM generation.

Timer T0 of µC 1 is set to give an interrupt request at 165µs (90µs) to start the ADC process. Five successive ADC's are carried out by µC 1, with a duration of 9.7µs each. The ADC process goes in parallel to the control algorithm, which is only interrupted by a single PEC data transfer after each ADC has finished. The PEC (peripheral event controller) allows to respond to an interrupt request with a single data transfer, which only consumes one instruction cycle and does not require to save and restore the machine status. Sampled data is written by the PEC to a "sample" data array.

As mentioned, both microcontrollers communicate with the high-speed synchronous serial interface (SSC). At 350µs µC 2 initiates a data transfer for nine variables. Each transfer takes about 3.3µs, so that a complete transfer duration of about 30µs results. The receiving data is written into a shift register of the µC 1. After a data byte is completely received it is transferred to a receive buffer register, from where a PEC data transfer writes the data to the "receive" array. In that way the reception of the transferred data takes place parallel to the control algorithm.

Timing of µC 2

At the very beginning of the control cycle, µC 1 produces a signal to µC 2, which causes an external interrupt request procedure to be started in µC 2, to synchronise the execution starting time of both microcontrollers.

At the beginning, the "sample" array of µC 2 is read out, which contains the sampled data from the ADC process.

ADC is started at 280µs by an interrupt request generation with timer T5. As it is the case in µC 1 the sampled data is transferred by PEC movements.

The interrupt capabilities of timer T6 are used for data transfer with the fast serial link. Normally, the SSC sending should be provided by the respective PEC. However, the implementation on the laboratory hardware with the fastest transmission rate of 5 MBaud was not functional with PEC transfers, probably as a consequence of the wiring connection of the two pre-designed controller boards as mentioned in [f23]. A proper board design with two microcontrollers on the same board should rid this problem. A T6 interrupt procedure is used for data transfer initiations, which interrupts the main control routine for about 30µs as shown in figure C.4.

The tasks carried out by the respective microcontroller are listed below. Not all of them may be needed during certain control applications. Chapter 3 and chapter 5 also give the tasks for each microcontroller, but specified for the particular control application.

µC 1 tasks:
sampling and ADC of three controlled currents
sampling and ADC of two potentiometer
complete inner current control loop including PWM
calculation of rotor position and speed from encoder signals
speed loop
remaining control algorithms

µC 1 tasks:
sampling and ADC of stator current and voltage
sampling and ADC of two potentiometer
power calculation and power control loop
angle calculation from stator voltage vector
remaining control algorithms

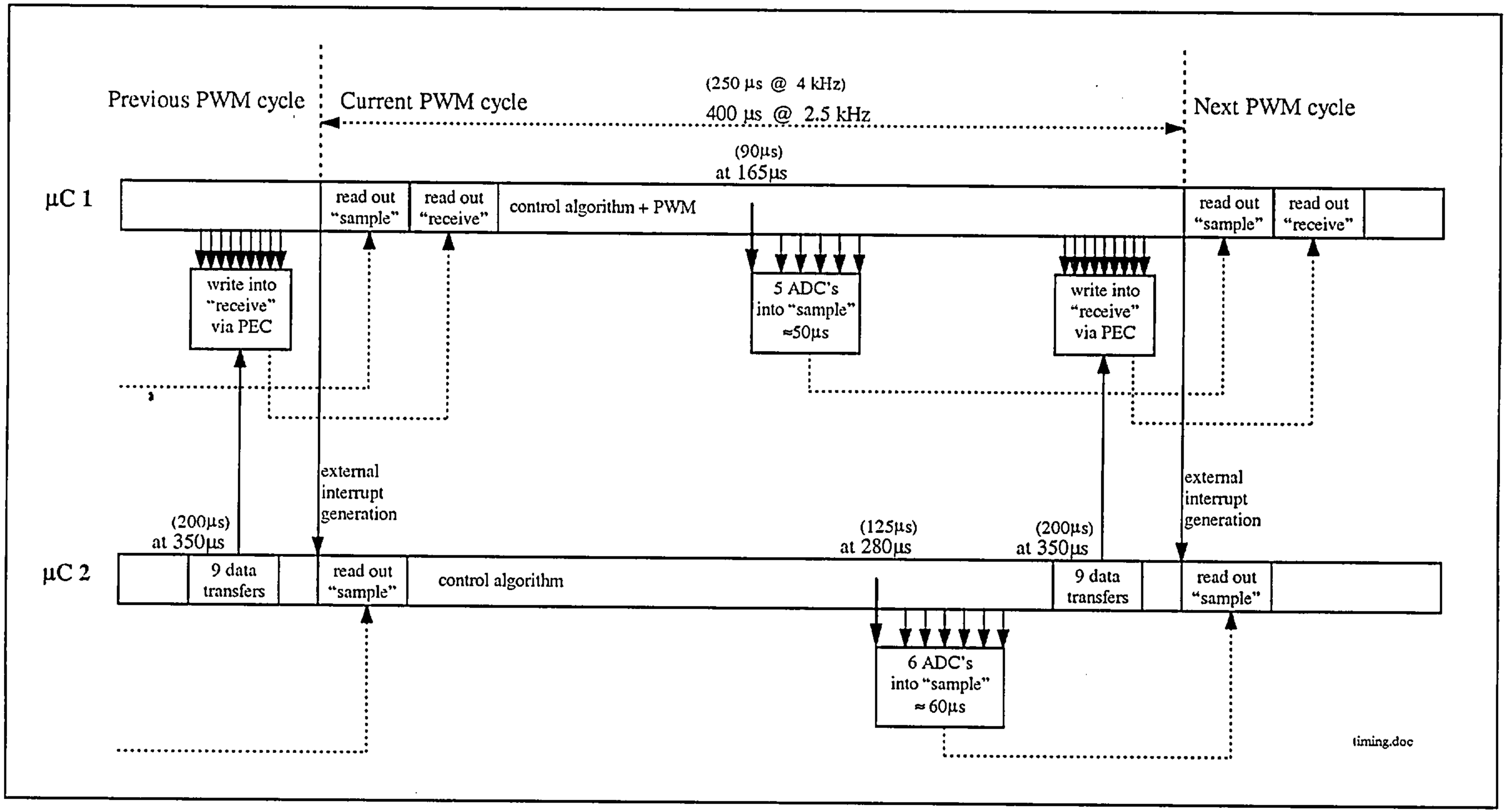

Figure C.4: Microcontroller timing

Appendix D

Influence of Turns-Ratio and Iron-Loss Resistor on Machine Equations

In the derivation of the dynamic model as well as the field oriented control description of the SDFM and CDFM the influence of a possible turns-ratio was ignored to keep simplicity and clearness in the involved equations. This appendix describes the necessary referral process needed for dynamic machine equations in case a turns-ratio is present.
Furthermore, the relationship between the per-phase equivalent circuit parameters and the d-q-model parameters is described.
Finally, the effect of an iron-loss resistor on the dynamic machine equations is clarified. Although the field oriented control results of the SDFM and CDFM justify the neglect of the iron-loss resistor in the dynamic machine equations, the steady state machine equations include the iron-loss resistor for simulation and modeling purposes. Since the steady state machine model can be derived from the dynamic machine model the presence of the iron-loss resistor in the dynamic machine equations is elaborated. Also, the influence on the torque equations is highlighted.

D.1 Referral Process due to Turns-Ratio

The stator and rotor voltage space vectors are defined in their natural reference frame as

$$\bar{v}_1^a = R_1 \bar{i}_1^a + \frac{d\bar{\Psi}_1^a}{dt} \tag{D.1}$$

$$\bar{v}_2^b = R_2 \bar{i}_2^b + \frac{d\bar{\Psi}_2^b}{dt} \tag{D.2}$$

where the stator and rotor flux linkages be expressed in terms of the stator and rotor current vectors as

$$\bar{\Psi}_1^a = L_1 \bar{i}_1^a + L_m \bar{i}_2^a \tag{D.3}$$

$$\bar{\Psi}_2^b = L_2 \bar{i}_2^b + L_m \bar{i}_1^b \tag{D.4}$$

where

$$\bar{i}_2^a = \bar{i}_2^b e^{j\Theta_r}$$

$$\bar{i}_1^b = \bar{i}_1^a e^{-j\Theta_r}$$

Equations (D.1)-(D.4) define the stator and rotor quantities on the stator side and rotor side respectively. The equations are not referred to the other machine side. The different parameters are

R_1 and R_2 are the stator and rotor resistance per phase

L_1 and L_2 are the stator and rotor self inductance per phase

L_m is the mutual inductance between stator and rotor windings

If there is a turns-ratio involved, between the stator and rotor windings with

$$a = \frac{N_1}{N_2}$$

as the effective turns-ratio, then it is useful to refer all quantities to the same number of turns, which is usually the stator number of turns.

The rotor quantities will be referred to the stator number of turns with following referred values (primed).

$$\bar{v}'^{b}_{2} = a\bar{v}^{b}_{2}$$

$$\bar{i}'^{b}_{2} = \frac{1}{a}\bar{i}^{b}_{2}$$

$$\bar{\Psi}'^{b}_{2} = a\bar{\Psi}^{b}_{2}$$

$$R'_2 = a^2 R_2$$

$$L'_2 = a^2 L_2$$

furthermore, for the inductance values can be written

$$L_{mag} = L_{mag1} = aL_m$$

$$L_m = \sqrt{L_{mag1} L_{mag2}}$$

$$L'_{mag2} = a^2 L_{mag2} = L_{mag1}$$

$$L_1 = (1+\sigma_1)L_{mag}$$

$$L_2 = (1+\sigma_2)L_{mag2}$$

$$L'_2 = a^2 L_2 = a^2(1+\sigma_2)L_{mag2} = (1+\sigma_2)L_{mag}$$

where

L_{mag} and L_{mag1} are the stator referred stator magnetising inductances

L_{mag2} is the rotor referred rotor magnetising inductance

L'_{mag2} is the stator referred rotor magnetising inductance

L'_2 is the stator referred rotor self inductance

σ_1 is the stator leakage factor

σ_2 is the rotor leakage factor

The space vectors referred to the stator number of turns can now be written as

$$\bar{v}_1^a = R_1 \bar{i}_1^a + \frac{d\bar{\Psi}_1^a}{dt}$$

$$\bar{v}'^b_2 = R'_2 \bar{i}'^b_2 + \frac{d\bar{\Psi}'^b_2}{dt}$$

$$\bar{\Psi}_1^a = L_1 \bar{i}_1^a + L_{mag} \bar{i}'^a_2$$

$$\bar{\Psi}'^b_2 = L'_2 \bar{i}'^b_2 + L_{mag} \bar{i}_1^b$$

$$\bar{i}'^a_2 = \bar{i}'^b_2 e^{j\Theta_r}$$

$$\bar{i}_1^b = \bar{i}_1^a e^{-j\Theta_r}$$

The torque is defined as

$$T_e = -\frac{3}{2} p_A \frac{L_m}{L_1} (\bar{\Psi}_1^a \times \bar{i}_2^a)$$

and by using referred values

$$T_e = -\frac{3}{2} p_A \frac{L_{mag}}{L_1} (\bar{\Psi}_1^a \times \bar{i}'^a_2)$$

D.2 Relationship between Parameters from the Per-Phase Equivalent Circuit and the Dynamic D-Q-Model Parameters

For obtaining the parameters of an induction machine the standard short-circuit and a no-load test can be carried out. The parameters, which are calculated from those tests are

- a: effective turns ratio
- R_1: stator per-phase resistance
- R_2: rotor per-phase resistance (R'_2 referred to stator side)
- $L_{\sigma 1}$: stator leakage inductance
- $L_{\sigma 2}$: rotor leakage inductance ($L'_{\sigma 2}$ referred to stator side)
- L_{mag}: magnetising inductance
- R_{fe}: iron loss resistance

The d-q-model parameters are related to the calculated parameters from the machine tests as

Stator resistance: $R_1 = R_1$

Rotor resistance: $R_2 = R_2 = \frac{R'_2}{a^2}$

Iron loss resistance: $R_{fe} = R_{fe}$

Stator self inductance: $L_1 = L_{\sigma 1} + L_{mag}$

Rotor self inductance: $L_2 = \frac{L'_2}{a^2} = \frac{L'_{\sigma 2} + L_{mag}}{a^2}$

Magnetising inductance: $L_{mag} = L_{mag} = aL_m$

Figure D.1 shows the different definitions on a steady state per-phase equivalent circuit for a SDFM.

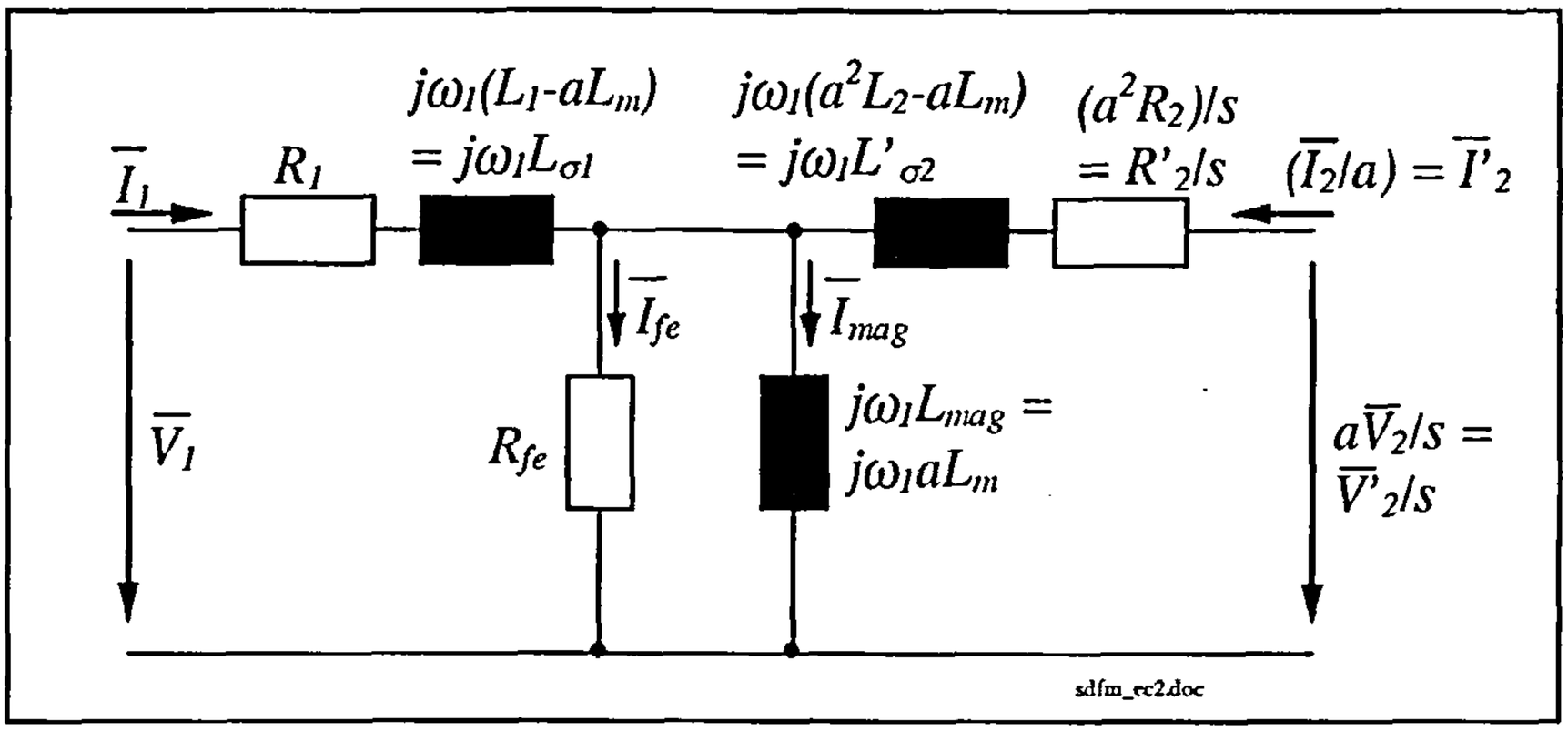

Figure D.1: Parameter definitions of the steady state per-phase equivalent circuit of the SDFM

D.3 Dynamic SDFM Model Including Iron-Loss Resistor

The dynamic machine model, ignoring the presence of an iron-loss resistor, of the SDFM with unity turns-ratio in a general reference frame is developed in section 3.1.3 of chapter 3. For convenience the space vector equations are repeated at this place

$$\bar{v}_1^g = R_1 \bar{i}_1^g + \frac{d\bar{\Psi}_1^g}{dt} + j\omega_1 \bar{\Psi}_1^g$$

$$\bar{v}_2^g = R_2 \bar{i}_2^g + \frac{d\bar{\Psi}_2^g}{dt} + j(\omega_g - \omega_1)\bar{\Psi}_2^g$$

$$\bar{\Psi}_1^g = L_1 \bar{i}_1^g + L_m \bar{i}_2^g$$

$$\bar{\Psi}_2^g = L_2 \bar{i}_2^g + L_m \bar{i}_1^g$$

The core losses are symbolised by a resistor parallel to the magnetising inductance as shown in figure D.1. For simplicity, this resistor represents the iron-losses of the machine concentrated on the primary side and is assumed to remain constant for all operating conditions. The modified dynamic equations of the SDFM on account of the iron-loss resistor are, following [f21]

$$\bar{v}_1^g = R_1 \bar{i}_1^g + \frac{d\overline{\Psi}_1^g}{dt} + j\omega_1 \overline{\Psi}_1^g$$

$$\bar{v}_2^g = R_2 \bar{i}_2^g + \frac{d\overline{\Psi}_2^g}{dt} + j(\omega_g - \omega_1)\overline{\Psi}_2^g$$

$$\overline{\Psi}_1^g = L_{\sigma 1} \bar{i}_1^g + \overline{\Psi}_m^g$$

$$\overline{\Psi}_2^g = L_{\sigma 2} \bar{i}_2^g + \overline{\Psi}_m^g$$

with

$$\overline{\Psi}_m^g = L_m \bar{i}_m^g$$

as the magnetising flux linkage space vector. The current space vector relationship follows as

$$\bar{i}_1^g + \bar{i}_2^g = \bar{i}_{fe}^g + \bar{i}_m^g$$

and the additional equation for the iron-loss path as

$$R_{fe} \bar{i}_{fe}^g = \frac{d\overline{\Psi}_m^g}{dt} + \omega_g \overline{\Psi}_m^g$$

The electromagnetic torque developed by a SDFM ignoring core losses can be written as

$$T_e = -\frac{3}{2} p_A \frac{L_m}{L_1} (\overline{\Psi}_1^g \times \bar{i}_2^g) \qquad \text{(D.5)}$$

Taking account of the iron-losses and expressing the torque as a function of the stator flux vector and the rotor current vector leads to

$$T_e = -\frac{3}{2} p_A [(\overline{\Psi}_1^g \times \bar{i}_2^g) - L_{\sigma 1} (\bar{i}_1^g \times \bar{i}_2^g)] \qquad \text{(D.6)}$$

Part of the developed machine torque of the SDFM is used to feed iron core losses, so that the effective shaft torque, described by (D.6), is partly smaller than that expressed by equation (D.5).

Alternatively, the developed shaft torque can be written as

$$T_e = -\frac{3}{2} p_A (\overline{\Psi}_m^g \times \bar{i}_2^g) \qquad \text{(D.7)}$$

or

$$T_e = -\frac{3}{2} p_A L_m (\bar{i}_m^g \times \bar{i}_2^g)$$

Equation (D.7) points out, that a stator flux oriented control of the SDFM introduces a slight error due to false orientation. For correct field orientation with impressed rotor current control the magnetising flux space vector must be used.

Appendix E

Simulation of SDFM and CDFM

The simulation of the steady state, dynamic and control behaviour of the SDFM and the CDFM is an important tool in familiarising oneself with the machine system.
This chapter describes the steady state and the dynamic simulation arrangements used during work. First the steady state model of the SDFM and the CDFM is characterised. After that, dynamic simulation with SIMULINK and with C are described.

E.1 Steady State Simulation with MATLAB

Steady state calculations are carried out by using MATLAB. MATLAB [f26] is a technical computing environment for high performance numeric computation and visualisation. It is in wide spread use nowadays. The beauty of MATLAB compared to other programming languages, e.g. PASCAL, C, is that complex calculations can be performed without defining an array for a two-dimensional number. The complex number is a built-in feature. This makes it very attractive for computations of electrical systems. Additionally, MATLAB allows to plot and manipulate data after calculations, because the data is saved in the background, the so called workspace.

The steady state calculations of the SDFM and the CDFM are based on the per-phase equivalent circuit equations. Turns-ratio, pole pair number and iron loss resistor are included in the equivalent circuit. All machine quantities are referred to their original machine side, so that they deliver the quantities as they would appear on the respective machine terminals.

Various programs have been written, allowing to input different input variables and to calculate the remaining machine quantities. In this section all basic machine equation are lead out from which the various programs were derived.

When using an equivalent circuit for calculations it is common to use per-phase rms values for the machine variables and to multiply the calculated per-phase torque, power and loss results by 3 to get the overall machine results.

Steady state calculations derived from the d-q-model of the machine use peak values for the machine electrical quantities representing the values on the d-axis and q-axis of the system. Although, the initial derivation of the d-q-model compared to the per-phase equivalent circuit model is of a completely different nature the performed calculations are both based on the complex number system. The equivalent circuit model for real and imaginary parts and the d-q-model for d-axis and q-axis quantities. It is therefore straight forward to utilise the per-phase equivalent circuit calculations for d-q-model calculations. In the d-q-model the quantities are peak values and the torque, power and loss results are multiplied by a factor of 1.5.

The description of the steady state model for the SDFM and the CDFM in the following uses the per-phase equivalent circuit approach.

E.1.1 Steady State Model of the SDFM

The per-phase equivalent circuit for the SDFM consisting of two sub-networks is shown in figure E.1. All quantities are referred to their actual machine side.

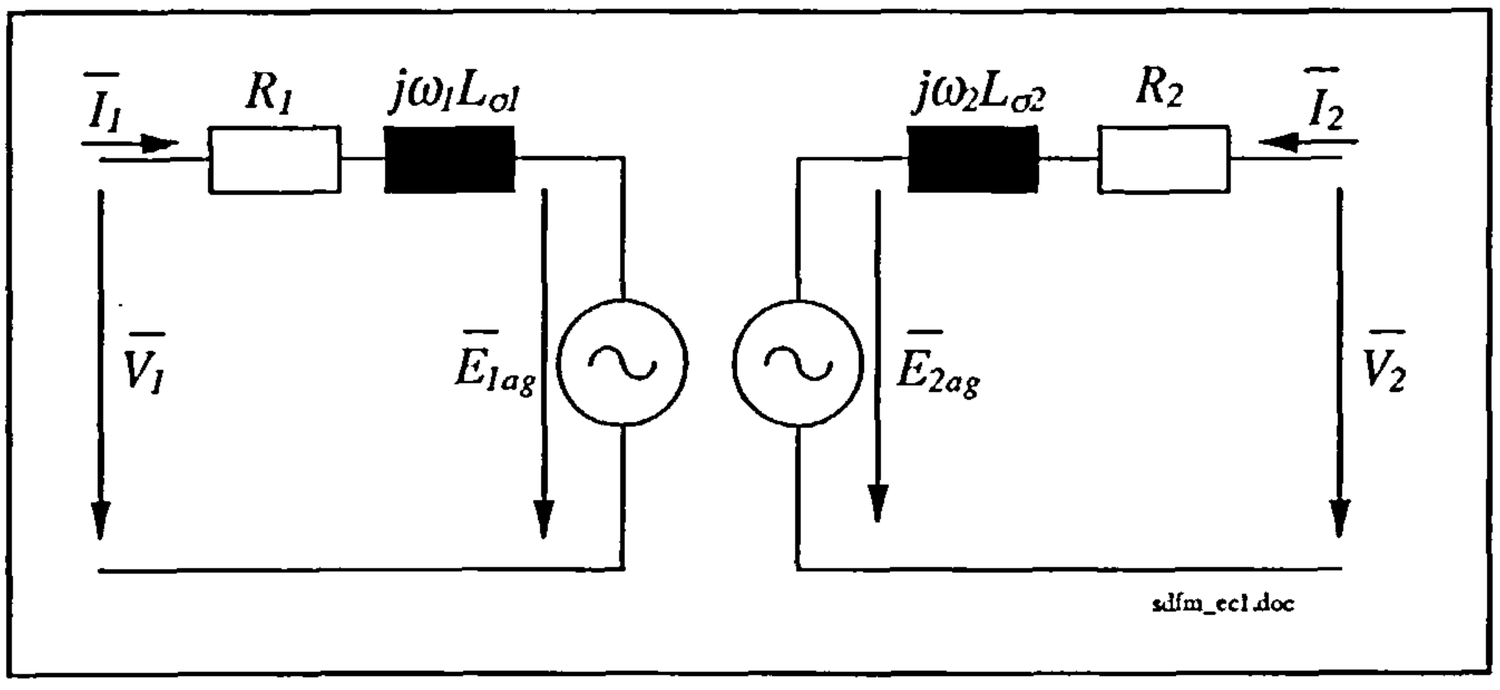

Figure E.1: Non-referred SDFM per-phase equivalent circuit

The per-phase equations of the SDFM are equal to the equations of machine A of the CDFM and shall therefore not be elaborated explicitly. It shall be referred to the CDFM section.

Although throughout this work all calculations are based on the equivalent circuit in figure E.1, the side 1 referred equivalent circuit is given next for the sake of completeness. Similar to the known referred cage induction machine equivalent circuit, all quantities are referred to the stator side and only stator frequency is present in the whole system.

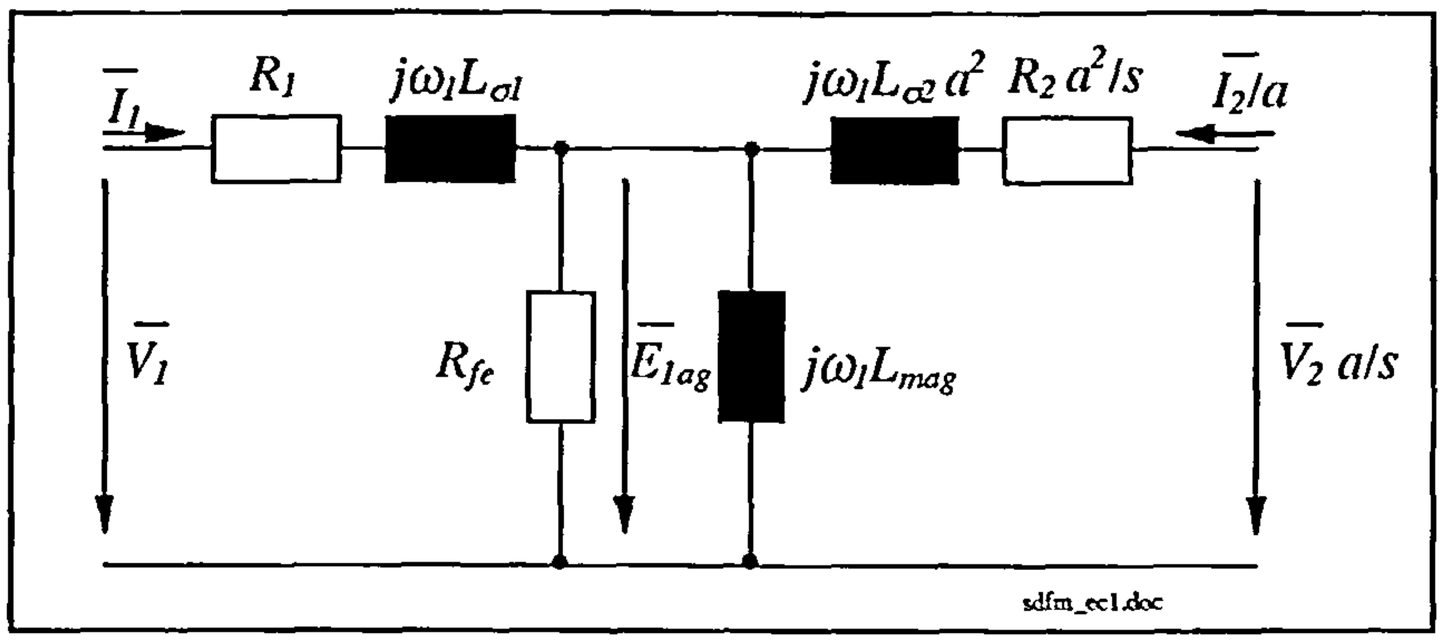

Figure E.2: Referred SDFM per-phase equivalent circuit

E.1.2 Steady State Model of the CDFM

The description of the CDFM equivalent circuit in this section considers only the positive phase sequence rotor connection, since this is the relevant case. The differences of the negative phase sequence rotor connection circuit are explained in chapter 4.

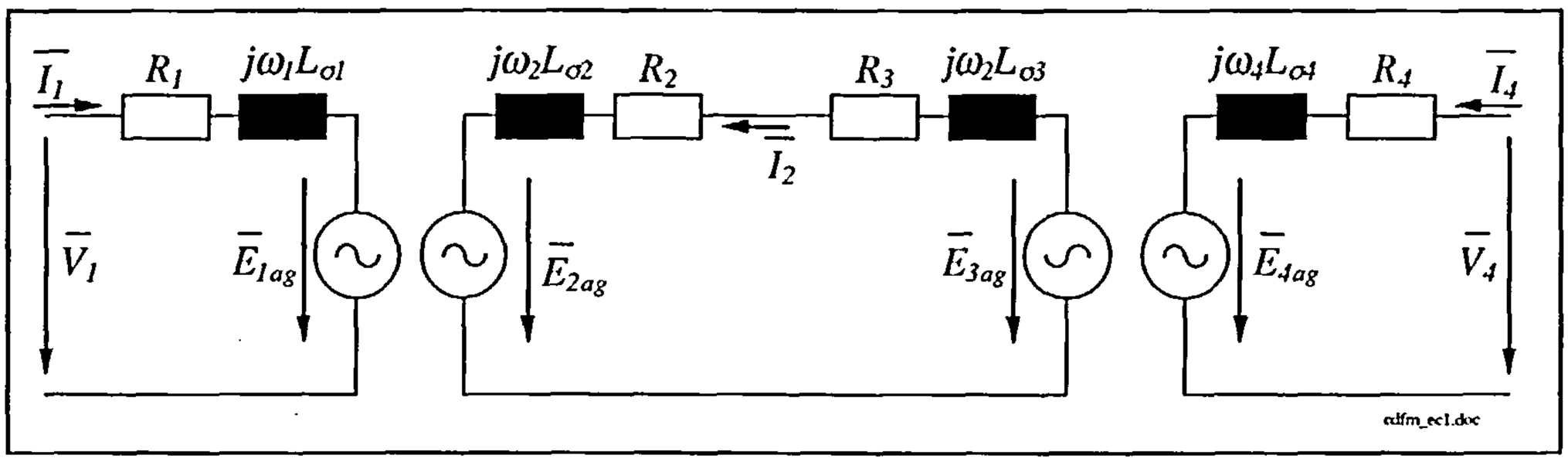

Figure E.3: Non-referred CDFM per-phase equivalent circuit (positive rotor connection)

The CDFM per-phase equivalent circuit, as already introduced in chapter 4, consist of three sub-networks. Side 1, the rotor and side 4 network, as displayed in figure E.3.
The calculations on the CDFM steady state behaviour is performed with the connection of two SDFM's, machine A and machine B and therefore uses four different machine sides. The rotor circuit in figure E.3 is the closed rotor circuit loop of side 2 with side 3.
Each machine may have a different set of parameters.

The voltage phasor equations for the individual machine sides are as

$$\overline{V}_1 = \overline{Z}_1 \overline{I}_1 + \overline{E}_{1ag}$$
$$\overline{V}_2 = \overline{Z}_2 \overline{I}_2 + \overline{E}_{2ag}$$
$$\overline{V}_3 = \overline{Z}_3 \overline{I}_3 + \overline{E}_{3ag}$$
$$\overline{V}_4 = \overline{Z}_4 \overline{I}_4 + \overline{E}_{4ag}$$

with the air-gap voltages of

$$\overline{E}_{1ag} = (\bar{I}_1 + \frac{\bar{I}_2}{a})^* \overline{Z}_{magA}$$

$$\overline{E}_{2ag} = \overline{E}_{1ag} \frac{s_A}{a} \qquad \text{(E.1)}$$

$$\overline{E}_{3ag} = (\bar{I}_3 + \frac{\bar{I}_4}{b})^* \overline{Z}_{magB}$$

$$\overline{E}_{4ag} = \overline{E}_{3ag} \frac{s_B}{b} \qquad \text{(E.2)}$$

The air-gap voltages are the induced e.m.f.'s due to the mutual air-gap flux linkage in the machine. Equation (E.1) constitutes the mathematical connection between side 1 and side 2 and equation (E.2) the connection for side 3 and side 4. The machine connection is accomplished with the positive phase sequence rotor connection constraints of

$$\bar{I}_2 = -\bar{I}_3$$
$$\overline{V}_2 = \overline{V}_3$$

and

$$\omega_2 = \omega_3$$

The slip in (E.1) and (E.2) is defined as

$$s_A = \frac{\omega_2}{\omega_1}$$

$$s_B = \frac{\omega_4}{\omega_3} \qquad \text{(E.3)}$$

with ω_1, ω_2 , ω_3, and ω_4 as the angular frequencies in electrical rad/s of the respective machine sides. Together with the mechanical rotor speed ω_r in electrical rad/s the frequency relation between side 1 and 2 is given by

$$\omega_1 = \omega_{rA} + \omega_2$$

and for side 3 and side 4 by

$$\omega_3 = \omega_{rB} + \omega_4$$

Using the number of pole pairs p_A and p_B the relation between the rotor speed in electrical and mechanical rad/s is obtained by

$$\omega_{rA} = p_A \omega_m$$

$$\omega_{rB} = p_B \omega_m$$

The turns-ratio definition of the individual machines follows as

$$a = \frac{\textit{effective number of turns on side 1}}{\textit{effective number of turns on side 2}}$$

$$b = \frac{\textit{effective number of turns on side 3}}{\textit{effective number of turns on side 4}}$$

It has to be noted, that for the definitions of the angular frequencies in equation (E.3) and for the turns ratio of machine B, side 3 is seen as it's primary side and side 4 as the secondary side.

Impedances are defined as

$$\bar{Z}_1 = R_1 + j\omega_1 L_{\sigma 1}$$

$$\bar{Z}_2 = R_2 + j\omega_2 L_{\sigma 2}$$

$$\bar{Z}_3 = R_3 + j\omega_3 L_{\sigma 3}$$

$$\bar{Z}_4 = R_4 + j\omega_4 L_{\sigma 4}$$

$$\bar{Z}_{magA} = \frac{1}{\bar{Y}_{magA}}$$

$$\bar{Y}_{magA} = \frac{1}{R_{feA}} + \frac{1}{j\omega_1 L_{magA}}$$

$$\bar{Z}_{magB} = \frac{1}{\bar{Y}_{magB}}$$

$$\bar{Y}_{magB} = \frac{1}{R_{feB}} + \frac{1}{j\omega_3 L_{magB}}$$

where

R_1, R_2, R_3 and R_4 are the per-phase resistances

$L_{\sigma 1}$, $L_{\sigma 2}$, $L_{\sigma 3}$ and $L_{\sigma 4}$ are the per-phase leakage inductances

R_{feA} and R_{feB} are the iron loss resistances

L_{magA} and L_{magB} are the magnetising inductances

Considering the magnetising path of each individual machine the magnetising currents for the different machine sides are

$$\bar{I}_{mag1} = \frac{\bar{E}_{1ag}}{j\omega_1 L_{magA}} \quad \text{and} \quad \bar{I}_{mag2} = \frac{\bar{E}_{2ag}}{j\omega_2 \frac{L_{magA}}{a^2}} = \bar{I}_{mag1} * a$$

$$\bar{I}_{mag3} = \frac{\bar{E}_{3ag}}{j\omega_3 L_{magB}} \quad \text{and} \quad \bar{I}_{mag4} = \frac{\bar{E}_{4ag}}{j\omega_4 \frac{L_{magB}}{b^2}} = \bar{I}_{mag3} * b$$

and for the currents through the iron loss resistor

$$\bar{I}_{fe1} = \frac{\bar{E}_{1ag}}{R_{feA}} \quad \text{and} \quad \bar{I}_{fe2} = \frac{\bar{E}_{2ag}}{\frac{s_A R_{feA}}{a^2}} = \bar{I}_{fe1} * a$$

$$\bar{I}_{fe3} = \frac{\bar{E}_{3ag}}{R_{feB}} \quad \text{and} \quad \bar{I}_{fe4} = \frac{\bar{E}_{4ag}}{\frac{s_B R_{feB}}{b^2}} = \bar{I}_{fe3} * b$$

The currents take following relation to each other

$$\bar{I}_1 + \frac{\bar{I}_2}{a} = \bar{I}_{fe1} + \bar{I}_{mag1}$$

$$\bar{I}_3 + \frac{\bar{I}_4}{b} = \bar{I}_{fe3} + \bar{I}_{mag3}$$

The per-phase flux linkage equations are

$$\overline{\Psi}_{mag1} = L_{magA} * \bar{I}_{mag1}$$

$$\overline{\Psi}_{mag2} = \frac{L_{magA}}{a^2} * \bar{I}_{mag2} = \frac{\overline{\Psi}_{mag1}}{a}$$

$$\overline{\Psi}_{mag3} = L_{magB} * \bar{I}_{mag3}$$

$$\overline{\Psi}_{mag4} = \frac{L_{magB}}{b^2} * \bar{I}_{mag4} = \frac{\overline{\Psi}_{mag3}}{b}$$

$$\overline{\Psi}_1 = L_{\sigma 1}\bar{I}_1 + \overline{\Psi}_{mag1}$$

$$\overline{\Psi}_2 = L_{\sigma 2}\bar{I}_2 + \overline{\Psi}_{mag2}$$

$$\overline{\Psi}_3 = L_{\sigma 3}\bar{I}_3 + \overline{\Psi}_{mag3}$$

$$\overline{\Psi}_4 = L_{\sigma 4}\bar{I}_4 + \overline{\Psi}_{mag4}$$

The apparent power definitions for the individual machine terminals are

$$S_1 = 3 * \overline{V}_1 conj(\bar{I}_1)$$

$$S_2 = 3 * \overline{V}_2 conj(\bar{I}_2)$$

$$S_3 = 3 * \overline{V}_3 conj(\bar{I}_3)$$

$$S_4 = 3 * \overline{V}_4 conj(\bar{I}_4)$$

Real power: (power is positive, when flowing into system)

$$P_1 = real(S_1)$$

$$P_2 = real(S_2)$$

$$P_3 = real(S_3)$$

$$P_4 = real(S_4)$$

Reactive power: (inductive is positive, capacitive is negative)

$$Q_1 = imag(S_1)$$

$$Q_2 = imag(S_2)$$

$$Q_3 = imag(S_3)$$

$$Q_4 = imag(S_4)$$

At the rotor connection point

$$P_2 = -P_3$$
$$Q_2 = -Q_3$$

The copper losses in each machine section are calculated as:

$$Cu_{loss1} = 3 * \left|\bar{I}_1\right|^2 R_1$$
$$Cu_{loss2} = 3 * \left|\bar{I}_2\right|^2 R_2$$
$$Cu_{loss3} = 3 * \left|\bar{I}_3\right|^2 R_3$$
$$Cu_{loss4} = 3 * \left|\bar{I}_4\right|^2 R_4$$
$$Cu_{lossA} = Cu_{loss1} + Cu_{loss2}$$
$$Cu_{lossB} = Cu_{loss3} + Cu_{loss4}$$

and the iron losses for each machine (iron losses of machine A are concentrated on side 1, those for machine B on side 3)

$$Fe_{lossA} = 3 * \frac{|\bar{E}_{1ag}|^2}{R_{feA}}$$
$$Fe_{lossB} = 3 * \frac{|\bar{E}_{3ag}|^2}{R_{feB}}$$

The torque developed by the individual machines is the cross product of the magnetising current and the secondary current referred onto the primary side.

$$T_{eA} = -3 * p_A * L_{magA} * \bar{I}_{mag1} \times \frac{\bar{I}_2}{a}$$
$$T_{eB} = -3 * p_B * L_{magB} * \bar{I}_{mag3} \times \frac{\bar{I}_4}{b}$$
$$T_{eAB} = T_{eA} + T_{eB}$$

Mechanical power:

$$P_{mechA} = -\omega_m T_{eA}$$
$$P_{mechB} = -\omega_m T_{eB}$$

or when considering the power flow in machine

$$P_{mechA} = -(1 - s_A) * (P_1 - (Cu_{loss1} + Fe_{lossA}))$$
$$P_{mechB} = -(1 - s_B) * (P_3 - (Cu_{loss3} + Fe_{lossB}))$$

For completeness, the side 1 referred equivalent circuit of the CDFM is displayed in figure E.4.

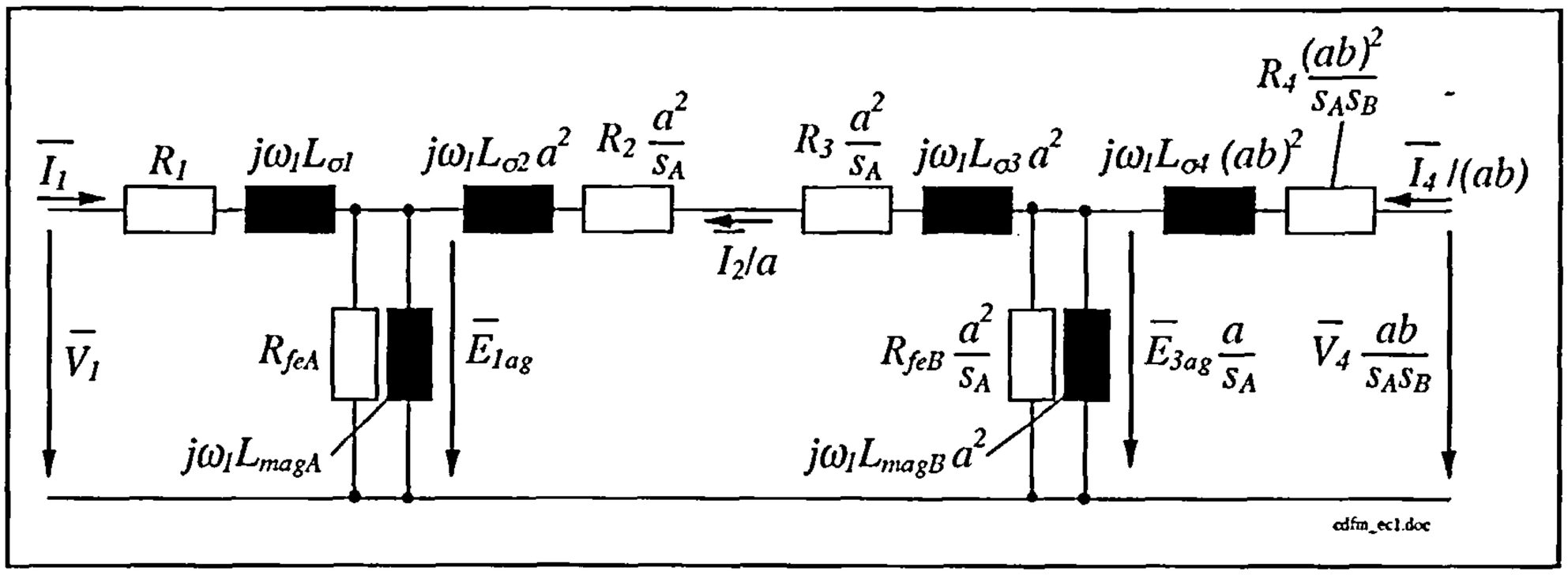

Figure E.4: Referred CDFM per-phase equivalent circuit (positive rotor connection)

E.1.3 Harmonic Steady State Model Derivation of the SDFM System

In this section the harmonic model for the SDFM system is derived as used for the harmonic current prediction process in chapter 7.

The system equations are

$$\overline{V}_{1v} = \overline{Z}_{11v}\overline{I}_{1v} + \overline{Z}_{magv}\frac{1}{a}\overline{I}_{2v} \tag{E.4}$$

$$\overline{V}_{2v} = \overline{Z}_{22v}\overline{I}_{2v} + \overline{Z}_{magv}\frac{s_v}{a}\overline{I}_{1v} \tag{E.5}$$

$$\overline{V}_{1v} = \overline{V}_{sv} + \overline{Z}_{sv}\overline{I}_{sv} \tag{E.6}$$

$$\overline{V}_{1v} = \overline{V}_{yv} + \overline{Z}_{yv}\overline{I}_{yv} \tag{E.7}$$

$$\overline{I}_{1v} = -\overline{I}_{sv} - \overline{I}_{yv} \tag{E.8}$$

and the impedance definitions are

$$\overline{Z}_{1v} = j\omega_{1v}L_{\sigma 1}$$

$$\overline{Z}_{2v} = j\omega_{2v}L_{\sigma 2}$$

$$\overline{Z}_{magv} = j\omega_{1v}L_{mag}$$

$$\overline{Z}_{yv} = j\omega_{1v}L_{y}$$

$$\overline{Z}_{sv} = j\omega_{1v}L_{s}$$

$$\overline{Z}_{11v} = \overline{Z}_{1v} + \overline{Z}_{magv}$$

$$\overline{Z}_{22v} = \overline{Z}_{2v} + \overline{Z}_{magv}\frac{s_v}{a^2}$$

Substituting (E.4) into (E.6) yields

$$\bar{Z}_{11v}\bar{I}_{1v} + \bar{Z}_{magv}\frac{1}{a}\bar{I}_{2v} = \bar{V}_{sv} + \bar{Z}_{sv}\bar{I}_{sv} \tag{E.9}$$

and with (E.8) results in

$$\bar{V}_{sv} = -(\bar{Z}_{11v} + \bar{Z}_{sv})\bar{I}_{sv} - \bar{Z}_{11v}\bar{I}_{yv} + \bar{Z}_{magv}\frac{1}{a}\bar{I}_{2v} \tag{E.10}$$

Substituting (E.4) into (E.7) yields

$$\bar{Z}_{11v}\bar{I}_{1v} + \bar{Z}_{magv}\frac{1}{a}\bar{I}_{2v} = \bar{V}_{yv} + \bar{Z}_{yv}\bar{I}_{yv} \tag{E.11}$$

and with (E.8) results in

$$\bar{V}_{yv} = -\bar{Z}_{11v}\bar{I}_{sv} - (\bar{Z}_{11v} + \bar{Z}_{yv})\bar{I}_{yv} + \bar{Z}_{magv}\frac{1}{a}\bar{I}_{2v} \tag{E.12}$$

Substituting (E.8) into (E.5) gives

$$\bar{V}_{2v} = -\bar{Z}_{magv}\frac{s_v}{a}\bar{I}_{sv} - \bar{Z}_{magv}\frac{s_v}{a}\bar{I}_{yv} + \bar{Z}_{22v}\bar{I}_{2v} \tag{E.13}$$

Using matrix formation (E.19), (E.12) and (E.13) can be written as

$$\begin{bmatrix}\bar{V}_{sv}\\ \bar{V}_{yv}\\ \bar{V}_{2v}\end{bmatrix} = \begin{bmatrix} -(\bar{Z}_{11v} + \bar{Z}_{sv}) & -\bar{Z}_{11v} & \bar{Z}_{magv}\frac{1}{a}\\ -\bar{Z}_{11v} & -(\bar{Z}_{11v} + \bar{Z}_{yv}) & \bar{Z}_{magv}\frac{1}{a}\\ -\bar{Z}_{magv}\frac{s_v}{a} & -\bar{Z}_{magv}\frac{s_v}{a} & \bar{Z}_{22v}\end{bmatrix}\begin{bmatrix}\bar{I}_{sv}\\ \bar{I}_{yv}\\ \bar{I}_{2v}\end{bmatrix} \tag{E.14}$$

E.1.4 Harmonic Steady State Model Derivation of the CDFM System

In this section the harmonic model for the CDFM system is derived as used for the harmonic current prediction process in chapter 7.

The machine equations are

$$\bar{V}_{1v} = \bar{Z}_{11v}\bar{I}_{1v} + \bar{Z}_{magAv}\frac{1}{a}\bar{I}_{2v} \tag{E.15}$$

$$\bar{V}_{2v} = \bar{Z}_{22v}\bar{I}_{2v} + \bar{Z}_{magAv}\frac{s_{Av}}{a}\bar{I}_{1v} \tag{E.16}$$

$$\bar{V}_{2v} = -\bar{Z}_{33v}\bar{I}_{2v} + \bar{Z}_{magBv}\frac{1}{b}\bar{I}_{4v} \tag{E.17}$$

$$\bar{V}_{4v} = \bar{Z}_{44v}\bar{I}_{4v} - \bar{Z}_{magBv}\frac{s_{Bv}}{b}\bar{I}_{2v} \tag{E.18}$$

with the slips of

$$s_{Av} = \frac{\omega_{2v}}{\omega_{1v}} \approx 1$$

$$s_{Bv} = \frac{\omega_{4v}}{\omega_{2v}} \approx 1$$

The remaining quantities of the CDFM system are

$$\bar{V}_{xv} = \bar{V}_{sv} + \bar{Z}_{sv}\bar{I}_{sv} \quad \text{(E.19)}$$

$$\bar{V}_{xv} = \bar{V}_{yv} + \bar{Z}_{yv}\bar{I}_{yv} \quad \text{(E.20)}$$

$$\bar{V}_{xv} = \bar{V}_{1v} + \bar{Z}_{x1v}\bar{I}_{x1v} \quad \text{(E.21)}$$

$$\bar{V}_{1v} = \bar{Z}_{x2v}\bar{I}_{x2v} \quad \text{(E.22)}$$

and

$$\bar{I}_{x1v} = -\bar{I}_{sv} - \bar{I}_{yv} \quad \text{(E.23)}$$

$$\bar{I}_{1v} = -\bar{I}_{x2v} - \bar{I}_{sv} - \bar{I}_{yv} \quad \text{(E.24)}$$

The impedance definitions are

$$\bar{Z}_{1v} = j\omega_{1v}L_{\sigma 1}$$

$$\bar{Z}_{2v} = j\omega_{2v}L_{\sigma 2}$$

$$\bar{Z}_{magAv} = j\omega_{1v}L_{magA}$$

$$\bar{Z}_{3v} = j\omega_{2v}L_{\sigma 3}$$

$$\bar{Z}_{4v} = j\omega_{4v}L_{\sigma 4}$$

$$\bar{Z}_{magBv} = j\omega_{2v}L_{magB}$$

$$\bar{Z}_{yv} = j\omega_{1v}L_{y}$$

$$\bar{Z}_{sv} = j\omega_{1v}L_{s}$$

$$\bar{Z}_{x1v} = j\omega_{1v}(1-x)L_{x}$$

$$\bar{Z}_{x2v} = j\omega_{1v}xL_{x}$$

$$\bar{Z}_{11v} = \bar{Z}_{1v} + \bar{Z}_{magAv}$$

$$\bar{Z}_{22v} = \bar{Z}_{2v} + \bar{Z}_{magAv}\frac{s_{Av}}{a^2}$$

$$\bar{Z}_{33v} = \bar{Z}_{3v} + \bar{Z}_{magBv}$$

$$\bar{Z}_{44v} = \bar{Z}_{4v} + \bar{Z}_{magBv}\frac{s_{Bv}}{b^2}$$

Substituting (E.16) into (E.17) gives

$$\bar{I}_{2v} = \bar{Z}_{av}\bar{I}_{4v} - \bar{Z}_{bv}\bar{I}_{1v} \quad \text{(E.25)}$$

with

$$\bar{Z}_{av} = \frac{\bar{Z}_{magB}\frac{1}{b}}{\bar{Z}_{22v} + \bar{Z}_{33v}} \qquad \bar{Z}_{bv} = \frac{\bar{Z}_{magA}\frac{s_{Av}}{a}}{\bar{Z}_{22v} + \bar{Z}_{33v}}$$

Substituting (E.15), (E.19) into (E.21) yields

$$\bar{V}_{sv} = (\bar{Z}_{cv} - \bar{Z}_{x1v} - \bar{Z}_{sv})\bar{I}_{sv} + (\bar{Z}_{cv} - \bar{Z}_{x1v})\bar{I}_{yv} + \bar{Z}_{magAv}\frac{1}{a}\bar{Z}_{av}\bar{I}_{4v} + \bar{Z}_{cv}\bar{I}_{x2v} \tag{E.26}$$

with $\bar{Z}_{cv} = \bar{Z}_{magAv}\frac{1}{a}\bar{Z}_{bv} - \bar{Z}_{11v}$

Rearranging (E.15), (E.20) with (E.21) gives

$$\bar{V}_{yv} = (\bar{Z}_{cv} - \bar{Z}_{x1v})\bar{I}_{sv} + (\bar{Z}_{cv} - \bar{Z}_{yv} - \bar{Z}_{x1v})\bar{I}_{yv} + \bar{Z}_{magAv}\frac{1}{a}\bar{Z}_{av}\bar{I}_{4v} + \bar{Z}_{cv}\bar{I}_{x2v} \tag{E.27}$$

and with (E.25) in (E.18) with the help of (E.24)

$$\bar{V}_{4v} = -\bar{Z}_{magBv}\frac{s_{Bv}}{b}\bar{Z}_{bv}\bar{I}_{sv} - \bar{Z}_{magBv}\frac{s_{Bv}}{b}\bar{Z}_{bv}\bar{I}_{yv} + (\bar{Z}_{44} - \bar{Z}_{magBv}\frac{s_{Bv}}{b}\bar{Z}_{av})\bar{I}_{4v} - \bar{Z}_{magBv}\frac{s_{Bv}}{b}\bar{Z}_{bv}\bar{I}_{x2v} \tag{E.28}$$

Substituting (E.22) into (E.15) and combining with (E.24) and (E.25) gives

$$0 = \bar{Z}_{cv}\bar{I}_{sv} + \bar{Z}_{cv}\bar{I}_{yv} + \bar{Z}_{magAv}\frac{1}{a}\bar{Z}_{av}\bar{I}_{4v} + (\bar{Z}_{cv} - \bar{Z}_{x2v})\bar{I}_{x2v} \tag{E.29}$$

Using matrix formation (E.26) - (E.29) can be written as

$$\begin{bmatrix} \bar{V}_{sv} \\ \bar{V}_{yv} \\ \bar{V}_{4v} \\ 0 \end{bmatrix} = \begin{bmatrix} \bar{Z}_{cv} - \bar{Z}_{x1v} - \bar{Z}_{sv} & \bar{Z}_{cv} - \bar{Z}_{x1v} & \bar{Z}_{magAv}\frac{1}{a}\bar{Z}_{av} & \bar{Z}_{cv} \\ \bar{Z}_{cv} - \bar{Z}_{x1v} & \bar{Z}_{cv} - \bar{Z}_{x1v} - \bar{Z}_{sv} & \bar{Z}_{magAv}\frac{1}{a}\bar{Z}_{av} & \bar{Z}_{cv} \\ -\bar{Z}_{magBv}\frac{s_{Bv}}{b}\bar{Z}_{bv} & -\bar{Z}_{magBv}\frac{s_{Bv}}{b}\bar{Z}_{bv} & \bar{Z}_{44v} - \bar{Z}_{magBv}\frac{s_{Bv}}{b}\bar{Z}_{av} & -\bar{Z}_{magBv}\frac{s_{Bv}}{b}\bar{Z}_{bv} \\ \bar{Z}_{cv} & \bar{Z}_{cv} & \bar{Z}_{magAv}\frac{1}{a}\bar{Z}_{av} & \bar{Z}_{cv} - \bar{Z}_{x2v} \end{bmatrix} \begin{bmatrix} \bar{I}_{sv} \\ \bar{I}_{yv} \\ \bar{I}_{4v} \\ \bar{I}_{x2v} \end{bmatrix} \tag{E.30}$$

E.2 Dynamic Simulation with SIMULINK

Dynamic simulation of the SDFM and CDFM machine system including the field oriented control was carried out by using SIMULINK. As an extension to MATLAB, SIMULINK is

a toolbox for simulating dynamic systems.

By connecting toolbox blocks, it is possible to create a complete model of a SDFM or a CDFM. The simulation of the dynamic system is based on a two-axis d-q-model of the machines. All simulated quantities are referred on their machine side and can be transferred to any particular reference frame by "reference frame transformation blocks" as will be seen later.

The SIMULINK modeling assumes an ideal current source for the inverter. Therefore the demand currents for the inner current control loop are directly fed into the machine model. Additionally, the model ignores iron losses and saturation and is based on the dynamic model of the SDFM and CDFM as presented in chapter 3 and chapter 4, respectively.

E.2.1 Dynamic Simulation of the SDFM

As it is the case in the steady state simulations, the model of the SDFM can be regarded as a subsection of the CDFM and is thus not treated independently, but it shall be referred to the CDFM model.

Simulation results for the stator flux oriented control of the SDFM are presented in figure E.18 for the inner current loop and E.19 for the power control loop. Parameters of the experimental machines are used and the simulation time step is 0.0002 s. The simulations include the mechanical dynamics of the system. The demand values in both cases where chosen, that they match the demand values of the experimental results presented in chapter 3. As it can be seen the simulation results have a very good agreement with the experimental results and it proves that the assumption of an ideal current source is justified and that the influence of iron losses is negligible.

E.2.2 Dynamic Simulation of the CDFM

The description of the CDFM model is given for the stator flux oriented control where the side 4 currents are directly fed into the machine model. From that point on it is easy to extend the model for various other simulations. Figure E.5 shows the complete model with the inputs and the outputs of the system.

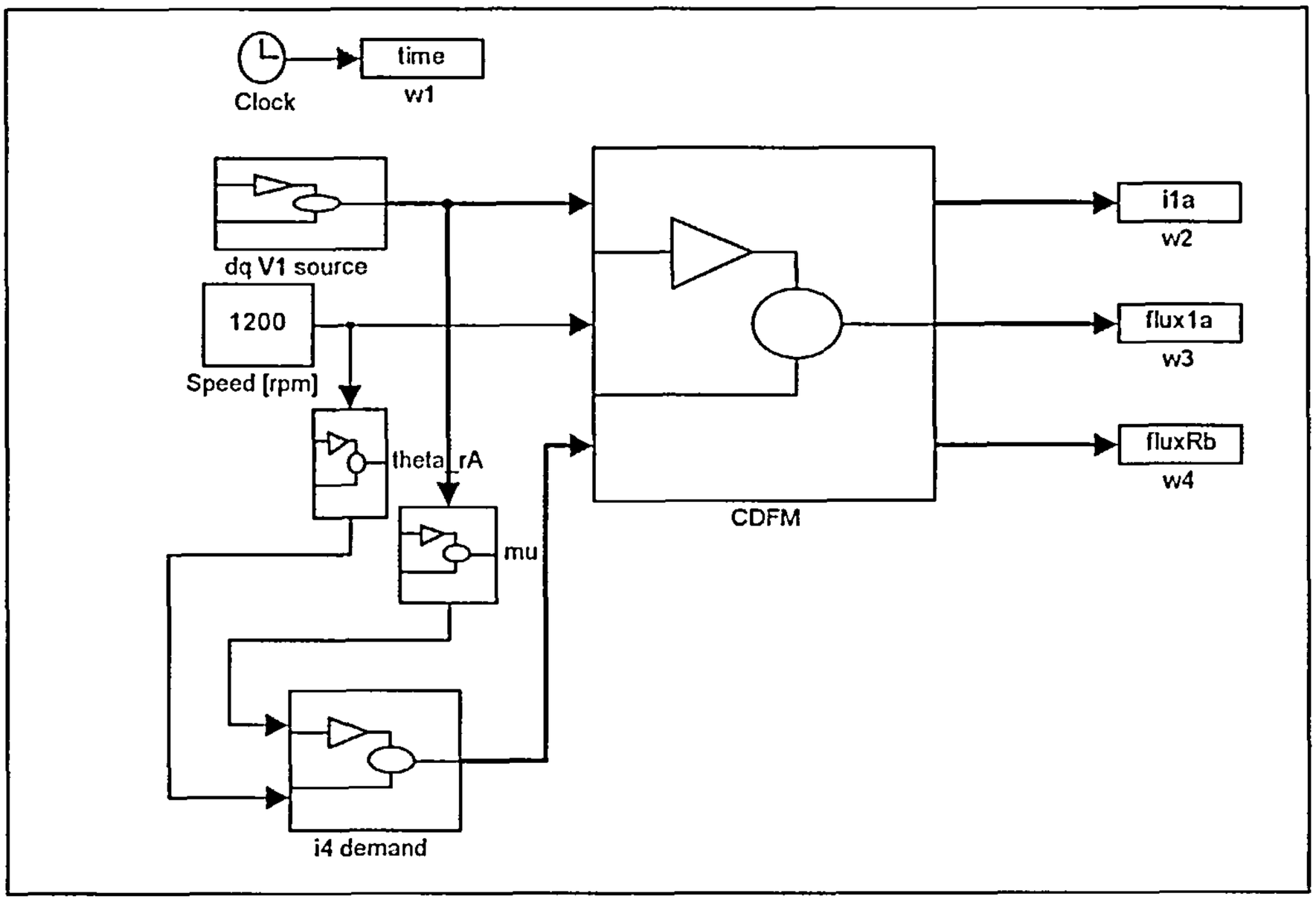

Figure E.5: Model of the CDFM for stator flux orientation

The inputs to the machine model are the d-q-voltage of side 1, the side 4 d-q-current and the constant speed. In this case mechanical dynamics are not included in the model.

Block - "dq V1 source"

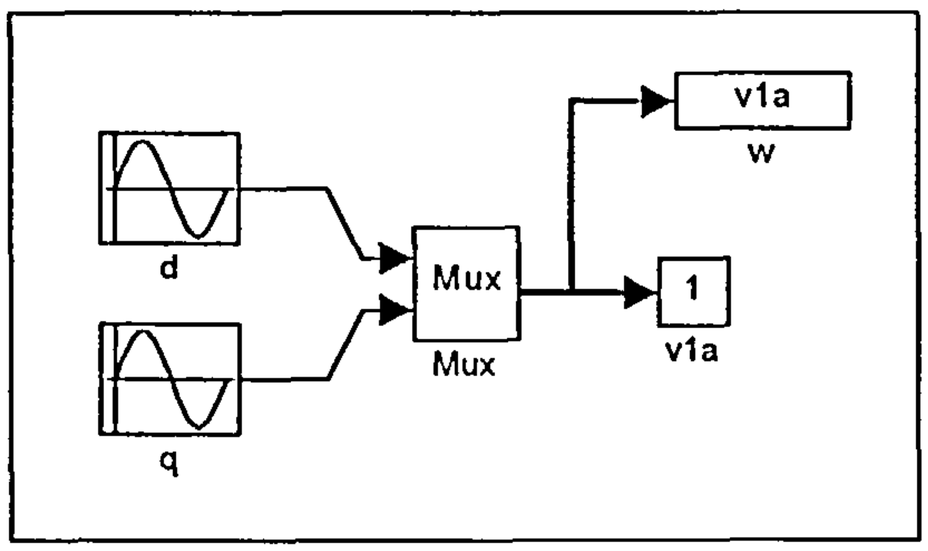

Figure E.6: v1 source

Figure E.6 shows the content of the block "dq V1 source". Two sinusoidal voltage sources are 90° phase shifted so that they constitute the d-axis and q-axis voltage of side 1.

Block - "theta_rA"

The rotor position angle in electrical rad/s is simply calculated by an integration of the mechanical speed in rpm, including a factor for the pole pair number. The mathematical equivalent to figure E.7 is

$$\Theta_{rA} = \frac{p_A 2\pi}{60} \int speed \; dt$$

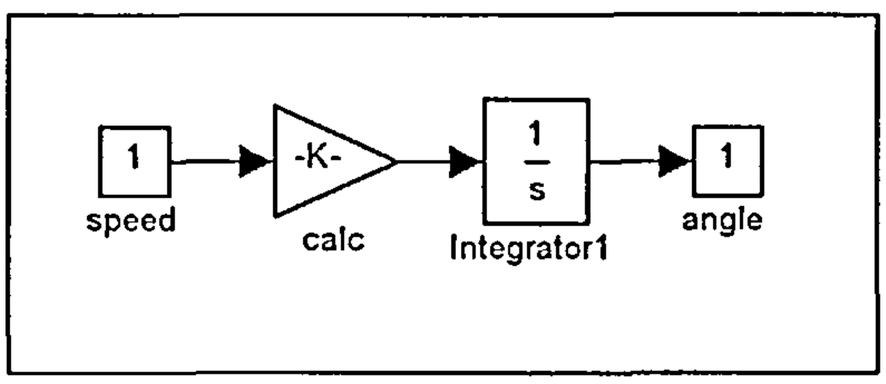

Figure E.7: Rotor position angle calculation

Block - "mu"

The angle μ (mu) of the excitation reference frame for the stator flux oriented control can be calculated with the help of the position of the side 1 voltage vector. A cartesian-to-polar transformation of the voltage vector delivers the angle of the vector. A subsequent subtraction of 90° yields the desired side 1 flux linkage angle μ in the stationary reference frame. It is illustrated in figure E.8.

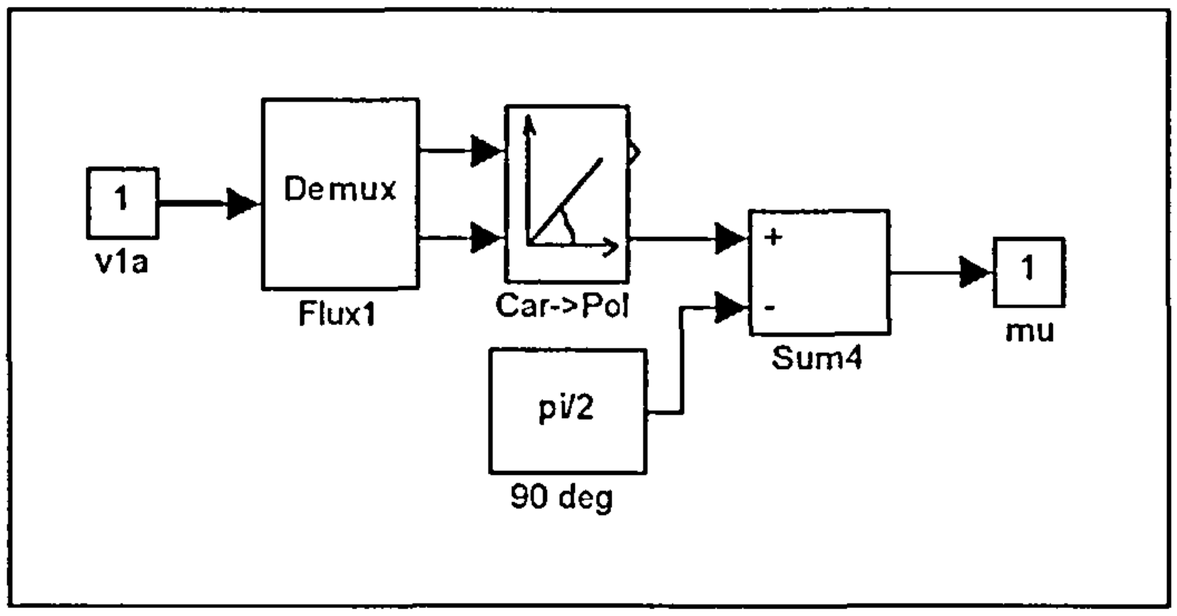

Figure E.8: Calculation of μ

Block - "i4 demand"

The input demand steps of the side 4 current components are DC-values in the "e"-frame, as displayed in figure E.9. To transfer the current from the "e"-frame to the side 4 "d"-frame a reference frame transformation has to be carried out. The necessary angle for the transformation is made up from the angle μ of the "e" reference frame and the angle Θ_{rAB} of the "d" reference frame. The block "Gain 1" in figure E.9 contains the pole pair numbers of the individual machines, $(p_A+p_B)/p_A$, to calculate the angle Θ_{rAB} form Θ_{rA}. Both, the d-q-values and the angle for the transformation are fed to the block "e -> d".

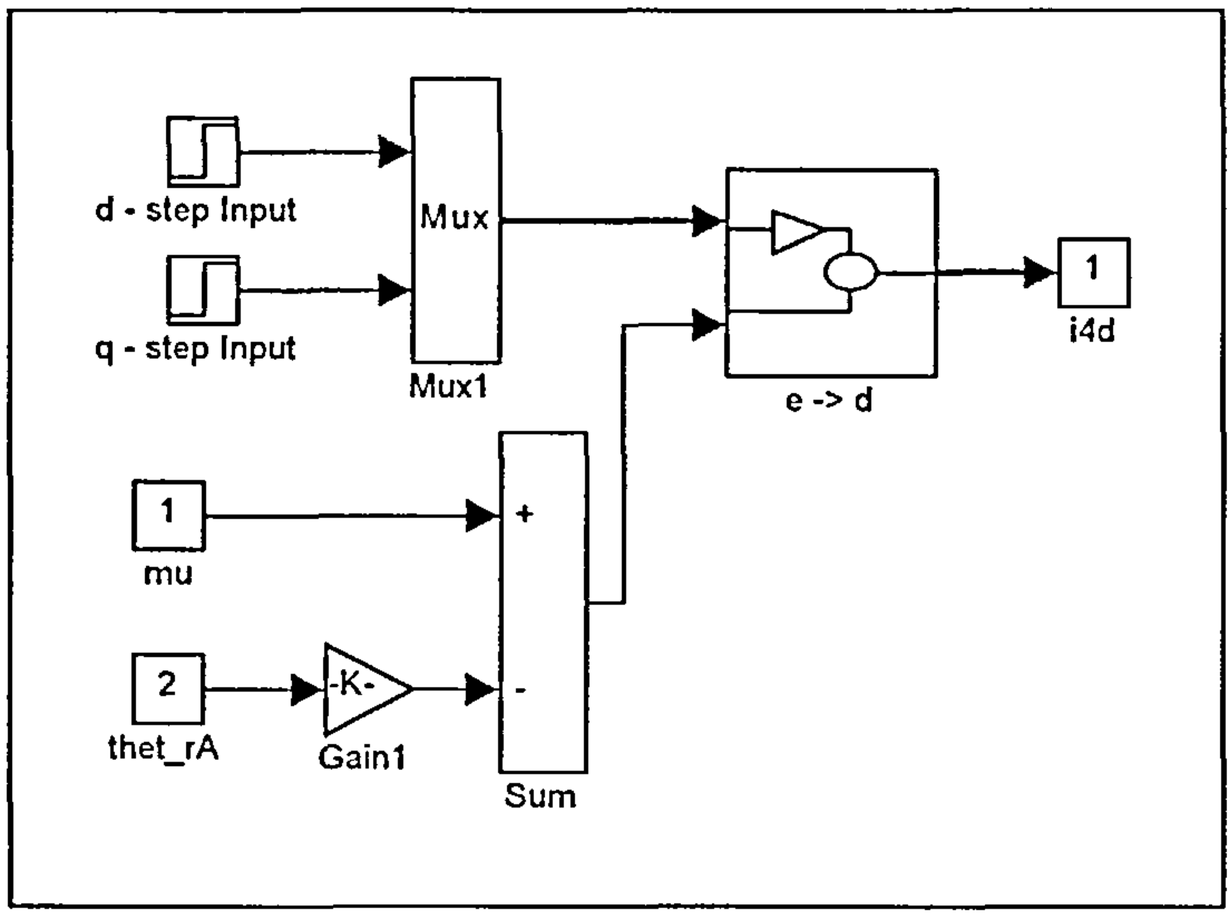

Figure E.9: i4e step input

Block - "e -> d"

This block contains a factor depending on a "positive" transformation of the type e^{jangle} or a "negative" transformation of the type $e^{-jangle}$.

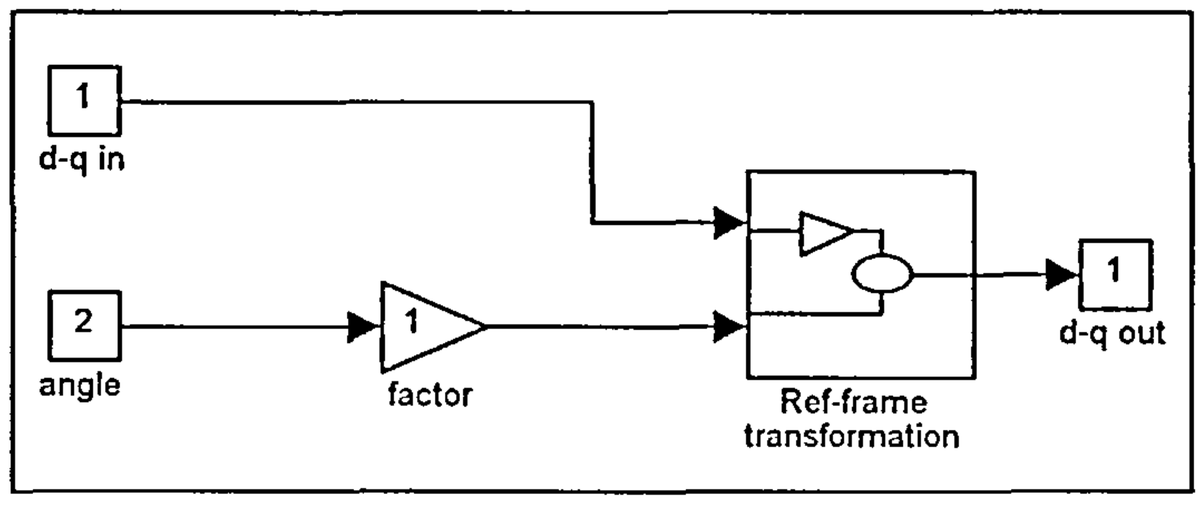

Figure E.10: Reference frame transformation

Block - "Ref-frame transformation"

In this block, displayed in figure E.11, the actual vector transformation takes place. The mathematical equivalent to that block is

$$\begin{bmatrix} d\_out \\ q\_out \end{bmatrix} = \begin{bmatrix} cos\ angle & -sin\ angle \\ sin\ angle & cos\ angle \end{bmatrix} \begin{bmatrix} d\_in \\ q\_in \end{bmatrix}$$

As mentioned the angle is either of a positive sign or a negative, depending on the type of transformation.

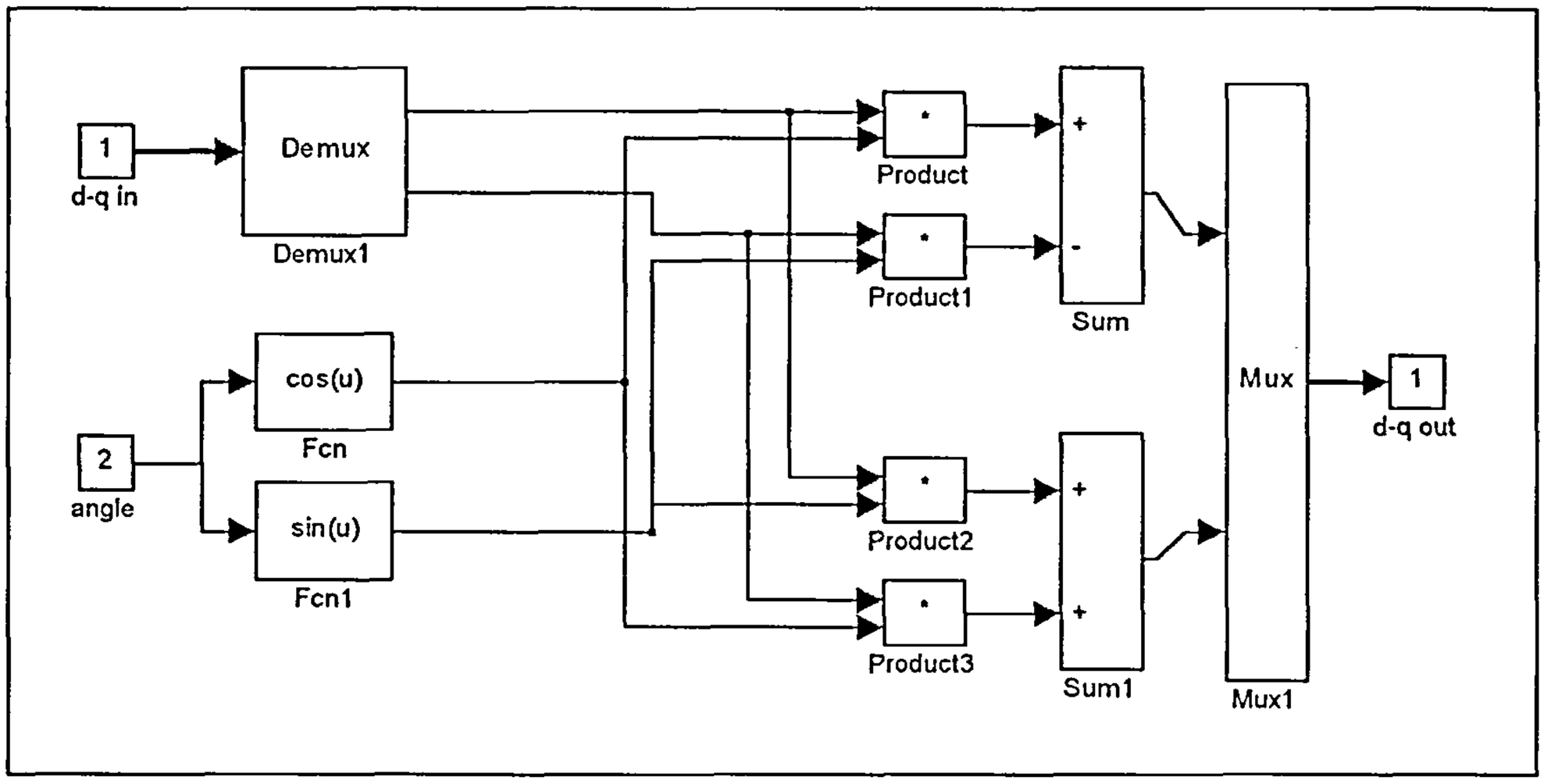

Figure E.11: Reference frame transformation

Cascadation of two machine models

The CDFM is modeled as a cascadation of two wound rotor induction machine models, as shown in figure E.12. The two machine models are connected with so called connection blocks. One for the side 2 and side 3 voltages and one for the side 2 and side 3 currents. As mentioned, each individual machine model can be used as a model for a SDFM

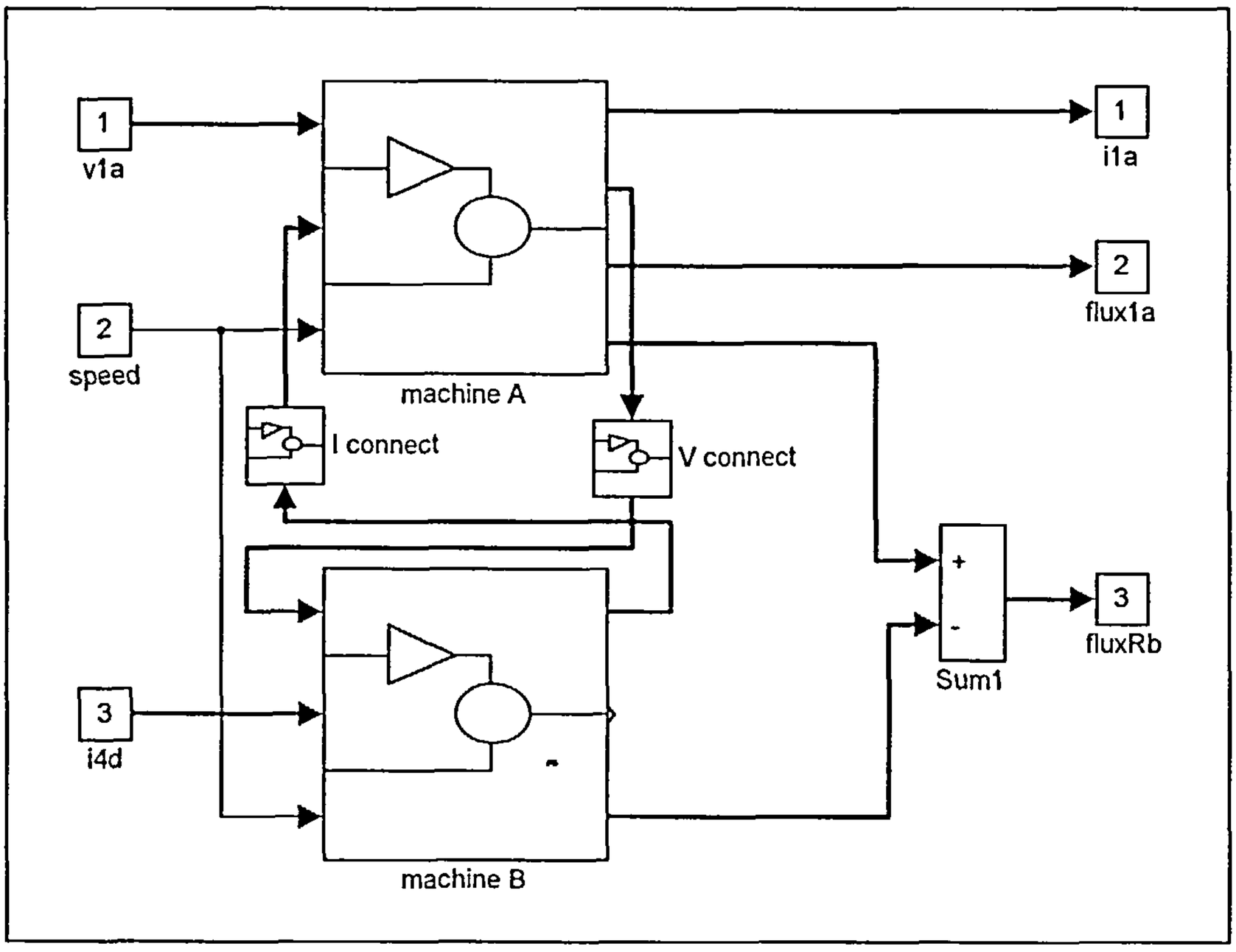

Figure E.12: CDFM - cascadation of machine A and machine B

Block - "V connect"

The positive phase sequence rotor connection of the individual machines follows the constraints of

$\bar{v}_2 = \bar{v}_3$ for the voltage vector connection

$\bar{i}_2 = -\bar{i}_3$ for the current vector connection (Block "I connect")

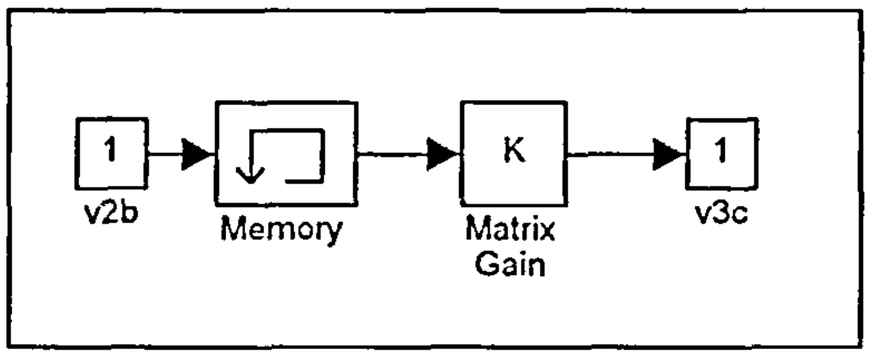

Figure E.13: Connection block

The "Matrix Gain" block contains the necessary matrix for the connection of the voltage vectors as

$$K = \begin{bmatrix} 1 & 0 \\ 0 & 1 \end{bmatrix}$$

and

$$K = \begin{bmatrix} -1 & 0 \\ 0 & -1 \end{bmatrix}$$

for the current connection block.

The "Memory" block constitutes a unit delay for breaking up algebraic loops. It is contained in both connection blocks.

Block - machine A

The inputs to the machine model are the side 1 voltage vector and the side 2 current vector and the mechanical speed. The different blocks, figure E.14, create the remaining machine quantities.

All machine quantities are calculated in their natural reference frame. It is therefore necessary to include some reference frame transformation blocks in the machine model to rotate the quantities onto the desired reference frame, when involved in further calculations.

The heart of the machine model is the state space block with the flux linkage as the state variable. The machine equations are rearranged that they follow the state space equations of

$$\frac{dx}{dt} = Ax + Bu$$
$$y = Cx + Du$$

where

$$A = [-R1\ L1^{-1}] \qquad x = [\Psi^a_{d1}\ \Psi^a_{q1}]^T$$
$$B = [I, R1\ LmA\ L1^{-1}] \qquad u = [v^a_{d1}\ v^a_{q1}\ i^a_{d2}\ i^a_{q2}]^T$$
$$C = [L1^{-1}, I] \qquad y = [i^a_{d1}\ i^a_{q1}\ \Psi^a_{d2}\ \Psi^a_{q2}]^T$$
$$D = [O, -LmA\ L1^{-1}; O, O]$$

with

$$R1 = \begin{bmatrix} R_1 & 0 \\ 0 & R_1 \end{bmatrix} \qquad R2 = \begin{bmatrix} R_2 & 0 \\ 0 & R_2 \end{bmatrix}$$
$$L1 = \begin{bmatrix} L_1 & 0 \\ 0 & L_1 \end{bmatrix} \qquad L2 = \begin{bmatrix} L_2 & 0 \\ 0 & L_2 \end{bmatrix} \qquad LmA = \begin{bmatrix} L_{mA} & 0 \\ 0 & L_{mA} \end{bmatrix}$$
$$I = \begin{bmatrix} 1 & 0 \\ 0 & 1 \end{bmatrix} \qquad O = \begin{bmatrix} 0 & 0 \\ 0 & 0 \end{bmatrix}$$

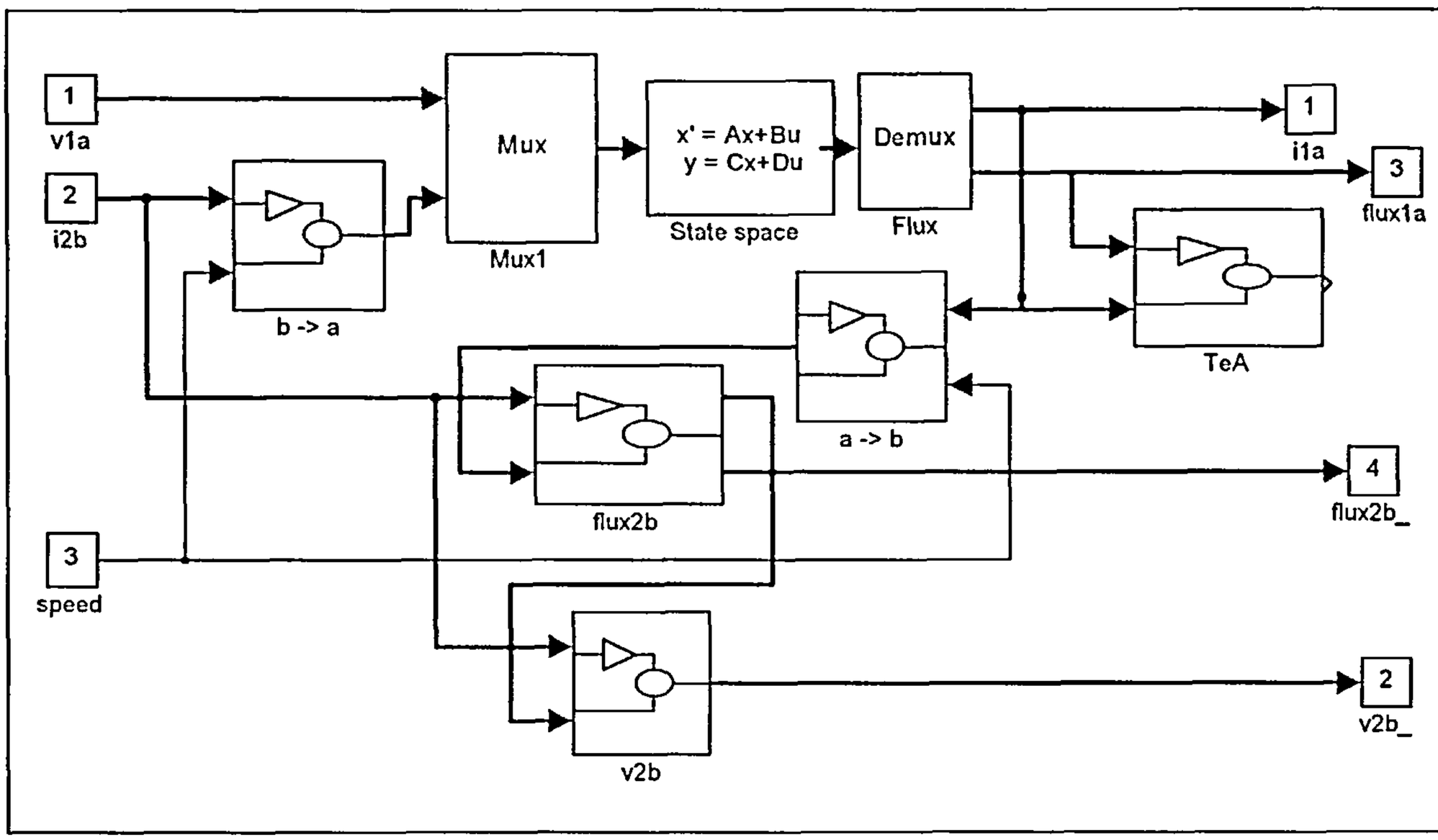

Figure E.14: Model of machine A

Block - "flux2b"

The calculation of the side 2 flux linkage follows the equation of

$$\overline{\Psi}^b_2 = L_2 \bar{i}^b_2 + L_{mA} \bar{i}^b_1$$

Side 1 and side 2 current vectors in the "b"-frame are the inputs to the block. The output is

the flux linkage vector and the derivative of the flux vector. The block is shown in figure E.15, where the matrix gain "L" contains the appropriate inductance parameters.

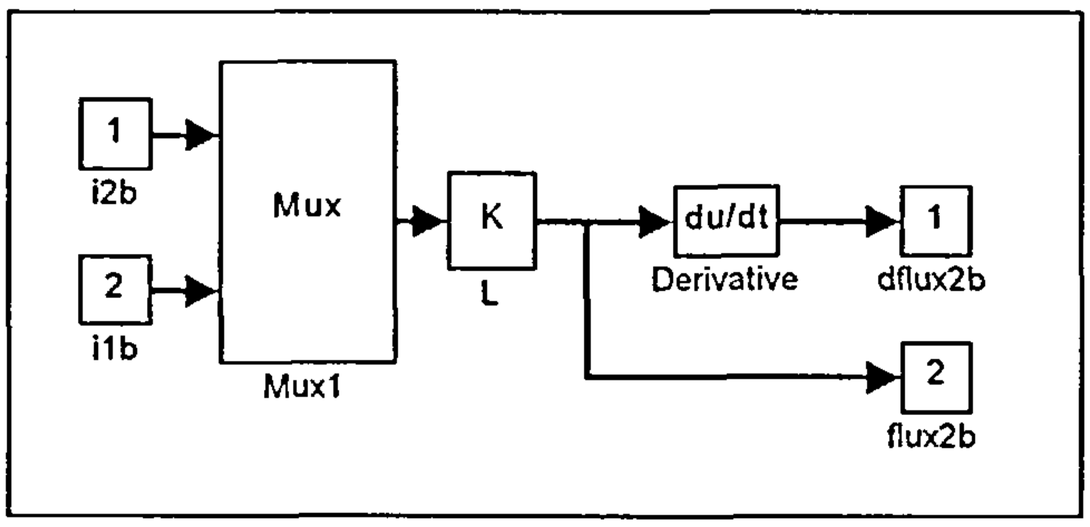

Figure E.15: Flux calculation

Block - "TeA"

The torque calculation of the machine A model utilises the outputs of the state space block, which are the side 1 current and flux linkage vector.

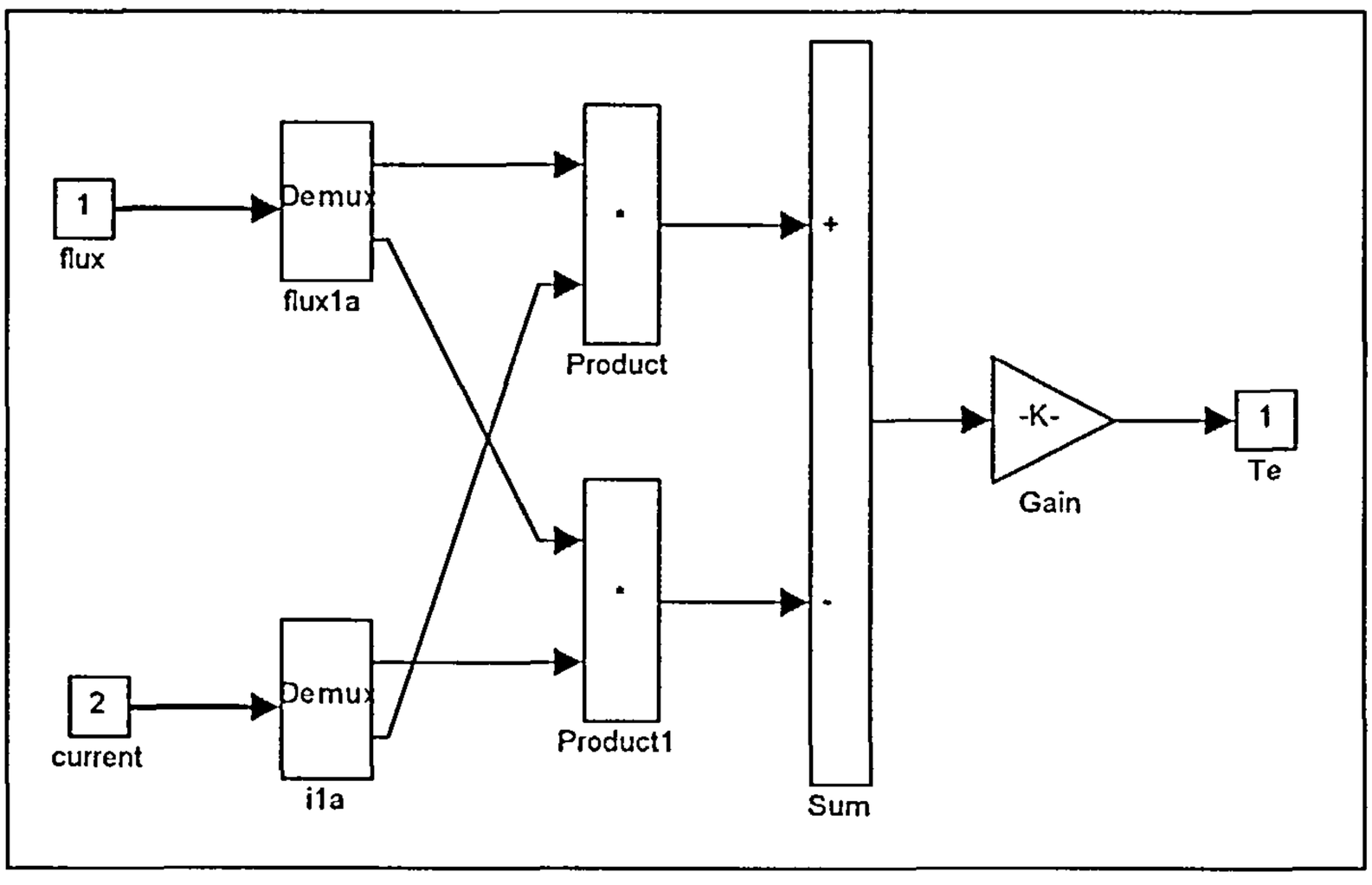

Figure E.16: Torque calculation

The blocks in figure E.16 are equivalent to the mathematical equation of

$$T_{eA} = \frac{3}{2} p_A (\overline{\Psi}_1^a \times \bar{i}_1^a)$$

Block - "v2b"

To calculate the side 2 voltage vector the side 2 current and the derivative of the side 2 flux

linkage vector are needed as inputs. The calculation of is equivalent to

$$\bar{v}_2^b = R_2 \bar{i}_2^b + \frac{d\bar{\Psi}_2^b}{dt}$$

The matrix gain block "R"in figure E.17 contains the side 2 rotor resistance values.

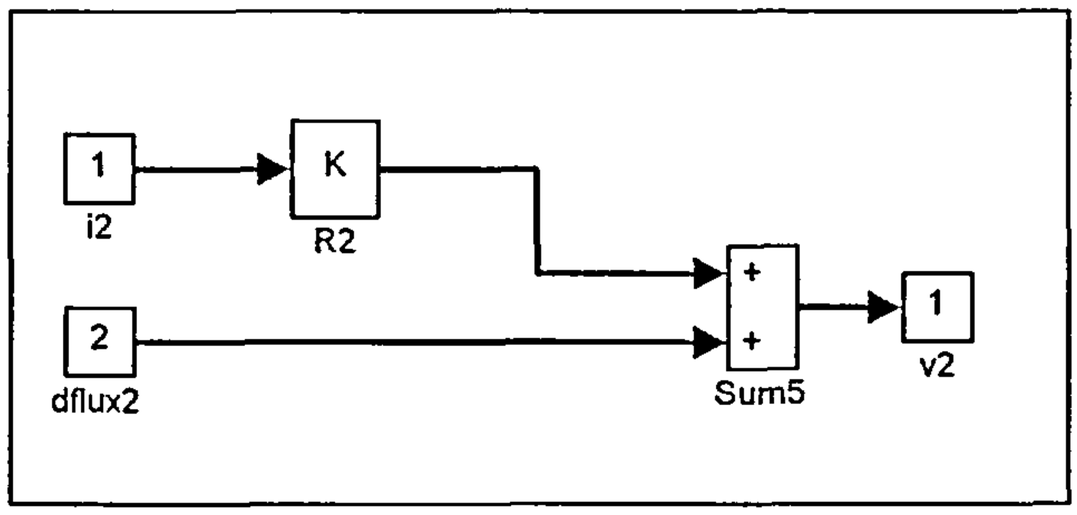

Figure E.17: Voltage calculation

The model of machine B has the same structure as the model of machine A.

Simulation results

Several field oriented control schemes are simulated and the important control variables are displayed. Parameters used for simulations are taken from a 30 kW SF-CDFM [Krebs]. This was done to study the effect of the different control schemes on a machine with larger rating, compared to the experimental CDFM.

The parameters are:

$p_A = p_B = 2$

$P_{1\,rated} = 30$ kW

$n_{m\,rated} = 1500$ rpm

$V_{1\,rated} = 400$ V

$T_{eAB\,rated} = 200$ Nm

$R_1 = R_4 = 0.74\ \Omega$

$R_2 = R_3 = 0.75\ \Omega$

$L_1 = L_4 = 0.14$ H

$L_{\sigma 1} = L_{\sigma 4} = 0.0025$ H

$L_{\sigma 2} = L_{\sigma 3} = 0.003$ H

For all simulations a time step of 0.0002 s was chosen.

Figure E.20 shows the simulation results for the combined flux control [Bauer], with a d-component current input and a torque demand input.

Figure E.21 gives the simulation results for the simplified inner current control loop of the combined flux control with inputs for both components of the side 4 current. Figure E.22 has the results for the outer power control loop.

Figure E.23 and figure E.24 show the results for the inner current loop and the outer power control loop for stator flux oriented control of the CDFM.

Generally, the simulated cases confirm the machine behaviour found from the experimental results.

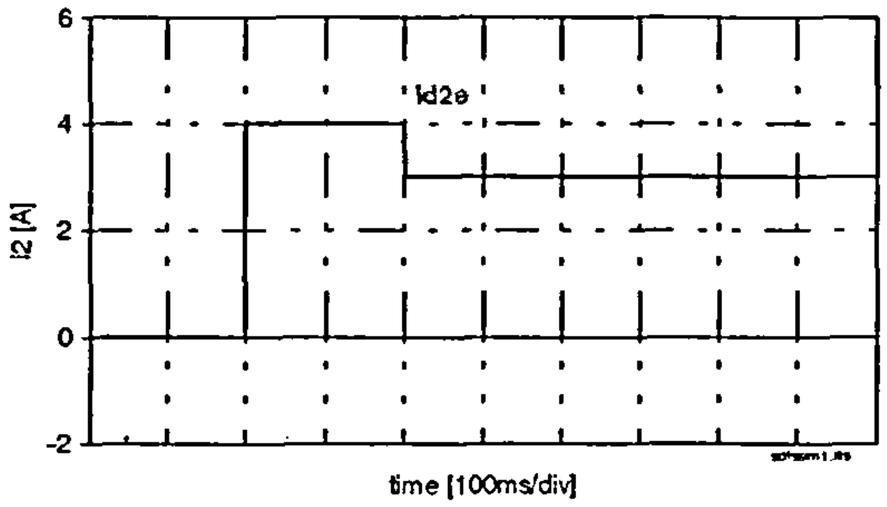

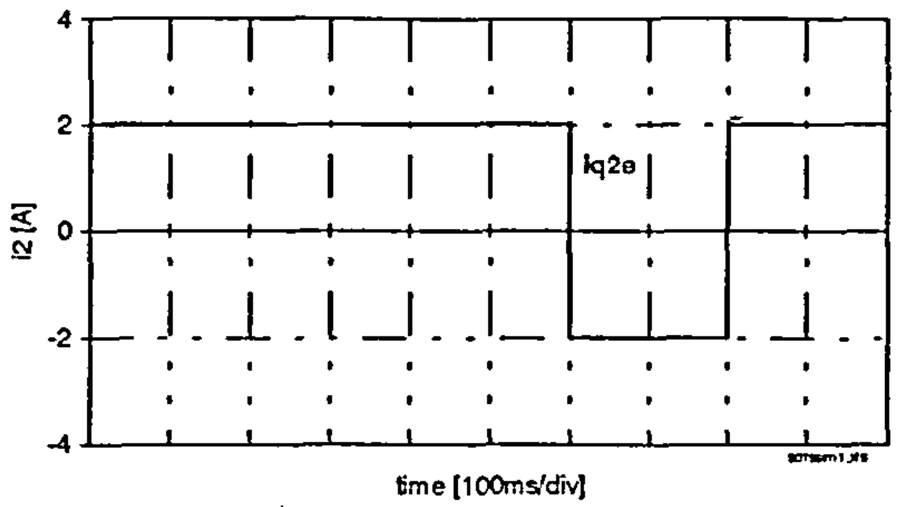

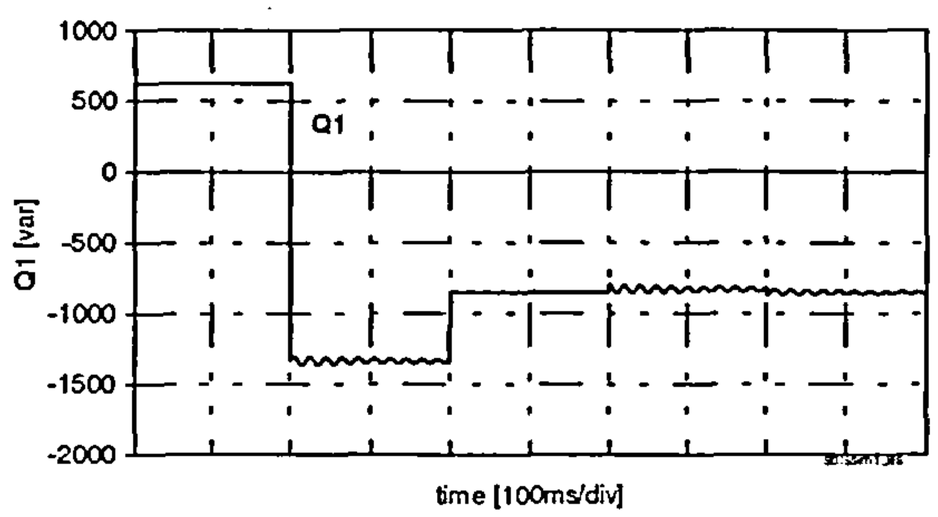

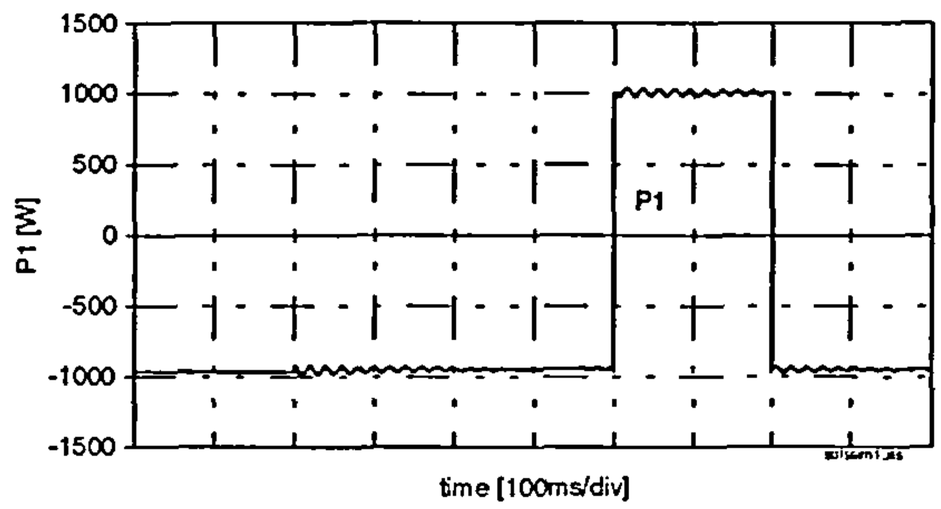

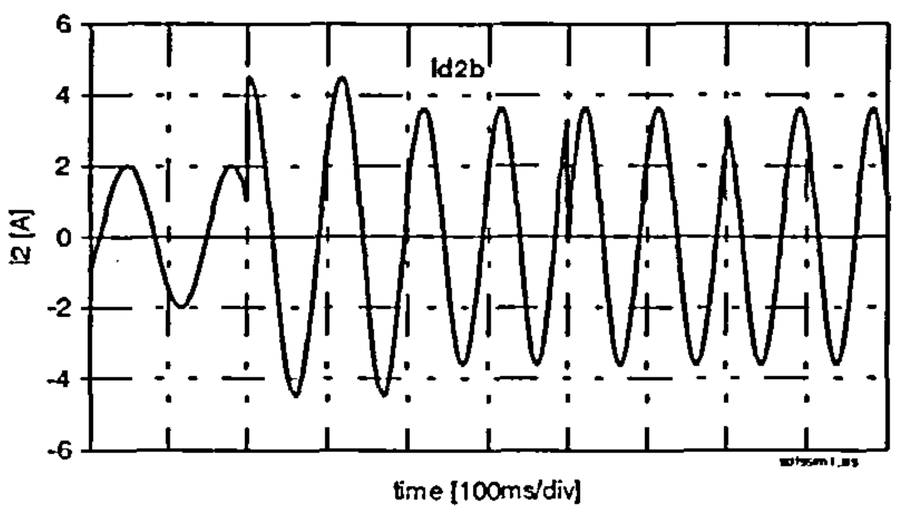

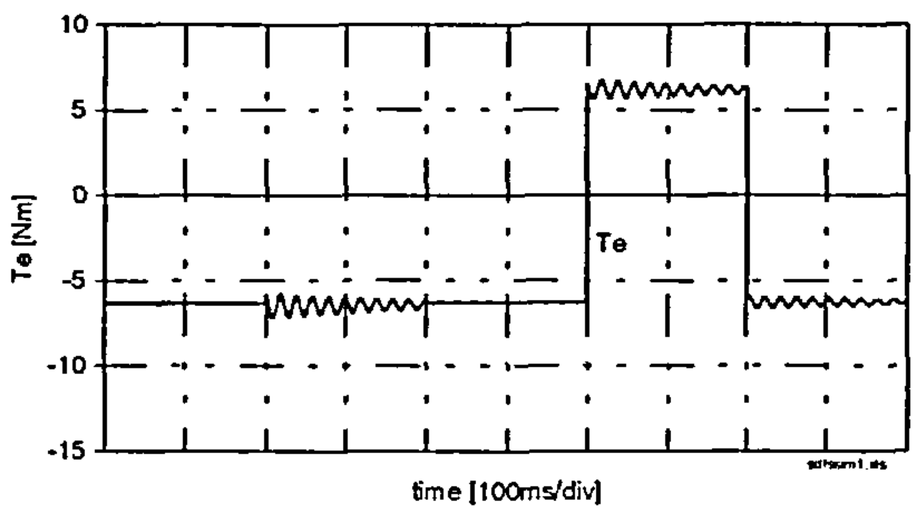

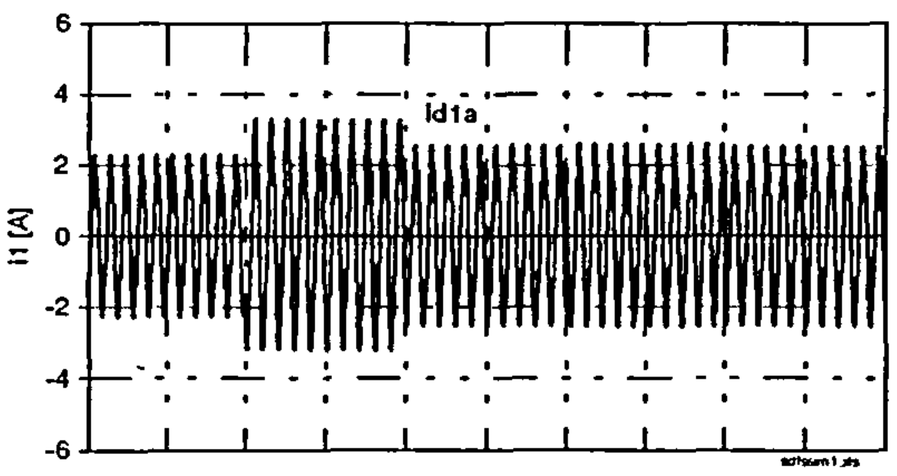

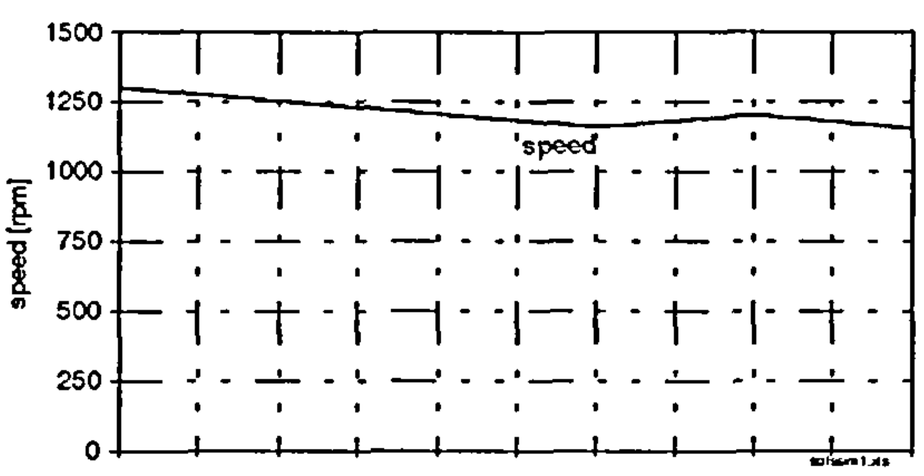

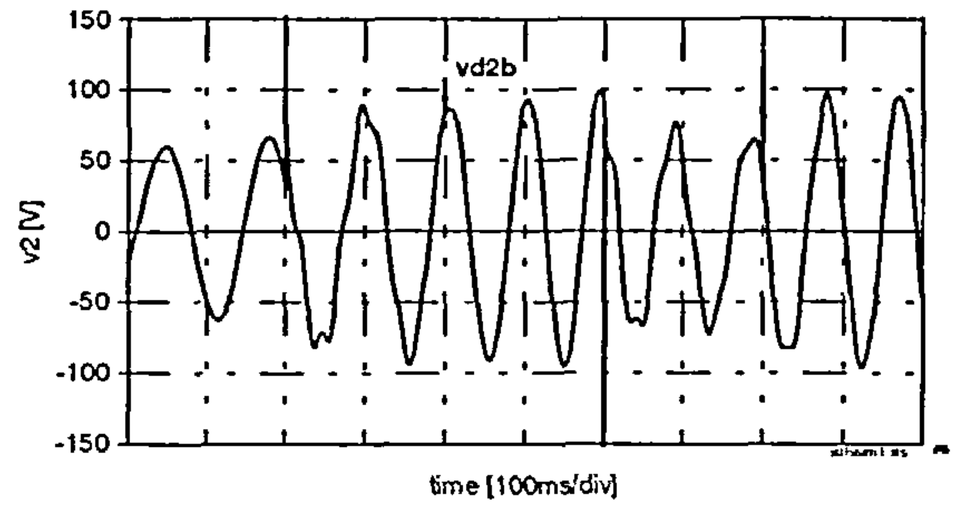

Figure E.18: Simulated SDFM dynamics for stator flux oriented control - current control loop

(i_{d2}^{e}* = 0 to 4 to 3 A , i_{q2}^{e}* = 2 to 0 to 2 A, dt = 0.0002 s)

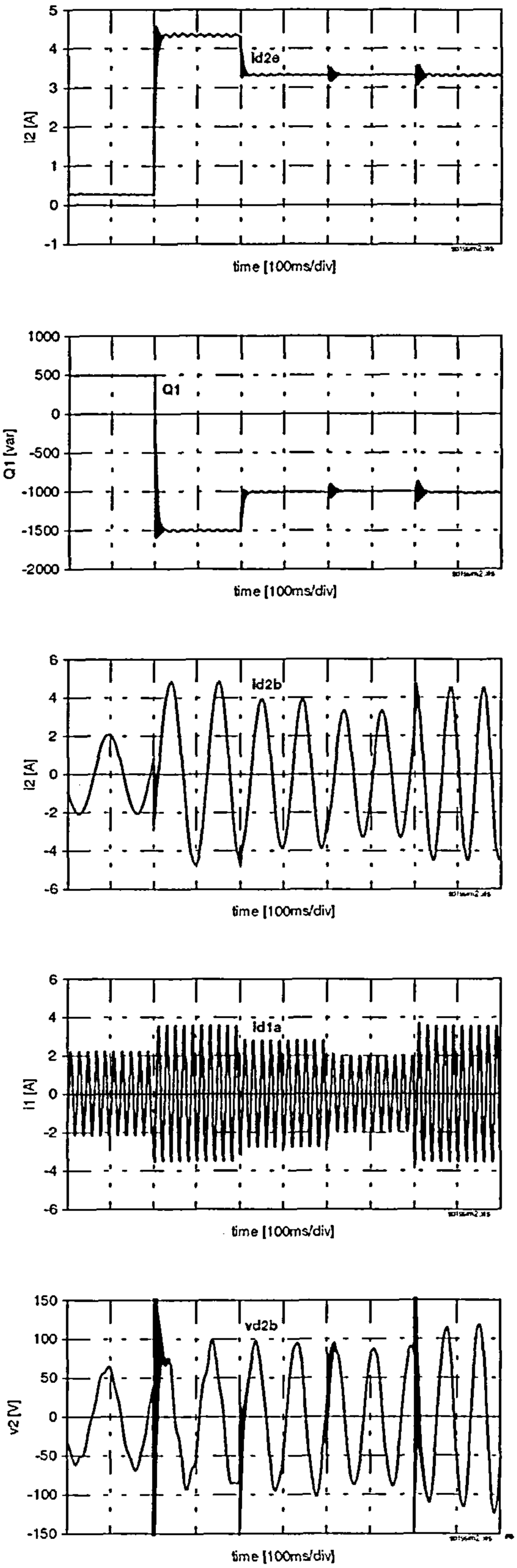

Figure E.19: Simulated SDFM dynamics for stator flux oriented control - power control loop

(Q_1^* = 500 to -1500 to -1000 var , P_1^* = -1000 to 0 to -1500 W, dt = 0.0002 s)

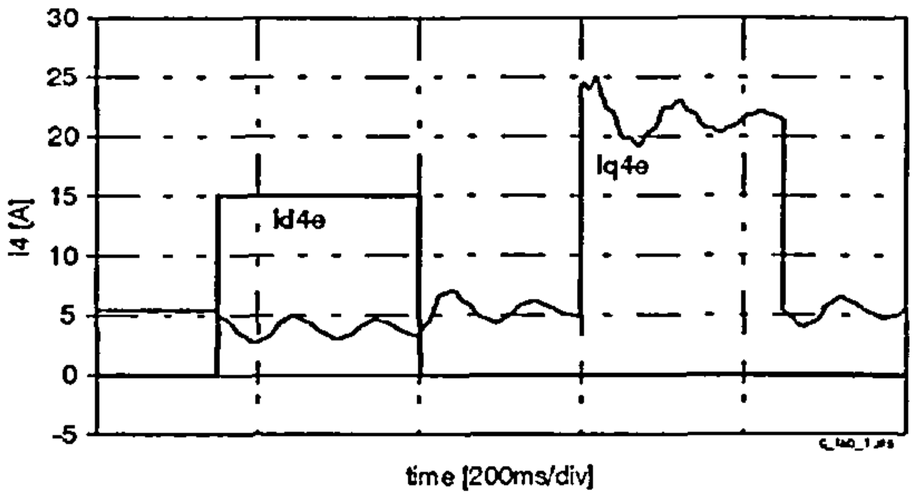

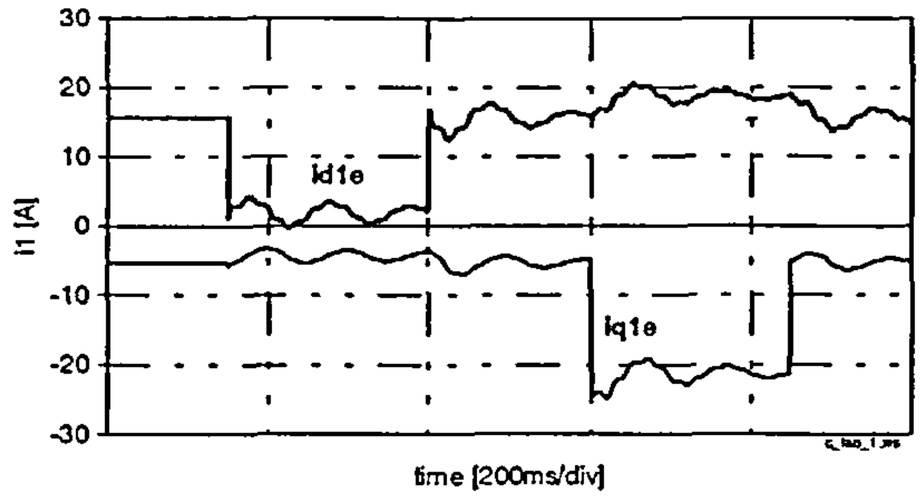

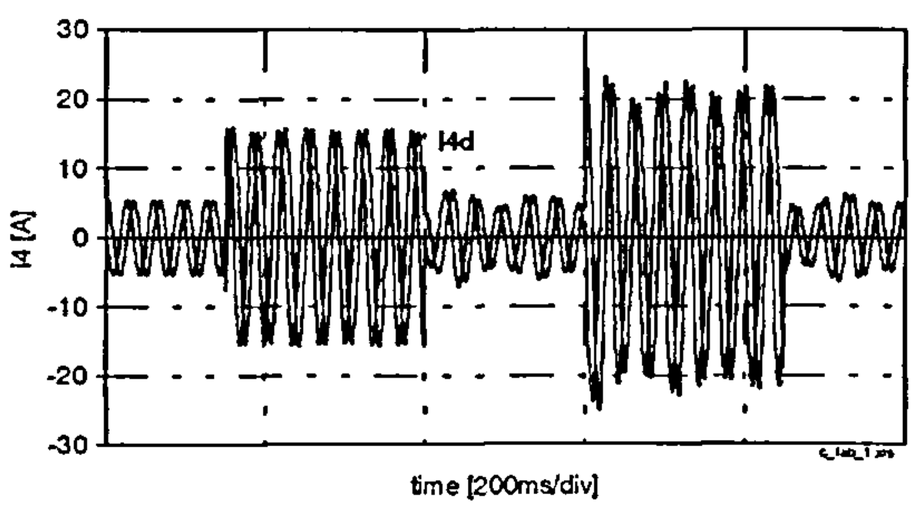

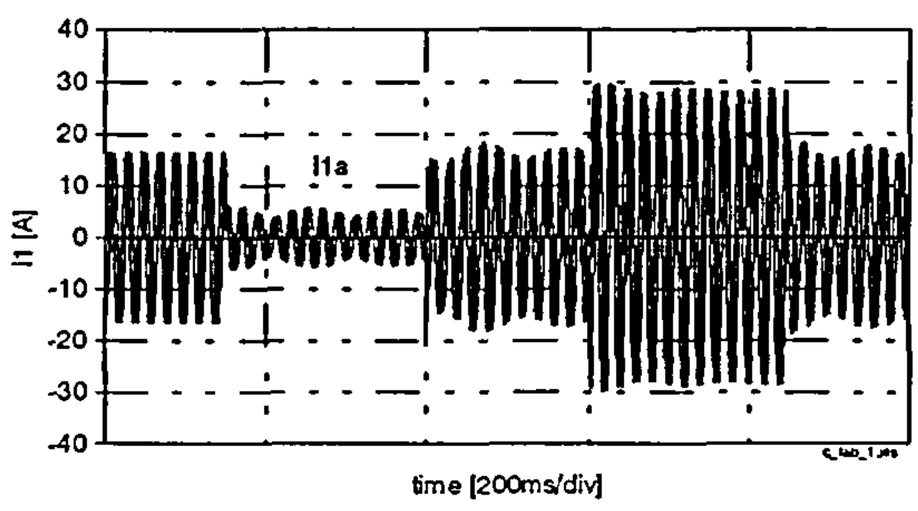

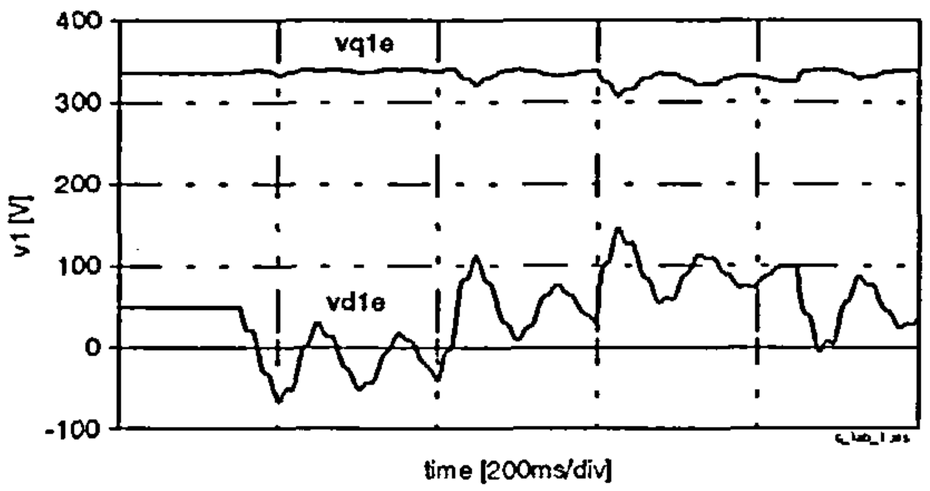

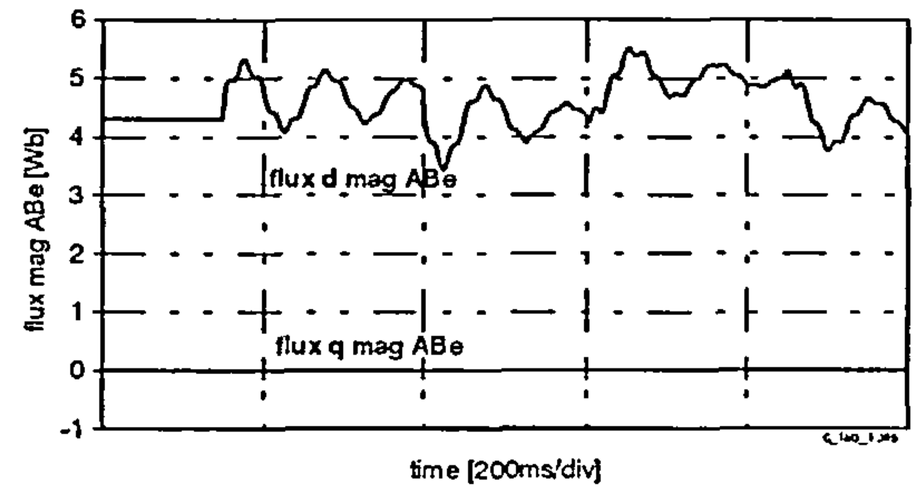

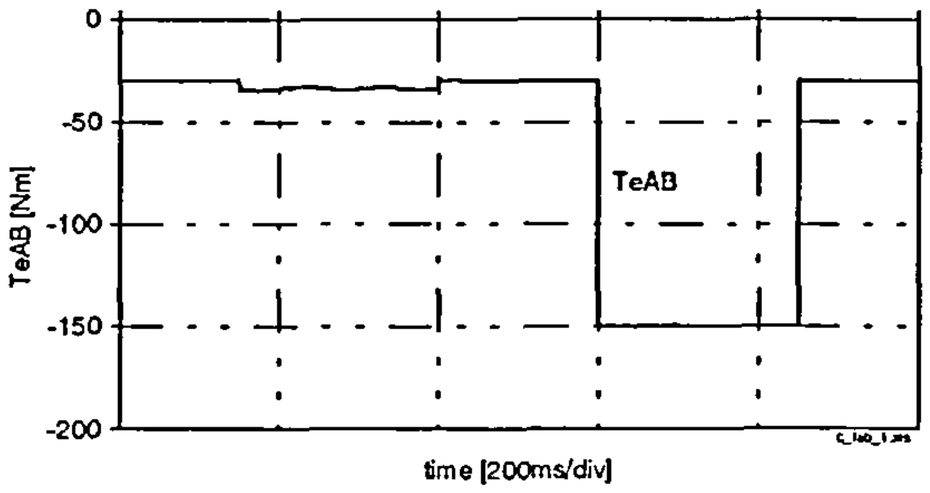

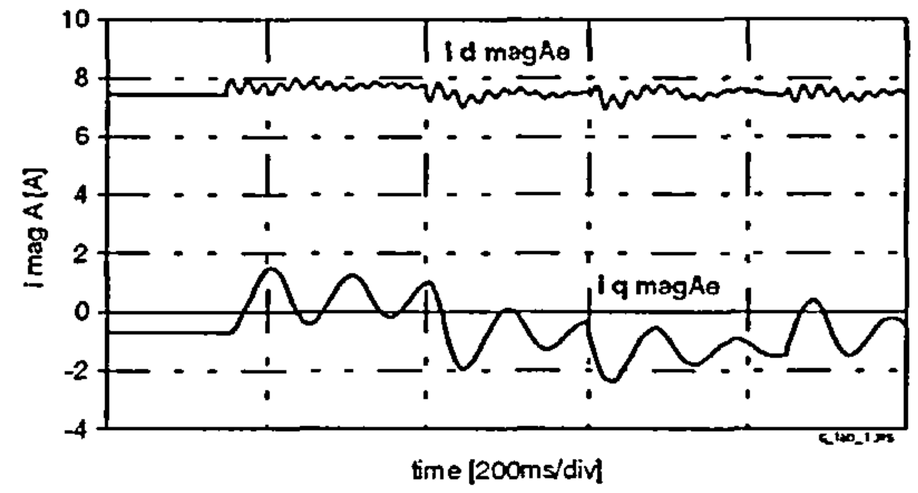

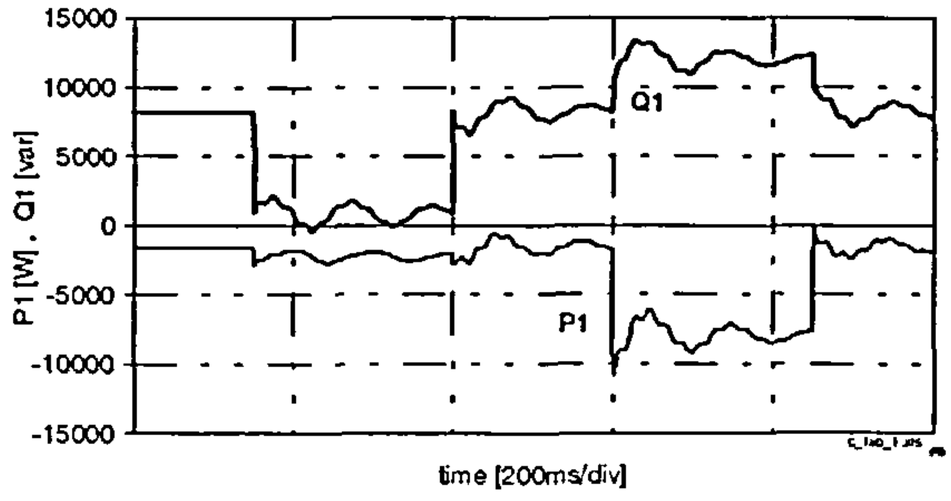

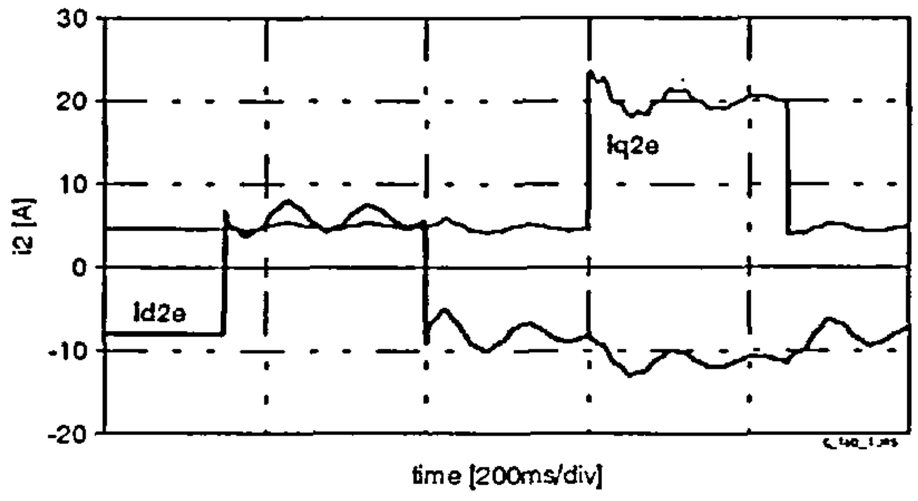

Figure E.20: Simulated CDFM dynamics of the combined flux control - control as in [b15]

(i_{d4}^{e*} = 0 to 15 A , T_{eAB}^{*} = -30 to -150 Nm, n_m = 1200 rpm, dt = 0.0002 s)

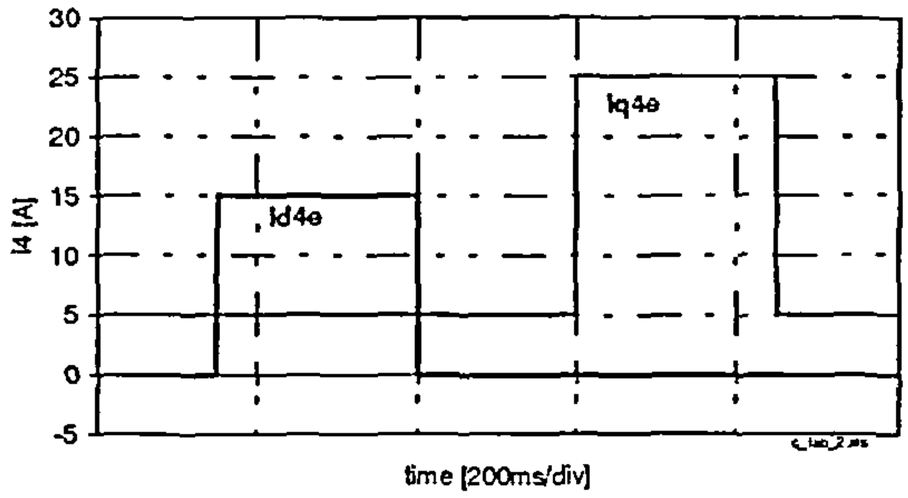

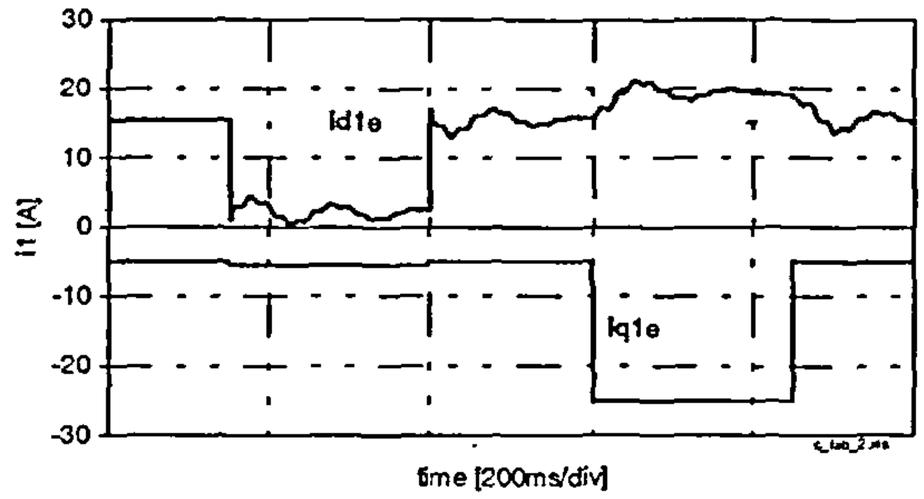

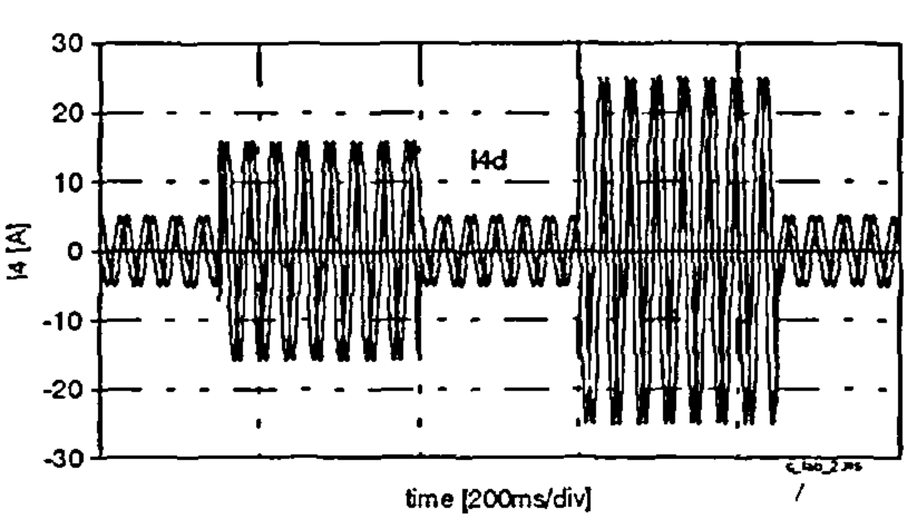

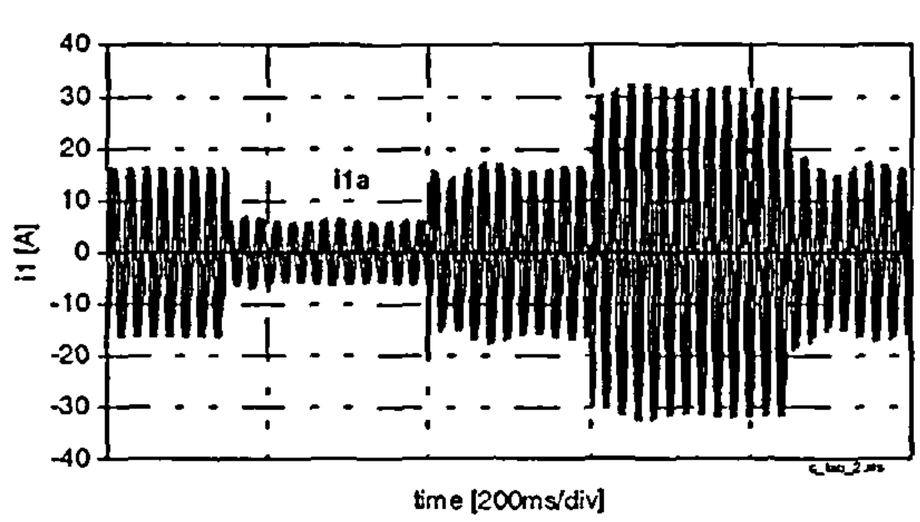

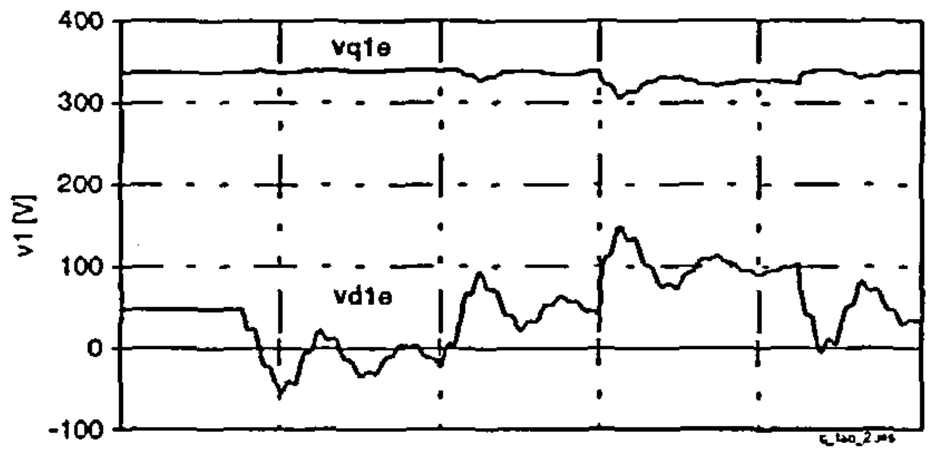

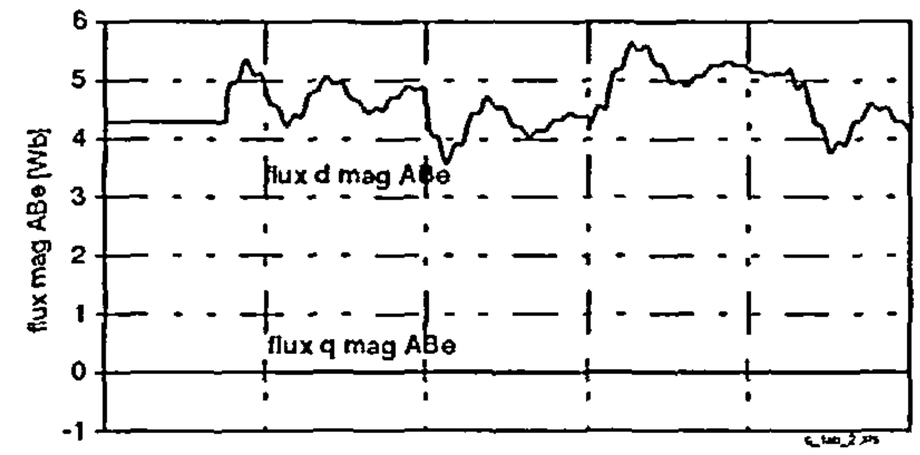

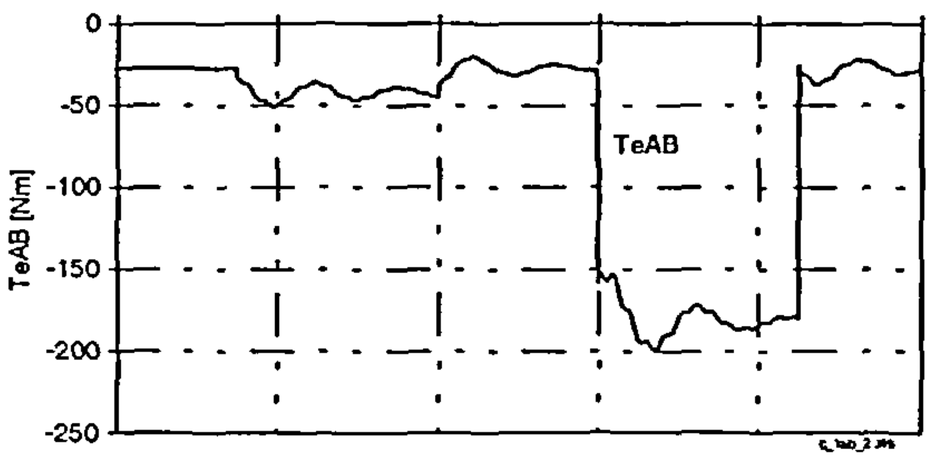

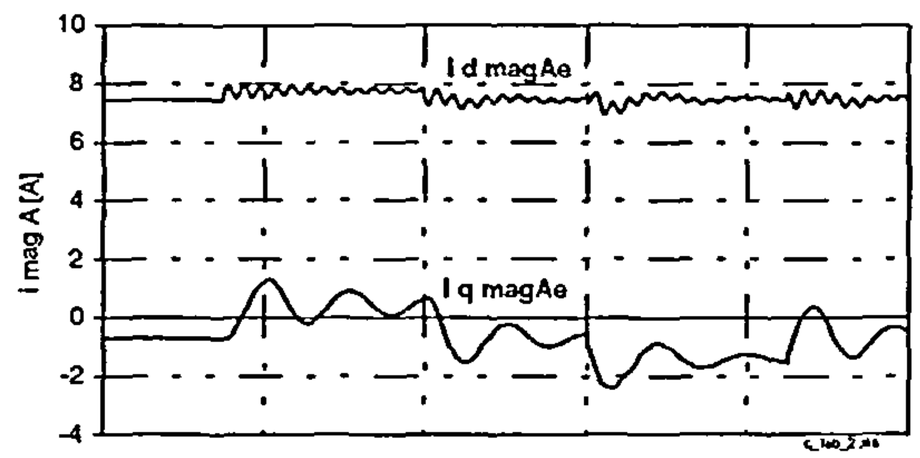

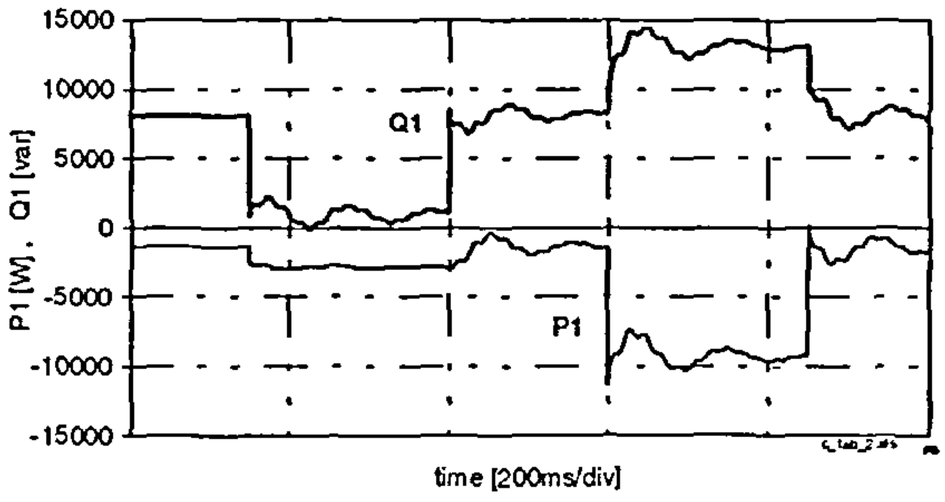

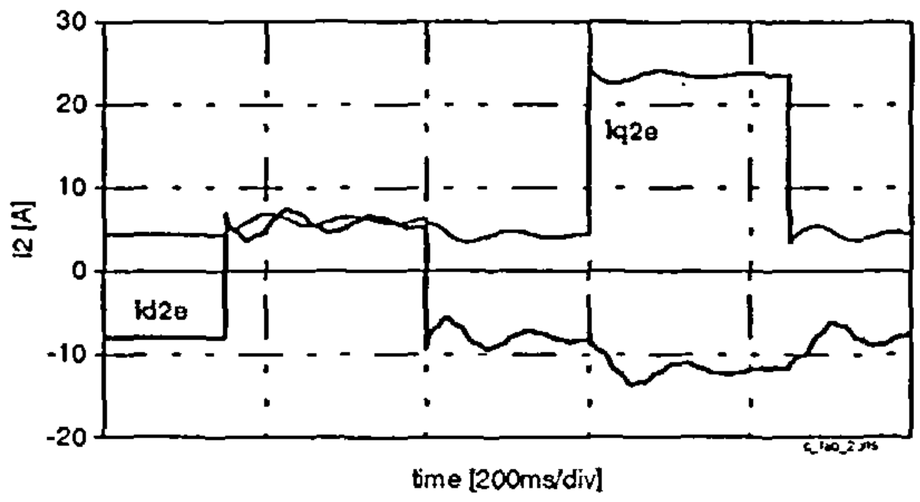

Figure E.21: Simulated CDFM dynamics of the combined flux control - simplified current control loop

($i_{d4}^{e*} = 0$ to 15 A , $i_{q4}^{e*} = 5$ to 25 A, $n_m = 1200$ rpm, dt = 0.0002 s)

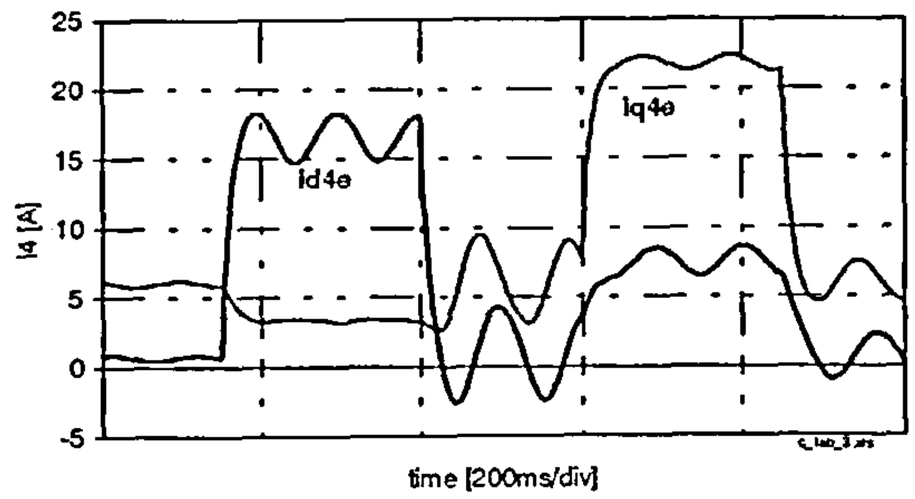

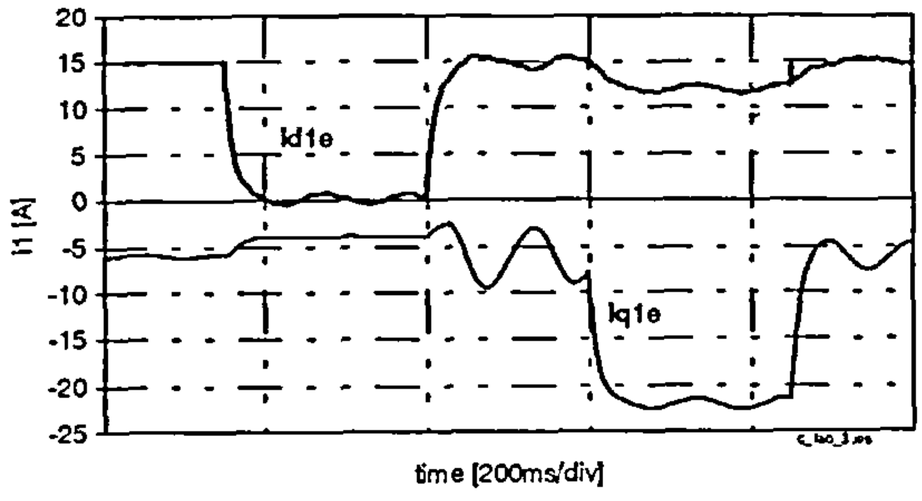

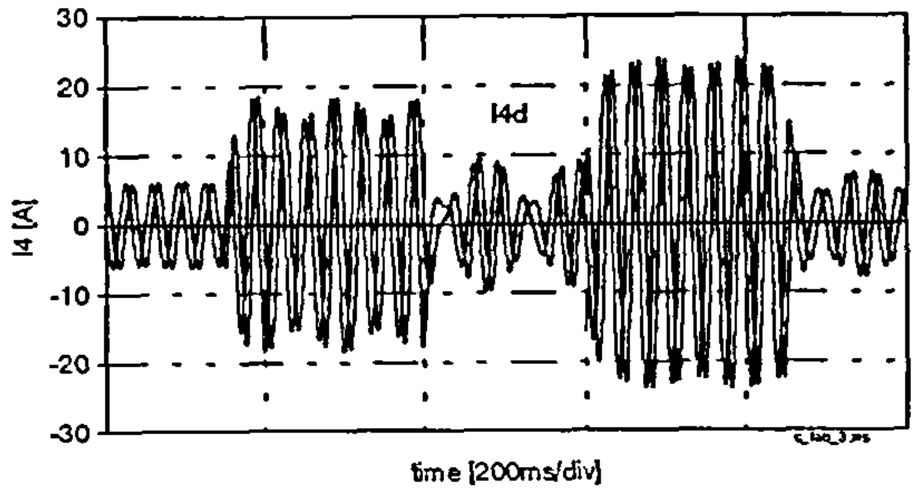

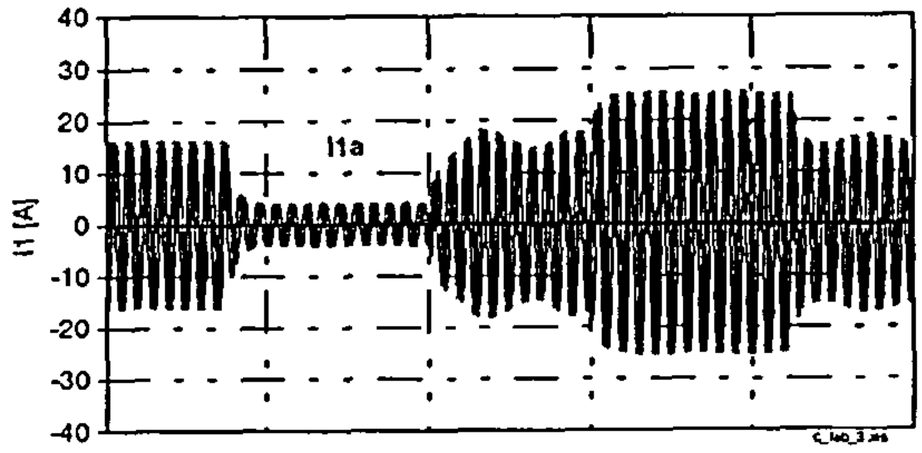

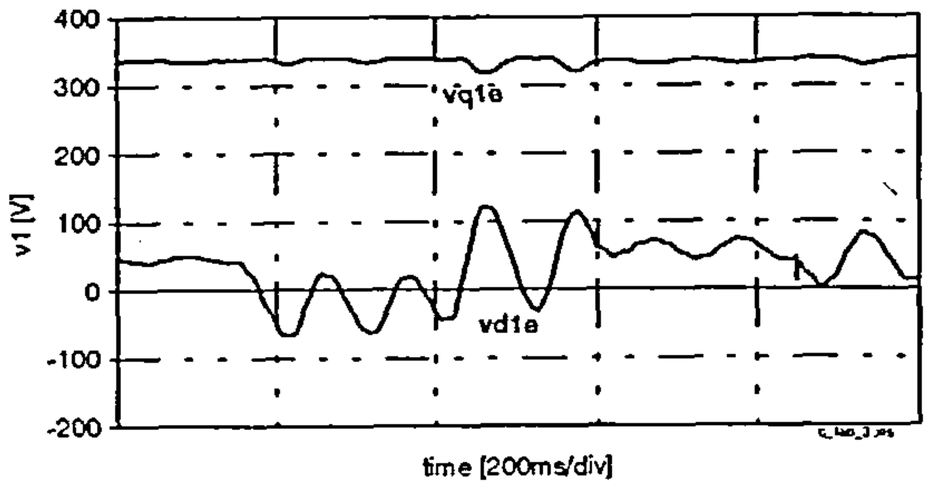

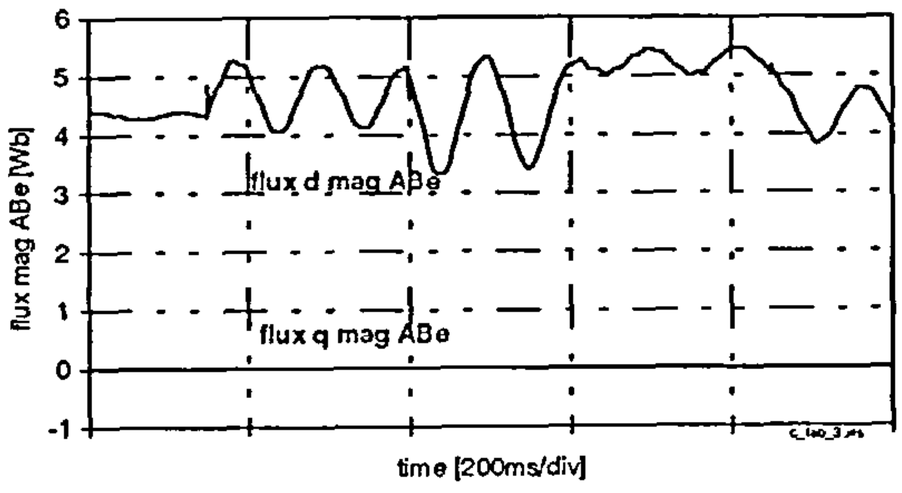

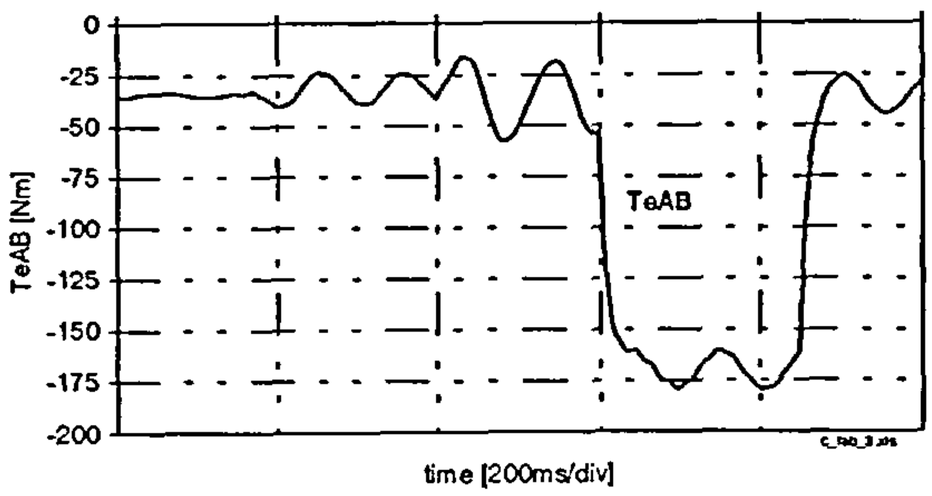

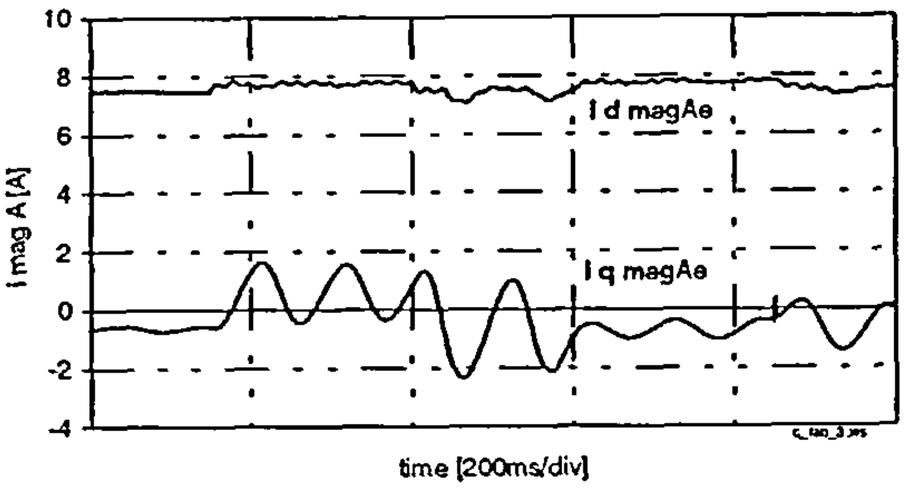

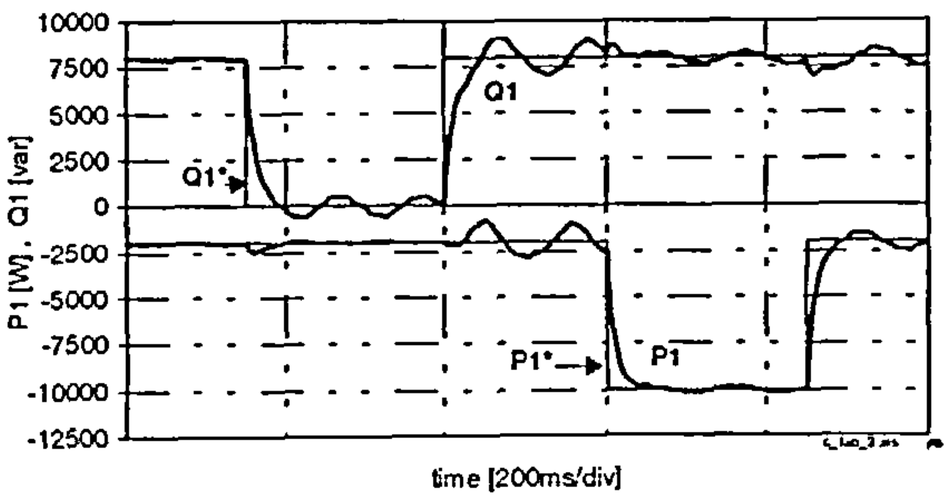

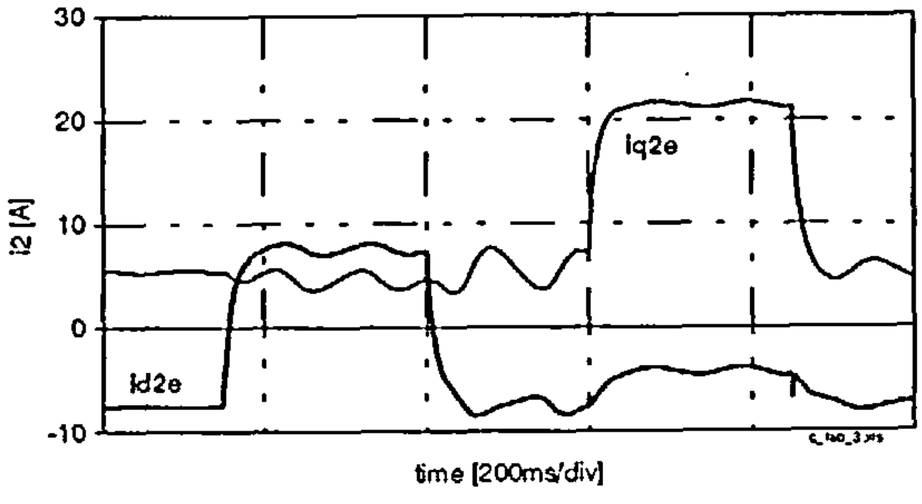

Figure E.22: Simulated CDFM dynamics of the combined flux control - simplified power control loop

(Q_1^* = 8000 to 0 var , P_1^* = -2000 to -10000 W, n_m = 1200 rpm, dt = 0.0002 s)

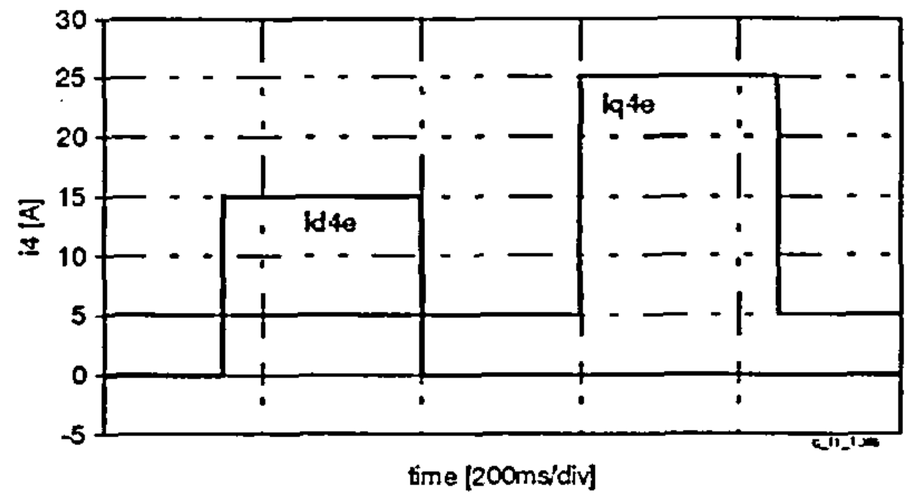

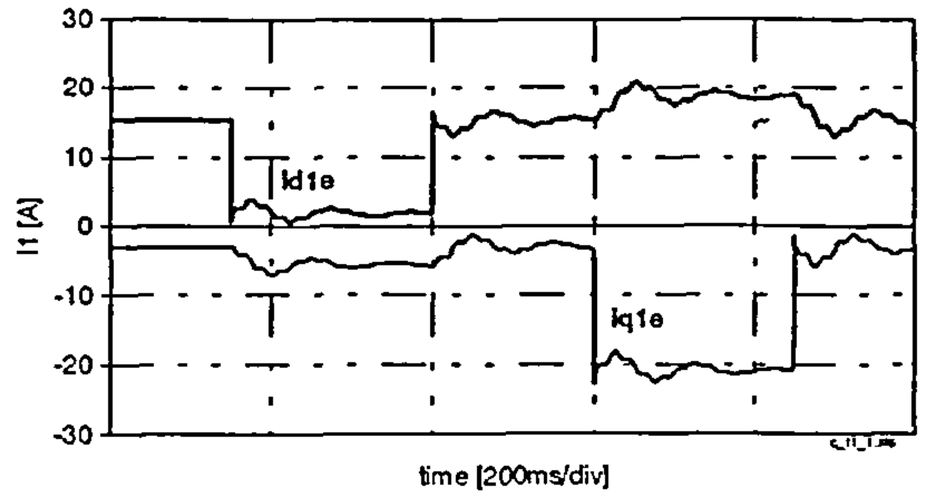

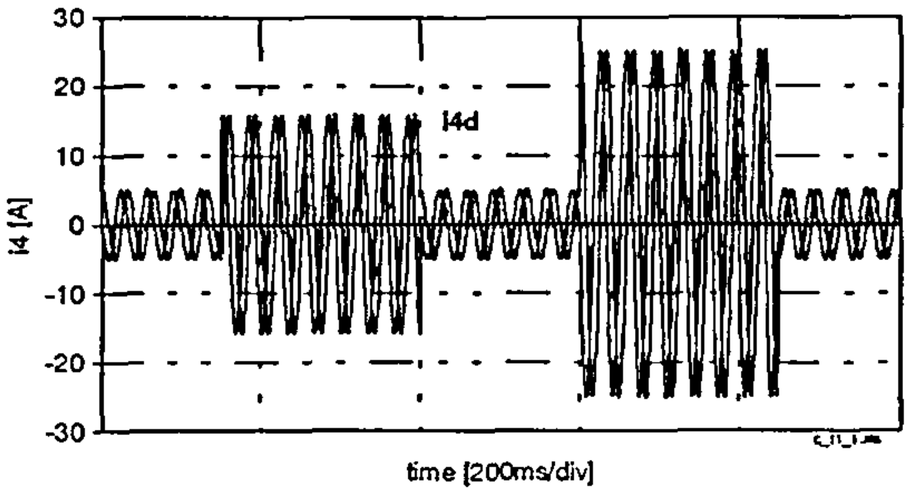

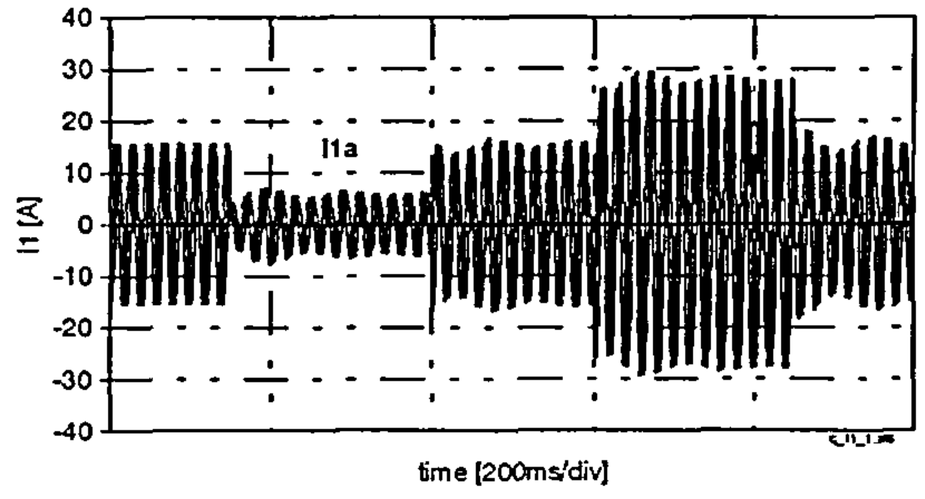

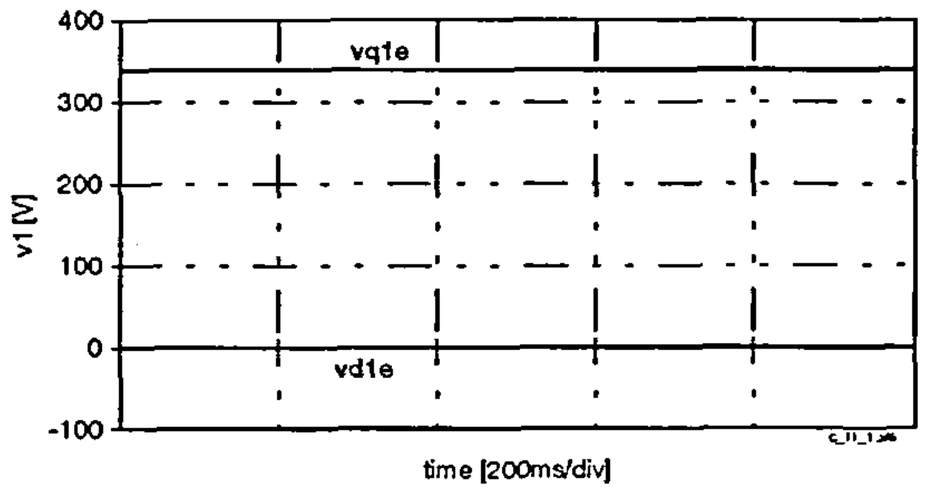

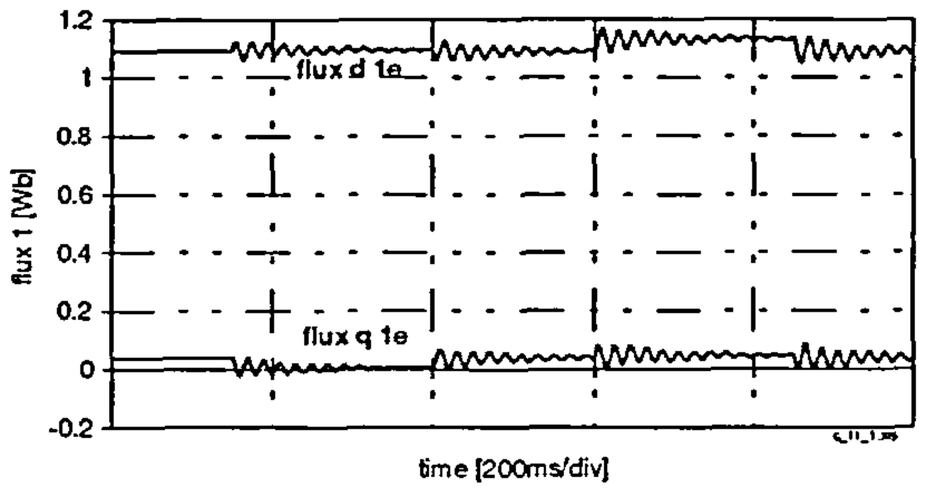

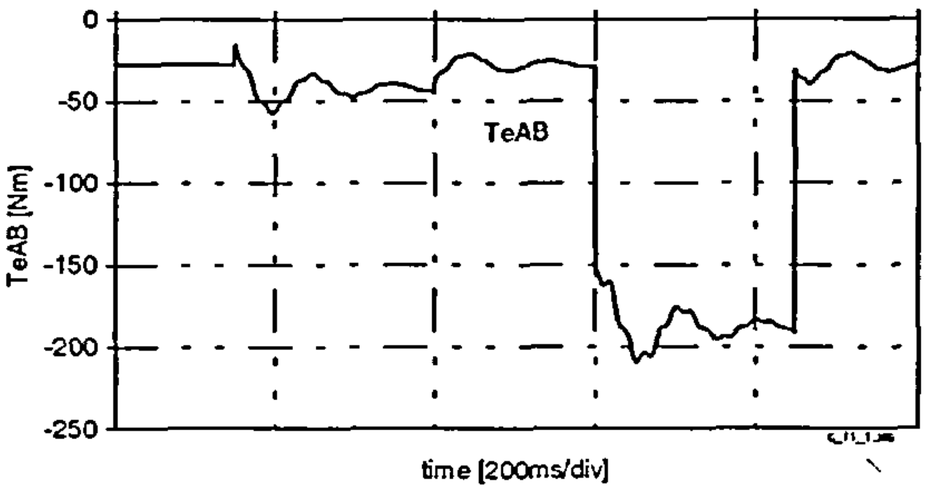

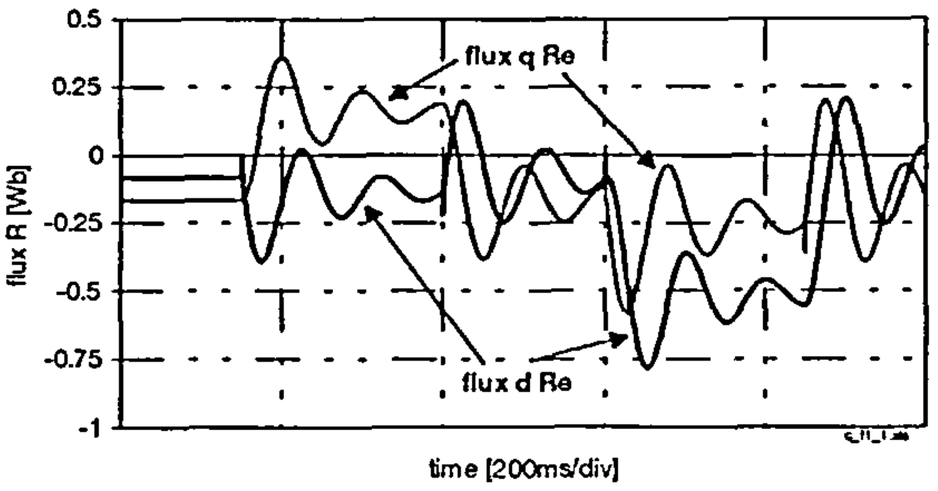

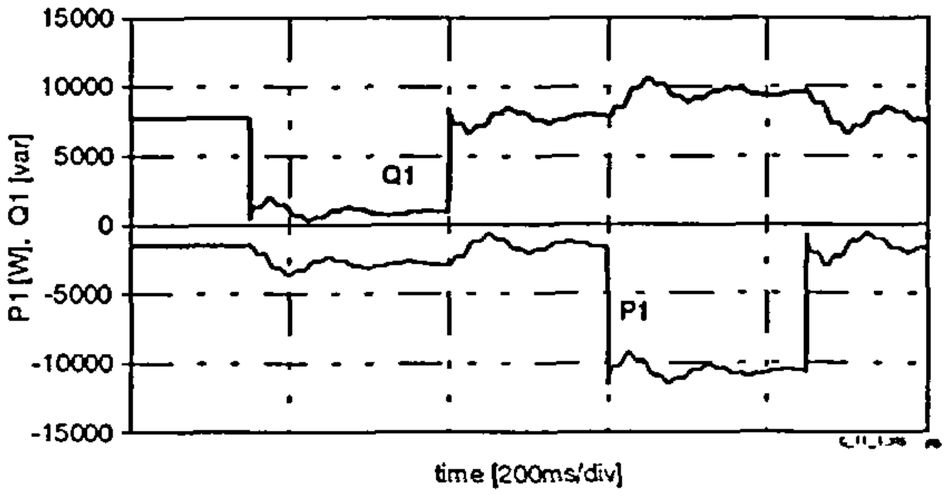

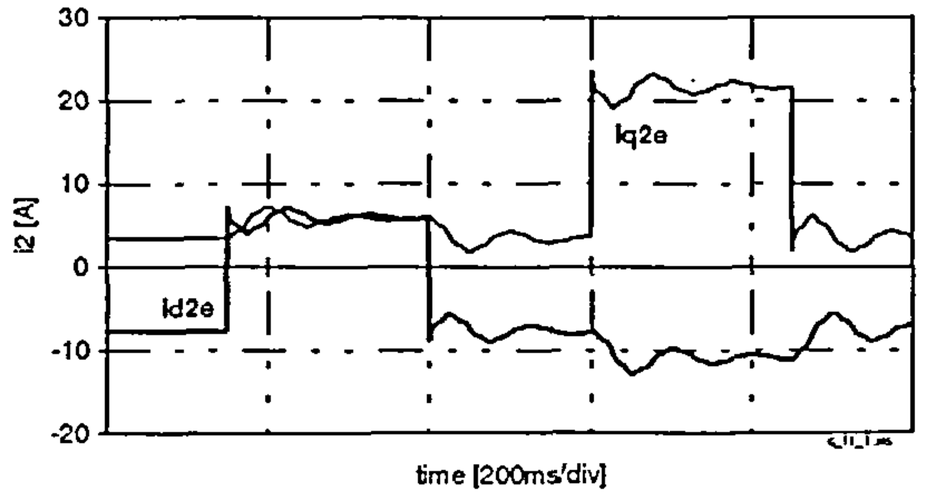

Figure E.23: Simulated CDFM dynamics of the stator flux control - current control loop

(i_{d4}^{e}* = 0 to 15 A , i_{q4}^{e}* = 5 to 25 A, n_m = 1200 rpm, dt = 0.0002 s)

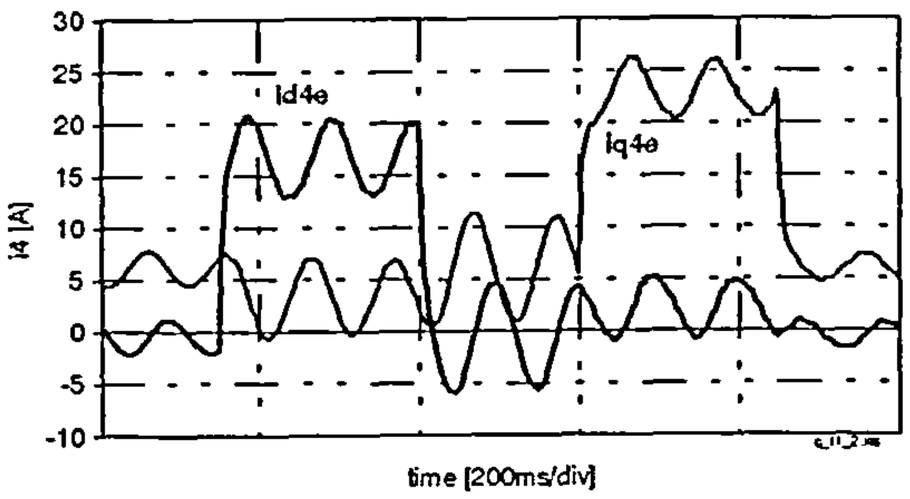

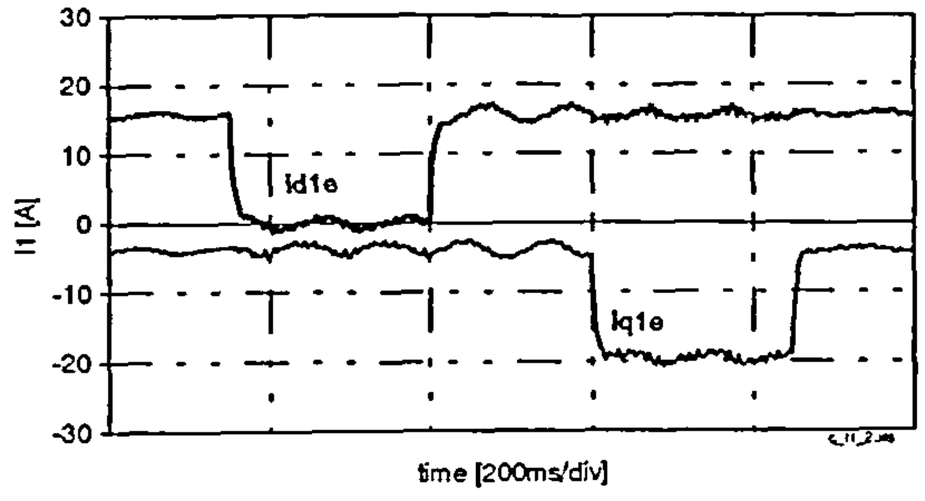

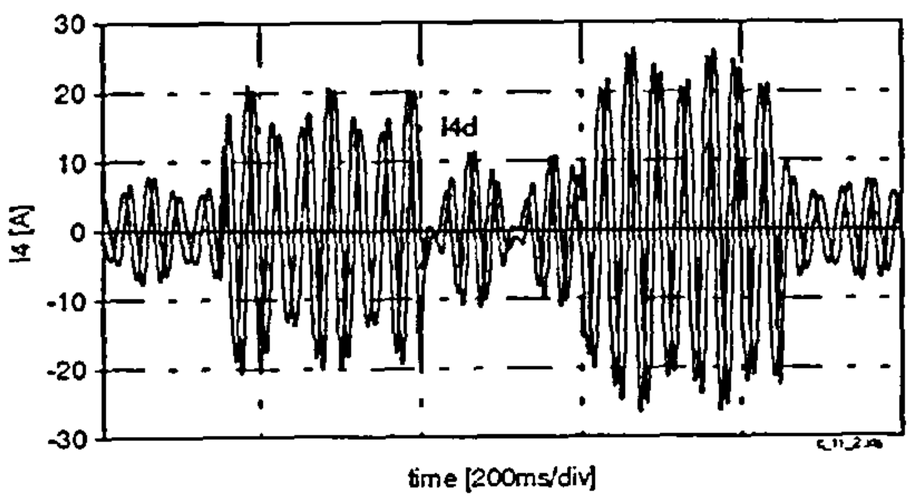

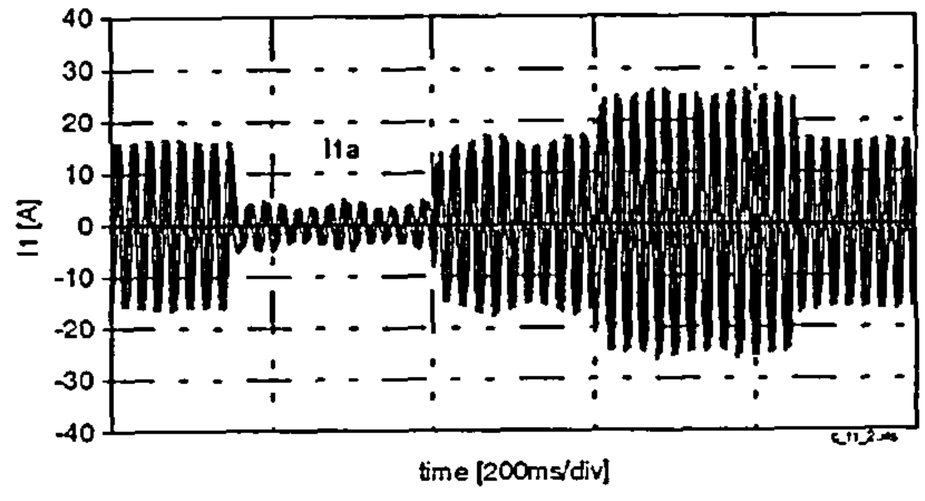

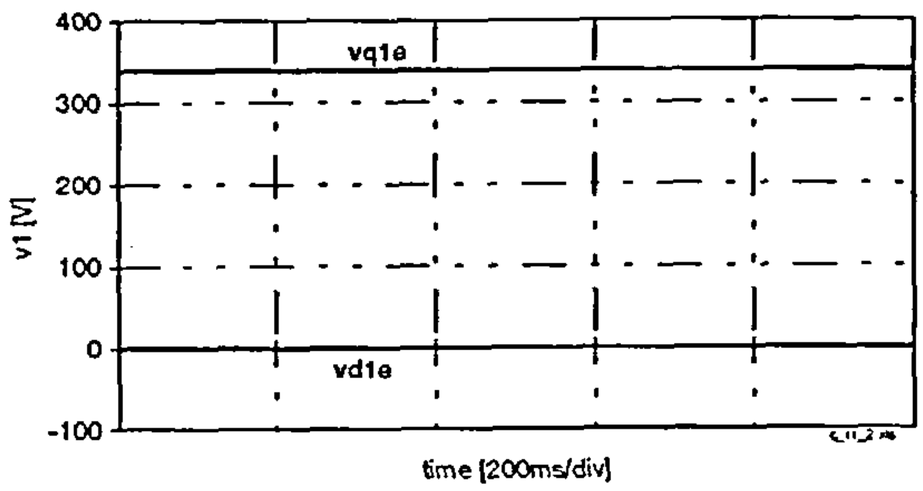

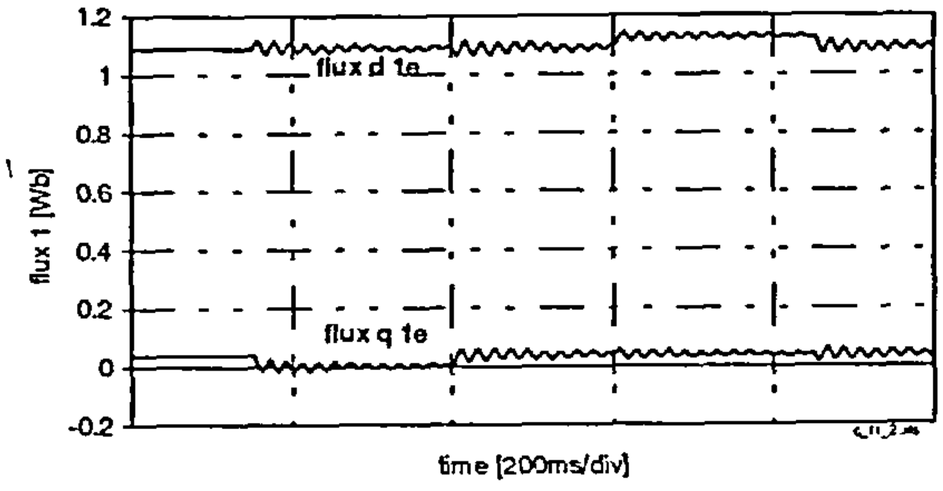

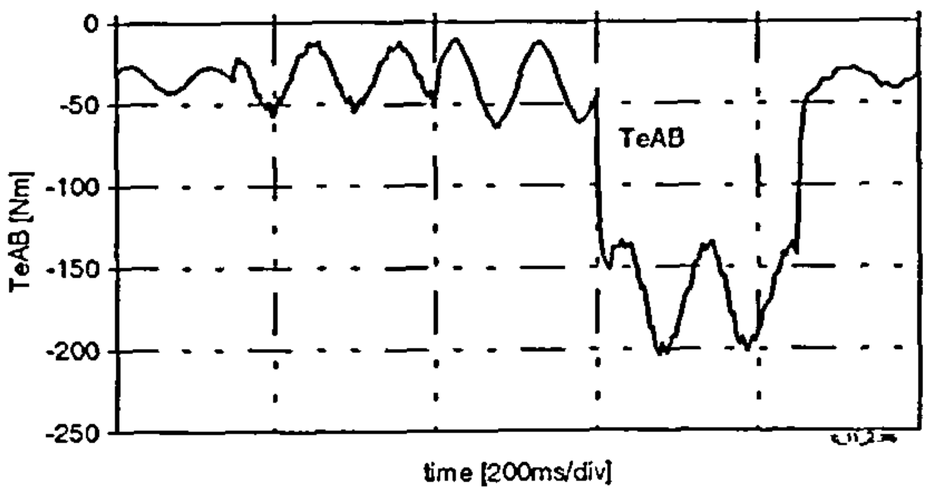

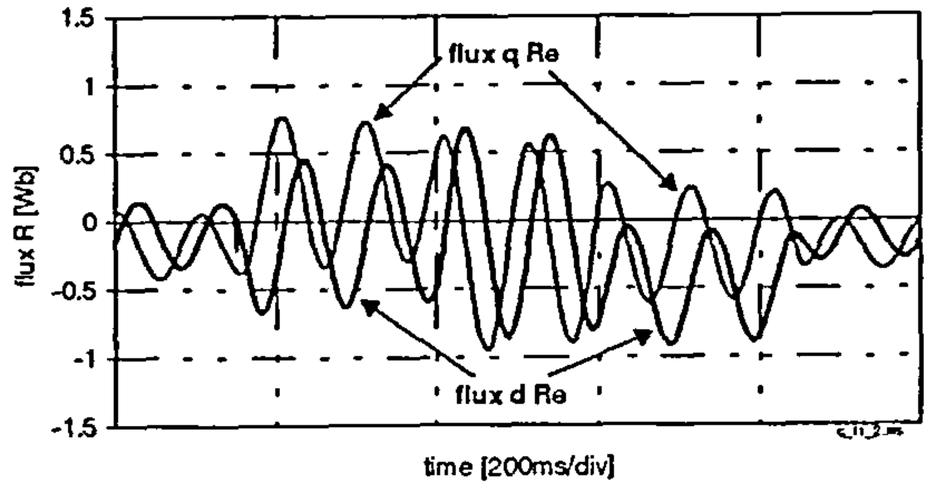

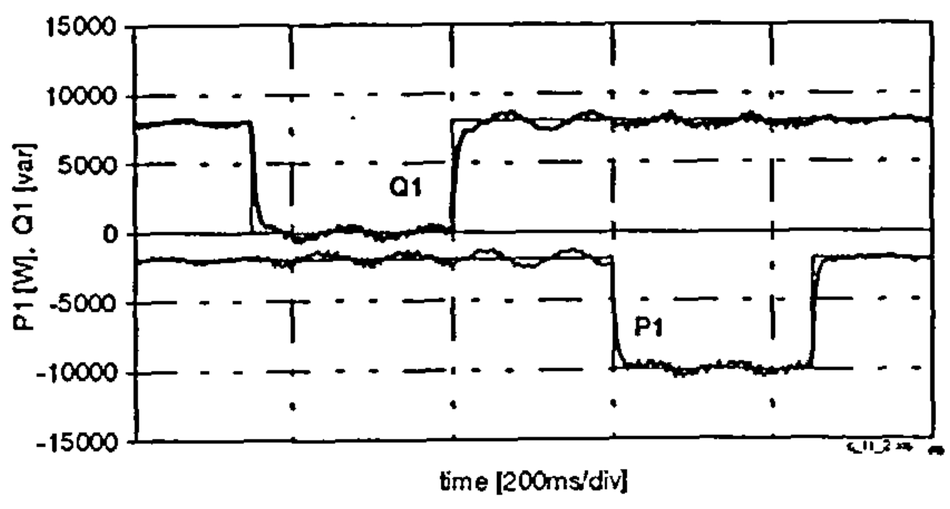

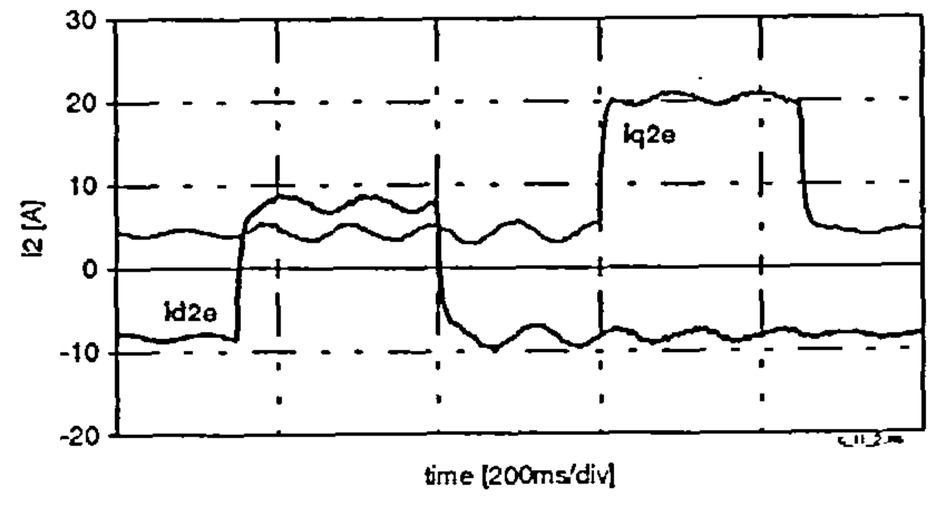

Figure E.24: Simulated CDFM dynamics of the stator flux control - power control loop

(Q_1^* = 8000 to 0 var , P_1^* = -2000 to -10000 W, n_m = 1200 rpm, dt = 0.0002 s)

E.3 Dynamic Simulation with C

The dynamic simulation with SIMULINK, SDFM or CDFM, assumes a perfect inverter with an impressed current, which is directly fed into the machine model. It is therefore not necessary to simulate a current control loop. Additionally, all quantities are perfect sinusoids. The actual system, however employs a voltage source inverter and it makes it inevitable to perform a current control loop to ensure that the demanded current values exist in the machine.
A dynamic control model, written in C and run in BORLAND C++ [f25] takes account of the voltage source inverter and the switching of the inverter.

It must be said straight away, that the computational effort is larger for the C program than for the respective SIMULINK simulation, caused by the additional current control loop. As will be seen, the results from the C simulation are generally not much different to the results obtained from the SIMULINK simulations, which justifies the SIMULINK model as the main simulation tool used during work. Furthermore, it is much easier and much faster to make changes to the existing SIMULINK model than to the C software.
Nevertheless, since a dynamic simulation program in C was developed initially, it is described in the following and simulation results are shown for the SDFM control. Also, the developed inverter switching simulation is needed for the time-step simulation of the inverter voltage for the harmonic prediction process as described in chapter 7.

In order to visualise the simulated quantities a display program was written in C, which is linked to the main simulation program in the compilation process. It allows to display eight different quantities during simulation.

The complete simulation flow-chart for the stator flux oriented control of the SDFM is shown in figure E.25 and further explained next

After the initialising process the main-loop starts. Here, the stator voltage is calculated for each simulation time-step.
Setting time values for t_{slow} and t_{fast} allows to emulate the sampling time of the real implementation. Since the power control loop has to have a smaller bandwidth than the current control loop, the sampling time can be less. In the real implementation the sampling frequency for the power control loop is the same as for the current control loop, but to shorten computational effort, in the simulation the PI-control for the power loop is only performed with a reduced sampling frequency.

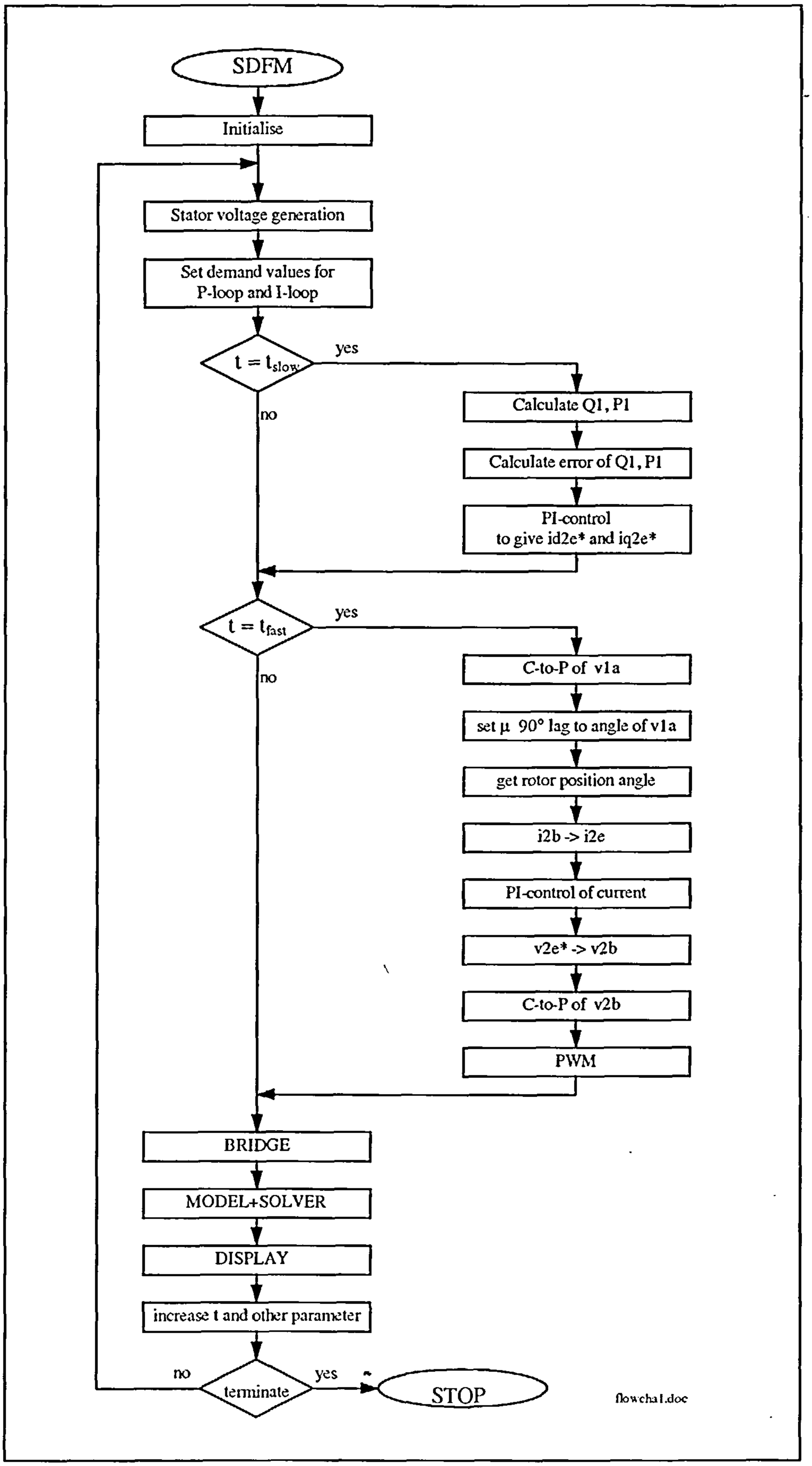

Figure E.25: Flow-chart for the C simulation of the SDFM

The current control loop is executed depending on the sampling frequency set by t_{fast}. The final step in the current control loop is a PWM-function. This function, simulating space vector PWM, carries out following tasks:

- Determining sextant
- Setting of the switching sequence of the involved voltage vectors
- Limiting voltage vector to linear boundary
- Calculation of the PWM sub-cycle times, need by BRIDGE-function

The BRIDGE-function is called at every simulation step. It generates d-q inverter voltages based on the switching sequence and on the cycle times provided by the PWM-function. No dead time simulation is included.

The MODEL-function contains the SDFM machine model. A 4th-order Runge-Kutta SOLVER-function is called by the MODEL-function to solve the machine equations at every simulation time-step.

The DISPLAY-function allows a screen display of the set quantities during simulation. The display interval variable must be set in the initialising routine, so that only every so often of the simulation time step a screen display takes place, which helps to minimise simulation running time.

The simulation process can be interrupted any time by mouse or keyboard click.

E.3.1 Dynamic Simulation of the SDFM

Dynamic simulation results of the field oriented SDFM control are shown in figure E.26 for the inner current control loop and in E.27 for the power control loop. Comparing the results to the SIMULINK results in figure E.18 and E.19 shows that there are no major differences. However, the C simulation introduces ripple on some quantities, which are a consequence of the simulated closed control loop, especially for the power control loop.

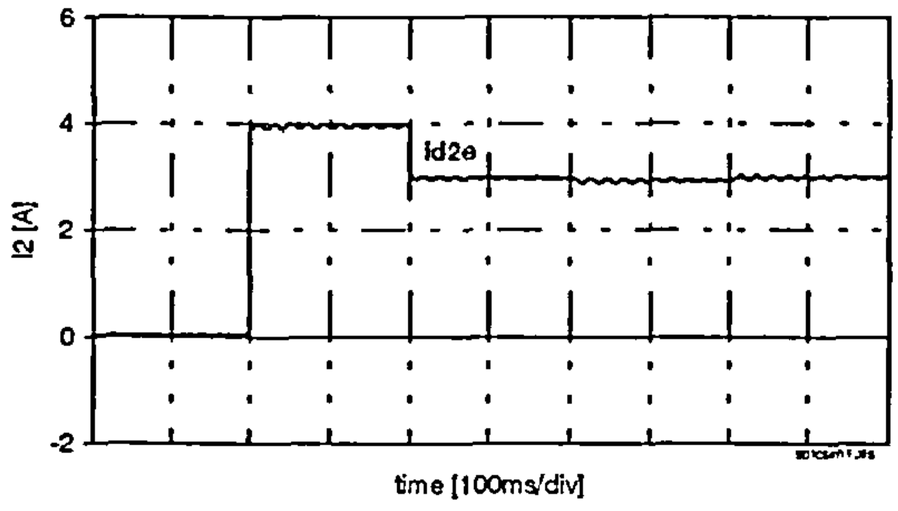

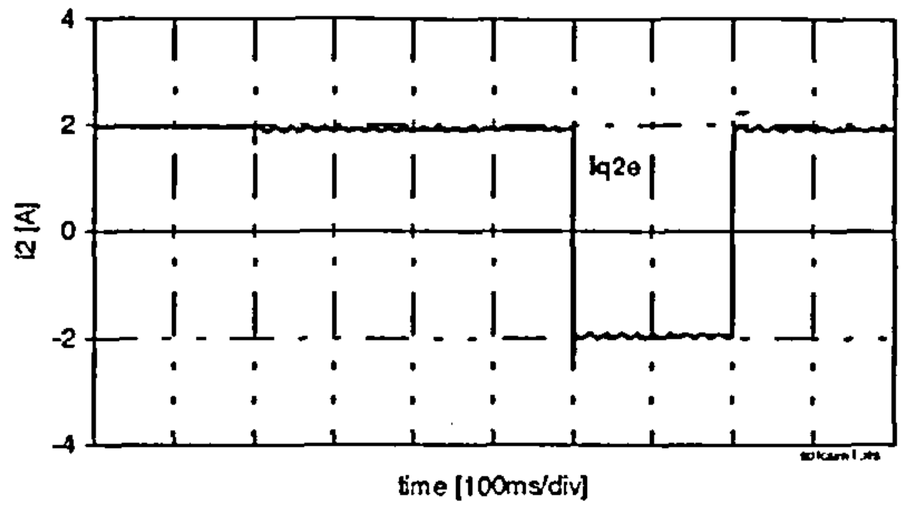

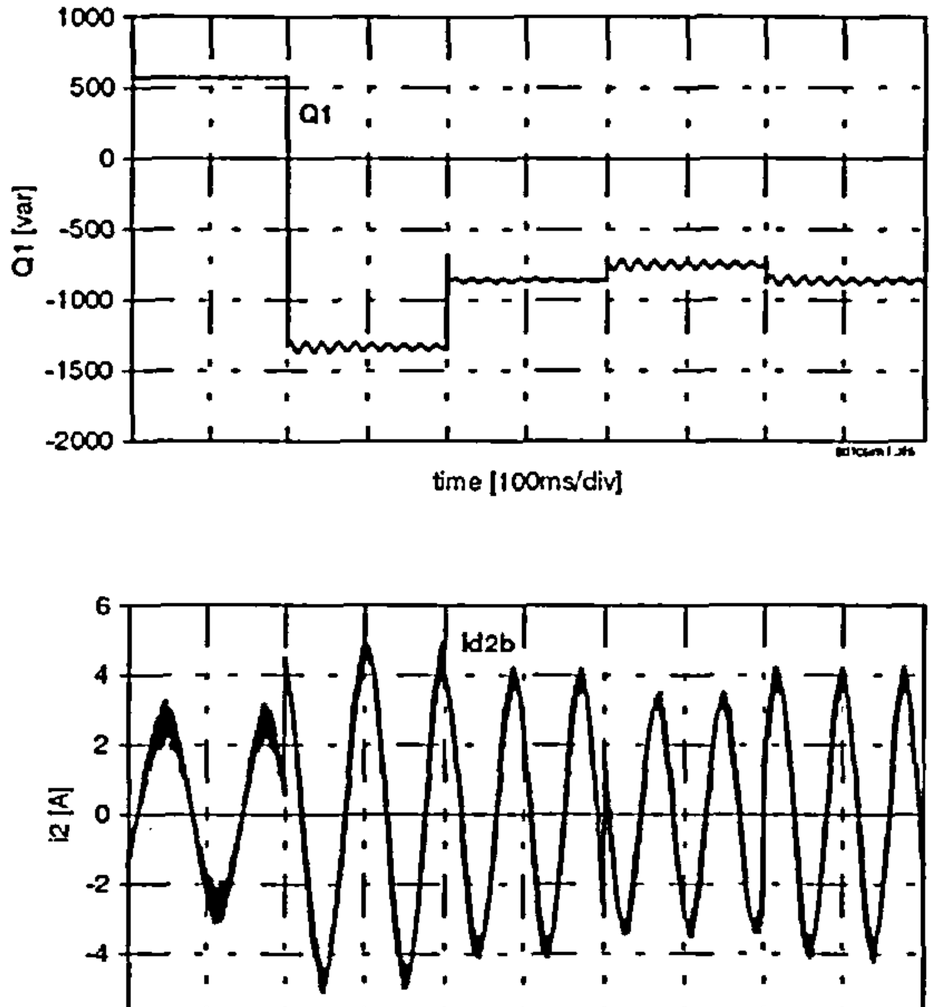

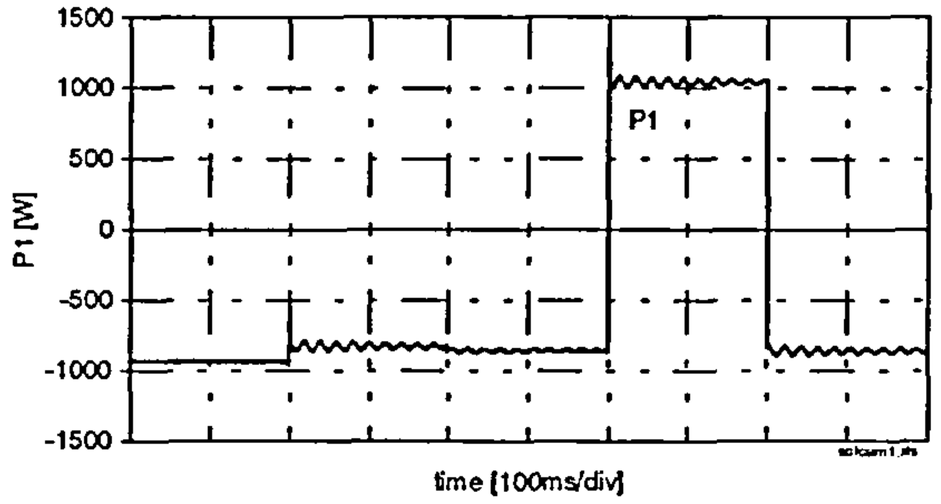

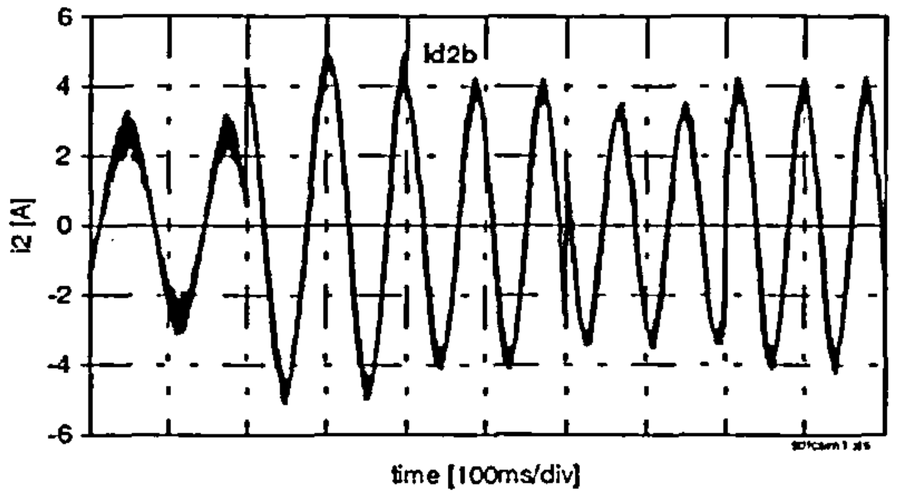

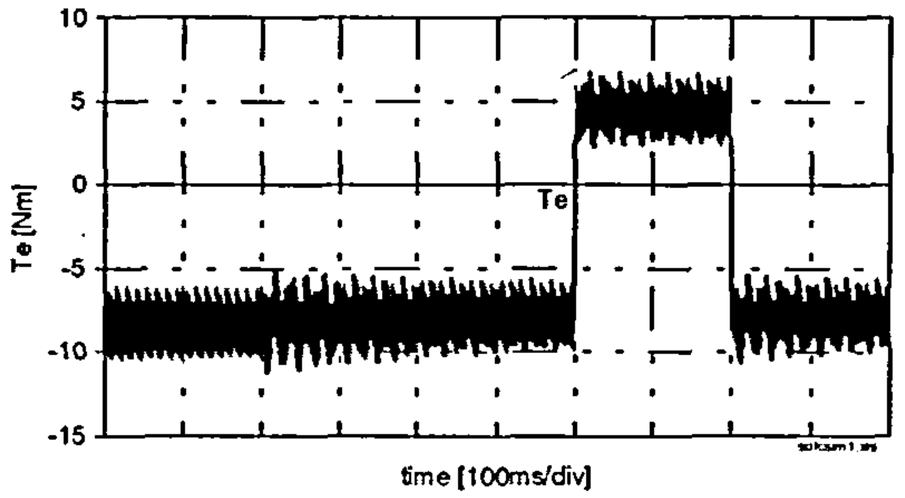

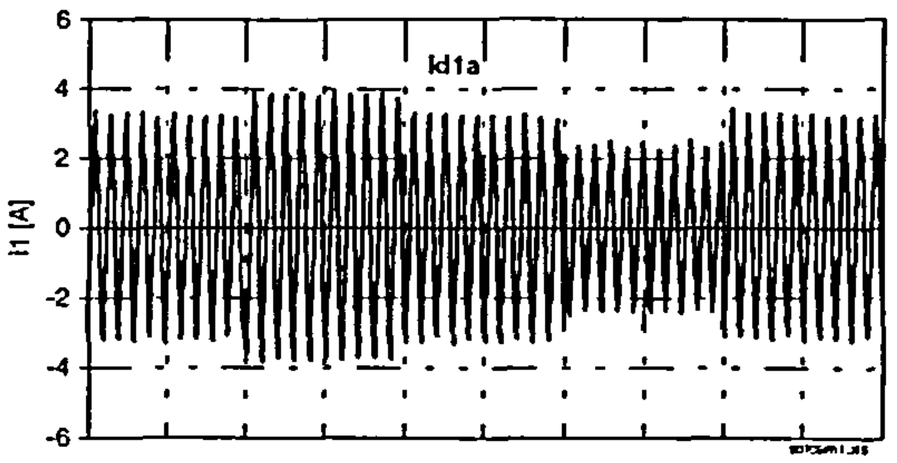

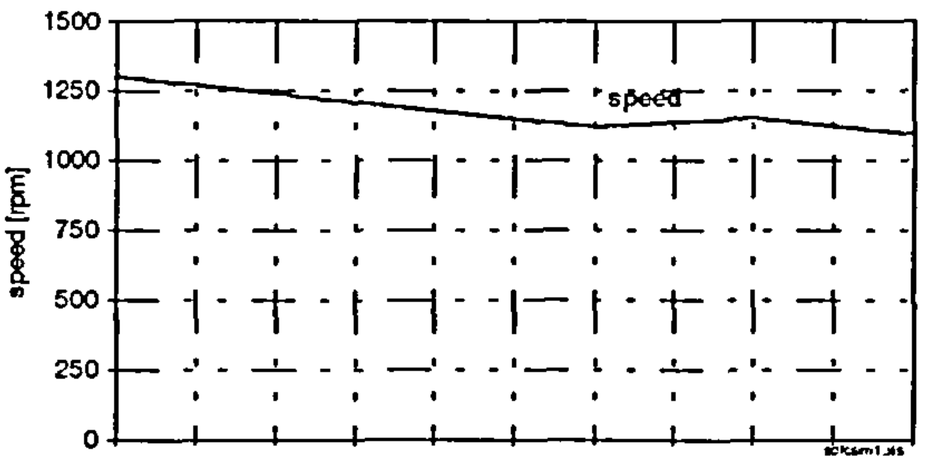

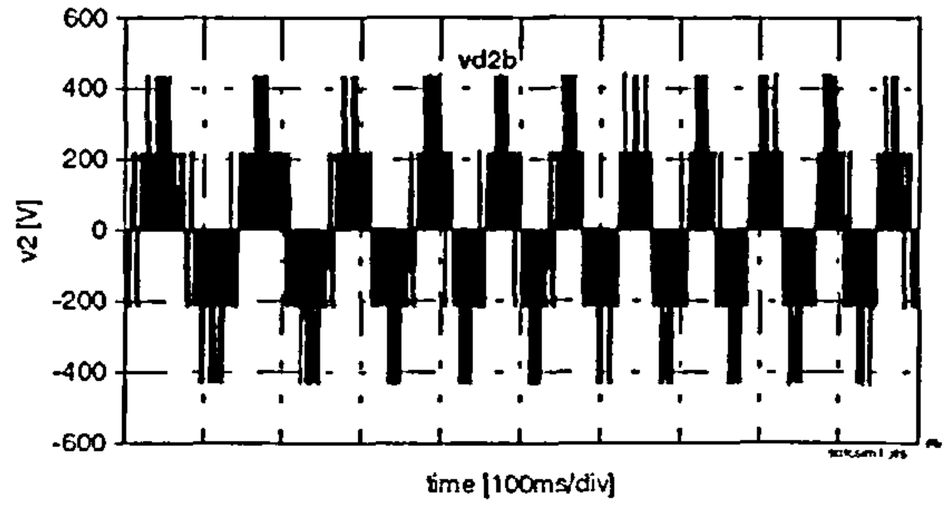

Figure E.26: C- simulated SDFM dynamics of the stator flux control - current control loop

($i_{d2}^{e*} = 0$ to 4 to 3 A , $i_{q2}^{e*} = 2$ to 0 to 2 A , dt = 0.0002s)

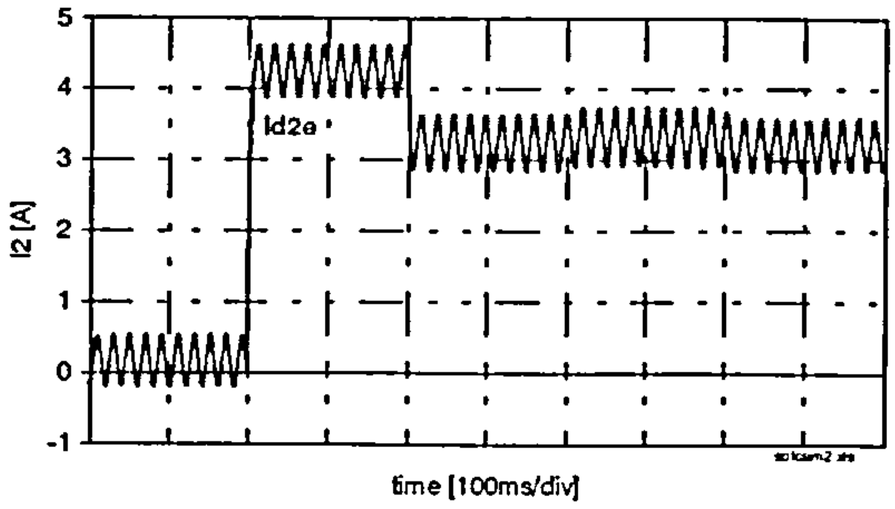

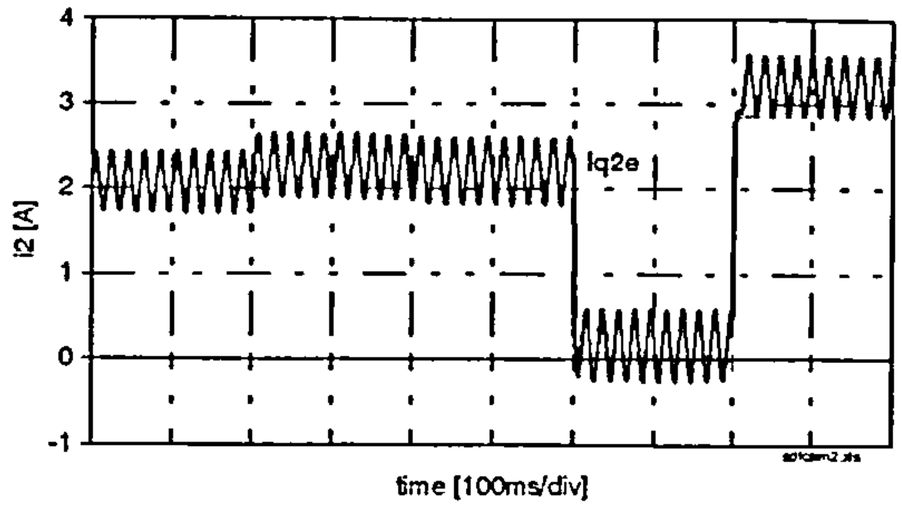

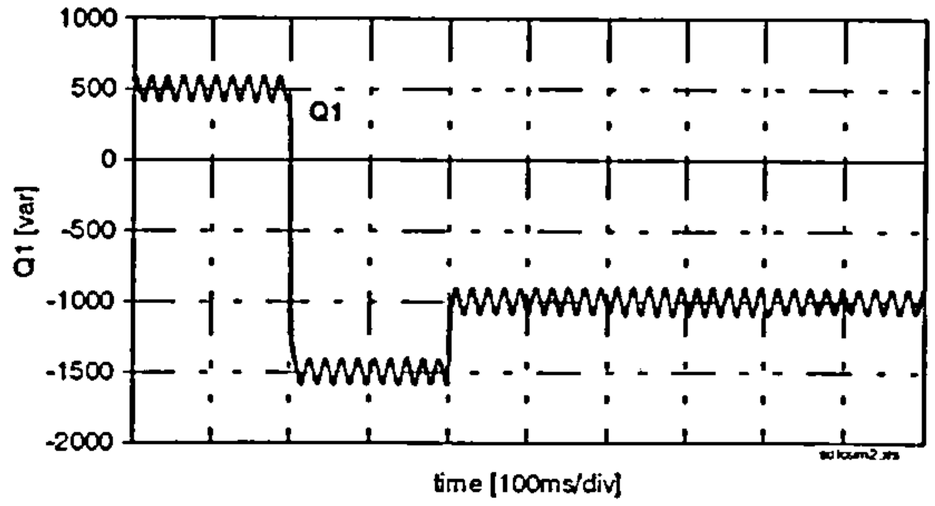

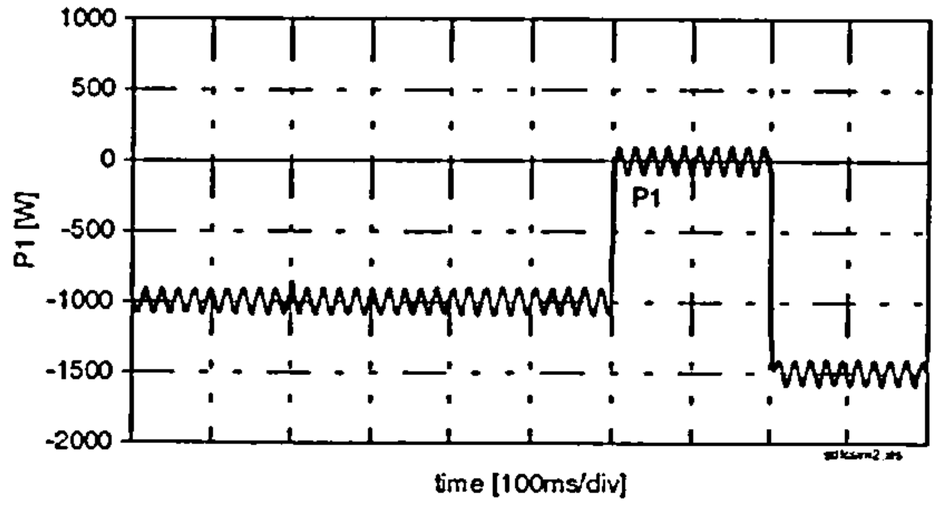

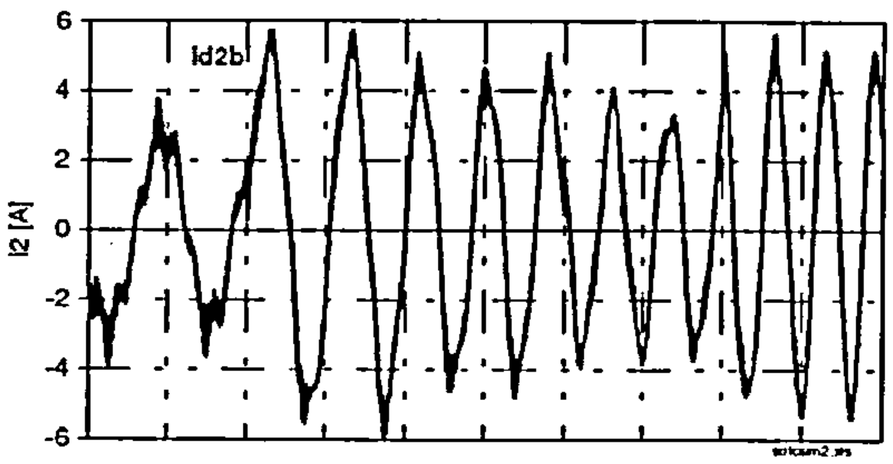

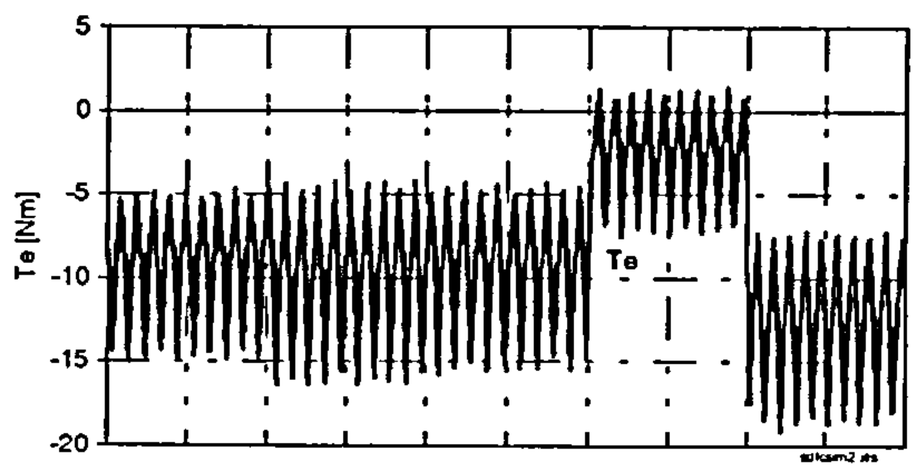

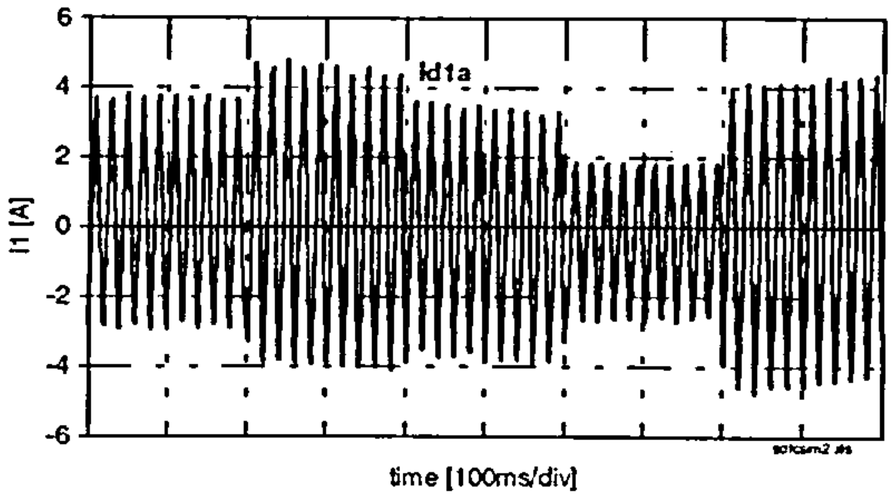

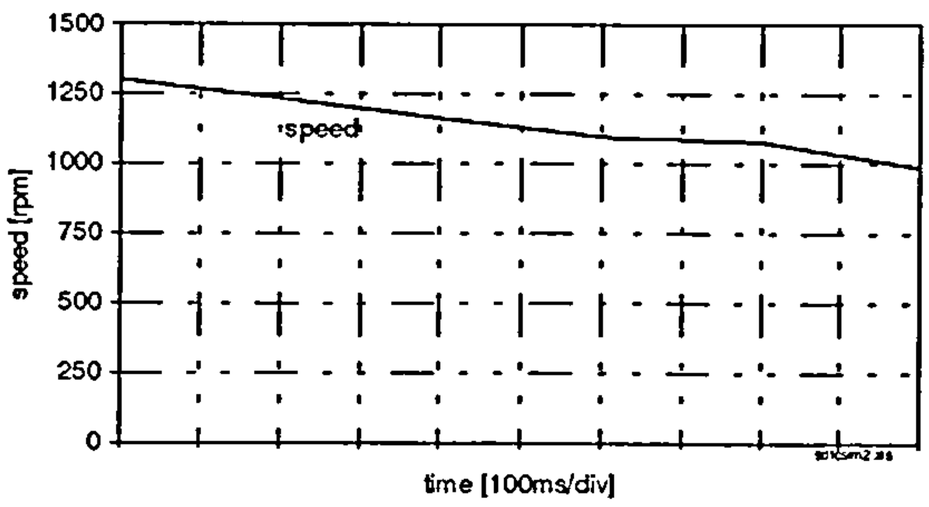

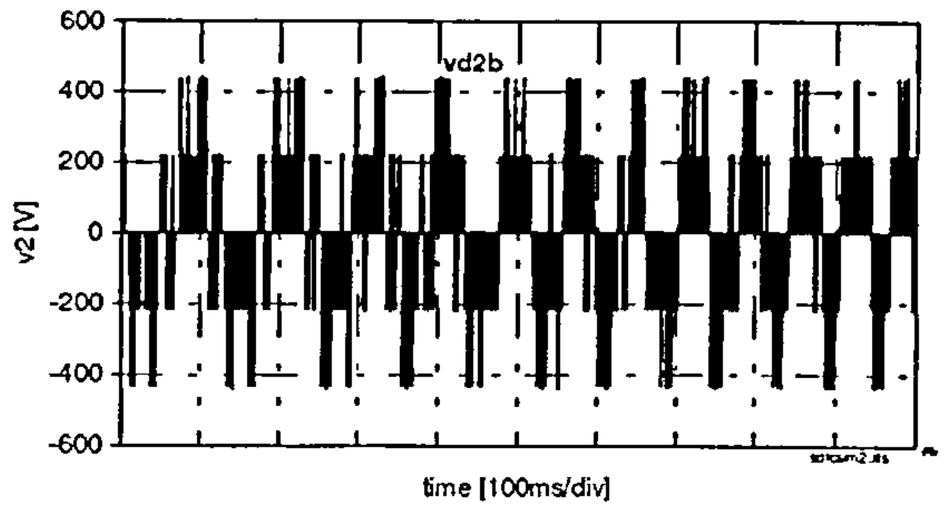

Figure E.27: C- simulated SDFM dynamics of the stator flux control - power control loop

(Q_1^* = 500 to -1500 to 1000 var , P_1^* = -1000 to 0 to -1500 W , dt = 0.0002s)

Appendix F

FFT

This appendix gives a brief introduction and description of the important features of Fast Fourier Transformation as used for analysing various waveforms in chapter 7.

F.1 Fourier Series

A *periodic* function, satisfying the Dirichlet criterias, can be expanded into the sum of an infinite number of harmonically related sine and cosine terms of the form [f9]

$$f(t)=\frac{a_0}{2}+\sum_{n=1}^{\infty}[a_n cos(n\omega_0 t)+b_n sin(n\omega_0 t)]$$

with ω_0 as fundamental frequency ($\omega_0=\frac{2\pi}{T}$) and $n\omega_0$ as frequency of the harmonics (n=2,3,4,...).

The Fourier coefficients are calculated as

$$a_0=\frac{2}{T}\int_0^T f(t)dt$$

$$a_n=\frac{2}{T}\int_0^T f(t)cos(n\omega_0 t)dt$$

$$b_n=\frac{2}{T}\int_0^T f(t)sin(n\omega_0 t)dt$$

with T being the period of the fundamental function. A significant point to observe for the *periodic* signal is that its spectrum is discrete, consisting only of components at dc, the fundamental frequency and integer multiples of the fundamental.
In contrast to this the frequency spectrum of a *nonperiodic* signal is continuous, consisting of components at all frequencies over the range for which it is nonzero. Instead of a Fourier series a Fourier transform must be used.

F.2 Discrete Fourier Transform (DFT)

To use the digital computer as calculation aid, the time continuous signal has to be sampled and digitised. This leads from the continuous Fourier transform to the discrete Fourier transform.

For a sampled *periodic* signal the frequency spectral can be calculated as [f9]

$$X(k)=\frac{1}{N}\sum_{n=0}^{N-1}x(n)e^{-j\frac{2\pi kn}{N}}$$

where X(k) is the kth component of the spectrum at the frequency kΔf, with Δf being the frequency resolution, N is the number of samples.

Since the DFT is an approximation of the Fourier transform of a continuous-time signal in the discrete-time domain, one has to be aware of possible sources of errors in the final result. These sources are *aliasing* and *leakage* [f9].

Aliasing occurs if the sampling frequency is not sufficiently high enough. As a result some actual high frequency components appear as lower frequency aliases that "fold back" around the Nyquist point. A solution to this problem is to ensure that the sampling rate is at least twice that of the highest frequency component having significant amplitude. In many cases, the signal may be filtered with a low-pass analog filter before sampling to ensure no components higher than the Nyquist frequency appear.
Leakage is the effect, when the magnitude of a single frequency is "smeared" around that particular frequency rather than having a sharp edge to its neighbouring frequencies. The primary source of the leakage is the discontinuity introduced in the periodic extension of a sequence. To avoid this source of error the number of periods sampled need to be an integer value.

F.3 Fast Fourier Transform (FFT)

The FFT is an algorithm that reduces the computational effort needed for the DFT remarkably. The number of computations required for the FFT are approximately $N \log_2 N$, compared to N^2 for the DFT.

The FFT-function within MATLAB was used for harmonic analysis of the various waveforms.

F.4 Selection of DFT or FFT Parameters

This section helps to summarise the important parameter relationships that must be considered when using the DFT or FFT.

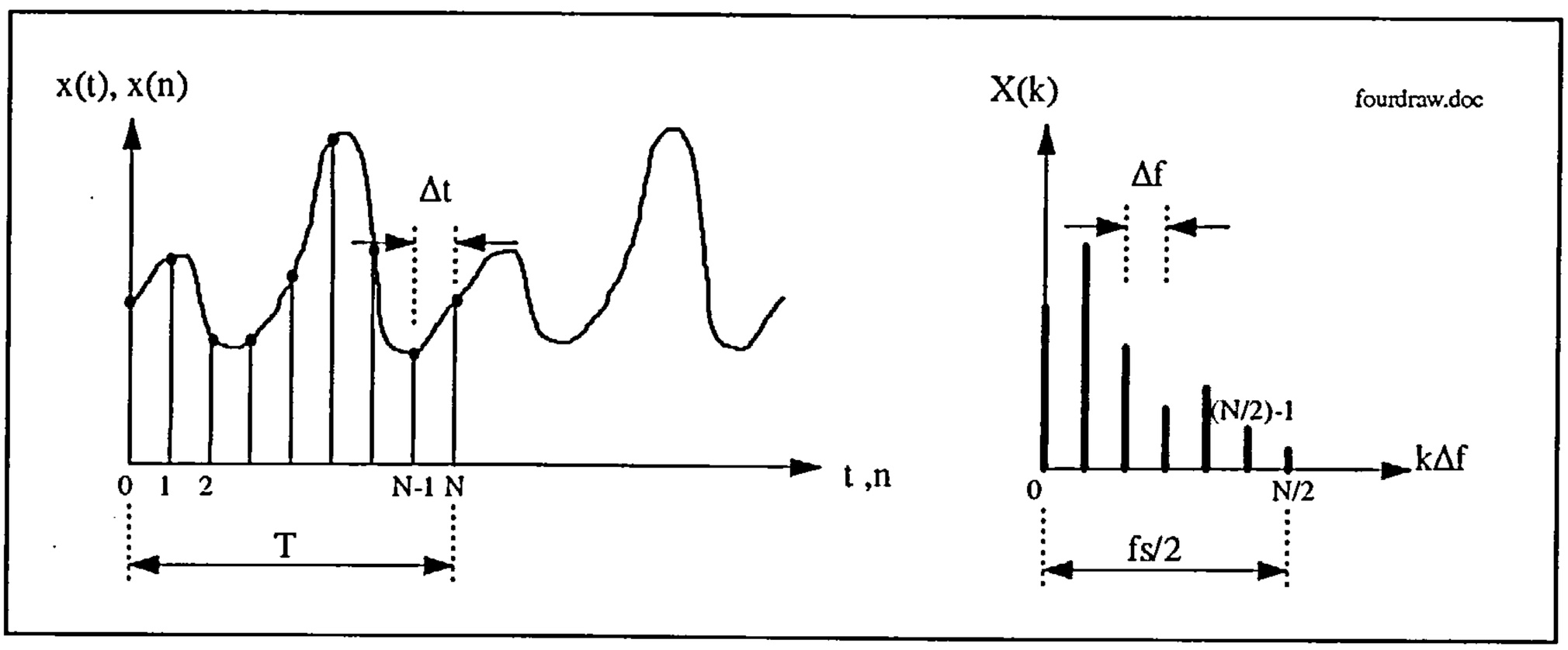

Figure F.1: Illustration of some properties of the DFT or FFT

In order to avoid aliasing it is necessary that

$$f_s \geq 2 f_{max}$$

where f_s is the sampling frequency and f_{max} the highest possible frequency in the spectrum. This gives for the sample time step

$$\Delta t = \frac{1}{f_s}$$

For a certain frequency resolution Δf the number of samples N must be chosen accordingly to

$$\Delta f = \frac{f_s}{N}$$

Appendix G

PWM and Waveforms

After an explanation of sinusoidal and space vector PWM this appendix describes the applied PWM principle of the microcontroller 80C167. In the second part, various waveforms of the SDFM and CDFM system are displayed, which were analysed in chapter 7.

G.1 PWM

High performance control of electrical machines, such as field orientation, relies on the fact that desired machine quantities have to be actually present in the machine. The switching signals for the voltage source inverter have therefore to be created in a certain way, so that the voltage, demanded from the current control loop, appears at the machine terminals. Two common pulse width modulation techniques are described in the following as well as the PWM method as implemented in the used microcontroller.

G.1.1 Sinusoidal PWM

Sinusoidal PWM (also called Suboscillation method) compares a reference signal to a carrier triangular signal as displayed in figure G.1 for a single leg of a 3-phase inverter. Each time when the two signals cross each other the switching state of the inverter leg changes.

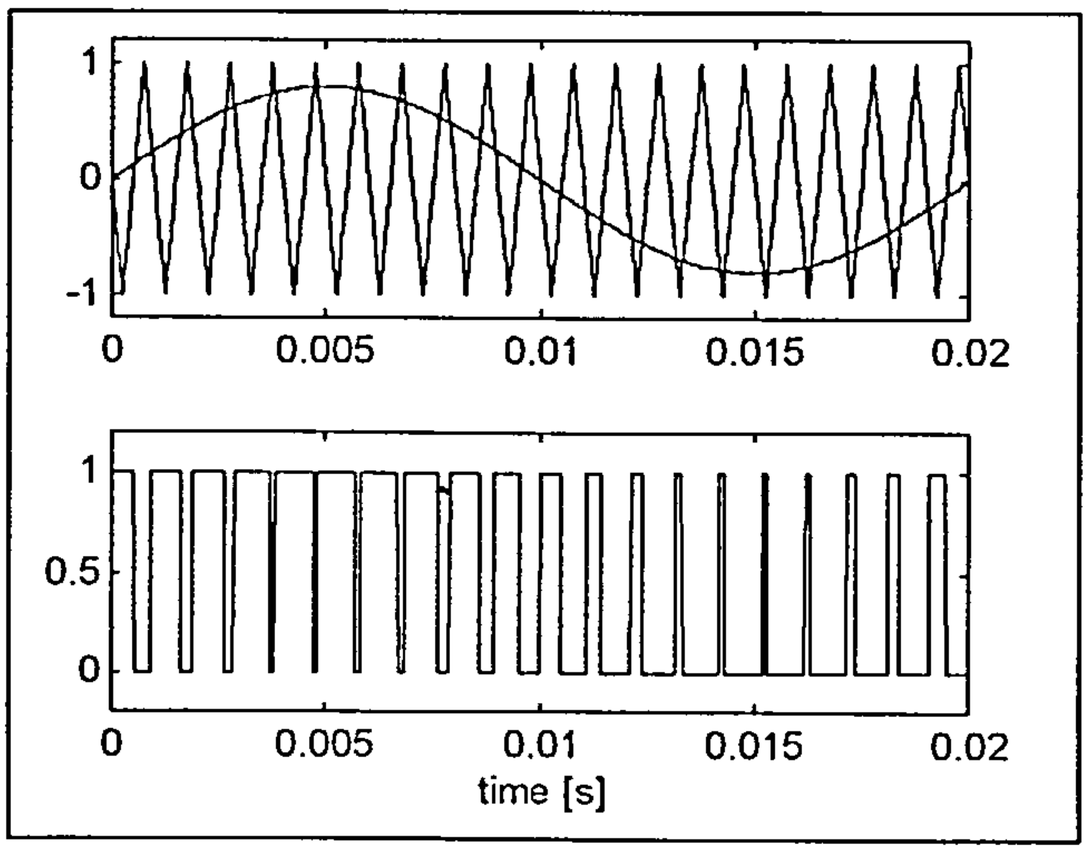

Figure G.1: Sinusoidal PWM principle

Applying that for each single inverter leg generates the 3-phase voltage at the machine terminals. The maximum fundamental rms line-line voltage at the inverter terminals take the value

$$V_{llrmsload} = \frac{\sqrt{6}}{4} V_{dc} = 0.612\, V_{dc} \qquad \text{(G.1)}$$

This is for the maximum modulation index of $m_i = 1$, where the peak of the reference signal is equal to the peak of the triangular carrier signal. The value reached by equation (G.1) is about 78 % of that produced by square-wave operation.

G.1.2 Space Vector PWM [f16-f18]

In comparison to the PWM method mentioned above, the space vector PWM (SVPWM) calculates the switching instances for the inverter legs from a 2-dimensional voltage vector. The 3-phase inverter in figure G.2 with the six switches can produce eight different switching conditions or states.

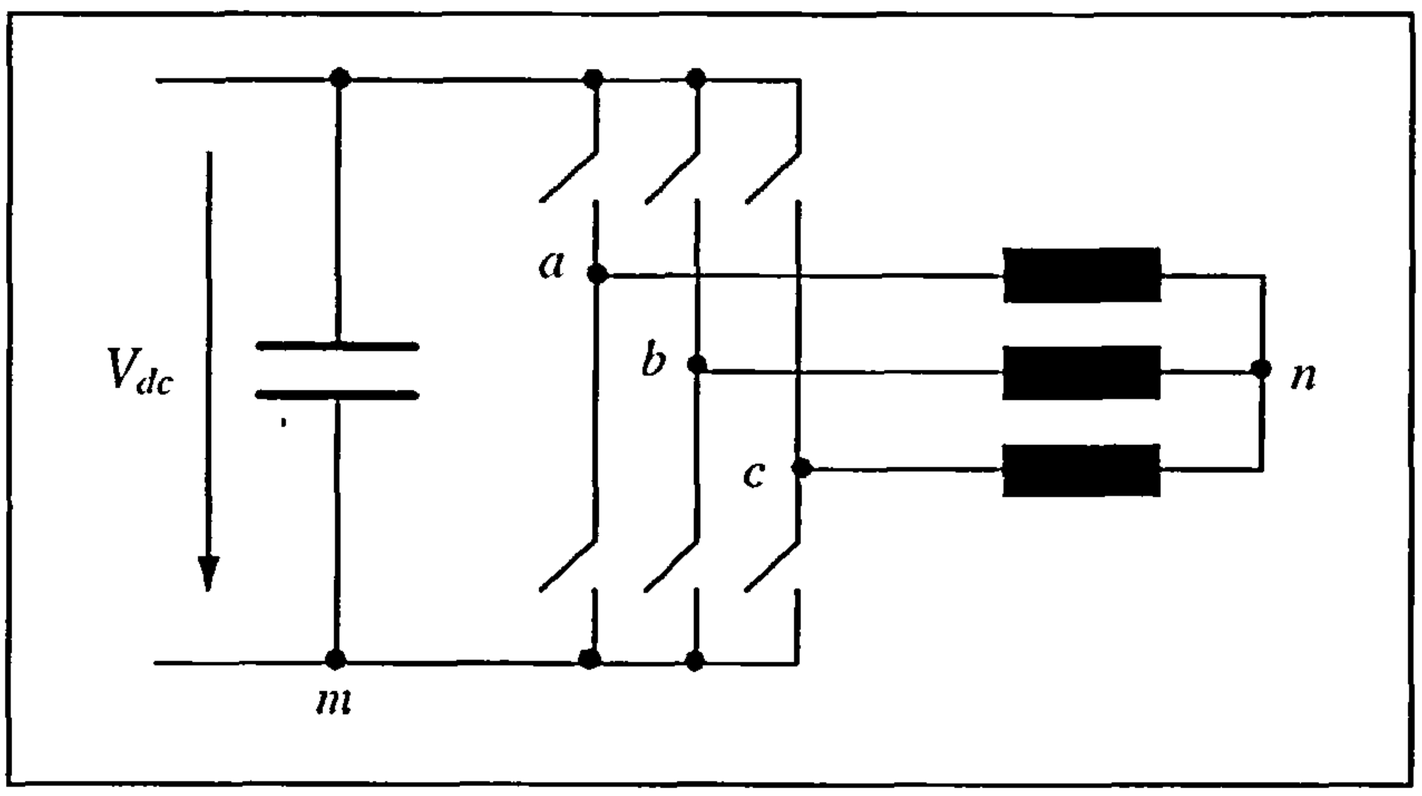

Figure G.2: Inverter with connected load

There are six active voltage vectors ($\bar{v}_1, \bar{v}_2, \bar{v}_3, \bar{v}_4, \bar{v}_5, \bar{v}_6$), which are aligned with the phases *a*, *b* and *c* either in positive or negative direction. There is also the possibility to create two so-called zero voltage vectors ($\bar{v}_0, \bar{v}_7$). The zero voltage vectors result, when either all upper or all lower switches are closed. The resulting 2-dimensional plane put up by the individual active voltage vectors is displayed in figure G.3 and constitutes a sextant with the zero voltage vectors at the origin with zero magnitude.

Depending on the switching state, the load can be connected to the d.c.-link in eight different ways as displayed in figure G.4. For the states 1 - 6, the three phase load is connected across the d.c.-link in six distinguished patterns. For the zero sequence, the load is either connected to the upper or to the lower rail of the d.c.-link. At that instant there is no voltage across the load.

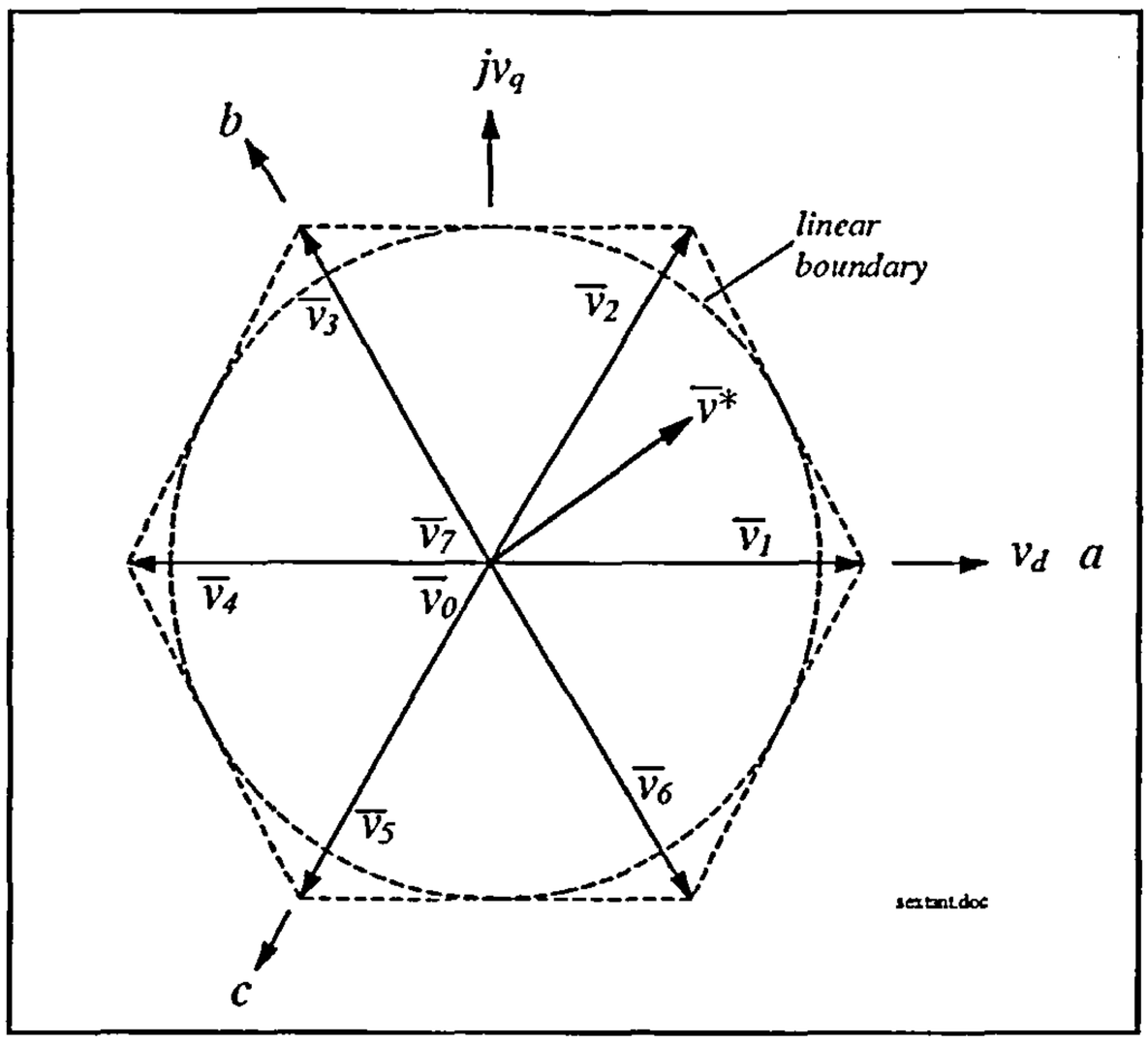

Figure G.3: Voltage vectors

The switching state can be symbolised by a digital number, one digit representing each phase. A "1" stands for a closed upper switch in the respective inverter leg, otherwise for a "0", the upper switch is open and the lower switch is closed, e.g. switching state 1 is symbolised by "100". In this case the load phase *a* is connected to the positive d.c.-link rail and load phases *b* and *c* are connected to the negative d.c.-link rail (figure G.4). At that instant 2/3 of the d.c.-link voltage are across the load phase *a* and 1/3 of the d.c.-link voltage is across the load phases *b* and *c*.

Table G.1 summarises the eight switching conditions and shows the resulting voltage values for the line-line load voltages (v_{ab}, v_{bc}, v_{ca}), the phase load voltages (v_{an}, v_{bn}, v_{cn}) and the d-q-voltage vectors (v_d, v_q). All voltage values are normalised with the d.c.-link voltage.

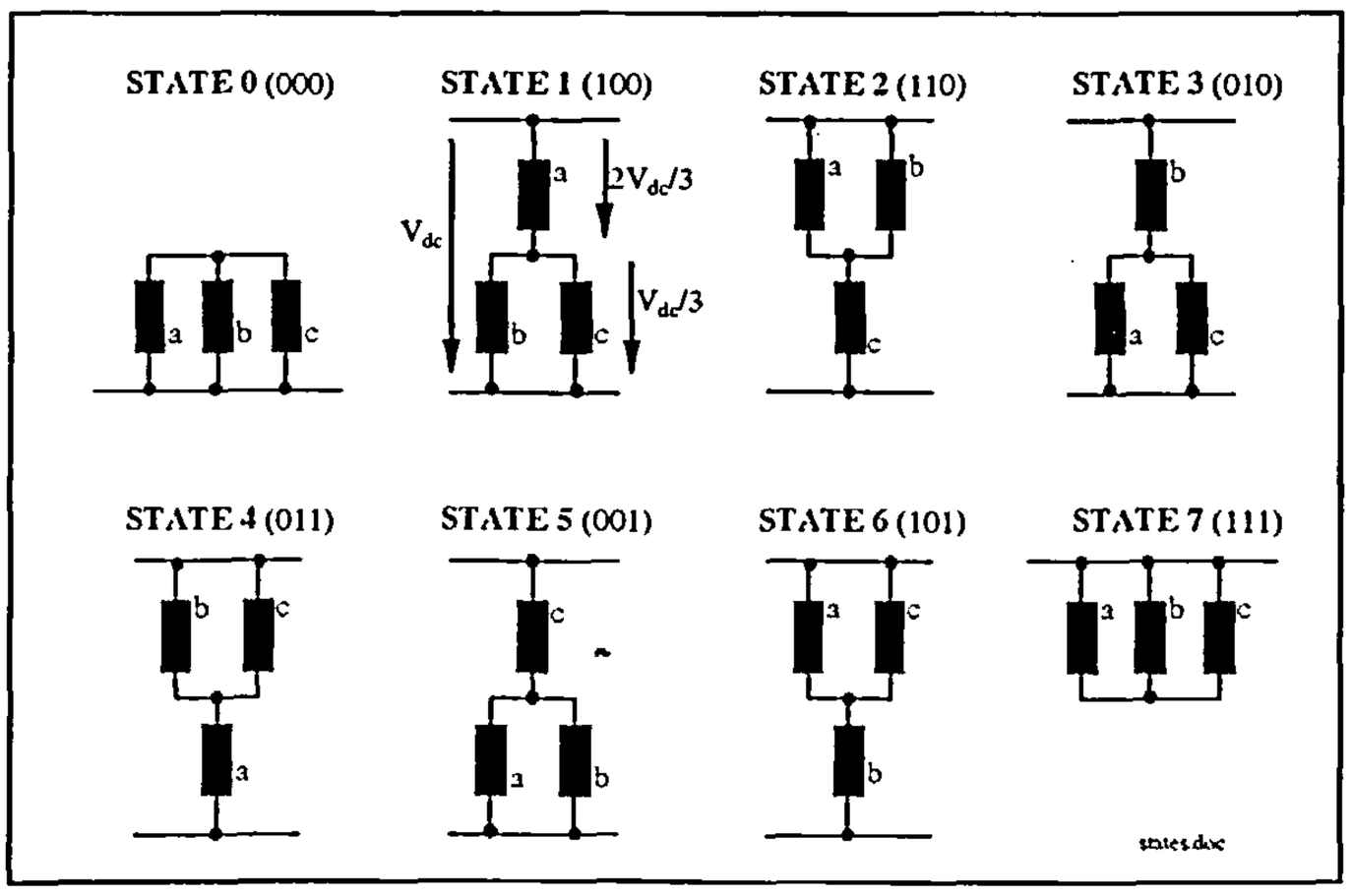

Figure G.4: Switching states

State	*Vector*	$\frac{v_{ab}}{V_{dc}}$	$\frac{v_{bc}}{V_{dc}}$	$\frac{v_{ca}}{V_{dc}}$	$\frac{v_{an}}{V_{dc}}$	$\frac{v_{bn}}{V_{dc}}$	$\frac{v_{cn}}{V_{dc}}$	$\frac{v_d}{V_{dc}}$	$\frac{v_q}{V_{dc}}$
000	$\bar{v}_0$	*0*	*0*	*0*	*0*	*0*	*0*	*0*	*0*
100	$\bar{v}_1$	*1*	*0*	*-1*	*2/3*	*-1/3*	*-1/3*	*2/3*	*0*
110	$\bar{v}_2$	*0*	*1*	*-1*	*1/3*	*1/3*	*-2/3*	*1/3*	*1/√3*
010	$\bar{v}_3$	*-1*	*1*	*0*	*-1/3*	*2/3*	*-1/3*	*-1/3*	*1/√3*
011	$\bar{v}_4$	*-1*	*0*	*1*	*-2/3*	*1/3*	*1/3*	*-2/3*	*0*
001	$\bar{v}_5$	*0*	*-1*	*1*	*-1/3*	*-1/3*	*2/3*	*-1/3*	*-1/√3*
101	$\bar{v}_6$	*1*	*-1*	*0*	*1/3*	*-2/3*	*1/3*	*1/3*	*-1/√3*
111	$\bar{v}_7$	*0*	*0*	*0*	*0*	*0*	*0*	*0*	*0*

table.doc

Table G.1: Switching states and voltage values

SVPWM is based on the concept of approximating a rotating reference voltage space vector $\bar{v}^*$ with those physically realisable on a 3-phase inverter.

Figure G.3 shows the reference voltage vector in the first sextant put up by the active voltage vectors $\bar{v}_1$ and $\bar{v}_2$. The magnitude of the voltage vectors $\bar{v}_I$ and $\bar{v}_{II}$, aligned to $\bar{v}_1$ and $\bar{v}_2$, which give the vectorial sum for $\bar{v}^*$ is calculated as

$$|\bar{v}_I| = \frac{sin(60°-\alpha)}{sin60°}|\bar{v}^*| \tag{G.2}$$

$$|\bar{v}_{II}| = \frac{sin\alpha}{sin60°}|\bar{v}^*| \tag{G.3}$$

$\bar{v}_I$ is always aligned with the positive active voltage vectors ($\bar{v}_1, \bar{v}_3, \bar{v}_5$) and $\bar{v}_{II}$ is always aligned with the negative active voltage vectors ($\bar{v}_2, \bar{v}_4, \bar{v}_6$), depending in which sextant the reference voltage vector is present. The angle α represents the intrasextant displacement of the reference voltage vector relative to the respective positive active voltage vector.

The duration for how long a certain active voltage vector is switched on to approximate the reference voltage vector within one switching cycle is calculated as

$$T_I = \frac{T_{cycle}}{2}\frac{|\bar{v}_I|}{\frac{2}{3}V_{dc}} \tag{G.4}$$

$$T_{II} = \frac{T_{cycle}}{2}\frac{|\bar{v}_{II}|}{\frac{2}{3}V_{dc}} \tag{G.5}$$

The remaining cycle time is filled up with the switching of the zero voltage vectors and the duration time for those is

$$T_0 = T_{cycle} - T_I - T_{II} \tag{G.6}$$

It has to be mentioned that the reference voltage vector is assumed to be constant during one switching cycle for sufficient high switching frequency.

In order to obtain minimum switching transitions of each inverter leg, within one switching cycle, it is necessary to arrange the switching sequence in such a way that the transition from one state to the next is performed by switching only one inverter leg. This can be achieved with following sequence

$$\overline{v}_0 \rightarrow \overline{v}_I \rightarrow \overline{v}_{II} \rightarrow \overline{v}_7 \rightarrow \overline{v}_7 \rightarrow \overline{v}_{II} \rightarrow \overline{v}_I \rightarrow \overline{v}_0$$

A switching pattern in that order keeps the switching losses low, because in one period each switch is just once in an on-state and off-state. Figure G.5 exemplifies the switching sequence for the reference vector in the first sextant as seen in figure G.3.

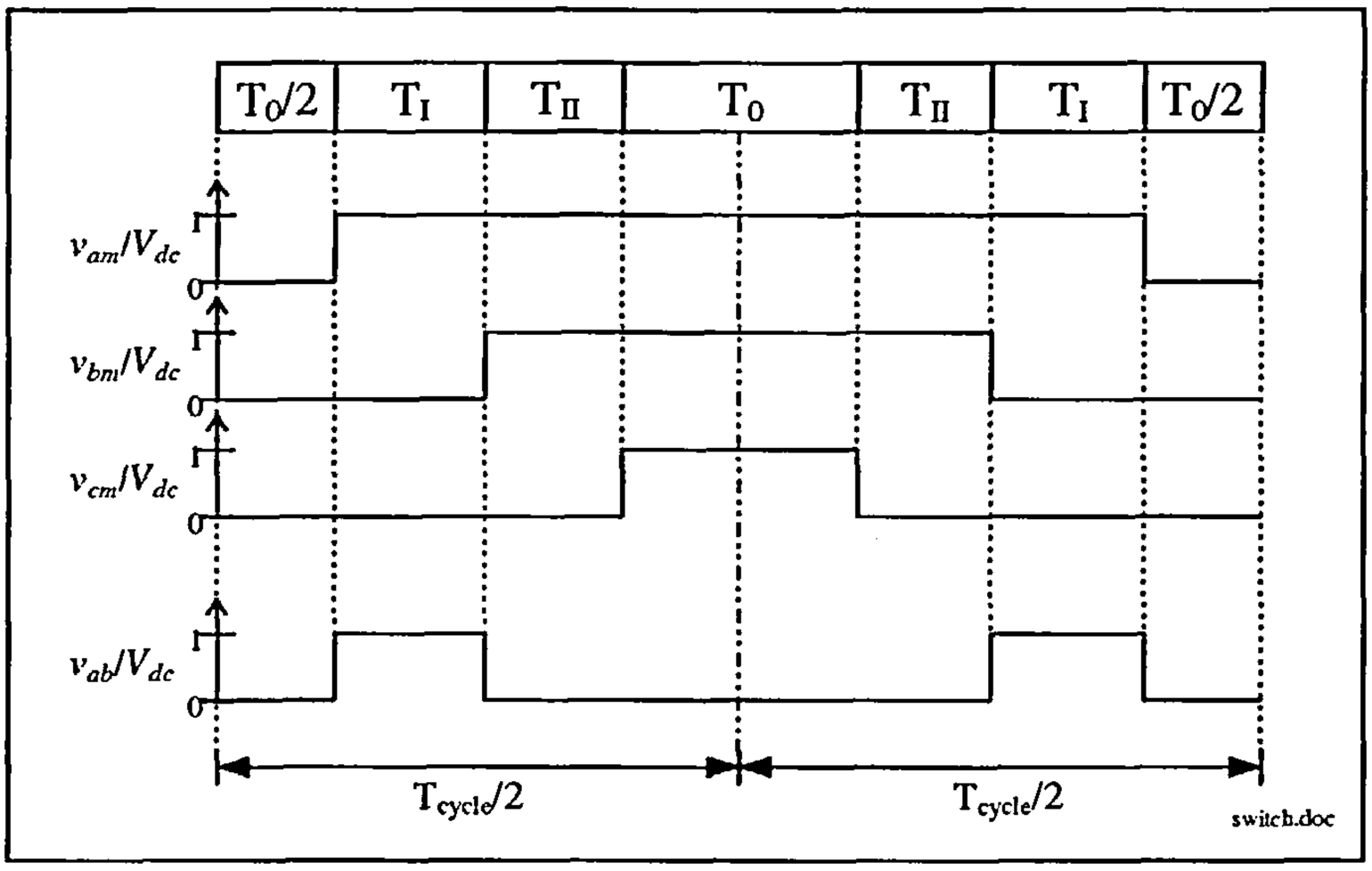

Figure G.5: Pulse pattern for SVPWM

Simulated switching waveforms are shown in figure G.6. There, the modulated fundamental frequency is underlaid and has a frequency of 50 Hz. The modulation index is *0.8*, the switching frequency is *2.5 kHz* and the sample frequency is *50kS/s*. Depending on the switching instance the voltage values as listed in table G.1 are resulting.

SVPWM allows to produce a larger fundamental output voltage than sinusoidal PWM at the maximum linear modulation index. The maximum linear modulation index $m_i=1$ is reached, when the reference voltage vector reaches the circle as shown in figure G.3. At that linear boundary, the zero switching times become zero and only active switching times remain. At that point, the maximum fundamental rms line-line voltage at the inverter terminals takes the value

$$V_{llrmsload} = \frac{1}{\sqrt{2}} V_{dc} = 0.707\, V_{dc} \qquad \text{(G.7)}$$

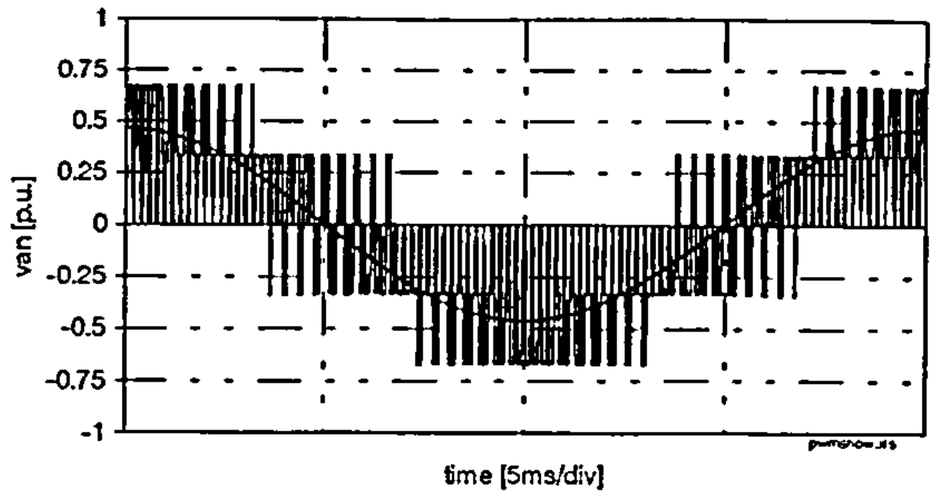

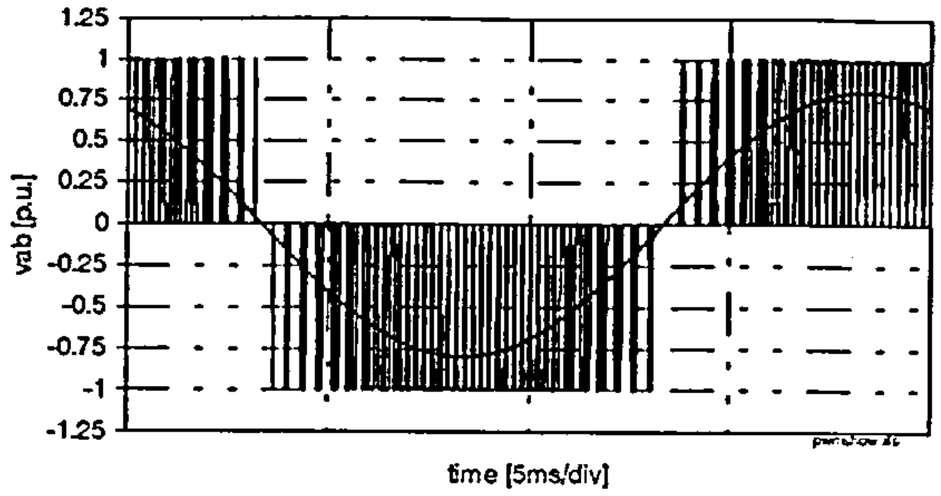

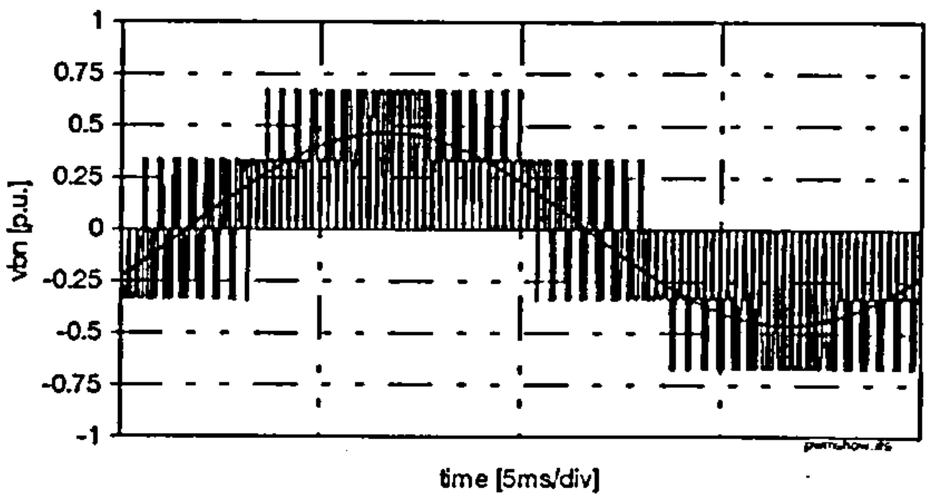

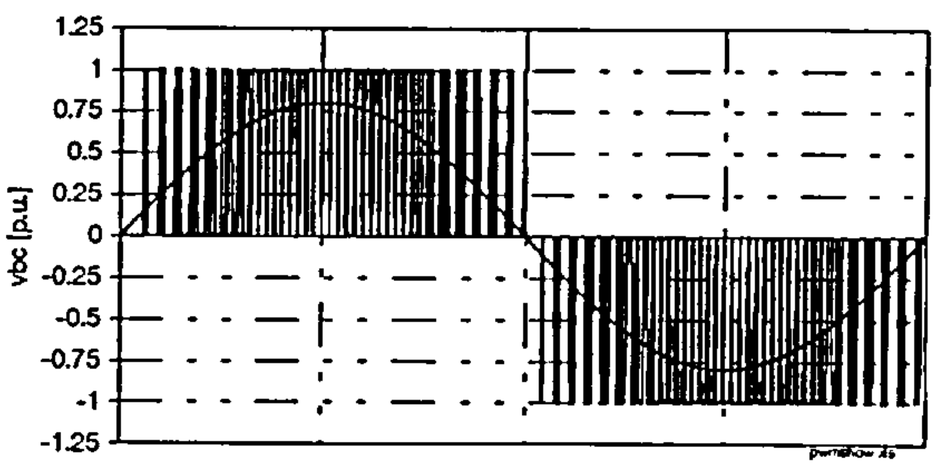

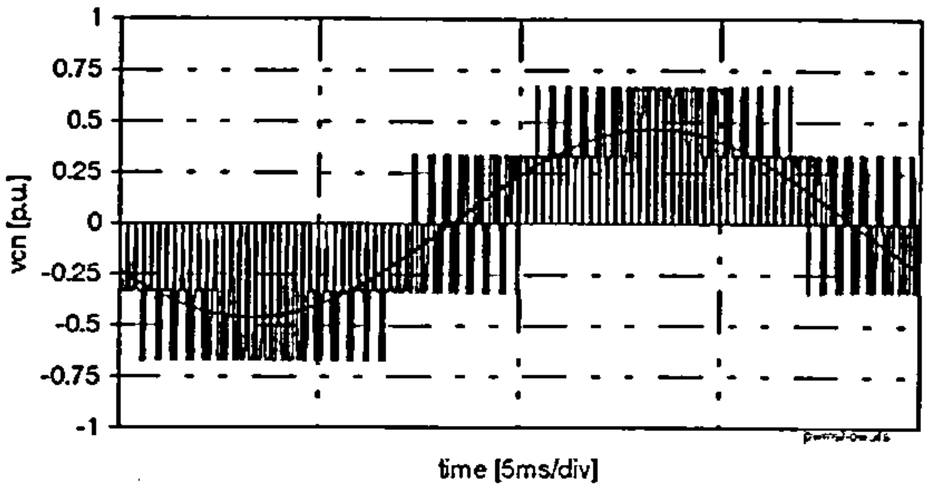

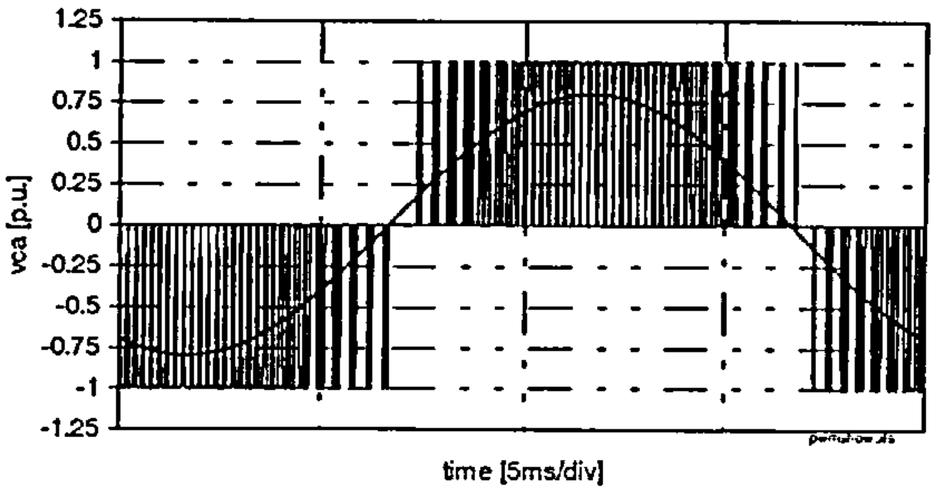

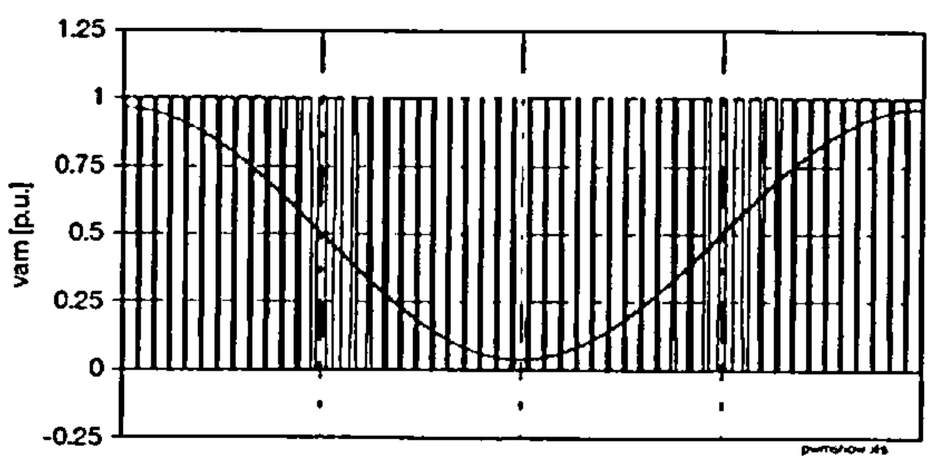

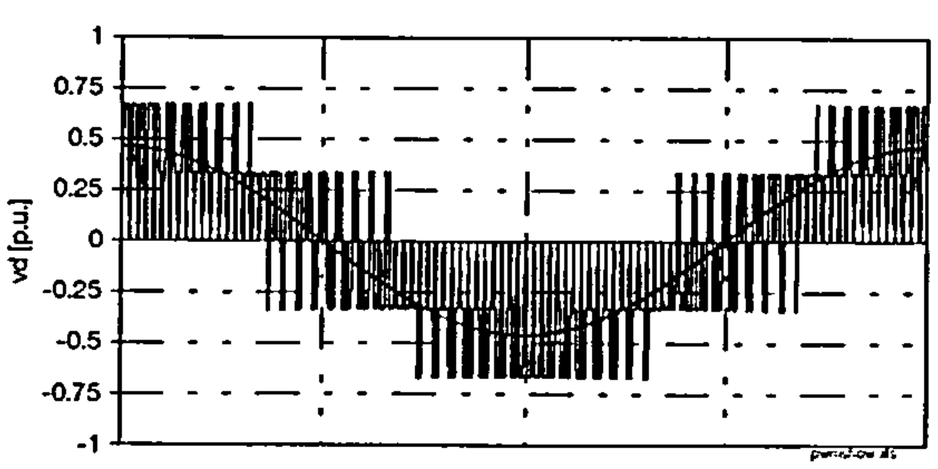

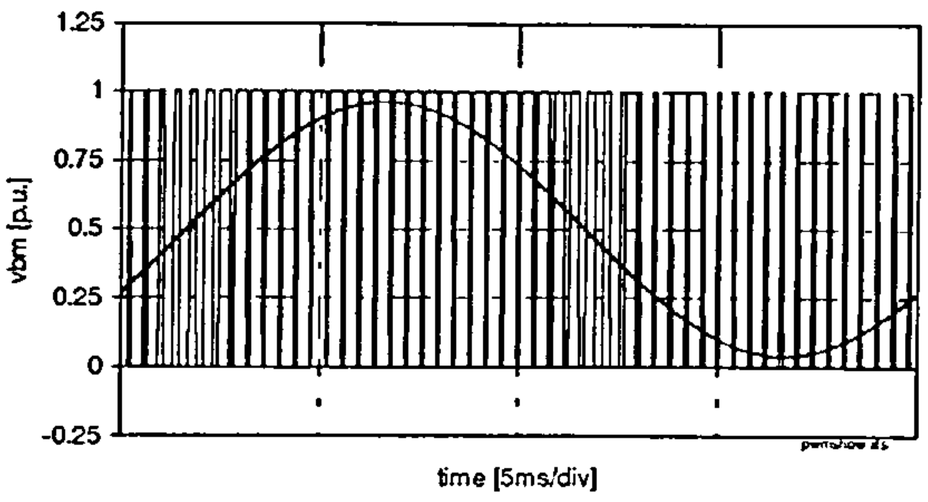

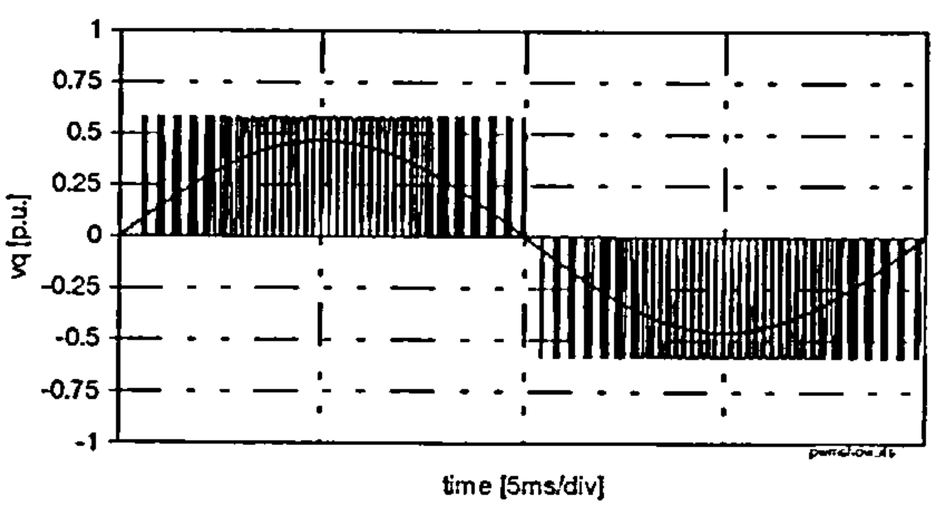

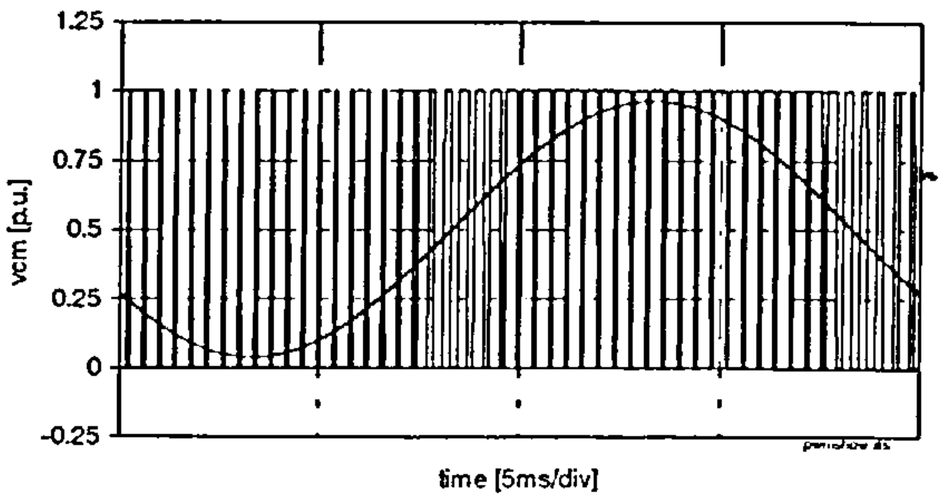

Figure G.6: Simulated switching waveforms for SVPWM

($m_i = 0.8$, $f_1 = 50$ Hz, $f_c = 2.5$ kHz, 50kS/s)

The value reached by equation (G.7) is about 91 % of that produced by square-wave operation.
Overmodulation is reached for further increasing the magnitude of the reference voltage vector and is explained in [f16].

Chapter 7 showed the frequency spectrum of the inverter line-line voltage. There, it can be seen that for low modulation index the harmonic side-band centered around the even multiples of the switching frequency have a larger magnitude than that centered around the odd multiples of the switching frequency. As elaborated in [f17], the placement of the zero voltage vector is responsible for that. In SVPWM the zero vectors are arranged in a way that the resulting line-line voltage of the inverter is switched twice during one switching cycle. Figure G.5 shows the switching pulses for the line-line voltage v_{ab}. For increasing modulation index the line-line voltage pulses take up more and more space within one half of the switching period and that leads to an increase in the odd multiple side-bands. The side-band centered around the even multiples of the switching frequency decrease in magnitude.
To demonstrate the effect of the modulation index upon the inverter line-line voltage harmonics, figure G.7 illustrates four different frequency spectra of simulated SVPWM voltage waveforms.

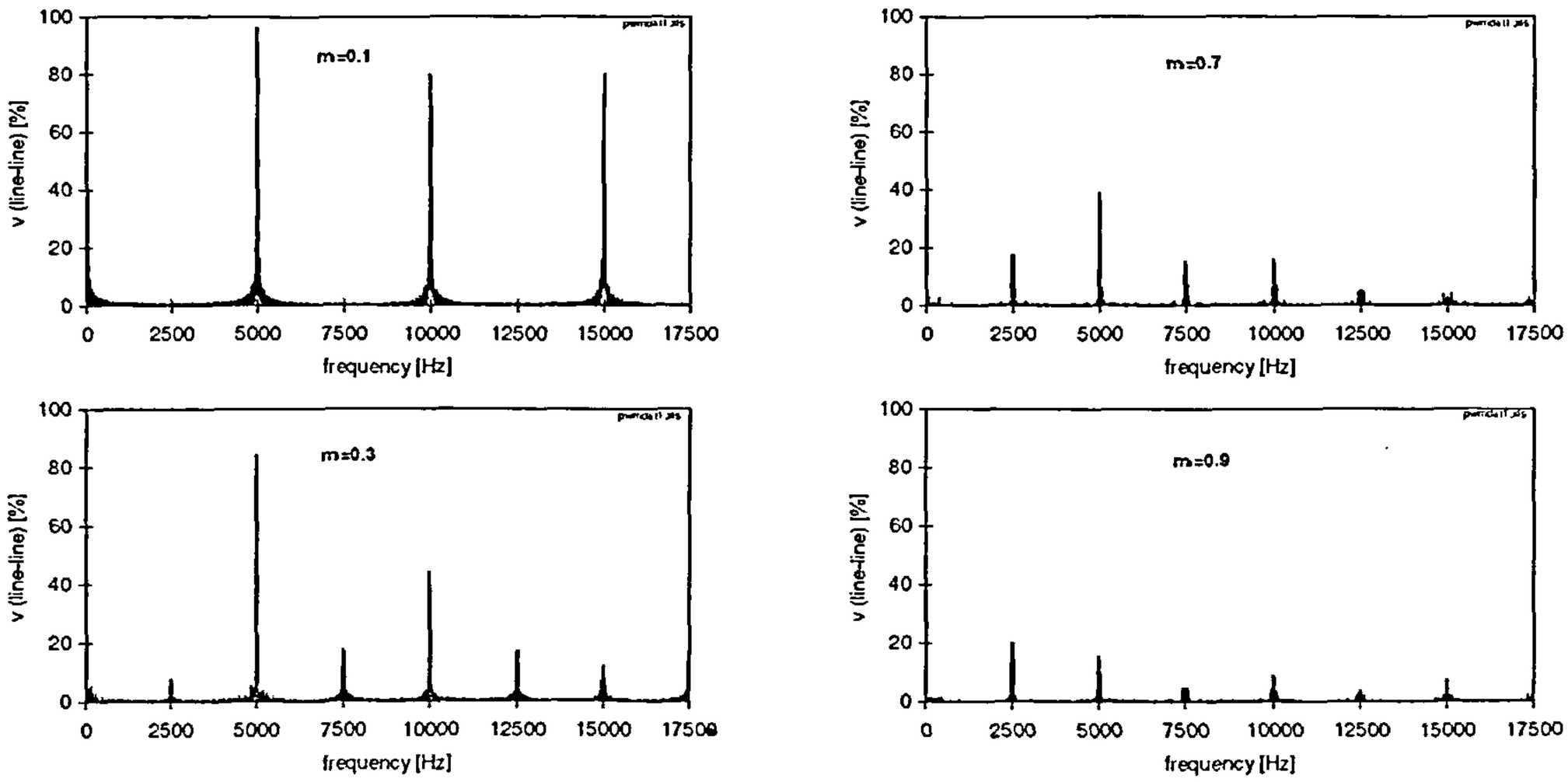

Figure G.7: Frequency spectra of simulated SVPWM inverter line-line voltages for various modulation indices (f_{c_m} = 2.5 kHz , 50 kS/s)

G.1.3 PWM with the Microcontroller 80C167 [f22]

The PWM module of the 80C167 consists of four independent PWM channels and four different operating modes are available. The PWM mode "Symmetrical PWM (center aligned PWM)" was used during laboratory work.

The PWM unit generates three PWM signals. External electronic circuitry creates the remaining three signals by inversion of the generated PWM signal and adds dead-time to produce the six PWM outputs for the inverter.

Similar to sinusoidal PWM, a reference signal is compared to a carrier triangular signal to create a switching signal at the crossing points. Although the applied PWM principle of the 80C167 can be described as symmetrical regular sampling PWM [f16], the digital form of sinusoidal PWM, the resulting pulse pattern is the same as for SVPWM.
The 80C167 PWM principle is explained with the help of figure G.8, where the PWM signal generation for PWM channel 1 is shown.
The switching frequency is determined by the content of the PWM period register PP1. The timer PT1 is counting up until it reaches the value of the PP1 register. Upon the next count pulse the count direction is reversed and the timer starts counting down until it reaches the digital value zero. In that way the triangular carrier signal is created as shown in figure G.8 for 8 steps.

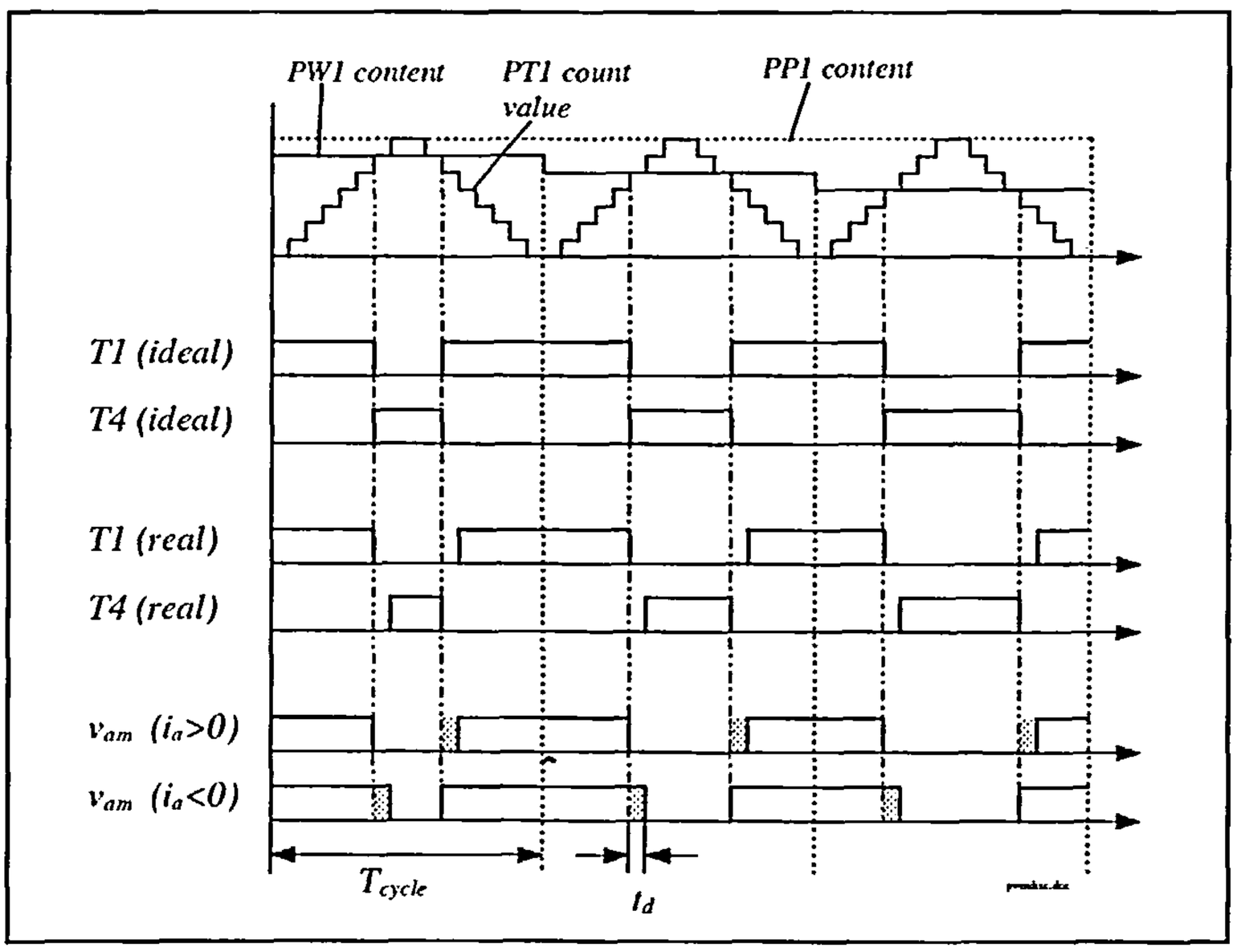

Figure G.8: PWM generation with 80C167

The digital reference value for the PWM channel 1 must be written to the pulse width register PW1. A 2-to-3 transformation of the voltage vector, demanded by the PI-controllers of the current control loop, produces the three PWM reference values.
The channel 1 PWM output signal of the 80C167 (*T4 (ideal)* in figure G.8) is switched to a high level, when the content of PT1 equals the content of PW1. The signal is switched back to a low level when the time of PT1 counted down to a value below the content of PW1. The complement of *T4 (ideal)* gives *T1 (ideal)*. With added dead-time the signals *T1 (real)* and *T4 (real)* constitute the switching signals for the upper and lower switch of the first inverter leg.
Depending on the current direction of phase *a*, the voltage v_{am} (see figure G.2 for nomenclature) is resulting as indicated in figure G.8.

The left picture of figure G.9 shows experimental pulse patterns of the terminal voltages v_{am}, v_{bm} and v_{cm} for 4 kHz switching frequency. It clearly demonstrates the centering of the pulses relative to each other as exemplified in figure G.5 for SVPWM.
The right picture of figure G.9 gives the voltage v_{am}, the respective phase current of i_2 and the line-line inverter voltage v_{ab} for a switching frequency of 2.5 kHz. As already indicated in figure G.5, the line-line voltage has an effective pulse frequency of double the switching frequency. This is also reflected in the phase current, where a ripple of double the switching frequency is clearly visible.

The complete inverter current and voltage waveforms are shown in figure G.10. The current has a sinusoidal waveform with the superimposed ripples as analysed in chapter 7. The line-line and phase voltage take a waveform as simulated in the previous section.

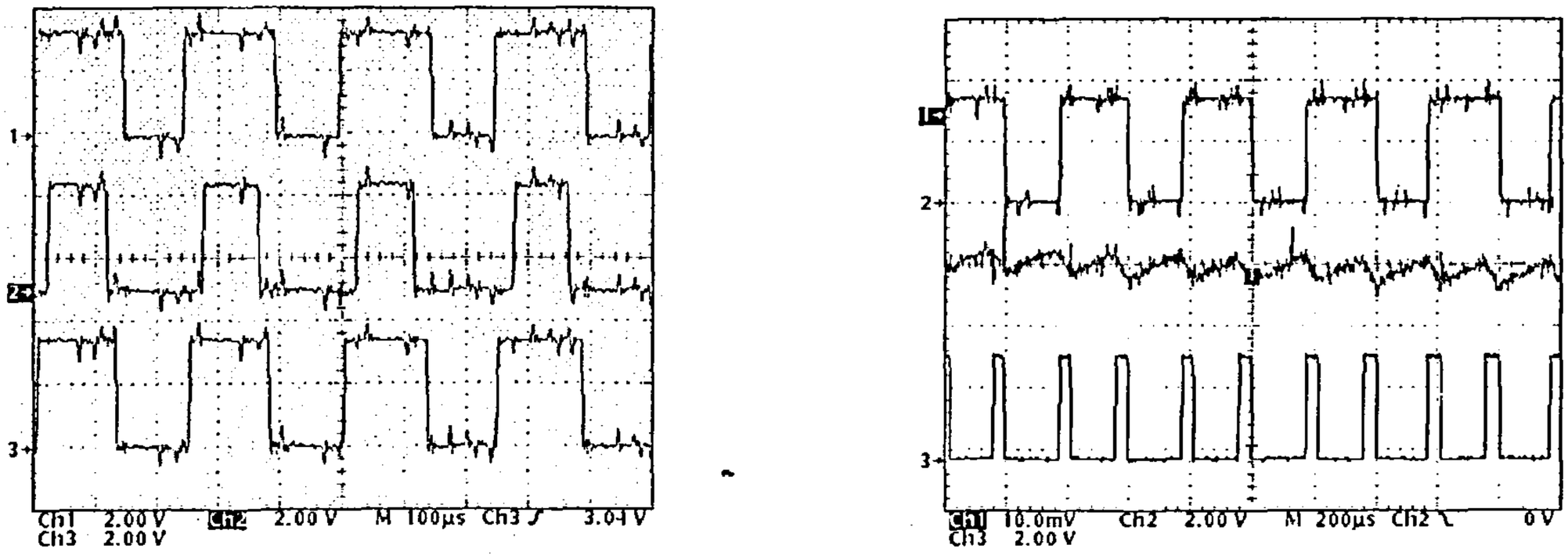

Figure G.9: PWM waveforms v_{am}, v_{bm}, v_{cm} and v_{am}, i_a, v_{ab}

(left: v_{am}, v_{bm}, v_{cm} [400V/div] right: v_{am} [400V/div], i_a [1A/div], v_{ab} [400V/div] all at 500kS/s)

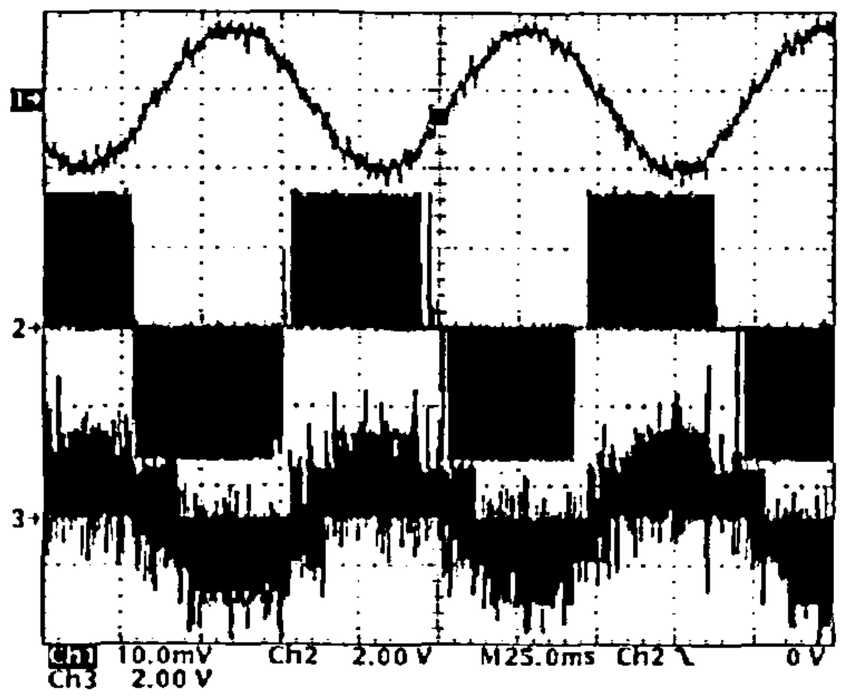

Figure G.10: Machine-side inverter waveforms i_2, v_2 *(line-line) and* v_2 *(phase)*
(from top: i_2 [5A/div] *v2 (line-line)* [400V/div] *v2 (phase)* [400V/div] all at 10kS/s)

G.2 Waveforms

Chapter 7 dealt with the frequency analysis of various waveforms. In this section some of the investigated waveform quantities are displayed.
Starting with the supply line-line and phase voltage in figure G.11. Figure G.12 gives the machine current of the SDFM system and figure G.13 displays current waveforms of the CDFM system. Finally, in figure G.14 the current waveform of the line-side inverter and the voltage across the inductor of the line-side inverter are illustrated.

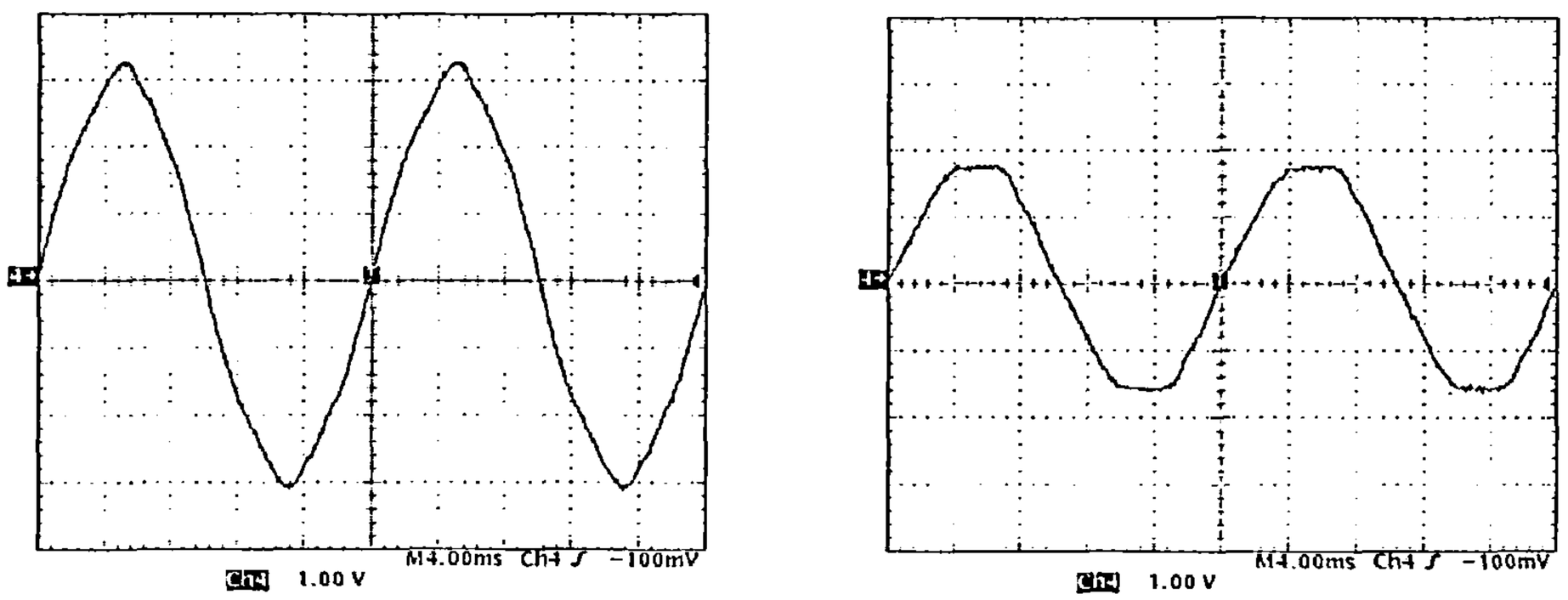

Figure G.11: Supply voltage waveforms v_1 *(line-line) and* v_1 *(phase)*
(left: *v1* (line-line) [200V/div] right: *v1* (phase) [200V/div] both at 25kS/s)

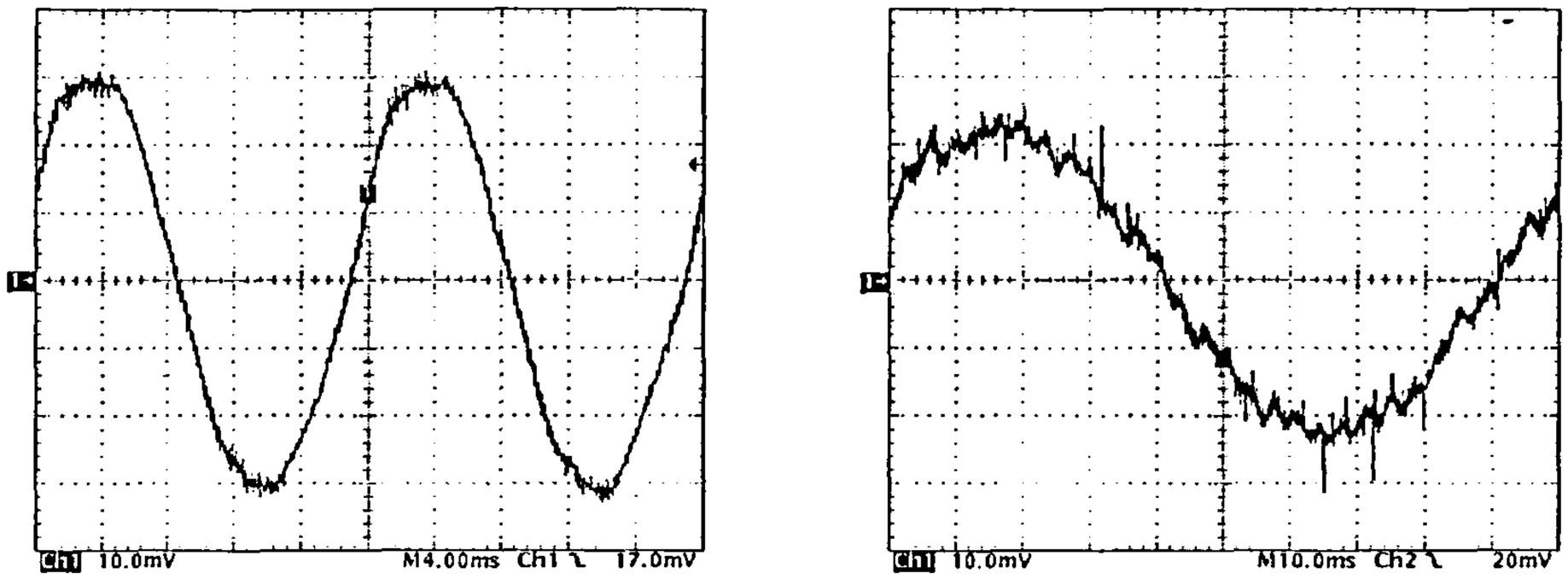

Figure G.12: SDFM current waveforms i_1 and i_2

(left: i_1 [1A/div] right: i_2 [2A/div] both at 25 kS/s)

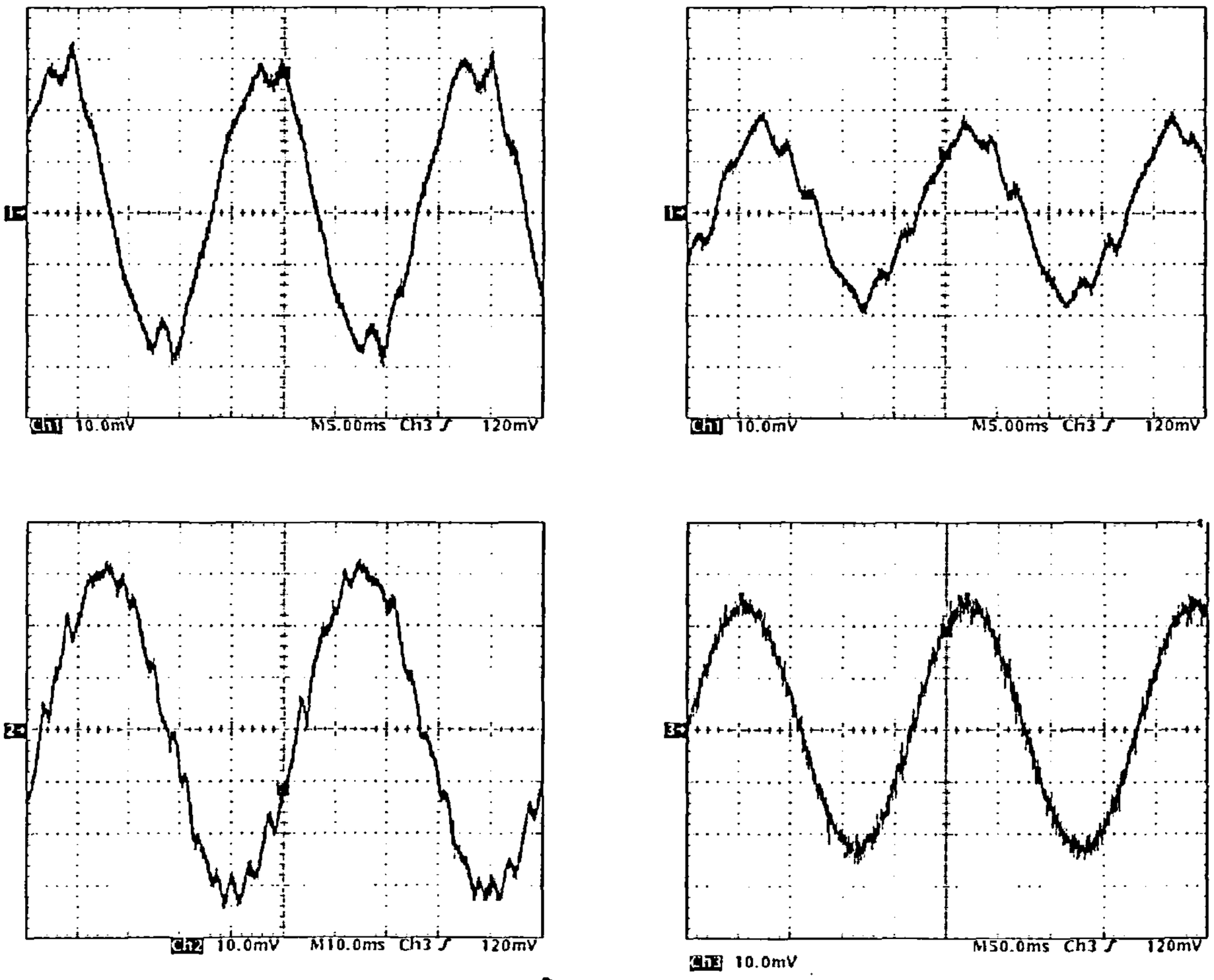

Figure G.13: CDFM current waveforms i_1, i_{x1}, i_2 and i_4

(top: left: i_1 [2A/div] right: i_{x1} [1A/div] both at 100kS/s

bottom: left: i_2 [1A/div] at 50kS/s right: i_4 [2A/div] at 10kS/s)

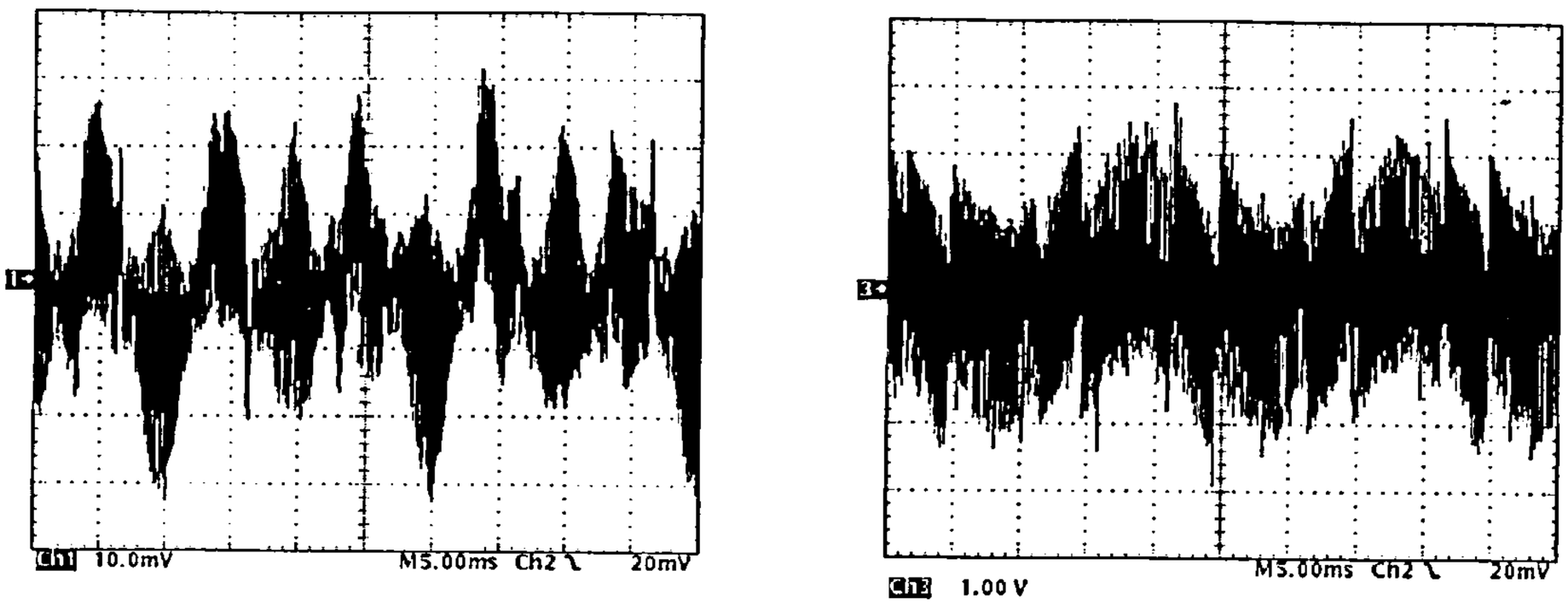

Figure G.14: Line-side inverter waveforms i_y and *voltage across inductor*

(left: i_y [1A/div] right: voltage across inductor [200V/div] both at 500kS/s)

References and Publications

The reference list is devided into six groups depending on the subject they refer to.

a - SDFM

[a1] Riaz, M.: **"Energy conversion properties of induction machines in variable-speed constant-frequency generating systems"**, AIEE Trans. on Applications and Industry, p.II, v.78, pp.25-30, 1959

[a2] Leonhard, W.: **"Field oriented control of a variable speed alternator connected to the constant frequency line"**, IEEE Conf. on Control of Power Systems, pp.149-153, 1979

[a3] Vicatos, M.S. / Tegopoulos, J.A.: **"Steady state analysis of a doubly-fed induction generator under sunchronous operation"**, IEEE-EC Trans., v.4, n.3, pp.495-501, 1989

[a4] Yamamoto, M. / Motoyoshi, O.: **"Active and reactive power control for doubly-fed wound rotor induction generator"**, IEEE-PE Trans., v.6, n.4, pp.624-629, 1991

[a5] Rifai, M.B. / Ortmeyer, T.H.: **"Dynamic analysis of a doubly-fed generator in power system applications"**, Electric Machines and Power Systems, v.21, pp.141-150, 1993

[a6] Arsudis, D.: **"Doppeltgespeister Drehstromgenerator mit Spannungs-zwischenkreis-Umrichter im Rotorkreis für Windkraftanlagen"**, Dissertation, Fakultät für Maschinenbau und Elektrotechnik, Techn. Universität Braunschweig, 1989

[a7] Arsudis, D. / Vollstedt, W.: **"Sensorlose Regelung einer doppeltgespeisten Asynchronmaschine mit geringen Netzrückwirkungen"**, Archiv für Elektrotechnik, v.74, pp.89-97, 1990

[a8] Bogalecka, E.: **"Power control of a double fed induction generator without speed or position sensor"**, EPE'93 Proc., pp.224-228, 1993

[a9] Xu, L. / Cheng, W.: **"Torque and reactive power control of a doubly-fed induction machine by position sensorless scheme"**, IEEE-IA Trans., v.31, n.3, pp.636-642, 1995

[a10] Refoufi, L. / Pillay, P.: **"Harmonic analysis of slip power recovery induction motor drives"**, IEEE-EC Trans., v.9, n.4, pp.665-672, 1994

[a11] Hombu, M. / Futami, M. / Miyazaki, S. / Kubota, Y. / Bando, A. / Azusawa, N.: **"Harmonics analysis on a slip-power recovery system fed by a d.c.-link GTO converter"**, EPE'95 Proc., pp.3.239-3.244, 1995

[a12] Tang, Y. / Xu, L.: **"A flexible active and reactive power control strategy for a variable speed constant frequency generating system"**, IEEE-PESC Proc., pp.568-573, 1993

[a13] Tang, Y. / Xu, L.: **"Vector control and fuzzy logic control of doubly-fed variable speed drives with DSP implementation"**, IEEE-EC Trans., v.10, n.4, pp.661-668, 1995

[a14] Atkinson, D.J. / Lakin, R.A. / Jones, R.: **"A vector controlled doubly-fed induction generator for a variable-speed wind turbine application"**, Trans. of the Inst. Measurement and Control, v.19, n.1, pp.2-12, 1997

[a15] Pena, R. / Clare, J.C. / Asher, G.M.: **"Doubly-fed induction generator using back-to-back PWM converters and its application to variable-speed wind-energy generation"**, IEE Proc. - Electr. Power Appl.,v.143, n.3, pp.231-241, 1996

[a16] Heller, M. / Schumacher, W.: **"Stability analysis of doubly-fed induction machines in stator flux reference frame"**, EPE'97 Proc., pp.2.707-2.710, 1997

b - CDFM / SF-CDFM

[b1] Smith, B.H.: **"Synchronous bahaviour of doubly-fed twin stator induction machine"**, IEEE-PAS Trans., v.86, n.10, pp.1227-1236, 1967

[b2] Cook, C.D. / Smith, B.H.: **"Stability and stabilisation of doubly-fed single-frame cascade induction machines"**, IEE Proc., v.126, n.11, pp.1168-1174, 1979

[b3] Cook, C.D. / Smith, B.H.: **"Effects of machine parameter values on dynamic response and stability regions of doubly-fed cascade induction machines"**, IEE-B Proc., v.130, n.2, pp.137-142, 1983

[b4] Nonaka, S. / Oguchi, K.: **"Brushless wound-rotor induction motor driven by self-controlled reversible frequency converter"**, Electrical Engineering in Japan, v.97, n.2, pp.40-48, 1977

[b5] Ortmeyer, T.H. / Borger, W.U.: **"Brushless generation with cascaded doubly fed machines"**, IEEE 1983 National Aerospace and Electronics Conference, Dayton, Ohio, pp.1420-1425, 1983

[b6] Weimer, J.A. / Ortmeyer, T.H.: **"Experimental cascaded doubly fed variable speed constant frequency generator system"**, IEEE 1984 National Aerospace and Electronics Conference, Dayton, Ohio, pp.444-451, 1984

[b7] Ortmeyer, T.H. / Borger, W.U.: **"Control of cascaded doubly fed machines for generator applications"**, IEEE-PAS Trans., v.103, n.9, pp.2564-2571, 1984

[b8] Ortmeyer, T.H. / Weimer, J.A.: **"Implementation of CDFM generator control"**, IEEE-AES Trans., v.22, n.4, pp.349-355, 1986

[b9] Ortmeyer, T.H.: **"CDFM generator steady state operating characteristics"**, IEEE

1986 National Aerospace and Electronics Conference, Dayton, Ohio, pp.312-319, 1986

[b10] Ortmeyer, T.H.: **"Negative frequency aspects of doubly-fed machine analysis"**, Proc. of the IEEE, v.71, n.8, p.1017, 1983

[b11] Koczara, W. / Haydock, L. / Holmes, P.G. / Patterson, E.B. / Morly, D.: **"A cycloconverter brushless cascaded induction motor"**, IEE Conf., n.341, pp.208-212, 1991

[b12] Sathiakumar, S. / Koczara, W.: **"Modified asynchronous cascade machine system"**, Electric Machines and Power Systems, v.25, pp.485-496, 1997

[b13] Sathiakumar, S. / Koczara, W.: **"Performance study of the modified asynchronous cascade machine system"**, Electric Machines and Power Systems, v.25, pp.497-508, 1997

[b14] Bauer, F.: **"Neues Steuerverfahren für die doppeltgespeiste Maschinenkaskade"**, etzArchiv, v.7, n.8 , pp.275-278, 1985

[b15] Bauer, F.: **"Die doppeltgespeiste Maschinenkaskade als feldorientierter Antrieb"**, Dissertation, Fakultät für Elektrotechnik, Universität Karlsruhe, 1986

[b16] Krebs, S.: **"New method to control cascaded doubly-fed machines in the state space"**, ETEP, v.5, n.1 , pp.55-61, 1995

[b17] Krebs, S.: **"Doppeltgespeiste Maschinenkaskade als feldorientierter Antrieb"**, Dissertation, Fakultät für Elektrotechnik, Universität Karlsruhe, 1994

[b18] Antriebstechnik GmbH FAURNDAU: **"Informations on SD-drives"**, Göppingen

c - BDFM

[c1] Hunt, L.J.: **"A new type of induction motor"**, IEE, v.39, pp.648-667, 1907

[c2] Hunt, L.J.: **"The cascade induction motor"**, IEE, v.52, pp.406-434, 1924

[c3] Creedy, F.: **"Some developments in multispeed cascade induction motors"**, IEE, v.59. pp.511-532, 1921

[c4] Broadway, A.R.W. / Burbridge, L.: **"Self-cascaded machine: a low-speed motor or high-frequency brushless alternator"**, IEE Proc., v.117, n.7, pp.1277-1290, 1970

[c5] Broadway, A.R.W / Cook, B.J. / Neal, P.W.: **"Brushless cascade alternator"**, IEE Proc., v.121, n.12, pp.1529-1535, 1974

[c6] Kusko, A. / Somuah, C.B.: **"Speed control of a single frame cascade induction motor with slip power pump back"**, IEEE-IA Trans., v.14, n.2, pp.97-105, 1978

[c7] Oguchi, K. / Suzuki, H.: **"Speed control of a brushless Static Kramer Drive"**, IEEE-IA Trans., v.17, n.1, pp.22-27, 1981

[c8] Shibata, F. / Taka, K.: **"A self cascaded induction generator combined with a separately controlled inverter and a synchronous condenser"**, IEEE-IA Trans., v.28, n.4, pp.797-807, 1992

[c9] Perera, B.S.P. / Smith, B.H.: **"Brushless constant frequency generation using single frame cascade induction machines"**, Electric Machines and Power Systems, v.19, pp.399-413, 1991

[c10] Perera, B.S.P. / Smith, B.H.: **"A novel model for single frame cascade induction machine having a multicircuit rotor winding"**, Electric Machines and Power Systems, v.21, pp.783-802, 1993

[c11] Wallace, A.K. / Spee, R. / Lauw, H.K.: **"Dynamic modelling of brushless doubly-fed machines"**, IEEE IAS annual meeting, pp.329-334, 1989

[c12] Li, R. / Wallace, A.K. / Spee, R. / Wang, Y.: **"Two axis model development of cage-rotor brushless doubly-fed machines"**, IEEE-EC Trans., v.63, n.3, pp.453-460, 1991

[c13] Li, R. / Wallace, A.K. / Spee, R.: **"Dynamic simulation of brushless doubly-fed machines"**, IEEE-EC Trans., v.63, n.3, pp.445-452, 1991

[c14] Brassfield, W. / Spee, R.: **"Direct torque control for brushless doubly-fed machines"**, IEEE-IAS annual meeting, pp.615-622, 1992

[c15] Wallace, A.K. / Spee, R. / Alexander, G.C.: **"The brushless doubly-fed machine: Its advantages, applications and design methods"**, IEE 6th International Conference on Electrical Machines and Drives, Conference Publication 376, pp.511-517, 1993

[c16] Zhou, D. / Spee, R. / Wallace, A.K.: **"Model reference adaptive speed control for doubly-fed machines"**, IEEE-IECON Proc., v.2, pp.1175-1180, 1993

[c17] Li, R. / Spee, R. / Wallace, A.K. / Alexander, G.C.: **"Synchronous drive performance of brushless doubly-fed motors"**, IEEE-IA Trans., v.30, n.4, pp.963-970, 1994

[c18] Brune, C.S. / Spee, R. / Wallace, A.K.: **"Experimental evaluation of a variable-speed doubly-fed wind power generation system"**, IEEE-IA Trans., v.30, n.3, pp.648-655, 1994

[c19] Gorti, B.V. / Zhou, D. / Spee, R. / Wallace, A.K. / Alexander, G.C.: **"Development of a brushless doubly-fed machine for limited pump drive in a waste-water treatment plant"**, IEEE-IA annual meeting, pp.523-529, 1994

[c20] Li, R. / Wallace, A.: **"Determination of converter control algorithms for brushless doubly-fed induction motor drives using Floquet and Lyapunov techniques"**, IEEE-PE Trans., v.10, n.1, pp.78-85, 1995

[c21] Ferreira, A.C. / Williamson, S.: **"Iron loss and saturation in brushless doubly-fed**

machines", IEEE-IAS annual meeting, pp.97-103, 1997

[c22] Williamson, S. / Boger, M.S.: **"Impact of inter-bar currents on the performance of the brushless doubly-fed motor"**, IEEE-IAS annual meeting, pp.188-195, 1997

[c23] Williamson, S. / Ferreira, A.C. / Wallace, A.K.: **"Generalised theory of the brushless doubly-fed machine. part 1: analysis"**, IEE-B Proc., v.144, n.2, pp.111-122, 1997

[c24] Williamson, S. / Ferreira, A.C.: **"Generalised theory of the brushless doubly-fed machine. part 2: model verification and performance"**, IEE-B Proc., v.144, n.2, pp.123-129, 1997

[c25] Zhou, D. / Spée. R. / Alexander, G.C.: **"Experimental evaluation of a rotor flux oriented control algorithm for brushless doubly-fed machines"**, IEEE-PE Trans., v.12, n.1, pp.72-78, 1997

[c26] Zhou, D. / Spée. R. / Alexander, G.C. / Wallace, A.K.: **"A simplified method for dynamic control of brushless doubly-fed machines"**, IEEE-IECON, v.2, pp.946-951, 1996

[c27] Zhou, D. / Spée. R.: **"Field oriented control development for brushless doubly-fed machines"**, IEEE-IAS annual meeting, pp.304-310, 1997

[c28] Liao, Y.: **"Design of a brushless doubly-fed induction motor for adjustable speed drive applications"**, IEEE-IAS annual meeting, v.2, pp.850-855, 1996

d - DFRM

[d1] Broadway, A.R.W.: **"Cageless induction machine"**, IEE, v.118, n.11, pp. 1593-1600, 1971

[d2] Broadway, A.R.W. / Tan, S.C.F.: **"Brushless stator-controlled synchronous-induction machine"**, IEE, v.120, n.8, pp.860-866, 1973

[d3] Xu, L. / Tang, Y.: **"A novel wind-power generating system using field oriented controlled doubly-excited brushless reluctance machine"**, IEEE-IAS annual meeting, v.1, pp.408-413, 1992

[d4] Xu, L. / Liang, F. / Lipo, T.A.: **"Transient model of a doubly excited reluctance motor"**, IEEE-EC Trans., v.6, n.1, pp.126-133, 1991

[d5] Liang, F. / Xu, L. / Lipo, T.A.: **"d-q analysis of a variable speed doubly ac excited reluctance motor"**, Electric Machines and Power Systems, v.19, n.2, pp.125-138, 1991

[d6] Xu, L. / Tang, Y. / Ye, L.: **"Comparison study of rotor structures of doubly excited brushless reluctance machine by finite element analysis"**, IEEE-EC Trans., v.9, n.1, pp.165-171, 1994

[d7] Xu, L. / Zhen, L. / Kim, E.H.: **"Field orientation control of a doubly excited brushless reluctance machine"**, IEEE-IAS annual meeting, pp.319-325, 1996

[d8] Liao, Y. / Sun, C.: **"A novel position sensorless control scheme for doubly-fed reluctance motor drives"**, IEEE-IA Trans., v.30, n.5, pp.1210-1218, 1994

[d9] Tang, Y. / Xu, L.: **"Adaptive fuzzy control of a variable speed power generating system with doubly excited reluctance machine"**, IEEE-PESC Proc., pp.377-384, 1994

[d10] Xu, L. / Wang, F.: **"Comparative study of magnetic coupling of a doubly-fed brushless machine with reluctance and cage rotors"**, IEEE-IAS annual meeting, pp.326-332, 1997

e - Tandem

[e1] Smith, B.H.: **"Theory and performance of a twin stator induction machine"**, IEEE-PAS Trans., v.85, n.2, pp.123-131, 1966

[e2] Levy, D.: **"Analysis of a double-stator induction machine used for a variable-speed constant-frequency small-scale hydro/wind electric power generator"**, Electric Power Systems Research, v.11, pp.205-223, 1986

[e3] Perahia, J. / Nayar, C.V.: **"Power controller for a wind turbine driven tandem induction generator"**, Electric Machines and Power Systems, v.19, pp.599-624, 1991

[e4] Perahia, J. / Nayar, C.V.: **"Analysis of a series-delta connected tandem induction motor"**, Electric Machines and Power Systems, v.23, pp.221-231, 1995

f - other

[f1] Say, M.G.: **"Alternating current machines"**, 5th ed., Longman Scientific & Technical, 1983

[f2] Leonhard, W.: **"Control of electric drives"**, 2nd edition, Springer-Verlag, Berlin, 1996

[f3] Vas, P.: **"Vector control of a.c. machines"**, Oxford University Press, Oxford, 1990

[f4] Hindmarsh, J.: **"Electrical machines and their applications"**, 4th edition, Butterworth-Heinemann Ltd, Oxford, 1984

[f5] Murphy, J.M.D.: **"Thyristor control of a.c. motors"**, Pergamon Press, Oxford, 1973

[f6] Finney, D.: **"Variable frequency a.c. motor drive systems"**, ISBN 0 86341 114 2, 1988

[f7] Fitzgerald, A.E. / Kingsley, C. / Umans, S.D.: **"Electric machinery"**, 5th edition, McGraw-Hill, London, 1992

[f8] Fischer, R.: **"Elektrische Maschinen"**, 7. Auflage, Hanser, München, 1989

[f9] Stanley, W.D.: **"Digital signal processing"**, 2nd edition, Reston Publishing Company Inc., Reston, 1984

[f10] McGeorge, H.D.: **"Marine electrical equipment and practice"**, 2nd ed., BH Newness

[f11] Hultgren, K.J.: **"VSCF cycloconverter ships service power equipment"**, Naval Engineers Journal, pp.46-62, 1992

[f12] Elbuluk, M.E. / Kankam, M.D.: **"Potential starter/generator technologies for future aerospace applications"**, IEEE-AES Systems Magazine, pp.24-31, 1997

[f13] Eggert, B.: **"1.5 MW wind power station with low a.c.-line distortion using a standard doubly-fed generator system with field orientation control"**, EPE'97 Proc., pp.2.739-2.742, 1997

[f14] Edvardsen, P.A. / Nestli,, T.F. / Kolstad, H.: **"Steady state power flow and efficiency optimising analysis of a variable speed constant frequency generating system"**, EPE'97 Proc., pp.2.691-2.694, 1997

[f15] Holtz, J.: **"State of the art of controlled a.c. drives without speed sensors"**, Int. Journal of Electronics, v.80, n.2, pp.249-263, 1996

[f16] Holtz, J.: **"Pulsewidth modulation for electronic power conversion"**, Proc. of the IEEE, v.82, n.8, pp.1194-1214, 1994

[f17] Holmes, D.G.: **"The significance of zero space vector placement for carrier based PWM schemes"**, IEEE-IA Trans., v.32, n.5, pp.1122-1129, 1996

[f18] van der Broek, H.W./ Skudelny, H.C. / Stanke, G.V.: **"Analysis and realisation of a pulsewidth modulator based on voltage space vectors"**, IEEE-IA Trans., v.24, n.1, pp.142-150, 1988

[f19] Kleinkauf, W. / Leonhard, W. / et al: **"Betriebsverhalten von Windenergie-anlagen"**, Band 1, BMFT Forschungsbericht T 84-154(1), 1984

[f20] Williamson, S.: **"The induction motor - a state-of-the-ark technology?"**, IEE - Power Engineering Journal, v.10, n.6, pp.247-254, 1996

[f21] Levi, E.: **"Rotor flux oriented control of induction machines considering the core loss"**, Electric Machines and Power Systems, v.24, pp.37-50, 1994

[f22] 16-Bit Microcontrollers, C167, User's Manual 02.96, Version 2.0, SIEMENS AG, Munich, 1996

[f23] Errata Sheet C167-LM, AD, Release 1.0, Siemens AG, 1994

[f24] Robert BOSCH GmbH: **"Technical Infromations on Servodyn-D Power Converter"**, 1995

[f25] Borland International Inc.: **"Borland C++ for Windows, Version 3.1"**

[f26] The MathWorks Inc.: **"MATLAB for Windows, Version 4.2c.1"**

[f27] Lander, C.W.: **"Power electronics"**, 3rd ed., McGraw-Hill, London, 1993

Publications resulting from this work

Nicholson, G. / Atkinson, D.J. / Hopfensperger, B. / Lakin, R.A.: **"Variable speed cascade induction generator system for wind turbines"**, ETSU report for the DTI, ETSU W/33/00450/REP, 1996

Hopfensperger, B. / Atkinson, D.J. / Lakin, R.A.: **"Kaskadierte doppeltgespeiste Maschinen als drehzahlvariable Generatorsysteme: Ein Überblick"**, German Wind Energy Conf. DEWEK'96, pp.129-132, 1996

Hopfensperger, B. / Atkinson, D.J. / Lakin, R.A.: **"Application of vector control to the cascaded induction machine for wind power generation schemes"**, EPE'97 Proc., pp.2.701-2.706, 1997

Hopfensperger, B. / Atkinson, D.J. / Lakin, R.A.: **"Stator flux oriented control of a cascaded doubly-fed induction machine"**, Paper submitted to the IEE, 1998